Compatibilisation of 1D/2D graphitic nanomaterials and poly(propylene) via non-covalent functionalisation with poly(acrylate)s

by

Jaipal Ajay Gupta

A thesis submitted in partial fulfilment of the requirements for the degree of Doctor of Philosophy in Engineering

University of Warwick

Warwick Manufacturing Group

International Institute for Nanocomposites Manufacturing

June 2018

Table of Contents

Table of contents ii

List of figures and schemes x

List of tables xxiv

List of equations xxvii

Acknowledgements xxviii

Declaration of authorship xxix

Summary xxx

Abbreviations and terminology xxxii

Chapter 1 Introduction

1.1 Background 1

1.2 Applications of nanostructured filled polymer composite materials 1

1.3 The research problem 1

1.4 The research strategy 4

1.5 Structure of thesis 5

1.6 Contribution to knowledge 7

1.7 Aims and objectives 8

1.8 References 9

Chapter 2 Literature Review

2.1 Introduction 11

2.2 Carbon based fillers 11

2.2.1 Carbon nanotubes (CNTs) 12

2.2.2 Graphene 18
2.3 Composites of Polymers and nanostructured fillers (Nanocomposites) 23
2.4 Processing and Functionalisation 30
2.4.1 Processing 30
2.4.2 Covalent functionalisation 32
2.4.3 Non-covalent functionalisation 34
2.5 Poly(propylene) PP 43
2.6 Synthesis of polymer compatibiliser for non-covalent functionalisation 46
2.6.1 Controlled living radical polymerisation 47
2.6.2 Reversible addition fragmentation chain-transfer polymerisation 48
2.6.3 Cu(0)-mediated living radical polymerisation 50
2.7 Concluding remarks 53
2.8 References 54

Chapter 3 Materials and Methods

3.1 Materials 60
3.1.1 Poly(propylene) (PP) 60
3.1.2 Multi-Walled Carbon Nanotubes (MWCNTs) 60
3.1.3 Graphene Nanoplatelets (GNPs) 60
3.1.4 Lauryl Acrylate (LA) 60
3.1.5 2-Phenyl ethyl Acrylate (2PEA) 60
3.1.6 Copper (0) Wire 61
3.1.7 *Tris*-(2-(dimethylamino)ethyl)amine (Me_6TREN) 61
3.1.8 Hostasol-ATRP initiator 61
3.1.9 Pyrene-ATRP initiator 61
3.1.10 General reagent and solvents 61
3.2 Sample Preparation 62

3.2.1 Synthesis of *Tris*-(2-(dimethylamino)ethyl)amine (Me_6TREN) 62
3.2.2 Cyanomethyl dodecyltrithiocarbonate 63
3.2.3 Typical RAFT polymerisation procedure 63
3.2.4 Typical Cu(0)-mediated polymerisation procedure 64
3.2.5 Typical protocol for solution mixing of MWCNTs/GNPs with poly(acrylate)s 65
3.2.6 Typical (nano)composite preparation procedure 65
3.2.7 Composite compositions 67
3.3 Characterisation and Processing Methods 70
3.3.1 X-Ray Photo-Electron Spectroscopy (XPS) 70
3.3.2 Twin-Screw Extrusion (Melt/Compounding) and Injection Moulding 70
3.3.3 Nuclear Magnetic Resonance Spectroscopy (NMR) 70
3.3.4 Differential Scanning Calorimetry (DSC) 70
3.3.5 Thermo-gravimetric Analysis (TGA) 71
3.3.6 Fourier Transform Infra-Red Spectroscopy (FTIR) 71
3.3.7 Static Mechanical Tensile Testing 71
3.3.8 Dynamic Mechanical Thermal Analysis (DMTA) 71
3.3.9 Parallel Plate Oscillatory Rheometry 72
3.3.10 Scanning Electron Microscopy (SEM) 72
3.3.11 Transmission Electron Microscopy (TEM) 73
3.3.12 Wide Angle X-Ray Scattering (WAXD) / Small Angle X-Ray Scattering (SAXS) 73
3.3.13 Raman Spectroscopy 74
3.3.14 Volume Resistivity 74
3.3.15 Size-Exclusion Chromatography (SEC) 75
3.3.16 Matrix-Assisted-Laser-Desorption-Ionisation Time-of-Flight Mass Spectrometry (MALDI-TOF-MS) 75
3.3.17 Droplet Shape Analysis (DSA) (Contact angle) 76

3.3.18 High resolution Mass spectrometry – Electrospray ionisation – Time of flight (HRMS – ESI – TOF) 76
3.3.19 UV-Vis spectroscopy 76
3.3.20 Fluorescence spectroscopy 76
3.3.21 Density measurements 76
3.4 References 77

Chapter 4 Results and Discussion I

Non-covalent functionalisation of MWCNTs with poly(lauryl acrylate) polymerised by Cu(0)-mediated and RAFT methods

4.1 Introduction 79
4.2 Synthesis and characterisation of poly(lauryl acrylate) P[LA] via RAFT 82
4.2.1 Synthesis and characterisation of cyanomethyl dodecyltrithiocarbonate 82
4.2.2 Synthesis and characterisation of P[LA] via RAFT 83
4.3 Synthesis and characterisation of poly(lauryl acrylate) P[LA] via Cu(0)-mediated LRP 86
4.3.1 Synthesis and characterisation of Me6TREN ligand 86
4.3.2 Synthesis and characterisation of P[LA] via Cu(0)-mediated LRP 86
4.3.3 Synthesis and characterisation of P[LA] via Cu(0)-mediated LRP using Hostasol-ATRP initiator 90
4.3.4 Synthesis and characterisation of P[LA] via Cu(0)-mediated LRP using Pyrene-ATRP initiator 93
4.4 Thermal stability of poly(acrylates) 96
4.4.1 Thermal stability of P[LA] synthesised using RAFT polymerisation 96
4.4.2 Thermal stability of P[LA] synthesised using Cu(0)-mediated LRP 100
4.4.3 Thermal stability of P[LA] via Cu(0)-mediated LRP using Hostasol-ATRP initiator ... 104
4.4.4 Thermal stability of P[LA] via Cu(0)-mediated LRP using Pyrene-ATRP initiator 108
4.5 Characterisation of the MWCNTs and GNPs used in this study 110

4.5.1 Electron microscopy imaging of the MWCNTs (NC7000) used in this study 110

4.5.2 Raman Spectroscopy of MWCNTs 113

4.5.3 X-ray photo-electron spectroscopy (XPS) of MWCNTs 114

4.6 Composites of MWCNTs and P[LA] 116

4.6.1 Synthesis and characterisation composites of MWCNTs and P[LA] synthesised using RAFT polymerisation 116

4.6.2 Synthesis and characterisation composites of MWCNTs and P[LA] synthesised using Cu(0)-LRP 118

4.7 Characterisation of Poly(propylene) 125

4.8 Conclusions 127

4.9 References 129

Chapter 5 Results and Discussion II

Plasticisation and compatibilisation of poly(propylene) with poly(lauryl acrylate) modified MWCNTs

5.1 Introduction 132

5.1.1 Synthesis and characterisation of P[LA] 133

5.1.2 Twin-screw melt compounded and injection moulding 134

5.1.3 Sample identification and nomenclature 135

5.2 Characterisation of composites of PP, MWCNTs and P[LA] 137

5.3 Conclusions 167

5.4 References 169

Chapter 6 Results and Discussion III

Synthesis and characterisation of composites of PP and PP filled with graphene nano-platelets (GNPs) functionalised by poly(lauryl acrylate) P[LA]

6.1 Introduction 172
6.2 Characterisation of GNPs 174
6.2.1 Electron microscopy of GNPs 175
6.2.2 Raman spectroscopy of GNPs 176
6.2.3 X-ray photoelectron spectroscopy of GNPs 178
6.3 Characterisation of composites of PP, GNPs and poly(lauryl acrylate) P[LA] 180
6.4 Conclusions 199
6.5 References 201

Chapter 7 Results and Discussion IV

Synthesis and characterisation of homopolymers and co-polymers of poly(lauryl acrylate) P[LA] and 2-phenyl ethyl acrylate P[2PEA] and their composites with multi-walled carbon nanotubes (MWCNTs) and graphene nano-platelets (GNPs)

7.1 Introduction 203
7.2 Synthesis of homopolymers and co-polymers of P[LA] and P[2PEA] 205
7.2.1 Synthesis of homopolymers of P[LA] 205
7.2.2 Synthesis of homopolymers of P[2PEA] 207
7.2.3 Synthesis of co-polymers of P[LA] and P[2PEA] 209
7.3 Homopolymers and copolymers of P[LA] and P[2PEA] 213
7.3.1 TGA of homopolymers and co-polymers of P[LA] and P[2PEA] 213
7.3.2 DSC of homopolymers and copolymers of P[LA] and P[2PEA] 214
7.3.3 Oscillatory rheology of homopolymers and copolymers of P[LA] and P[2PEA] 217
7.4 Composites of MWCNTs and GNPs with homopolymers and copolymers of P[LA] and P[2PEA] 219
7.4.1 Composites of MWCNTs with homopolymers and copolymers of P[LA] and P[2PEA] 219

7.4.2 Composites of GNPs with homopolymers and copolymers of P[LA] and P[2PEA].....233

7.5 Conclusions.....240

7.6 References.....241

Chapter 8 Results and Discussion V

Characterisation of composites of PP and PP filled with multi-walled carbon nanotubes (MWCNTs) and graphene nano-platelets (GNPs) functionalised with homo-polymers and co-polymers of poly(lauryl acrylate) P[LA] and 2-phenyl ethyl acrylate P[2PEA]

8.1 Introduction.....243

8.2 Characterisation of composites of PP, MWCNTs or GNPs with poly(acrylate)s.....246

8.3 Conclusion.....273

8.4 References.....276

Chapter 9 Conclusions and Recommendations for Future Work

9.1 Conclusions.....278

9.2 Recommendations for Future Work.....286

Journal Papers and Conference Presentations 288

1 Polymer chemistry paper **2016** 291

2 Polymer paper **2017** 309

6 & 7 EPF & WMG **2015** poster.....325

8 Macro group **2016** poster 326

9 & 10 WMG & Warwick Polymer poster **2016** 327

11 *IX*th ECNP **2016**.....328

13 8th Asia-Europe Symposium **2017**.....330

14 EPF **2017** 331

15 World polymer congress **2018** 332

Appendix 333

List of Figures and Schemes

Figure 2.1 Schematic illustration of the arc-discharge method for the production of CNTs 12

Figure 2.2 Schematic illustration of the laser ablation method for the production of CNTs 13

Figure 2.3 TEM micrograph of a MWCNT 16

Figure 2.4 Diagram showing the different ways a graphene sheet can rolled into a CNT .16

Figure 2.5 AFM micrographs showing 'sword and sheath' fracture of a MWCNT 18

Figure 2.6 A schematic showing the 2D structure of graphene and its ability to be wrapped into 0D fullerenes, 1D CNTs and 3D graphite.....19

Figure 2.7 TEM micrograph of a fractured CNT/PS film.....25

Figure 2.8 Schematic showing morphological states of a) phase separated, b) intercalated and c) exfoliated GNPs 28

Figure 2.9 Surface initiated ATRP grafting of the MWCNT-Br with LA or SA.....34

Figure 2.10 π – π stacking interactions.....36

Figure 2.11 Schematic showing pyrene functionalised polymers for CNT binding.....37

Figure 2.12 Synthesis of poly(methyl methacrylate-co-(1-pyrene) methyl-2-methyl-2-propenoate) copolymer.....37

Figure 2.13 a) Copolymer modification of CNT via a one-pot strategy and b) TEM of functionalised CNT 38

Figure 2.14 C-H – π interaction during polymer/CNT wrapping 39

Figure 2.15 Schematic of the synthesis of a amphiphilic block copolymer.....40

Figure 2.16 Schematic of electrostatic adsorption between a negatively charged MWCNT and positively charged PANI molecule.....42

Figure 2.17 Schematic of a spherulite showing lamella and amorphous regions 44

Figure 2.18 Radial α-spherulites of iPP a) negative (α_{11}) 413 K b) positive (α_1) 393 K 45

Figure 2.19 Schematic representing the non-covalent (π-π) interactions between a polymer compatibiliser, MWCNTs and the lamella of PP 46

Figure 2.20 Schematic showing mechanism for RAFT 48

Figure 2.21 Simplified mechanism of Cu(0)-mediated LRP 52

Figure 3.1 Schematic representation of the typical protocol adopted for preparation of composite materials 65

Scheme 4.1 Schematic representation of P[LA] wrapping around/on a CNT 81

Figure 4.1 ^{1}H NMR spectrum of cyanomethyl dodecyltrithiocarbonate recorded in $CDCl_3$ 82

Scheme 4.2 Synthetic strategy for the polymerisation of LA *via* RAFT 83

Figure 4.2 ^{1}H NMR of P[LA] (**B**) synthesised *via* RAFT polymerisation 84

Figure 4.3 SEC traces of P[LA] synthesised *via* RAFT polymerisation. P[LA] (**A-C**) defined in Table 4.1 84

Figure 4.4 DSC traces of P[LA] synthesised *via* RAFT. P[LA] (**A-C**) defined in Table 4.1 85

Scheme 4.3 Synthetic strategy for polymerisation of LA *via* Cu(0)-mediated LRP 86

Figure 4.5 ^{1}H NMR of P[LA] synthesised *via* Cu(0)-mediated LRP 87

Figure 4.6 SEC traces of P[LA] synthesised *via* Cu(0)-mediated LRP. P[LA] (**D-F**) defined in Table 4.2 88

Figure 4.7 DSC traces of P[LA] synthesised *via* Cu(0)-mediated LRP. P[LA] (**D-F**) defined in Table 4.2 89

Scheme 4.4 Schematic representation of Hostasol end-functionalised P[LA] *via* Cu(0)-mediated LRP 90

Scheme 4.5 Synthetic strategy for polymerisation of LA *via* Cu(0)-mediated LRP using Hostasol-ATRP initiator 91

Figure 4.8 ^{1}H NMR of P[LA] synthesised *via* Cu(0)-mediated LRP using a Hostasol-ATRP initiator 91

Figure 4.9 SEC trace of P[LA] synthesised *via* Cu(0)-mediated LRP using Hostasol-ATRP initiator 92

Scheme 4.6 Schematic representation of pyrene end-functionalised P[LA] *via* Cu(0)-mediated LRP 93

Scheme 4.7 Synthetic strategy for polymerisation of LA *via* Cu(0)-mediated LRP using Pyrene-ATRP initiator 93

Figure 4.10 ^{1}H NMR of P[LA] synthesised *via* Cu(0)-mediated LRP using a Pyrene-ATRP initiator 94

Figure 4.11 SEC trace of P[LA] synthesised *via* Cu(0)-mediated LRP using Pyrene-ATRP initiator 95

Figure 4.12 TGA and DTA curves of P[LA] synthesised *via* RAFT polymerisation. P[LA] (**A-C**) defined in Table 4.1 96

Figure 4.13 SEC traces of P[LA] after thermal treatment at 200 °C under an air atmosphere as a function of time; 0 min. ($M_{n,\,SEC}$ = 2.5 kDa, $Đ$ =1.13), 30 min. ($M_{n,\,SEC}$ = 2.5 kDa, $Đ$ =1.13). P[LA] (**A**) defined in Table 4.1. All peaks are normalised to a maximum intensity of 1 98

Figure 4.14 MALDI-TOF-MS spectra of P[LA] synthesised *via* RAFT before (a) and after (b) thermal treatment at 200 °C for 30 min in an air atmosphere 98

Scheme 4.8 Description of degradation products following the MALDI analysis of P[LA] synthesised *via* RAFT (a) before and (b) after thermal treatment (200 °C, 30 min.) 99

Figure 4.15 NMR of P[LA] synthesised *via* RAFT ($M_{n,\,SEC}$ = 2.5 kDa, $Đ$ = 1.13) before and after thermal treatment at 200 °C under an air atmosphere as a function of time 100

Figure 4.16 TGA and DTA curves of P[LA] synthesised *via* Cu(0)-mediated LRP polymerisation. P[LA] (**D-F**) defined in table 4.2 101

Figure 4.17 SEC traces of P[LA] after thermal treatment at 200 °C under an air atmosphere as a function of time; 0 min. ($M_{n,\,SEC}$ = 2.1 kDa, $Đ$ =1.11), 30 min. ($M_{n,\,SEC}$ = 2.1 kDa, $Đ$ =1.11). P[LA] (**D**) defined in table 4.2. All peaks are normalised to a maximum intensity of 1 101

Figure 4.18 MALDI-TOF-MS spectra of P[LA] synthesised via Cu(0)-mediated polymerisation before (a) and after (b) thermal treatment at 200 °C for 30 mins. in air ... 102

Scheme 4.9 Proposed degradation products following the MALDI-TOF-MS analysis of P[LA] synthesised *via* Cu(0)-mediated polymerisation (a) before and (b) after thermal treatment (200 °C, 30 min.) 102

Figure 4.19 NMR of P[LA] synthesised *via* Cu(0)-mediated polymerisation ($M_{n,\ SEC}$ = 2.1 kDa, $Đ$ = 1.11) before and after thermal treatment at 200 °C under an air atmosphere as a function of time 103

Figure 4.20 (a) TGA and (b) DTA curves of Hostasol-P[LA] synthesised *via* Cu(0)-mediated LRP using Hostasol-ATRP initiator. P[LA] properties given in table 4.2 and 4.3 105

Figure 4.21 DSC traces of P[LA] synthesised *via* Cu(0)-mediated LRP using Hostasol-ATRP initiator. P[LA] defined in table 4.2 and 4.3 106

Figure 4.22 FTIR spectra of Hostasol-ATRP as a function of temperature 107

Figure 4.23 (a) TGA and (b) DTA curves of P[LA] synthesised *via* Cu(0)-mediated LRP using Pyrene-ATRP initiator. P[LA] defined in table 4.2 and 4.4 109

Figure 4.24 SEM micrographs of MWCNTs (NC7000^{TM}) at a) x 15k magnification and b) x100k magnification 111

Figure 4.25 HRTEM images of un-functionalised MWCNTs at, a) x 400k, b) x 250k c) x 250k and d) x 150k magnification 112

Figure 4.26 Raman spectra for MWCNTs 113

Figure 4.27 XPS spectra of MWCNTs, a) survey scan, b) carbon 1s and c) oxygen 1s 115

Figure 4.28 (a) TGA weight loss curves and (b) DTA curves of P[LA] synthesised *via* RAFT and dispersed with MWCNTs. P[LA] (**A-C**) defined in table 4.1 P[LA] modified MWCNTs (**A-C**$_{(5/10)}$) defined in table 4.5 117

Figure 4.29 (a) TGA weight loss curves and (b) DTA curves of P[LA] synthesised *via* Cu(0)-mediated LRP and P[LA] coated MWCNTs. P[LA] (**D-F**) defined in table 4.2. P[LA] modified MWCNTs (**D-F**$_{(5/10)}$) defined in table 4.6 119

Figure 4.30 SEM micrographs of a) un-functionalised MWCNTs at a magnification 100k and b) P[LA] functionalised MWCNTs (**E$_{10}$**) x 100k 120

Figure 4.31 DSC traces of composites of P[LA] and MWCNTs 121

Figure 4.32 Raman spectra of composites of MWCNTs with homopolymers of P[LA] . 122

Figure 4.33 HRTEM images of (a) un-functionalised MWCNTs at 50k × magnification; (b) un-functionalised MWCNTs at 400k × magnification; (c) MWCNTs functionalised with P[LA] at 150k × magnification; (d) MWCNTs functionalised with P[LA] with red line to show inner and outer walls at 300k × magnification. (P[LA] (**B**) polymerised via Cu(0)-mediated polymerisation) 124

Figure 4.34 (a) TGA weight loss curves of MWCNTs premixed with P[LA] and melt mixed with iPP at 165 °C (b) DTA curves of MWCNTs premixed with P[LA] and melt mixed with PP at 165 °C. P[LA] (**D**) defined in table 4.2 125

Figure 4.35 SEC traces of PP before (as received) and after cryo-milling 126

Figure 5.1 SEC traces of P[LA] bulk synthesised *via* Cu(0)-mediated LRP. P[LA] bulk defined in Table 5.1 134

Figure 5.2 SEM micrographs of PP a) x 2k and b) x 12k, composites of PP and MWCNTs (1 wt% CNTs) c) x 25k and d) x 100k, composites of PP and P[LA] (4 wt% P[LA]) e) x 38k and f) x 80k, composites of PP and P[LA] functionalised MWCNTs (1 wt% CNT 4P[LA]) g) x 9k and h) x 110k, composites of PP and P[LA] functionalised MWCNTs (1 wt% CNT 1P[LA]) i) x 5k and j) x 90k magnification 139

Figure 5.3 Variation in (a) storage modulus (G'), (b) complex viscosity $|\eta^*|$ and (c) reciprocal of loss tangent ($(\tan \delta)^{-1}$) as a function of angular frequency (ω) for unfilled PP and composites of PP and MWCNTs and (d) Cole-Cole plot (G' versus G'') 141

Figure 5.4 Variation in (a) imaginary viscosity (η'') with real viscosity (η'), (b) complex viscosity ($|\eta^*|$) with complex modulus ($|G^*|$), (c) $(\tan \delta)^{-1}$ with G'' and (d) phase angle (δ) with the absolute value of ($|G^*|$) (Van Gurp-Palmen plot) for unfilled PP and composites of PP and MWCNTs 142

Figure 5.5 Variation in: (a) storage modulus (G'), (b) complex viscosity $|\eta^*|$ and (c) reciprocal of loss tangent ($(\tan \delta)^{-1}$) as a function of angular frequency (ω) for unfilled PP and composites of PP and P[LA] modified MWCNTs (1:4 MWCNT:P[LA]); and (d) Cole-Cole plot (G' versus G'') 143

Figure 5.6 Variation in (a) imaginary viscosity (η'') with real viscosity (η'), (b) complex viscosity ($|\eta^*|$) with complex modulus ($|G^*|$), (c) $(\tan \delta)^{-1}$ with G'' and (d) phase angle (δ) with the absolute value of ($|G^*|$) (Van Gurp-Palmen plot) for unfilled PP and composites of PP and P[LA] modified MWCNTs 144

Figure 5.7 Variation in: (a) storage modulus (G'), (b) complex viscosity $|\eta^*|$ and (c) reciprocal of loss tangent ($(\tan \delta)^{-1}$) as a function of angular frequency (ω) for unfilled PP and composites of PP and P[LA]; and (d) Cole-Cole plot (G' versus G'') 145

Figure 5.8 Variation in (a) imaginary viscosity (η'') with real viscosity (η'), (b) complex viscosity ($|\eta^*|$) with complex modulus ($|G^*|$), (c) $(\tan \delta)^{-1}$ with G'' and (d) phase angle (δ) with the absolute value of ($|G^*|$) (Van Gurp-Palmen plot) for unfilled PP and composites of PP and P[LA] 146

Figure 5.9 Stress vs strain curves for a) unfilled PP and composites of PP and MWCNTs, b) unfilled PP and composites of PP and P[LA], c) unfilled PP and composites of PP and 4P[LA] functionalised MWCNTs with a filler to compatibiliser ratio of 1:4 and d) unfilled PP and composites of PP and 1P[LA] functionalised MWCNTs with a filler to compatibiliser ratio of 1:1 148

Figure 5.10 Variation in, (a) Young's modulus (E), (b) yield strength (σ_Y), (c) fracture strength (σ_B) and (d) elongation at break (ε_B), as a function of MWCNT loading for composites of, PP/MWCNTs, PP/MWCNTs/4P[LA] and PP/MWCNTs/1P[LA]. Sample compositions described in table 5.2 149

Figure 5.11 Variation in, (a) Young's modulus (E), (b) yield stress (σ_Y), (c) stress at break (σ_B) and (d) elongation at break (ε_B), as a function of P[LA] loading for composites of PP/P[LA] 151

Figure 5.12 Variation in (a) tan δ (b) storage modulus (E') and (c) loss modulus (E'') for unfilled PP and composites of PP and MWCNTs 153

Figure 5.13 Variation in T_g obtained from tan δ maximum a) as function of MWCNT loading for composites of PP and unmodified MWCNTs, PP and 1:4 MWCNT:P[LA] modified MWCNTs and PP and 1:1 MWCNT:P[LA] modified MWCNTs and b) as function of P[LA] loading for composites of PP and P[LA]. Change in T_g obtained from loss modulus (E'') maximum c) as function of MWCNT loading for composites of PP and unmodified MWCNTs, PP and 1:4 MWCNT:P[LA] modified MWCNTs and PP and 1:1 MWCNT:P[LA] modified MWCNTs and d) as function of P[LA] loading for composites of PP and P[LA] 154

Figure 5.14 Variation in (a) tan δ (b) storage modulus (E') and (c) loss modulus (E'') of unfilled PP and composites of PP and P[LA] 155

Figure 5.15 Variation in (a) tan δ (b) storage modulus (*E'*) and (c) loss modulus (*E''*) of unfilled PP and P[LA] functionalised MWCNTs with a filler to compatibiliser ratio of 1:4 156

Figure 5.16 Variation in (a) tan δ (b) storage modulus (*E'*) and (c) loss modulus (*E''*) of unfilled PP and P[LA] functionalised MWCNTs with a filler to compatibiliser ratio of 1:1 157

Figure 5.17 DSC a) heating curves and b) cooling curves for unfilled PP and composites of PP and MWCNTs, c) heating curves and b) cooling curves for unfilled PP and composites of PP and P[LA], e) heating curves and f) cooling curves for unfilled PP and composites of PP and P[LA] functionalised MWCNTs (1:4 MWCNTs:P[LA]) and g) heating curves and (h) cooling curves for unfilled PP and composites of PP and P[LA] functionalised MWCNTs (1:1 MWCNTs:P[LA]) 161

Figure 5.18 WAXD diffractograms for a) unfilled PP and composites of PP and MWCNTs, b) unfilled PP and for blends of P[LA] and PP and c) unfilled PP and for composites of PP and P[LA] modified MWCNTs in a 1:4 MWCNTs:P[LA] 164

Figure 5.19 DC electrical conductivity (σ) as a function of MWCNT concentration (*Φ*) at a constant r.t. for unfilled PP, composites of PP and MWCNTs, composites of PP and P[LA] functionalised MWCNTs (1:4 MWCNT/P[LA]) and composites of PP and P[LA] functionalised MWCNTs (1:1 MWCNT/P[LA]) 165

Figure 6.1 Schematic representation of P[LA] interacting with a graphene sheet 173

Figure 6.2 SEM micrographs of GNPs at a) x 2k, and b) x 10k magnification. HRTEM images of un-functionalised GNPs at c) x 28.5k, d) x 46k, e) x 28.5k, and f) x 310k magnification 176

Figure 6.3 Raman spectra for the GNPs used in this study 177

Figure 6.4 XPS spectra of GNPs, a) survey scan, b) Carbon 1s and c) Oxygen 1s 179

Figure 6.5 SEM micrographs of composites of, PP and GNPs (1 wt% GNPs) at a) x 8k, b) x 80k, c) x 3k and d) x 5k magnification and composites of PP and P[LA] functionalised GNPs (1 wt% GNPs P[LA]) at e) x 5k, f) x 15k, g) x 80k and h) x 120k magnification .. 181

Figure 6.6 Stress vs strain curves for unfilled PP and composites of a) PP and GNPs and b) PP and P[LA] functionalised GNPs 183

Figure 6.7 Variation in a) Young's modulus (*E*), b) tensile stress (σ), c) strain at yield point (ε_y) and d) tensile strain at break (ε_B), as a function of GNP loading for composites of PP filled with GNPs and PP filled with P[LA] functionalised GNPs 185

Figure 6.8 DMTA traces for unfilled PP and composites of PP and GNPs, a) tanδ b) storage modulus (*E'*) and c) loss modulus (*E''*) as a function of temperature 187

Figure 6.9 DMTA traces for unfilled PP and composites of PP and P[LA] functionalised GNPs, a) tanδ b) storage modulus (*E'*) and c) loss modulus (*E''*) as a function of temperature 188

Figure 6.10 Change in T_g obtained from a) tanδ maxima and b) loss modulus (*E''*) maxima, for composites of PP/GNPs and PP/P[LA] modified GNPs 189

Figure 6.11 Variation in: (a) storage modulus (*G'*), (b) complex viscosity |η*| and (c) reciprocal of loss tangent ($(\tan \delta)^{-1}$) as a function of angular frequency (ω) for unfilled PP and composites of PP and GNPs and (d) Cole-Cole plot (*G'* verses *G''*) 191

Figure 6.12 Variation in: (a) storage modulus (*G'*), (b) complex viscosity |η*| and (c) reciprocal of loss tangent ($(\tan \delta)^{-1}$) as a function of angular frequency (ω) for unfilled PP and composites of PP and P[LA] functionalised GNPs and (d) Cole-Cole plot (*G'* verses *G''*) 192

Figure 6.13 DSC (a) heating curves and (b) cooling curves for, unfilled PP and composites of PP and GNPs. DSC (c) heating curves and (d) cooling curves for, unfilled PP and composites of PP and P[LA] functionalised GNPs 193

Figure 6.14 WAXS diffractograms for unfilled PP and for composites of a) PP and GNPs and b) PP and P[LA] functionalised GNPs 196

Figure 6.15 DC electrical conductivity (σ) verses GNP concentration (Φ) at a constant r.t (298K) 197

Figure 7.1 Schematic displaying the block copolymer (P[LA-*block*-2PEA]) interacting with MWCNTs within a poly(propylene matrix) 204

Figure 7.2 Schematic displaying the block copolymer interacting with GNPs within a poly(propylene) matrix 205

Scheme 7.1 Synthetic strategy for homo-polymerisation of LA *via* Cu(0)-mediated living radical polymerisation 206

Figure 7.3 ^{1}H NMR spectra of P[LA] of various molecular weights recorded in $CDCl_3$ synthesised *via* Cu(0)-mediated polymerisation 206

Figure 7.4 SEC traces of P[LA] of various molecular weights synthesised *via* Cu(0)-mediated polymerisation 207

Scheme 7.2 Synthetic strategy for homo-polymerisation of 2PEA *via* Cu(0)-mediated LRP 208

Figure 7.5 ^{1}H NMR spectra of P[2PEA] of various molecular weights recorded in $CDCl_3$ synthesised *via* Cu(0)-mediated polymerisation 209

Figure 7.6 SEC traces of P[2PEA] of various molecular weights synthesised *via* Cu(0)-mediated polymerisation 209

Scheme 7.3 Ball and stick schematics for the copolymer architectures of LA and 2PEA *via* Cu(0)-mediated LRP 210

Scheme 7.4 Synthetic strategy for co-polymerisation of LA and 2PEA *via* Cu(0)-mediated LRP 210

Figure 7.7 ^{1}H NMR spectra of co-polymers of P[LA] and P[2PEA] recorded in $CDCl_3$ synthesised *via* Cu(0)-mediated polymerisation 212

Figure 7.8 SEC traces of co-polymers of P[LA] and P[2PEA] synthesised *via* Cu(0)-mediated polymerisation 212

Figure 7.9 TGA and DTA curves of (a) homopolymers of P[LA], (b) homopolymers of P[2PEA] and (c) copolymers of P[LA] and P[2PEA] synthesised *via* Cu(0)-mediated LRP 214

Figure 7.10 DSC traces (first cooling and second heating cycle) of (a) homopolymers of P[LA], (b) homopolymers of P[2PEA] and (c) copolymers of P[LA] and P[2PEA] synthesised *via* Cu(0)-mediated LRP 216

Figure 7.11 Variation in: (a) storage modulus (*G'*), (b) loss modulus (*G''*) and (c) complex viscosity ($|\eta^*|$) as a function of angular frequency (ω) for homopolymers and copolymers of P[LA] and P[2PEA] at r.t. 218

Figure 7.12 SEM micrographs of composites of P[2PEA]10K and MWCNTs at a) x35k and b) x115k; of *stat*20K and MWCNTs at c) x35k and d) x80k and, of *block*20K and MWCNTs at e) x8k and f) x75k magnification 221

Figure 7.13 TEM images of composites *stat*20K and MWCNTs at a) x630k and b) x820k; and of *block*20K and MWCNTs at c) x94k and d) x390k magnification 222

Figure 7.14 a) Structure of di-block copolymer P[LA-*block*-2PEA] ($M_{n,GPC}$ = 19,000 Da, DPn = 1.15) (b) Ultrasonication and mechanical stirring of P[LA-*block*-2PEA] with MWCNTs in $CHCl_3$ (c) HRTEM image depicting evidence for non-covalent functionalization.....223

Figure 7.15 a) TEM image of the *block* 20K MWCNT and b) HRTEM image of boxed region in (a). (c) Low magnification dark-field STEM image of *block* 20K MWCNT and (d) HR STEM image of boxed region in (c) 223

Figure 7.16 Carbon K-edge spectra of a) graphite presenting two peaks of the ($sp^2 + 2p_z$) bonding and b) diamond showing only one major peak of the sp^3 bonding.....224

Figure 7.17 EELS analysis. a) High magnification STEM image clearly showing ~15nm coating of the block copolymer on a MWCNT. b) Carbon K-edge EELS spectra (high-loss) from the green boxed region in (a) from regions A and B, where the peaks at 285 and 292 eV correspond to electron transitions from the 1s level to π* and σ* states, respectively. c) and d) individual maps of the fitting components from peaks A and B in (a).....225

Figure 7.18 DMA and rheological analysis. Variation of a) tan δ and b) storage modulus (*E'*), verses temperature for PLA-b-P2PEA (*block* 20K) and its composite with MWCNTs. Variation (at RT) of (c) storage modulus (*G'*) and (d) complex viscosity ($|\eta^*|$), as a function of angular frequency (ω) for PLA-*b*-P2PEA and its composite with MWCNTs 226

Figure 7.19 Small and wide-angle X- ray scattering data (SAXS/WAXS) of pure copolymer (*block* 20K), MWCNTs and corresponding blend, with molecular packing detail. (a): WAXS patterns of pure MWCNT and MWCNT blend displaying prominent (002) and (100) graphite peaks but, absent in the pure block copolymer pattern. (b): SAXS patterns of pure block copolymer at 30 °C (pre and post-heating to 100 °C), indicating regular lamellar structure. (c): SAXS patterns of pure MWCNT and MWCNT block copolymer blend, where q* at 0.039 Å is still observed in the copolymer blend. (d): Computed correlation function of pure block copolymer SAXS profile displaying long period (Lp) as ~ 156 Å. (e): Lamellar structure of block copolymer with length-scales extracted from the correlation function; Lp = 156 Å, hard block (Hb) is the P[LA] block

being ~ 100 Å and soft block (Sb) being P[PEA] block being ~ 56 Å. (f): Schematic of block copolymer on surface of a MWCNT with indication of length-scale in SAXS.....227

Figure 7.20 a) TGA and b) DTA curves of composites of MWCNTs with homopolymers and copolymers of P[LA] and P[2PEA] 230

Figure 7.21 DSC traces of composites of MWCNTs with homopolymers and copolymers of P[LA] and P[2PEA].....230

Figure 7.22 Raman spectra of MWCNTs alone and composites of MWCNTs with homopolymers and copolymers of P[LA] and P[2PEA] 231

Figure 7.23 SEM micrographs of composites of GNPs and poly(acrylate). P[LA] 10K GNPs a) x25k and b) x150k; P[2PEA] 20K GNPs c) x5k and d) x50k; *stat* 20K e) x10k and f) x100k; *block* 20K g) x7k and x70k magnification 234

Figure 7.24 TEM images of unfunctionalised GNPs a) x1,050k and b) x1,050k. Composites of GNPs and poly(acrylate). *Stat* 20K GNPs c) x650k and d) x1,050k. *Block* 20K GNPs e) x190k and f) x1,050k magnification.....235

Figure 7.25 (a) TGA and (b) DTA curves of composites of GNPs with homopolymers and copolymers of P[LA] and P[2PEA] 236

Figure 7.26 DSC traces of composites of GNPs with homopolymers and copolymers of P[LA] and P[2PEA] 237

Figure 7.27 Raman spectra for neat GNPs and composites of GNPs with homopolymers and copolymers of P[LA] and P[2PEA] 238

Figure 7.28 Variation (at RT) of (a) storage modulus (G') and (b) complex viscosity ($|\eta^*|$), as a function of angular frequency (ω) for a composite of *block* 20K and GNPs 239

Scheme 8.1 Schematic representation for the non-covalent compatibilisation of P[LA-*block*-2PEA] with MWCNTs within a PP matrix.....245

Figure 8.1 SEM micrographs of unfilled PP at **a**) x2.5k, **b**) x3k, **c**) PP/P[LA]10K at x35k, **d**) PP/P[2PEA]10K at x28k, **e**) PP/*block*20K at x23k, **f**) PP/*stat* 20K at x11k, **g**) P[LA]10K/ MWCNTs at x110k, **h**) P[2PEA]10K/MWCNTs at x110k, **i**) *block* 20K/MWCNTs at x95k, **j**) *stat* 20K/MWCNTs at x130k, **k**) P[LA]10K/GNPs at x80k, **l**) P[2PEA]10K/GNPs at x50k, **m**) *block* 20K/GNPs at x40k and **n**) *stat* 20KGNPs at x25k magnification.....248

Figure 8.2 Variation in (a) storage modulus (G'), (b) complex viscosity ($|\eta^*|$) and (c) reciprocal of loss tangent ($(\tan \delta)^{-1}$) as a function of angular frequency (ω) for unfilled PP and composites of PP blended with homo and co-polymers of P[LA] and P[2PEA]; and (d) Cole-Cole plot (G' versus G'').....252

Figure 8.3 Variation in (a) storage modulus (G'), (b) complex viscosity ($|\eta^*|$) and (c) reciprocal of loss tangent ($(\tan \delta)^{-1}$) as a function of angular frequency (ω) for unfilled PP and composites of PP blended with MWCNTs functionalised with homo and co-polymers of P[LA] and P[2PEA]; and (d) Cole-Cole plot (G' versus G'') 254

Figure 8.4 Variation in (a) storage modulus (G'), (b) complex viscosity ($|\eta^*|$) and (c) reciprocal of loss tangent ($(tan\ \delta)^{-1}$) as a function of angular frequency (ω) for unfilled PP and composites of PP blended with GNPs functionalised with homo and co-polymers of P[LA] and P[2PEA]; and (d) Cole-Cole plot (G' versus G'').....255

Figure 8.5 Stress vs strain curves for unfilled PP and composites of **a**) PP blended with homo and co-polymers of P[LA] and P[2PEA], **b**) PP blended with MWCNTs functionalised with homo and co-polymers of P[LA] and P[2PEA] and **c**) PP blended with GNPs functionalised with homo and co-polymers of P[LA] and P[2PEA].....256

Figure 8.6 Mechanical properties for unfilled PP and composites of PP blended with homo and co-polymers of P[LA] and P[2PEA], **a**) Young's Modulus (E), **b**) tensile strength (σ), **c**) yield strain (ε_Y) and **d**) elongation at break (ε_B). Mechanical properties for unfilled PP and composites of PP blended with MWCNTs functionalised with homo and co-polymers of P[LA] and P[2PEA], **e**) Young's Modulus (E), **f**) tensile strength (σ), **g**) yield strain (ε_Y) and **h**) elongation at break (ε_B). Mechanical properties for unfilled PP and composites of PP blended with GNPs functionalised with homo and co-polymers of P[LA] and P[2PEA], **i**) Young's Modulus (E), **j**) tensile strength (σ), **k**) yield strain (ε_Y) and **l**) elongation at break (ε_B).....258

Figure 8.7 a) DMTA tan δ traces as a function of temperature and **b**) comparisons for change in T_g by tan δ peak and E'' peak, for unfilled PP and composites of PP blended with homo and co-polymers of P[LA] and P[2PEA]. **c**) DMTA tan δ traces as a function of temperature and **d**) comparisons for change in T_g by tan δ peak and E'' peak, for unfilled PP and composites of PP blended with MWCNTs functionalised with homo and co-polymers of P[LA] and P[2PEA]. **e**) DMTA tan δ traces as a function of temperature and **f**) comparisons for change in T_g by tan δ peak and E'' peak, for unfilled PP and composites of

PP blended with GNPs functionalised with homo and co-polymers of P[LA] and P[2PEA] 262

Figure 8.8 DMTA traces for unfilled PP and composites of PP blended with homo and co-polymers of P[LA] and P[2PEA], **a**) storage modulus (*E′*) and **b**) loss modulus (*E″*) as a function of temperature. DMTA traces for unfilled PP and composites of PP blended with MWCNTs functionalised with homo and co-polymers of P[LA] and P[2PEA], **c**) storage modulus (*E′*) and **d**) loss modulus (*E″*) as a function of temperature. DMTA traces for unfilled PP and composites of PP blended with GNPs functionalised with homo and co-polymers of P[LA] and P[2PEA], **e**) storage modulus (*E′*) and **f**) loss modulus (*E″*) as a function of temperature 265

Figure 8.9 DSC **a**) heating curves and **b**) cooling curves for unfilled PP and composites of PP blended with homo and co-polymers of P[LA] and P[2PEA]. DSC **c**) heating curves and **d**) cooling curves for unfilled PP and composites of PP blended with MWCNTs functionalised homo and co-polymers of P[LA] and P[2PEA]. DSC **e**) heating curves and **f**) cooling curves for unfilled PP and composites of PP blended with GNPs functionalised with homo and co-polymers of P[LA] and P[2PEA] 268

Figure 8.10 WAXD diffractograms of PP and **a**) composites of PP and poly(acrylates), **b**) composites of PP blended with MWCNTs functionalised with homo and co-polymers of P[LA] and P[2PEA] and **c**) composites of PP blended with GNPs functionalised with homo and co-polymers of P[LA] and P[2PEA] 271

Appendix 1. ^{1}H NMR of LA monomer for polymer synthesis 333

Appendix 2. ^{1}H NMR of AIBN initiator for RAFT polymerisation 333

Appendix 3. ^{1}H NMR of EBiB initiator for Cu(0)-mediated LRP 334

Appendix 4. ^{1}H NMR of Me_6TREN ligand for Cu(0)-mediated LRP 334

Appendix 5. DSC trace of lauryl acrylate (LA) monomer 335

Appendix 6. ^{1}H NMR of Hostasol-ATRP initiator 335

Appendix 7. ^{1}H NMR of 2PEA monomer for polymerisations 336

Appendix 8. TGA of cyanomethyl dodecyltrithiocarbonate RAFT agent 336

Appendix 9. TGA of lauryl acrylate (LA) monomer 337

Appendix 10. a) TGA and b) DTA of common reagents 338

Appendix 11. a) image of Thermo-Scientific Haake^{TM} Mini-Lab II twin-screw micro-compounder, b) image of Thermo-Scientific Haake^{TM} Mini-Jet Pro piston injection moulding system and c) images of the moulds used to prepare test specimens with the Mini-Jet Pro.....339

List of Tables

Table 2.1 d-spacings and corresponding miller indices of iPP 45

Table 3.1 Blending ratios (wt%) for PP and composites of PP, poly(lauryl acrylate) P[LA] (M_n = 11,500, $Đ$ = 1.15) and MWCNTs and corresponding composite nomenclature 67

Table 3.2 Blending ratios (wt%) for PP and composites of PP, P[LA] (M_n = 11,500, $Đ$ = 1.15) and GNPs and corresponding composite nomenclature 68

Table 3.3 Blending ratios (wt%) for PP and composites of PP, poly(acrylate), MWCNTs, GNPs and corresponding composite nomenclature 69

Table 4.1 Theoretical and experimental data for the preparation of initial polymers of LA *via* RAFT polymerisation process and the associated number average molar masses 83

Table 4.2 Theoretical and experimental data for the preparation of initial polymers of LA *via* Cu(0)-mediated LRP polymerisation process and the associated number average molar masses 87

Table 4.3 Theoretical and experimental data for the preparation of P[LA] *via* Cu(0)-mediated LRP polymerisation process, using a Hostasol-ATRP initiator and the associated number average molar masses 91

Table 4.4 Theoretical and experimental data for the preparation of P[LA] *via* Cu(0)-mediated LRP polymerisation process, using a pyrene-ATRP initiator and the associated number average molar masses 94

Table 4.5 Relative proportions (wt%) of P[LA] (synthesised using RAFT) and MWCNTs before and after adsorption.....117

Table 4.6 Relative proportions (wt%) of P[LA] (synthesised using Cu(0)-mediated polymerisation) and MWCNTs before and after adsorption.....118

Table 4.7 Raman properties of MWCNTs and composites of MWCNTs with homopolymers of P[LA] 122

Table 4.8 Raman properties of MWCNTs and composites of MWCNTs with homopolymers of P[LA] 123

Table 4.9 SEC analysis of isotactic PP before and after cryo-milling 127

Table 5.1 Theoretical and experimental data for the preparation of bulk P[LA] *via* Cu(0)-mediated LRP process and the associated conversion, number average molar masses and dispersity 133

Table 5.2 List of materials loadings used of PP, MWCNTs and P[LA] in the production of the composites 136

Table 5.3 Change in tensile mechanical properties for PP and composites of PP, P[LA] and MWCNTs. Definitions are described in table 5.2 150

Table 5.4 Calorimetric data observed from DSC and crystalline content (X_c) determined by DSC and WAXD for PP and composites of PP, P[LA] and MWCNTs 162

Table 6.1 Composite Formulation 174

Table 6.2 Change in mechanical properties for PP and composites of PP, GNPs and P[LA]. 184

Table 6.3 Calorimetric data observed from DSC and crystalline content (Xc) determined from DSC for PP and composites of PP and GNPs 194

Table 7.1 Theoretical and experimental data for the preparation of homo-polymers of P[LA] *via* Cu(0)-mediated LRP process and the associated number average molar masses 206

Table 7.2 Theoretical and experimental data for the preparation of homo-polymers of P[2PEA] *via* Cu(0)-mediated LRP process and the associated number average molar masses 208

Table 7.3 Theoretical and experimental data for the preparation of co-polymers of LA and 2PEA *via* Cu(0)-mediated LRP process and the associated number average molar masses 211

Table 7.4 Descriptions of loadings of poly(acrylate)s and filler in the composites 219

Table 7.5 Raman bands for neat MWCNTs and composites of MWCNTs with homopolymers and copolymers of P[LA] and P[2PEA] 232

Table 7.6 Raman properties of MWCNTs and composites of MWCNTs with homopolymers and copolymers of P[LA] and P[2PEA] 232

Table 7.7 Raman peaks for GNPs and composites of GNPs with homopolymers and copolymers of P[LA] and P[2PEA] 238

Table 7.8 Raman of GNPs and composites of GNPs with homopolymers and copolymers of P[LA] and P[2PEA] 239

Table 8.1 Loadings of PP, filler and poly(acrylate) in the composites studied 244

Table 8.2 Calorimetric data observed from DSC and crystalline content (X_c) determined from DSC for PP and composites of; PP blended with homo and co-polymers of P[LA] and P[2PEA], PP blended with MWCNTs functionalised homo and co-polymers of P[LA] and P[2PEA] and PP blended with GNPs functionalised homo and co-polymers of P[LA] and P[2PEA] 269

Table 8.3 Crystallographic properties of composites of PP, GNPs/MWCNTs and poly(acrylate)s listing the relative intensity ratios between the β(300) and α(040) reflections 272

Appendix 12. Mechanical properties for unfilled PP and composites of PP and poly(acrylates), PP blended with MWCNTs functionalised with homo and co-polymers of P[LA] and P[2PEA] and PP blended with GNPs functionalised with homo and co-polymers of P[LA] and P[2PEA] 340

List of Equations

Equation 1 (Electrical) Electrical resistivity formula 75

Equation 2 (Rheology) Dynamic frequency sweeps with a sinusoidal stress, τ, formula 141

Equation 3 (Rheology) The linear response of the material in terms of strain, γ_r, formula 141

Equation 4 (Rheology) Resultant function in terms of strain formula 141

Equation 5 (Electrical) Stauffer and Aharony formula for relationship between electrical conductivity and carbon black concentration 166

Equation 6 (SAXS) Correlation function for SAXS profile 228

Equation 7 (SAXS) Correlation function for SAXS profile 228

Acknowledgements

I would like to acknowledge the University of Warwick and WMG for their financial contribution and the opportunity to undertake this research project.

A special thank you to my supervisors, Prof. Tony McNally, Dr. Chaoying Wan and Prof. David Haddleton. I am truly grateful for your support and guidance.

I give special thanks and recognition to Martin Worrall for his support, advice, guidance and friendship throughout my PhD.

I acknowledge the input of Dr. Daniel Keddie for his assistance regarding the practical experimental procedure for the synthesis of the RAFT agent. I acknowledge the assistance of Dr. Ellen Heeley from Open University for the synchrotron and SAXS measurements.

Within the University of Warwick, I would like to extend my thanks to the technicians and researchers across both WMG and the Department of Chemistry whom without I would not have been able to have completed my PhD.

Finally, I would like to thank my friends, family and the members of the International Institute for Nanocomposites Manufacturing (IINM) for all their lasting support.

Declaration of Authorship

This thesis is submitted to the University of Warwick in support of my application for the degree of Doctor of Philosophy. It has been composed by myself and has not been submitted in any previous application for any degree to any other university or higher education institution or as any part of any other submission to the University of Warwick. It describes the work carried out from August 2014 to January 2018.

Except otherwise indicated, the work presented (including data generated and data analysis) herein was carried out by the author and is not the product of collaboration.

Parts of this thesis have been published and submitted to journals during the PhD period by the author as detailed in the list of publications at the end of this thesis.

Signed and dated:

Summary

1D and 2D graphitic materials (carbon nanotubes (CNTs) and graphene nanoplatelets (GNPs)) are of great interest due to their extraordinary electrical, thermal, mechanical and optical properties rarely found in bulk materials. The transfer of such properties to polymers has been limited and the development of scalable, cost-effective, multi-functional composite materials not fully realised. Polymers filled with 1D and 2D graphitic nanomaterials have uses in a wide range of applications and industries ranging from aerospace and automotive to personal care and high-tech products. Growing global economic development has sharply increased the world's energy needs and in particular, our energy storage needs. In addition, they have potential applications in electronics, sensors and energy conversion. Another application in the area of personal care has shown that CNT-polymer composites can be used to speed up the process of bone-regeneration by being used as tissue scaffold materials. An application of interest is to use graphitic nanomaterials to produce composites with high mechanical performance (stiffness and strength) with low filler quantity providing innovative light-weighting solutions. Further potential applications of 1D and 2D graphitic nanomaterials include; touch screens, capacitors, spintronic devices, fuel cells, conductive films, high frequency circuits and flexible electronics. The development of such innovative materials requires the nanofiller to be homogenously dispersed within the polymer matrix, e.g. poly(propylene)(PP). The formation of an interconnected filler network structure at a low percolation threshold will result in the enhancement of electrical and thermal conductivity. In addition, efficient interfacial adhesion and stress transfer between filler and polymer results in improved mechanical strength and stiffness. However, poor compatibility between filler and the PP matrix prevents efficient homogenous dispersion and network formation. To address this major technical challenge, the use of a polymer compatibiliser which non-covalently functionalised graphitic nanomaterials was explored. By way of example, poly(lauryl acrylate) P[LA] was selected based upon its known compatibility with PP and it was proposed that it would also non-covalently functionalise such fillers via CH-π wrapping. P[LA] was synthesised using controlled living radical polymerisation methods and was shown to both be thermally stable for extrusion and physisorbed onto the surface of MWCNTs. For composites of PP, P[LA] and either MWCNTs or GNPs evidence was obtained confirming that P[LA] improved filler dispersion however, the most notable observation was a significant reduction in T_g of PP which was associated with P[LA]

plasticising PP. Further polymer compatibilisers based on copolymers (statistical and block) of P[LA] and poly(2-phenyl ethyl acrylate) P[2PEA] where also synthesised and their potential to non-covalently functionalise CNTs and GNPs via both CH-π wrapping and π-π stacking examined. A range of characterisation techniques were employed to thoroughly understand the behaviour of these compatibilisers when added to composites of MWCNTs/GNPs and PP. Evidence for π-π stacking of P[2PEA] onto the surface of both graphitic fillers was observed from extensive electron microscopy observations. The potential of P[LA-*co*-2PEA] block copolymers as compatibilisers for 1D and 2D graphitic materials and PP was proven. The use of poly(acrylate)s as compatibilisers to assist the dispersion of 1D and 2D graphitic nanofillers in a PP has proven to be a concept with limited potential to alter the mechanical, electrical and thermal properties of polymers. The excellent thermal stability demonstrated by poly(acrylate)s for the purpose of melt blending with PP provides scope for further work through alternative functionalisation strategies e.g. covalent functionalisation. Throughout the project, the discussion has centred around the use of P[LA] and P[2PEA] due their potential to adsorb onto surface of 1D and 2D graphitic fillers and promote their dispersion in a PP matrix however, further work should investigate a range of poly(acrylate)s with various structures, chemistries, molecular weights and dispersities. For example, the use poly(acrylate)s with longer side chains such as poly(octadecyl acrylate) or poly(acrylate)s containing aromatic side chains with a greater number of benzene rings such as pyrene, for example pyrene acrylate. It is evident that the viscosity of the compatibilising polymer influences the extent of dispersion of the compatibiliser in the PP and matrix and therefore, it would be interesting to investigate if there is a correlation between the viscosity of the polymer compatibiliser and the extent of its dispersion in the PP matrix. GNPs with a greater aspect ratio are predicted to achieve percolation at lower loadings, increase electrical and thermal conductivity as well as improve the mechanical properties. Additionally, it would be interesting to explore what GNP quantity is required to achieve electrical and rheological percolation with the same type of GNPs and correlate those findings with graphenes with different aspect ratios to understand the role of flake dimensions. It is clear, P[LA] is not particularly successful in compatibilising the GNPs used in this study. In addition, it would useful to conduct dynamic cross-polarized optical microscopy and WAXS/SAXS scattering experiments during heating and cooling to investigate trans-crystallinity phenomena at the interface between GNPs and the PP matrix.

Abbreviations and Terminology

MWCNTs	Multi-Walled Carbon Nanotubes
GNPs	Graphene Nanoplatelets
SWCNTs	Single-walled carbon nanotubes
CNTs	Carbon nanotubes
iPP	(isotactic) Poly(propylene)
PP	Poly(propylene)
LRP	Living radical polymerisation
ATRP	Atom transfer radical polymerisation
CLRP	Controlled living radical polymerisation
RAFT	Reversible addition – fragmentation chain transfer polymerisation
CTA	Chain transfer agent
SET-LRP	Single electron transfer – living radical polymerisation
P[LA]	Poly[lauryl acrylate]
P[2PEA]	Poly[2-phenyl ethyl acrylate]
P[LA-*block*-2PEA]	Poly(lauryl acrylate-*block*-2-phenyl ethyl acrylate)
P[LA-*stat*-2PEA]	Poly(lauryl acrylate-*statistical*-2-phenyl ethyl acrylate)
Hostasol-P[LA]	P[LA] polymerised using a Hostasol functionalised initiator
Pyrene-P[LA]	P[LA] polymerised using a Pyrene functionalised initiator
EBiB	Ethyl α-bromoisobutyrate
DMA	Dynamic mechanical analysis
DMTA	Dynamic mechanical thermal analysis
TGA	Thermo-gravimetric analysis
DSC	Differential scanning calorimetry
GPC	Gel permeation chromatography
SEC	Size exclusion chromatography
PDi (*Đ*)	Poly dispersity
NMR	Nuclear magnetic resonance spectroscopy

FTIR	Fourier transform infrared spectroscopy
UV-Vis	Ultra-violet visible spectroscopy
SEM	Scanning electron microscopy
HRTEM	High resolution transmission electron microscopy
EELS	Electron energy loss spectroscopy
XPS	X-ray photoelectron spectroscopy
XRD	X-ray diffraction
SAXS	Small angle X-ray scattering
WAXS	Wide angle X-ray scattering
WAXD	Wide angle X-ray diffraction

Chapter 1 Introduction

1.1 Background

The rapid development of nanotechnology over past 30 years has precipitated the development of new materials with nano-meter scale dimensions. In particular, 1D and 2D graphitic nanomaterials (graphene and carbon nanotubes (CNTs)) are of great interest due to their unique properties which are rarely found in bulk materials.[1] Facilitating the use of these materials and their exceptional properties has remained a serious challenge and progress has been limited. Academic and industrial researchers have applied tremendous levels of effort into trying to take advantage of these properties at the macro-scale however, lack of detailed understanding with regards to the behaviour of these materials on the nanoscale has retarded progress.

1.2 Applications of nanostructured filled polymer composite materials

Polymers filled with 1D and 2D graphitic nanomaterials have uses in a wide range of applications and industries ranging from aerospace and automotive to personal care and high-tech products. Growing global economic development has sharply increased the world's energy needs and energy storage needs. Smartphones and computers as well as electric vehicles require an ever-higher quantity of energy storage. The exceptionally high electrical properties of graphitic nanomaterials has led to the production of novel lithium ion batteries with remarkable charging and discharging rates.[2] In addition, they have potential applications in electronics, sensors and energy conversion.[2] Another application in the area of personal care has shown that CNT-polymer composites can be used to speed up the process of bone-regeneration by being used as tissue scaffold materials. An application of interest is to use graphitic nanomaterials to produce composites with high mechanical performance (stiffness and strength) with low filler quantity providing innovative light-weighting solutions. Further potential applications of 1D and 2D graphitic nanomaterials include; touch screens, capacitors, spintronic devices, fuel cells, conductive films, high frequency circuits and flexible electronics.[3]

1.3 The research problem

Polymer materials, both commodity and engineering polymers (e.g. PP, HDPE, Nylon) are used in a wide range of applications due to their good processing properties and the ease at which they can be scaled, as well as their low cost of production. However, they

are typically electrically and thermally insulating and mostly only suitable for non-load bearing components which limits their use. Applications which require high electrical and thermal conductivity combined with enhanced mechanical strength and stiffness tend to resort to metals to fulfil their needs (e.g. copper, steel). In the modern age of sustainability, efficiency and high cost of production, new materials are sought after which meet certain criteria such as; high electrical and thermal conductivity, high mechanical strength and stiffness, lightweight, low cost of production, scalable and longevity. In the last three decades, polymer materials have provided many of these solutions in terms of low cost and scalability which has led to their wide scale use ranging from packaging to consumer electronics. However, further improvements to polymers are possible if additional functionalities can be added to the matrix material. Thus, there is the need for an additional component which has very different properties to those of the neat polymer. The addition of nanometre scale particles to polymer systems has attracted substantial interest due to the possibility of producing composites with exceptional electrical, thermal and mechanical properties with the addition of only a small weight/volume percentage of nanofiller (<5 wt%). Polymer encapsulation has been commonly selected as the system of choice when looking to magnify the outstanding properties of nanomaterials and has generated a new field of materials science known as 'nanocomposites'. Polymer composites reinforced with nanoscale inclusions differ greatly from the traditional particulate and fibre-reinforced composites, where challenges including dispersion, distribution and interfacial adhesion become more of a stumbling block. One of the key advantages of reducing the reinforcement size from the micro-meter to the nano-meter scale is to offer multi-functional properties in contrast to traditional composites which are focused on primarily on improvements in mechanical properties (stiffness and strength). Carbon nanotubes (CNTs) and graphene are cylindrical and sheet shaped nanostructures made entirely of carbon. CNTs are referred to as 1D graphitic carbon allotropes because of their high aspect ratios (ratio of length to diameter). Graphene is referred to as a 2D graphitic carbon allotrope because it represents a single layer of graphite and it is a single atom thick. Graphene is a single-atom-thick sheet of carbon atoms arranged in a hexagonal lattice and has been reported to be the world's thinnest, strongest and stiffest material, as well as being an excellent conductor of both heat and electricity.[3] CNTs have been shown to be thermally stable up to 2800 °C, to have a thermal conductivity twice that of diamond and electron mobilities over a thousand times higher than copper wire. In addition, CNTs possess a high elastic modulus, in the order of

~1 TPa. Graphene also has many similar properties to that of CNTs. On their own, it can be difficult to utilise the exceptional properties of these carbon nanofillers due to their nanoscale as they are difficult to handle and produced in powder form. It makes sense to combine the outstanding properties of nanofillers with commodity and engineering polymers, e.g. poly(propylene), poly(amide) to produce composites which can be easily processed and moulded. It has been theorised that the outstanding properties of carbon nanomaterials can be optimised if the nanofillers are homogenously dispersed and distributed within the polymer matrix. There is a preference for the formation of a network structure to be achieved at a low percolation threshold to optimise the electrical and thermal conductivity of the unfilled polymer. Mixing nanofillers with thermoplastics is typically performed under solvent-free conditions using extrusion however, the thermodynamics of mixing is not favourable and prevents the two systems from mixing effectively and homogenously. The aromatic, highly electronic, sp^2 hybridized structure of nano-fillers have extremely poor compatibility with the neutral, sp^3 hybridized structure of poly(propylene) (PP). A range of methods can be used to functionalise graphitic fillers including, covalent functionalisation comprising of 'grafting to' and 'grafting from' the surface of the nano-filler. Extensive research into covalent functionalisation of graphitic nanofillers has been conducted and a review of literature has indicated improvements in the properties of the composite materials are possible (see chapter 2). For example, polymer grafting to the surface has rendered the fillers soluble in a wide range of solvents and improved their interfacial compatibility with polymer matrices. However, it is the hexagonal sp^2 arrangement of carbon atoms that gives graphitic nanofillers their exceptional properties and the introduction of covalent bonds on the surface introduces defects which will inevitably reduce the maximum potential for the filler to reinforce the composite. The process of covalent functionalisation destroys the regular sp^2 structure reducing the intrinsic properties of these fillers. Additionally, industry will only seek to use graphitic nanofillers with their existing infrastructure if the improvement in properties justifies the added cost. From a composites perspective, the covalent functionalisation strategy is not regarded as the optimal approach. Moreover, any covalent functionalisation will only add to the cost of an already very expensive nano-filler.

The non-covalent functionalisation strategy is regarded as a more optimal approach whereby there is no attachment of functional groups to the graphitic nanofiller surface which preserves the intrinsic properties. Polymers containing pyrene derivatives have been investigated for non-covalent functionalisation however, studies have been limited to solvent

based systems. This project seeks to develop a polymer based compatibiliser which can promote non-covalently, compatibility between graphitic nanofillers and the polymer matrix (using e.g. CH-π and π-π interactions) during melt mixing in the extruder.[2-5] To the best of my knowledge, there have been no investigations into the use of controlled living radical polymerisation techniques (RAFT and Cu(0)-mediated LRP), to synthesise polymers which are thermally stable for processing with PP in an extruder, designed to non-covalently functionalise MWCNTs and GNPs, through the use of either CH-π and/or π-π interactions. In addition, studies correlating the poly(acrylate) (compatibiliser) structure and architecture to the properties of the composite have not been performed extensively. It has however been known that long chain alkyl polyacrylates demonstrate high solubility within PP from the research by ICI ltd.

1.4 The research strategy

The main goal of this project was to study the fundamental characteristics of 1D and 2D graphitic nanomaterials when encapsulated within a polymer matrix, by way of example poly(propylene) (PP) and to understand the causes and effects of poor dispersion and weak interfacial adhesion between the nano-fillers and the PP matrix. Ultimately, a range of poly(acrylate)s were synthesised and studied with the aim of improving mechanical, electrical and thermal properties of PP. The effective stress transfer between filler and polymer and other properties of composites of polymers and CNTs/GNPs are very much governed by the extent of interfacial interaction between the polymer matrix and the filler and the use of poly(acrylate)s as non-covalent compatibilisers was explored to improve the interfacial interaction between both components.

In the first instance, the best possible methods to functionalise the surface of CNTs and GNPs were explored. Possible methods to achieve this are π-π stacking or polymer wrapping through CH–π adsorption. Another possibility is to synthesise diblock and triblock copolymers with one block binding with the filler and the other with the polymer matrix.[6, 7] For triblock copolymers, the centre block will position the polymer chain at the filler - PP matrix interface.[8] The polymer architecture was also assessed in terms of whether linear polymers, star shaped polymers or polymer brushes are the most effective compatibilisers for PP/CNT or PP/GNP composites.[9] Non-covalent functionalisation involved designing and synthesising a polymeric based compatibiliser that had three characteristics, 1) it non-covalently binds to the surface of the filler via different mechanisms, such as CH-π wrapping

and π-π stacking, 2) it prefers to reside at the interface between the filler and polymer matrix and, 3) it has good compatibility with the polymer matrix and for PP, it was able to co-crystallise with the crystal lamella of PP. Many studies have been carried out in the area of non-covalent functionalisation of CNTs and graphene for reinforcement of a polymer matrix prepared where the composite materials is prepared via melt mixing however, few have demonstrated highly dispersed systems with worthwhile increases in mechanical, electrical and thermal properties.[10, 11] The surface of the filler is comprised of sp^2 bonded carbon atoms with p-type orbitals pointing perpendicular to the surface of the filler. It is this feature that we are looking to use to bind the compatibiliser to via CH-π wrapping or π-π stacking.[12] Notwithstanding, the thermal stability of the polymeric compatibiliser must be sufficient such that it will not degrade during melt mixing with PP, typically (~200 °C).

Thermoplastics such as PP can ideally be blended with fillers when they are in the melt phase. Melt compounding using extrusion is an ideal method for blending functionalised fillers with PP to produce nanocomposites/blends that can also be injection moulded into standard shapes for characterisation such as dog bones for static mechanical analysis, rectangular bars for electrical and dynamic mechanical analysis (DMA) and disks for oscillatory rheology measurements. A further but central requirement is that any polymer bound to CNTs and GNPs should be thermally and mechanically stable during extrusion. Thermal stability is a key aspect of the thesis as any polymer synthesised by RAFT and Cu(0)-mediated methods must be thermally stable during extrusion with PP because, if the polymer degrades in the extruder then it will no longer be able to bind to the filler and reinforcement will not be realised.[13-16] It is known from the published literature that poly(lauryl acrylate) P[LA] is able to co-crystallise with PP due to its long chain hydrophobic alkyl side groups.[17]

1.5 Structure of thesis

The hypothesis for chapter 4 was to use P[LA] as a compatibiliser for CNTs and GNPs where it is anticipated that the polymer will ‘wrap’ via CH-π type binding mechanisms to the filler and where P[LA]s ability to co-crystallise the PP is a means of bridging interfacial incompatibility. P[LA] was synthesised using RAFT[18] and Cu(0)-mediated methods[19, 20] and subsequently characterised using TGA to investigate its thermal stability both independently and when absorbed onto the surface of MWCNTs.[13-15, 21-24] The

investigations into the thermal stability of P[LA] determined its suitability for extrusion with PP.

Chapter 5 investigated the potential for P[LA] to functionalise the surface of CNTs via CH-π polymer wrapping during melt mixing with PP via twin screw-extrusion. Blends of P[LA], MWCNTs and PP were produced including varying the P[LA] to MWCNT ratio of 1:1 and 4:1 to investigate the quantity of P[LA] required to absorb onto the surface of the MWCNTs. In addition, the MWCNT loading was varied from 0.01 wt% to 5 wt% to determine the percolation threshold and the change in percolation threshold with the addition of P[LA] loading.

Subsequently, chapter 6 investigated the application of P[LA] to non-covalently functionalise graphene nanoplatelets (GNPs) via melt-compounding with PP and the resulting composites were characterised. Mechanical, thermo-mechanical, thermal, rheological and crystallization properties were studied to effectively understand the behaviour of the P[LA]/GNP complex when dispersed in PP compared to un-functionalised GNPs.

Furthermore, chapter 7 studied the application of copolymers of P[LA] and 2-pheneyl ethyl acrylate[25] [P(2PEA)] to functionalise CNTs and GNPs. The copolymers were synthesised using Cu(0)-mediated LRP. As well as thermal stability, non-covalent π-π interactions between P[2PEA] and CNTs/GNPs were investigated and how changing the poly(acrylate) architecture (i.e. statistical or block copolymer) influences the non-covalent interactions. P[2PEA] was chosen as means of providing stronger π-π interactions with the filler surface compared to P[LA]. Electron microscopy, TGA, DSC, and Raman were employed to obtain evidence of the non-covalent interactions.

Finally, chapter 8 investigated the application of P[LA] and P[2PEA] copolymers and their composites with PP. Furthermore, the effect of the copolymers of P[LA] and P[2PEA] on the dispersion and therefore the mechanical, electrical, thermal, thermo-mechanical and rheological properties of their composites with MWCNTs/GNPs and PP was also investigated. The ratio of poly(acrylate) to filler concentration was fixed at a ratio of 4:1 and the filler loading was also fixed to 1 wt% to maintain the emphasis of the investigation on the poly(acrylate) structure.

1.6 Contribution to knowledge

The work conducted within this research project provides a significant contribution to knowledge in the field of polymer composite materials science. The research conducted is of importance to the scientific community and provides a benefit to society by developing new materials for important applications such as, light weighting, energy storage and conversion, as well as many others detailed in the literature review. The primary value from the research is from the design, synthesis, characterisation, analysis and evaluation of poly(acrylate)s and their composites with MWCNTs/GNPs and PP. It is important to understand the thermal stability of poly(acrylate)s (and therefore similar polymers produced using controlled living radical methods) and their suitability for melt mixing with PP (and therefore similar thermoplastics) during extrusion.

For many decades, extensive research has been conducted in the field of controlled living radical polymer synthesis and its fundamental polymerisation mechanisms. The studies have extended to use a broad range monomer types and structures. Such efforts have led to developments of polymer systems with ever increasing structures, architectures and behaviours. However, applications of such complex polymers in industry has been limited to small scale applications such as drug delivery. A lack of knowledge and understanding on the suitability of such polymer systems with existing polymer processing techniques including extrusion is limited and therefore, this research looks to fill the gap in the knowledge by determining the suitability of such polymer systems with existing polymer processing methods to expand their applications and develop new multifunctional products. It is unknown to which temperatures poly(acrylate)s are thermally stable to and by which thermal degradation mechanisms they follow when synthesised using controlled living radical polymerisation techniques including RAFT and Cu(0)-mediated LRP.

As well as understanding the thermal and thermomechanical properties of poly(acrylate) systems, the application of such polymers for non-covalently compatibilising MWCNTs and GNPs with PP has yet to have been explored. The challenge of overcoming the lack of compatibility between 1D and 2D graphitic materials with thermoplastic systems has been widely studied however, most of solutions in literature have focused on a covalent functionalisation approach to improving the thermodynamics of mixing. To date, the use of controlled living radical polymerisation polymers to non-covalently functionalise graphitic nanomaterials for blending with thermoplastics and the characterisation of the resulting

composites has not been explored. This project will study the CH-π non-covalent interactions of long chain hydrophobic P[LA] polymers with MWCNTs and GNPs and whether any evidence of polymer wrapping onto the surface of the graphitic nanofillers can be observed. Investigations were conducted into the potential of P[LA] to non-covalently functionalise MWCNTs and GNPs through the production of composites of P[LA], MWCNTs/GNPs and PP and to characterise the composites to determine the ability of P[LA] to improve the dispersion of the graphitic nanofillers. The synthesise and characterisation of copolymers of P[LA] and P[2PEA] was investigated and the use of poly(acrylate)s containing pendent aromatic groups to non-covalently (π-π) adsorbing onto the surface of the graphitic fillers was studied. In addition, investigations into the potential for homo and copolymers of P[LA] and P[2PEA] to improve the dispersion of composites of MWCNTs/GNPs and PP by characterising the properties of the composite were performed.

1.7 Aims and objectives

The **aims** of this project are to;

- Improve the interfacial adhesion between the surface of 1D and 2D graphitic fillers (MWCNTs and GNPs) and a polymer matrix (PP) without affecting the structure or altering the intrinsic properties of the fillers.
- Improve the dispersion and interfacial adhesion of MWCNTs and GNPs with PP using poly(acrylate)s synthesised using controlled living radical polymerisation techniques.
- Confirm the mechanism for non-covalent functionalisation of MWCNTs and GNPs with poly(acrylates).
- Prepare via melt mixing and characterise composites of poly(acrylate) functionalised MWCNTs/GNPs with PP.
- Correlate the structure and architecture of the poly(acrylate)s with the properties of their composites with MWCNTs/GNPs and PP to support the hypothesis of using controlled living radical polymers (CLRP) to effectively compatibilise graphitic nanofillers for composite applications.

The **objectives** of this project are;

- Characterise the purity, structure and size of MWCNTs and GNPs using XPS, Raman, SEM and TEM.
- Determine the thermal degradation mechanisms of poly(lauryl acrylate) P[LA] synthesised using RAFT and Cu(0)-mediated LRP using TGA, GPC, NMR and MS.
- Establish the presence of non-covalent (CH-π, polymer wrapping,) interactions between the P[LA] and MWCNTs/GNPs using TGA, Raman, SEM and TEM.
- Prepare and characterise homo and copolymers of P[LA] and P[2PEA] using Cu(0)-mediated LRP. Investigate the thermal stability of homo and copolymers of P[LA] and P[2PEA] using TGA.
- Establish the presence of non-covalent (CH-π and π-π,) interactions between copolymers of P[LA] and P[2PEA] and MWCNTs/GNPs using TGA, Raman, SEM and TEM.
- Prepare and characterise composites of poly(acrylate), MWCNTs/GNPs and PP to determine the consequences of adding poly(acrylate)s to composites of MWCNTs/GNPs and PP by evaluating their; mechanical properties (static tensile testing), electrical properties (DC electrical conductivity), thermo-mechanical properties (DMTA), rheological properties (oscillatory shear rheology), thermal properties (DSC) and morphological properties (SEM/TEM).

1.8 References

1. G. Pandey and E. T. Thostenson, *Polym. Rev.*, 2012, **52**, 355-416.
2. P. Bilalis, D. Katsigiannopoulos, A. Avgeropoulos and G. Sakellariou, *R. Soc. Chem. Adv.*, 2014, **4**, 2911-2934.
3. V. Georgakilas, M. Otyepka, A. B. Bourlinos, V. Chandra, N. Kim, K. C. Kemp, P. Hobza, R. Zboril and K. S. Kim, *Chem. Rev.*, 2012, **112**, 6156-6214.
4. S. Meuer, L. Braun and R. Zentel, *Macromol. Chem. Phys.*, 2009, **210**, 1528-1535.
5. T. Fujigaya and N. Nakashima, *Sci. Tech. Adv. Mater.*, 2015, **16**, 1-21.
6. J. Y. T. Chong, D. J. Keddie, A. Postma, X. Mulet, B. J. Boyd and C. J. Drummond, *Colloids Surf., A*, 2015, **470**, 60-69.
7. J. Y. T. Chong, X. Mulet, A. Postma, D. J. Keddie, L. J. Waddington, B. J. Boyd and C. J. Drummond, *Soft Matter*, 2014, **10**, 6666-6676.

8. M. J. Nasrullah, A. Vora and D. C. Webster, *Macromol. Chem. Phys.*, 2011, **212**, 539-549.
9. L. P. Yang and C. Y. Pan, *Macromol. Chem. Phys.*, 2008, **209**, 783-793.
10. X. L. Xie, Y. W. Mai and X. P. Zhou, *Mater. Sci. Eng. R-Rep.*, 2005, **49**, 89-112.
11. P. C. Ma, N. A. Siddiqui, G. Marom and J. K. Kim, *Compos. Part A*, 2010, **41**, 1345-1367.
12. B. Yang, Y. Zhao, X. Ren, X. Y. Zhang, C. K. Fu, Y. L. Zhang, Y. Wei and L. Tao, *Polym. Chem.*, 2015, **6**, 509-513.
13. O. Altintas, K. Riazi, R. Lee, C. Y. Lin, M. L. Coote, M. Wilhelm and C. Barner-Kowollik, *Macromolecules*, 2013, **46**, 8079-8091.
14. O. Altintas, M. Abbasi, K. Riazi, A. S. Goldmann, N. Dingenouts, M. Wilhelm and C. Barner-Kowollik, *Polym. Chem.*, 2014, **5**, 5009-5019.
15. B. Chong, G. Moad, E. Rizzardo, M. Skidmore and S. H. Thang, *Aust. J. Chem.*, 2006, **59**, 755-762.
16. E. V. Chernikova, A. V. Plutalova, E. S. Garina and D. V. Vishnevetsky, *Polym. Chem.*, 2016, **7**, 3622-3632.
17. G. Moad, G. Li, R. Pfaendner, A. Postma, E. Rizzardo, S. Thang and H. Wermter, in *Controlled/Living Radical Polymerization*, ed. K. Matyjaszewski, American Chemical Society, 2006, vol. 944, ch. 35, pp. 514-532.
18. K. L. Chen, Y. H. Zhao and X. Y. Yuan, *Chem. Res. Chin. Univ.*, 2014, **30**, 339-342.
19. A. Anastasaki, C. Waldron, V. Nikolaou, P. Wilson, R. McHale, T. Smith and D. M. Haddleton, *Polym. Chem.*, 2013, **4**, 4113-4119.
20. A. Anastasaki, V. Nikolaou, A. Simula, J. Godfrey, M. X. Li, G. Nurumbetov, P. Wilson and D. M. Haddleton, *Macromolecules*, 2014, **47**, 3852-3859.
21. O. Altintas, T. Josse, M. Abbasi, J. De Winter, V. Trouillet, P. Gerbaux, M. Wilhelm and C. Barner-Kowollik, *Polym. Chem.*, 2015, **6**, 2854-2868.
22. O. Altintas, T. Josse, J. De Winter, N. M. Matsumoto, P. Gerbaux, M. Wilhelm and C. Barner-Kowollik, *Polym. Chem.*, 2015, **6**, 6931-6935.
23. H. Willcock and R. K. O'Reilly, *Polym. Chem.*, 2010, **1**, 149-157.
24. A. Postma, T. P. Davis, G. Moad and M. S. O'Shea, *Macromolecules*, 2005, **38**, 5371-5374.
25. U. Senthilkumar, K. Ganesan and B. S. R. Reddy, *J. Polym. Res.*, 2003, **10**, 21-29.

Chapter 2 Literature Review

2.1 Introduction

A composite is a material made from two or more components. Traditional composite materials such as steel reinforced concrete and fibre-filled resins have revolutionised modern society with new materials, new products and an ever-increasing number of applications. However, there has been greater demand for newer materials with improved properties.[1] Multifunctional polymer composites have received a great deal of attention recently due to their exceptional properties.[2] Nanometre scale reinforcing particles such as; clay silicates, calcium carbonates, carbon nanotubes (CNTs) and graphene have excited great interest as they can be used as fillers in polymer matrices.[3] Conventional micro fillers such as mica, talc, fibre glass, metal powders and carbon black have been incorporated into polymer matrices however but, large volume fractions (20-60 wt%) are required to achieve improved mechanical, electrical and thermal properties.[4] Such large quantities of filler prevent efficient processing and are not cost effective.[3] In contrast, theoretically CNTs and graphene are able to achieve similar if not better performance with only a fraction of the loading compared to traditional fillers.

2.2 Carbon based fillers

Carbon is one of the most versatile naturally occurring elements available. Its ability to form strong and stable covalent bonds with other elements, especially with itself, makes it the backbone for most modern materials. Its place as a group fourteen, row two element gives carbon its special properties as it can not only form strong covalent bonds but it can form four of them.[5] The presence of both sp^3 and sp^2 hybridised bonds in many carbon-based materials provide them with unique mechanical, electrical and thermal properties. Carbon black (CB) consists of spherical aggregated particles with diameters ranging from tens to hundreds of nanometres.[4] CB is a widely used conductive filler due to its high supply, low density and cost and good electrical properties. However, impractical quantities of carbon black are required to achieve electrical percolation in polymer composites for example; ~11 vol% for HDPE/CB, ~20 wt% for PVC/CB and ~20 wt% for poly(urethane)/CB.[4] CNTs and graphene are considered very interesting materials due to the fact they have at least one dimension on the nanometre scale and therefore, their properties can be understood using quantum mechanical theory.[6]

2.2.1 Carbon nanotubes (CNTs)

Since the observation made over two decades ago by Iijima[7], research interest in CNTs has grown exponentially. CNTs have appeared as a very encouraging material in a variety of research fields from polymer composites to biotechnology and energy storage.[8] CNTs have found potential applications in electronics, sensors, energy storage and conversion devices as a result of their exceptional electrical and thermal conductivity properties.[8, 9] Applications include the tips of atomic force microscopes (AFM) which require sharp and stiff materials, as well as CNT fibres for artificial muscles controlled using low voltages.[9] In addition, CNTs have been explored as electrode materials in organic light emitting diodes (OLED's), fuel cells, super-capacitors, dye-sensitized solar cells, additives for lithium ion batteries and field effect transistors.[9] Regardless of the application proposed, they are almost always used by inclusion in a polymer.[9]

CNTs were first synthesised using an arc-discharge evaporation method. This method involves growing needle like, tubular carbon at the negative end of an electrode. The size of the CNTs first synthesised ranged from a few nanometres in diameter to a few tens of nanometres in diameter and consisted of multiple layers of concentric graphene cylinders now known as multi-walled carbon nanotubes (MWCNTs).[4, 7]

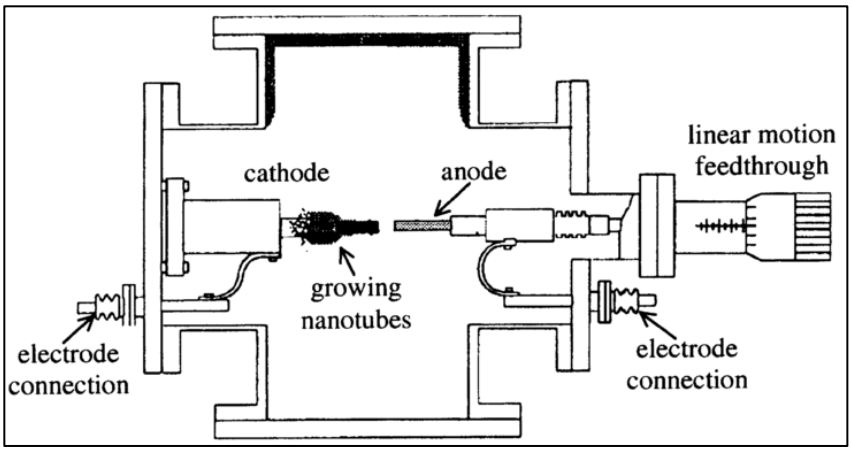

Figure 2.1 Schematic illustration of the arc-discharge method for the production of CNTs.[10]

The arc-discharge method (figure 2.1) involves using an anode and cathode, each made of very high purity graphite electrodes enclosed under a helium atmosphere. A very

high voltage is applied and a stable arc is formed between the two electrodes. The anode graphite then degrades and the CNTs grow on the surface of the cathode. The distance between the anode and cathode are kept constant. The size of the electrodes and doping them with metallic catalyst particles can be used to control the morphology of the CNTs produced.[10] The process produces a mixture of graphitic components contaminated with catalytic metals and require purification.[9]

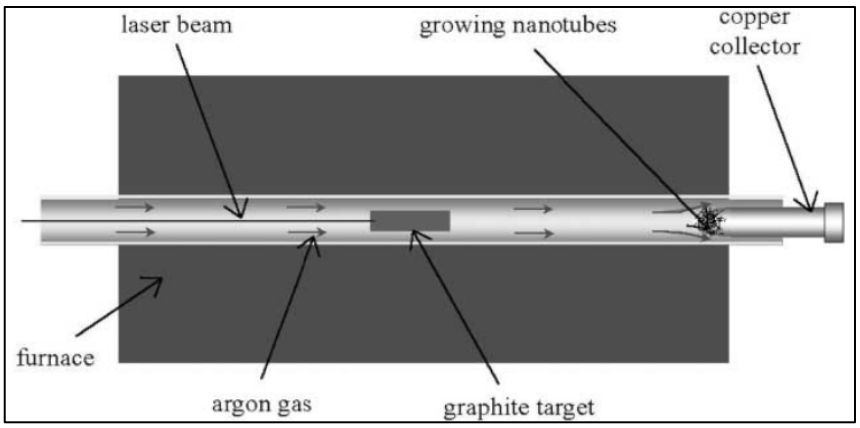

Figure 2.2 Schematic illustration of the laser ablation method for the production of CNTs.[10]

Laser ablation (figure 2.2) involves using a pulsed laser to vaporise graphite in a controlled atmosphere oven at a temperature close to 1200 °C under inert gas.[9] The method also allows the morphology of the CNTs to be changed by doping the graphite target with metals. Using cobalt and nickel doped graphite produces SWCNTs.[10] However, laser ablation is very expensive and not suitable for large scale production.[9] CNTs can also be synthesised from the thermal decomposition of hydrocarbon species on a metal substrate.[9] They are then graphitised by heat treatment and the CNTs are subsequently grown directly using chemical vapour deposition (CVD). However, this method also produces other forms of graphitic carbon such as soot and fullerenes.[7] It is therefore important to consider the purity of the CNTs that are used because the presence of other forms of carbon can influence the compatibilisation chemistry between the CNT and the polymer matrix. A significant advantage of using CVD over other techniques is that the technique is a continuous process because the carbon source can be continually fed in as a gas. However, since hydrocarbons polarise readily on surfaces heated above 600 ^{o}C, this causes significant formation of amorphous carbon deposits and therefore, further purification is required. In contrast to other

methods, CVD can be used to synthesise aligned CNTs with controlled tube diameter and length ranges. This is carried out by using plasma-enhanced CVD (PECVD).[2,11] Gas-phase catalytic growth from carbon monoxide can also be used to synthesise CNTs. High pressure conversion of carbon monoxide (HiPco) works well for the synthesis of SWCNTs with reports showing high purity and yields at 1200 °C and 10 atm.[10] In summary, arc-discharge and laser ablation are not effective methods to synthesise CNTs as they have limitations with regards to scale-up. Only a small amount of graphite can be used each time. For CNTs to become more commercially available, they should be synthesised in large quantities with relatively low cost. As all the above methods are unable to produce defect free CNTs, it is important to choose a method that produces CNTs with a relatively low number of defects and impurities. Subsequent purification steps can be costly and therefore, the use of CVD is presently the most cost-effective solution because gas-phase processes produce CNTs with fewer impurities and scale-up is relatively not too costly.[10, 12, 13]

Many researchers have reported results showing the unique and outstanding physical, optical, thermal and mechanical properties of the tubular structure of carbon.[8] A selection of unique properties include exceptional electrical and thermal conductivity as well as superior mechanical stiffness, high charge carrying density and tensile strength.[3, 8-10] It is not surprising so much time and effort has been applied to trying to realise the potential of CNTs when they are thermally stable up to 2800 °C (in a vacuum) along with thermal conductivity twice that of diamond and an electron mobility 1000 times higher than copper, in their purest form.[9, 10] The excellent electronic properties can be controlled to be either metallic or semi-conducting by changing chiral symmetry, with metallic SWCNTs calculated to have electric current densities in the region of 4 x 10^9 A cm^{-2}, over 1000 times higher than metals.[9] SWCNTs have also shown to have electron mobilities in the region of ~100,000 cm^2 V^{-1} s^{-1} , higher than silicon.[9] MWCNTs have shown to have electrical conductivities in the region of 10^5 S cm^{-1} and current densities of 10^8 A cm^{-2}, lower than SWCNTs.[9] In addition, the calculated conductance of an average nanotube is ~10 $k\Omega^{-1}$.[14] Values for the thermal conductivity of CNTs have been quoted to be in the region of 3000 – 3500 W m^{-1} K^{-1} axially which is an order of magnitude greater than copper, 385 $Wm^{-1}K^{-1}$.[9, 15] Values for thermally conductivity at RT of SWCNTs are ~ 3500 $Wm^{-1}K^{-1}$ with MWCNTs achieving ~3000 $Wm^{-1}K^{-1}$. Crystalline 'ropes' of SWCNTs achieved ~1750-5800 $Wm^{-1}K^{-1}$. The values reported were in excess of the best bulk crystalline thermal conductor, diamond, reported to be ~1000-

2200 $Wm^{-1}K^{-1}$. Indeed, molecular dynamics simulations have reported values of up to ~6600 Wm^{-1} K^{-1} are possible for an isolated CNT at RT.[16]

Spectroscopy characterisation show CNTs adsorb from the far ultra-violet (200 nm) to the far infrared 200 μm resulting in the CNTs appearing black.[9] Mechanical simulations of CNTs show them to be very resilient and can sustain extreme strain with very little evidence of brittleness or plasticity. CNTs subjected to plastic deformation under tensile stress, are able to undergo a Stone-Wales transformation where the hexagonal structure transforms into two pentagons and two heptagons.[10, 17] Theoretical and experimental studies on MWCNTs and graphene have shown they have an extremely high elastic modulus, with values in the order of 1 TPa which is comparable to other allotropes of carbon such as diamond (1.2 TPa) and fracture strains of ~5-10%.[4, 14] MWCNTs are strong along in the axial direction with Young's modulus in the range of 270-950 GPa and tensile strength in the range of 11-63 GPa, depending on the type and structure of the MWCNT.[9] Additionally, examination of the literature has also shown that tensile strengths 10-100 times higher than the strongest type of steel have been reported for CNTs.[10, 18] MWCNTs have also shown to have a toughness of ~770 Jg^{-1}.[14] For SWCNTs, the mechanical properties are similar with Young's moduli between ~0.32-1.47 TPa and, tensile strengths in the range of 10-52 GPa and toughness of ~770 Jg^{-1}.[14]

CNTs have a large aspect ratio (typically in the range of 100-1000) which gives CNTs a very high effective surface area, ideal for reinforcement. The cylindrical hexagonal arrangement of carbon atoms bonded in a sp^2 framework gives the CNTs their extremely high tensile moduli, strength and toughness.[3, 7-9, 19] Due to the fact that each carbon atom is bonded to three other carbon atoms, this allows the fourth, non-bonding electron free to travel in the delocalised network of p-type orbitals which gives the CNTs their high electrical conductivity and high electron mobility.[20] The structure of CNTs is somewhat similar to that of graphene that has been rolled into a tubular structure.[9, 21] The surface of CNTs consist of a 2D sheet of carbon atoms hexagonally arranged where each carbon atom is bonded to 3 other carbon atoms with a bond angle of 120°. In comparison, for diamond each carbon atom is bonded to four other carbon atoms in a tetrahedral arrangement with a bond angle of 109°. CNTs can be produced as single-walled (SWCNTs) or multi-walled (MWCNTs) (figure 2.3) where multiple tubes are inside each other.[9] The atomic structure of CNTs greatly depends on the arrangement of the hexagons and this can be described in terms of chirality.[10]

Diameters of MWCNTs are typically in the range of 10 to 50 nanometres with lengths in the order of a few microns.[4] The concentric cylinders within MWCNTs have a spacing of ~0.34 nm between adjacent layers.[22] In general, the cost of MWCNTs is lower than that of SWCNTs due to production challenges.[21]

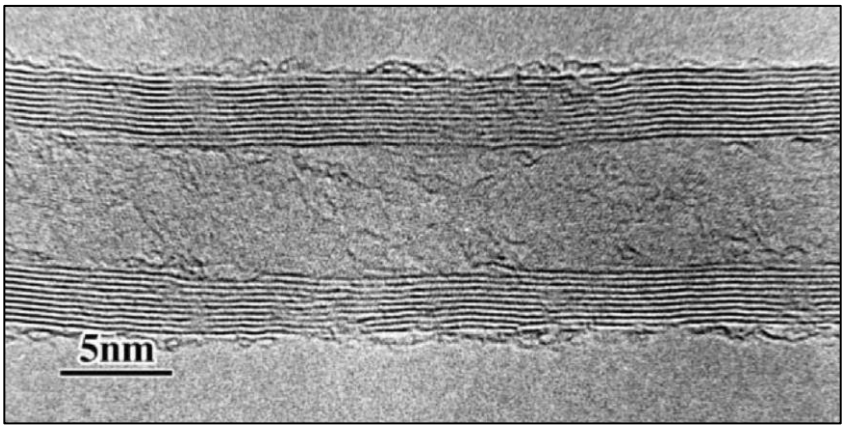

Figure 2.3 TEM micrograph of a MWCNT.[10]

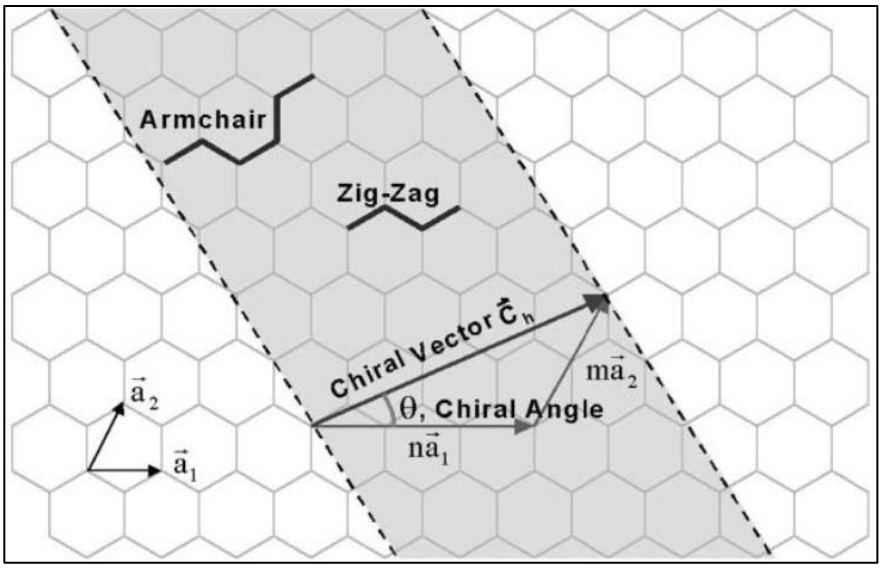

Figure 2.4 Diagram showing the different ways a graphene sheet can rolled into a CNT.[10]

Figure 2.4 shows how the chiral angle, θ, and the chiral vector, C_h, determines which type of CNT is present.[23] When the chiral angle is at its minimum (0°), the structure is referred to as 'zig-zag' and when the angle is at its maximum (30°), the structure is referred to as 'armchair'. C_h is used to characterise the CNT structure and is denoted using the vector

notation (n, m), where n denotes the number of horizontal hexagons and m denotes the number of vertical hexagons in the repeat unit. In the case of zig-zag, the CNT has a roll-up vector of (n, 0) and for the arm-chair structure, the roll-up vector is (n, n).[23] The chiral vector also determines the diameter of the nanotube.[10] It is important to consider the chirality of the CNT used as this determines its specific properties.[23] The mechanical properties of CNTs are not greatly affected by chirality but, the electronic properties of CNTs are strongly dependant on the orientation of the hexagons within the CNT. This is because, if the all the hexagons are arranged in a highly symmetrical behaviour, this makes it easier for the free electrons to tunnel between neighbouring carbon atoms. In turn, the electron mobility increases and the CNTs behave in a metallic way. This gives CNTs their unique properties of being able to be both metallic and semi-conducting depending on their symmetry.[10] The chiral indices (n, m) can be used to predict the properties of CNTs, for example, a SWCNT is metallic if its chiral index ($2n+m$) is divisible by 3. If not, it is considered a semi-conductor.[23]

The properties of CNTs depend on the arrangement of the sheets (how they are rolled together), the diameter, the length of the tube and their structure. All CNTs synthesised using current methods, cannot be produced completely defect free. Due to the methods used to manufacture CNTs, all have defects and this can greatly change the morphology of the nanotube. In addition to defects, the number of walls in the CNT greatly affects its morphology.[24] It is not only important to synthesise high purity, low defect CNTs but, it is also important to characterise them effectively. However, due to their nano-scale features, it can be very challenging to obtain direct property measurements. Atomic force microscopy (AFM) has been used to directly measure the stiffness and strength of the CNTs. AFM showed MWCNTs to have a bending elastic modulus of 1.26 TPa and an average bending strength of 14.2 ± 8 GPa. Tensile measurements have also been carried out on MWCNTs by attaching a single nanotube between two opposing AFM tips and loading the nanotube under tension. The outer most tube failed first followed by the inner tubes being pulled out in a ‘sword and sheath’ or ‘telescopic’ failure type mechanism (figure 2.5). The results showed the outer most wall of the CNT to have a tensile strength of 10-60 GPa and an elastic modulus of 270-950 GPa. Interestingly, ropes of MWCNTs have a tensile strength and modulus of 3.6 and 450 GPa respectively, which shows the presence of defects from the CVD synthesis process has a significant influence on the strength of CNTs.[10, 19, 25]

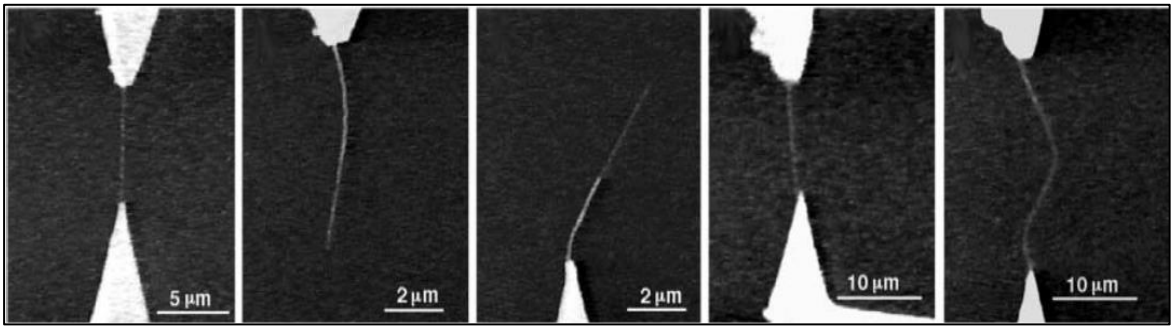

Figure 2.5 AFM micrographs showing 'sword and sheath' fracture of a MWCNT.[10]

In addition to the use of AFM, transmission electron microscopy (TEM) and scanning transmission electron microscopy (STEM) are excellent tools for characterising CNTs. TEM provides high special resolution, morphology, atomic/crystallographic structure as well as qualitative and quantitative compositional analysis using energy dispersive X-ray spectroscopy (EDS) and electron energy loss spectroscopy (EELS).[26] EDS can provide data on elemental composition such as the carbon to oxygen ratio and presence of metal catalysts. Where EDS provides elemental composition, X-ray photoelectron spectroscopy (XPS) can provide quantitative data on the type of bonding present such as, type of oxygen functional groups present and ratio of sp^2 to sp^3 bonding in CNTs.[27] Electron energy loss spectroscopy (EELS) is an analytical technique coupled with STEM, which measures the kinetic energy change (loss) after the electrons have interacted with the nuclei of the sample. EELS can provide structural and chemical information about a material with atomic level spatial resolution with energy resolutions of 1 eV. Analysis of the inner-shell ionization edges provide details on the fine structure of materials and hence can be used to distinguish the non-covalent functionalisation of polymers onto the surface of the filler, for example by analysing differences in bond character.[28, 29]

2.2.2 Graphene

Since the awarding of the Nobel Prize in physics in 2010 to Professors Andre Geim and Konstantin Novoselov[30, 31], the research on graphene and graphene related materials has accelerated exponentially. Research on graphene has shown it to exhibit exceptional electrical, mechanical, thermal and optical properties and has excited the scientific community with its potential applications.[30, 32] Graphene is a planar two dimensional material made of a hexagonally arranged monolayer of carbon atoms covalently bonded

together in a sp^2 structure.[9] It is a single layer of graphite and a single atom thick (less than 1 nm) of carbon atoms in a honeycomb lattice.[9, 16] This can be considered as a building block for all other types of graphitic materials with other dimensionalities. Fullerenes which are considered 'zero' dimensional (0D), can be produced by wrapping graphene into a ball, CNTs which are considered as 'one' dimensional (1D) can be produced by wrapping graphene into a tubular structure and graphite which is considered 'three' dimensional (3D) can be produced by stacking graphene sheets (2D) together (figure 2.6).[30] Initially, the hypothesis was that the isolation of mono-layer graphene was not possible as calculations suggested the structure was thermodynamically unstable as the sheets would roll up into scrolls. In fact, this hypothesis is still under debate as the majority of commercially available graphene is crumpled and rolled-up and not perfectly planar and flat.[32]

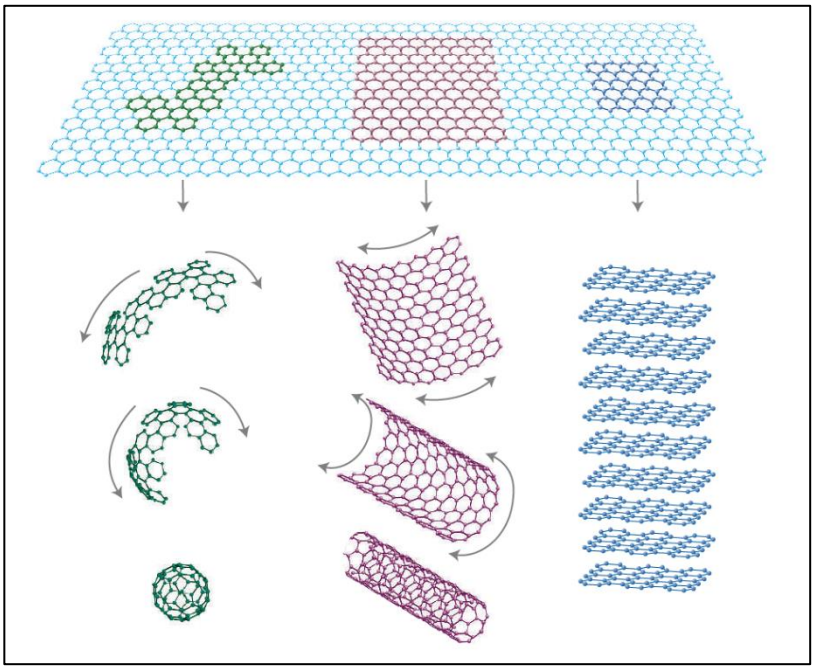

Figure 2.6 A schematic showing the 2D structure of graphene and its ability to be wrapped into 0D fullerenes, 1D CNTs and 3D graphite.[30]

The chiral index notation (*n*,*m*) can also be applied to graphene as well as CNTs when defining the sheet edge structure. Upon the unzipping of a SWCNT, the chirality of the SWCNT inversely correlates to the chirality of the graphene sheet edge. A SWCNT which has an armchair chirality will produce a graphene nano-ribbon (GNR) with zigzag edges and vice versa. However, after subjecting the GNR to joule heating the sheet edges

become achiral.[23] Mono-layer graphene is very difficult to produce on sufficient scales for use in (nano)composites, especially defect free graphene.[33] Currently, completely monolayer defect free graphene is produced in very small quantities at extremely high cost and reserved only for electronic applications. Typical methods used for the synthesis of graphene include; micro-mechanical cleavage, arc-discharge, CVD and reduction of graphene oxide.[9] Other methods include ultra-sonication of graphite powder in solvent and unzipping of CNTs to produce nano-ribbons.[9] Defect free mono-layer graphene is generally produced using chemical vapour deposition (CVD) on metal substrates such as copper using methane/H_2 mixtures.[32] The process involves decomposition of hydrocarbons in the presence of catalytic metal as substrate layers under high temperature and high vacuum. In the case of Nickel(Ni), graphitic crystals form instead of graphene which can be overcome by depositing less than 300 nm thick layers of Ni on SiO_2/Si substrates.[32] Graphene can also be synthesised by thermal degradation of silicon carbide (SiC) during CVD.[30] The methods allows the possibility of producing macroscopic sized graphene sheets through epitaxial growth of thin graphitic films on a 6H-SiC substrate.[9, 32] Mono-layer graphene is not suitable for use in composites due to high cost. Hence, multi- or possible few-layer graphene is preferred for composite applications as it is produced by more cost effective means such as high shear exfoliation of graphite flakes.[34] The thinner forms of graphite are known as graphene nanoplatelets (GNPs). The definition of GNPs covers all types graphene that ranges from 100 nm thick to few layer graphene (< 10 layers).[32] Coleman *et al.* undertook large-scale exfoliation as means of producing high volumes of graphene for composite applications. They used water-surfactant solutions to disperse and exfoliate graphite during high shear exfoliation.[32] They found graphite can be exfoliated when the local shear rate surpasses the critical value of ~10^4 s^{-1}.[34] Arc-discharge evaporation of graphite can be used to generally produce, bi-layer, tri-layer and multi-layer graphene. The process is ideal for electronic applications where boron and nitrogen can be used during the synthesis to dope the graphene sheets during production.[9] An alternative method for producing defect free mono-layer graphene is to use micro-mechanical cleaving of bulk graphite.[32] The process involves attaching scotch adhesive tape to a polished graphite surface and repeated peeling of a single layer of graphene. The process requires highly orientated pyrolytic graphite or high quality natural graphite.[32] The limitations with such an approach are that only a very small percentage of the flakes lifted would be single layer and the process is not practical for scale up. However, the method produces high quality graphene crystallites which are difficult to

achieve with other techniques.[9, 30] Liquid phase exfoliation has also been employed as a means of preparing graphene through the use of vigorous mechanical stirring in solvent and high power ultrasonication.[32] The use of organic solvents such as dimethyl formamide (DMF) and *N*-methylpyrrolidone (NMP) along with ultrasonication and purification produced >50 % monolayer suspensions of graphene. The material contained minimal defects and low levels of oxidation however, the sheets were relatively small with the lateral dimensions no greater than a few microns.[32] Typically, chemical exfoliation of graphite is used to separate the graphene sheets. Hummer's method involves the use of acid treatment (HNO_3/H_2O_2 and HNO_3/H_2SO_4) to introduce oxygen based functional groups between the layers to produce graphene oxide (GO). After exfoliation, the GO would be reduced to graphene by means of reduction, typically involving hydrazine.[35] Chemical exfoliation can result in intercalated graphene where the graphene layers are separated by intercalated atoms between the atomic planes where each graphene sheet is considered as an isolated layer in a 3D matrix.[30] The method is ideal for large scale synthesis of graphene however, the quality of graphene produced is poor as the graphene has a varied layer distribution and significant number of defects.[9] The GO produced by chemical exfoliation is heavily oxygenated and bears hydroxyl and epoxide groups on the basal planes as well as carbonyl and carboxyl groups on the sheet edges.

As well as graphene sheets, graphene nano-ribbons (GNRs) can also be produced by the 'unzipping' of MWCNTs by either oxidation or argon plasma etching. The technique produces high quality, well-defined graphene shapes which are suitable for a variety of applications.[32] GNRs are graphene strips with widths <50 nm and can considered as unzipped SWCNTs. GNRs can be either metallic or semi-conducting depending on their edge structure and width.[23] The properties of graphene are dependent on the number of layers in each flake. The electronic properties are determined by the number of layers and ten is considered the transition from graphene to graphite in terms of electronic properties.[30] Mono-layer and bi-layer graphene are considered to be zero-band gap semiconductors.[36] Graphene has shown to have exceptional charge carrying mobility.[32] The charge carriers have shown to have concentrations, n as high as 10^{13} cm^{-2} and mobilities, μ can exceed 15,000 cm^2 V^{-1} s^{-1} at RT, along with current densities six orders of magnitude higher than copper.[9, 30] In addition, studies have shown graphene charge carriers to exhibit zero effective mass and travel micron distances without being scattered.[32] Single layer graphene has low-

lying electrons causing it to behave like massless relativistic Dirac fermions which gives rise to unique phenomena such as the quantum spin Hall effect, suppression of weak localisation, deviation from adiabatic Born-Oppenheimer approximation and enhanced Coulomb interaction.[16] Graphene exhibits unusual energy dissipation relation giving it exceptional thermal properties with thermal conductivities through phononic transport measured to be in the region ~5,300 $Wm^{-1}K^{-1}$, greater than other highly conductive materials such as CNTs, copper and gold.[1, 9, 15, 16]

Mono-layer graphene has shown to have excellent mechanical properties with a Young's modulus in the region of ~1100 GPa and tensile strength of 130 GPa.[9] Furthermore, graphene is impermeable to gases such as oxygen.[1, 32] Characterisation of graphene typically involves the utilisation of a range of techniques, including high-resolution transmission electron microscopy (HR-TEM) and atomic force microscopy (AFM) which can determine the number of layers in a graphene flake. AFM is the considered useful when characterising graphene with typical resolutions of ~30 nm (due to convolution) however, HR-TEM provides resolutions as high as ~0.2 nm as the interatomic spacing in graphite is 0.335 nm.[32] However, for graphene flakes less than ~ 5 Å thick, differentiating between mono-layer and bi-layer graphene becomes increasing challenging.[30] Graphene absorbance is independent of wavelength with monolayer graphene absorbing ~2.3% of visible light.[32] Such optical activity enables characterisation of inter-atomic layers by HR-TEM. However, a limitation of HR-TEM is that for few-layer graphene samples, carbon becomes optically transparent when in focus and sufficient contrast with the substrate can be difficult to obtain. As a possible solution, ellipsometry can be used to characterise such samples whereby the change in dielectric function of plane polarised light can distinguish between individual graphene layers.[32] Wide-angle X-ray scattering (WAXS) of graphene can also be used to characterise graphene layers. Graphite has a characteristic sharp peak (002) Bragg reflection at 2θ = ~26 ° (Cu-K_α, d = 0.154 nm). As the number of layers decreases, the peak becomes broader and the Scherrer formula describes such a relationship.[32] As well as characterising the number of layers present in a graphene sample, the surface area is also a critical property of the material. Brunauer-Emmett-Teller (BET) theory is used to determine the surface area of materials by measuring the physical gas adsorption on the surface. Monolayer graphene has been shown to have a surface area of ~2630 m^2/g and the surface area decreases as the number of layers increase.[32] Raman spectroscopy is widely used to characterise the purity of

graphene and CNTs by determining the number of defects present in the material. Carbon-carbon bonds exhibit strong Raman scattering and therefore, it's possible to use Raman to differentiate between mono-layer, bi-layer and tri-layer graphene. The Raman spectrum of graphene contains three characteristic peaks, *D*, *G* and *G′*. The *D* band (~1350 cm^{-1}) is as a result of inelastic scattering of phonons caused by a disorder or defect present in the graphene, for example, dangling bonds on sheet edges. The *G* band (~1580 cm^{-1}) is associated with the tangential in-plane vibrational stretching mode of the carbon-carbon bond. The *G′* band (~2690 cm^{-1}) peak is a second order overtone of the in-plane vibration of the *D* band. Raman can determine the quality of graphene by taking the ratio between the *D* band and the *G* band intensities.[32, 37, 38] Nano-indention is a method of directly determining the mechanical properties of graphene by suspending a graphene sample over a hole of 1.0-1.5 μm in diameter on a silicon substrate and applying a force by means of an AFM tip.[32]

2.3 Composites of Polymers and nanostructured fillers (Nanocomposites)

In order to utilise the outstanding properties of CNTs and graphene, one of the potential applications is their incorporation in to polymer matrices to produce composite materials where at least one component has nanoscale structural features.[1, 9] By incorporating 1D and 2D graphitic fillers into polymers matrices, it is possible to translate the exceptional properties these fillers possess, in part, to the polymer matrix. The possibility of producing ultra-high strength, electrically and thermally conducting polymer nanocomposites has led to intense research in the growing field with the number of potential applications for such materials growing.[2, 9] In particular, the possibility of significantly enhancing the mechanical properties and electrical/thermal conductivity of a polymer matrix using a small addition of filler, offer scope for developing new and interesting composite materials.[10, 21] As a consequence of the exceptional properties available, it has long been considered to use them as functional fillers to reinforce commodity and engineering polymers, such as poly(propylene) (PP), poly(ethylene) (PE), poly(ethylene terephthalate) (PET) and poly(ether ether ketone) (PEEK). It is anticipated that the unique mechanical properties of the fillers could be transferred to a matrix that can melt processed then an entirely new class of light weight, super-strong, advanced composites could be produced. There is huge demand for strong, lightweight materials with high electrical and/or thermal conductivity.[15] The applications of polymeric materials could then be extended to; electromagnetic shielding, energy storage and harvesting as well as biocomposites where load bearing was a

concern.[21] However, to realise the potential application of polymer nanocomposites, the interactions between the filler and the polymer matrix must be fully understood.[9] Various products containing graphene composites have already become commercially available, such as in high end sporting goods like tennis rackets and golf clubs which make use of increased strength with a reduction in weight. However, in both instances it has been reported that no property improvements were achieved and that the manufacturers simply added graphene for public relations (PR) purposes. In addition, MWCNTs have been used in electrostatic-discharge components to enhance the electrical conductivity of polymer matrices,[9, 39, 40] and in a range of automotive applications where anti-static properties are required for fuel transmission, e.g. fuel pipes.

To utilise the outstanding properties of CNTs and graphene, they first must be uniformly and homogeneously dispersed and distributed within a polymer matrix.[1] The typical industrially relevant method for dispersion within polymer matrices is melt-compounding however, other methods have also been studied, such as melt spinning, solution mixing, ultrasonication and *in-situ* polymerisation.[21] The interface between the filler surface and the polymer matrix is very important because, a strong adhesive interaction between the two components will produce the composite with the best mechanical and electrical properties,[9] where the former requires effective stress transfer at the interface. The choice of mixing method is largely dependent on the properties of the polymer such as whether to use solution mixing in a solvent or melt-mixing in an extruder (solvent-free). Melt-mixing is preferred by industry as it does not require the use of environmentally harmful solvents and the polymers can be processed in a continuous processes.[9, 41]

Many factors must be considered so optimal properties of the nanocomposite can be attained, such as filler volume fraction, method and extent of dispersion in the polymer matrix, filler-polymer interactions and type of polymer matrix used.[3] It has been shown that by adding a small amount of CNTs to poly(styrene) (PS) (1 wt%), the tensile strength of PS can increase by 25% and the elastic stiffness by 40% relative to the unfilled polymer. Figure 2.7 shows a transmission electron micrograph (TEM) of a CNT/poly(styrene) film and the mechanism of fracture when subjected to tensile stress. The CNTs are pulled out of the film. The results clearly showed how CNTs can reinforce the PS matrix however, to achieve optimum strength and stiffness, strong interfacial adhesion between CNTs and the polymer matrix is required.[10]

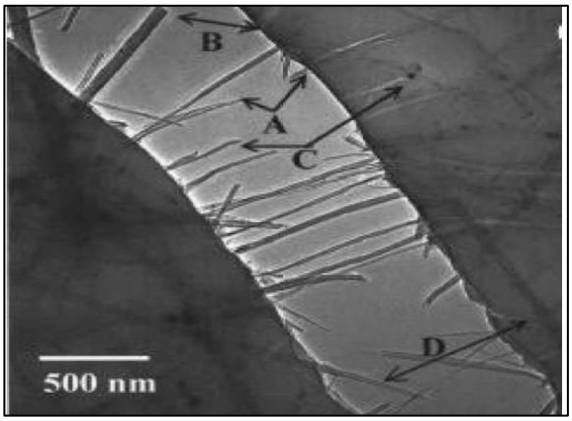

Figure 2.7 TEM micrograph of a fractured CNT/PS film.[10]

McNally *et al*. prepared composites of poly(ethylene) PE and MWCNTs using melt compounding. Exhaustive examination using microscopy across length scales and WAXD indicated a well dispersed system but some agglomerates of MWCNTs were still present. Raman spectroscopy showed an up-shift of 17 cm^{-1} of the *G*-band and electrical conductivity increased by 16 orders of magnitude (from 10^{-20} to 10^{-4} S cm^{-1}) on addition of 10 wt% MWCNT to PE however, percolation was observed at 7.5 wt%. A rheological percolation was achieved at 7.5 wt% as determined from oscillatory rheological measurements confirming the presence of an interconnected nanotube network structure resulting in 'pseudo-solid' like behaviour observed by increase in storage modulus (G').[42]

Various composites of CNTs and epoxies have been produced using the solution mixing method. The incorporation of MWCNTs into an epoxy resin resulted in an increase in tensile strength of 35% compared to neat epoxy.[9] Addition of SWCNTs to the epoxy resulted in an increase in Young's modulus of 50% and tensile strength of 20% relative to neat epoxy resin. In addition to the use of solution mixing, composites of epoxy with aligned CNTs have been produced which showed Young's modulus and tensile strength to increase by 716% and 160% respectively, compared to neat epoxy in the direction of the aligned CNTs. Without doubt, the incorporation of CNTs leads to an improvement in mechanical properties however, the challenge is to uniformly disperse and align the CNTs as this leads to the greatest improvement in composite properties.[9] In the case of composites of epoxy and CNTs, reports have shown percolation to have been achieved at loadings as low as 0.005 wt% CNTs. After some alignment of the CNTs in the epoxy, the percolation threshold decreased to 0.0025 wt% with conductivities of 10^{-3} S m^{-1} at loadings of 0.01 wt% reported.[9]

Enhancements in electrical and thermal conductivity are related in part to the extent of nanofiller dispersion and, can be measured by means of percolation theory. The conductive fillers such as CNTs and graphene form conductive interconnecting pathways that enable electrons to pass from one end of the material to the other through a pathway created by the conductive filler. The critical concentration of conductive filler required to form continuous conducting paths and impart conductivity is known as the percolation threshold.[4] The extent of dispersion of a conductive filler within a polymer matrix can be estimated by the percolation threshold, as the lower the percolation threshold, the less filler is required to achieve percolation.[9, 43] However, percolation does not necessarily directly correlate to dispersion as it is possible to obtain highly percolated systems whilst simultaneously being highly agglomerated and poorly dispersed. Nonetheless, the work herein assumes that changes in percolation can be construed as relative changes in dispersion.

Enhanced stiffness and strength can be achieved by the addition of very low loadings of nanofiller(s). Significant improvement in properties can be achieved with the addition of less than 1 wt% filler, such as in the case of Nylon where the Young's modulus increases by ca. 27% with the addition of 1 wt% MWCNTs.[3] Pötschke *et al*, compression moulded composites of poly(carbonate) with MWCNTs, and achieved a rheological and electrical percolation between 1-2 wt% loading.[44] Their work used HRTEM to quantify dispersion of the compression moulded plaques however, such methods are surface measurements not necessarily representative compared to methods such as using electrical and rheological percolation which are more effective at measuring the bulk properties because, they are through thickness measurements.

Recent studies have shown that blends of PP and SWCNTs with loadings of up to 1 wt% led to an increase in Young's modulus and tensile strength of the PP.[3] Bhattacharyya *et al*. prepared composites of PP and SWCNTs *via* melt blending. Their results showed the CNTs increased crystallisation rate (nucleating effect), reduced spherulite size and narrowed spherulite distribution.[21]

Zhou *et al*. investigated the effects of MWCNT size and content on the thermal stability of PP. Results demonstrated increased thermal stability of PP with increasing MWCNT loading, increasing aspect ratio and decreasing nanotube diameter. The thermal stability of PP increased by as much as ~30 °C upon addition of 5 wt% MWCNTs and was

attributed to the formation of tortuous paths by the CNTs which absorb and dissipate the thermal energy throughout the PP.[21] Zhou *et al.* produced composites of PP and MWCNTs with loadings up to 10 wt% *via* melt mixing at 190 °C for 10 min. The blends were subsequently compression moulded. Their results showed poor dispersion, even at low MWCNT loadings. The MWCNTs were observed to be present in micrometre clusters with other areas of the matrix containing no MWCNTs at all. Volume resistivity measurements revealed an electrical percolation at a relatively high 8 wt% loading. Mechanical properties revealed a ~5% increase in tensile strength for up to a 1 wt% loading and a decrease in elongation at break with increasing filler content, i.e. MWCNT addition embrittled the PP. Thermal analysis also confirmed increased crystallisation rate and decreased crystallite size distribution for up to a 0.5 wt% loading.[4] Zhang *et al.* prepared composites of SWCNTs and PP by coating the surface of solvent swollen PP powders with CNTs and subsequent compression moulding. They obtained an electrical conductivity percolation threshold of only 0.3 wt% by forming a network structure. The CNTs nucleated the crystallisation of PP at a 0.1 wt% loading. The formation of the γ phase was also detected, which would weaken the mechanical properties of the composite which were not measured.[45] Xiao *et al.* prepared composites of MWCNTs and PP by means of dynamic packing injection moulding where oscillatory shear is applied to the melt composite during the injection moulding process. The tensile strength increased from 50.5 to 59 MPa and the impact strength increased by almost 50% at 0.6 wt% loadings. The improvements were attributed to improved dispersion and shear stress induced nanotube orientation.[46]

As well as polymer/CNT composites, significant attention has been directed towards polymer/graphene composites. Polymer GNP composites can be present in various degrees of GNP exfoliation ranging from phase separated composites to intercalated and exfoliated composites (figure 2.8). Intercalated composites retain a stacked GNP structure but increased interlayer spacing, whereas exfoliated composites lose the stacked structure of the GNPs. Wide angle X-ray diffraction (WAXD), small-angle X-ray scattering (SAXS) and TEM can be used to accurately determine morphology and dispersion.[33]

Bafana *et al*. produced composites of PP and GNPs with loadings of 0.5-5 wt%. Their resulted showed increases in thermal stability of the composite with increasing GNP loading of ~66 °C compared to neat PP, for the highest loading. The result is consistent with the incorporation of CNTs within PP. Melt rheological results showed decrease in storage (G')

and loss (G'') moduli with increasing angular frequency. Viscosity increased at low shear rates however and, rheological percolation as seen with CNTs was not evident when GNP was added. Significant changes in dynamic mechanical thermal analysis (DMTA) properties were not observed with increasing GNP loading.[47]

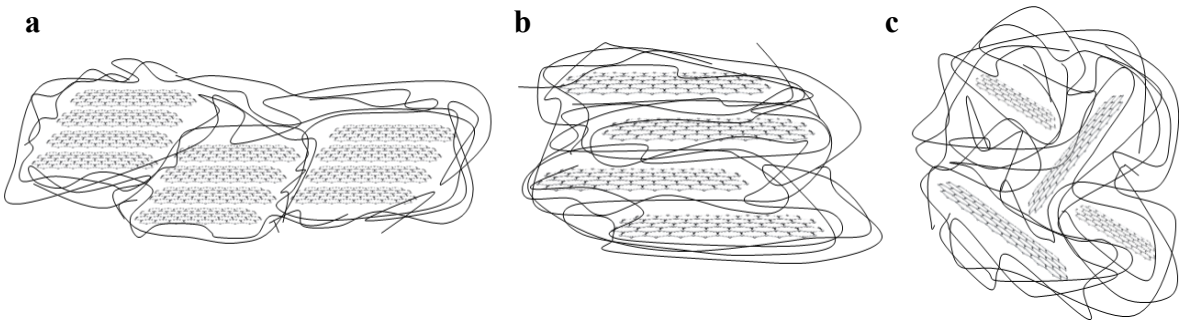

Figure 2.8. Schematic showing morphological states of a) phase separated, b) intercalated and c) exfoliated GNPs.[33]

In addition, Qaiss *et al.* produced composites of high density poly(ethylene) HDPE with graphene nanoribbons using melt compounding. They compared their results with composites of CNTs and HDPE and concluded the composites containing the graphene nanoribbons had significantly improved rheological, thermal and mechanical properties relative to the composites with the CNTs.[9] Liu *et al.* looked at the differences between graphene and CNTs in terms of percolation thresholds in HDPE. Composites with graphene and HDPE had a significantly higher percolation threshold, 1 wt% compared to CNTs, 0.15 wt%. In addition, the CNT composite showed greater conductivities at identical filler loadings. Such differences are down to the structural differences between the graphene and CNTs, where graphene sheets tend to fold and crumple whereas CNTs a relatively rigid and maintain networked structures at significantly reduced loadings.[9]

In the case of graphene/poly(styrene) composites, percolations have been measured at 0.1 vol% with conductivities of 0.1 Sm^{-1} at 1 vol% loadings.[9] Stankovich *et al*. produced graphene/PS composites via complete exfoliation of graphite and molecular-level dispersion of chemically modified graphene sheets.[1] Chemical modification involved oxidation of pristine graphite and mild ultrasonication in water to produce stable dispersions consisting of entirely 1 nm thick sheets of graphene oxide (GO). The GO was subsequently treated with

organic isocyanates to reduce the hydrophilicity of the sheets. The chemically modified GO was solution mixed with PS and subsequently reduced to induce electrical conductivity.[1]

When studying the effect of adding fillers such as CNTs and graphene into polymer matrices, it is important to consider their interaction with the polymer matrix and how the filler structure and properties influences their dispersion in the polymer matrix. For example, graphene is a planer material with high specific surface area and therefore, theoretically its flat structure allows the sheets to slide between the polymer chains in the matrix. This specific property can result in the interfacial contact area between the filler and the polymer matrix to be relatively large compared to CNTs which are a single dimensional material and have less interfacial surface area contact with the polymer matrix in the case of individually dispersed CNTs and graphene. Such differences, should allow graphene to have greater reinforcement capabilities compared to CNTs as greater amount of stress is transferrable at the interface from the polymer matrix to the graphene compared to CNTs.[9]

There are many challenges which must be resolved before new advanced composites with enhanced properties can be made. These include, poor dispersion of the filler within the polymer matrix, slipping of the CNTs and sheets due to poor compatibilisation with the polymer matrix and aggregation of the CNTs into ropes and the graphene into stacks which reduces the aspect ratio of the reinforcement.[10] The poor solubility of CNTs and graphene(s) in aqueous and organic solvents is also problematic for their incorporation into polymer matrices, if solution mixing is of interest.[8, 48]

Many different methods have been attempted to improve the dispersion of CNTs and graphene within polymer matrices however, very few, if any have been able to successfully address this major problem. This is because, the 1D and 2D fillers form bundles and agglomerates due to their strong cohesive intrinsic Van der Waals interactions (-5.9 kJ/mol) between themselves and this hinders them from dispersing individually and uniformly in solvents and polymer matrices.[8, 15] Poor dispersion and large agglomerates can lead to significantly reduced properties of the polymer as they disrupt the crystal structure of the polymer[49], and can also act as stress concentrators. However, if CNTs and graphene could be dispersed uniformly with minimal agglomerations in a semi-crystalline polymer matrix such as poly(propylene) PP, then this would lead to significantly enhanced mechanical properties of the (nano)composite. The reason for this is that the CNTs behave as a strong nucleating effect and can alter PP crystallisation behaviour.[10, 50]

2.4 Processing and Functionalisation

2.4.1 Processing

Surface functionalisation of the filler can improve dispersion and improve the interfacial interactions between filler and polymer matrix. Limited homogeneous distribution of the filler and controlling their orientation is problematic and therefore, the large expected surface area cannot be created.[2, 51] The separation of individual tubes and sheets, homogenous distribution and parallel alignment cannot be achieved without functionalisation. The role of functionalisation is to promote dispersion and interfacial adhesion without affecting the intrinsic properties of the filler.[9, 51] Melt-compounding is often used as an effective method for dispersing the fillers into the polymer matrix. The application of high shear can provide enough mechanical energy to help de-bundle CNT agglomerates and exfoliate graphene stacks.[52] Parameters such as, the mixing process (e.g. screw profile of extruder, residence time, screw speed) are important for controlling composite properties. Changing such parameters can influence the extent of dispersion such as, increased residence time and screw-speed, the incorporation of a recirculating design and use of high shear screw profiles. These parameters have to be taken into account when assessing the properties of the composites.[51] The dispersion of CNTs and graphene can be improved through multiple extrusions however, this process does not improve the interfacial adhesion between the filler and the polymer matrix. The composites can be subsequently moulded into various shapes. The technique is particularly favourable in industry as the process does not require the use of solvents and surfactants as would be required with the solution mixing approach.[9] Mayoral *et al*. showed the mixing of MWCNTs in PP was strongly influenced by energy, torque, residence time and temperature of the mixer. Increasing the rotor speed and mixing time resulted in decrease in percolation threshold.[53] In addition, the screw-profile of the extruder has also shown to influence the dispersion.[54]

An alternative approach to melt mixing is solution mixing which typically involves dispersing the CNTs or graphene into a solvent by way of ultrasonication. Ultrasonication energy can be applied either by use of a sonication bath or by means of a higher energy ultrasonication probe tip. The use of sonication exerts high energy vibrational energy onto the filler and helps to de-bundle the CNT ropes and exfoliate the graphene stacks. Solution mixing of polymer matrices with CNTs or graphene has been explored by many groups. As means of improving the dispersion and homogenous mixing of the filler with the polymer

matrix, the polymer matrix is dissolved in an organic solvent and the filler is added and dispersed with ultrasonication. One limitation with the use of solution mixing is that sustained exposure to organic solvents and dissolved oxygen can cause degradation of the polymer matrix not to mention the environmental and cost implications of using organic solvents when scaling up production commercially.[8] The use of solution mixing as a method for dispersion of CNTs and graphene can be applicable to thermoset and thermoplastic polymers such as; epoxy, poly(vinyl alcohol) PVA, poly(methyl methacrylate) PMMA, poly(urethane), poly(styrene) PS and many others with similar properties. The process involves simply dissolution of the polymer in an appropriate solvent followed by addition of the filler and use of ultrasonication and mechanical stirring to disentangle the CNT bundles and graphene sheets. The composite is subsequently precipitated and moulded accordingly. The major limitation with such a process is the poor dispersion of the fillers in the solvents used hence the filler is not homogenously dispersed in the composite. The use of surfactants can aid dispersion however, they decrease the properties of the composite.[9] However, a major drawback with ultrasonication is that sustained high energy exposure can lead to damage and destruction of the fillers. Such damage leads to reduced mechanical and electrical properties of the fillers which makes the resultant composite less promising. However, minor ultrasonication for low times (less than 10 mins) can promote exfoliation prior to further functionalisation to prevent re-aggregation can be advantageous as damage is minimised.[9]

CNTs and graphene solely consist of carbon atoms (except for heteroatom defects) and this gives them a low surface free energy, and limited functional groups required for coupling. To overcome the lack of dispersion, some researchers have used surfactants as a processing aids however, this has little effect on interfacial adhesion due to the weak interactions involved.[51] A common surfactant used to disperse CNTs and graphene particles is sodium dodecylsulfate (SDS) or surfactants analogous to SDS which makes use of CH-π type hydrophobic interactions to disperse the nanomaterials with in various solvents.[55]

Additionally, the use of melt compounding and solution mixing, *in-situ* polymerisation of the monomer in the presence of CNTs or graphene has been used to promote uniform homogenous dispersion of the fillers into the polymer matrix. The method is suitable for polymers which are insoluble in solvents and are thermally instable for melt compounding such as poly(pyrrole) and poly(aniline). The major limitation of the method is

that it is difficult to polymerise monomers of common thermoplastics in the presence of such fillers as they require stringent conditions which are often difficult to achieve in a laboratory set up.[9]

To develop composites of polymers and 1D/2D fillers with significantly better performance, the main challenges of good filler dispersion, controlled orientation, strong interfacial adhesion, and an electrical conduction path require the use of new techniques such as the use of a functionalising compatibiliser. Chemical functionalisation of the filler can improve solubility and improve interfacial adhesion by shielding the Van der Waals interactions, the binding to the surface of the filler facilitating effective stress transfer from the polymer matrix to the filler through compatibilisation.[51, 56] Covalent or non-covalent functionalisation of CNTs or graphene are the two main approaches that can be used to overcome these limitations of carbon based fillers.[8]

2.4.2 Covalent functionalisation

Many different methods have been employed to try and improve the compatibility of the interaction between the surface of the fillers and the polymer matrix. One strategy is to covalently alter the surface of the filler. This method involves the conversion of a small number of sp^2 carbons into sp^3 and the introduction of functional groups onto the surface of the filler. The functional groups mainly consist of oxygen and nitrogen based moieties such as, alcohols, esters, carboxylic acids, amines, amides and epoxides. The presence of such functional groups allow scope for post modification functionalisation such as 'grafting from' and 'grafting to' strategies which involves either attaching further molecules 'to the surface' or growing molecules 'from the surface', such as polymers for example.[8, 57] With the general acceptance that surface modification of the fillers is required, there are a few methods which can be used to achieve this, by way of example, chemical treatment and polymer grafting.

Acid treatments can be used to introduce functional groups onto the surface such as hydroxyls, acids or epoxides. However, this process results in scission of the CNTs and graphene and significantly increases the number of defect sites.[58] Oxidation of CNTs and graphene can lead to excessive surface damage (destruction of π-orbital structure) and significant reduction in mechanical and electronic properties (loss of electron-acceptor/electron-transport properties). Oxidation generally produces carboxylic acid type functional groups on the surface which can be used to ionically interact with

compatibilisers.[22] Acid treatment involves treating the filler with HNO_3/H_2O_2 and HNO_3/H_2SO_4.[14]

In addition to acid treatment, fluorination of CNTs is a popular method for covalent functionalisation because, the nanotube walls are expected to be inert. Functionalisation density and coverage can easily be controlled by fluorination and the fluorine atoms can be subsequently substituted by alkyl groups using alkyl lithium and Grignard reagents.[22] Another example is the 1,3-dipolar cycloaddition of CNTs with phenol which can be further functionalised with polymers.[14]

Polymer grafting is a possible solution as it results in improving solubility in aqueous and organic solvents as well as polymer matrices, depending on the nature of the grafted polymer.[8] One example of the 'graft from' strategy is to attach a free radical initiator, 2,2' – azobisisobutyronitrile, (AIBN) to open some of the π-bonds on the surface of the filler. The surface of the CNTs were then polymerised using free radical polymerisation with poly(methyl methacrylate) (PMMA). The method is known as surface initiated free radical polymerisation and it is a covalent method because, a carbon – carbon bond is being formed between the CNT and the compatibilising polymer.[10] A major drawback of using this type of approach is that the sp^2 structure of the CNTs is damaged and some intrinsic properties of CNTs (electrical and thermal conductivity) become significantly weaker even though compatibilisation can be significantly improved.

A similar approach is to use radical chemistry. Methods such as reversible addition-fragmentation chain-transfer polymerisation (RAFT) and atom transfer radical polymerisation (ATRP) can be used to grow polymers from the surface of CNTs which are covalently attached. In addition, the use of long apolar acrylates such as poly(lauryl acrylate) P(LA) and poly(stearyl acrylate) P(SA) are expected to facilitate good compatibility with PP due to their structural similarity with the polymer matrix. Hvilsted *et al.* polymerised P(LA) and P(SA) from the surface of MWCNTs by creating a bromo-initiator on the CNT surface using UV irradiation (figure 2.9).[59] CNTs were subsequently polymerised using ATRP to create covalently functionalised CNTs with P(LA). The covalently modified CNTs were melt mixed with PP. Dielectric spectroscopy measurements indicated an improvement in dispersion however, the mechanical properties of the composite were not measured.[59]

Covalent functionalisation of the filler is not an effective way of producing polymer composites because, the fillers have defects already and further damage to their surface

chemistry prevents the filler from improving the properties of the polymer composite. The major draw-back with the covalent functionalisation approach is the structural damage of the CNTs and graphene. Key properties of the fillers including conductivity (electrical and thermal) and mechanical strength are altered and significantly diminished as the method destroys their regular symmetrical hexagonal structure.[8] Covalent functionalisation can facilitate improved load transfer and more uniform dispersion due to the stronger interactions between the filler and the polymer matrix compared to non-covalent functionalisation however, the loss in intrinsic properties is too great for the method to be feasible.

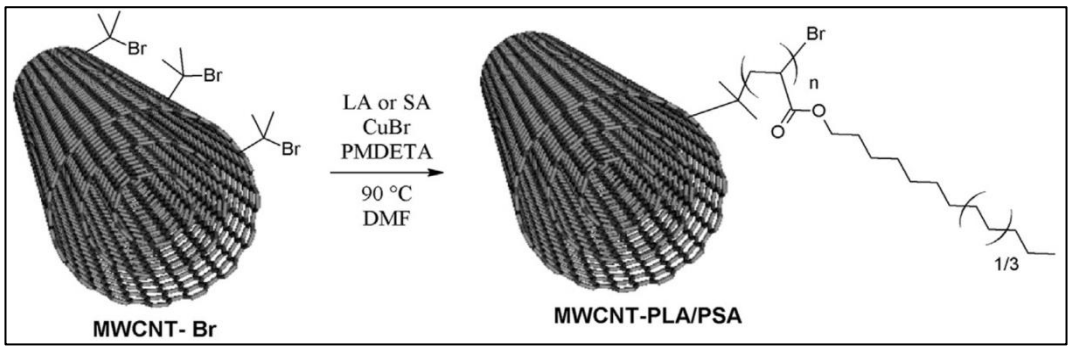

Figure 2.9 Surface initiated ATRP grafting of the MWCNT-Br with LA or SA.[59]

The only viable strategy to unlock the true potential of CNTs and graphene for composite applications is to functionalise them in a non-covalent manner so that filler reinforcement of the polymer is maximised without significantly altering the intrinsic properties of the filler derived from the ratio of sp^2 to sp^3 hybridisation.[8]

2.4.3 Non-covalent functionalisation

In contrast to covalent functionalisation, non-covalent functionalisation involves grafting polymers to the surface of the filler through various types of interactions. The interactions are individually very weak compared to a covalent carbon-carbon bond however, they make use of the cooperative effect of multiple weak interactions based on higher levels of grafting to the filler.[8] Non-covalent functionalisation is an ideal approach to improving the dispersion of the filler and interfacial adhesion whilst maximising gains in composite properties. Such an approach can preserve the desired properties of the filler, while improving their solubility's with both polar and non-polar sovents.[22]

The reasoning for the limited success with regards to non-covalent functionalisation of carbon-based nanomaterials is the lack of characterisation and understanding of the physical and electronic processes associated with the interface between the functionalising material and the carbon nano-material. Understanding the type and strength of interaction is key to effectivity functionalising the carbon nanomaterial because, not only does the compatibiliser have to adsorb onto the carbon nano-material, the adsorption must be uniform and homogeneous, effective at dispersing the carbon nanomaterial and strong enough to maintain adsorption during high shear mixing and under static and dynamic stress. The nanotube solubility, dispersion and interfacial stress transfer must be optimised to prevent interfacial slippage and this requires the interface to be carefully engineered.[14]

The understanding of adsorption kinetics of functionalising molecules onto the surface of carbon nanomaterials is key to producing an efficient compatibilising polymer. CNTs and graphene are carbonaceous materials with strong affinities to organic molecules due to their hydrophobic surfaces.[60] Adsorption is a surface based phenomenon and involves the adsorbate (functionalising molecule) coming into direct contact with the adsorbent (CNT or graphene). The adsorption process is classified into physisorption (weak non-covalent interactions) and chemisorption (strong covalent bonding). Van der Waals is the fundamental interacting force between molecules even though the interaction is very weak.[60] Van der Waals interactions result from transient shifts in electron density causing instantaneous and induced dipoles and require the adsorbent to be very close to the adsorbate. Another type of physisorption is hydrogen bonding which is a charged interaction, a result of donor and acceptor atoms. Aromatic-aromatic physisorption interactions are also as a result of charged electrostatic potentials.[61]

The main strategies for non-covalent functionalisation involve matching the electronic nature of the carbon nanomaterial. The use of π-π interactions is the most common method of non-covalent functionalisation as the aromatic groups are able to π-π stack together and form relatively strong interactions.[62] In addition, CH-π, polymer wrapping, ionic interactions and plasma polymerisation-treatment have also demonstrated effective functionalisation strategies for carbon nanomaterials.[14, 22] Various types of molecules can be adsorbed onto the surface of CNTs and graphene such as, polar and non-polar organic molecules, charged inorganic compounds, functionalised aromatics, proteins via a range of interactions as well as metal nanoparticles.[63-65]

The phenomenon of π-π stacking involves electrostatic attraction between two benzene rings. As shown in figure 2.10, a benzene ring (monomer unit for a CNT and graphene) contains a high concentration of electron density above and below the ring which leaves the ring itself electropositive. Depending on the angle at which the two benzene rings interact, the interaction can be attractive or repulsive.[66]

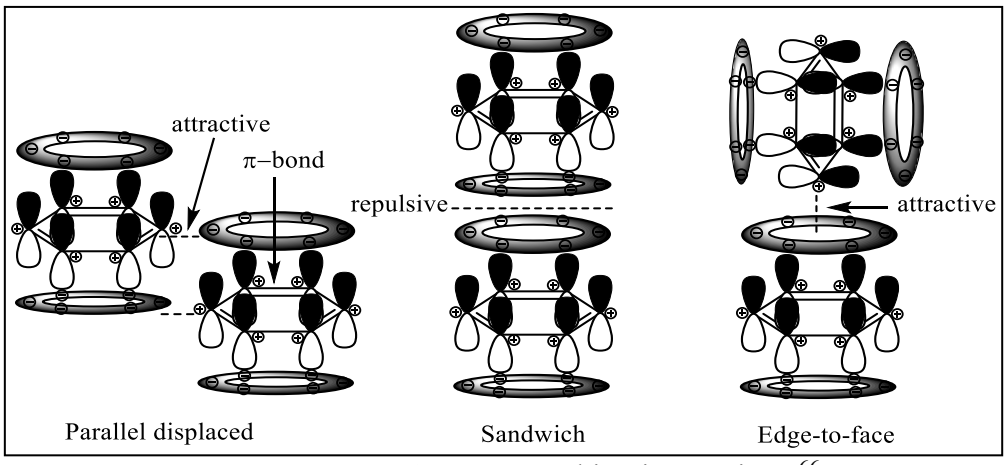

Figure 2.10 π – π stacking interactions.[66]

Pyrene is essentially a small section of the surface of a CNT or graphene and hence can adsorb onto the surface of the filler by the same π-π interactions which cause the CNTs and graphene sheets to aggregate. Their aromatic structure is similar to graphite.[8] Pyrene can be incorporated into polymers by either modifying it into an initiator or monomer unit. One of the advantages of using pyrene is its fluorescence properties which can be used to determine and confirm adsorption onto the surface of carbon nanomaterials *via* quantitative fluorescence quenching.[67]

Zentel *et al*. synthesised a diblock co-polymer with one block made of poly(methyl methacrylate) (PMMA) and the second block made of a pyrene side chain functionalised acrylate (figure 2.11).[68] The authors looked at how strongly a pyrene end-functionalised polymer binds to CNTs compared to a pyrene side chain functionalised polymer. They also studied how varying the distance between pyrene on the side chain and the back-bone affected the strength of the binding. They concluded that having the spacer between the side chain and the backbone and a maximum number of anchoring units of 20 gave optimal binding. A major drawback with this work was that they only investigated the dispersion of the CNTs in a solvent. In-order for the nanocomposites to be useful, ideally the mode of

preparation has to be melt blending therefore, thermal stability of the functional group also needs to be taken into consideration.[68]

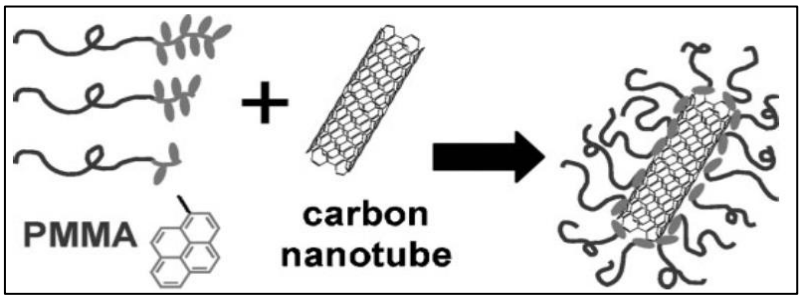

Figure 2.11 Schematic showing pyrene functionalised polymers for CNT binding.[68]

Jérôme *et al.* copolymerised (1-pyrene)methyl 2-methyl-2-propanoate (PyMMP) with methyl methacrylate (MMA) and 2-(dimethylamino)ethyl methacrylate (DEAEMA) by means of atom transfer radical polymerisation (ATRP) (figure 2.12). They concluded that stable dispersions in an organic solvent required a polymer to CNT ratio of at least 2:1. Increased polymer content improved dispersion and increased pyrene content also improved dispersion. However, changes in molecular weight had little effect when the pyrene content was kept constant showing the adsorption is directly controlled by the pyrene moiety.[8]

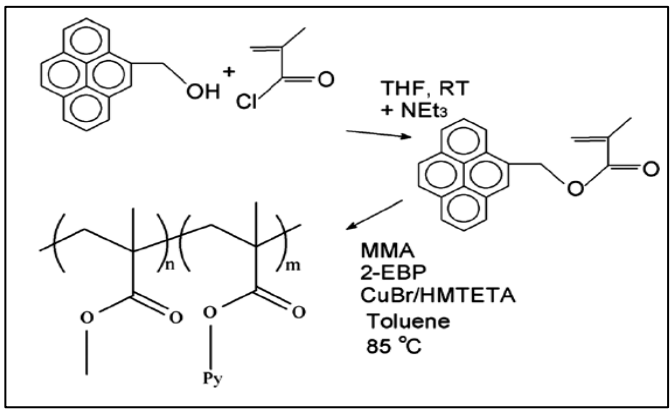

Figure 2.12 Synthesis of poly(methyl methacrylate-*co*-(1-pyrene) methyl-2-methyl-2-propenoate) copolymer.[8]

Adronov *et al.* produced copolymers, both random and block of various systems incorporating pyrene. They concluded that increasing pyrene content resulted in stronger polymer-SWCNT interactions. The use of statistical pyrene containing copolymers resulted

in reduced solubility compared with block co-polymers where one of the blocks contained a pyrene moiety. The reasoning behind this was the dispersing block was free to extend into solution and the pyrene block was able to completely adsorb onto the surface of the SWCNT which was not possible in the case of the statistical copolymer.[8] Dai *et al*. used a bifunctional molecule, *N*-succinimidyl-1-pyrenebutanoate to irreversibly adsorb onto the surface of SWCNTs in DMF or methanol. Furthermore, the succinimidyl ester groups are reactive to nucleophilic substitution and they were able to attach proteins to the surface of SWCNTs using this bifunctional compatibiliser.[22] In addition, Guldi and Prato *et al*. also used pyrene derivatives to produce hybrid materials with strong electron donor/acceptor properties. Pyrene has shown in many cases, it is able to easily and effectively adsorb onto the surface of carbon based nanomaterials showing π-π interactions are an effective approach to non-covalently functionalising carbon based nanomaterials.[22] Yang *et al*. reported the use of a hexa-component system where they combined the Ugi reaction, π-π stacking (pyrene-CNT) and *in-situ* RAFT polymerisation in a one pot reaction with MWCNTs (figure 2.13a).[48]

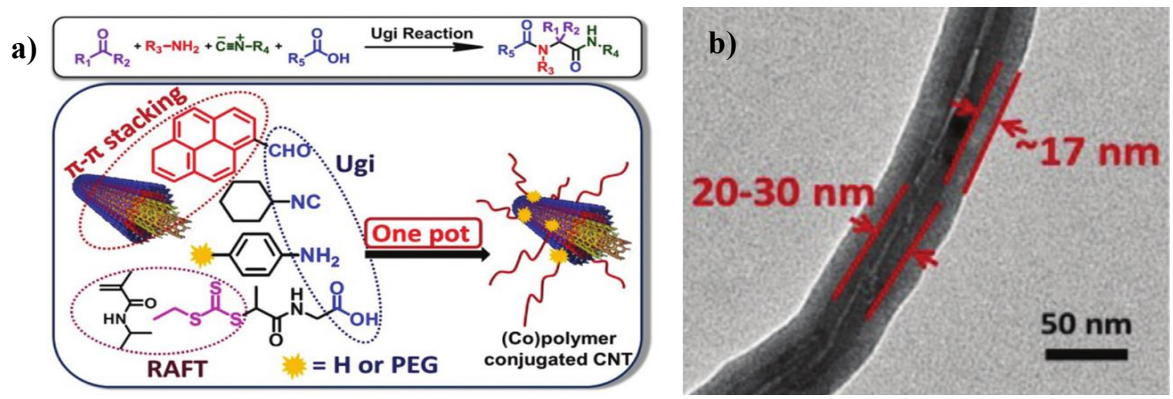

Figure 2.13 a) Copolymer modification of CNT *via* a one-pot strategy and b) TEM of functionalised CNT.[48]

The one-pot strategy composed a click reaction, RAFT polymerisation and supramolecular interactions, which resulted in a high grafting density and good dispersion in both organic and aqueous media. The polymer contained mid-chain pendent pyrene groups which were able to adsorb onto the surface of MWCNTs and form a thick polymer film (~17 nm) (figure 2.13b) observed by TEM and therefore, showing pyrene based polymers are able to successfully non-covalently functionalise MWCNTs.[48] In addition to the use of pyrene based polymers to non-covalently functionalise CNTs and graphene, other

aromatic type polymers have also been considered. For example, the use of styrene based polymers. Xie *et al.* used polystyrene-*g*-(glycidyl methacrylate-*co*-styrene) copolymers to non-covalently functionalise CNTs and grafted the co-polymer to the polymer matrix (PS) to improve interfacial adhesion. The styrene component of the co-polymer adsorbed onto the CNTs via π-π stacking and the glycidyl methacrylate group dispersed the nanotube in the solvent.[8] Shvartzman-Cohen *et al*. has shown the dispersion of SWCNTs using micelles of di-block co-polymers in water. They produced electron deficient molecules which interacted with the electron rich SWCNTs to form donor-acceptor complexes similar to π-π complexes.[2] Chen *et al*. used a rigid, fixed polymer, poly(aryleneethynylene) containing alternating aromatic alkyne units in the back bone to irreversibly and non-covalently functionalise SWCNTs. Evidence for π-π interactions were determined by shifts in the polymer peaks in the ^{1}H NMR spectrum and fluorescence quenching from optical microscopy.[69]

It is also possible to adsorb polymers onto the surface of carbon fillers using carbon-hydrogen groups (CH groups) and π systems in the form of CH- π interactions which have been known for years.[2] Even though the comparative strength of a CH-π interaction is relatively weak compared to a hydrogen bond, the cumulative effect is significant enough to influence the filler-polymer interaction.[2, 8] CH – π interactions (figure 2.14) occur when a polymer wraps around a CNT or adsorbs onto a graphene sheet. The interaction is similar to a hydrogen bond where the more electronegative carbon polarises the C-H bond causing the delta positive hydrogen to be attracted to the negatively charged electron cloud above the benzene ring.[70]

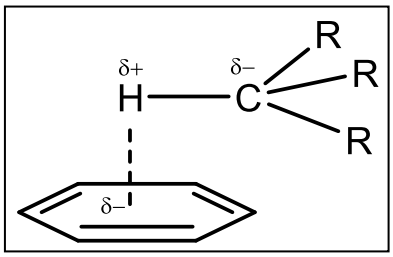

Figure 2.14 C-H – π interaction during polymer/CNT wrapping.

Baskaran *et al*. used long chain polymer molecules which contain numerous CH moieties to adsorb onto MWCNTs and reported that non-covalent CH wrapping is a general

phenomenon that occurs between polymers and CNTs.[2] The authors identified shifted IR and Raman frequency bands to confirm the interaction.[8]

Additionally, the use of long chain alkyl groups, temperature responsive SWCNT dispersions have also been developed with the use of poly(*N*-isopropylacrylamide) P(NIPAm) making use of its lower critical solution temperature (LCST) of ≈ 32 °C. The P(NIPAm) interacted with the SWCNT using the alkyl hydrocarbon backbone and isopropyl side chains through non-specific Van der Waals and hydrophobic interactions. The interesting property with this system is that even though the interaction in solution is relatively weak, they were able to reversibly switch between dispersed and aggregated states by altering the temperature across its LCST.[8] In conclusion, it's possible to use hydrophobic polymer chains to non-covalently wrap CNTs as a means of dispersing CNTs and graphene.

Other polymers such as poly(2-ethyl-2-oxazoline) (PEOX) and poly(acrylic acid) (PAA) have also been shown to provide strong and stable dispersions in aqueous and polar organic solvents. To further understand the CH-π binding mechanism, Naito *et al*. studied the correlation between polymer stiffness and the polymer wrapping on the surface of SWCNTs using poly(dialkylsilane) (PSi)s. The polymer side-chains facilitated strong CH-π interactions. In addition, the polymer architecture has also been considered where the use of hyper-branched poly(ethylene) (HBPE) can effectively solubilise MWCNTs in solution.[8]

Armaroli *et al*. synthesised a block copolymer using RAFT that is capable of efficiently dispersing SWCNTs in aqueous media (figure 2.15). The authors synthesised an amphiphilic block copolymer. Fluorescence and atomic force microscopy measurements showed quenching of the semiconducting analogues normally emitted by SWCNTs. However, this was carried out in aqueous media and therefore, does not directly relate to the polymers' ability to compatibilise CNTs within a polymer matrix in the melt.[71]

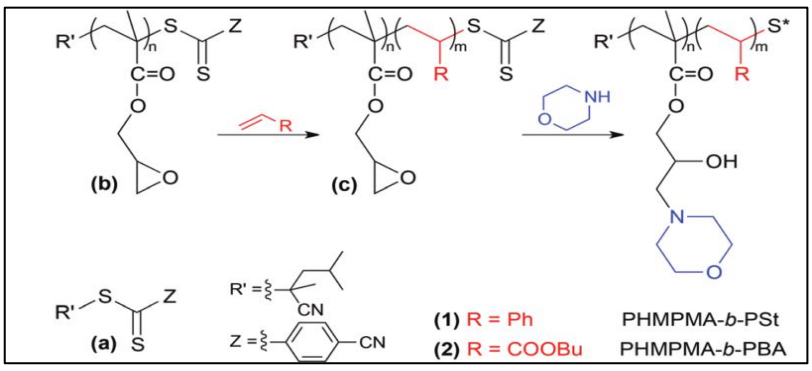

Figure 2.15 Schematic of the synthesis of a amphiphilic block copolymer.[71]

Smalley *et al*. have reported the use of speciality polymers such as poly(vinyl pyrrolidone) and poly(styrene sulfonate) to non-covalently wrap SWCNTs.[2] Stoddart *el al.* has also shown to use poly(metaphenylene vinylene) to wrap SWCNTs in solution. However, the concept of polymer wrapping has only been shown to be present with very few specific polymers.[2]

The non-covalent functionalisation strategies discussed have been predominantly applied using a solution mixing approach. The strategies must be applied using a melt-mixing approach for them to relevant for PP. The molecules discussed can only be applicable if they are thermally stable for extrusion during processing. Examination of literature revealed very limited work has been carried out in the area of non-covalent functionalisation of 1D and 2D graphitic fillers for melt mixing with thermoplastics. For example, Müller *et al*. used polyoxyethylene cetyl ether to improve the dispersion of MWCNTs with linear low-density polyethylene (LLDPE). The composite was nearly free of MWCNT agglomerates and the dispersion improved with increasing ethylene glycol repeating units in the additive backbone. Electrical percolation reduced to 1 wt% upon additive addition and MWCNT loadings of 2 wt% and 8 wt% resulted in increases in strain at break of 113% compared to the corresponding composite without additive.[72] In addition, maleic anhydride grafted PP has been used as a way of introducing polarity into the PP matrix to improve the compatibilisation between the fillers and the matrix.[73] Cohen *et al* further functionalised the polymer matrix by producing pyridine modified polyethylene which was melt-mixed with MWCNTs. Rheological percolations reduced to 0.8 wt% from 1.4 wt% upon addition of 5 wt% pyridine modified polyethylene.[74]

A particular non-covalent functionalisation strategy of interest is the use of conducting polymers and their interaction with CNTs and graphene via π-π stacking. Conducting polymers such as poly(thiophenes) have already been established in many technological applications which mirror the potential applications of CNTs and graphene.[8] By way of example, the electrical conductivity of poly(3-hexylthiophene) (P3HT) can be controlled by altering its stereo-regularity. Nandi *et al.* studied composites of MWCNTs and P3HT and their results indicated increases in electrical conductivity and mechanical properties relative to unfilled P3HT.[8] To further improve the interaction with CNTs and graphene, Yang *et al.* functionalised P3HT with pyrene and dispersed SWCNTs in the polymer. The polymer interacted with the SWCNTs by means of π-π interactions between

the pyrene and the SWCNTs. Their results indicated the size of the SWCNT bundles was reduced and the authors were able to cast films of the composite material. Fluorescence measurements showed 100% quenching confirming pyrene could be a possible route to the non-covalent functionalisation of CNTs and graphene.[8]

Furthermore, in addition to the use of π-π and CH-π interactions, it is also possible to use ionic interactions to non-covalently functionalise CNTs and graphene. CNTs and graphene naturally contain various levels of defects. These defects can be present either on the main body of the nanotube/sheet or on the ends of the CNTs/sheet edges. Such defects are mainly present in the form of oxygen functional groups such as carboxylic acids. These defects naturally give the fillers an inherent negative charge and therefore, it is possible to use such charges to ionically interact with the filler by means of using positively charged polymers. Yan *et al.* demonstrated the use of polyaniline (PANI) as means of functionalising MWCNTs and confirmed this by Raman and FT-IR spectroscopy (figure 2.16).

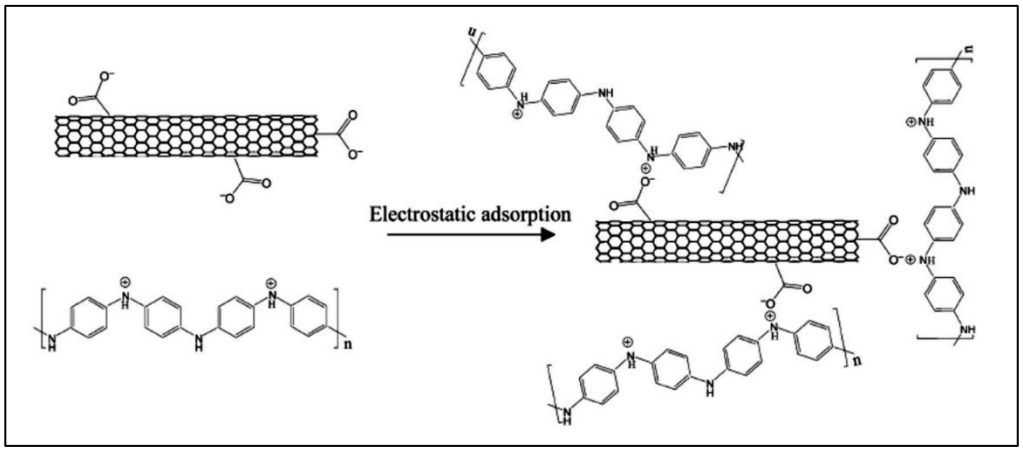

Figure 2.16 Schematic of electrostatic adsorption between a negatively charged MWCNT and positively charged PANI molecule.[8]

In conclusion, non-covalent functionalisation has been shown to effectively disperse CNTs and graphene in solutions. The method allows the mechanical and electrical properties of the CNTs and graphene to be maintained. CH-π, π-π and ionic interactions are the main interaction possible between polymers and the fillers and they are strong enough to form stable dispersion in various solvents.[8]

2.5 Poly(propylene) PP

The production of a (nano)composite involves dispersing the functionalised carbon nanomaterial (filler) within a polymer matrix. The polymer matrix chosen for this project is polypropylene. Polypropylene (PP) is a commodity thermoplastic polymer and is one of the largest produced polymers in the world with an estimated annual global production of 55 million metric tons.[75] It is a commodity plastic used in a very wide range of applications such as a packaging material for foods, clothing, toys, films, medical care, automotive and as parts for many different household appliances. PP can be used for both flexible packaging, in which case it is rolled into films and rigid packaging, such as containers and caps.[3, 75] PP is versatile because, it is a thermoplastic rather than a thermoset. PP can be re-melted several times and remoulded into any size and shape with limited effects on its properties. It is a high throughput material because, once the mould has been machined for the product, the product can be extruded and injection moulded at high speeds in a continuous process. Melt-compounding is a versatile technique and the wide spread use of extrusion and injection moulding has led to global production of polymer products at extremely low cost. High grade injection moulders are able to rapidly produce products with highly controlled shape, texture and reproducibility.[3] However, there are some disadvantages to using PP, which are that a new mould has to be machined every time the size and shape of the product changes and the extruders and moulders can be very expensive. In addition, a large amount of energy is required to melt PP above its melting temperature, (170 ^{o}C – 220 ^{o}C). Moreover, due to the fact the production rate is very high, the economies of scale allow the cost of the product produced to be very low and therefore, it is one of the most widely used polymers globally.

The aim of this project is to combine the exceptional mechanical and electrical/thermal properties of CNTs and graphene and to combine them with the exceptional processing properties of PP. This would produce a new type of advanced material with exceptional mechanical and electrical properties but, it can also be extruded and injection moulded into any size and shape and recycled. Reinforced PP would be able to replace a lot of the current thermoset polymers used as a recyclable alternative, but with advanced functional properties.[76] The project will focus on working with isotactic PP (iPP). iPP has the greatest commercial importance over syndiotactic and atactic PP due to its high crystallinity. For example, atactic PP is amorphous and syndiotactic PP has lower crystallinity than iPP. High crystallinity gives iPP a good benchmark in terms of mechanical

and processing properties. Polymorphism is a description of the different ways the polymer can pack and crystallise to form different crystal structures. iPP has a number of polymorphs but, the three most common are monoclinic (α), hexagonal (β) and triclinic (γ). The α form is the highest quantity form in iPP but, small amounts of β can be present depending on crystallisation kinetics. The β form can be selectively induced by using β nucleating agents and the γ form can be produced in low molecular weight PP or high-pressure crystallisation.[77-79] MWCNTs and GNPs are known to nucleate polymers cooled from the melt and increase the crystallinity as well nucleate the β phase of PP. It is important to characterise changes in crystallinity and determine the local micro-structure of the fillers. The fillers may reside within the inter-lamellae spacing as well as the amorphous phase and this can be affected by functionalisation.[80] After PP is cooled from the melt, the polymer chains align and form a localised ordered structure. This region is referred to as lamellae (figure 2.17). Crystallisation in polymers is induced by a nucleus. The nucleus initiates lamellar formations and sufficient branching result in the formation of spherulites. In the case of iPP, it is referred to as being a semi-crystalline polymer as its degree of crystallinity ranges between 10 – 85% depending on the stereo-regularity of the polymer chains and the cooling conditions. It is not possible to achieve 100% crystallinity because, even though it is thermodynamically favourable for all the polymer chains to align, steric hindrance and entanglement prevents that from happening. Crystal nucleation occurs when two parallel chains are close enough to crystallise. Due to the fact that crystallisation is an exothermic process, the latent heat of fusion (~210 J g^{-1}) released helps to direct nearby polymers to also align themselves and this kick starts a chain reaction of crystal growth. It is also possible to use a heterogeneous nucleating agents such as CNTs and graphene which induce crystallisation by providing a framework for the polymer chains to align themselves against.[81, 82]

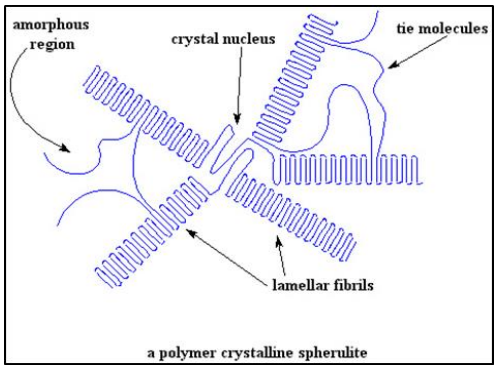

Figure 2.17 Schematic of a spherulite showing lamella and amorphous regions.[81]

Crystallisation of polymer occurs at temperatures significantly below the melting point, for example iPP melts at ~165 °C but crystallises at ~125 °C. Crystallisation usually occurs at a constant rate and the crystallisation kinetics are controlled by secondary nucleation mechanisms rather than a dissipation of latent heat of fusion, as is the case for metals.[82] Spherulites form birefringent disk-like formations centred around a random crystal nuclei and grow radially at a constant rate (figure 2.18). The spherulites subsequently come into contact with each other forming various polygonal shapes which correspond to the polymorph of the crystal.[83]

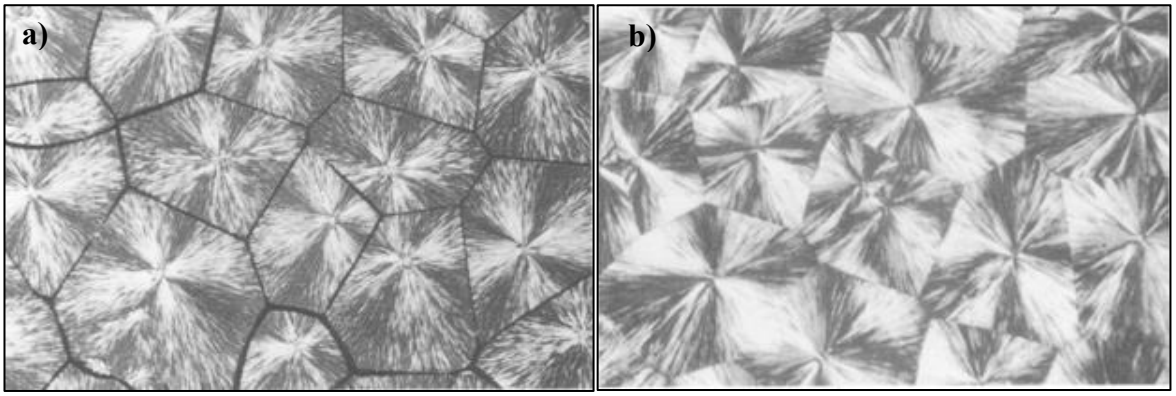

Figure 2.18 Radial α-spherulites of iPP a) negative (α_{11}) 413 K b) positive (α_1) 393 K.[83]

Table 2.1 d-spacings and corresponding miller indices of iPP.[84]

$(hkl)_\alpha$	$(hkl)_\beta$	$(hkl)_\gamma$	D (Å)	2θ (λ = 1 Å)
		(111)	6.39	8.98
(110)			6.26	9.16
		(113)	5.86	9.79
	(300)		5.50	10.43
(040)		(008)	5.24	10.95
(130)			4.78	12.01
		(117)	4.38	13.11
(111)	(311)	(202)	4.17	13.77
$(13\bar{1})$/(041)		(026)	4.05	14.18
		(206)	3.63	15.83
(150)/(060)			3.51	16.38
		(00 12)	3.47	16.57
(200)			3.28	17.54

The degree of crystallinity can be measured using a variety of different techniques such as differential scanning calorimetry (DSC), X-ray diffraction (XRD), and nuclear magnetic resonance spectroscopy (NMR). DSC shows the amount of thermal energy released/absorbed when a polymer crystallises/melts and this measurement can be used to determine if crystallinity increases or decreases and what affects the use of a nucleating agent (filler) can have on the glass transition temperature (T_g ~ -20 °C), as well as melting (T_m) and crystallisation (T_c) temperatures.[81] XRD can characterise the different type of polymorphs in iPP and the peaks can be analysed to measure the degree of crystallinity.[85] Table 2.1 describes the Miller indices for the corresponding polymorphs in iPP.[84, 86]

2.6 Synthesis of polymer compatibiliser for non-covalent functionalisation

The hypothesis is to use a polymer based compatibiliser as opposed to a non-polymer based compatibiliser because, use of a compatibiliser other than a polymer would most likely lead to phase separation between the compatibiliser and the polymer matrix and therefore hinder, bulk compatibilisation. Not only is the interaction between the filler and the compatibiliser crucial but, the interaction between the compatibiliser and the polymer matrix must also be considered and therefore, it is believed the use of a polymer compatibiliser must be the optimal solution for this system (Figure 2.19). In order to develop a polymer with highly specific properties, the polymer structure must be controllable. A polymer with controllable monomer sequence, molecular weight, dispersity and architecture must be made and therefore, a polymer will need to be tailored and synthesised for the specific system.

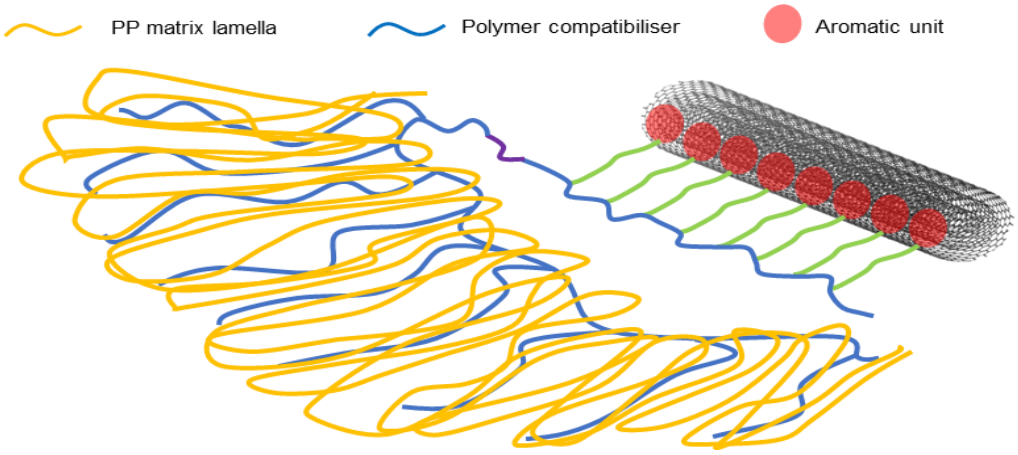

Figure 2.19 Schematic representing the non-covalent (π-π) interactions between a polymer compatibiliser, MWCNTs and the lamella of PP.

The non-covalent functionalisation of MWCNTs relies on efficient compatibilization and a method to predict effective solubility between the compatibiliser and the MWCNTs is to use Hansen solubility parameters. Effective solubilisation of the MWCNTs in PP will lead to reduction is agglomerates. The Hansen solubility parameter uses a combination of non-polar, permeant dipole-permeant dipole and hydrogen bonding interactions to determine the cohesive energy between mediums. Such parameters are important when considering the type of compatibiliser being synthesised however, such parameters will be considered in this work.[87]

Any potential benefit from the addition of MWCNTs to PP in terms of mechanical performance can be predicted using the Cox-Krenchel model which quantitatively applies the rules of mixtures and elastic behaviour of aligned particles under equal strain conditions. Such models describe limited potential in improvements in mechanical performance due to low loading of filler however, such models are primarily developed macroscopic aligned-fibre systems. Such models are not sufficiently suitable when applying to nano scale reinforcements as the model assumes the polymer matrix properties are unaffected by the addition of the filler which is not the case.[88]

2.6.1 Controlled living radical polymerisation

There are many different polymerisation techniques available with the most common technique used being free radical polymerisation. Free radical polymerisation involves using a radical source which acts as the radical initiator such as 2,2' – azobisisobutyronitrile (AIBN). The AIBN decomposes thermally and the radicals reacts with a reactive alkene bond on the monomer unit in a 'head to tail' mechanism. The alkene bond then has a radical on the end which can then react with another monomer unit and this process repeats until all of the monomer is consumed. The active chain end then undergoes chain transfer. It can terminate by recombination with another initiator radical. An alternative is for the chain end to undergo disproportionation where the active chain end removes a hydrogen from the adjacent carbon forming an alkene and the hydrogen transfers to another active chain end which subsequently forms an alkane. The major disadvantage of using free radical polymerisation is that the initiation step is very slow which means new chains are being generated throughout the polymerisation. This causes the dispersity ($Đ$) to increase and can make it very difficult to control the molecular weight of the polymer and the end group fidelity is also very poor.[81]

A much improved alternative to free radical polymerisation is living radical polymerisation (LRP) which is often referred to as reversible deactivation radical polymerisation (RDRP).[89] In an ideal 'living' polymerisation, the initiation step is very fast compared to the rate of propagation so all of the chains start growing at the same time. They also all grow at the same rate with very low levels of irreversible chain transfer or termination. Following these rules, the molecular weight distribution (dispersity) is very narrow (<1.2) with very high end-group fidelity which can also be chain extended. This technique allows the possibility to formulate multi-block polymers with defined end-group functionality. This method opens the possibility to synthesise polymers with complex architectures with a pre-defined molecular weight because, the number average degree of polymerisation (DP_n) is the monomer concentration divided by the initiator concentration.[81] Techniques such as nitroxide mediated polymerisation (NMP)[90], reversible addition-fragmentation chain transfer polymerisation (RAFT)[91-94], atom transfer radical polymerisation (ATRP)[95] and Cu(0)-mediated LRP are all variations of LRP as they all demonstrate remarkable control in polymer molecular weight, end-group functionality, dispersity and architecture.[89, 96]

2.6.2 Reversible addition fragmentation chain-transfer polymerisation

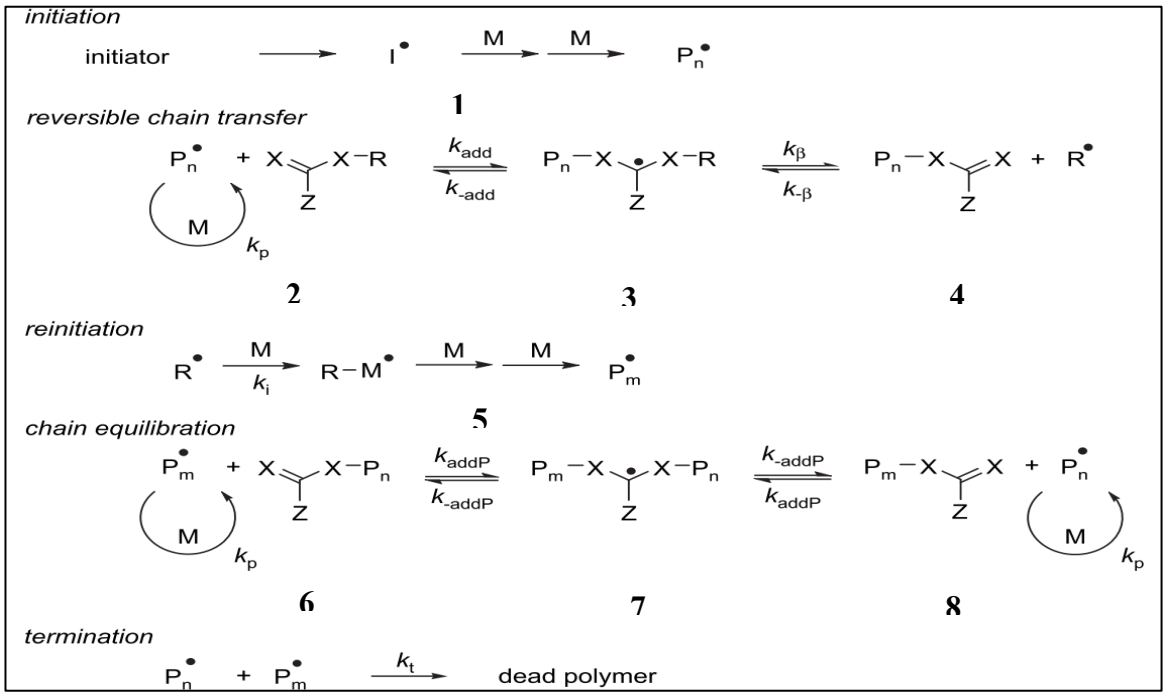

Figure 2.20 Schematic showing mechanism for RAFT.[97]

Reversible addition-fragmentation chain transfer polymerisation (RAFT) is a polymerisation technique which can polymerise monomer units which possess a carbon – carbon double bond (alkene). Any molecule containing an alkene could theoretically be polymerised but, typically monomers include acrylates, methacrylates, styrene, acrylamides and many others. RAFT yields reversible deactivation of propagating radicals through the process of degenerate chain transfer.[91, 98]

The main component used in RAFT is the chain transfer agent (CTA) (also known as the RAFT agent) which reversibly regulates the rate of propagation of the active polymer chain end and therefore, provides its 'living' characteristics.[99] The RAFT agent itself does not initiate or terminate the polymerisation. The process of initiation requires the addition of an external radical generator such as AIBN. In fact, all things being equal, RAFT is simply free radical polymerisation with the addition of a CTA to control the rate of propagation. Figure 2.20 shows the mechanism for RAFT.[91, 97] Initially, a radical generator such as AIBN homolytically cleaves at elevated temperatures to generate radicals. The radicals are extremely reactive and they initiate polymerisation by reacting with the alkene on the monomer units in a 'head to tail' mechanism (**1**). After the polymerisation of a few monomer units, the active polymer chain end reacts with the X on the CTA agent (X=C group) (**2**) and the chain transfer agent transfers (**3**) the radical to the R group (**4**). The initiator generated polymer chain has now become dormant. Furthermore, the R group propagates with further monomer units and the R group chain has now become active (**5**). After the addition of monomer units on the R group chain, the active polymer chain end will recombine (**4**) with the CTA with same mechanism (**3**) and the previous dormant polymer chain will become active again (**2**) and the R-group chain becomes dormant. The process repeats until all of the monomer is consumed. Essentially, the role of the CTA is to reversibly activate/deactivate the growing polymer chains by reversibly switching them between a dormant/active state equilibrium (**6 – 7 – 8**).[91, 100, 101]

With reference to figure 2.20, usually X is a sulphur atom (thiocarbonylthio group) but, it can also be a CH_2. The Z group determines the addition and fragmentation rates because it will determine the stability of the radical intermediate. Trithiocarbonates are the most reactive RAFT agents as they have sulphur atoms adjacent to the thiocarbonylthio group as they help to maintain the double bond character of the thiocarbonylthio group which makes it more reactive towards radicals. The CTA has to be reactive enough so that the

propagating radicals react with the CTA but also, stable enough so that the R group can homolytically cleave. The R group is very important in RAFT because, this strongly determines the level of control provided by the CTA agent. The R group must have good leaving group ability so that it can homolytically dissociate but, it also must have a very high re-initiation efficiency. If the re-initiation efficiency is low, this will cause high levels of termination and the dispersity will increase.[91, 97]

The polymerisation efficiency of the CTA greatly depends on the electronic properties of the monomer. Monomers can be groups into two classes, 'more activated' monomers (MAMs) and 'less activated' monomers (LAMs). MAMs are monomers containing doubles bonds which are conjugated, for example to an aromatic system in the case of styrene or a carbonyl in the case of methacrylates and acrylates. LAMs are adjacent to a saturated carbon, nitrogen or oxygen as in the case of vinyl acetate or *N*-vinylpyrrolidone. MAMs are less reactive to radical addition and therefore require the use of more activated CTA such as trithiocarbonates. LAMs are more reactive to radical addition and they require less activated CTA such as *O*-alkyl xanthates. In summary, the choice of RAFT agent is highly dependent on the type of monomer used and therefore, this must be considered during the design of the compatibiliser.[91]

RAFT is a very versatile technique because, it can be used to polymerise a wide range monomers including, acrylates, methacrylates, acrylonitrile, styrenes, vinyl monomers and almost anything with a carbon – carbon double (C=C) bond. The monomers also do not require special protection and the CTA can be used in a wide range of solvents including aqueous and protic solvents. The major advantage of using RAFT is that it is a relatively easy technique to implement. However, it can be difficult to select the correct CTA for the required monomer/solvent system and the synthesis of the CTA can be challenging at times.[91, 97]

2.6.3 Cu(0)-mediated living radical polymerisation

An alternative to using RAFT is Cu(0)-mediated living radical polymerisation (Cu(0)-mediated LRP). The technique is a widely applied and useful technique for controlling the polymerisation of vinyl monomers.[102] This technique also has the ability to propagate polymer chains to completion with negligible levels of termination or chain transfer. The exact mechanism of the polymerisation is still under debate however the current belief is that the dormant chains are activated through a heterogeneous outer-sphere electron

transfer process. The process involves the decomposition of a tertiary substituted alkyl halide initiator into a carbon centred radical and a halide anion and process is catalysed using Cu(0). The carbon centred radical from the initiator is then able react with an unsaturated alkene and propagate the polymerisation.[89, 102-104]

The use of Cu(0)-mediated LRP allows easy access and fast polymerisation (conversion < 3h) of acrylates, methacrylates, and acrylamides to well-defined narrow dispersities ($Đ \sim 1.1$) and controlled molecular weight polymers under ambient conditions. As reported in the literature,[89] Cu(0)-mediated LRP is able to polymerise a range of monomers, and it especially works well for acrylates yielding dispersity values in the range of 1.05 – 1.10, even up to almost full conversion with little quantifiable bimolecular termination. It is therefore, an excellent tool to use when trying to synthesise polymers that require controlled architectures, as is the case for the non-covalent functionalisation of CNTs and graphene.[89, 102-104]

The polymerisation technique is highly versatile compared to techniques such as anionic polymerisation, as it is able to be utilised in a wide range of solvents such as; H_2O, alcohols, ionic liquids, and many others. A wide range of monomers (more activated monomers containing electron withdrawing groups) can be used including acrylates, methacrylates, and acrylamides which can be unprotected such as in the case of sugar moieties. The polymerisations can be carried out at ambient temperature and pressure which is ideal, as chain transfer tends to be more prevalent at higher temperatures. The polymerisations are quick to set up (less than 15 mins) and simply require mild deoxygenation via nitrogen bubbling. The copper catalyst can easily be removed using filtration leaving only minor copper residues which can be completely removed by dialysis. A significant but not critical limitation of Cu(0)-mediated LRP is to polymerise less activated monomers such as vinyl acetate and vinyl pyrrolidone including acidic monomers as these are unable to form the Cu complex required during polymerisation.[89, 105, 106]

The mechanism of Cu(0)-mediated LRP consists of using copper which is at the centre of the reaction. The polymerisation involves the use of Cu(0) as the activator and Cu(II) Br_2 as the deactivator in a polar solvent such as isopropyl alcohol. The Cu(0) forms a complex with the ligand tris[2-(dimethylamino)ethyl]amine (Me_6-Tren), see figure 2.21. This complex is known as the activator and the complex initiates rapid polymerisation via a tertiary substituted alkyl halide initiator such as ethyl α-bromoisobutyrate. The

polymerisation proceeds via the mechanism whereby the [Cu(0)-Me_6-Tren] complex homolytically cleaves the carbon-halide bond on the initiator to produce a stabilised tertiary radical and this radical is able to propagate with the monomer and complete the polymerisation as shown in figure 2.21.[89]

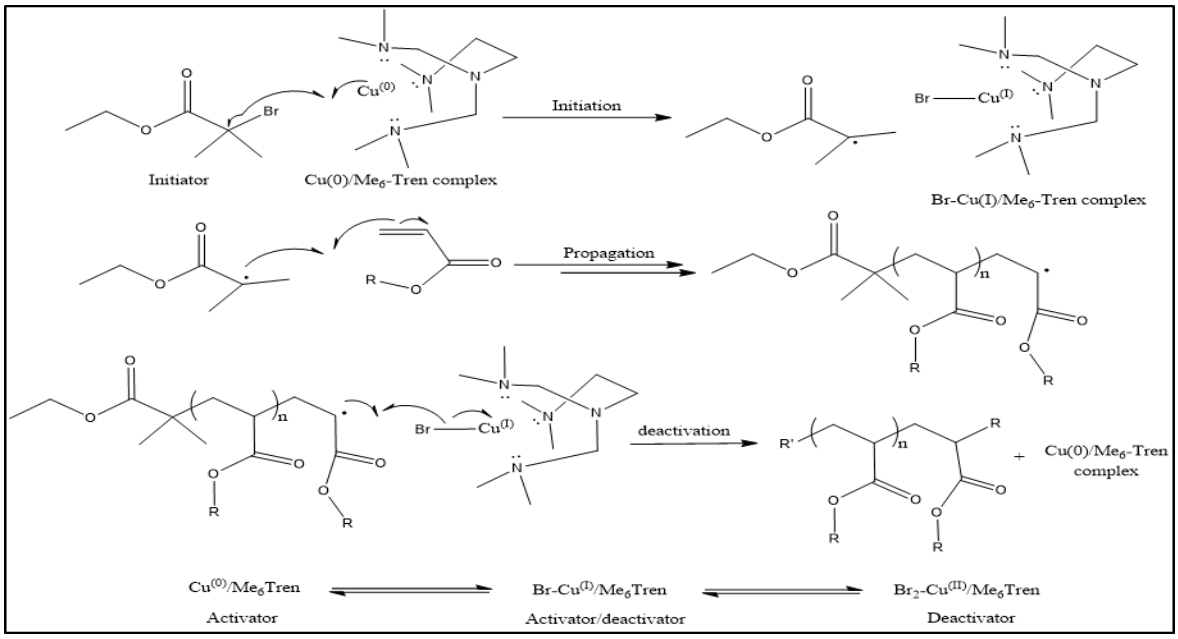

Figure 2.21 Simplified mechanism of Cu(0)-mediated LRP.

The use of Cu(0) and Cu(II)Br_2 is key to ensuring the polymerisation is controlled. Initially, Cu(0) is highly reactive and is able to rapidly initiate all initiator molecules instantly to ensure they start the polymerisation at the same time. Subsequently, the equilibrium between Cu(0), Cu(I) and Cu(II) governs the rate of propagation where Cu(II)Br_2 recombines (deactivates) with the propagating chain end to halt the polymerisation followed by reactivation by either Cu(0) or Cu(I) to restart the polymerisation. Essentially, the role of the equilibrium is to ensure all of the propagating chains are polymerising at the same time and at the same rate to ensure they all finish at the same time and thus achieve controlled dispersity and controlled molecular weight. The activation/deactivation is considerably faster than the rate of propagation and therefore, there is limited opportunity for the polymer chains to terminate, undergo recombination or chain transfer, which leads to excellent end group fidelity.[89]

The excellent end group fidelity achieved by Cu(0)-mediated LRP enables the synthesis of sequence controlled-multiblock copolymers. Prior to the introduction of Cu(0)-

mediated LRP, the growing polymer chain required stringent purification in order to maintain high end-group fidelity due to low conversion and high levels of termination. As Cu(0)-mediated LRP produces quantitative conversion in every cycle, no purification methods are required between intermediate monomer additions and hence, Cu(0)-mediated LRP has catalysed the growth in the production of multiblock copolymers with complex architectures such as stars and hyperbranched structures. Such properties make it an excellent technique for the purpose of designing and producing multiblock polymers for the compatibilisation of CNTs and GNPs within a polymer matrix such as PP.[89]

2.7 Concluding remarks

In conclusion, CNTs and GNPs have been selected for their exceptional mechanical, electrical and thermal properties. The fillers can be directly loaded into polymer matrices using melt compounding, however the Van der Waals forces between the CNTs and GNPs results in poor dispersion and interfacial adhesion. Twin screw extrusion is not efficient at achieving homogenous dispersions even with high rotor speeds and long residence times. To overcome the poor dispersion of the nano-fillers within the polymer matrices, functionalisation is required. Non-covalent functionalisation relies on weak intermolecular interactions such as π-π, CH-π and polymer wrapping and therefore, adsorption kinetics must be considered. It is hypothesised, the optimal compatibilising molecule would be a polymer due to the fact the compatibiliser is required to co-crystallise with PP and irreversibly adsorb to the surface of the fillers. The use of the controlled living radical polymerisation techniques such as RAFT and Cu(0)-mediated LRP can be utilised to produce well defined polymers with controlled molar masses, dispersity and architecture. They can be used to synthesis bi-functional polymers which are able to compatibilise with the polymer matrix and the filler. In conclusion, the project will focus on the synthesis and characterisation of various polymer compatibilisers, specifically for aiding and improving the dispersion of MWCNTs and GNPs in PP. The composites will be produced using twin-screw melt compounding and the composites extensively characterised to determine how the structure and properties of the polymer affects the properties of the composite. In addition, the non-covalent adsorption onto the surface of the fillers will extensively characterised. The polymer compatibilisers will be in the form of homo and copolymers which are capable of wrapping the fillers using

either CH-π or π-π type interactions as well co-crystallise with PP matrix to bridge the incompatibility and improve dispersion during melt-mixing.

2.8 References

1. S. Stankovich, D. A. Dikin, G. H. B. Dommett, K. M. Kohlhaas, E. J. Zimney, E. A. Stach, R. D. Piner, S. T. Nguyen and R. S. Ruoff, *Nature*, 2006, **442**, 282-286.
2. D. Baskaran, J. W. Mays and M. S. Bratcher, *Chem. Mater.*, 2005, **17**, 3389-3397.
3. S. P. Bao and S. C. Tjong, *Mater. Sci. Eng. A*, 2008, **485**, 508-516.
4. Z. Zhou, S. F. Wang, Y. Zhang and Y. X. Zhang, *J. Appl. Polym. Sci.*, 2006, **102**, 4823-4830.
5. S. J. Blanksby and G. B. Ellison, *Acc. Chem. Res.*, 2003, **36**, 255-263.
6. Y. N. Xia, P. D. Yang, Y. G. Sun, Y. Y. Wu, B. Mayers, B. Gates, Y. D. Yin, F. Kim and Y. Q. Yan, *Adv. Mater.*, 2003, **15**, 353-389.
7. S. Iijima, *Nature*, 1991, **354**, 56-58.
8. P. Bilalis, D. Katsigiannopoulos, A. Avgeropoulos and G. Sakellariou, *R. Soc. Chem. Adv.*, 2014, **4**, 2911-2934.
9. X. M. Sun, H. Sun, H. P. Li and H. S. Peng, *Adv. Mater.*, 2013, **25**, 5153-5176.
10. E. T. Thostenson, Z. F. Ren and T. W. Chou, *Compos. Sci. Technol.*, 2001, **61**, 1899-1912.
11. C. M. White, R. Banks, I. Hamerton and J. F. Watts, *Prog. Org. Coat.*, 2016, **90**, 44-53.
12. M. Morsy, M. Helal, M. El-Okr and M. Ibrahim, *Spectrochim. Acta Mol. Biomol. Spectros.*, 2014, **132**, 594-598.
13. W. W. Liu, S. P. Chai, A. R. Mohamed and U. Hashim, *J. Ind. Eng. Chem.*, 2014, **20**, 1171-1185.
14. M. T. Byrne and Y. K. Gun'ko, *Adv. Mater.*, 2010, **22**, 1672-1688.
15. S. H. Song, K. H. Park, B. H. Kim, Y. W. Choi, G. H. Jun, D. J. Lee, B. S. Kong, K. W. Paik and S. Jeon, *Adv. Mater.*, 2013, **25**, 732-737.
16. A. A. Balandin, S. Ghosh, W. Z. Bao, I. Calizo, D. Teweldebrhan, F. Miao and C. N. Lau, *Nano Lett.*, 2008, **8**, 902-907.
17. B. I. Yakobson, G. Samsonidze and G. G. Samsonidze, *Carbon*, 2000, **38**, 1675-1680.

18. M. M. J. Treacy, T. W. Ebbesen and J. M. Gibson, *Nature*, 1996, **381**, 678-680.
19. J. P. Salvetat, G. A. D. Briggs, J. M. Bonard, R. R. Bacsa, A. J. Kulik, T. Stockli, N. A. Burnham and L. Forro, *Phys. Rev. Lett.*, 1999, **82**, 944-947.
20. G. Miquelard-Garnier, A. Guinault, D. Fromonteil, S. Delalande and C. Sollogoub, *Polymer*, 2013, **54**, 4290-4297.
21. T. Y. Zhou, G. C. P. Tsui, J. Z. Liang, S. Y. Zou, C. Y. Tang and V. Miskovic-Stankovic, *Compos. Part B*, 2016, **90**, 107-114.
22. Y. L. Zhao and J. F. Stoddart, *Acc. Chem. Res.*, 2009, **42**, 1161-1171.
23. D. Q. Zhang, J. Yang and Y. Li, *Small*, 2013, **9**, 1284-1304.
24. M. S. de Luna, L. Pellegrino, M. Daghetta, C. V. Mazzocchia, D. Acierno and G. Filippone, *Compos. Sci. Technol.*, 2013, **85**, 17-22.
25. B. I. Yakobson, C. J. Brabec and J. Bernholc, *Phys. Rev. Lett.*, 1996, **76**, 2511-2514.
26. M. Caplovicova, T. Danis, D. Buc, L. Caplovic, J. Janik and I. Bello, *Ultramicroscopy*, 2007, **107**, 692-697.
27. V. Georgakilas, M. Otyepka, A. B. Bourlinos, V. Chandra, N. Kim, K. C. Kemp, P. Hobza, R. Zboril and K. S. Kim, *Chem. Rev.*, 2012, **112**, 6156-6214.
28. R. F. Egerton, *Rep. Prog. Phys.*, 2009, **72**, 1-25.
29. A. E. Goode, N. D. M. Hine, S. Chen, S. D. Bergin, M. S. P. Shaffer, M. P. Ryan, P. D. Haynes, A. E. Porter and D. W. McComb, *Chem. Commun.*, 2014, **50**, 6744-6747.
30. A. K. Geim and K. S. Novoselov, *Nat. Mater.*, 2007, **6**, 183-191.
31. K. S. Novoselov, A. K. Geim, S. V. Morozov, D. Jiang, Y. Zhang, S. V. Dubonos, I. V. Grigorieva and A. A. Firsov, *Science*, 2004, **306**, 666-669.
32. R. J. Young, I. A. Kinloch, L. Gong and K. S. Novoselov, *Compos. Sci. Technol.*, 2012, **72**, 1459-1476.
33. J. R. Potts, D. R. Dreyer, C. W. Bielawski and R. S. Ruoff, *Polymer*, 2011, **52**, 5-25.
34. K. R. Paton, E. Varrla, C. Backes, R. J. Smith, U. Khan, A. O'Neill, C. Boland, M. Lotya, O. M. Istrate, P. King, T. Higgins, S. Barwich, P. May, P. Puczkarski, I. Ahmed, M. Moebius, H. Pettersson, E. Long, J. Coelho, S. E. O'Brien, E. K. McGuire, B. M. Sanchez, G. S. Duesberg, N. McEvoy, T. J. Pennycook, C.

Downing, A. Crossley, V. Nicolosi and J. N. Coleman, *Nat. Mater.*, 2014, **13**, 624-630.

35. C. Valles, I. A. Kinloch, R. J. Young, N. R. Wilson and J. P. Rourke, *Compos. Sci. Technol.*, 2013, **88**, 158-164.
36. A. H. Castro Neto, F. Guinea, N. M. R. Peres, K. S. Novoselov and A. K. Geim, *Rev. Mod. Phys.*, 2009, **81**, 109-162.
37. L. M. Malard, M. A. Pimenta, G. Dresselhaus and M. S. Dresselhaus, *Phys. Rep.*, 2009, **473**, 51-87.
38. M. S. Dresselhaus, G. Dresselhaus, R. Saito and A. Jorio, *Phys. Rep.*, 2005, **409**, 47-99.
39. E. T. Thostenson, C. Y. Li and T. W. Chou, *Compos. Sci. Technol.*, 2005, **65**, 491-516.
40. J. N. Coleman, U. Khan, W. J. Blau and Y. K. Gun'ko, *Carbon*, 2006, **44**, 1624-1652.
41. T. McNally and P. Pötschke, in *Polymer–carbon nanotube composites: preparation, properties and applications*, Woodhead Publishing Ltd, Cambridge, UK, 1st edn., 2011, pp. 428-481.
42. T. McNally, P. Pötschke, P. Halley, M. Murphy, D. Martin, S. E. J. Bell, G. P. Brennan, D. Bein, P. Lemoine and J. P. Quinn, *Polymer*, 2005, **46**, 8222-8232.
43. D. S. Bangarusampath, H. Ruckdaschel, V. Altstadt, J. K. W. Sandler, D. Garray and M. S. P. Shaffer, *Chem. Phys. Lett.*, 2009, **482**, 105-109.
44. P. Pötschke, T. D. Fornes and D. R. Paul, *Polymer*, 2002, **43**, 3247-3255.
45. X. Zhang, X. R. Yan, Q. L. He, H. G. Wei, J. Long, J. Guo, H. B. Gu, J. F. Yu, J. J. Liu, D. W. Ding, L. Y. Sun, S. Y. Wei and Z. H. Guo, *ACS Appl. Mater. Interfaces*, 2015, **7**, 6125-6138.
46. Y. Xiao, X. Q. Zhang, W. Cao, K. Wang, H. Tan, Q. Zhang, R. N. Du and Q. Fu, *J. Appl. Polym. Sci.*, 2007, **104**, 1880-1886.
47. A. P. Bafana, X. R. Yan, X. Wei, M. Patel, Z. H. Guo, S. Y. Wei and E. K. Wujcik, *Compos. Part B*, 2017, **109**, 101-107.
48. B. Yang, Y. Zhao, X. Ren, X. Y. Zhang, C. K. Fu, Y. L. Zhang, Y. Wei and L. Tao, *Polym. Chem.*, 2015, **6**, 509-513.
49. Q. X. Li, J. S. Church, A. Kafi, M. Naebe and B. L. Fox, *J. Nanopart. Res.*, 2014, **16**, 2513.

50. J. N. Coleman, U. Khan and Y. K. Gun'ko, *Adv. Mater.*, 2006, **18**, 689-706.
51. M. Supova, G. S. Martynkova and K. Barabaszova, *Sci. Adv. Mater.*, 2011, **3**, 1-25.
52. R. M. Novais, F. Simon, M. C. Paiva and J. A. Covas, *Compos. Part A*, 2012, **43**, 2189-2198.
53. B. Mayoral, J. Lopes and T. McNally, *Macromol. Mater. Eng.*, 2014, **299**, 609-621.
54. B. Mayoral, G. Garrett and T. McNally, *Macromol. Mater. Eng.*, 2014, **299**, 748-756.
55. J. R. Yu, N. Grossiord, C. E. Koning and J. Loos, *Carbon*, 2007, **45**, 618-623.
56. S. P. Lonkar, Y. S. Deshmukh and A. A. Abdala, *Nano Res.*, 2015, **8**, 1039-1074.
57. C. M. Homenick, G. Lawson and A. Adronov, *Polym. Rev.*, 2007, **47**, 265-290.
58. A. Alam, C. Y. Wan and T. McNally, *Eur. Polym. J.*, 2017, **87**, 422-448.
59. A. E. Daugaard, K. Jankova and S. Hvilsted, *Polymer*, 2014, **55**, 481-487.
60. S. J. Zhang, T. Shao, H. S. Kose and T. Karanfil, *Environ. Sci. Technol.*, 2012, **31**, 79-85.
61. E. V. Anslyn and D. A. Dougherty, *Modern Physical Organic Chemistry*, Wilsted and Taylor Publishing Services, United States of America, 2006.
62. K. Yang, L. Z. Zhu and B. S. Xing, *Environ. Sci. Technol.*, 2006, **40**, 1855-1861.
63. W. Chen, L. Duan, L. L. Wang and D. Q. Zhu, *Environ. Sci. Technol.*, 2008, **42**, 6862-6868.
64. W. Chen, L. Duan and D. Q. Zhu, *Environ. Sci. Technol.*, 2007, **41**, 8295-8300.
65. R. J. Chen, Y. G. Zhang, D. W. Wang and H. J. Dai, *J. Am. Chem. Soc.*, 2001, **123**, 3838-3839.
66. C. R. Martinez and B. L. Iverson, *Chem. Sci.*, 2012, **3**, 2191-2201.
67. M. Zhao, L. Y. Yang, R. C. Zhang, J. Dong, H. F. Dong, Y. Q. Wen, X. W. Zhan, G. Wang, Y. F. Lu and G. J. Wang, *Polymer*, 2013, **54**, 297-302.
68. S. Meuer, L. Braun and R. Zentel, *Macromol. Chem. Phys.*, 2009, **210**, 1528-1535.
69. J. Chen, H. Y. Liu, W. A. Weimer, M. D. Halls, D. H. Waldeck and G. C. Walker, *J. Am. Chem. Soc.*, 2002, **124**, 9034-9035.
70. T. Fujigaya and N. Nakashima, *Sci. Tech. Adv. Mater.*, 2015, **16**, 1-21.
71. E. Pavoni, E. Bandini, M. Benaglia, J. K. Molloy, G. Bergamini, P. Ceroni and N. Armaroli, *Polym. Chem.*, 2014, **5**, 6148-6150.
72. M. T. Muller, P. Pötschke and B. Voit, *Polymer*, 2015, **66**, 210-221.
73. S. H. Lee, E. Cho, S. H. Jeon and J. R. Youn, *Carbon*, 2007, **45**, 2810-2822.

74. E. Cohen, A. Ophir, S. Kenig, C. Barry and J. Mead, *Macromol. Mater. Eng.*, 2013, **298**, 419-428.
75. *Market Study: Polypropylene*, Ceresana, http://www.ceresana.com/en/market-studies/plastics/polypropylene/, 3rd edn., 10/08/2014.
76. M. P. Stevens, *Polymer Chemistry: An Introduction*, Oxford University Press, New York, 3rd edn., 1999.
77. R. Thomann, C. Wang, J. Kressler and R. Mulhaupt, *Macromolecules*, 1996, **29**, 8425-8434.
78. K. Nakamura, S. Shimizu, S. Umemoto, A. Thierry, B. Lotz and N. Okui, *Polym. J.*, 2008, **40**, 915-922.
79. C. Angelloz, R. Fulchiron, A. Douillard, B. Chabert, R. Fillit, A. Vautrin and L. David, *Macromolecules*, 2000, **33**, 4138-4145.
80. S. J. Chin, S. Vempati, P. Dawson, M. Knite, A. Linarts, K. Ozols and T. McNally, *Polymer*, 2015, **58**, 209-221.
81. G. G. Odian, *Principles of polymerisation*, Wiley, New York, 3rd edn., 1991.
82. J. Karger-Kocsis, in *Polypropylene: An A-Z reference*, Kluwer Academic, Dordrecht, 1999, pp. 136, 295, 332.
83. J. Varga, *J. Mater. Sci.*, 1992, **27**, 2557-2579.
84. A. T. Jones, J. M. Aizlewood and D. R. Beckett, *Macromol. Chem. Phys.*, 1964, **75**, 134-158.
85. A. R. Bhattacharyya, T. V. Sreekumar, T. Liu, S. Kumar, L. M. Ericson, R. H. Hauge and R. E. Smalley, *Polymer*, 2003, **44**, 2373-2377.
86. B. Zhang, J. B. Chen, X. L. Zhang and C. Y. Shen, *J. Appl. Polym. Sci.*, 2011, **120**, 3255-3264.
87. S. Detriche, G. Zorzini, J. F. Colomer, A. Fonseca and J. B. Nagy, *J. Nanosci. Nanotechnol.*, 2008, **8**, 6082-6092.
88. W. Wang, P. Ciselli, E. Kuznetsov, T. Peijs and A. H. Barber, *Philosophical Transactions of the Royal Society a-Mathematical Physical and Engineering Sciences*, 2008, **366**, 1613-1626.
89. A. Anastasaki, V. Nikolaou and D. M. Haddleton, *Polym. Chem.*, 2016, **7**, 1002-1026.
90. C. J. Hawker, A. W. Bosman and E. Harth, *Chem. Rev.*, 2001, **101**, 3661-3688.

91. D. J. Keddie, G. Moad, E. Rizzardo and S. H. Thang, *Macromolecules*, 2012, **45**, 5321-5342.
92. N. G. Engelis, A. Anastasaki, G. Nurumbetov, N. P. Truong, V. Nikolaou, A. Shegiwal, M. R. Whittaker, T. P. Davis and D. M. Haddleton, *Nat. Chem.*, 2017, **9**, 171-178.
93. D. J. Keddie, *Chem. Soc. Rev.*, 2014, **43**, 496-505.
94. J. T. Lai, D. Filla and R. Shea, *Macromolecules*, 2002, **35**, 6754-6756.
95. J. Lad, S. Harrisson, G. Mantovani and D. M. Haddleton, *Dalton Trans.*, 2003, DOI: 10.1039/b303888b, 4175-4180.
96. W. A. Braunecker and K. Matyjaszewski, *Prog. Polym. Sci.*, 2007, **32**, 93-146.
97. G. Moad, E. Rizzardo and S. H. Thang, *Polymer*, 2008, **49**, 1079-1131.
98. S. Perrier and P. Takolpuckdee, *J. Polym. Sci. Part A: Polym. Chem.*, 2005, **43**, 5347-5393.
99. J. Skey and R. K. O'Reilly, *Chem. Commun.*, 2008, DOI: 10.1039/b804260h, 4183-4185.
100. G. Moad, E. Rizzardo and S. H. Thang, *Aust. J. Chem.*, 2009, **62**, 1402-1472.
101. G. Moad, in *Controlled Radical Polymerization: Mechanisms*, American Chemical Society, 2015, vol. 1187, ch. 12, pp. 211-246.
102. Q. Zhang, P. Wilson, Z. D. Li, R. McHale, J. Godfrey, A. Anastasaki, C. Waldron and D. M. Haddleton, *J. Am. Chem. Soc.*, 2013, **135**, 7355-7363.
103. C. Waldron, A. Anastasaki, R. McHale, P. Wilson, Z. D. Li, T. Smith and D. M. Haddleton, *Polym. Chem.*, 2014, **5**, 892-898.
104. B. M. Rosen and V. Percec, *Chem. Rev.*, 2009, **109**, 5069-5119.
105. K. Matyjaszewski, *Macromolecules*, 2012, **45**, 4015-4039.
106. K. Matyjaszewski and J. H. Xia, *Chem. Rev.*, 2001, **101**, 2921-2990.

Chapter 3 Materials and Methods

3.1 Materials

3.1.1 Poly(propylene) (PP)

Injection moulding grade isotactic poly(propylene) (PP), grade H734-52RNA ($M_{n,SEC}$ = 56,000, $Đ$ = 4.3 had a melting temperature range of 165 – 180 °C, density = 0.945 g cm^{-3} and a melt flow rate (MFR) of 52 g/10 min at 230 °C and 2.16 kg (ISO 1133D) was supplied by Braskem Europe GmbH in pellet form.

3.1.2 Multi-Walled Carbon Nanotubes (MWCNTs)

Non-functionalised commercially available thin multi-walled carbon nanotubes (MWCNTs) produced by a catalytic carbon vapour deposition (CCVD) process with an average diameter of 9.5 nm and average length of 1.5 μm (grade NC7000, purity: >90%) were purchased from Nanocyl S.A., Belgium and used as received. The density of these MWCNTs was reported to be 1.85 g cm^{-3},[1] and the oxygen to carbon ratio 0.0045:1,[2] respectively.

3.1.3 Graphene Nanoplatelets (GNPs)

Mechanical materials Grade Elicarb® graphene few-layer nanoplatelet powder (product code: SP8082) (GNPs) were kindly donated by Thomas Swan & Company Ltd. The nanoplatelets were reported (by Thomas Swan Ltd) to have; a typical lateral size <5 μm, an aspect ratio of ~ 500, a sheet resistance of <22 Ω/m (measured using a 25 μm film via a four-point probe method), a I_D/I_G ratio of 0.07 – 0.1 and $I_D/I_{D'}$ ratio of 3.5 – 5.0, a surface area of 30 – 50 m^2g^{-1}, a sp^2 content of 98%, an average plate thickness between 5 and 7 layers, reported to contain 4% surfactant residues and 4% inorganic residues.

3.1.4 Lauryl Acrylate (LA)

Lauryl acrylate (LA) was purchased from Sigma Aldrich and passed through a column of basic alumina immediately prior to use in order to remove inhibitors. Lauryl acrylate has a density of 0.884 g ml^{-1} (Sigma-Aldrich).

3.1.5 2-Phenyl ethyl Acrylate (2PEA)

2-Phenyl ethyl Acrylate (2PEA) was purchased from Polysciences Europe GmbH and passed through a column of basic alumina immediately prior to use in order to remove inhibitors.

3.1.6 Copper (0) Wire

Cu(0)-wire (gauge 0.25 mm) was purchased from Comax Engineering Wires and pre-activated by immersion in conc. HCl prior to use.

3.1.7 *Tris*-(2-(dimethylamino)ethyl)amine (Me_6TREN)

Tris-(2-(dimethylamino)ethyl)amine (Me_6TREN) was synthesised following a previously published procedure,[3] degassed and stored in a fridge under nitrogen prior to use. Me_6TREN has a density of 0.862 g ml^{-1} (Sigma-Aldrich).

3.1.8 Hostasol-ATRP initiator

Hostasol-ATRP initiator (Hostasol-ATRP) was kindly donated by Prof. David Haddleton (University of Warwick). Hostasol was modified into an ATRP initiator by Haddleton group in the following way. Hostasol (thioxantheno[2,1,9-dej]isochromene-1,3-dione) was supplied by Clariant. Hostasol was firstly modified into Hostasol-OH (2-(8-Hydroxy-3,6-dioxaoctyl)thioxantheno [2,1,9- dej]isoqiunoline-1,3-dione) by reacting with 5-aminopentol with the aid of *p*-toluenesulfonic acid to produce a bright orange solid.[4] The Hostasol-OH was modified into a Hostasol-ATRP initiator by reacting with α-Bromoisobutyryl bromide to produce a bright orange solid.[4, 5]

3.1.9 Pyrene-ATRP initiator

Pyrene-ATRP initiator (Pyrene-ATRP) was kindly donated by Prof. David Haddleton (University of Warwick).

3.1.10 General reagent and solvents

1-Dodecanethiol, anhydrous tetrahydrofuran, potassium tert-butoxide, carbon disulfide, chloroacetonitrile, chloroform, formaldehyde, methanol, sodium chloride, sodium sulfate, ethyl acetate, n-hexane, trimethylamine, ethyl 2-bromoisobutyrate (EBiB) (density = 1.329 gml^{-1}), copper(II) bromide, Tris(2-aminoethyl)amine (TREN), anhydrous toluene, 2,2'-Azobis(2-methylpropionitrile) [AIBN] and isopropanol (IPA) were purchased from Sigma Aldrich or Fisher Scientific and were all used as received. Filter paper was obtained from Fisher (cellulose) with a pore size of 20-25 μm.

3.2 Sample Preparation

3.2.1 Synthesis of *Tris*-(2-(dimethylamino)ethyl)amine (Me_6TREN)

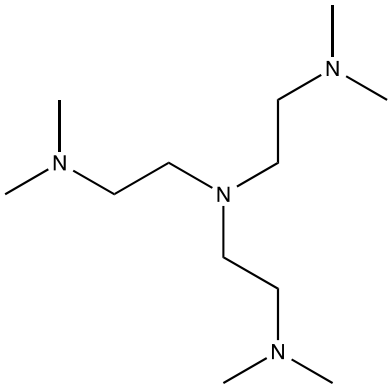

(N,N,N',N',N'',N''-hexamethyl-[trisaminoethyl]amine, Me_6-TREN)

Me_6TREN was synthesised following the previously published procedure by Ciampolini and Nardi[3] degassed and stored in a fridge under nitrogen prior to use.[6]

Formaldehyde 37% v/v (270.9 ml, 3.64 mol) and formic acid (320 ml, 8.15 mol) were added to a 1L RB flask, immersed in an ice bath. Tris(2-aminoethyl)amine (50 ml, 0.33 mol) was added drop-wise over a period of 1h, with vigorous stirring. The rate of addition was adjusted to limit the formation of carbon dioxide. The reaction mixture was subsequently refluxed at 120 ºC for 12h (until the evolution of carbon dioxide had ceased). After cooling to ambient temperature, the volatiles were removed by rotary evaporation to give an orange-yellow oil. After cooling the reaction mixture in an ice bath, the pH was adjusted to pH 10 with a saturated sodium hydroxide solution[a]. The oil was extracted using 3 x 150 ml of chloroform. The combined organic layers were concentrated by rotary evaporation to yield an orange-yellow layer. The oil was distilled under reduced pressure[b] (75-79 ºC, 10^{-3} mbar) to yield a colourless oil (25.33 g, 63% yield).

a) Upon adjustment to pH 10, the product precipitates out of the solution to form an oily layer. This required a large amount of saturated NaOH solution.

b) The first fraction (waste) was removed using a cryo-distillation technique. Then, the second fraction, the product, was extracted under reduced pressure (75-79 ºC, 10^{-3} mbar).

^{1}H NMR ($CDCl_3$, 400 MHz, 298 K), δ (ppm): 2.25 (t, 6H, J=7.03 Hz, $(CH_3)_2$-N-CH_2-C***H***$_2$-N-R) and 2.00 (t, 6H, J=7.03 Hz, $(CH_3)_2$-N-C***H***$_2$-CH_2-N-R), 1.86 (s, 18H, (C***H***$_3)_2$-N-R).

^{13}C NMR ($CDCl_3$, 400 MHz, 298 K), δ(ppm): 57.5 $(CH_3)_2$-N-***C***H_2-CH_2-N-R), 53.1$(CH_3)_2$-N-CH_2-***C***H_2-N-R), 45.9 (***C***$H_3)_2$-N-R).

IR (neat) (cm^{-1}): 1034, 1125 ($\nu_{C\text{-}N}$).

ESI-MS (m/z, Da): [M^+] 231.2 (230.25 Th)

3.2.2 Cyanomethyl dodecyltrithiocarbonate

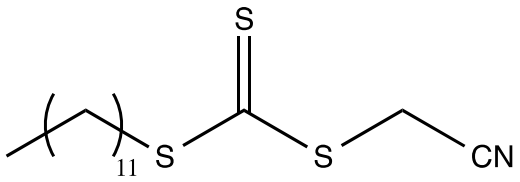

1-Dodecanethiol (12.75 g, 63 mmol, 1 eq) was dissolved in 100 mL dry THF. Potassium tert-butoxide (7.07 g, 63 mmol, 1 eq) was added to the solution with stirring at ambient temperature. The solution became thick and cloudy. After stirring for 15 minutes, carbon disulfide, CS_2 (9.6 g, 126 mmol, 2 eq) was added and the solution stirred for a further 30 minutes. Subsequently, chloroacetonitrile (4.75 g 63 mmol, 1 eq) was added and the mixture stirred for a further 24 hours. The solution was diluted with deionised water and extracted with chloroform (3 × 100 mL), washed with brine (2 × 100 mL) and dried with sodium sulphate. The product was then filtered and the solvent removed under reduced pressure. The crude product was purified by column chromatography through silica eluting with 1:9 ethyl acetate/n-hexane. The product was re-crystallised with n-hexane to give the desired product cyanomethyl dodecyltrithiocarbonate (19.22 g, 60 mmol, 96 %). ^{1}H NMR ($CDCl_3$, 400 MHz, 298 K), δ (ppm): 4.16 (s, 2H, -C***H***$_2$-CN), 3.42 (t, J = 7.34 Hz, 2H, -CH_2-C***H***$_2$-S(C=S)S), 1.73 (m, 2H, -C***H***$_2$-CH_2-S(C=S)S), 1.5-1.2 (m, 18H, CH_3-(C***H***$_2)_9$-CH_2-) 0.89 (t, J = 6.70 Hz, 3H, C***H***$_3$-$(CH_2)_9$-CH_2-). ^{13}C NMR ($CDCl_3$, 400 MHz, 298 K), δ (ppm): 218.8, 114.7, 38.0, 31.9, 29.6, 29.5, 29.4, 29.3, 29.0, 28.9, 27.8, 22.7, 21.3, 14.1. IR (neat) (cm^{-1}): 2900 (C-H), 2850 (C-H), 2250 (C≡N), 1460, 1370, 1075 (S-(C=S)-S), 850, 810, 720. HRMS (ESI) m/z ($C_{15}H_{27}S_3N$ [M+H^+] requires 318.13) observed 318.14. The data concurs with that reported by Chong *et al.*[6, 7]

3.2.3 Typical RAFT polymerisation procedure

The typical procedure for RAFT polymerisation of lauryl acrylate was adapted from a previously reported literature method.[8] Cyanomethyl dodecyltrithiocarbonate (RAFT agent) (63.5 mg, 0.2 mmol, 1.0 mol equiv.), lauryl acrylate (LA, 2.26 mL, 8.32 mmol, 42.0 mol equiv.), 2,2′-azobis(2-methylpropionitrile) (AIBN, 0.3 mg, 2 μmol, 0.01 mol equiv.) and a magnetic stir bar were charged to a polymerisation Schlenk tube and dissolved in 3 mL of anhydrous toluene. A rubber septum was used to seal the Schlenk tube and the mixture degassed via sparging with argon for 20 min. The Schlenk tube was placed in an oil bath heated at 60 °C for 24 h. Toluene was removed using reduced pressure and then the polymer was precipitated by the addition of cold methanol and water (4:1 v/v) from chloroform. Samples of the reaction mixture were carefully removed at the end of the polymerisation for ^{1}H NMR, mass spectroscopy and GPC analyses. The samples for ^{1}H NMR spectroscopy were diluted in $CDCl_3$, while samples for GPC and MS were diluted with chloroform and tetrahydrofuran (THF), respectively.[6]

3.2.4 Typical Cu(0)-mediated polymerisation procedure

P[LA] was synthesised using the procedure described by Anastasaki *et al*.[9, 10] Ethyl 2-bromoisobutyrate (EBiB, 2.31 mL, 3.07 g, 15.8 mmol, 1.00 mol equiv.), *n*-lauryl acrylate (LA, 180 mL, 159.12 g, 662 mmol, 42.0 mol equiv. relative to initiator molecule), $Cu^{II}Br_2$ (176 mg, 0.79 mmol, 0.05 mol equiv. relative to bromo functionality), IPA (180 mL) and a magnetic stir bar wrapped with pre-activated copper wire (15 cm) were charged to a polymerisation reactor vessel prior to sealing with a rubber septum and the mixture deoxygenated with argon sparging for 15 min. *via* a needle. Me_6TREN (0.758 mL, 0.653 g, 2.84 mmol, 0.18 mol equiv. relative to bromo functionality) was added *via* a deoxygenated, air tight syringe to start the reaction and the polymerisation was allowed to proceed for 24h at ambient temperature. Samples of the reaction mixture were carefully removed at the end of the polymerisation for ^{1}H NMR, and GPC analysis. The samples for ^{1}H NMR spectroscopy were diluted in $CDCl_3$, while the GPC samples were diluted with chloroform and then passed through a column of basic alumina to remove the copper salts. The lauryl acrylate polymer was precipitated in a mixture of cold methanol and water (4:1 v/v) from chloroform to remove copper salts and dried overnight in a vacuum oven.[6] Homopolymers and copolymers of P[LA] and P[2PEA] were polymerised using the procedure described above with identical molar equivalent ratios. Volumes and masses were altered as required

following the controlled living radical equation of $DP_n = [M]/[I]$ where, DP_n is the degree of polymerisation, [M] is the monomer concentration and [I] is the initiator concentration.

Synthesis of P[LA-*stat*-2PEA] involved combining LA and 2PEA at the monomer addition stage. Synthesis of P[LA-*block*-2PEA] involved first polymerising LA using the procedure above. Subsequently, P[LA] was considered as a macro-initiator for the synthesis of the 2PEA block and polymerised using the procedure above.

3.2.5 Typical protocol for solution mixing of MWCNTs/GNPs with poly(acrylate)s

Solution mixing of MWCNTs/GNPs with poly(acrylates) was based on a previously published procedure.[6] MWCNTs [50 mg (5 wt%) and 100 mg (10 wt%)] were dispersed in chloroform (100 mL) *via* ultrasonication for 3 minutes at ambient temperature. Solutions of MWCNTs mixed with P[LA] were sonicated using a Fisher ultrasonic bath (S30H) at 50 Hz, 280 W. Subsequently, 1 g of P[LA] was added to the dispersion and the mixture was again sonicated for 3 mins. A magnetic stirrer bar was added to the reaction vessel and the mixture stirred vigorously for 1 hour. The mixture was filtered using a Buchner funnel. The filter cake was collected and dried overnight in a vacuum oven at ambient temperature.[6]

3.2.6 Typical (nano)composite preparation procedure

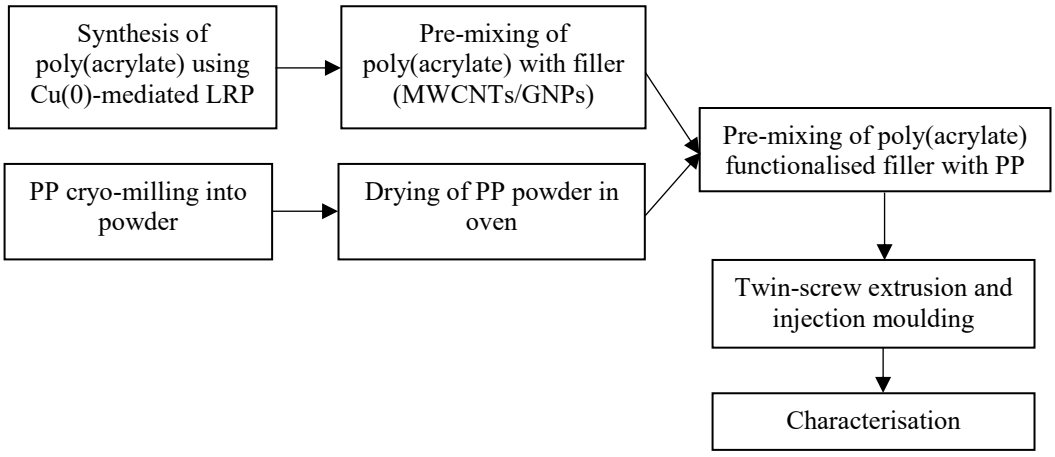

Figure 3.1 Schematic representation of the typical protocol adopted for preparation of composite materials.

Composites were prepared based on previously published procedures and adapted as required (Figure 3.1).[1, 11-16] The PP pellets were ground to a powder (μm diameter particles), using a SPEX® SamplePrep Freezer Mill 6870 (Stanmore, UK) to improve mixing between the PP and the fillers. The pellets (25 g batch) were pre-cooled for 12 min., followed by two

5 min. grinding cycles at 15 Hz. Between each cycle, the sample was cooled for a 2 min. interval. A liquid nitrogen bath was used for cooling to prevent shear heating which could degrade the material. The PP powder was dried in a vacuum oven at 30 ºC for 12h prior to processing. FTIR was employed to assess if any degradation had taken place as a consequence of the grinding process. No PP degradation was observed, at any time, using this methodology.

The PP and fillers (MWCNTs/GNPs) were in powder form and the poly(acrylates) were in liquid form. Composites were prepared by dry blending (pre-functionalising) the filler powder with a given ratio of poly(acrylate) polymer and subsequently dry blending with a given ratio of PP (blend compositions described in section 3.2.7) by manually mixing in a glass beaker using a spatula. The pre-blend was then fed into the hopper of a Haake™ Mini-Lab II micro-compounder fitted with two conical co-rotating screws and which facilitates recirculation of the mixture within a chamber of volume 5 cm^3. The composite material was processed for 5 min. at 100 rpm and 170 ºC (conditions previously optimised with unfilled PP in a control experiment). After 5 min., the (nano)composite was extruded through a 3.90 x 1.20 mm rectangular die directly into the hot melt chamber of a micro-injection moulding machine. Samples were injection moulded using a piston injection moulding system (Thermo-Scientific Haake™ MiniJet Pro) to produce standard dumbbell-shaped test specimens conforming to ASTM D638 V, disk samples (d = 25, h = 1.5 mm) for oscillatory rheology measurements and bar samples (80 x 10 x 4 mm) for DMTA studies. The injection temperature was set to 190 ºC and the mould temperature to 70 ºC with an injection pressure of 350 bar. (Neat PP was also extruded and injection moulded using the same parameters for the purpose of comparison). Composite samples were subsequently characterised using a range of techniques described section 3.3.

3.2.7 Composite compositions

The following tables describe the compositions of each mixture used to make the composites and the corresponding nomenclature adopted.

Table 3.1 Blending ratios (wt%) for PP and composites of PP, poly(lauryl acrylate) P[LA] (M_n = 11,500, $Đ$ = 1.15) and MWCNTs and corresponding composite nomenclature.

Composite composition (wt %)	Nomenclature
PP (100)	PP
PP(99.99)/CNT(0.01)	0.01 wt% CNT
PP(99.9)/CNT(0.1)	0.1 wt% CNT
PP(99.7)/CNT(0.3)	0.3 wt% CNT
PP(99.5)/CNT(0.5)	0.5 wt% CNT
PP(99)/CNT(1)	1 wt% CNT
PP(97)/CNT(3)	3 wt% CNT
PP(95)/CNT(5)	5 wt% CNT
PP(99.96)/P[LA](0.04)	0.04 wt% P[LA]
PP(99.6)/P[LA](0.4)	0.4 wt% P[LA]
PP(98.8)/P[LA](1.2)	1.2 wt% P[LA]
PP(98)/P[LA](2)	2 wt% P[LA]
PP(96)/P[LA](4)	4 wt% P[LA]
PP(88)/P[LA](12)	12 wt% P[LA]
PP(80)/P[LA](20)	20 wt% P[LA]
PP(99.95)/CNT(0.01)/P[LA](0.04)	0.01 wt% CNT 4P[LA]
PP(99.5)/CNT(0.1)/P[LA](0.4)	0.1 wt% CNT 4P[LA]
PP(98.5)/CNT(0.3)/P[LA](1.2)	0.3 wt% CNT 4P[LA]
PP(97.5)/CNT(0.5)/P[LA](2)	0.5 wt% CNT 4P[LA]
PP(95)/CNT(1)/P[LA](4)	1 wt% CNT 4P[LA]
PP(85)/CNT(3)/P[LA](12)	3 wt% CNT 4P[LA]
PP(75)/CNT(5)/P[LA](20)	5 wt% CNT 4P[LA]
PP(99.98)/CNT(0.01)/P[LA](0.01)	0.01 wt% CNT 1P[LA]
PP(99.8)/CNT(0.1)/P[LA](0.1)	0.1 wt% CNT 1P[LA]
PP(99.4)/CNT(0.3)/P[LA](0.3)	0.3 wt% CNT 1P[LA]

PP(99)/CNT(0.5)/P[LA](0.5)	0.5 wt% CNT 1P[LA]
PP(98)/CNT(1)/P[LA](1)	1 wt% CNT 1P[LA]
PP(94)/CNT(3)/P[LA](3)	3 wt% CNT 1P[LA]
PP(90)/CNT(5)/P[LA](5)	5 wt% CNT 1P[LA]

Table 3.2 Blending ratios (wt%) for PP and composites of PP, P[LA] (M_n = 11,500, $Đ$ = 1.15) and GNPs and corresponding composite nomenclature.

Composite composition (wt %)	**Nomenclature**
PP(100)	PP
PP(99.9) / GNPs(0.1)	0.1 wt% GNPs
PP(99.7) / GNPs(0.3)	0.3 wt% GNPs
PP(99.5) / GNPs(0.5)	0.5 wt% GNPs
PP(99.25) / GNPs(0.75)	0.75 wt% GNPs
PP(99) / GNPs(1)	1 wt% GNPs
PP(97) / GNPs(3)	3 wt% GNPs
PP(95) / GNPs(5)	5 wt% GNPs
PP(99.5) / P[LA] 10K(0.4) / GNPs(0.1)	0.1 wt% GNPs P[LA]
PP(98.5) / P[LA] 10K(1.2) / GNPs(0.3)	0.3 wt% GNPs P[LA]
PP(97.5) / P[LA] 10K(2) / GNPs(0.5)	0.5 wt% GNPs P[LA]
PP(96.25) / P[LA] 10K(3) / GNPs(0.75)	0.75 wt% GNPs P[LA]
PP(95) / P[LA] 10K(4) / GNPs(1)	1 wt% GNPs P[LA]
PP(85) / P[LA] 10K(12) / GNPs(3)	3 wt% GNPs P[LA]
PP(75) / P[LA] 10K(20) / GNPs(5)	5 wt% GNPs P[LA]

Table 3.3 Blending ratios (wt%) for PP and composites of PP, poly(acrylate), MWCNTs, GNPs and corresponding composite nomenclature.

Composite composition (wt %)	**Nomenclature**
PP(100)	PP
PP(99)/MWCNTs(1)	PP MWCNTs
PP(95)/P[LA] 5K(4)/MWCNTs(1)	P[LA] 5K MWCNTs
PP(95)/P[LA] 10K(4)/MWCNTs(1)	P[LA] 10K MWCNTs
PP(95)/P[LA] 20K(4)/MWCNTs(1)	P[LA] 20K MWCNTs
PP(95)/P[2PEA] 5K(4)/MWCNTs(1)	P[2PEA] 5K MWCNTs
PP(95)/P[2PEA] 10K(4)/MWCNTs(1)	P[2PEA] 10K MWCNTs
PP(95)/P[2PEA] 20K(4)/MWCNTs(1)	P[2PEA] 20K MWCNTs
PP(95)/*block* 20K(4)/MWCNTs(1)	*block* 20K MWCNTs
PP(95)/*stat* 20K(4)/MWCNTs(1)	*stat* 20K MWCNTs
PP(99)/GNPs(1)	PP GNPs
PP(95)/P[LA] 5K(4)/GNPs(1)	P[LA] 5K GNPs
PP(95)/P[LA] 10K(4)/GNPs(1)	P[LA] 10K GNPs
PP(95)/P[LA] 20K(4)/GNPs(1)	P[LA] 20K GNPs
PP(95)/P[2PEA] 5K(4)/GNPs(1)	P[2PEA] 5K GNPs
PP(95)/P[2PEA] 10K(4)/GNPs(1)	P[2PEA] 10K GNPs
PP(95)/P[2PEA] 20K(4)/GNPs(1)	P[2PEA] 20K GNPs
PP(95)/*block* 20K(4)/GNPs(1)	*block* 20K GNPs
PP(95)/*stat* 20K(4)/GNPs(1)	*stat* 20K GNPs
PP(96)/P[LA] 10K(4)	PP P[LA] 10K
PP(96)/P[2PEA] 10K(4)	PP P[2PEA] 10K
PP(96)/*block* 20K (4)	PP *block* 20K
PP(96)/*stat* 20K (4)	PP *stat* 20K

3.3 Characterisation and Processing Methods

3.3.1 X-Ray Photo-Electron Spectroscopy (XPS)

XPS measurements of MWCNTs and GNPs were performed using a Kratos Axis Ultra delay-line-detector XPS equipped with a magnetic immersion lens and charge neutralisation system with the spherical mirror and concentric hemispherical analysers. Measurements were analysed using CasaXPS analysis software.

3.3.2 Twin-Screw Extrusion (Melt/Compounding) and Injection Moulding

The Thermo Scientific Haake™ Mini-Lab II micro-compounder was fitted with two conical co-rotating screws and the machine facilitates recirculation of compound within a chamber of volume 5 cm^3. The twin-screw extruder was employed with a barrel temperature set to 170 °C, a screw speed of 100 rpm and a recirculation time of 5 min. Both the PP, and the fillers were dried at 70°C overnight prior to mixing.

3.3.3 Nuclear Magnetic Resonance Spectroscopy (NMR)

^1H and ^{13}C NMR spectra were recorded on a Bruker DPX-300 and Bruker DPX-400 spectrometer in $CDCl_3$. All chemical shifts are reported in ppm (δ) relative to a tetramethylsilane zero standard and referenced to the chemical shifts of deuterated solvent resonance (^1H and ^{13}C). Monomer conversions were determined *via* ^1H NMR spectroscopy by comparing the integrals of monomeric vinyl protons to the terminal methyl protons on the P(LA).

3.3.4 Differential Scanning Calorimetry (DSC)

A Mettler Toledo (DSC1, model 700, 400W) equipped with FRS5 thermocouple sensor, robotic sample changer and evaluated using a STARe Version 15.01 software package was used to study the thermal properties of all the materials. The instrument was calibrated using Indium and Zinc standards. Non-isothermal scans were performed under nitrogen (20 cm^3 min^{-1}) using the following procedure: samples of 10 ± 1 mg were inserted (aluminium pan with pieced lid) in the instrument at 200 °C and held at this temperature for 2 min. to eliminate thermal history, then cooled from 200 °C to 80 °C at -10 K/min., re-heated from 80 °C to 200 ºC at 10 K/min. and, cooled again from 200 °C to 80 °C at -10 K/min., then finally heated from 80 °C to 200 °C at 10 K/min. The thermograms were used to determine the onset melting temperature, crystallisation temperature (T_c), peak melting temperature (T_m), enthalpy of melting (ΔH_m) and crystallisation (ΔH_c). The degree of

crystallinity for PP was calculated by dividing the (ΔH_m) or (ΔH_c) for the sample by the enthalpy of melting for a theoretically 100% crystalline PP (ΔH°_f = 207.1 J/g).[17]

3.3.5 Thermo-gravimetric Analysis (TGA)

Thermo-gravimetric analysis (TGA) was carried out using a Mettler Toledo TGA1-STARe system under the flow of nitrogen (40-60 cm^3/min). The sample weights ranged from 10-15 mg and were loaded into 70 µL alumina pans. The samples were heated from r.t. to 800 °C at a constant heating rate of 10 K min^{-1}. Decomposition temperatures were determined from the onset of weight loss from both the weight % and first derivative curves.

3.3.6 Fourier Transform Infra-Red Spectroscopy (FTIR)

FTIR measurements were taken using a Bruker Tensor 27 spectrometer equipped with an attenuated total reflectance (ATR) crystal and specac golden gate heating stage. Spectra were recoded the OPUS analysis software in the range of 400 – 6000 cm^{-1} at r.t. The resolution was set to 2 cm^{-1} and averaged over 12 scans to acquire each spectrum.

3.3.7 Static Mechanical Tensile Testing

Tensile tests were performed to measure the modulus (MPa), ultimate tensile strength (MPa) and strain at break (%) using a Shimadzu Autograph AGS-X fitted with a 10 kN load cell, equipped with a twin TRViewX non-contact digital video extensometer (500 and 120 mm field of view) using the Trapezium X Version 1.4 software package. The standard dumbbell-shaped test specimens (ASTM D638 V) with an extensometer gauge length of 7.62 mm were deformed using a constant crosshead speed of 10 mm/min and data acquisition rate of 100 points/s. The distance between the grips was 25.4 mm. Five replicates of each sample were run to obtain an average and standard deviation values. To obtain the elastic modulus, a linear regression technique was utilized to define the slope of the stress-stain curve in the initial region before yield, taken to be a strain range of 0.05% and 0.25% determined by published standard BS EN ISO 527-1:2012.

3.3.8 Dynamic Mechanical Thermal Analysis (DMTA)

DMTA measurements (storage modulus (*E*'), loss modulus (*E*'') and loss factor (tanδ)) were carried out using a Triton Tritec 2000 DMA equipped with a standard air oven. Composite samples were studied using the dual cantilever geometry with a free length of 17.5 mm, width of 10 mm and thickness of 4 mm. A clamp mass of 5.66, geometry constant of 2.043 x 10^{-4} and strain factor of 3.918 were used. Samples taken from injection moulded

bars were used and cut to the required length (50 mm). The samples were cooled with liquid nitrogen and heated from -80 °C to 140 °C at a heating rate of 2 K/min with a single dynamic frequency of 1 Hz and a static displacement of 15 μm.

Poly(acrylates) and their composites with MWCNTs and GNPs were performed under compression geometry with a single dynamic frequency of 1 Hz and a static displacement of 50 μm. A thickness of 1.5 mm and diameter of 7 mm was used with; a clamp mass of 3.70, a geometry constant of 2.566×10^{-2} and a strain factor 6.67×10^{2}. The samples were cooled with liquid nitrogen and heated from -100 °C to 200 °C at a heating rate of 2 K/min.

3.3.9 Parallel Plate Oscillatory Rheometry

The rheological behaviour of the nanocomposites was studied using a Thermo Scientific Haake MARS III rheometer equipped with a parallel-plate geometry (plate diameter = 25 mm, gap set to 1 mm). Oscillatory amplitude stress sweeps were first undertaken over a stress range of 0.1 to 100 Pa at a fixed temperature and frequency of 180 °C and 1 Hz, respectively. The test indicated the region in which the deformation was small enough for the storage modulus (G') to be independent of deformation. Under such conditions the viscoelastic properties of the material became apparent. The injection moulded disk was initially inserted onto the plates and heated to 180 °C and allowed to melt before being squeezed from a thickness of 1.65 mm to a thickness of 1 mm. The sample of 1 mm thickness, was then subjected to dynamic oscillation frequency sweeps of 0.1 to 100 Hz and back, under a controlled stress at 100 Pa, under an air atmosphere. The poly(acrylates) and their composites with GNPs and MWCNTs were subjected to dynamic oscillation frequency sweeps of 0.1 to 100 Hz under a controlled stress at 100 Pa at r.t. They were also subjected to a temperature ramp between r.t and 250 °C at a fixed frequency of 1 Hz and controlled stress at 100 Pa at a heating rate of 5 K/min.

3.3.10 Scanning Electron Microscopy (SEM)

Scanning electron microscope micrographs were obtained using a Zeiss sigma field emission SEM. The instrument is fitted with a Gemini column. For measurements using the SE2 detector, a working distance of 8 mm was used and an acceleration voltage of 10 kV. For measurements using the InLens detector, a working distance of 2.5 mm was used and an acceleration voltage of 3 kV. Prior to imaging, the samples were cryo-fractured by placing them in a bath of liquid nitrogen for 30 mins., then removing them and immediately

fracturing them using a hammer and vice. The fractured surface was mounted on an aluminium SEM stub with the aid of carbon adhesive tape with the fractured surface in the vertical up direction. The sample was subsequently sputter coated (10 nm) using an Au/Pt metal target (Cressington 108 auto) equipped with a digital thickness controller and the procedure performed under a weak argon atmosphere.

3.3.11 Transmission Electron Microscopy (TEM)

TEM imaging of samples were performed using a FEI Talos F200X microscope. Poly(acrylate) and their composites were imaged by first dissolving the sample (10 mg/ml) in chloroform and dropping the sample onto a lacey carbon coated 200 mesh copper grids purchased from Agar scientific. PP composite samples were prepared by sectioning ultra-thin samples, typically between 50 and 100 nm thick using a Lycia RM2245 ultracryo-microtome equipped with Diatome 35° dry diamond knife performed at -40 °C. STEM-EELS was performed in an JEOL ARM 200F microscope, with an accelerating voltage of 80 kV, energy resolution of ~1.2 eV, dispersion of 0.25 eV/channel and convergence and collection semi-angles of 29 and 100 *mrad* respectively. EELS spectra were processed by removing background of the form AEr, corrected for multiple scattering and aligning the 1s–p* peak maximum to ~285.5 eV. Data were recorded with a dose of less than 200 electrons per $Å^2$ to minimise the effect on CNT graphitic structure. The acquisition time for the low-loss and the carbon K-edge spectra was ~0.2s and ~20s, respectively. Also, the sample was heated at 50˚ under vacuum overnight.

3.3.12 Wide Angle X-Ray Scattering (WAXD) / Small Angle X-Ray Scattering (SAXS)

Wide-angle X-ray diffraction (WAXD) was used to characterise the crystalline structure of the composites. WAXD spectra of the MWCNTs, GNPs and composite materials were collected using a PANalytical Empyrean X-ray diffractometer equipped with a Co ($K_{\alpha 1}$ (λ) = 1.789 Å) source and PIXcel^{3D} detector. A tube voltage of 45 kV and current of 40 amps was employed. The measurements were carried out under reflectance mode using a stage spinner (composite disk-shaped samples mounted using minimal plasticine inside the metal holder) with a revolution speed of 1 rps. The patterns were collected in the 2θ range of $5^{\circ} – 60^{\circ}$. The step size selected was a 2θ value of 0.01313° and the time per step was 1.6 seconds. The values for 2θ and d-spacing were calculated using Bragg's law, $n\lambda=2d\sin\theta$ where; λ is the wavelength of the X-ray source, θ is the angle between the incident rays and the surface of the crystal (Bragg angle), d is the spacing between the interatomic layers, and

when n is an integer, the incident rays and surface rays are in phase and a peak is observed.[18] Crystallinity calculations were determined using PANalytical HighScore Plus analysis software (V4.6a) whereby, a bending factor of 10 and a granularity of 20 are used to determine the amorphous halo. The percent crystallinity is defined as the ratio of area from the crystalline peaks to the sum of the crystalline and amorphous areas.

SAXS/WAXS data was collected using a Xenocs Xeuss 2.0 laboratory beamline instrument with a Cu Kα source (λ = 1.54 Å). SAXS/WAXS data were collected on Pilatus 300K and Pilatus 100K detector systems, respectively, calibrated with silver behenate. The sample to detector distance was 2490 mm for SAXS (an evacuated chamber was positioned between the sample and SAXS detector to reduce air scattering and absorption) and 162 mm for WAXS (positioned in the evacuated sample chamber). A Linkam HFSX350 temperature control stage (with Kapton windows), was used to house the samples and positioned vertically in the instrument's evacuated sample chamber. Static 2D SAXS/WAXS data was taken at a frame rate of 60 s. Time-resolved SAXS/WAXS data was also obtained for the copolymer sample at a frame rate of 30 s where the samples were heated to 200 ºC and then cooled to -50 ºC at 5 ºC min^{-1}.

3.3.13 Raman Spectroscopy

Raman spectra were collected using a Renishaw inVia Reflex confocal Raman microscope (Gonzo) equipped with a 532 nm solid state laser and x5, x20, x50 objectives. The spectra were collected using a Renishaw CCD detector (Visible – NIR). The laser (10 mW) was spot focused on the sample (100 μm x 3 mm) with an exposure time of 2 mins and a minimum of 5 collections. No melting of the polymers was detected throughout the experiment. The Raman scattering was collected in a standard 180° backscattering geometry.

3.3.14 Volume Resistivity

Volume resistivity was measured using a two-point probe method on injection moulded test bars (length 18 mm, width 9.4 mm, thickness 3.25 mm) prepared by coating each end with silver conducting paint and attaching copper tape over the conducting paint to minimise contact resistance. An electrometer (Keithley, Ohio, USA, model 6517B) was used to measure volume resistivity using an applied voltage of 1 V. The surfaces of all samples were cleaned with ethanol prior to measurement. According to ASTM D4496 and D257, the measured volume resistance, R_v, was converted to volume resistivity, ρ_v, using equation (1);

$$\rho_v = R_v A / t \quad (1)$$

where A is the effective area of the measured electrode and t is the specimen thickness.

3.3.15 Size-Exclusion Chromatography (SEC)

Size exclusion chromatography (SEC) measurements of polymers were conducted using an Agilent 390-LC MDS fitted with differential refractive index (DRI), dual light scattering (LS), and viscometry (VS) detectors equipped with 2 x PLgel mixed c-columns (300 x 7.5 mm), 1 x PLgel 5 μm guard column (50 x 7.5 mm) and auto-sampler. Low molar mass linear poly(methyl methacrylate) standards in the range 200 to 1.0 x 10^6 g mol^{-1} were used to calibrate the system. All samples were passed through a 0.45 μm PTFE filter prior to analysis. The eluent was chloroform with 2% trimethylamine at a flow rate of 1.0 mL min^{-1} at 30 °C. SEC data was analysed using Cirrus v3.3.

SEC of PP was conducted using an Agilent PL220 instrument equipped with differential refractive index (DRI), viscometry (VS) and dual angle light scatter (LS 90 + 15) detectors. The system was equipped with 2 x PLgel Mixed D columns (300 x 7.5 mm) and a PLgel 5 μm guard column. The mobile phase was TCB with 250 PPM BHT (butylated hydroxytoluene) additive. Samples were run at 1 ml/min at 160'C. Polystyrene standards (Agilent EasyVials) were used to create a third order calibration. Analyte samples were filtered through a stainless-steel frit with 10 μm pore size before injection. Respectively, experimental molar mass ($M_{n,SEC}$) and dispersity ($Đ$) values of synthesized polymers were determined by conventional calibration using Agilent GPC/SEC software.

3.3.16 Matrix-Assisted-Laser-Desorption-Ionisation Time-of-Flight Mass Spectrometry (MALDI-TOF-MS)

MALDI-TOF-MS was conducted using a Bruker Daltonics Ultraflex II MALDI-TOF mass spectrometer, equipped with a nitrogen laser delivering 2 ns laser pulses at 337 nm with positive ion ToF detection per-formed using an accelerating voltage of 25 kV. Solutions in tetrahydrofuran (50 μL) of trans-2-[3-(4-tert-butylphenyl)-2-methyl-2-propyldene] malonitrile (DCTB) as a matrix (saturated solution), sodium iodide as cationization agent (1.0 mg mL^{-1}) and sample (1.0 mg mL^{-1}) were mixed, and 0.7 μL of the mixture was applied to the target plate. Spectra were recorded in reflector mode calibrating PEG-Me 1100 kDa.

3.3.17 Droplet Shape Analysis (DSA) (Contact angle)

Contact angle measurements were performed on poly(acrylate) functionalised MWCNTs and GNPs using a Krüss droplet shape analyser 100. Contact angle (sessile drop) measurements were performed by dropping a small microliter droplet (10 μL) of purified water to the surface of the sample and measuring the contact angle between the droplet and the surface of the sample using a high precision camera determined by the DSA100 analysis software.

3.3.18 High resolution Mass spectrometry – Electrospray ionisation – Time of flight (HRMS – ESI – TOF)

HRMS – ESI – TOF was performed using a Bruker MicroTOF, Bruker MaXis II, MaXis Plus and MaXis Impact machine. Samples were dissolved in chloroform and diluted to a concentration of 2-3 mg/ml prior to insertion.

3.3.19 UV-Vis spectroscopy

UV-Vis spectroscopy spectra were recorded using an Agilent Cary 60 UV-Vis spectrometer with a wavelength range of 200 – 1000 nm. Samples were dissolved in chloroform and measured using a Quartz 6030 UV cuvette (10 x 10 mm). Spectra from solid-state UV-Vis spectroscopy were recorded using a Shimadzu UV-2600 UV-Vis-NIR spectrophotometer equipped with an integrating sphere for solid samples. The mode of operation is total diffuse reflectance.

3.3.20 Fluorescence spectroscopy

Fluorescence spectroscopy was recorded using an Agilent Cary Eclipse Fluorescence spectrometer. Samples were dissolved in chloroform and measured using a Quartz 6030 UV cuvette (10 x 10 mm).

3.3.21 Density measurements

The density of iPP and P[LA] was measured using a Mettler Toledo NewClassic Balance (Model ME204) with attached density kit using water as the displacement fluid.

3.4 References

1. S. J. Chin, S. Vempati, P. Dawson, M. Knite, A. Linarts, K. Ozols and T. McNally, *Polymer*, 2015, **58**, 209-221.
2. B. Krause, T. Villmow, R. Boldt, M. Mende, G. Petzold and P. Pötschke, *Compos. Sci. Technol.*, 2011, **71**, 1145-1153.
3. M. Ciampolini and N. Nardi, *Inorg. Chem.*, 1966, **5**, 41-44.
4. A. J. Limer, A. K. Rullay, V. San Miguel, C. Peinado, S. Keely, E. Fitzpatrick, S. D. Carrington, D. Brayden and D. M. Haddleton, *React. Funct. Polym.*, 2006, **66**, 51-64.
5. J. Nicolas, V. San Miguel, G. Mantovani and D. M. Haddleton, *Chem. Commun.*, 2006, DOI: 10.1039/b609935a, 4697-4699.
6. J. Gupta, D. J. Keddie, C. Y. Wan, D. M. Haddleton and T. McNally, *Polym. Chem.*, 2016, **7**, 3884-3896.
7. Y. K. Chong, G. Moad, E. Rizzardo and S. H. Thang, *Macromolecules*, 2007, **40**, 4446-4455.
8. J. Y. T. Chong, D. J. Keddie, A. Postma, X. Mulet, B. J. Boyd and C. J. Drummond, *Colloids Surf., A*, 2015, **470**, 60-69.
9. A. Anastasaki, C. Waldron, V. Nikolaou, P. Wilson, R. McHale, T. Smith and D. M. Haddleton, *Polym. Chem.*, 2013, **4**, 4113-4119.
10. C. Waldron, A. Anastasaki, R. McHale, P. Wilson, Z. D. Li, T. Smith and D. M. Haddleton, *Polym. Chem.*, 2014, **5**, 892-898.
11. C. Roman, M. García-Morales, J. Gupta and T. McNally, *Polymer*, 2017, **118**, 1-11.
12. T. McNally, P. Pötschke, P. Halley, M. Murphy, D. Martin, S. E. J. Bell, G. P. Brennan, D. Bein, P. Lemoine and J. P. Quinn, *Polymer*, 2005, **46**, 8222-8232.
13. T. McNally and P. Pötschke, *Polymer–carbon nanotube composites: preparation, properties and applications*, Woodhead Publishing Ltd, Cambridge, UK, 2011.
14. C. McClory, T. McNally, G. P. Brennan and J. Erskine, *J. Appl. Polym. Sci.*, 2007, **105**, 1003-1011.
15. B. Mayoral, J. Lopes and T. McNally, *Macromol. Mater. Eng.*, 2014, **299**, 609-621.
16. C. McClory, T. McNally, M. Baxendale, P. Pötschke, W. Blau and M. Ruether, *Eur. Polym. J.*, 2010, **46**, 854-868.
17. J. Karger-Kocsis, in *Polypropylene: An A-Z reference*, ed. J. Karger-Kocsis, Kluwer Academic, Dordrecht, 1st edn., 1999.

18. D. F. Wu, Y. R. Sun, L. Wu and M. Zhang, *J. Appl. Polym. Sci.*, 2008, **108**, 1506-1513.

Chapter 4 Results and Discussion I

Non-covalent functionalisation of MWCNTs with poly(lauryl acrylate) polymerised by Cu(0)-mediated and RAFT methods

4.1 Introduction

Over the last decade, new polymerisation methods have been developed which can produce well-defined polymers with targeted molar masses, controlled narrow dispersities and complex architectures with specific functionality, e.g. hyper-branched and star polymers.[1] Such polymerisation techniques make use of controlled living radical polymerisation (LRP) techniques such as reversible addition-fragmentation chain transfer polymerisation (RAFT)[2-5] and Cu(0)-mediated living radical polymerisation (Cu(0)-mediated LRP).[6-8] They are referred to as reversible deactivation radical polymerisation (RDRP) techniques. Polymers produced by such methods have not been fully characterised in terms of their thermal stability during melt processing as in extrusion and injection moulding. The detailed understanding of the thermal and thermo-mechanical stability of polymers synthesised using RDRP techniques and their suitability for melt processing is limited.[9, 10] A lack of understanding regarding the thermal and thermo-mechanical stability of such polymers has resulted in limited melt processing *via* extrusion. It is important to understand the consequences of high shear stresses and temperatures during melt processing in order to expand the use of RDRP polymers in industry.[9] Critically, the effects of thermal and thermo-mechanical stress on the molecular structure of functional polymers will need to be considered because their ability to withstand both during the melt mixing will be the determining factor enable their use as compatibilisers for carbon nanotubes (CNT) and graphene with polymers, such as PP and P[LA].[11-13] Whilst thermolysis has been applied as a method for transformation of functional chain-ends,[14, 15] limited work has been carried out with respect to understanding the effects of high shear and temperature during processing. Altintas *et al*. have shown that the molar mass of trithiocarbonate mid-chain functional polymers decreased at elevated temperatures (~200 °C). However, trithiocarbonate end-functionalised polymers resisted thermal degradation under identical conditions.[16] Star-shaped polymers containing a trithiocarbonate moiety were more susceptible to thermal degradation compared to linear analogues.[17]

Limited solubility in solvents and polymers due to strong Van der Waals interactions lead to strongly bound agglomerates and therefore hinders development of polymer nanocomposites.[18] Poorly controlled dispersion and limited distribution of CNTs and graphene within the polymer matrix prevents widespread application of such materials. In addition, the interface between the CNTs and the polymer matrix needs to be carefully understood in order to improve dispersion and interfacial adhesion between filler and polymer.[19]

To improve dispersion and promote interfacial adhesion, the use of a compatibilising polymer has been proposed. The properties of the polymer should be such that it can selectively and non-covalently adsorb onto the surface of the CNTs and improve compatibility with the polymer matrix whilst remaining thermally stable during extrusion. Such polymers will be synthesised using RDRP methods such as RAFT and Cu(0)-mediated LRP. The use of RDRP polymers for non-covalent functionalisation of carbon based 1D and 2D materials has yet to have been fully explored.

The use of non-covalent functionalisation preserves the inherent properties of the CNTs and graphene, while improving dispersion and interfacial adhesion with polymer matrices. For example, aromatic compounds such as, Hostasol (a pigment) and pyrene employ π-π stacking and hydrophobic compounds such as, lauryl acrylate are attracted via hydrophobic interactions to bind to the surface of CNTs and graphene.[20] A combination of π-π stacking and hydrophobic adsorption can drive self-assembly of the polymer around the CNT in the form of wrapping. Polymer wrapping around a CNT is entropically unfavourable however, the reduction in surface energy of the CNTs in the dispersion media makes the wrapping process thermodynamically favourable.[21]

It is well known from the literature that methacrylate polymers have degradation temperatures in the region of 200 °C due to the radical catalysed ‘unzipping’ of the methacrylate polymer backbone. However, investigations into the thermal stability of acrylates prepared via RDRP methods have not been as detailed. Herein, the non-covalent wrapping of poly(lauryl acrylate)s P[LA] over MWCNTs is investigated, (Scheme 4.1) synthesised by both Cu(0)-mediated[22] and RAFT[23] polymerisation methods. The thermal stability of P[LA] synthesised both those methods was evaluated by TGA and supported by size exclusion chromatography (SEC), matrix-assisted laser desorption/ionization mass spectrometry (MALDI-TOF MS) and TEM. Comparisons between the thermal stability of

acrylates synthesised by Cu(0)-mediated and RAFT has not been reported often[24] and therefore, the hypothesis is to compare the thermal stability of the same polymer produced by the two different polymerisation techniques.

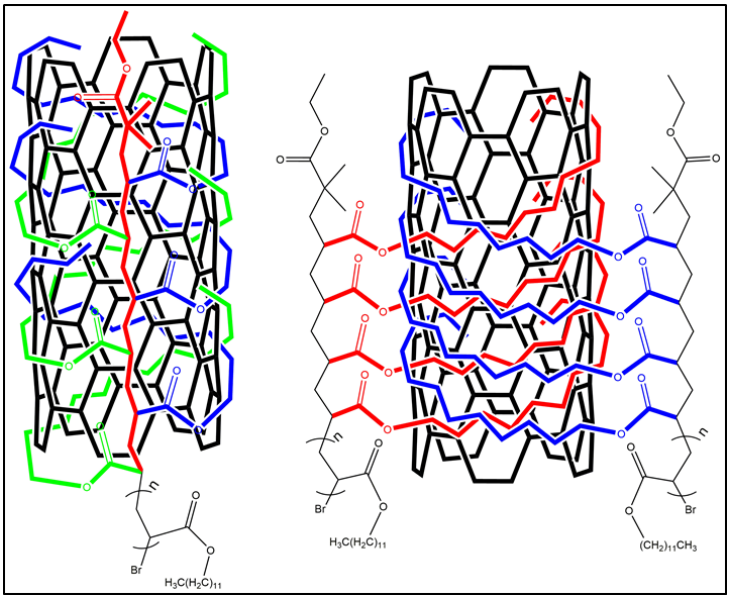

Scheme 4.1 Schematic representation of P[LA] wrapping around/on a CNT.

By way of example, poly(lauryl acrylate) P[LA] was chosen as it known to be able to co-crystallise with poly(propylene) PP.[25] P[LA] is a typical hydrophobic poly(acrylate) and has shown to have good compatibility with isotactic PP because its long hydrophobic chains can co-crystallise with the hydrophobic chains in PP.[26] The hypothesis is to non-covalently coat the surface of the CNTs with P[LA] *via* CH-π type intermolecular adsorption and hence improve the interfacial disparity between the CNTs and the PP matrix.

In addition to the investigation of non-covalent functionalisation poly(lauryl acrylate) (P[LA]) with MWCNTs, the effect of using aromatic initiators to produce aromatic end-functionalised P[LA] and its effect on non-covalently functionalising MWCNTs was also investigated. The thermal stability of P[LA] and aromatic end-functionalised P[LA] was investigated to establish suitability for melt mixing (extrusion).

4.2 Synthesis and characterisation of poly(lauryl acrylate) P[LA] *via* RAFT

The polymerisation of lauryl acrylate (LA) using RAFT requires a chain-transfer agent (CTA). The CTA agent, cyanomethyl dodecyltrithiocarbonate was chosen as it has shown to be good at controlling the polymerisation of hydrophobic acrylates.[27] Upon successful synthesis of the CTA agent, LA can be polymerised by combining the monomer (LA), the CTA agent, initiator and solvent. The ^{1}H NMR of LA and AIBN (Appendix 1 and 2 respectively) have been performed to establish a baseline for the polymerisation of LA monomer and the spectra show the reagents have been obtained with high purity.

4.2.1 Synthesis and characterisation of cyanomethyl dodecyltrithiocarbonate

The CTA, cyanomethyl dodecyltrithiocarbonate was prepared *via* alkylation of a dodecylcarbodithioate salt[28] with chloroacetonitrile, adapting the synthesis method detailed by Chong *et al*.[29] Figure 4.1 shows the ^{1}H NMR for cyanomethyl dodecyltrithiocarbonate. The peaks are very clear and sharp with very minimal traces of impurity and showing the RAFT agent can be accessed *via* this route in high purity. The RAFT agent was obtained in high yield (98%).

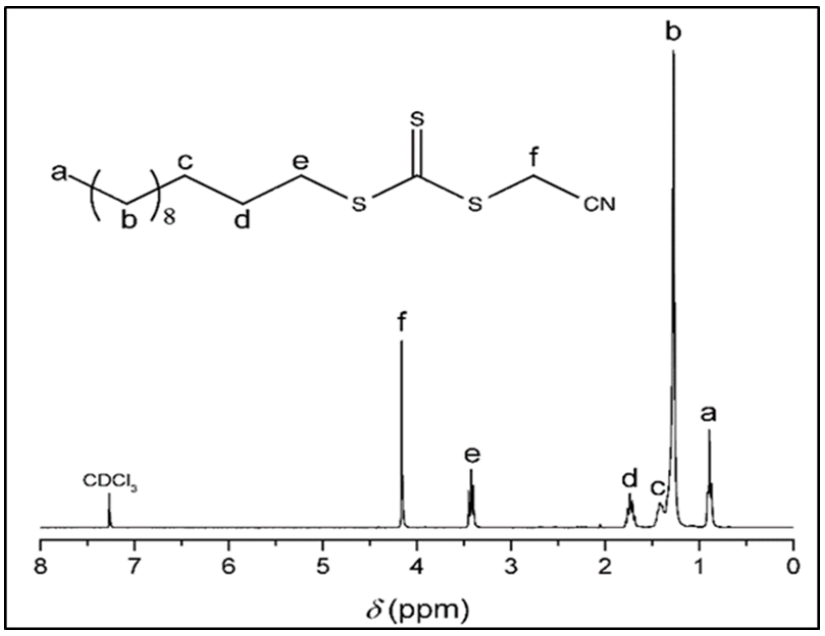

Figure 4.1. ^{1}H NMR spectrum of cyanomethyl dodecyltrithiocarbonate recorded in $CDCl_3$.

The synthesis was adapted using a non-nucleophilic base, potassium *tert*-butoxide as opposed to the use of sodium hydride (NaH). Potassium *tert*-butoxide showed greatly

improved results compared to other strong bases, in that the work up is simplified and there are fewer undesired side reactions.[28, 30]

4.2.2 Synthesis and characterisation of P[LA] *via* RAFT

Lauryl acrylate was polymerised using RAFT (Scheme 4.2) and has been previously reported by Chen *et al*.[31] The polymerisation of long, hydrophobic polymer chains has been reported.[23] As listed in Table 4.1, the RAFT polymerisation of LA in toluene produced poly(lauryl acrylate) (P[LA]) with a range of targeted degrees of polymerisation (DP_n = 25, 50 and 100, $M_{n,th}$ = 6,000 – 24,000 g mol^{-1}). The polymerisation involved combining the LA, CTA, solvent and AIBN in a reaction vessel and heating to 60 °C to thermally initiate the AIBN initiator. After a 24-hour period, a polymer was obtained and characterised. P[LA] with three molecular weights were prepared to investigate how molecular weight effects the polymers thermal stability and its ability to non-covalently wrap MWCNTs.

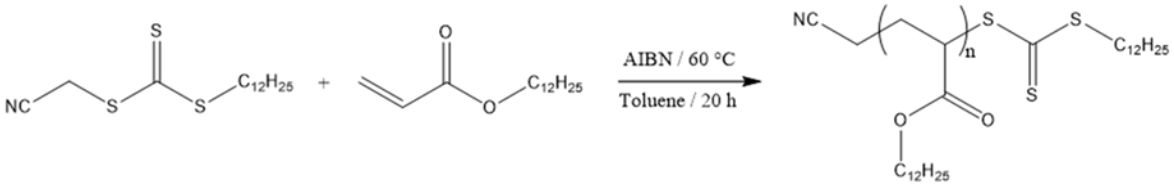

Scheme 4.2 Synthetic strategy for the polymerisation of LA *via* RAFT.

Table 4.1 Theoretical and experimental data for the preparation of initial polymers of LA *via* RAFT polymerisation process and the associated number average molar masses.

Nomenclature	[LA]/[RAFT]^a	Conv.^{b} [%]	$M_{n,\,th}$ [g mol^{-1}]	$M_{n,\,GPC}$ ^{c} [g mol^{-1}]	$Đ$ ^{c}
A	25	95	6 000	5 300	1.11
B	50	95	12 000	13 800	1.24
C	100	90	24 000	21 500	1.30

^{a}[RAFT]:[AIBN] = [1]:[0.05]. ^{b} ^{1}H NMR. ^{c}$CHCl_3$ SEC analysis *via* RI detection using linear PMMA standards.

Figure 4.2 shows the ^{1}H NMR spectrum of a particular P[LA] polymer chain (**B**) synthesised using RAFT. The spectrum shows high levels of quantitative conversion (~95%) with traces of any unreacted monomer not visible after purification which would be present between (6.5-5.5 ppm, Appendix 1). Conversion decreased with higher molar masses due to possible phase separation between the monomer and polymer during the reaction, preventing all of the monomer being consumed.

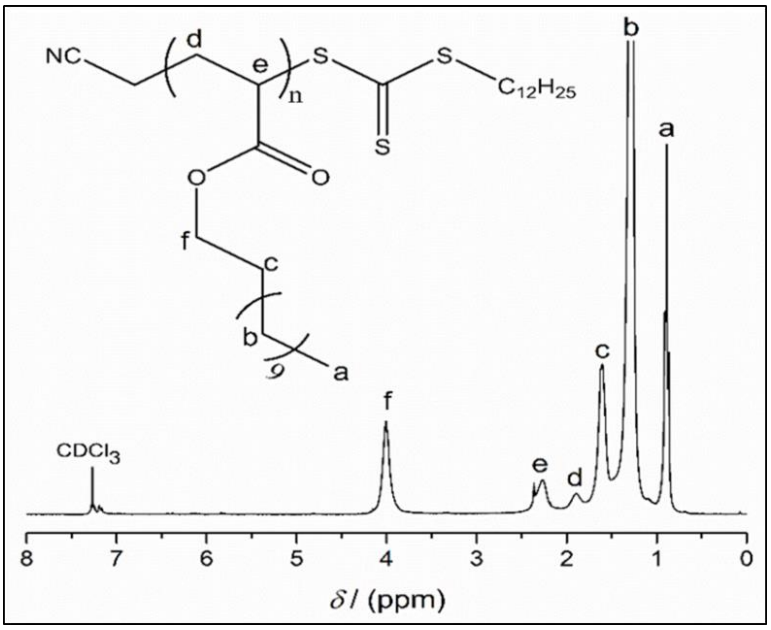

Figure 4.2 ^{1}H NMR of P[LA] (**B**) synthesised *via* RAFT polymerisation.

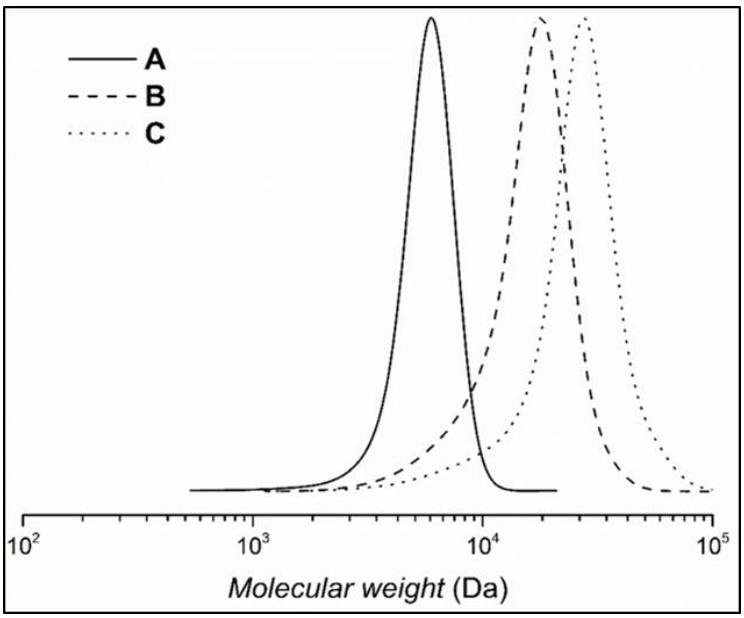

Figure 4.3 SEC traces of P[LA] synthesised *via* RAFT polymerisation. P[LA] (**A-C**) defined in Table 4.1.

SEC analysis (Figure 4.3) revealed the polymerisations were in good agreement with theoretical M_n however, the dispersity increased with increasing M_n (Table 4.1). The M_n increased with increasing monomer to RAFT agent ratio, confirming good control. Low molar mass tailing was observed for high molar mass polymers suggesting further optimisation is required with obtained molecular weights of $M_{n,GPC}$ = 5,300, 13,800, 21,500 g mol^{-1}.

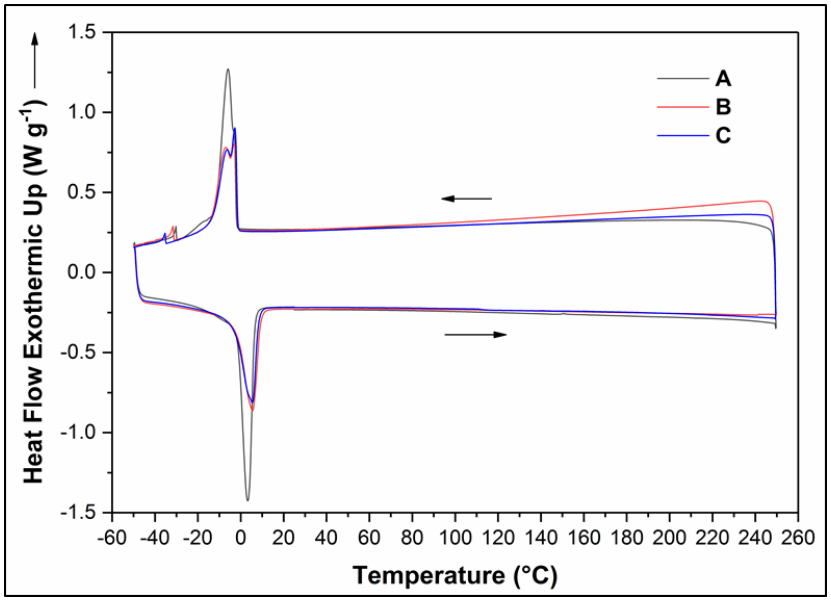

Figure 4.4 DSC traces of P[LA] synthesised *via* RAFT. P[LA] (**A-C**) defined in Table 4.1.

DSC traces of P[LA] synthesised by RAFT (Figure 4.4) indicate a single-phase transition exhibited by P[LA]. P[LA] undergoes a melting transition (T_m) at ~2 °C and a crystallisation transition (T_c) at ~ -10 °C. A small shoulder is observed at ~ -20 °C which can be attributed to unreacted (or small oligomer) LA determined from the DSC trace of LA monomer (Appendix 5). Very small peaks at ~ -30 °C can be attributed to unreacted reagents or impurities such as AIBN initiator and CTA agent.

In summary, LA was polymerised successfully using RAFT demonstrated by high levels of quantitative conversion confirmed by ^{1}H NMR and a linear increase in molecular weight by SEC. The cyanomethyl dodecyltrithiocarbonate CTA works well with LA producing polymers with controlled molecular weight and narrow dispersity.

4.3 Synthesis and characterisation of poly(lauryl acrylate) P[LA] *via* Cu(0)-mediated LRP

Polymerisation of LA using Cu(0)-mediated LRP requires the use of a ligand, Me_6TREN which complexes the copper during the polymerisation. The ligand-copper complex is subsequently able to undergo homolytic halide transfer from the initiator to the metal centre and therefore, initiate the polymerisation process. The initiator, EBiB, is a typical hydrophobic initiator and suitable for the polymerisation of hydrophobic monomers. The ^{1}H NMR of EBiB (Appendix 3) shows the initiator is of high purity.

4.3.1 Synthesis and characterisation of Me_6TREN ligand

Me6TREN ligand was synthesised according to a previously published procedure.[32] The ^{1}H NMR of Me_6TREN (Appendix 4) shows the ligand was synthesised with high purity and complete methylation of the amine moieties in TREN. In addition, ^{13}C NMR, FTIR and high resolution – electrospray ionisation – mass spectrometry (HR–ESI–MS) confirmed the molecular structure of Me_6TREN as detailed in section 3.2.1.

4.3.2 Synthesis and characterisation of P[LA] *via* Cu(0)-mediated LRP

The polymerisation of LA *via* Cu(0)-mediated LRP (Scheme 4.3) in IPA solvent was performed using the adapted procedure detailed by Anastasaki *et al*.[22] Scheme 4.3 shows schematically the polymerisation strategy and table 4.2 lists the targeted degrees of polymerisation (DP = 25, 50, 100, $M_{n,th}$ = 6 000-24 000 g mol^{-1}).[22] The molecular weight was adjusted by altering the ratio between monomer (LA) and initiator (EBiB). P[LA] polymers with three molecular weights were investigated to study the effect of molecular weight on thermal stability and P[LA] ability to non-covalently wrap MWCNTs.

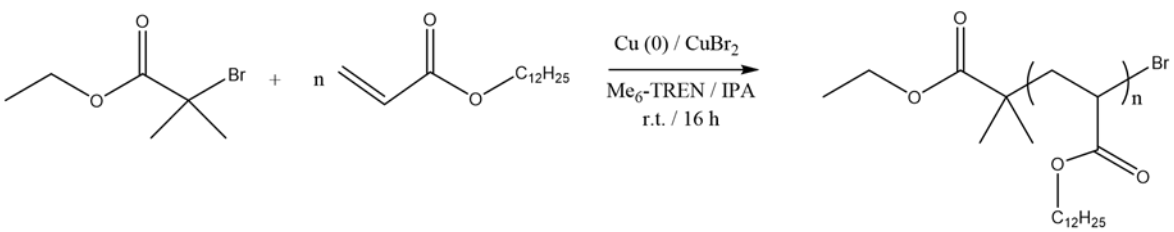

Scheme 4.3 Synthetic strategy for polymerisation of LA *via* Cu(0)-mediated LRP.

^{1}H NMR of P[LA] polymerised using Cu(0)-mediated LRP (Figure 4.5) revealed polymerisations achieved excellent conversion (~98%) and high levels of purity after purification. The spectrum shows minimal levels of monomer impurity (6.5-5.5 ppm). Conversion decreased with higher molar masses due to possible phase separation between the monomer and polymer during the reaction, preventing all the monomer being consumed.

Table 4.2 Theoretical and experimental data for the preparation of initial polymers of LA *via* Cu(0)-mediated LRP polymerisation process and the associated number average molar masses.

Nomenclature	[LA]/[I]	Conv.^{a} [%]	$M_{n,\,th}$ [g mol^{-1}]	$M_{n,\,GPC}$ ^{b} [g mol^{-1}]	$Đ$ ^{b}
D	25	98	6 000	5 500	1.14
E	50	97	12 000	11 900	1.17
F	100	95	24 000	17 500	1.25

^{a} ^{1}H NMR. ^{b}$CHCl_3$ SEC analysis *via* RI detection using linear PMMA standards.

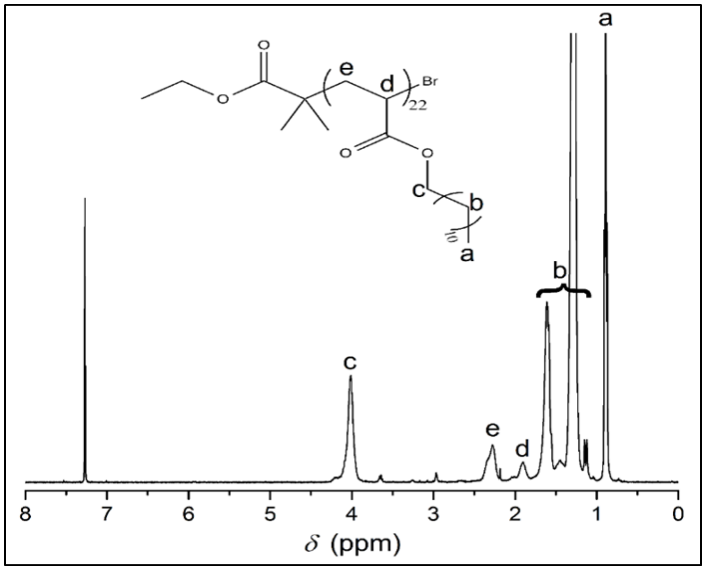

Figure 4.5 ^{1}H NMR of P[LA] synthesised *via* Cu(0)-mediated LRP.

Table 4.2 and figure 4.6 confirm the linear increase in molar mass with increasing monomer concentration. There was good agreement with theoretical M_n and low dispersity ($Đ \approx 1.2$; Table 4.2) with obtained molecular weights of $M_{n,GPC}$ = 5,500, 11,900, 17,500 g

mol^{-1}. Low molar mass tailing can also be observed causing broadening dispersities for the two higher molar mass polymers.

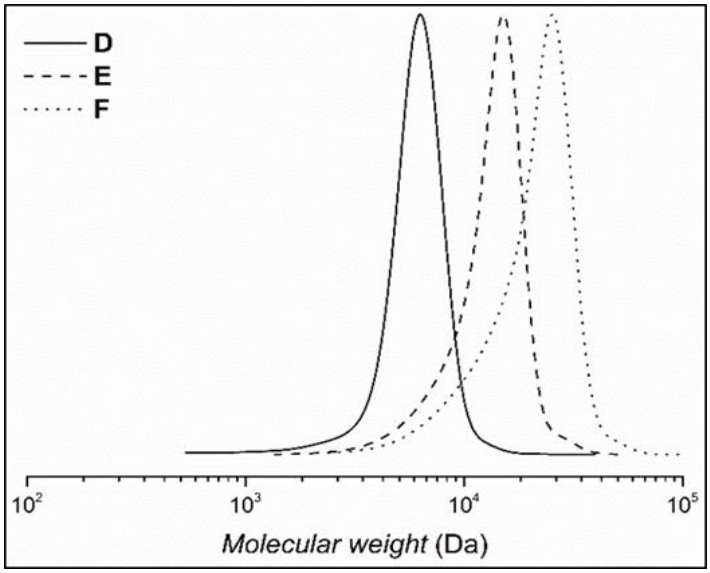

Figure 4.6 SEC traces of P[LA] synthesised *via* Cu(0)-mediated LRP. P[LA] (**D-F**) defined in Table 4.2.

In summary, LA was polymerised successfully using Cu(0)-mediated LRP demonstrated by high levels of quantitative conversion by ^{1}H NMR and linear increase in molecular weight by SEC. The polymerisation of LA using Cu(0)-mediated LRP is simpler than that of RAFT because, Cu(0)-mediated LRP does not require the use of a RAFT agent and can be performed at ambient temperature. The increased temperature of polymerisation required with RAFT increases the rate of chain-transfer and hence reduces control due to the higher probability of chain-transfer. Reduced control for the polymerisation of LA *via* RAFT can be observed from increased dispersities obtained for P[LA] *via* RAFT compared to P[LA] synthesised by Cu(0)-mediated LRP (Table 4.1 and 4.2). Therefore, it was decided that subsequent polymerisations will be carried out *via* the use of Cu(0)-mediated LRP because, the method is simpler and produces polymers with narrower dispersities.

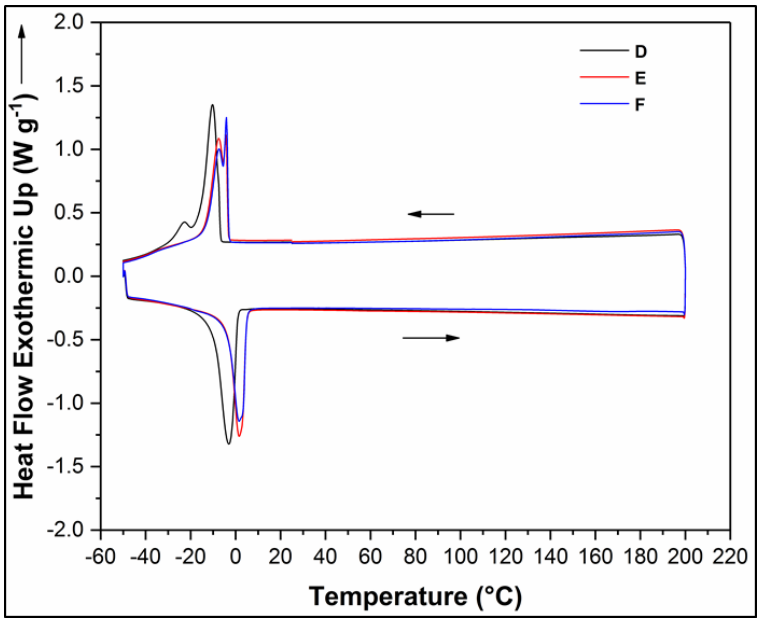

Figure 4.7 DSC traces of P[LA] synthesised *via* Cu(0)-mediated LRP. P[LA] (**D-F**) defined in Table 4.2.

Figure 4.7 displays differential scanning calorimetry (DSC) trace of P[LA] synthesised by Cu(0)-mediated LRP is shown in Figure 4.7. It was assumed that the end groups will not have a significant effect on the DSC trace of P[LA] due to the end groups relative size being very small compared to the bulk polymer chain. The DSC traces reveal a crystallisation temperature (T_c) of ~ -10 °C and a melting temperature (T_m) of ~ 2 °C. The presence of a T_m and T_c is expected as the long hydrophobic polymer chains are able to align, pack together and subsequently form crystal structures. The formation of crystal structures by P[LA] is imperative as it is required to co-crystallise with PP. The first order phase transition is independent of molecular weight for molecular weights above ~10,000 g mol^{-1} however, the lower molecular weight P[LA] (**D**) has a lower T_m and T_c showing the phase transition is dependent on molecular weight for molecular weights below ~10,000 g mol^{-1}. For P[LA](**D**) a shoulder at ~ -20 °C is observed which could potentially be from unreacted monomer or short chain oligomers. The DSC trace for LA monomer is included in appendix 5. The trace of LA shows similar first order phase transitions as those with P[LA] with a T_c of ~ -17 °C and T_m of ~ 7 °C. The monomer is also able to crystallise and melt due to the packing of the lauryl chains. The shoulder at ~ -20 °C for P[LA](**D**) appears at a similar temperature to the T_c of the monomer confirming the shoulder is as a result of unreacted

monomer. In addition, the polymerisation of LA leads to an increase of T_c by ~ 15 °C and decrease in T_m by ~ 5 °C.

4.3.3 Synthesis and characterisation of P[LA] *via* Cu(0)-mediated LRP using Hostasol-ATRP initiator.

After establishing the successful polymerisation of P[LA] using Cu(0)-mediated LRP, the use of various aromatic initiators were investigated. In addition to the CH-π polymer wrapping approach, it was proposed that the use of aromatic type moieties would be required to improve the non-covalent binding to the surface of MWCNTs. One possible solution was the use of Hostasol (thioxantheno[2,1,9-dej]isochromene-1,3-dione) an aromatic orange fluorescent pigment with excellent heat resistance properties. Pigments are routinely added to polymers. Hostasol could be adapted to be a Cu(0)-mediated LRP initiator and subsequently used for the polymerisation of LA which would combine the CH-π wrapping of the P[LA] backbone and the π-π stacking between the Hostasol and the CNT (or any aromatic graphitic filler). It was proposed that such a 'polymer' would effectively bind to the surface of CNTs or graphene as illustrated in Scheme 4.4.

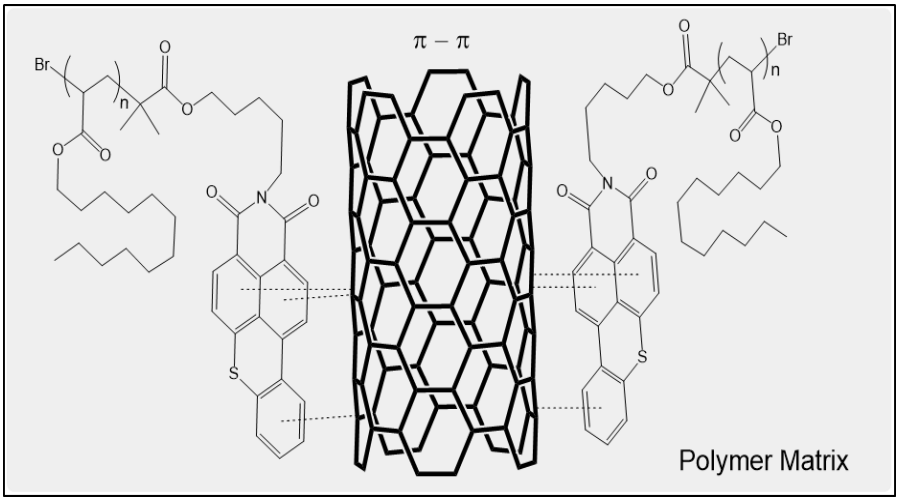

Scheme 4.4 Schematic representation of Hostasol end-functionalised P[LA] *via* Cu(0)-mediated LRP.

Hostasol modified Cu(0)-mediated initiator (Hostasol-ATRP) was kindly provided by Prof. David Haddleton (University of Warwick) and was subsequently used to polymerise LA *via* Cu(0)-mediated LRP as displayed in Scheme 4.5. Prior to polymerisation, the Hostasol-ATRP initiator was characterised by ^{1}H NMR (Appendix 6) in order to establish a baseline for the polymerisation.

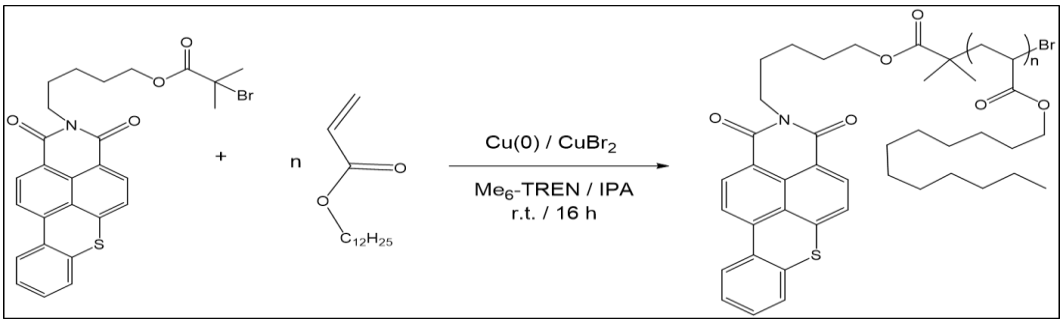

Scheme 4.5 Synthetic strategy for polymerisation of LA *via* Cu(0)-mediated LRP using Hostasol-ATRP initiator.

Table 4.3 Theoretical and experimental data for the preparation of P[LA] *via* Cu(0)-mediated LRP polymerisation process, using a Hostasol-ATRP initiator and the associated number average molar masses.

Nomenclature	[LA]/[I]	Conv.[a] [%]	$M_{n,\,th}$ [g mol^{-1}]	$M_{n,\,GPC}$ [b] [g mol^{-1}]	$Đ$ [b]
Hostasol-P[LA]	100	85	24 000	10 000	1.50

[a] ^{1}H NMR. [b]THF SEC analysis *via* RI detection using linear PMMA standards.

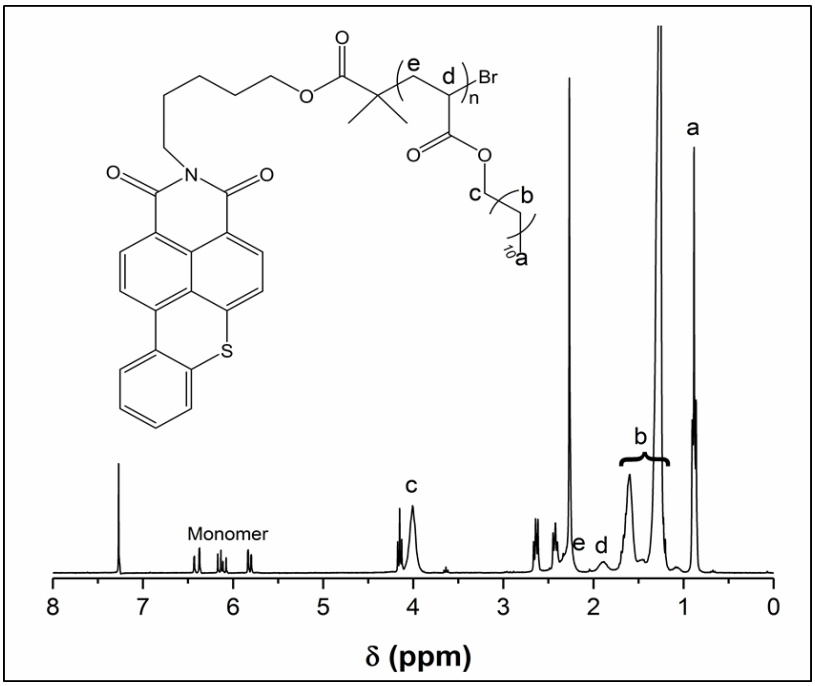

Figure 4.8 ^{1}H NMR of P[LA] synthesised *via* Cu(0)-mediated LRP using a Hostasol-ATRP initiator.

Hostasol-ATRP was polymerised with LA using Cu(0)-mediated LRP with identical experimental procedures as those used for homopolymers of LA (Scheme 4.5). Table 4.3 lists the targeted degrees of polymerisation (DP = 100, $M_{n,th}$ = 24 000 g mol^{-1}). Hostasol end-functionalised P[LA] (Hostasol-P[LA]) was produced with a single molecular weight as its thermal stability and interactions with MWCNTs were initially studied prior to investigating the effect of altering the molecular weight of P[LA]. Figure 4.8 shows the ^{1}H NMR of Hostasol-P[LA] and confirms the polymer was successfully synthesised however, conversion was limited to 85%. Monomer conversion is ~ 10% below that obtained for homopolymers of P[LA] suggesting the Hostasol end group is influencing the polymerisation at high conversion. The presence of LA monomer can be observed at (6.5-5.5 ppm). Additionally, the SEC trace of Hostasol-P[LA], figure 4.9, reveals poor agreement with theoretical M_n and broad dispersity ($Đ \approx 1.5$; table 4.3) through the presence of low molar mass tailing. The results indicate the polymerisation requires further optimisation to increase the conversion and narrow the dispersity. Optimisation can be conducted by changing the polymerisation solvent as well as the concentrations of Cu(0)/$CuBr_2$/Me_6TREN. Prior to optimisation, the thermal stability and extent of binding to MWCNTs was investigated.

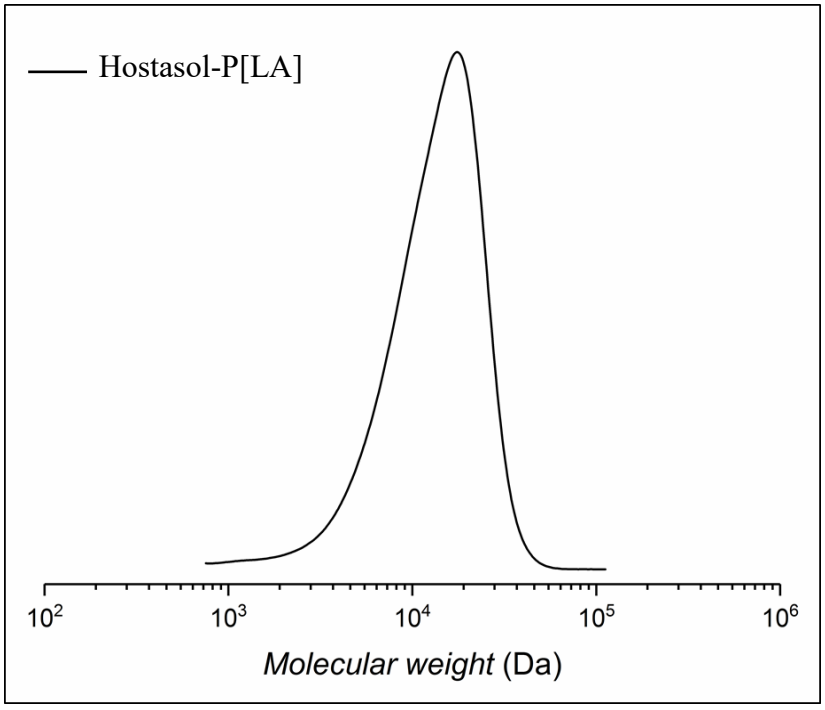

Figure 4.9 SEC trace of P[LA] synthesised *via* Cu(0)-mediated LRP using Hostasol-ATRP initiator.

4.3.4 Synthesis and characterisation of P[LA] via Cu(0)-mediated LRP using pyrene-ATRP initiator.

In addition to the use of Hostasol for the synthesis of aromatic end-functionalised P[LA], the use of pyrene was also studied as it has been proposed to have similar or greater potential to non-covalently bind to the surface of CNTs through a combination of CH-π wrapping of the P[LA] backbone and π-π stacking between the pyrene and the CNT (Scheme 4.6). P[LA] was polymerised using a pyrene molecule functionalised with an ATRP initiator (Pyrene-ATRP) (Scheme 4.7).

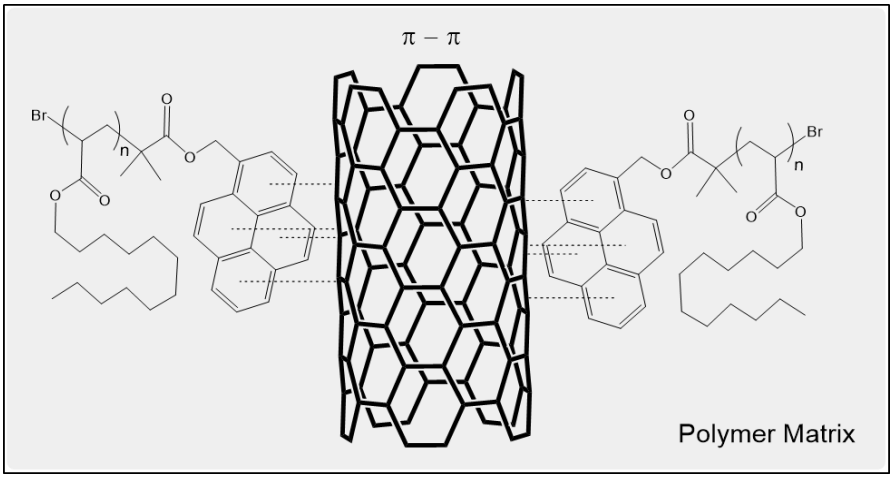

Scheme 4.6 Schematic representation of pyrene end-functionalised P[LA] *via* Cu(0)-mediated LRP.

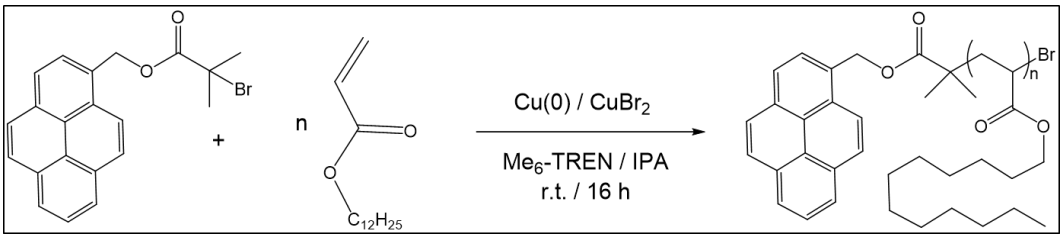

Scheme 4.7 Synthetic strategy for polymerisation of LA *via* Cu(0)-mediated LRP using Pyrene-ATRP initiator.

LA was polymerised *via* Cu(0)-mediated LRP with the pyrene-ATRP initiator using experimental procedures as those used with the homo-polymerisation of LA (Scheme 4.7). Table 4.4 lists the targeted degrees of polymerisation (DP = 100, $M_{n,th}$ = 24000 g mol^{-1}). Pyrene end-functionalised P[LA] (Pyrene-P[LA]) was also produced with a single molecular weight as its thermal stability and interactions with MWCNTs must first be investigated,

prior to investigating the effect of altering the molecular weight on the thermal stability of pyrene end-functionalised P[LA].

Table 4.4 Theoretical and experimental data for the preparation of P[LA] *via* Cu(0)-mediated LRP polymerisation process, using a pyrene-ATRP initiator and the associated number average molar masses.

Nomenclature	[LA]/[I]	Conv.[a] [%]	$M_{n,\,th}$ [g mol^{-1}]	$M_{n,\,GPC}$ [b] [g mol^{-1}]	$Đ$ [b]
Pyrene-P[LA]	100	95	24 000	14 100	1.52

[a] ^{1}H NMR. [b]$CHCl_3$ SEC analysis *via* RI detection using linear PMMA standards.

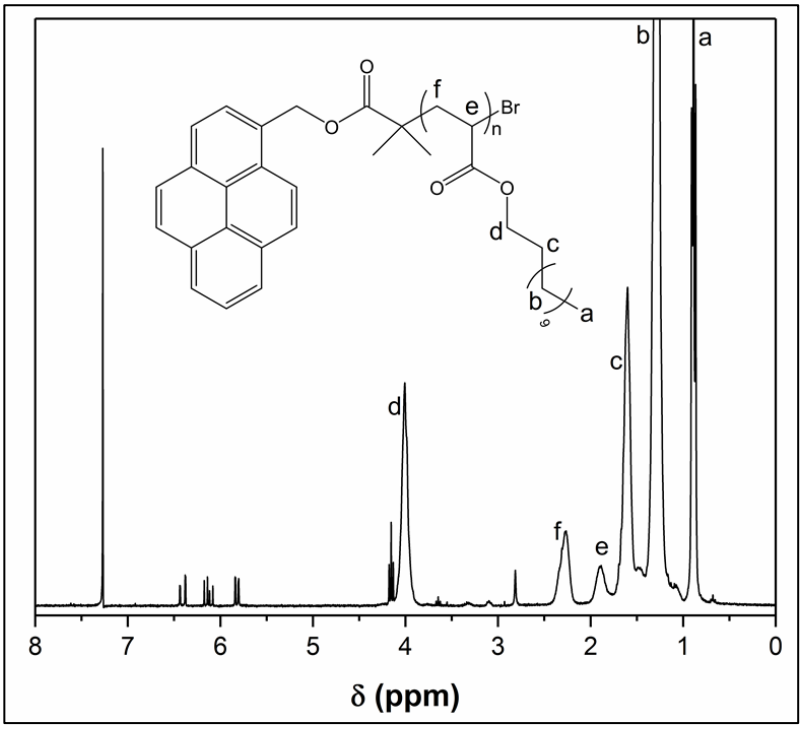

Figure 4.10 ^{1}H NMR of P[LA] synthesised *via* Cu(0)-mediated LRP using a Pyrene-ATRP initiator.

Figure 4.10 shows the ^{1}H NMR of pyrene-P[LA] and shows the polymer was successfully synthesised with a conversion of ~95% (Table 4.4). The presence of LA monomer can be observed at (6.5-5.5 ppm) showing further optimisation is possible. The

presence of the pyrene end group could be influencing the polymerisation at high conversion, preventing the polymerisation completing to full conversion.

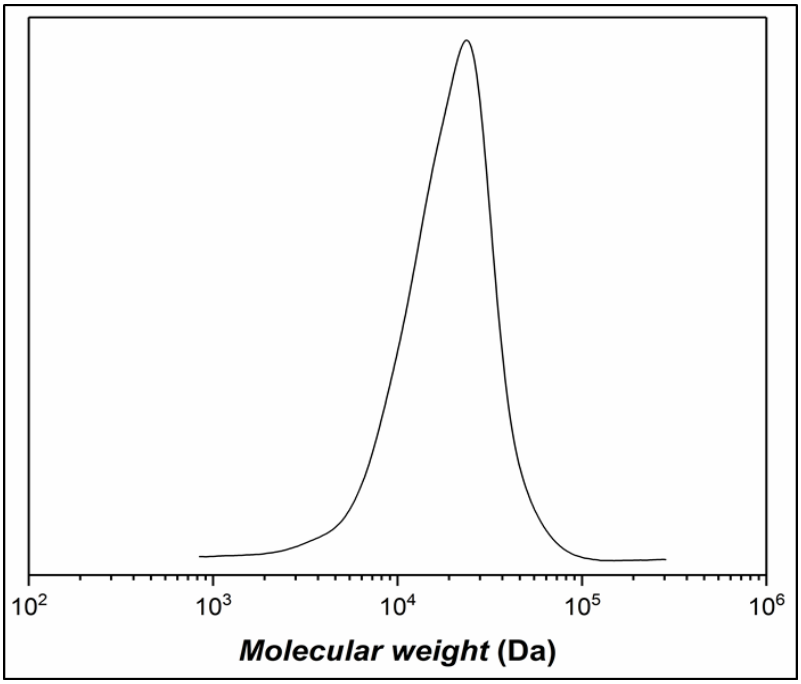

Figure 4.11 SEC trace of P[LA] synthesised *via* Cu(0)-mediated LRP using Pyrene-ATRP initiator.

Figure 4.11 shows the SEC trace of pyrene-P[LA] and reveals poor agreement with theoretical M_n and broad dispersity ($Đ \approx 1.52$; table 4.4) through the presence of low molar mass tailing. The results indicate the polymerisation requires optimisation to increase the conversion and narrow the dispersity. Optimisation can be conducted by altering the polymerisation solvent as well as concentrations of Cu(0)/$CuBr_2$/Me_6TREN. Prior to optimisation, the thermal stability and binding to MWCNTs should be investigated.

4.4 Thermal stability of poly(acrylates)

Thermogravimetric analysis (TGA) was carried out to investigate the thermal stability of P[LA] and aromatic end-functionalised P[LA]s prior to melt processing.

4.4.1 Thermal stability of P[LA] synthesised using RAFT polymerisation

Homopolymers of P[LA] synthesised *via* RAFT were analysed by TGA (Figure 4.12). The onset of degradation occurred at ~340-350 °C with 95% mass loss having occurred by ~440-450 °C for homopolymers **B** and **C**. Homopolymer **A**, which is the lowest molar mass P[LA] showed a lower onset of degradation at ~250-260 °C.

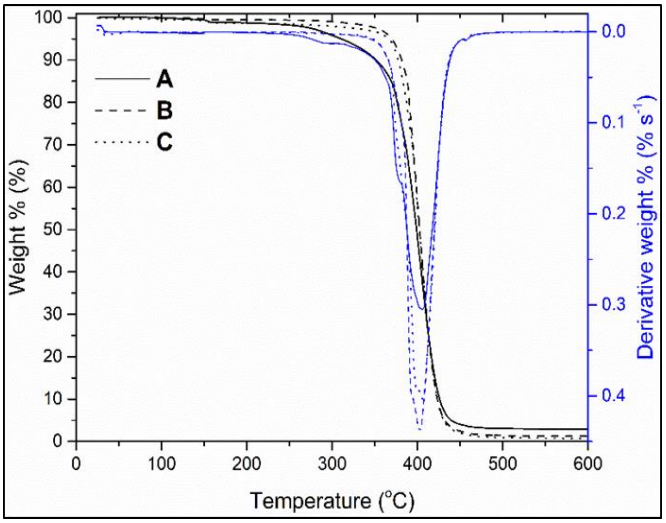

Figure 4.12 TGA and DTA curves of P[LA] synthesised *via* RAFT polymerisation. P[LA] (**A-C**) defined in Table 4.1.

The lower onset of degradation for homopolymer **A** can be explained due to its lower molar mass, M_n = 5.3 kDa and given the cyanomethyl dodecyltrithiocarbonate RAFT agent has a molar mass of 317.96 Da. On average, ~6 wt% of the homopolymer **A** is the RAFT agent and therefore the ~ 6 wt% mass loss observed at 250-260 °C for homopolymer **A** can be attributed to the thermal degradation of the RAFT end group, by assessing the TGA of the RAFT agent alone (Appendix 8). The onset of thermal degradation for the RAFT agent occurs between ~200-260 °C *via* thermal degradation mechanisms previously published in literature.[33] Some examples are illustrated in scheme 4.8. Typically, thermal elimination of the RAFT end groups results in the formation of an unsaturated chain-end with the complete

removal of sulphur. For the higher molar mass polymers, **B** and **C** the weight percentage of the RAFT group relative to the molar mass of the polymer is considerably lower and therefore, the thermal degradation of the RAFT end group is not apparent for those polymers. In addition, the TGA of the LA monomer showed onset of monomer degradation occurs at ~140-150 °C (Appendix 9). The degradation temperature is significant as any traces of un-polymerised monomer would be degraded during the melt-processing of the polymer and therefore polymerisation to high conversion and high purification is important to prevent degradation of unreacted monomer during extrusion. Therefore, mass loss at 250-260 °C for homopolymer **A** could contain a component from the degradation of unreacted monomer.

It is worth noting, the thermal degradation of the RAFT end group almost certainly leads to the production of free radicals which appears to not have a significant influence on the onset of degradation of the P[LA] backbone. Additionally, polymer **A** exhibits a shoulder at ~370-380 °C which could possibly be attributed to the thermal degradation of an intermediary compound formed during the pyrolysis of the RAFT end group.[33] Importantly, P[LA] does not exhibit a radical induced 'unzipping' commonly seen with methacrylates such as poly(methyl methacrylate) (PMMA) in which depolymerisation is observed at ~300 °C.

The TGA data indicated P[LA] is sufficiently thermally stable for the extrusion up to at least 250 °C and therefore, it should be possible to blend P[LA] with PP for the purpose of improving MWCNT dispersion and compatibility with the PP matrix. It appears the thermal stability of P[LA] is not affected by the thermal decomposition of the RAFT end group.

To further explore the effect of the thermal degradation of the RAFT end group on the polymer backbone, molar mass analyses using size exclusion chromatography (SEC) and matrix-assisted laser-desorption ionisation time of flight mass spectrometry (MALDI-TOF MS) were performed on P[LA] synthesised by RAFT, before and after subjecting the polymers to elevated temperatures of 200 °C for 30 mins in an air atmosphere to simulate the effects of heating during extrusion. Figure 4.13 shows the effect of thermal treatment on the molar mass of P[LA] (**A**) using SEC. Limited if any change in molar mass distribution was observed. The result confirmed the end groups of P[LA] do not affect the thermal stability of the P[LA] and its potential for use in melt processing.

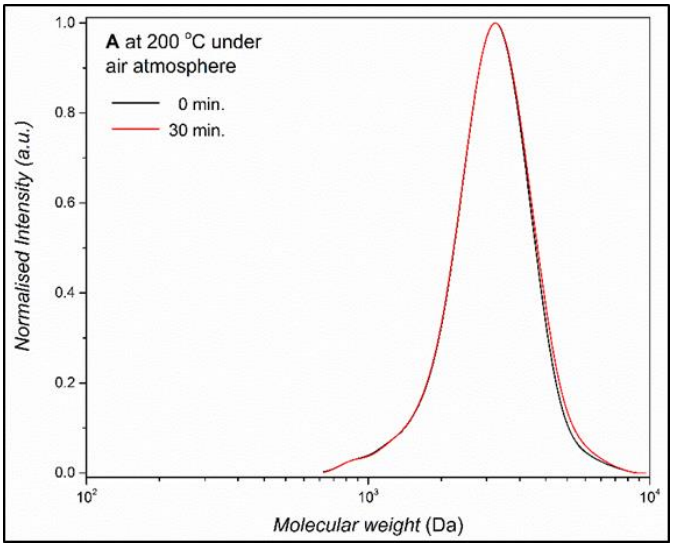

Figure 4.13 SEC traces of P[LA] after thermal treatment at 200 °C under an air atmosphere as a function of time; 0 min. ($M_{n,\,SEC}$ = 2.5 kDa, $Đ$ =1.13), 30 min. ($M_{n,\,SEC}$ = 2.5 kDa, $Đ$ =1.13). P[LA] (**A**) defined in Table 4.1. All peaks are normalised to a maximum intensity of 1.

MALDI-TOF-MS was used to further investigate the thermal characteristics of P[LA]. Figure 4.14 clearly shows the molecular structure of P[LA] *via* RAFT changes when subjected to elevated temperatures, up to 200 °C. However, the repeating pattern of the peaks, separated by the relative molar mass of the monomer indicates the thermal degradation is not occurring at the polymer backbone.

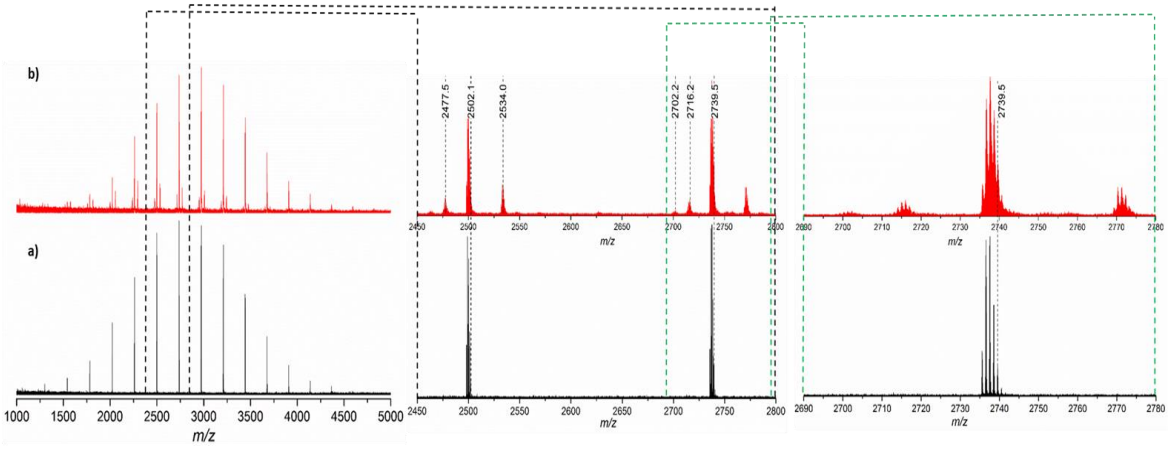

Figure 4.14 MALDI-TOF-MS spectra of P[LA] synthesised *via* RAFT before (a) and after (b) thermal treatment at 200 °C for 30 min in an air atmosphere.

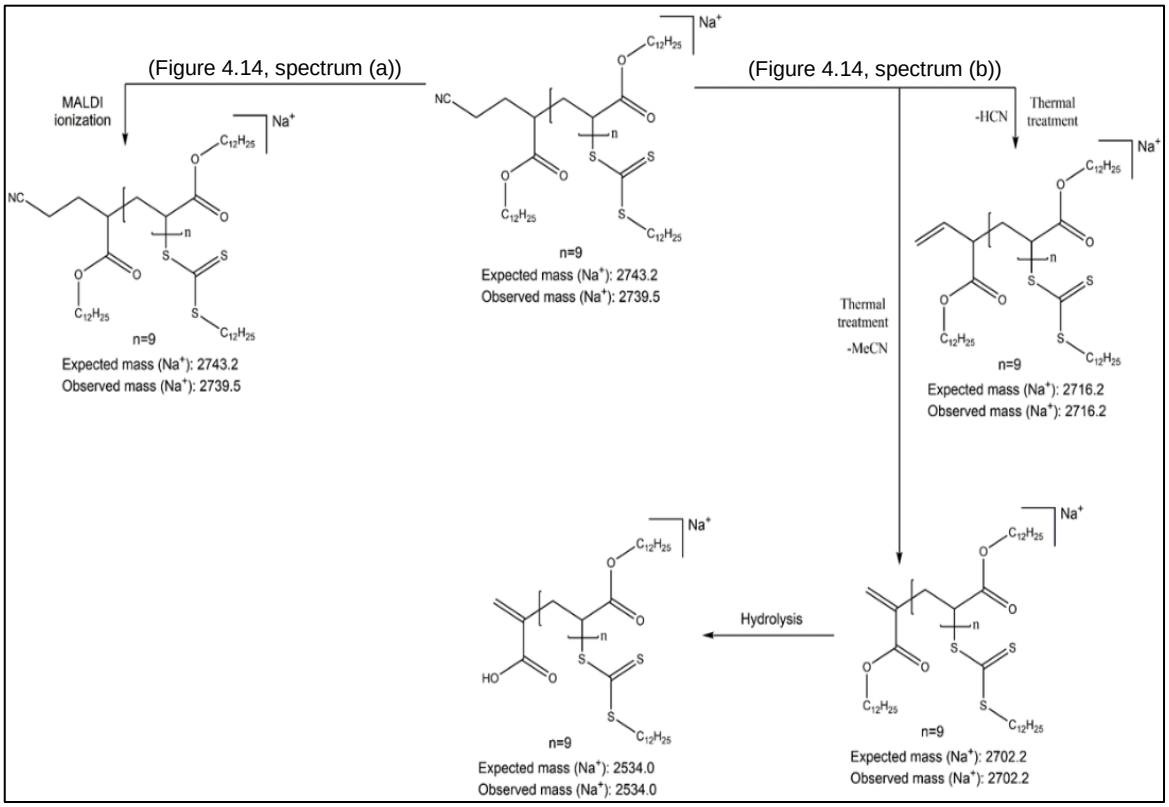

Scheme 4.8 Description of degradation products following the MALDI analysis of P[LA] synthesised *via* RAFT (a) before and (b) after thermal treatment (200 °C, 30 min.)

Possible structures for mass losses during degradation are displayed in scheme 4.8 and are in agreement with a recent report by Barner-Kowollik *et al*.[9] The main distributions are attributed to the polymer, *i.e. m/z* 2739 showing the majority of the polymer is unaffected by the thermal treatment. Mass loses at *m/z* 2702 and 2716 indicate the formation of an unsaturated species caused by the decomposition of the reactive nitrile group. Elimination of the nitrile group appears to have initiated the hydrolysis of a nearby ester. The loss of lauryl alcohol and elimination of the reactive nitrile group is consistent with the signal at *m/z* at 2534. Interestingly, thermal decomposition of the RAFT group was not observed in the MALDI-TOF-MS after thermal treatment suggesting, the trithiocarbonate group and the polymer backbone are thermally stable at 200 °C for 30 min.

Furthermore, NMR (Figure 4.15) was used to confirm the formation of the unsaturated chain end after thermal treatment. Due to the relative concentration of the unsaturated chain end being very low compared with the polymer side-chain, detection of the chain end was not possible.

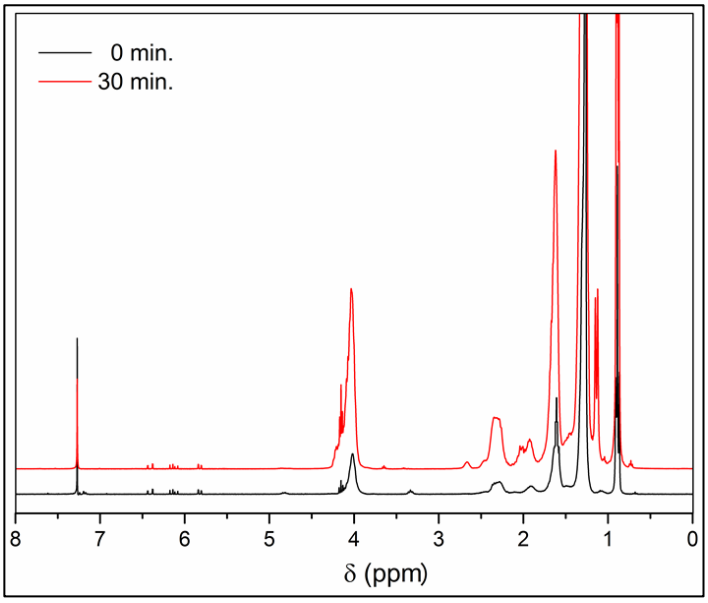

Figure 4.15 NMR of P[LA] synthesised *via* RAFT ($M_{n,\,SEC}$ = 2.5 kDa, $Đ$ = 1.13) before and after thermal treatment at 200 °C under an air atmosphere as a function of time.

4.4.2 Thermal stability of P[LA] synthesised using Cu(0)-mediated LRP

P[LA] synthesised by Cu(0)-mediated LRP has a similar thermal degradation profile to P[LA] synthesised by RAFT (Figure 4.16). The onset of thermal degradation occurred at ≈340-350 °C with 95% mass loss having occurred by 440-450 °C. Polymers **E** and **F** show a ≈2–3 wt% mass loss by 250 °C which could be attributed to the loss of unreacted LA monomer. The TGA of LA (Appendix 9) shows the onset of monomer degradation occurs at ≈140 - 150 °C. The data in Table 4.2 show the higher molar mass polymers **E** and **F** have lower conversions and therefore, unreacted monomer accounts for ≈2–3 wt% mass loss by 250 °C. A similar mass loss was also observed for P[LA] synthesised by RAFT. A shoulder placed between ≈290–300 °C indicates possible pyrolysis of end groups. It is possible the pyrolysis of the ethyl isobutyrate initiator occurs *via* an E_i (intramolecular elimination), also known as a thermal pericyclic *syn* elimination, to release ethylene[34]. In addition, the loss of the labile bromide end group can contribute to a total mass loss of ≈108 Da. On average, pyrolysis of the end groups could contribute a ≈2 wt% mass loss, for the lowest molar mass homopolymer **D**, resulting in the shoulder process observed between ≈290 – 300 °C.

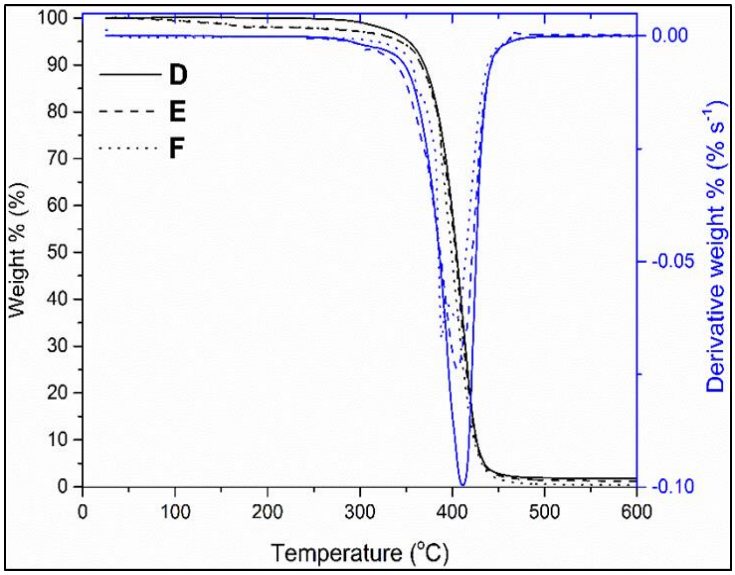

Figure 4.16 TGA and DTA curves of P[LA] synthesised *via* Cu(0)-mediated LRP polymerisation. P[LA] (**D-F**) defined in table 4.2.

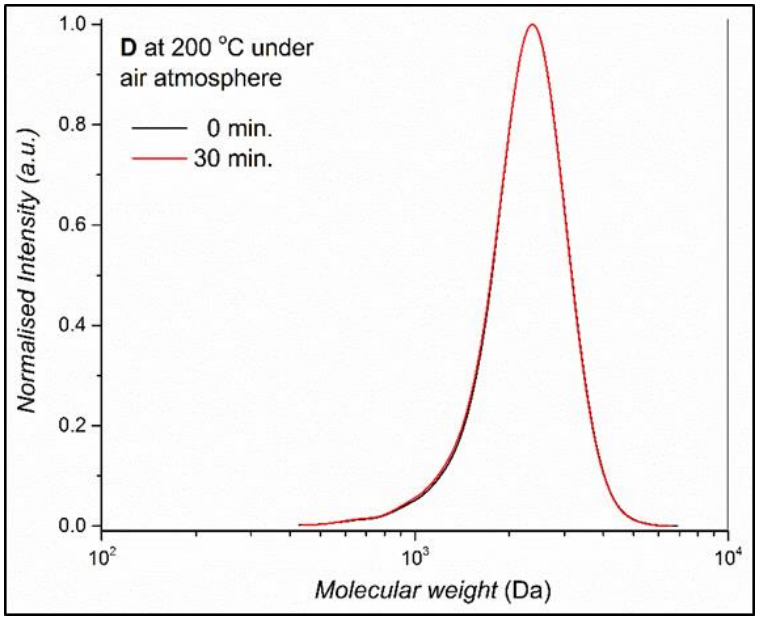

Figure 4.17 SEC traces of P[LA] after thermal treatment at 200 °C under an air atmosphere as a function of time; 0 min. ($M_{n,\,SEC}$ = 2.1 kDa, $Đ$ =1.11), 30 min. ($M_{n,\,SEC}$ = 2.1 kDa, $Đ$ =1.11). P[LA] (**D**) defined in table 4.2. All peaks are normalised to a maximum intensity of 1.

The effect of thermal treatment on the molar mass of P[LA] synthesised by Cu(0)-mediated LRP was also investigated using SEC analysis (Figure 4.17). Limited if any, change in molar mass distribution was observed for P[LA] (**D**) confirming the thermal

degradation of the end-groups does not affect the thermal stability of the P[LA] backbone and its potential use for melt processing with PP.

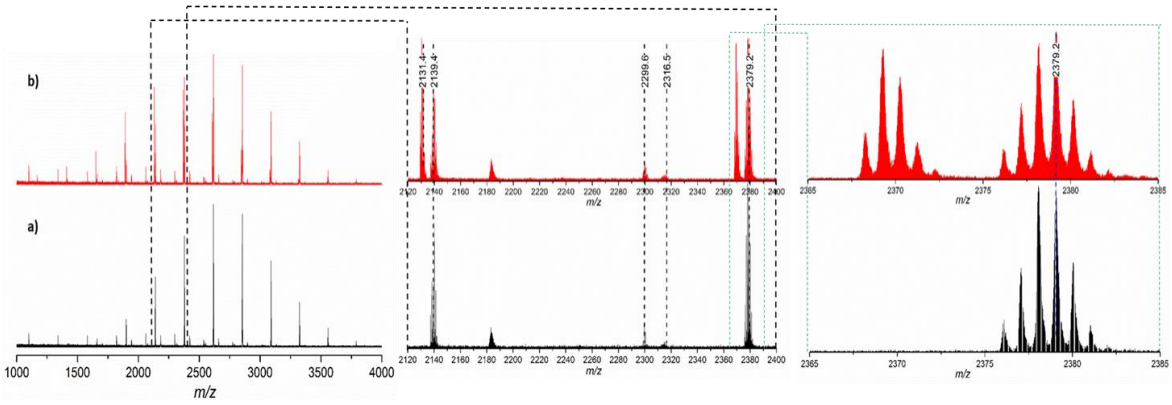

Figure 4.18 MALDI-TOF-MS spectra of P[LA] synthesised via Cu(0)-mediated polymerisation before (a) and after (b) thermal treatment at 200 °C for 30 mins. in air.

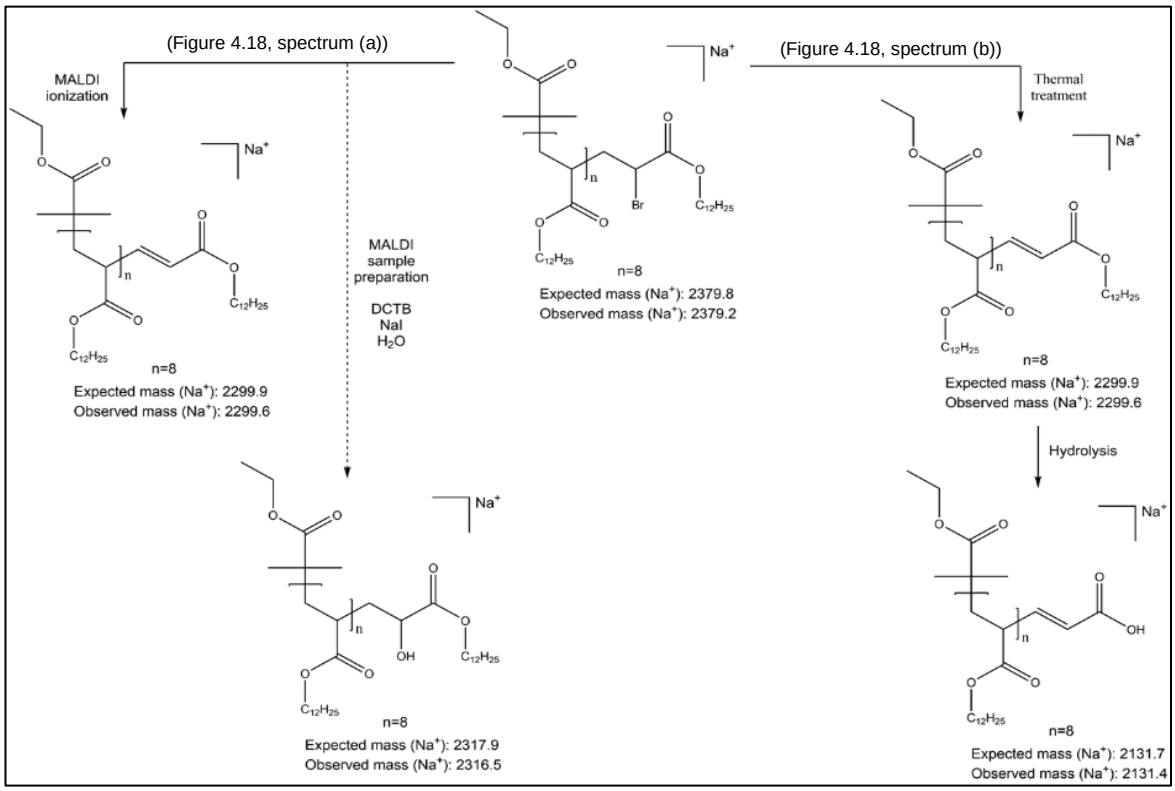

Scheme 4.9 Proposed degradation products from MALDI-TOF-MS analysis of P[LA] synthesised *via* Cu(0)-mediated polymerisation (a) before and (b) after thermal treatment (200 °C, 30 min.)

MALDI-TOF-MS analysis was also performed on P[LA] (**D**) synthesised by Cu(0)-mediated LRP (Figure 4.18). The mass loses observed (Scheme 4.9) are consistent with those reported recently by Barner-Kowollik *et al*.[9] Compared to the P[LA] synthesised by RAFT, ester hydrolysis is more apparent after the elimination of HBr. This is due to the acidic nature of HBr which causes increased hydrolysis compared with the nitrile group in the case of the RAFT polymer. Elimination of HBr and the possible substitution of a hydroxide moiety during the MALDI-TOF-MS ionisation process was also observed for the acrylate polymers *i.e. m/z* 2299 and 2316. Moreover, the subsequent hydrolysis of a nearby ester after elimination of HBr during thermal treatment *i.e. m/z* 2131, is also in agreement with the recent report by Barner-Kowollik *et al*.[9]

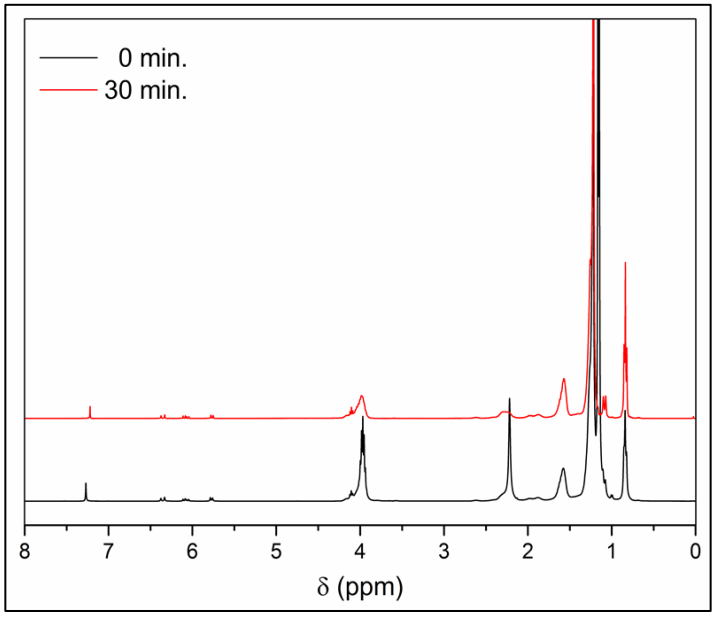

Figure 4.19 NMR of P[LA] synthesised *via* Cu(0)-mediated polymerisation ($M_{n,\,SEC}$ = 2.1 kDa, $Đ$ = 1.11) before and after thermal treatment at 200 °C under an air atmosphere as a function of time.

Identification of vinylic peaks at the end of the polymer chain was also attempted by NMR (Figure 4.19). Due to the relative concentration of the unsaturated chain end being very low compared the polymer side-chain, detection of the chain end was not possible.

In summary, P[LA] synthesised by RAFT and Cu(0)-mediated LRP is thermally stable when subjected to thermal treatment at 200 °C for 30 mins to simulate the effects of heating during extrusion. The polymer backbone remains unaffected, as seen by SEC and

MALDI-TOF analysis however, the end groups are thermally degraded. In the case of P[LA] synthesised by RAFT, the elimination of the nitrile group to form an unsaturated chain end and hydrolysis of a nearby ester are observed. In the case of P[LA] synthesised by Cu(0)-mediated LRP, elimination of the bromide end group to form an unsaturated chain end and hydrolysis of a nearby ester were observed. Critically, such eliminations have limited if any, effect on the polymer backbone at the temperatures required for the processing of PP in an extruder, typically 200 °C

4.4.3 Thermal stability of P[LA] *via* Cu(0)-mediated LRP using Hostasol-ATRP initiator.

After establishing the thermal stability of P[LA] synthesised by RAFT and Cu(0)-mediated LRP, the thermal stability of aromatic end-functionalised P[LA] synthesised using Cu(0)-mediated LRP was investigated. It is important to establish whether the aromatic end-groups are thermally stable at melt extrusion temperatures for PP to determine whether they can be used to functionalise MWCNTs during extrusion with PP.

Figure 4.20 a) and b) show the TGA and DTA curves of the Hostasol-ATRP initiator, Hostasol polymerised with LA (Hostasol-P[LA]), P[LA] (**E**) polymerised *via* Cu(0)-mediated LRP, MWCNTs and Hostasol-P[LA] blended with 10 wt% MWCNTs using solution mixing.

The onset of thermal degradation for the Hostasol-ATRP initiator occurs at ~240-250 °C with 95% mass loss having been completed by ~500 °C. The DTA curve indicates the degradation is a three-step process. The three-step degradation process suggests three separate areas of the Hostasol-ATRP initiator degrade at different temperatures. The first mass loss of ~20 wt% occurring at ~240-250 °C is likely to be the degradation of the ester group. The second mass loss event of a further ~20 wt% occurring at ~320-350 °C is likely to be the degradation of the imide group. Finally, the final degradation mass loss of ~60 wt% occurring at ~380-450 °C is likely to be the aromatic structure of the Hostasol molecule based on the relative mass losses. The onset for the degradation of the Hostasol-ATRP initiator is relatively close to the processing temperature of PP (~170-210 °C) suggesting it would not be suitable to use to functionalise P[LA]. P[LA] has a degradation temperature of ~350 °C and an aromatic initiator would be required to be thermally stable to at least ~300 °C for it to be suitable for processing with PP, in order to provide certainty that the Hostasol will not degrade under thermo-mechanical stress.

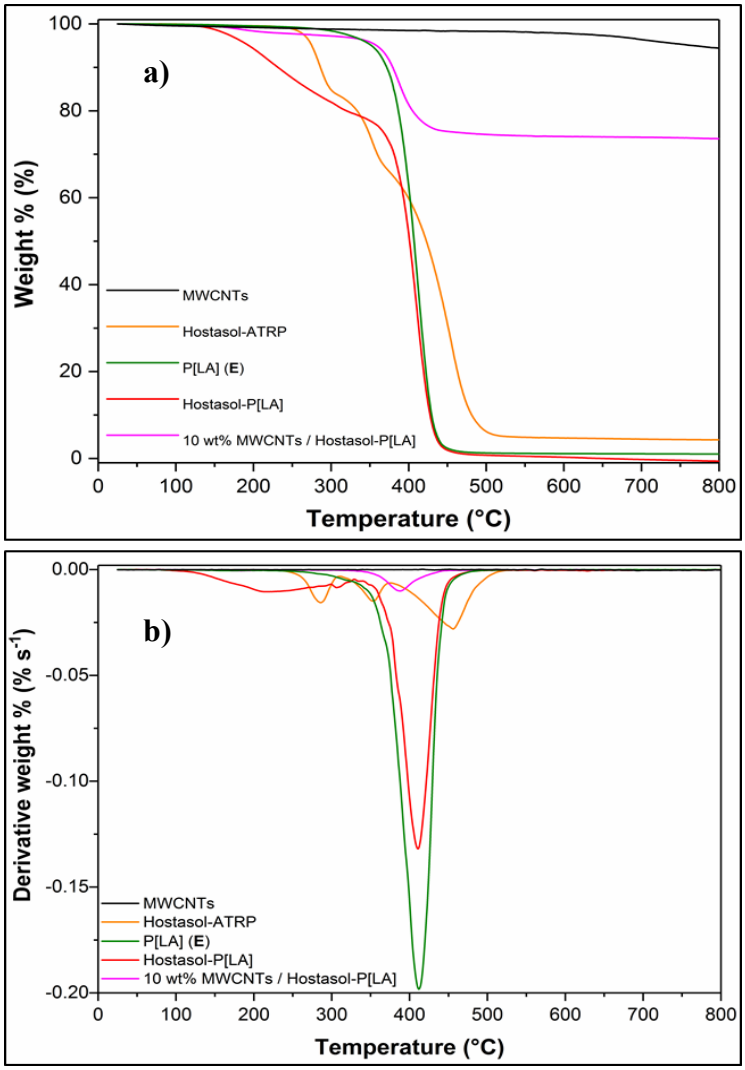

Figure 4.20 (a) TGA and (b) DTA curves of Hostasol-P[LA] synthesised *via* Cu(0)-mediated LRP using Hostasol-ATRP initiator. P[LA] properties given in table 4.2 and 4.3.

The Hostasol-P[LA] has an onset of degradation of ~140-150 °C suggesting the Hostasol is not as thermally stable when attached to P[LA] compared to Hostasol-ATRP. The degradation can also be attributed to unreacted monomer as the ^{1}H NMR (Figure 4.8) shows the presence of 15 wt% unreacted monomer. In contrast, the P[LA] (**E**) has an onset of degradation of 300-320 °C however, this polymer only has 3 wt% unreacted monomer. It can be argued that the onset of thermal degradation can be improved by improving purification and complete removal of unreacted monomer however, such a process is costly in an industrial environment. It is preferable to optimise the polymerisation to achieve high rates of conversion but, this was not pursued as Hostasol itself does not have the required thermal stability.

The TGA of MWCNTs has only a 4 wt% mass loss at 800 °C with onset occurring ~600 °C suggesting the presence of impurities such as metal catalysts and amorphous carbon. Hostasol-P[LA] was solution mixed with MWCNTs to determine if there is an interaction between the Hostasol and the MWCNTs. 10 wt% MWCNTs were solution mixed with Hostasol-P[LA] and the mixture was subsequently filtered and dried. The composite of MWCNTs and Hostasol-P[LA] showed a two-step degradation process. Initially, onset occurs at ~150-160 °C which can be attributed to the degradation of the Hostasol end group and unreacted LA monomer. The second degradation occurs at ~340-350 °C and can be attributed to the degradation of the P[LA] backbone confirmed with degradation of P[LA] (**E**). The TGA curve shows ~15 wt% mass remained at 800 °C indicating only ~15 wt% of P[LA] remained bound to the MWCNTs after solution mixing even though the MWCNTs were initially mixed with 90 wt% P[LA].

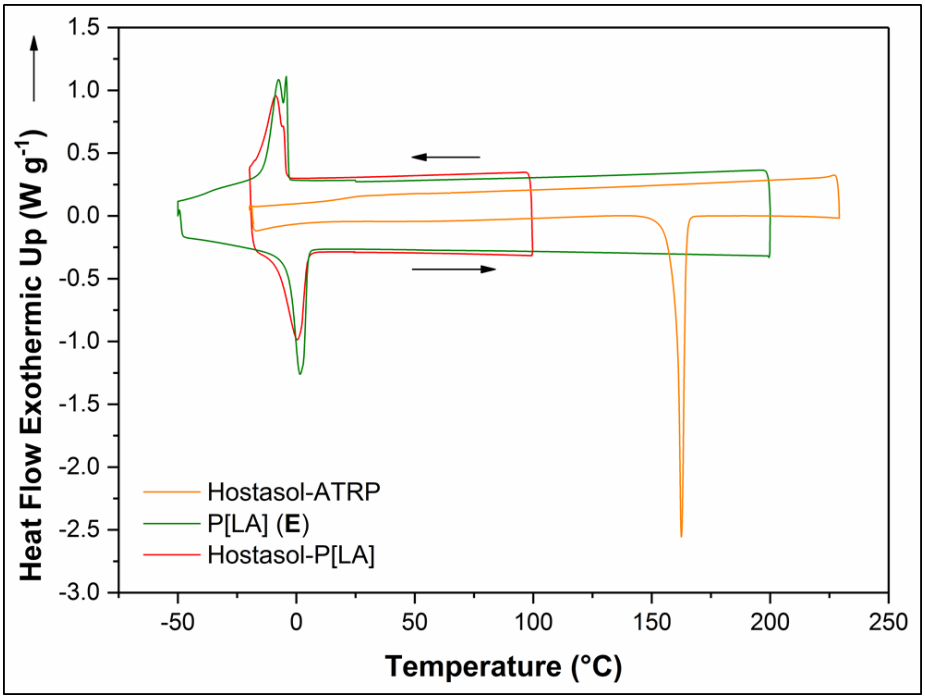

Figure 4.21 DSC traces of P[LA] synthesised *via* Cu(0)-mediated LRP using Hostasol-ATRP initiator. P[LA] defined in table 4.2 and 4.3.

DSC measurements (Figure 4.21) were performed on the Hostasol-ATRP initiator, Hostasol-P[LA] and P[LA] (**E**) to determine if the Hostasol has the required thermal stability. A significant melting or sublimation process was observed at ~165 °C for the

Hostasol-ATRP initiator suggesting the Hostasol is thermally altered after this temperature. To further determine if the thermal transition leads to changes in molecular structure of the Hostasol, variable temperature FTIR was used to investigate this behaviour.

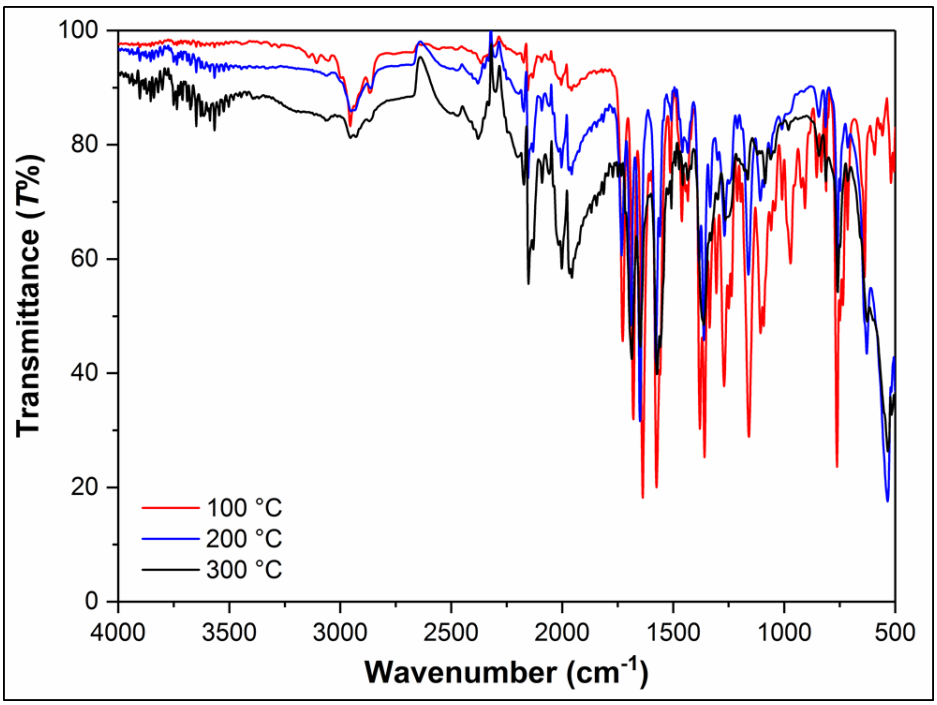

Figure 4.22 FTIR spectra of Hostasol-ATRP as a function of temperature.

The Hostasol-ATRP initiator was heated to temperatures ranging from r.t. to 300 °C and the FTIR spectra taken (Figure 4.22), of the spectra recorded at three temperatures are displayed for clarity. The FTIR spectra show the Hostasol-ATRP changes molecular structure when heated from r.t. to even 200 °C. The peaks in the range from ~700-1750 cm^{-1} decreased in intensity suggesting the functional groups such as the imide group (~1700-1650 cm^{-1}) and the ester group (1750-1735 cm^{-1}) degraded. Additionally, various changes in CH bending (700-500 cm^{-1}) and overtones (2300-1800 cm^{-1}) confirm changes in aromatic structure of the Hostasol.

In summary, it is not possible to use Hostasol end-functionalised P[LA] for the purpose of non-covalently functionalising MWCNTs using melt blending with PP. It is challenging to synthesise Hostasol-P[LA] with high conversions (>98%) so as to eliminate the presence of unreacted LA monomer which can degrade during melt mixing with PP.

Furthermore, TGA, DSC and FTIR measurements confirmed the Hostasol-ATRP initiator does not have the required thermal stability (>200 °C) for processing with PP.

4.4.4 Thermal stability of P[LA] *via* Cu(0)-mediated LRP using Pyrene-ATRP initiator.

To further explore the use of aromatic end-functionalised P[LA] for the non-covalent functionalisation of MWCNTs during extrusion with PP, pyrene end-functionalised P[LA] (pyrene-P[LA]) was synthesised using Cu(0)-mediated LRP using a pyrene initiator (pyrene-ATRP). Pyrene has shown to non-covalently bind to the surface of MWCNTs, discussed in chapter 2. Figure 4.23 a) and figure 4.23 b) show the TGA and DTA curves respectively of; pyrene-ATRP initiator, P[LA] polymerised with pyrene-ATRP initiator, P[LA] polymerised using standard initiator, MWCNTs and MWCNTs solution mixed with pyrene-P[LA].

Pyrene –ATRP had an onset of degradation of ~150-160 °C with 75% mass loss by ~550 °C. Pyrene-ATRP undergoes a three-step degradation process, similar to Hostasol-ATRP. The first degradation step occurs at ~150-160 °C with a mass loss of ~20 wt% which can be possibly be attributed to the degradation of the ester group. The second degradation step occurs at ~240-250 °C with a mass loss of ~20 wt% can possibly be attributed to the elimination of the alcohol functionality formed after the degradation of the ester group. The final degradation step occurs at ~400-450 °C with a mass loss of ~35 wt% which can possible be attributed to the degradation and carbonisation of the pyrene molecule itself. There is 25 wt% residual mass possibly due to the presence of carbon soot after degradation. Due to the fact that the pyrene-ATRP initiator has an onset of degradation at ~150-160 °C, it is not possible to use pyrene end-functionalised P[LA] to non-covalently functionalise MWCNTs.

Pyrene-P[LA] did not show such a low onset of degradation however, it is difficult to detect the degradation of the end group as its mass relative to the main polymer back bone is <1 wt%. MWCNTs were solution mixed with 90 wt% pyrene-P[LA] in chloroform before filtration and drying. The subsequent composite shows that only 20 wt% of pyrene-P[LA] was retained on the surface of the MWCNTs. This is a ~5 wt% increase on the amount of polymer retained on the surface of MWCNTs compared to that with Hostasol-P[LA]. Therefore, pyrene has a stronger non-covalent interaction with MWCNTs compared to Hostasol as more P[LA] was able to adsorb onto the surface of MWCNTs.

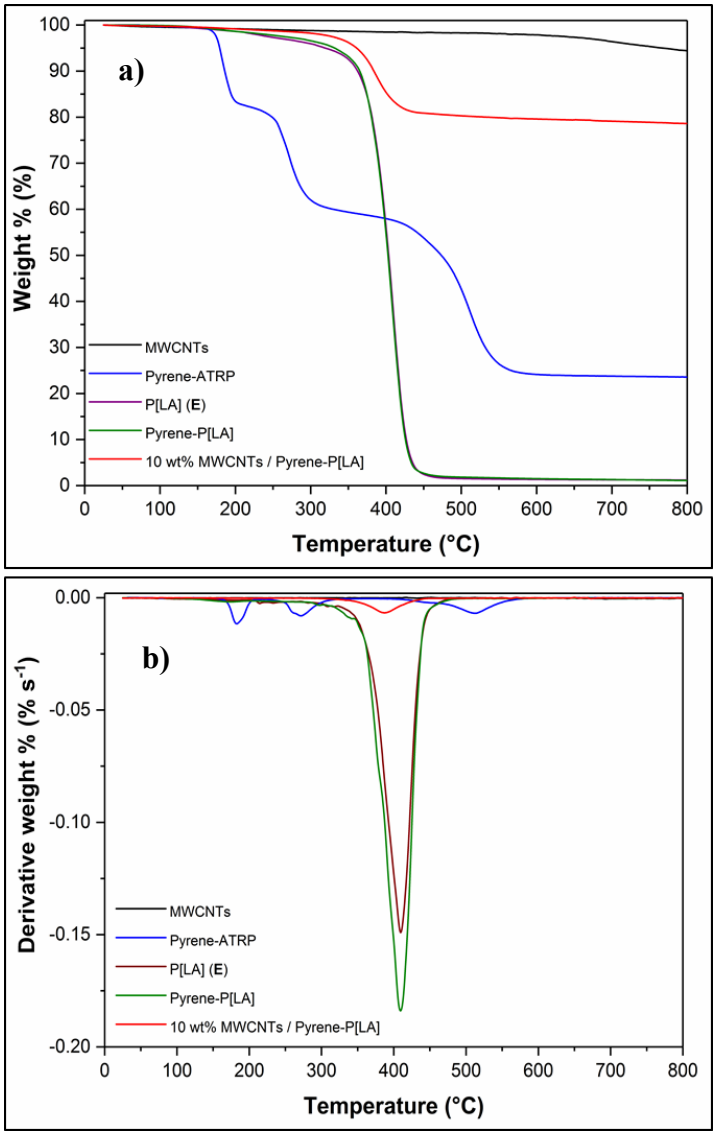

Figure 4.23 (a) TGA and (b) DTA curves of P[LA] synthesised *via* Cu(0)-mediated LRP using Pyrene-ATRP initiator. P[LA] defined in table 4.2 and 4.4.

In conclusion, TGA has shown that pyrene does not have the required thermal stability for use as an aromatic end functionalised moiety for P[LA]. It appears the ester bond linking the aromatic moiety to the polymer backbone may not be thermally stable to >300 °C and therefore, alternative methods of incorporating aromatic functionalities into poly(acrylates) is required, for example, the use of block copolymers with aromatic side-chain groups.

4.5 Characterisation of the MWCNTs and GNPs used in this study

In order to successfully characterise composites of poly(acrylates) with MWCNTs or GNPs, the MWCNTs have to be rigorously characterised as well as the poly(acrylates). A range of techniques were used to determine structure, morphology, diameter, purity, aspect ratio and quality of MWCNTs and GNPs used. The most common type of characterisation employed is electron microscopy (EM). EM in the form of scanning electron microscopy (SEM) and high-resolution transmission electron microscopy (HRTEM) provide detailed analysis of MWCNTs. TEM can be expanded to scanning transmission electron microscopy (STEM) which is excellent for accompanied spectroscopic analysis such as energy dispersive X-ray spectroscopy (EDX) and electron energy loss spectroscopy (EELS). EM provides visual observations of the materials with very high magnifications. Magnifications of up to x 10^9 can be achieved with high resolution TEM instruments that are aberration corrected.

In addition to using EM, Raman spectroscopy has shown to be an excellent tool for characterising the structure of the MWCNTs and GNPs. Carbon-carbon bonds are Raman active. Pulsing the bonds with specific energies causes Raman scatting which can be analysed to understand the structural characteristics such as defect density and presence of impurities.

X-ray photoelectron spectroscopy (XPS) can provide details on atomic distributions such as the C:O ratio. It is important to understand the quantity and type of oxygen functional groups on the surface of MWCNTs and GNPs to determine whether they require further treatment prior to use.

MWCNTs produced by Nanocyl™ (NC7000) are commercially grown using chemical vapour deposition (CVD) and were used as received without prior chemical treatment and therefore, it is important to accurately characterise them to better understand their interactions with polymers.

4.5.1 Electron microscopy imaging of the MWCNTs (NC7000) used in this study

Figure 4.24 shows the low magnification SEM micrographs of MWCNTs. The images show the agglomerates formed during the production process. The NC7000 are present in the form of agglomerates of c.a. 2-3 μm diameter. The tubes are highly entangled (Figure 4.24b). The ropes themselves are comingled together to form more loosely entangled

agglomerates ranging in sizes from c.a. 5 μm to 1 mm. EDX analysis performed by White *et al* revealed the presence of catalytic residue within the agglomerates of MWCNTs.[35] The main impurities for NC7000 are aluminium (5.9 wt%), iron (0.5 wt%), cobalt (0.2 wt%) and trace levels of sodium. Aluminium oxide is used as support particles and the Fe and Co as catalysts. The support particles are thought to be responsible for the highly entangled nature of the agglomerates as the rough surface of the support particles reduces alignment during growth.[35]

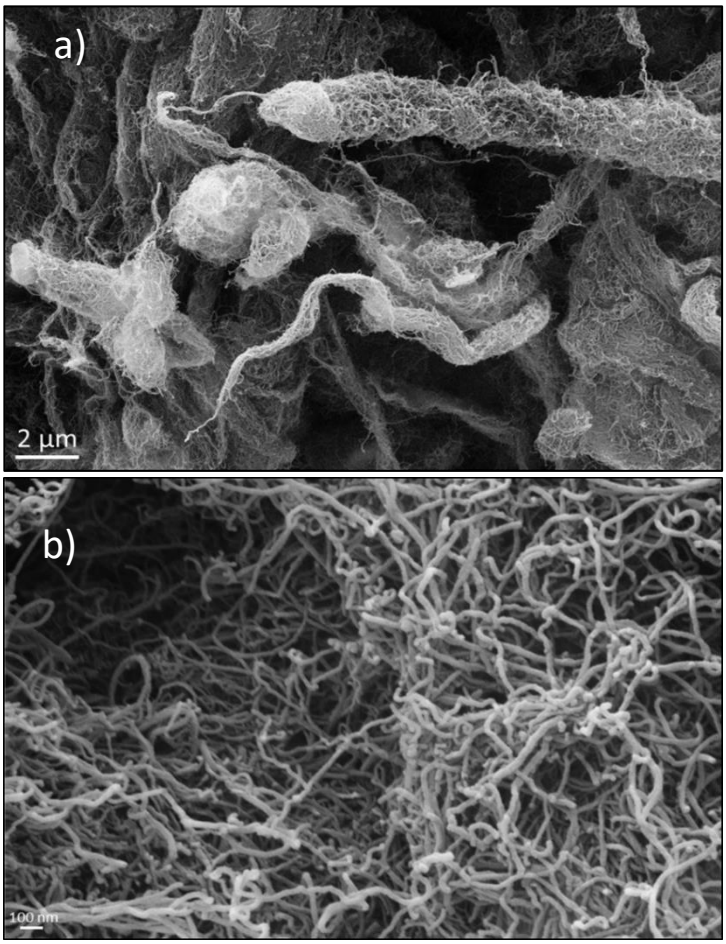

Figure 4.24 SEM micrographs of MWCNTs (NC7000^{TM}) at a) x 15k and b) x 100k magnification.

HRTEM is a valuable method for characterising the homogeneity of the MWCNTs and their morphology. The orientation of the wall, their graphitic character, and presence of impurities can easily be quantified by TEM.

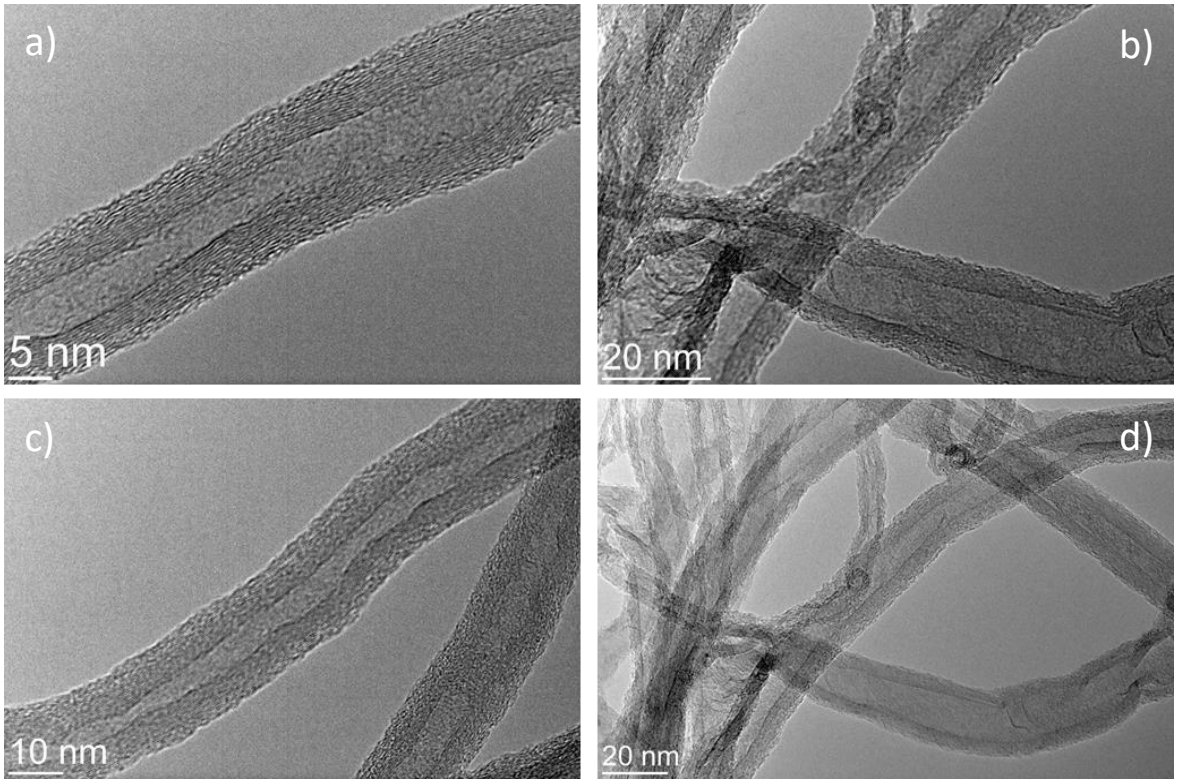

Figure 4.25 HRTEM images of un-functionalised MWCNTs at, a) x 400k, b) x 250k c) x 250k and d) x 150k magnification.

Figure 4.25 shows TEM images of un-functionalised MWCNTs at various magnifications. The images clearly show the multi-wall tubular structure of MWCNTs along with their hollow core. The number of walls these tubes have has been visually estimated to be in the region of 10-20 implying they would be excellent for mechanical reinforcement.

The outer walls are highly disordered whereas the inner walls are smooth and parallel with few voids. The walls themselves show areas of buckling and bending. Generally, the walls run parallel to the main axis however, twisting is common along longer tubes. Tube diameters range from 5-20 nm with lengths in the order of 1-2 μm. Krause *et al* reported the tubes to have a surface area of 250-300 m^2g^{-1} with a bulk density of 66 kgm^{-3}.[36]

4.5.2 Raman Spectroscopy of MWCNTs

Figure 4.26 shows the Raman spectra of these MWCNTs. The measurement was conducted using a 532 nm laser (2.33 eV). The Raman active symmetries are labelled as *A*, E_1 and E_2. The first order allowed C-C bond transition is known as the *G*-band (~1577 cm^{-1}). This is as a result of the in-plane vibration of an ideal sp^2 carbon-carbon bond. This vibration has a second order overtone known as the *G′* band (~2670 cm^{-1}) and, is used to infer long range order in the carbon-based structure. The disorder induced *D*-band (~1345 cm^{-1}) is a forbidden vibrational energy transition and results from defects in the structure of MWCNTs such as C-O bonds and dangling bonds.

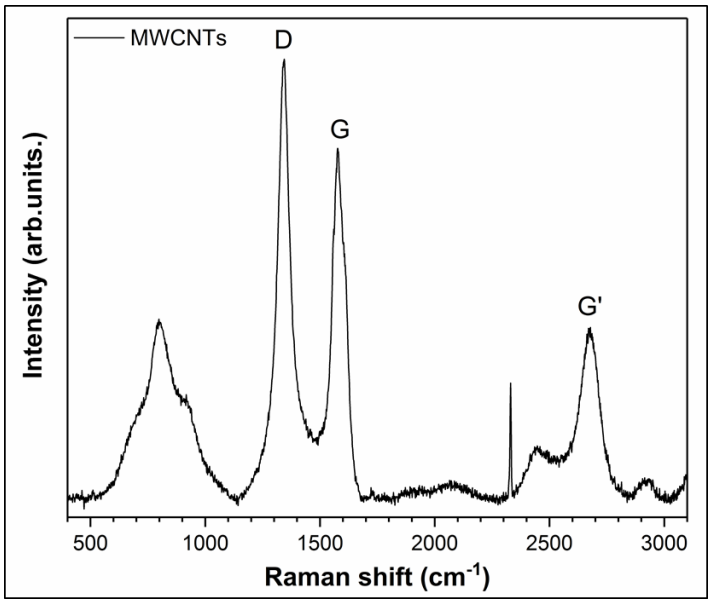

Figure 4.26 Raman spectra for MWCNTs.

The quality of the MWCNTs (or defect density) can be determined by calculating the ratio of intensities between the *D*-band and the *G*-band. The MWCNTs used in this project have a I_D/I_G ratio of 1.26. The relatively high ratio suggests the MWCNTs used contain a high number of defects. However, the high number can also be as a result of the presence of amorphous carbon. The value of I_D/I_G is similar to that obtained by White *et al* (I_D/I_G = 1.12) and they also suggested the possibility of a highly defective structure.[35] In addition, the $I_{G'}/I_G$ intensity ratio can be used as a better indicator of crystallinity as it has been proposed that defects reduce the double resonance process which reduces the *G′* band. The MWCNTs had a $I_{G'}/I_G$ = 0.46 which is similar to that measured by White *et al*.[35] However, it can be difficult to compare intensity ratios as they are highly dependent on the excitation wavelength.

Purification of the MWCNTs through washing with mild acidic solution can be used to remove the impurities however, this project was focused on the use of as produced commercially available MWCNTs and therefore, such purifications were not pursued.

4.5.3 X-ray photo-electron spectroscopy (XPS) of MWCNTs

XPS can be used to characterise the surface chemistry of the MWCNTs. Figure 4.27a shows the survey scan for the MWCNTs and a relative C:O ratio of 98:2 implying relatively low levels of oxidation and a high degree of graphitisation compared to more oxidised and purified MWCNTs which can have oxygen content of over 5 at%. A small proportion of the oxidation can be from oxidised catalysts such as aluminium oxide however, aluminium was not detected by XPS. The spectra mostly consists of the C1s peak at 284.0 eV with is corresponding KLL Auger. The O1s at 533 eV has a small peak and is due to carboxylic acids and esters mainly present on the tube edges.[35] Figure 4.27b shows the deconvolution for the C1s peak and the likely peaks present used to form the C1s peak. The majority of the peak is dominated by the carbon sp^2 bond showing there are little defects in the nanotube walls due to the lack of a carbon sp^3 peak. Figure 4.27b and figure 4.27c confirm the presence of oxygen functional groups which is as expected as all commercially available MWCNTs have some degree of oxygen on the surface.[35]

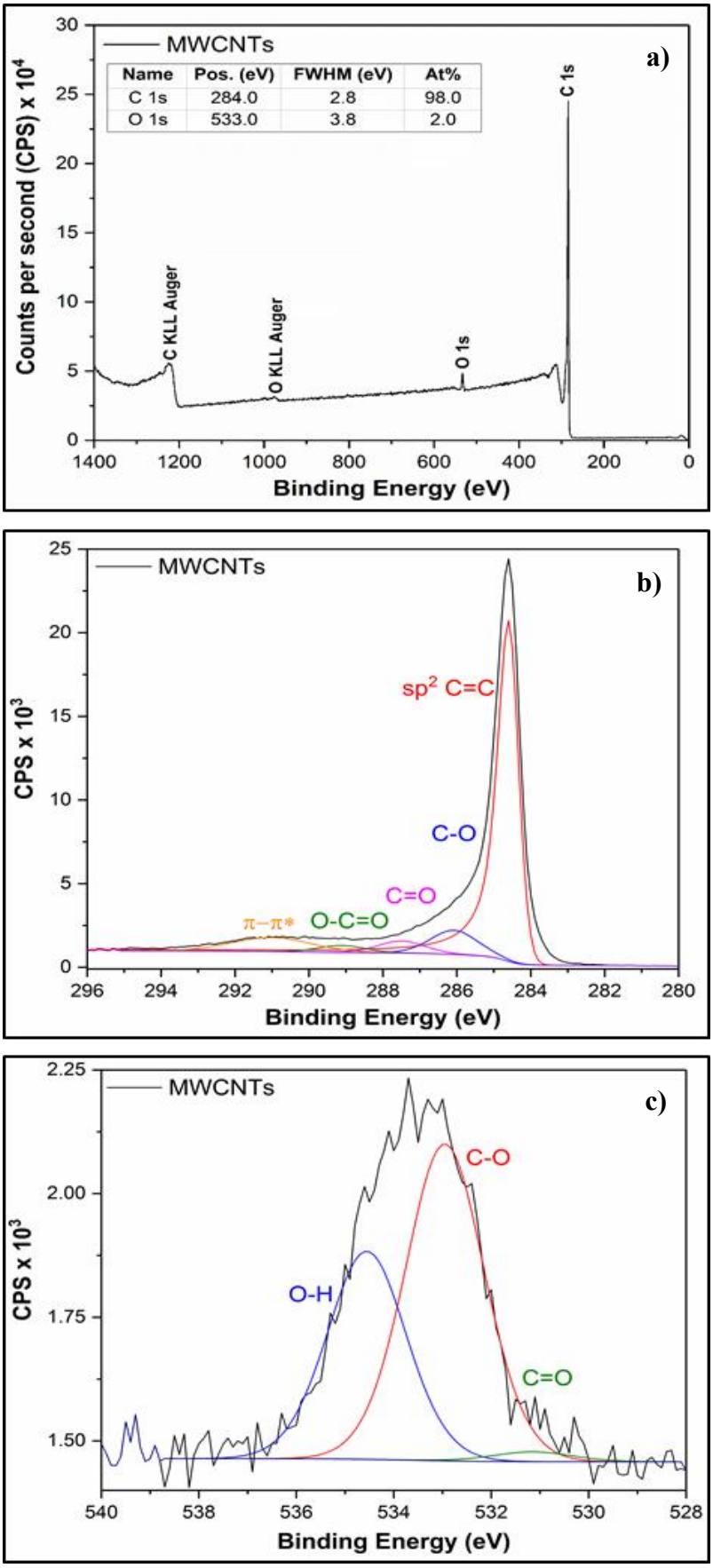

Figure 4.27 XPS spectra of MWCNTs, a) survey scan, b) carbon 1s and c) oxygen 1s.

4.6 Composites of MWCNTs and P[LA]

After establishing the thermal stability of P[LA] is suitable for melt mixing with PP, the non-covalent CH-π wrapping interaction between P[LA] and MWCNTs was investigated with the aim of improving the dispersion and interfacial adhesion between the MWCNTs and the PP matrix. In addition to the investigation of the interaction between MWCNTs and P[LA], the effect of using P[LA] synthesised by RAFT and Cu(0)-mediated LRP was compared to determine whether the P[LA] polymerised by both techniques effects its' interaction with the MWCNTs.

Initially, sonication and vigorous stirring was used to break up the MWCNT agglomerates in a chloroform solution. Care was taken not to sonicate the MWCNTs for a prolonged period of time >5 min, as this can damage the structural integrity of the MWCNTs. P[LA] was added to the dispersed MWCNT solutions, then briefly sonicated and vigorously stirred to allow adsorption of the polymer onto the MWCNT surfaces. There was no observable evidence of tube damage from extensive microscopic examination (SEM/HRTEM) across the length scales post sonication. The dispersion was subsequently filtered and dried. TGA was used to establish the quantity of P[LA] adsorbed onto the surface of MWCNTs.

4.6.1 Synthesis and characterisation composites of MWCNTs and P[LA] synthesised using RAFT polymerisation

P[LA] synthesised using RAFT was solution mixed with MWCNTs. The following investigation was used to determine whether P[LA] adsorbs onto the surface of MWCNTs and whether using P[LA] synthesised by RAFT or Cu(0)-mediated LRP influenced the strength of the non-covalent interaction and subsequently the quantity of P[LA] adsorbed onto the surface of the MWCNTs. Several variables were investigated such as, whether the molecular weight of P[LA] influenced the adsorption and the concentration of MWCNTs used in the initial dispersion, (*i.e.* does changing the mixing ratio between P[LA] and MWCNTs influence adsorption). Table 4.5 lists the various P[LA]/MWCNT combinations and the relative ratios of P[LA] to MWCNTs before and after filtration (i.e. for the P[LA] synthesised using RAFT).

Table 4.5 Relative proportions (wt%) of P[LA] (synthesised using RAFT) and MWCNTs before and after adsorption.

Nomenclature	P[LA]	Dispersion of P[LA]/MWCNT[a]		MWCNT adsorbed on P[LA][b]	
		P[LA]	MWCNT	MWCNT	P[LA]
A_5	A	95	5	88	12
A_{10}	A	90	10	84	16
B_5	B	95	5	79	21
B_{10}	B	90	10	86	14
C_5	C	95	5	81	19
C_{10}	C	90	10	78	22

[a] Dispersed in 100 ml $CHCl_3$. [b] TGA analysis of dried filter cake. P[LA] (**A-C**) defined in Table 4.1.

Initially, MWCNTs (5 wt% and 10 wt%) were dispersed in chloroform with P[LA] (90 wt% and 95 wt%, respectively) assisted by ultrasonication. The dispersion was subsequently filtered and dried to produce a (nano)composite film. P[LA]s with three different degrees of polymerisation and molar masses were chosen to investigate the effect of changing molar masses on the non-covalent wrapping/interaction with MWCNTs. After solution mixing P[LA] (synthesised using RAFT) with MWCNTs, the concentration of adsorption/coating was determined by TGA.

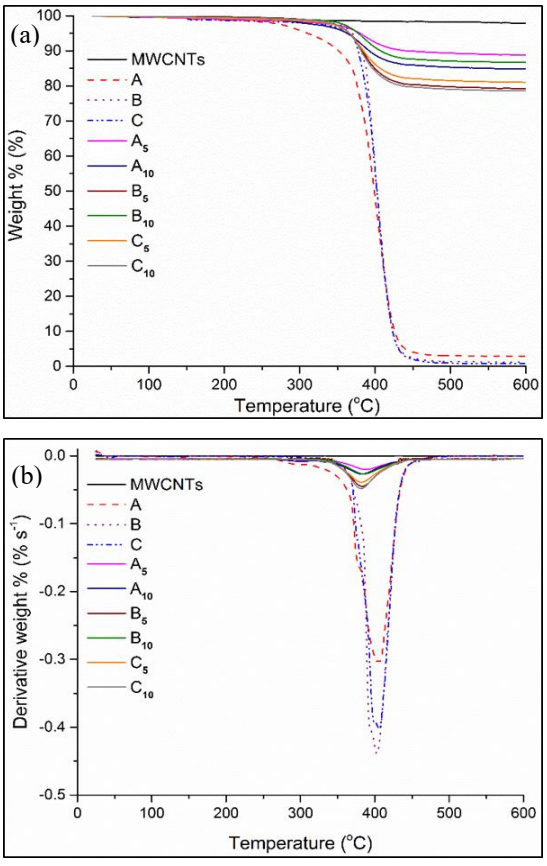

Figure 4.28 (a) TGA weight loss curves and (b) DTA curves of P[LA] synthesised *via* RAFT and dispersed with MWCNTs. P[LA] (**A-C**) defined in table 4.1 P[LA] modified MWCNTs (**A-C**$_{(5/10)}$) defined in table 4.5.

Figure 4.28 a) and b) show the TGA and DTA traces respectively and indicate an adsorption of ~10-25 wt% P[LA]. The onset of thermal degradation of P[LA] after adsorption appears to be unchanged at ~340-350 °C. In general, the higher the molar mass of the P[LA], the greater the level of adsorption. This is expected due to one part of the polymer chain being adsorbed whilst, the remainder of the polymer chain is more likely to adsorb onto the CNT surface via CH-π interactions. The MWCNTs are thermally stable in the whole temperature range studied (up to 600 °C), with only negligible mass loss due to the presence of amorphous carbon and other impurities. Additionally, increasing the amount of MWCNTs results in P[LA] adsorption as the MWCNT surface area available is increased, thus more polymer is able to adsorb. Higher concentrations of P[LA] adsorption was expected and therefore, other factors, possibly bound solvent could be preventing adsorption of more P[LA].

4.6.2 Synthesis and characterisation composites of MWCNTs and P[LA] synthesised using Cu(0)-LRP.

Table 4.6 lists the various P[LA]/MWCNT combinations and the relative ratios of P[LA] to MWCNTs before and after filtration, (i.e. for P[LA] synthesised using Cu(0)-mediated polymerisation). The TGA curves of MWCNTs coated with P[LA] synthesised *via* Cu(0)-mediated polymerisation (Figure 4.29a and b) indicate a more enhanced interaction in that P[LA] synthesised by this method has increased thermal stability of ~50 °C when adsorbed onto the surface of the MWCNTs and, a significantly greater concentration of this P[LA] adsorbs compared to P[LA] synthesised using RAFT. Un-bound P[LA] had an onset temperature for degradation of ~340-350 °C, but P[LA] bound to the surface of the MWCNTs had a higher onset temperature of ~400 – 410 °C.

Table 4.6 Relative proportions (wt%) of P[LA] (synthesised using Cu(0)-mediated polymerisation) and MWCNTs before and after adsorption.

Nomenclature	P[LA]	Dispersion of P[LA]/MWCNT[a]		MWCNT adsorbed on P[LA][b]	
		P[LA]	MWCNT	MWCNT	P[LA]
D_5	D	95	5	86	14
D_{10}	D	90	10	83	17
E_5	E	95	5	65	35
E_{10}	E	90	10	42	58
F_5	F	95	5	16	84
F_{10}	F	90	10	67	33

[a] Dispersed in 100 ml $CHCl_3$. [b] TGA analysis of dried filter cake. P[LA] (**D-F**) defined in Table 4.2.

Additionally, a clear trend was observed where the higher the molar mass of the P[LA], the greater the concentration of P[LA] adsorbed. In general, the increase in concentration of MWCNTs also results in an increase in the concentration of P[LA] adsorption. These observations are in agreement with that reported above for the P[LA] synthesised using RAFT. The increased thermal stability of P[LA] (see Figure 4.29a and b) confirms there is an interaction between the surface of the MWCNTs and the P[LA]. The increased thermal stability of P[LA] observed shows an interaction occurs between the surface of the MWCNTs and the P[LA]. However, it is unclear why this interaction is only observed with P[LA] synthesised by Cu(0)-mediated and not with RAFT. The difference in the thermal stability could be as a result of relative amounts of bound and un-bound P[LA]. It is possible the P[LA] synthesised by RAFT was adsorbed but poorly bound, however, the P[LA] synthesised by Cu(0)-mediated was bound. It is also possible P[LA] synthesised by Cu(0)-mediated reacts with the surface of MWCNTs which causes the delayed degradation of the polymer.

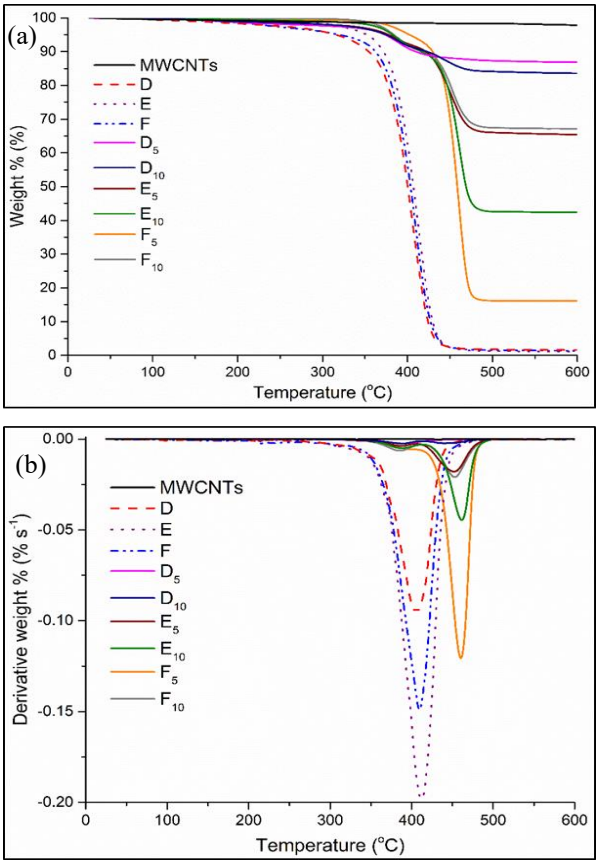

Figure 4.29 (a) TGA weight loss curves and (b) DTA curves of P[LA] synthesised *via* Cu(0)-mediated LRP and P[LA] coated MWCNTs. P[LA] (**D-F**) defined in table 4.2. P[LA] modified MWCNTs (**D-F**$_{(5/10)}$) defined in table 4.6.

As the LA polymerised by RAFT was carried out at higher temperatures, there is a greater degree of branching in the P[LA] synthesised by this method. The highly branched structure could prevent the P[LA] from adsorbing as effectively compared to the more linear P[LA] synthesised by Cu(0)-methods.[37]

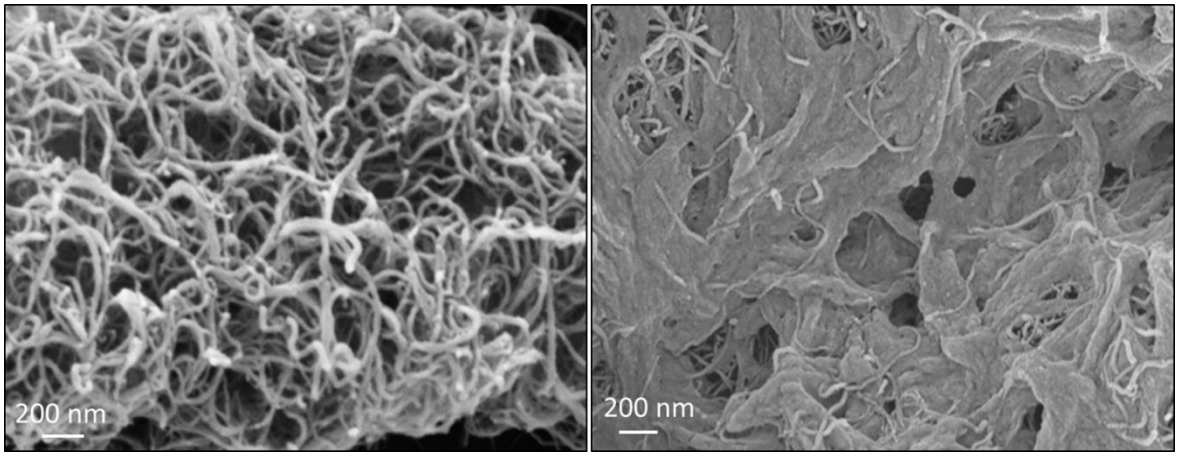

Figure 4.30 SEM micrographs of a) un-functionalised MWCNTs at a magnification 100k and b) P[LA] functionalised MWCNTs (**E_{10}**) x 100k.

Figure 4.30 shows the SEM micrographs of MWCNTs before and after functionalisation with P[LA]. As seen previously, figure 4.30 a) shows the highly entangled network of MWCNTs within a agglomerate. Upon addition of P[LA] to MWCNTs *via* solution mixing, the P[LA] is able to coat the MWCNTs and disentanglement of some MWCNTs can be observed. However, the image also shows the P[LA] is only able to coat the surface of the agglomerate and not disentangle the agglomerate itself. Even though P[LA] is able to non-covalently adsorb onto the surface of the MWCNT agglomerate, it is not however able to disentangle the agglomerate itself. Clearly, ultrasonication and solution mixing is not powerful enough to disentangle the MWCNT agglomerate. The project subsequently focused on using high shear twin screw extrusion to disperse the agglomerate and quantify the effect of P[LA] addition on MWCNT dispersion within a PP matrix.

Prior to producing blends of PP, P[LA] and MWCNTs, the effect of P[LA] on the surface of MWCNTs was analysed using DSC. MWCNTs were blended with P[LA] with a 1:4 ratio of MWCNTs to P[LA]. A ratio of 1:4 was chosen as the MWCNTs have a very high aspect ratio and therefore, a high surface area (>2000 m^2 g^{-1}) and low density. In order to enable significant coverage of the MWCNTs, a significant quantity of P[LA] was required

however, excessive P[LA] will significantly alter the properties of PP itself and therefore a ratio of 1:4 was selected as a reasonable quantity to start the study.

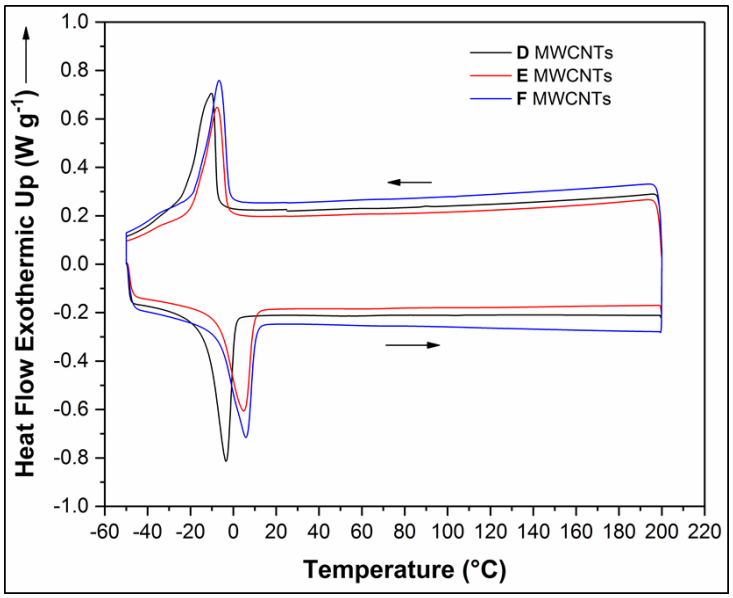

Figure 4.31 DSC traces of composites of P[LA] and MWCNTs.

Figure 4.31 shows the DSC traces of P[LA] (synthesised *via* Cu(0)-mediated LRP) blended with MWCNTs with a 1:4 ratio of MWCNTs to P[LA]. The DSC traces do not show a significant difference compared to P[LA] without MWCNTs (Figure 4.7) in terms of melting and crystallisation temperatures. The peaks appear to be broader suggesting the MWCNTs are disturbing the P[LA] crystallisation behaviour and therefore showing, the P[LA] is interacting with the MWCNTs.

Figure 4.32 shows the Raman spectroscopy of MWCNTs blended with P[LA] (synthesised *via* Cu(0)-mediated LRP) blended with MWCNTs in a 1:4 ratio of MWCNTs to P[LA]. The Raman spectra can be interpreted to establish if there is an interaction(s) between the P[LA] and the MWCNTs.

Table 4.7 lists the peak positions for the *D*, *G* and *G'* bands and, the full width at half height (FWHH) for each. The *D* bands shifted by ~3 cm^{-1} to higher wavenumbers after addition of P[LA]. The *G* band shifted by ~5 cm^{-1} and the *G'* also shifted to higher wavenumbers. It is challenging to determine the shift of the *G'* band as its peak is not as well defined as the *D* and *G* bands. Previously published results have demonstrated the upshifts in these bands associated with non-covalent functionalisation are as a result of stress acting on the interacting materials.[18, 38] In addition, table 4.8 lists the relative intensity ratios of the

bands and the relative gaps between the peaks. The (I_D / I_G) decreased by 0.1 on addition of P[LA] suggesting there is an interaction between the P[LA] and the MWCNTs. A decrease in relative intensity is also observed with the other bands.

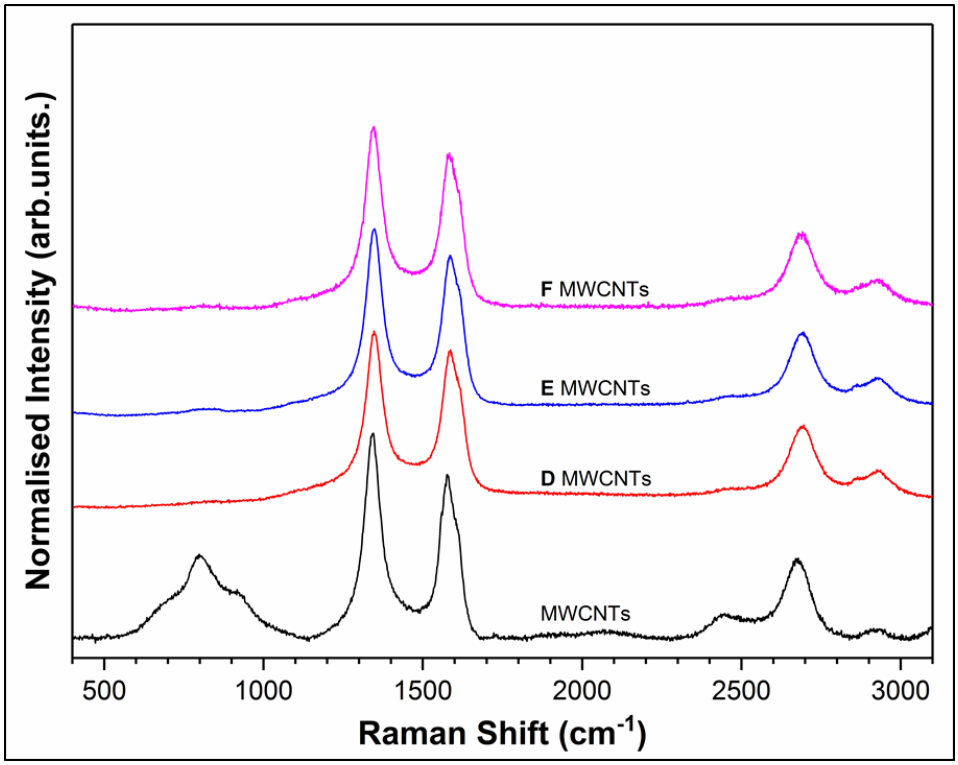

Figure 4.32 Raman spectra of composites of MWCNTs with homopolymers of P[LA].

Table 4.7 Raman properties of MWCNTs and composites of MWCNTs with homopolymers of P[LA].

Sample	D band peak (cm^{-1})	D band FWHH (cm^{-1})	G band peak (cm^{-1})	G band FWHH (cm^{-1})	G' band peak (cm^{-1})	G' band FWHH (cm^{-1})
MWCNTs	1344	63	1577	68	2674	101
D MWCNTs	1347	67	1583	76	2689	99
E MWCNTs	1347	63	1582	74	2690	105
F MWCNTs	1345	63	1583	74	2686	102

Table 4.8 Raman properties of MWCNTs and composites of MWCNTs with homopolymers of P[LA].

Sample	I_D / I_G	I_D / $I_{G'}$	$I_{G'}$ / I_G	G minus D (cm^{-1})	G' minus D (cm^{-1})	G' minus G (cm^{-1})
MWCNTs	1.26	2.71	2.16	232.0	1332.8	1100.8
D MWCNTs	1.13	2.35	2.08	236.8	1342.1	1105.3
E MWCNTs	1.18	2.49	2.11	235.2	1343.5	1108.4
F MWCNTs	1.17	2.40	2.05	238.5	1341.0	1102.6

Figure 4.33 a) and b) show the uncoated MWCNTs at different magnifications, the entangled tube structure and multi-walled morphology can be observed. P[LA] chains adsorbed onto the surface of MWCNTs can be seen due to the difference in phase contrast surrounding the MWCNTs in figure 4.33 c) and d). The red lines (figure 4.33d) indicate the outer and inner walls of the MWCNTs and help to show the presence of P[LA] radiating from the outer wall of the MWCNT. From the evidence presented, it is clear that P[LA] coats the MWCNTs through a combination of physical wrapping and CH-π interaction.

P[LA](**D**) modified MWCNTs were melt mixed with iPP in an extruder (5 mins at 80 rpm and 165 °C) and the thermally stability of the ternary composites prepared determined from the respective TGA and DTA curves, see figure 4.34. Interestingly, the thermal stability of iPP was increased on addition of MWCNTs alone, but that of P[LA](**D**) was unchanged. However, when all three components were melt mixed the thermal stability (below 460 °C) was intermediate between neat iPP and P[LA](**D**). Most importantly, the P[LA] component was thermally stable both during the extrusion cycle and via TGA post melt mixing.

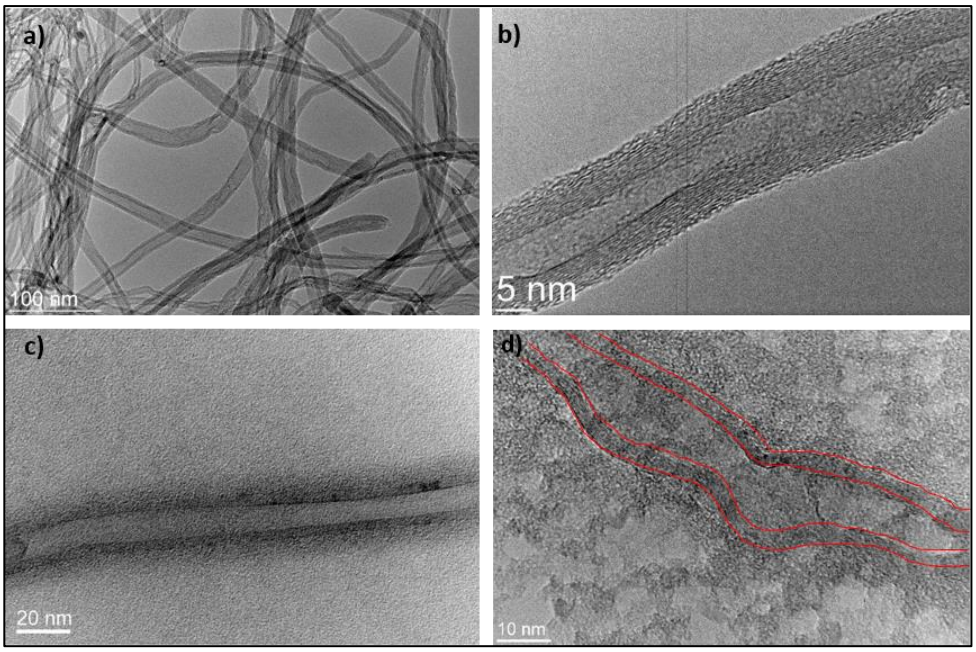

Figure 4.33 HRTEM images of (a) un-functionalised MWCNTs at 50k × magnification; (b) un-functionalised MWCNTs at 400k × magnification; (c) MWCNTs functionalised with P[LA] at 150k × magnification; (d) MWCNTs functionalised with P[LA] with red line to show inner and outer walls at 300k × magnification. (P[LA] (**B**) polymerised via Cu(0)-mediated polymerisation).

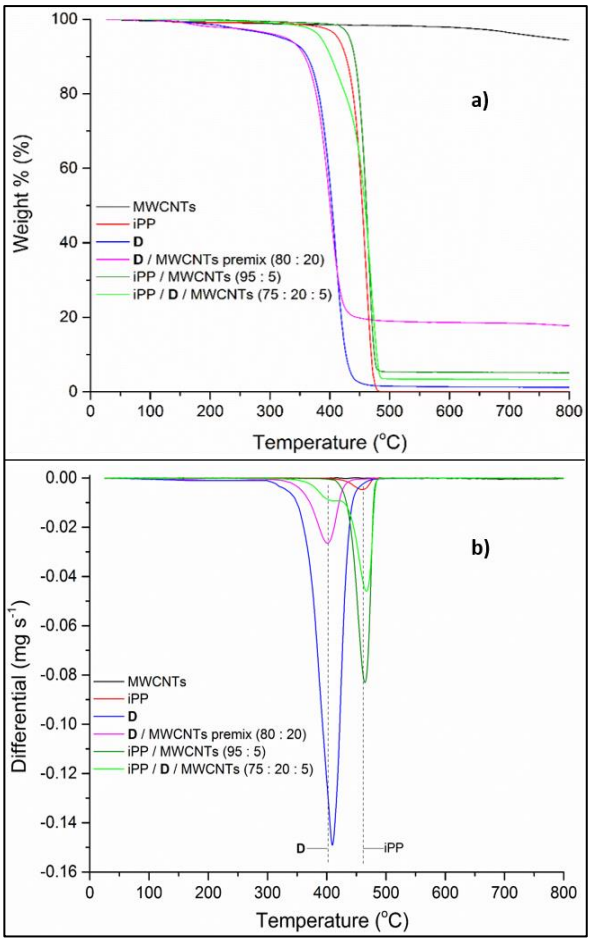

Figure 4.34 (a) TGA weight loss curves of MWCNTs premixed with P[LA] and melt mixed with iPP at 165 °C (b) DTA curves of MWCNTs premixed with P[LA] and melt mixed with PP at 165 °C. P[LA] (**D**) defined in table 4.2.

4.7 Characterisation of Poly(propylene)

After establishing the thermal stability of P[LA] synthesised by RAFT and Cu(0)-mediated methods were sufficient to enable their use as a compatibiliser, via a route of non-covalent functionalization, for MWCNTs and PP, the subsequent investigation was to produce and characterise composites of P[LA]-functionalised MWCNTs and PP.

The process of producing the PP based composites involved cryo-milling the PP pellets into a fine power to improve mixing between the PP and the P[LA] functionalised MWCNTs. The process of cryo-milling the PP was shown not to degrade the polymer, see figure 4.35. The SEC trace shows a significant change in molar mass distribution, before and after cryo-milling. The dispersity, $Đ$, increases considerably from 19.7 to 31.9 however the weight average molecular weight, M_w, is unchanged. This result can be explained by a large

increase in very small PP chains causing the distribution to widen however, the quantity of high molecular weight chains remains unchanged.

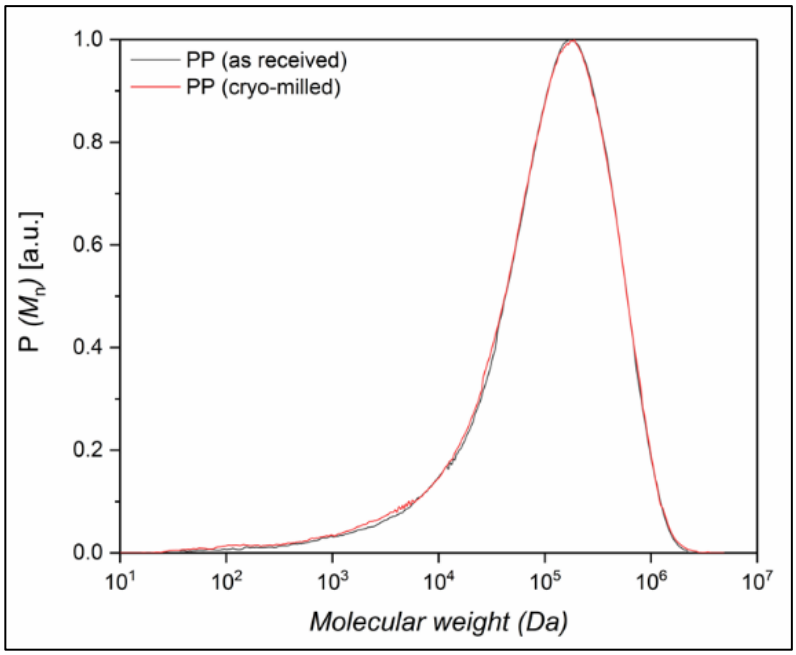

Figure 4.35 SEC traces of PP before (as received) and after cryo-milling.

Table 4.9 lists the molar masses of the as received PP and the cryo-milled PP. M_n quantifies the number average molar mass of PP. This is the total mass of all of the polymer molecules divided by the total number of molecules in the sample. Values of 11,000 g mol^{-1} before milling and 6,800 g mol^{-1} after milling suggested degradation of the polymer. However, PP is expected to have a considerably higher molar mass (>100,000 g mol^{-1}) suggesting that M_n is not accurately able to quantify the molar mass of the polymer. The reasoning is the polymer has an extremely wide polydispersity ($Đ$) which increases after milling. The milling process causes small amounts of chain scission which will decrease M_n and widen the dispersity. The low M_n is as a result of a large number of chains with low molar mass and a small number of chains with large molar mass. The M_n calculation gives significant weighting to the low molar mass chains and hence produces a low value for M_n which is not representative of the higher molar mass chains. Therefore, an alternative calculation is required.

Table 4.9 SEC analysis of isotactic PP before and after cryo-milling.

Nomenclature	$M_{n,\,GPC}$ [a] [g mol^{-1}]	$M_{w,\,GPC}$ [a] [g mol^{-1}]	$Đ$ [a]
PP (as received)	11,000	216,000	19.7
PP (cryo-milled)	6,800	215,000	31.9

[a] 1,2,4-Trichlorobenzene SEC analysis *via* RI detection using linear poly(styrene) standards.

M_w is the weight average molar mass. M_w gives greater weighting to the fewer higher molecular weight chains. Hence the M_w shows no significant change after cryo-milling confirming that cryo-milling does not affect the PP. Cryo-milling does however, produce a greater number of smaller molar mass chains but, they are not expected to significantly alter the processing properties of PP as the number of higher molecular weight chains are relatively unaffected and, they dominate the material properties. In addition, the calibration standards used, poly(styrene), behave differently compared to PP in solution and therefore, the molar masses cannot be accurately confirmed.

4.8 Conclusions

In summary, the thermal and thermo-mechanical stability of poly(lauryl acrylate) (P[LA]) synthesised using RAFT and Cu(0)-mediated LRP with and without aromatic initiators including, Hostasol and pyrene was determined. Its potential for MWCNT functionalisation and subsequent use in polymer processing with iPP was investigated. P[LA] of various molar masses were prepared *via* reversible addition-fragmentation chain transfer (RAFT) polymerisation and Cu(0)-mediated living radical polymerisation (Cu(0)-mediated LRP). P[LA] was prepared with the aim of non-covalent functionalisation of MWCNTs *via* solution mixing and the functionalisation strategy of CH-π and polymer wrapping. The purpose of the functionalisation was to improve dispersion and interfacial adhesion of MWCNTs with polymers such as isotactic poly(propylene) (PP).[11] Lauryl acrylate (LA) was polymerised using RAFT to a high conversion (95%) and furnished polymers in good agreement with theoretical M_n with dispersity increasing with increasing M_n. LA was polymerised using Cu(0)-mediated LRP to a high conversion (>98%), produced polymers in good agreement with theoretical M_n and low dispersity ($Đ \approx 1.2$) for lower molar

mass polymers. Low molar mass tailing was observed for P[LA] *via* Cu(0)-mediated polymerisation for higher molar masses polymers.[11] Thermo-gravimetric analysis (TGA) of P[LA] *via* RAFT showed onset of degradation occurred at ~340-350 °C however, this decreased to ~250-260 °C for lower molar mass polymers. TGA of the RAFT agent revealed an onset of degradation of ~200-250 °C. Free radicals generated from the thermal degradation of end groups did not influence the thermal stability of the P[LA] backbone and 'unzipping' commonly seen with methacrylates was not observed. TGA of P[LA] using Cu(0)-mediated LRP revealed similar degradation to that of P[LA] using RAFT. The thermal stability of P[LA] is sufficient for melt processing with PP.[11] TGA analysis of Hostasol and pyrene end-functionalised P[LA] revealed they are not thermally stable enough (> 200 °C) to be used to functionalise MWCNTs in an extruder with PP. P[LA] *via* RAFT was solution mixed with MWCNTs and showed an adoption of ~10-25 wt% P[LA] onto the surface of the MWCNTs. The onset of thermal degradation of the P[LA] remained unchanged after the adsorption on to the surface of the MWCNTs. P[LA] *via* the Cu(0)-mediated method adsorbed up to 85 wt% P[LA] and an increase in thermal stability of ~50 °C of the P[LA] was recorded. Increasing P[LA] and MWCNT concentration independently also resulted in an increase in the quantity of adsorption, possibly due to increased CH-π interactions. The increased thermal stability of the P[LA] after adsorbing onto the surface of MWCNTs could possibly be due to heat transfer from the P[LA] to the MWCNTs, resulting in delayed pyrolysis of P[LA]. Evidence from transmission electron micrographs (TEM) showed the P[LA] adsorbing onto the MWCNT surface.[11] Size exclusion chromatography (SEC) and matrix-assisted laser desorption/ionization time of flight mass spectrometry (MALDI-TOF) of P[LA] after heating to 200 °C for 30 mins in an air atmosphere showed loss of end groups but, the P[LA] backbone remained preserved for both polymer types. Evidence from transmission electron microscopy micrographs (TEM) show the P[LA] adsorbing onto the MWCNT surface. Melt processing of composites of P[LA] *via* Cu(0)-mediated LRP with MWCNTs and PP was possible as the P[LA] was thermally stable during both the extrusion and in the TGA when studies post melt mixing.[11] MWCNTs were characterised using electron microscopy, Raman spectroscopy and XPS. Characterisation revealed the tubes have diameters ranging from 5-20 nm and the number of walls in the region of 10-20. XPS reveals presence of 2 At% oxygen and Raman revealed a high intensity D band, possible due to presence of oxidised amorphous carbon.

The interactions between P[LA] and MWCNTs were characterised using SEM, TEM, DSC, and Raman which all revealed the presence of an interaction. Further investigations on the effect of functionalisation of P[LA] on the surface of MWCNTs were carried out by producing composites of PP, MWCNTs and P[LA] with various MWCNT concentrations and MWCNT to P[LA] ratios. The hypothesis is to investigate the wrapping of P[LA] on MWCNTs during a post extrusion and study if the wrapping of P[LA] leads to an improvement in mechanical, electrical and rheological properties of the composite compared to without the addition of P[LA]. Subsequently, the use of various fillers (e.g. GNPs) or poly(acrylate) architectures (e.g. block copolymers) and monomers will be investigated.

4.9 References

1. W. A. Braunecker and K. Matyjaszewski, *Prog. Polym. Sci.*, 2007, **32**, 93-146.
2. R. T. A. Mayadunne, E. Rizzardo, J. Chiefari, Y. K. Chong, G. Moad and S. H. Thang, *Macromolecules*, 1999, **32**, 6977-6980.
3. D. J. Keddie, *Chem. Soc. Rev.*, 2014, **43**, 496-505.
4. G. Moad, E. Rizzardo and S. H. Thang, *Aust. J. Chem.*, 2009, **62**, 1402-1472.
5. S. Perrier and P. Takolpuckdee, *J. Polym. Sci. Part A: Polym. Chem.*, 2005, **43**, 5347-5393.
6. A. Anastasaki, V. Nikolaou and D. M. Haddleton, *Polym. Chem.*, 2016, **7**, 1002-1026.
7. Q. Zhang, P. Wilson, Z. D. Li, R. McHale, J. Godfrey, A. Anastasaki, C. Waldron and D. M. Haddleton, *J. Am. Chem. Soc.*, 2013, **135**, 7355-7363.
8. B. M. Rosen and V. Percec, *Chem. Rev.*, 2009, **109**, 5069-5119.
9. O. Altintas, T. Josse, M. Abbasi, J. De Winter, V. Trouillet, P. Gerbaux, M. Wilhelm and C. Barner-Kowollik, *Polym. Chem.*, 2015, **6**, 2854-2868.
10. O. Altintas, T. Josse, J. De Winter, N. M. Matsumoto, P. Gerbaux, M. Wilhelm and C. Barner-Kowollik, *Polym. Chem.*, 2015, **6**, 6931-6935.
11. J. Gupta, D. J. Keddie, C. Y. Wan, D. M. Haddleton and T. McNally, *Polym. Chem.*, 2016, **7**, 3884-3896.
12. A. Anastasaki, V. Nikolaou, A. Simula, J. Godfrey, M. X. Li, G. Nurumbetov, P. Wilson and D. M. Haddleton, *Macromolecules*, 2014, **47**, 3852-3859.

13. C. Waldron, A. Anastasaki, R. McHale, P. Wilson, Z. D. Li, T. Smith and D. M. Haddleton, *Polym. Chem.*, 2014, **5**, 892-898.
14. B. Chong, G. Moad, E. Rizzardo, M. Skidmore and S. H. Thang, *Aust. J. Chem.*, 2006, **59**, 755-762.
15. A. Postma, T. P. Davis, G. Moad and M. S. O'Shea, *Macromolecules*, 2005, **38**, 5371-5374.
16. O. Altintas, K. Riazi, R. Lee, C. Y. Lin, M. L. Coote, M. Wilhelm and C. Barner-Kowollik, *Macromolecules*, 2013, **46**, 8079-8091.
17. O. Altintas, M. Abbasi, K. Riazi, A. S. Goldmann, N. Dingenouts, M. Wilhelm and C. Barner-Kowollik, *Polym. Chem.*, 2014, **5**, 5009-5019.
18. T. Fujigaya and N. Nakashima, *Sci. Tech. Adv. Mater.*, 2015, **16**, 1-21.
19. J. H. Du, J. Bai and H. M. Cheng, *Express Polym. Lett.*, 2007, **1**, 253-273.
20. Y. L. Zhao and J. F. Stoddart, *Acc. Chem. Res.*, 2009, **42**, 1161-1171.
21. S. W. Kim, T. Kim, Y. S. Kim, H. S. Choi, H. J. Lim, S. J. Yang and C. R. Park, *Carbon*, 2012, **50**, 3-33.
22. A. Anastasaki, C. Waldron, V. Nikolaou, P. Wilson, R. McHale, T. Smith and D. M. Haddleton, *Polym. Chem.*, 2013, **4**, 4113-4119.
23. J. Y. T. Chong, D. J. Keddie, A. Postma, X. Mulet, B. J. Boyd and C. J. Drummond, *Colloids Surf., A*, 2015, **470**, 60-69.
24. J. D. Moskowitz and J. S. Wiggins, *Polym. Degrad. Stab.*, 2016, **125**, 76-86.
25. A. E. Daugaard, K. Jankova and S. Hvilsted, *Polymer*, 2014, **55**, 481-487.
26. G. Moad, G. Li, R. Pfaendner, A. Postma, E. Rizzardo, S. Thang and H. Wermter, in *Controlled/Living Radical Polymerization*, ed. K. Matyjaszewski, American Chemical Society, 2006, vol. 944, ch. 35, pp. 514-532.
27. J. Y. T. Chong, X. Mulet, A. Postma, D. J. Keddie, L. J. Waddington, B. J. Boyd and C. J. Drummond, *Soft Matter*, 2014, **10**, 6666-6676.
28. D. J. Keddie, G. Moad, E. Rizzardo and S. H. Thang, *Macromolecules*, 2012, **45**, 5321-5342.
29. Y. K. Chong, G. Moad, E. Rizzardo and S. H. Thang, *Macromolecules*, 2007, **40**, 4446-4455.
30. D. J. Keddie, C. Guerrero-Sanchez, G. Moad, R. J. Mulder, E. Rizzardo and S. H. Thang, *Macromolecules*, 2012, **45**, 4205-4215.
31. K. L. Chen, Y. H. Zhao and X. Y. Yuan, *Chem. Res. Chin. Univ.*, 2014, **30**, 339-342.

32. M. Ciampolini and N. Nardi, *Inorg. Chem.*, 1966, **5**, 41-44.
33. H. Willcock and R. K. O'Reilly, *Polym. Chem.*, 2010, **1**, 149-157.
34. J. Clayden, N. Greeves, S. Warren and P. Wothers, in *Organic Chemistry*, ed. J. Clayden, Oxford University Press, Oxford, UK, 1st edn., 2001, ch. 38, pp. 1013-1014.
35. C. M. White, R. Banks, I. Hamerton and J. F. Watts, *Prog. Org. Coat.*, 2016, **90**, 44-53.
36. B. Krause, M. Mende, P. Pötschke and G. Petzold, *Carbon*, 2010, **48**, 2746-2754.
37. M. Gaborieau, S. P. S. Koo, P. Castignolles, T. Junkers and C. Barner-Kowollik, *Macromolecules*, 2010, **43**, 5492-5495.
38. M. S. Dresselhaus, G. Dresselhaus, R. Saito and A. Jorio, *Phys. Rep.*, 2005, **409**, 47-99.

Chapter 5 Results and Discussion II

Plasticisation and compatibilisation of poly(propylene) with poly(lauryl acrylate) surface modified MWCNTs

5.1 Introduction

CNT surface functionalisation is essential to overcome van der Waals interactions between neighbouring CNTs and subsequently improve dispersion and prevent re-agglomeration.[1] Many papers have focused on preparation and properties of composites of PP and MWCNTs through simple melt compounding or solution mixing of PP and unmodified MWCNTs.[2-13] Although the properties of the PP could be improved through these methods, the MWCNT content could be reduced to achieve similar efficiencies by improving the level of dispersion with functionalised MWCNTs.

Chapter 4 established that poly(lauryl acrylate) P[LA] synthesised using reversible deactivation radical polymerisation (RDRP) techniques is thermally stable that it can be melt mixed at the relevant processing conditions for PP. By way of example, P[LA] was selected based upon its known good compatibility with PP and because its hydrophobic chains are known to be able to co-crystallise with PP.[14] P[LA] was shown to adsorb onto the surface of MWCNTs (chapter 4) via a combination of hydrophobic interactions and possible CH-π wrapping interactions. TGA, SEM, TEM and Raman were used to characterise the CH-π wrapping of the P[LA] on the surface of the MWCNTs. As a result, this chapter reports the preparation via melt-blending and the characterisation of composites of PP with MWCNTs functionalised with P[LA] synthesised using Cu(0)-mediated polymerisation. Various loadings of MWCNTs and different MWCNTs:P[LA] ratios were used to understand how the properties of the composites change accordingly. It is proposed that the addition of P[LA] modified MWCNTs to PP will produce a nanocomposite with improved mechanical, electrical and thermal properties relative to unfilled PP and MWCNT filled PP. The mechanical and rheological properties and crystallisation behaviour of these composites were characterised to assess the role of P[LA] in plasticising and compatibilising PP and MWCNTs.

In chapter 2 it was described how poor dispersion and weak interfacial adhesion prevents significant improvement in properties of polymer/CNT composites and therefore, my hypothesis is that the use of P[LA] to pre-functionalise MWCNTs *via* CH-π wrapping

on the MWCNTs will overcome such limitations. Due to the non-polar chemical structure of PP chains, the use of P[LA] wrapping on the CNT surface is expected to provide efficient interfacial adhesion and improve CNT dispersion.[15] CNTs possess strong attractive interactions between themselves causing the formation of agglomerates, bundles, 'ropes' and yarns.[16, 17] Homogenous dispersion requires breaking the strong van der Waals interactions between neighbouring tubes. To increase the surface area of the CNTs and form a network structure, good compatibility between the MWCNTs and the PP matrix is required. P[LA] will be used to 'coat' the surface of the MWCNTs, prevent van der Waals interactions between neighbouring CNTs and improve compatibility with the PP matrix leading to formation of an interconnected network structure at low MWCNT loadings.

5.1.1 Synthesis and characterisation of P[LA]

P[LA] was produced in bulk using the Cu(0)-mediated LRP technique. TGA results in chapter 4 demonstrated the presence of non-covalent CH-π adsorption between P[LA] and MWCNTs, by way of increase in onset of the thermal degradation temperature of P[LA] by ~ 50 °C. The increase was only detected for P[LA] synthesised *via* Cu(0)-mediated LRP and not for P[LA] synthesised *via* RAFT. In addition, the use of RAFT requires the synthesis of a CTA agent, which is more challenging and costly to prepare, compared to the synthesis of Me_6TREN which is relatively straightforward.

LA was polymerised using the identical procedure as described in scheme 4.3. Table 5.1 lists the conversion and molecular weight data of the P[LA] used for the melt mixing with MWCNTs and PP. The density of P[LA] was measured to be 0.9 g cm^{-3}. The polymerisation proceeded with good conversion (~95%) and low dispersity ($Đ$ = 1.15).

Table 5.1 Theoretical and experimental data for the preparation of bulk P[LA] *via* Cu(0)-mediated LRP process and the associated conversion, number average molar masses and dispersity.

Nomenclature	[LA]/[I]	Conv.[a] [%]	$M_{n,\,th}$ [g mol^{-1}]	$M_{n,\,GPC}$ [b] [g mol^{-1}]	$Đ$ [b]
P[LA] bulk	42	95	10 100	11 500	1.15

[a] ^{1}H NMR. [b] $CHCl_3$ SEC analysis *via* RI detection using linear PMMA standards.

Figure 5.1 shows the SEC trace for bulk P[LA]. The SEC trace shows low molar mass tailing however, the dispersity, $Đ$, of 1.15 is good and the measured number average molar mass, $M_{n,\,GPC}$, of 11,500 g mol^{-1} is reasonably close to the theoretical number average molar mass, $M_{n,\,th}$, of 10,000 g mol^{-1} (Table 5.1). The differences in molar mass can be due to the use of PMMA standards for the linear calibration which have a significantly different hydrodynamic volume and behave differently in solution. A molar mass of ~10,000 g mol^{-1} was chosen as this lied in the central range for the molar masses of P[LA] analysed in chapter 4. The presence of ~5% unreacted LA monomer is considered to have a negligible effect on the processing of P[LA] with PP and MWCNTs.

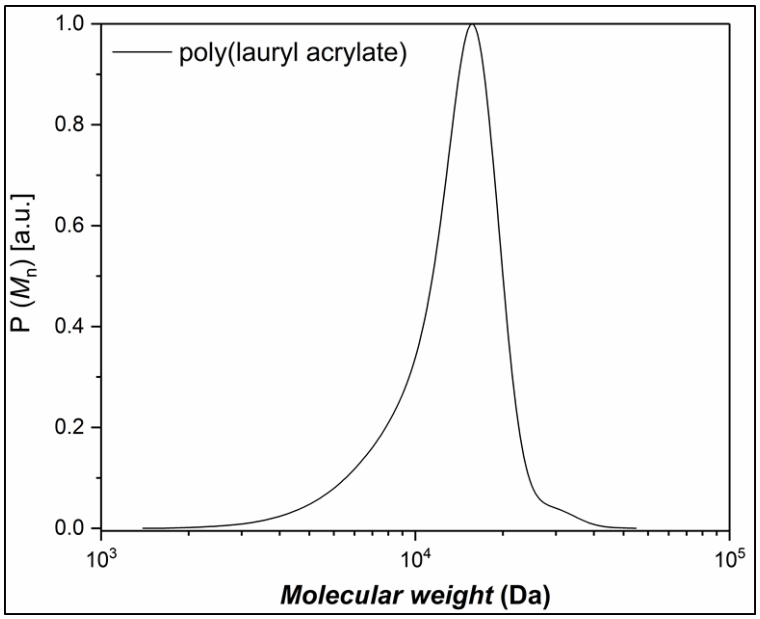

Figure 5.1 SEC traces of P[LA] bulk synthesised *via* Cu(0)-mediated LRP. P[LA] bulk defined in table 5.1.

5.1.2 Twin-screw melt compounding and injection moulding

Conical twin-screw melt compounding was used to prepare the composites (Appendix 11a). The instrument offers a short and well-defined dwell time. The micro-compounder is scaled down to a small size with compounding masses of ~8g ideal for material development. Larger extruders (>100 g) were not selected as they required the use of large quantities of MWCNTs/GNPs and P[LA] which were not available. Appendix 11a shows an image of the extruder used to produce the composites of PP, MWCNTs and P[LA].

The MWCNTs were firstly precisely weighed and pre-functionalised with P[LA]. The P[LA] was a high viscosity liquid at r.t and therefore, simple stirring in a beaker was used to produce a P[LA] functionalised MWCNT paste. Subsequently, the cryo-milled powdered PP was added and again stirred to ensure even coating of the P[LA] functionalised MWCNTs around the PP particles. The mixture was fed through the hopper and the co-rotating screws used to compound the mixture and the mixture was then recirculated. After 5 min. recirculation, the sample was ejected into the hot melt chamber of the injection moulding machine. The samples were subsequently injection moulded (Appendix 11b). It is important to consider the screw profile and how that affects the dispersion and agglomerate size.[18] Additionally, the screw speed and mixing time have to also be considered.[19] For this project, these parameters were fixed with the shallow screw profile, as shown in Appendix 11a. The screw speed was fixed at 100 rpm and residence time of 5 min. to allow sufficient mixing with minimal polymer degradation. Appendix 11b shows the injection moulding machine used to prepare the samples. A high pressure (>500 bar) gas powered piston is used to force the material into the moulds (Appendix 11c).

5.1.3 Sample identification and nomenclature

Table 5.2 lists the four sets of composites that were prepared and characterised. The first set involved blending the MWCNTs with PP with various MWCNT loadings to obtain a baseline for functionalisation. The second set examined the effect of adding P[LA] to PP without the presence of MWCNTs. The reasoning behind this is not all of the P[LA] will be 'bound' to the surface of the MWCNTs. A significant amount will be dispersed within the PP matrix and the effect of this is characterised. The amount of P[LA] added was identical for that of set three. The third set involved blending various loadings of P[LA] functionalised MWCNTs with PP with the ratio of P[LA] to MWCNTs kept constant at 4:1 P[LA]:MWCNTs. For example, the sample, 5 wt% CNT 4P[LA], has 5 wt% CNTs and 20 wt% P[LA]. The fourth set involved changing the ratio of P[LA] to MWCNTs to 1:1 P[LA]:MWCNTs.

Table 5.2 List of materials loadings used of PP, MWCNTs and P[LA] in the production of the composites.

Sample name (wt%)	Nomenclature[a]
PP (100)	PP
PP(99.99)/CNT(0.01)	0.01 wt% CNTs
PP(99.9)/CNT(0.1)	0.1 wt% CNTs
PP(99.7)/CNT(0.3)	0.3 wt% CNTs
PP(99.5)/CNT(0.5)	0.5 wt% CNTs
PP(99)/CNT(1)	1 wt% CNTs
PP(97)/CNT(3)	3 wt% CNTs
PP(95)/CNT(5)	5 wt% CNTs
PP(99.96)/P[LA](0.04)	0.04 wt% P[LA]
PP(99.6)/P[LA](0.4)	0.4 wt% P[LA]
PP(98.8)/P[LA](1.2)	1.2 wt% P[LA]
PP(98)/P[LA](2)	2 wt% P[LA]
PP(96)/P[LA](4)	4 wt% P[LA]
PP(88)/P[LA](12)	12 wt% P[LA]
PP(80)/P[LA](20)	20 wt% P[LA]
PP(99.95)/CNT(0.01)/P[LA](0.04)	0.01 wt% CNT 4P[LA]
PP(99.5)/CNT(0.1)/P[LA](0.4)	0.1 wt% CNT 4P[LA]
PP(98.5)/CNT(0.3)/P[LA](1.2)	0.3 wt% CNT 4P[LA]
PP(97.5)/CNT(0.5)/P[LA](2)	0.5 wt% CNT 4P[LA]
PP(95)/CNT(1)/P[LA](4)	1 wt% CNT 4P[LA]
PP(85)/CNT(3)/P[LA](12)	3 wt% CNT 4P[LA]
PP(75)/CNT(5)/P[LA](20)	5 wt% CNT 4P[LA]
PP(99.98)/CNT(0.01)/P[LA](0.01)	0.01 wt% CNT 1P[LA]
PP(99.8)/CNT(0.1)/P[LA](0.1)	0.1 wt% CNT 1P[LA]
PP(99.4)/CNT(0.3)/P[LA](0.3)	0.3 wt% CNT 1P[LA]
PP(99)/CNT(0.5)/P[LA](0.5)	0.5 wt% CNT 1P[LA]
PP(98)/CNT(1)/P[LA](1)	1 wt% CNT 1P[LA]
PP(94)/CNT(3)/P[LA](3)	3 wt% CNT 1P[LA]
PP(90)/CNT(5)/P[LA](5)	5 wt% CNT 1P[LA]

[a] MWCNTs have been abbreviated to CNT(s).

The composites were extensively characterised using a range of techniques including electron microscopy, static and dynamic mechanical analysis, DSC, oscillatory rheology, WAXS and electrical conductivity.

5.2 Characterisation of composites of PP, MWCNTs and P[LA]

A combination of techniques addressing structural, thermal, dynamic and static mechanical and rheological properties were used to rigorously understand this P[LA] induced plasticisation of PP and compatibilisation behaviour between PP and MWCNTs which in turn provide a framework to describe the electrical properties of the composites obtained.

Melt mixing achieved a highly dispersed and interconnected network of MWCNTs in the PP matrix as shown in the representative SEM micrographs, figure 5.2 c) and d). From figure 5.2 c) and d) the MWCNTs are poorly dispersed though the presence of agglomerates (~20-50 μm). SEM is not able to give a representative description of the extent of MWCNT dispersion and therefore, it is difficult to quantitatively determine dispersion using microscopy. Nevertheless, it is obvious from the cryo-fracture surfaces that there is some degree of MWCNT pull-out. The MWCNTs are only partially embedded in the PP matrix confirming the interfacial interaction between the PP and MWCNTs is still relatively poor. Further imaging shows clusters of MWCNTs agglomerates with other regions showing little or no MWCNT presence concluding distribution is not homogenous and the MWCNTs require functionalisation to further increase dispersion and interfacial adhesion with the matrix. The SEM micrographs of cryo-fractured surfaces of neat PP at various magnifications are shown in figure 5.2 a) and b) for relative comparison.

Agglomerate size and distribution was reduced upon addition of P[LA] functionalised MWCNTs, for loadings of MWCNTs:P[LA] of 1:4, see SEM, figure 5.2 g) and h). The addition of P[LA] as a compatibiliser had no significant effect on the dispersion of the MWCNTs in an already poorly dispersed system. Figure 5.2 d) shows there are regions where the MWCNTs have not completely dispersed within the PP. Figure 5.2 e) and f) show the SEM micrographs of composites of PP and 4 wt% P[LA]. The morphology is similar to that of neat PP, see SEM, figure 5.2 a) and b), showing the P[LA] is compatible with the PP matrix. A lack of compatibility of the P[LA] with the PP would result in phase separation of the P[LA] and the observation of a non-continuous morphology. P[LA] was chosen for its good compatibility with PP because its long, hydrophobic chains have shown to be able to co-crystallise with the lamella of the PP.[20] Changes to the loading ratio between MWCNTs:P[LA] to 1:1 led to increased agglomerate size and reduced dispersion, see SEM, figure 5.2 i) and j) compared to figure 5.2 h). A greater number of regions where MWCNTs

have not completely dispersed were observed within PP compared to the composite of MWCNTs:P[LA] of 1:4 and unmodified MWCNTs. The presence of large clusters (outlined in red) were still visible but the pull-out effect seemed to be reduced. The reduced pull-out effect can be explained by the lower homogenous dispersion and hence lower numbers of MWCNTs in the cryo-fracture surface.

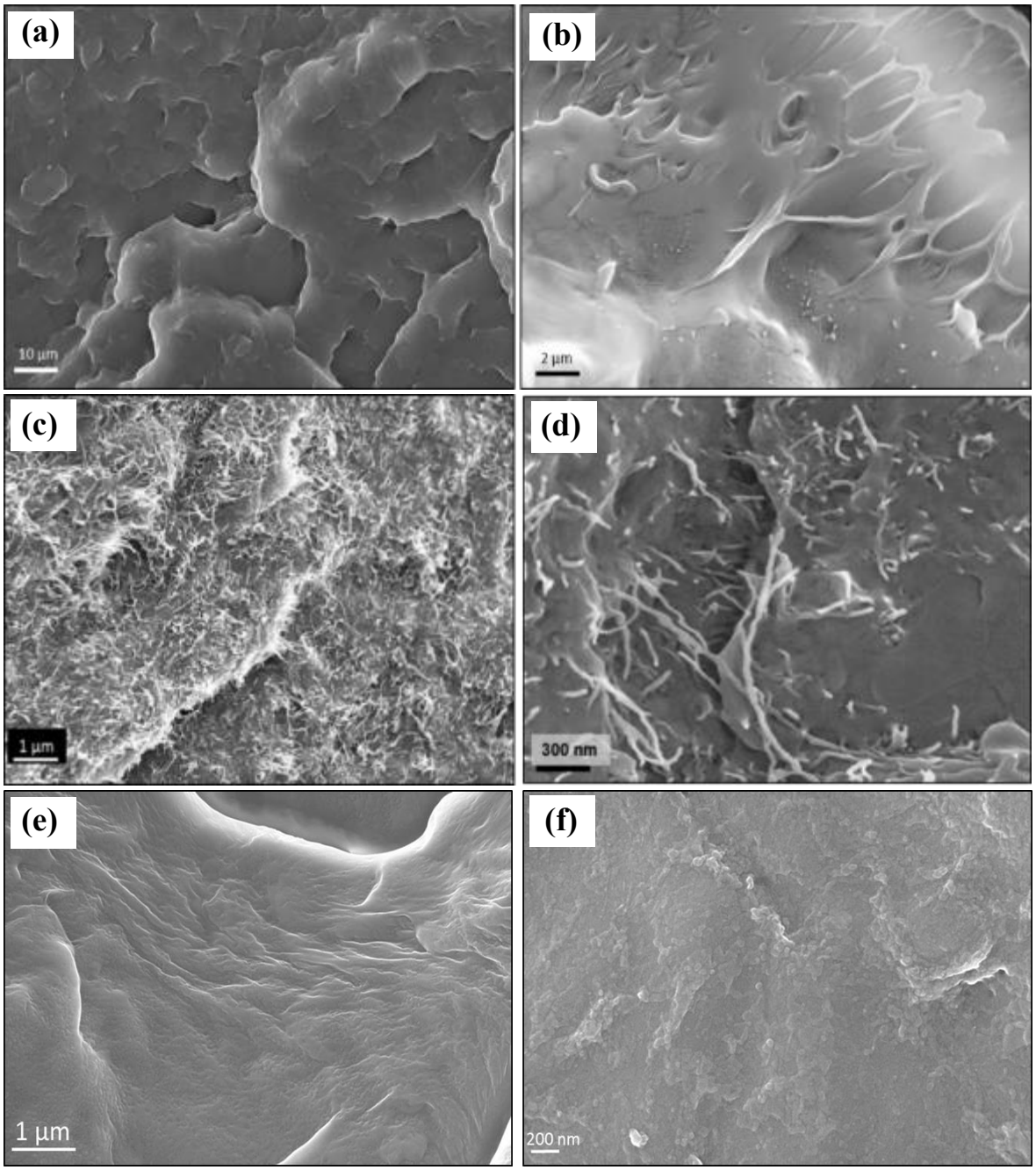

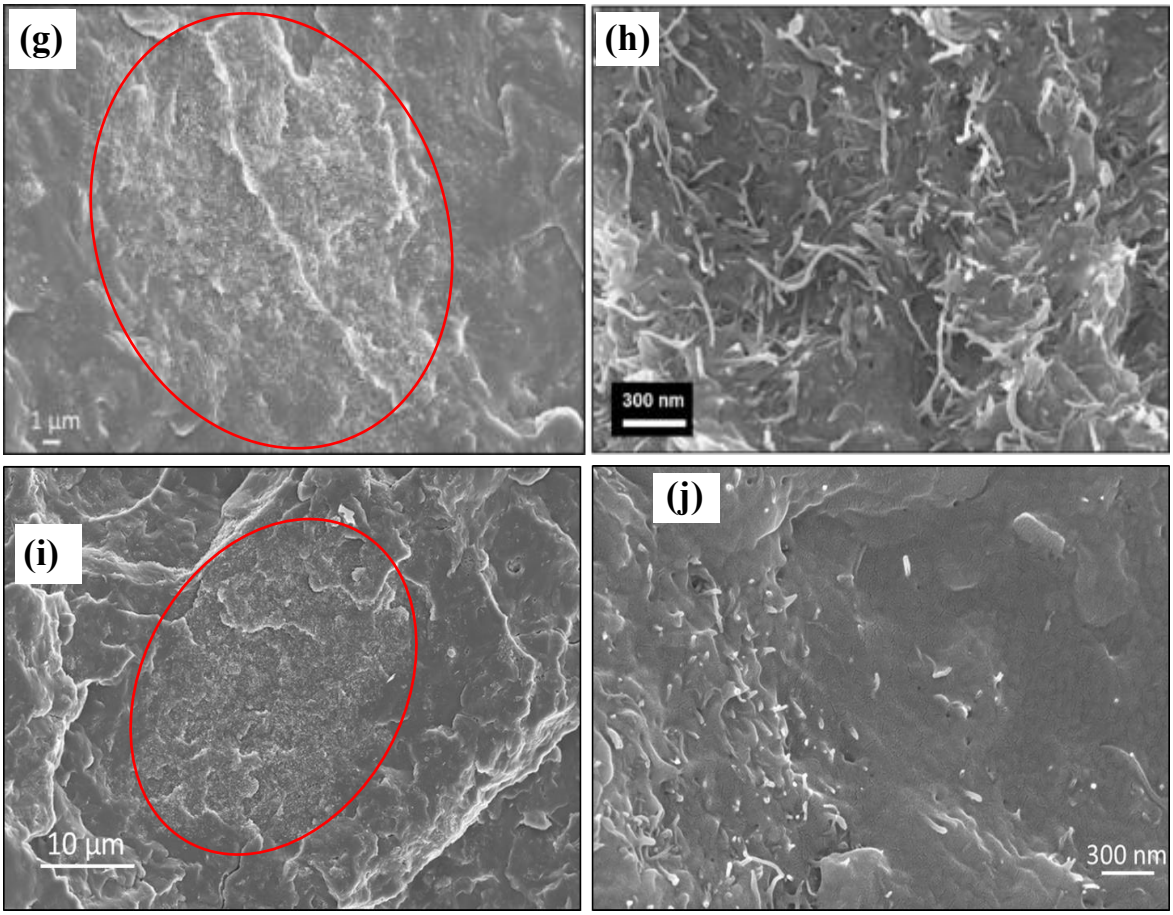

Figure 5.2 SEM micrographs of PP a) x 2k and b) x 12k, composites of PP and MWCNTs (1 wt% CNTs) c) x 25k and d) x 100k, composites of PP and P[LA] (4 wt% P[LA]) e) x 38k and f) x 80k, composites of PP and P[LA] functionalised MWCNTs (1 wt% CNT 4P[LA]) g) x 9k and h) x 110k, composites of PP and P[LA] functionalised MWCNTs (1 wt% CNT 1P[LA]) i) x 5k and j) x 90k magnification.

The reduced dispersion and increased agglomerate size for composites of PP and P[LA] modified MWCNTs with a ratio of MWCNTs:P[LA] of 1:1 relative to loadings of MWCNTs:P[LA] of 1:4 are attributed to the reduced quantity of P[LA] in blend.

In conclusion, the SEM images showed the micro-compounder was effective at achieving a poorly dispersed system of MWCNTs in the PP matrix producing an interconnected network. Agglomerates were reduced and relatively small showing the mixing parameters selected are suitable for the preparation of composites of this nature. Composites of PP and modified MWCNTs were poorly dispersed. CNT pull-out on the fracture surface was observed indicating weak interfacial adhesion between the MWCNTs and the PP. The addition of P[LA] in a ratio of 1:4 MWCNT:P[LA] further increased

dispersion and reduced agglomerate size and distribution. However, relatively weak interfacial adhesion remained with continued CNT pull-out and dispersion was not completely homogenous. A reduction in P[LA] loading to 1:1 MWCNTs:P[LA] reduced dispersion and increased agglomerate size relative to a P[LA] loading of 1:4 MWCNTs:P[LA] demonstrating that P[LA] is compatibilising the MWCNTs with PP. As expected, the P[LA] facilitates the separation of MWCNT bundles though CH-π wrapping via surface adsorption which prevents the van der Waals forces between the MWCNTs from agglomerating them together.

Further evidence for the increased dispersion, reduced agglomeration and the formation of interconnected networks was obtained using oscillatory rheology. In the first instance, a high degree of MWCNT dispersion throughout the PP matrix and conclusive evidence for a well-defined rheological percolation threshold at 0.5wt% was observed for composites of PP and unmodified MWCNTs (figure 5.3). An improved degree of dispersion and reduction of the rheological percolation threshold to 0.3wt% was observed upon addition of P[LA] functionalised MWCNTs at a ratio of 1:4 MWCNTs:P[LA] to the PP matrix (figure 5.5). The reduction in percolation threshold along with the SEM observations is further evidence that the addition of P[LA] leads to a more poorly dispersed system. Clearly the addition of P[LA] alters PP chain dynamics and interfacial interactions between the MWCNT filler and PP resulting in enhanced MWCNT dispersion, figure 5.2 h) and ultimately, this effects the viscoelastic properties of PP.

Since CNTs have an extremely high aspect ratio (length-to-diameter) up to 10^5, they have an ability to influence the rheological properties of polymer melts at very low loadings by hindering polymer chain dynamics. On MWCNT addition to polymers a dramatic increase in the storage modulus (G') and complex viscosity ($|\eta^*|$) as well as the detection of an apparent yield strength at low frequencies (< 1 rad/s) is typically observed. A 'pseudo-solid' like behaviour is observed upon formation of a percolated MWCNT network and the extent of filler dispersion, aspect ratio, and alignment can all be related to changes in (nano)composite viscoelasticity.[21]

In order to determine rheological percolation, oscillatory measurements were performed to indirectly assess the extent of MWCNT dispersion in the PP matrix and the effect of the addition of P[LA] modified MWCNTs on dispersion.[22] Dynamic frequency

sweeps with a sinusoidal stress, τ, is applied to the sample to explore the CNT network formation:

$$\tau(t) = \tau_0 \sin \omega t \tag{2}$$

where ω is the frequency at low amplitudes of strain, τ_0. The linear response of the material in terms of strain is:

$$\gamma_r = \gamma_0 \sin(\omega t + \delta) \tag{3}$$

where, δ is the phase angle or lag of the resultant strain wave. The G' is based on the amplitude of the 'in-phase strain' and the loss modulus (G'') on the 'out of phase strain'. The incorporation of these material functions resulting in the above equation becoming:

$$\gamma_r = G'(\omega)\sin(\omega t) + G''(\omega)\cos(\omega t) \tag{4}$$

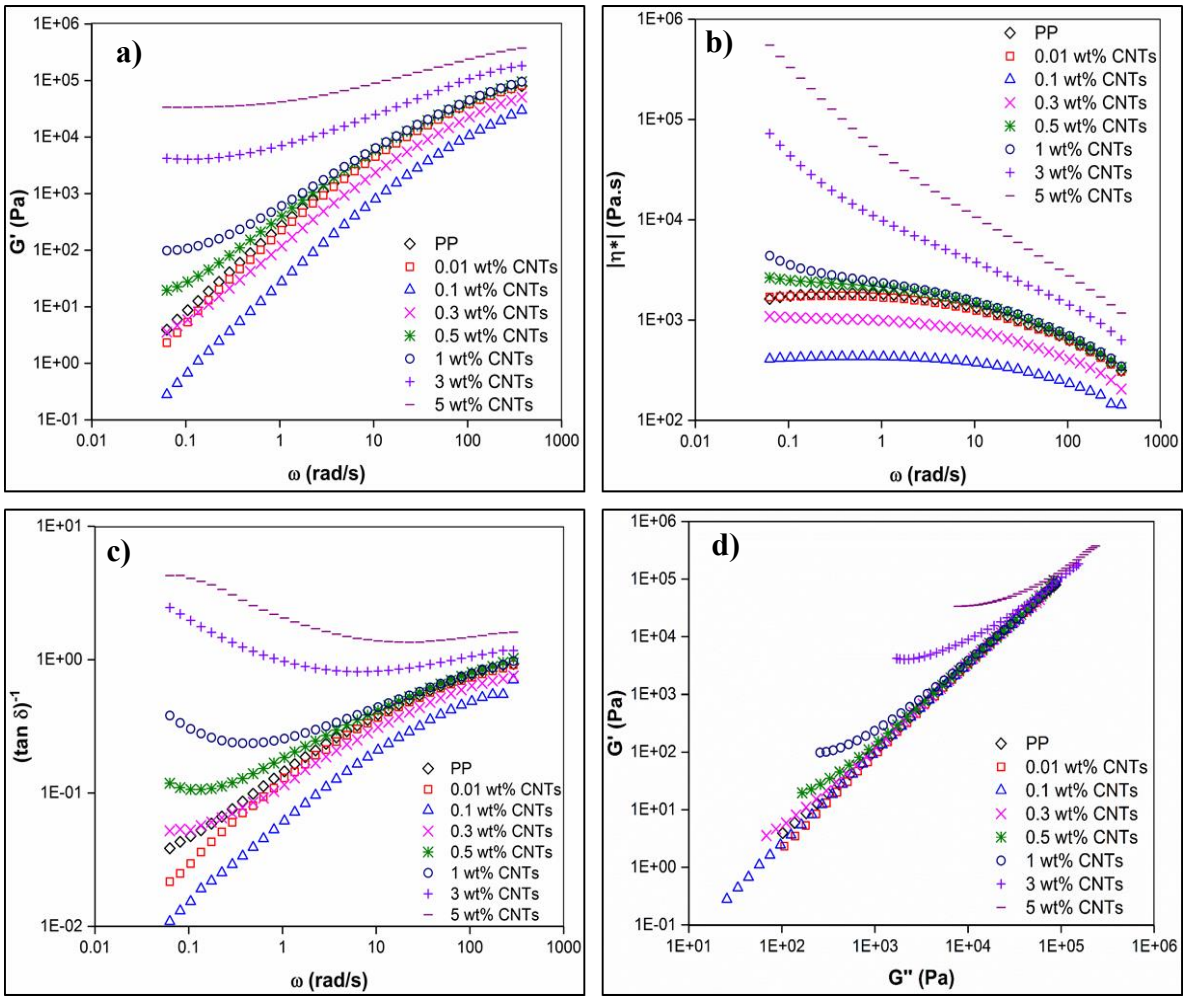

Figure 5.3 Variation in (a) storage modulus (G'), (b) complex viscosity $|\eta^*|$ and (c) reciprocal of loss tangent ($(\tan \delta)^{-1}$) as a function of angular frequency (ω) for unfilled PP and composites of PP and MWCNTs and (d) Cole-Cole plot (G' versus G'').

At low frequencies (e.g. ~ω = 0.1 rad/s) G', $|\eta^*|$ and tan δ^{-1} all increase with increasing MWCNT loading, G' by about 5 and $|\eta^*|$ by about 3 orders of magnitude on addition of 5 wt% MWCNTs, figures 5.3 a), b) and c). The formation of a plateau at low frequency for G' and the increase in $|\eta^*|$ and tan δ^{-1} as a function of frequency occurred at some MWCNT loading between 0.3wt% and 0.5wt%. A more accurate estimate for the rheological percolation can be obtained from constructing Cole-Cole (i.e. G' versus G''), see figure 5.3 d) and (η'' versus η'), see figure 5.4 a) and Van Gurp-Palmen (phase angle δ versus $|G^*|$) plots, see figure 5.4 d). The onset in the deviation from the linear relationship between G' and G'' and η'' and η' and the decrease in phase angle δ as a function of $|G^*|$ suggests the rheological percolation is closer to 0.5wt%. The MWCNTs are relatively well dispersed in the PP matrix and the PP relaxation times increase (see figure 5.4 a)) with increasing MWCNT loading as the MWCNTs hinder polymer chain mobility.

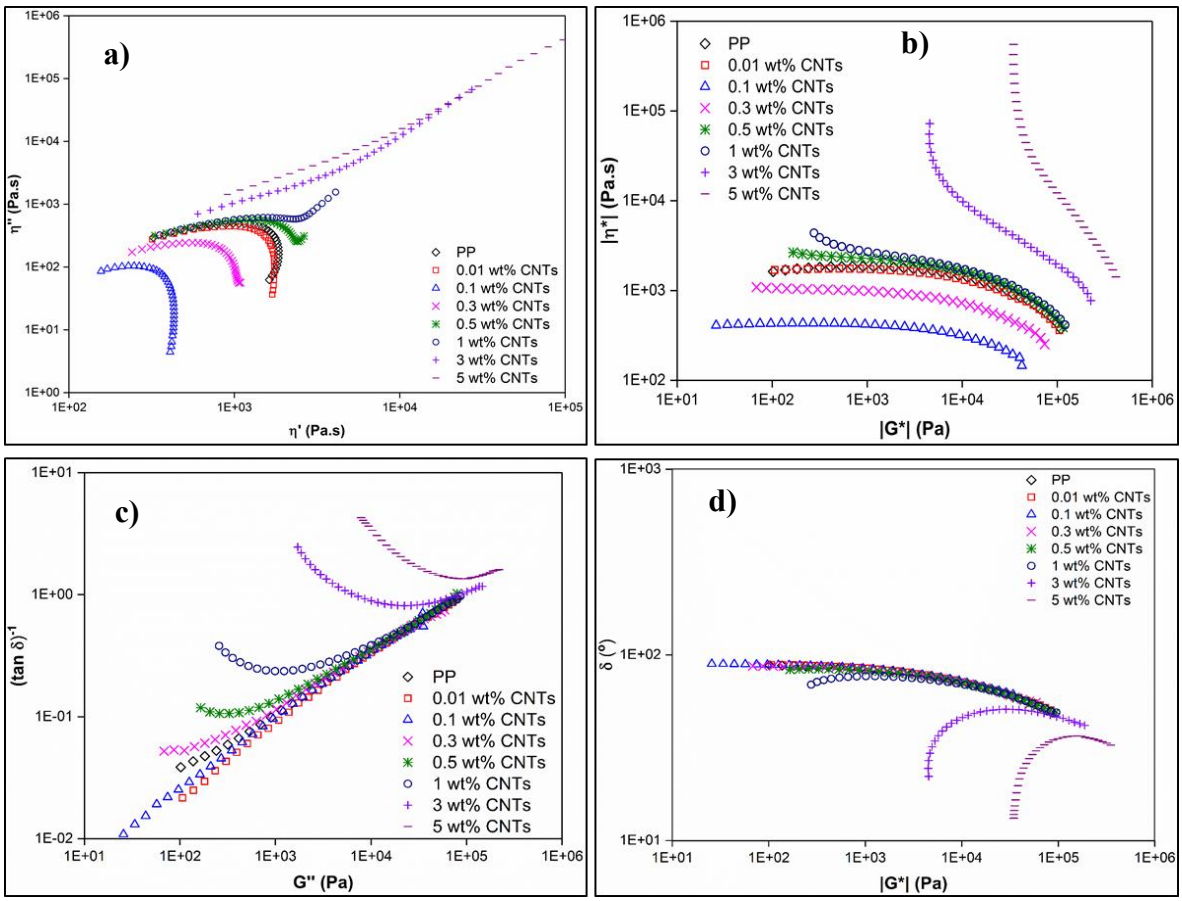

Figure 5.4 Variation in (a) imaginary viscosity (η'') with real viscosity (η'), (b) complex viscosity ($|\eta^*|$) with complex modulus ($|G^*|$), (c) $(\tan \delta)^{-1}$ with G'' and (d) phase angle (δ) with the absolute value of ($|G^*|$) (Van Gurp-Palmen plot) for unfilled PP and composites of PP and MWCNTs.

The effect of P[LA] addition on the viscoelastic response of PP and composites of PP and MWCNTs for a 1:4 ratio of MWCNTs:P[LA] and, rheological percolation can be seen in figure 5.5. From the plots of *G'*, $|\eta^*|$ and tan δ^{-1} as a function of frequency, the onset of rheological percolation is closer to 0.3 wt% MWCNTs, see figures 5.5 a), b) and c). Likewise, from the Cole-Cole (figure 5.5 d)) and Van Gurp-Palmen plots for the composites of PP with P[LA] modified MWCNTs, see figure 5.6 d), incorporation of P[LA] enhanced the MWCNT dispersion and distribution in the PP matrix resulting in a lower rheological percolation. Above percolation a large increase in $|\eta^*|$ was also observed, see figure 5.5 b). A reduced percolation threshold from ~0.5wt% to ~0.3wt% through network formation at lower loadings and enhanced dispersion for composites of PP and P[LA] modified MWCNTs relative to composites of PP and unmodified MWCNTs is in agreement with the observations made using SEM.

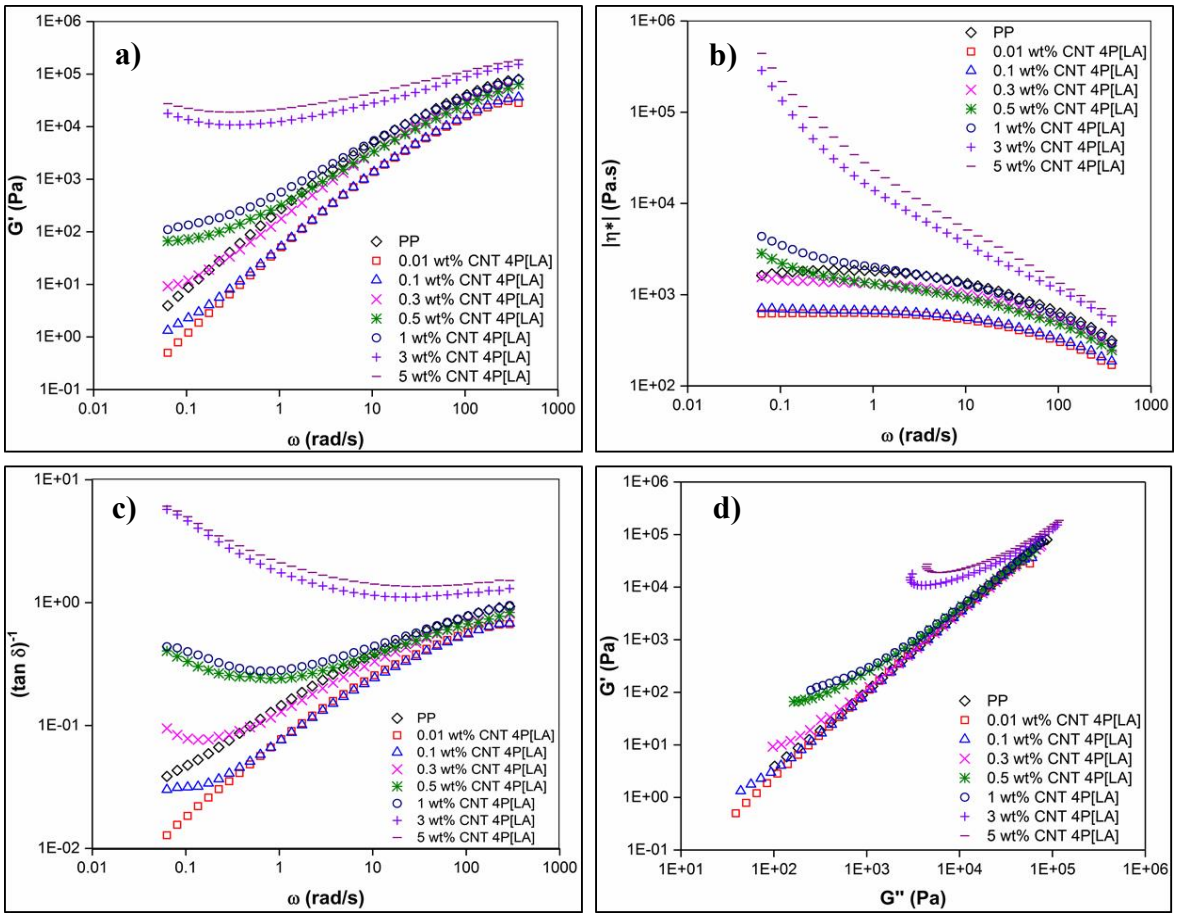

Figure 5.5 Variation in: (a) storage modulus (*G'*), (b) complex viscosity $|\eta^*|$ and (c) reciprocal of loss tangent ((tan $\delta)^{-1}$) as a function of angular frequency (ω) for unfilled PP and composites of PP and P[LA] modified MWCNTs (1:4 MWCNT:P[LA]); and (d) Cole-Cole plot (*G'* versus *G''*).

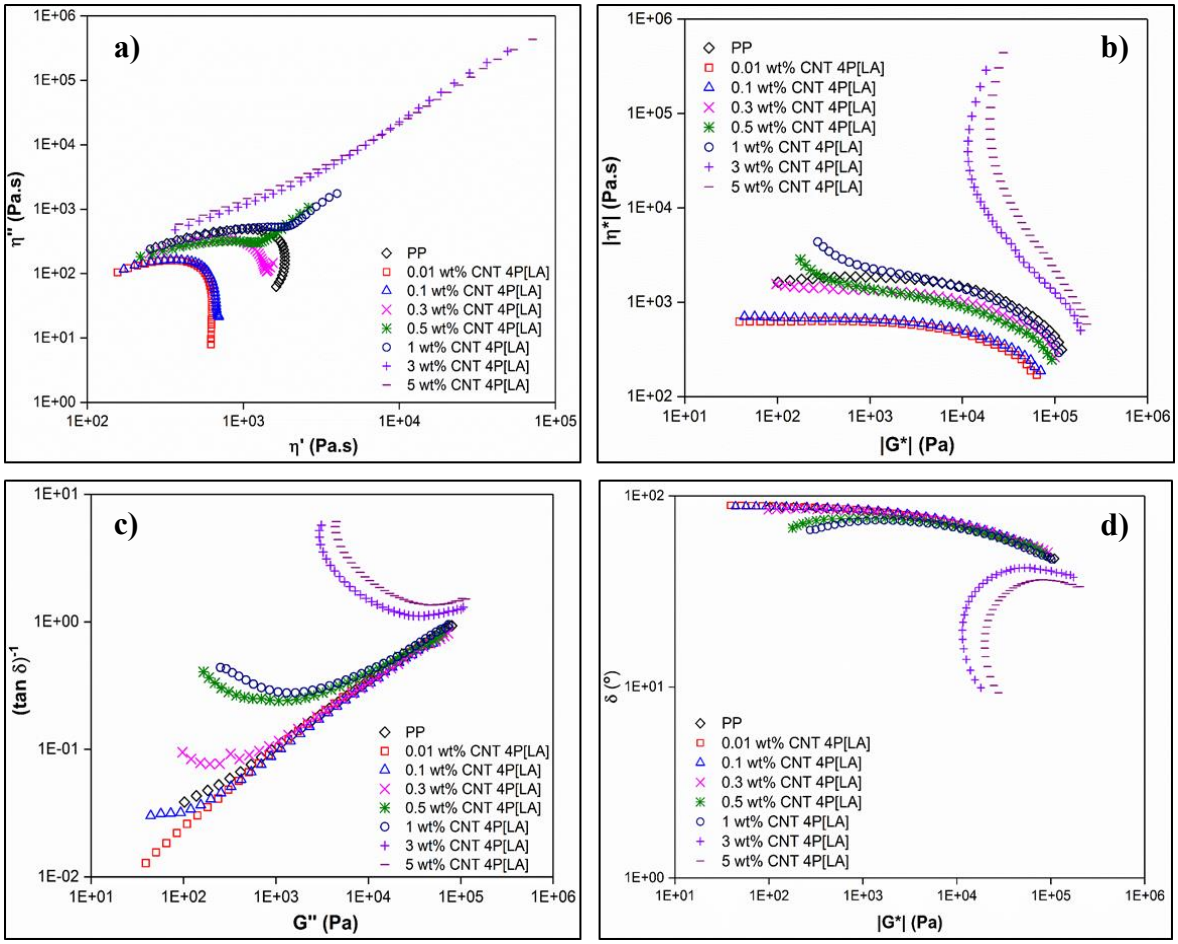

Figure 5.6 Variation in (a) imaginary viscosity (η'') with real viscosity (η'), (b) complex viscosity ($|\eta^*|$) with complex modulus ($|G^*|$), (c) $(\tan \delta)^{-1}$ with G'' and (d) phase angle (δ) with the absolute value of ($|G^*|$) (Van Gurp-Palmen plot) for unfilled PP and composites of PP and P[LA] modified MWCNTs.

The relaxation behaviour of the composites (related to the extent of MWCNT dispersion) can be examined by plotting log imaginary viscosity (η'') verses log real viscosity (η'), as function of MWCNT loading (figure 5.4a)). A well dispersed MWCNT system is expected to have a longer relaxation process and figure 5.4a shows an increase in relaxation time for unmodified MWCNT loadings greater than 0.3wt%. P[LA] functionalised MWCNTs (figure 5.6a)) showed an increase in relaxation time occurred for loadings greater than 0.1 wt%. Plots of $|\eta^*|$ verses $|G^*|$ (figure 5.6b)) and $(\tan \delta)^{-1}$ verses G'' (figure 5.6c)) also indicated of a more highly dispersed and percolated network of MWCNTs after the MWCNTs had been functionalised with P[LA]. The Van-Gurp Palmen plot shown in figure 5.4d)) demonstrates a difference in rheological response from 1 wt% MWCNT

loading compared with P[LA] functionalised MWCNTs (figure 5.6d) which demonstrated this response from 0.5 wt%, again indicating a reduction in the percolation threshold.

The effect of P[LA] itself on the viscoelastic response of the PP used in this study was isolated by performing the same oscillatory rheology measurements, see figure 5.7 and 5.8. As might be expected the addition of up to 20wt% P[LA] to PP resulted in a decrease in G' and $|\eta^*|$ as a function of frequency as well as PP relaxation times, further confirmation of the plasticising efficiency of P[LA] for PP.

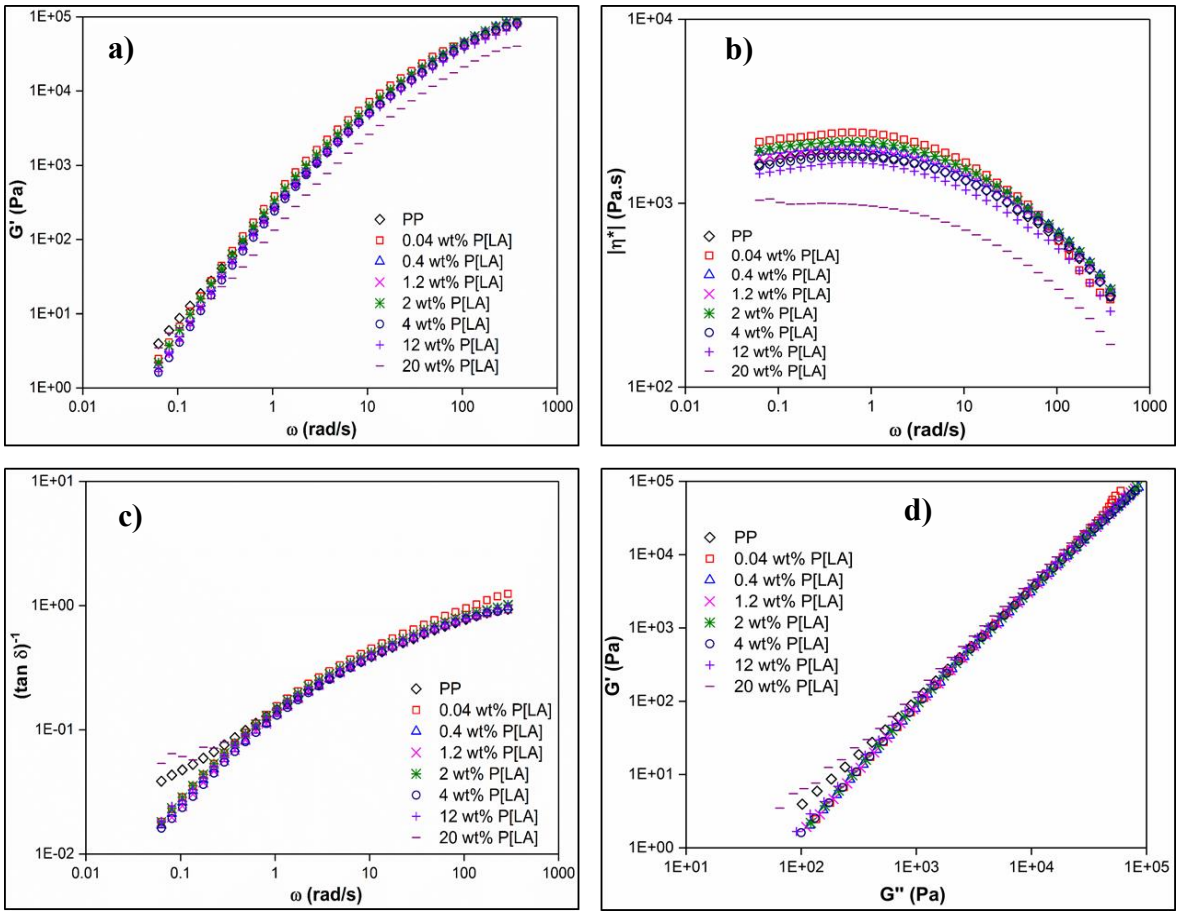

Figure 5.7 Variation in: (a) storage modulus (G'), (b) complex viscosity $|\eta^*|$ and (c) reciprocal of loss tangent ($(\tan \delta)^{-1}$) as a function of angular frequency (ω) for unfilled PP and composites of PP and P[LA]; and (d) Cole-Cole plot (G' versus G'').

Compared to the viscoelastic properties of neat PP, the addition of up to 10wt% P[LA] to PP has not significantly affected the properties and relaxation times of the composite, see figure 5.6 and 5.7. In addition, the lack of deviation of the responses from neat PP demonstrates good compatibility between the P[LA] and the PP and further evidence

of the plasticisation effect of P[LA] on PP. Deviations from neat PP would be an indication of phase separation due to reduced polymer chain dynamics however, such as an effect was not detected.

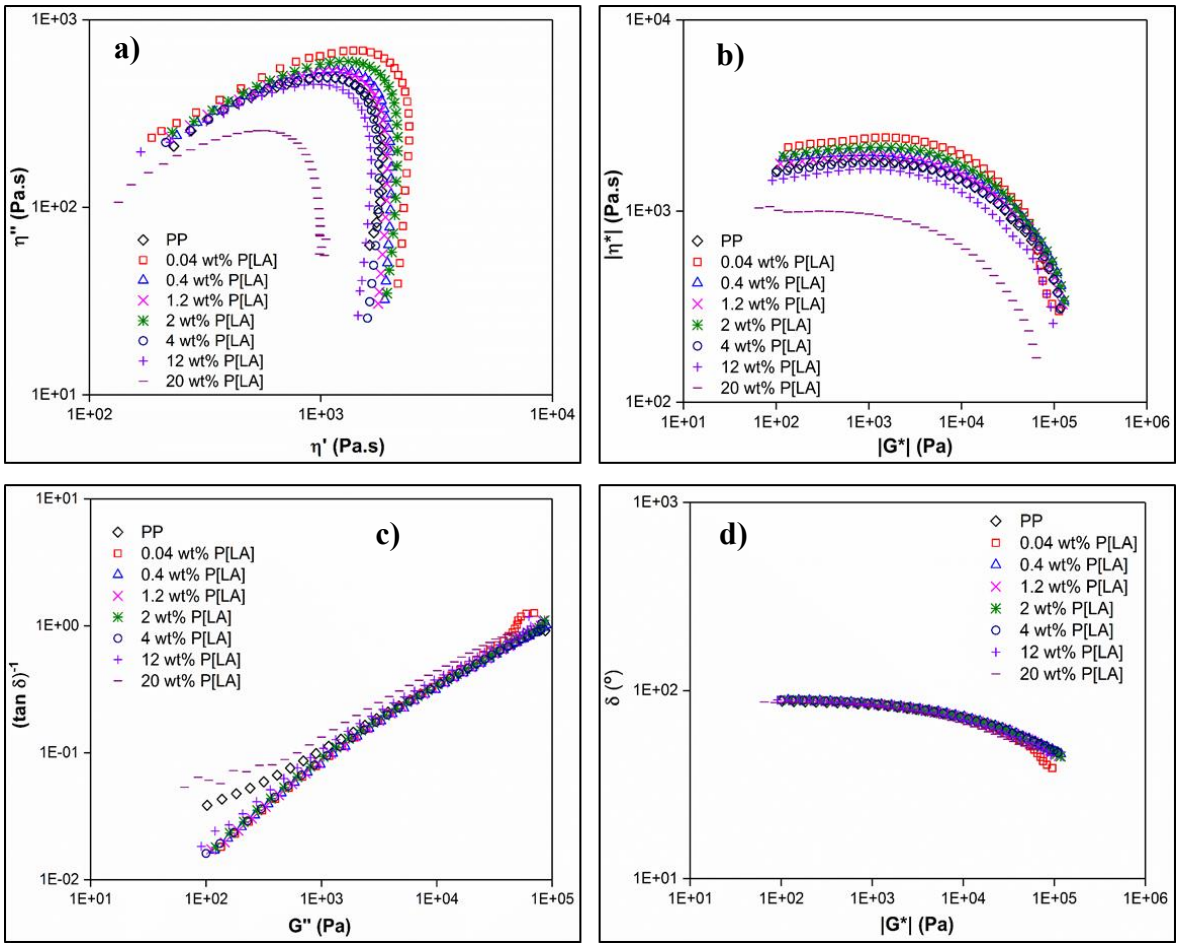

Figure 5.8 Variation in (a) imaginary viscosity (η'') with real viscosity (η'), (b) complex viscosity ($|\eta^*|$) with complex modulus ($|G^*|$), (c) $(\tan \delta)^{-1}$ with G'' and (d) phase angle (δ) with the absolute value of ($|G^*|$) (Van Gurp-Palmen plot) for unfilled PP and composites of PP and P[LA].

A combination of SEM and oscillatory rheology measurements have demonstrated the MWCNTs are well dispersed and network formation has been achieved. The addition of P[LA] has led to further increases in dispersion and reductions in percolation threshold. It is proposed the well dispersed systems will lead to notable increase in mechanical properties through the effect of interfacial stress transfer from the PP matrix to the MWCNTs under mechanical static tensile loading.

The r.t. static mechanical properties for composites of PP, MWCNTs and P[LA] were measured and their corresponding stress vs strain curves for composites of, PP and unmodified MWCNTs (figure 5.9a), PP and P[LA] (figure 5.9b), PP and P[LA] modified MWCNTs with a ratio of 1:4 MWCNTs:P[LA] (figure 5.9c), and PP and P[LA] modified MWCNTs with a ratio of 1:1 MWCNTs:P[LA] (figure 5.9d) are shown. Table 5.3 lists the Young's modulus (E), yield strength (σ_Y), fracture strength (σ_B) and elongation at break (ε_B) for the composites corresponding to the relevant stress vs strain curves.

A significant decrease in ε_B from ~270% for unfilled PP to ~5% after MWCNT addition was observed. Such a dramatic decrease of ~ 98% in ε_B even after the addition of 0.01 wt% MWCNTs is a common observation due to the highly anisotropic behaviour of the MWCNT particles.[23] The MWCNTs form highly entangled networks with the PP matrix. Unsurprisingly, even at modest loadings, the MWCNTs are defects within the PP matrix and hinder the movement of the polymer chains during uniaxial deformation leading to embrittlement. The effective stress transfer at the interface between CNTs and polymer matrix is limited. The ductile to brittle failure transition is very low at 0.01wt% MWCNT loading. There is no correlation between MWCNT loading and ε_B suggesting the flow of the polymer chains is fixed after the addition of MWCNTs as seen in figure 5.10 d). The E of PP (1.46 GPa) was not significantly altered by the addition of just MWCNTs up to a loading of 5wt%. For reference, the E decreased by ~20% at 0.1wt% MWCNT loading. A subsequent increase in MWCNT loading resulted in an increase in E returning to the same value for unfilled PP as shown in figure 5.10 a). A decrease in E suggests poor interfacial adhesion of the MWCNTs and lack of compatibility between the MWCNTs and the PP. The MWCNT agglomerates act as stress concentrators and poor interfacial adhesion leads to stress fractures causing a decrease in E. The σ_Y showed a similar pattern with a reduction of ~20% at 0.1 wt% MWCNT loading and a subsequent increase to neat PP levels at 5 wt% loading (figure 5.10 b). Overall, the addition of just MWCNTs had little change in σ_Y. The σ_B increased significantly (~50%) with increasing MWCNT loading. An increase of ~70% was observed for a 5 wt% MWCNT loading. Such an increase in σ_B is to be expected due to reduced ductility.

The addition of P[LA] modified MWCNTs with a ratio of 1:4 MWCNTs:P[LA] resulted in a reduction in E (~ -50%), σ_Y (~ -50%) and σ_B (~ -30%) compared to neat PP. However, an increase in ε_B (~ 50%) was observed compared to unmodified MWCNTs for a 5 wt% loading. With the exception of ε_B, all other results showed a decrease in mechanical

properties compared to the PP matrix. Clearly, the addition of P[LA] results in plasticisation of PP concomitantly assisting MWCNT dispersion and distribution in the PP matrix.

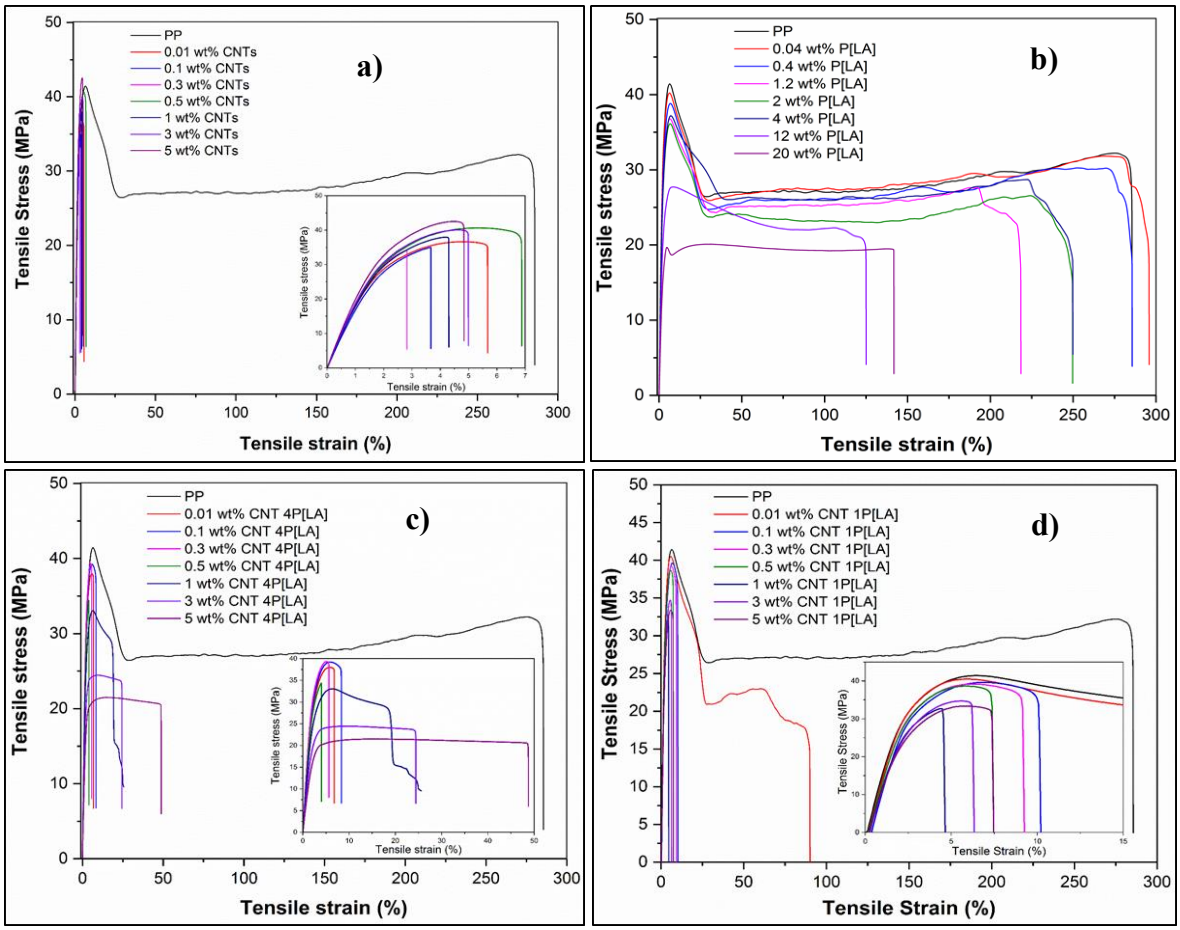

Figure 5.9 Stress vs strain curves for a) unfilled PP and composites of PP and MWCNTs, b) unfilled PP and composites of PP and P[LA], c) unfilled PP and composites of PP and 4P[LA] functionalised MWCNTs with a filler to compatibiliser ratio of 1:4 and d) unfilled PP and composites of PP and 1P[LA] functionalised MWCNTs with a filler to compatibiliser ratio of 1:1.

The addition of 1:4 MWCNT:P[LA] modified MWCNTs to PP resulted in the decrease in ε_B of about 80%, some 18% below that obtained when unmodified MWCNTs were added at the same 5wt% loading. Presumably, the P[LA] is having a plasticising effect on PP as well as promoting interfacial interaction between the MWCNTs and PP chains, facilitated by wrapping/coating of the P[LA] via CH-π interactions. To understand this behaviour further, the tensile properties of blends of PP and P[LA] were measured, where the P[LA] content was similar to that for the composites with 1:4 MWCNT:P[LA] modified MWCNTs.

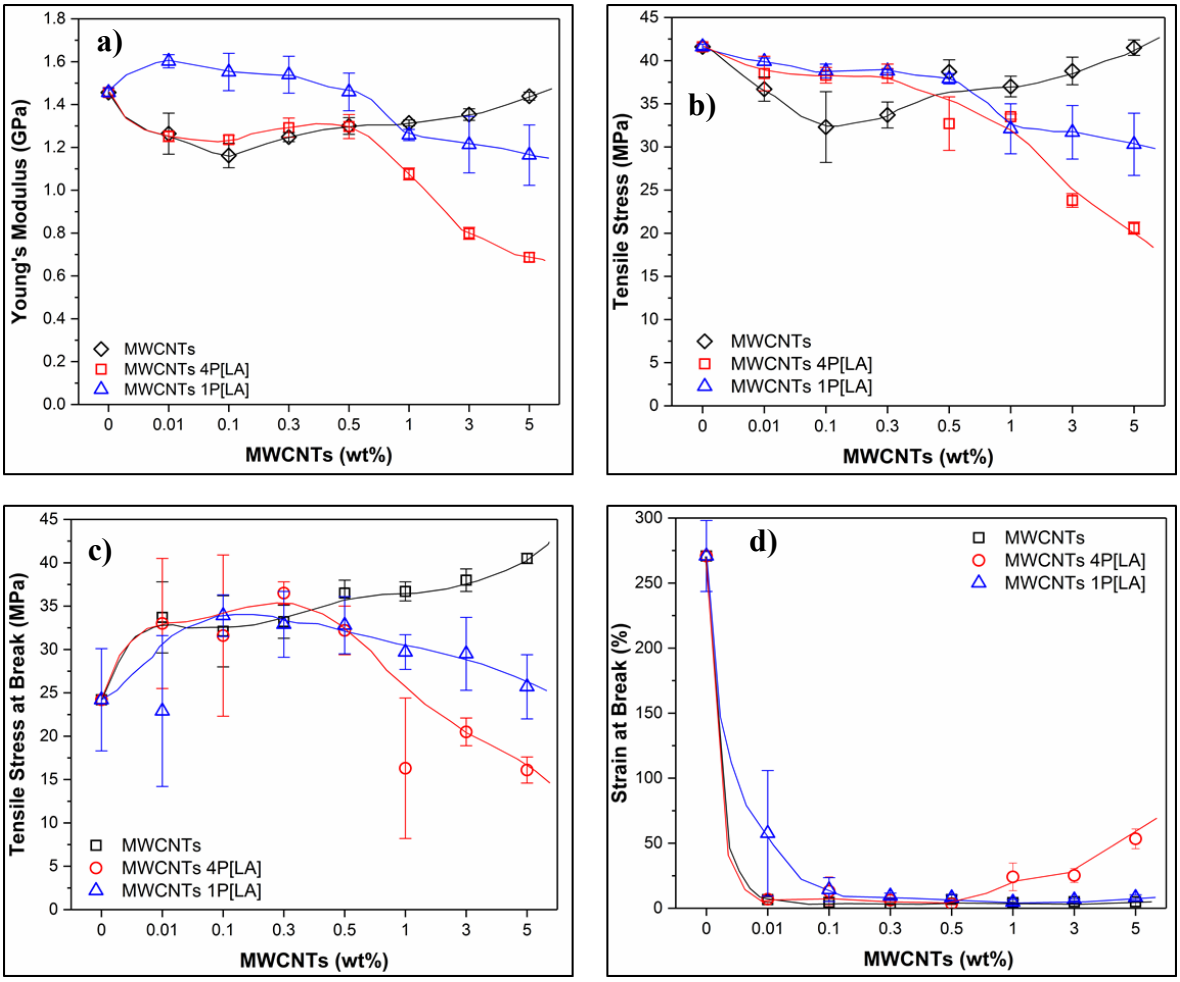

Figure 5.10 Variation in, (a) Young's modulus (E), (b) yield strength (σ_Y), (c) fracture strength (σ_B) and (d) elongation at break (ε_B), as a function of MWCNT loading for composites of, PP/MWCNTs, PP/MWCNTs/4P[LA] and PP/MWCNTs/1P[LA]. Sample compositions described in table 5.2.

For these blends, addition of P[LA] to PP resulted in a 50% decrease in stiffness and strength of PP, for a 20 wt% loading of P[LA], about a 20% decrease in σ_B, but critically little change in ε_B until the P[LA] content was greater than 4wt% (figure 5.11). At low loadings of P[LA], <2 wt%, E was not as significantly affected with a decrease of only ~10% (figure 5.11a). Significant changes were only observed after the addition of 2 wt% P[LA] for σ_Y, σ_B and ε_B suggesting that a plasticising effect was attained upon the addition of 2 wt% P[LA] (figure 5.11 b) c) and d)). The ductility and toughness of PP is retained upon P[LA] addition. The P[LA] is enabling the PP chains to slide past each other, increasing the free volume and therefore, causing a reduction in mechanical properties relative to neat PP.

Table 5.3 Change in tensile mechanical properties for PP and composites of PP, P[LA] and MWCNTs. Definitions are described in table 5.2

MWCNT loading (wt%)	Young's modulus (GPa)	↑ GPa (%)	Tensile stress (MPa)	↑ MPa (%)	Stress at break (MPa)	↑ MPa (%)	Strain at break (%)	↑ % (%)
PP	1.456 ± 0.021		41.6 ± 0.3		24.2 ± 5.9		270.8 ± 27.3	
0.01 wt% CNTs	1.264 ± 0.096	-13.2	36.7 ± 1.4	-11.6	33.7 ± 4.1	39.2	6.6 ± 2.0	-97.6
0.1 wt% CNTs	1.162 ± 0.057	-20.2	32.3 ± 4.1	-22.3	32.1 ± 4.1	32.4	4.5 ± 1.5	-98.3
0.3 wt% CNTs	1.248 ± 0.021	-14.2	33.7 ± 1.5	-18.9	33.2 ± 1.9	36.9	3.4 ± 0.6	-98.8
0.5 wt% CNTs	1.300 ± 0.039	-10.7	38.7 ± 1.4	-6.8	36.5 ± 1.5	50.5	6.7 ± 1.3	-97.5
1 wt% CNTs	1.314 ± 0.014	-9.8	37.0 ± 1.2	-10.9	36.7 ± 1.1	51.4	4.3 ± 0.7	-98.4
3 wt% CNTs	1.353 ± 0.027	-7.1	38.8 ± 1.6	-6.6	38.0 ± 1.3	57.0	5.0 ± 0.9	-98.2
5 wt% CNTs	1.439 ± 0.019	-1.2	41.5 ± 0.9	-0.2	40.5 ± 0.6	67.1	5.0 ± 0.7	-98.2
0.04 wt% P[LA]	1.448 ± 0.008	-0.5	40.5 ± 0.4	-2.5	19.1 ± 3.2	-21.3	273.1 ± 54.4	0.8
0.4 wt% P[LA]	1.382 ± 0.082	-5.1	39.1 ± 1.2	-6.0	20.1 ± 7.4	-17.1	280.9 ± 82.3	3.7
1.2 wt% P[LA]	1.312 ± 0.041	-9.9	37.7 ± 1.1	-9.3	15.0 ± 4.2	-38.0	274.0 ± 15.6	1.2
2 wt% P[LA]	1.254 ± 0.040	-13.9	35.9 ± 1.0	-13.6	16.2 ± 2.1	-33.0	277.5 ± 35.7	2.5
4 wt% P[LA]	1.189 ± 0.031	-18.3	36.8 ± 0.4	-11.4	17.3 ± 3.5	-28.7	277.1 ± 46.9	2.3
12 wt% P[LA]	0.954 ± 0.007	-34.5	28.7 ± 0.8	-31.0	14.3 ± 4.2	-41.0	192.9 ± 65.0	-28.8
20 wt% P[LA]	0.702 ± 0.011	-51.8	19.8 ± 0.4	-52.4	18.3 ± 0.7	-24.3	155.3 ± 33.7	-42.7
0.01 wt% CNTs 4P[LA]	1.252 ± 0.025	-14.0	38.5 ± 2.0	-7.3	33.0 ± 7.5	36.2	7.0 ± 2.0	-97.4
0.1 wt% CNTs 4P[LA]	1.236 ± 0.020	-15.1	38.3 ± 0.9	-7.8	31.6 ± 9.3	30.4	13.1 ± 11.0	-95.2
0.3 wt% CNTs 4P[LA]	1.292 ± 0.045	-11.3	38.5 ± 1.1	-7.4	36.5 ± 1.3	50.8	6.2 ± 1.1	-97.7
0.5 wt% CNTs 4P[LA]	1.297 ± 0.056	-10.9	32.7 ± 3.1	-21.3	32.2 ± 2.8	32.8	3.5 ± 0.8	-98.7
1 wt% CNTs 4P[LA]	1.076 ± 0.028	-26.1	33.5 ± 0.3	-19.3	16.3 ± 8.1	-32.9	24.1 ± 10.6	-91.1
3 wt% CNTs 4P[LA]	0.799 ± 0.028	-45.1	23.8 ± 0.8	-42.8	20.5 ± 1.6	-15.4	25.2 ± 5.4	-90.7
5 wt% CNTs 4P[LA]	0.687 ± 0.021	-52.8	20.6 ± 0.7	-50.3	16.1 ± 1.5	-33.6	53.4 ± 7.6	-80.3
0.01 wt% CNTs 1P[LA]	1.602 ± 0.031	10.0	39.9 ± 0.4	-4.1	22.9 ± 8.7	-5.4	57.6 ± 48.3	-78.7
0.1 wt% CNTs 1P[LA]	1.552 ± 0.087	6.6	38.8 ± 0.8	-6.7	33.9 ± 2.4	40.1	14.3 ± 9.2	-94.7
0.3 wt% CNTs 1P[LA]	1.539 ± 0.086	5.7	38.8 ± 0.2	-6.7	32.9 ± 3.8	36.0	9.3 ± 2.3	-96.6
0.5 wt% CNTs 1P[LA]	1.459 ± 0.088	0.2	37.9 ± 0.6	-8.9	32.8 ± 3.3	35.5	8.0 ± 2.2	-97.0
1 wt% CNTs 1P[LA]	1.258 ± 0.026	-13.6	32.1 ± 2.9	-22.8	29.7 ± 2.0	22.7	4.7 ± 1.9	-98.3
3 wt% CNTs 1P[LA]	1.213 ± 0.132	-16.7	31.7 ± 3.1	-23.8	29.5 ± 4.2	21.9	6.4 ± 0.8	-97.6
5 wt% CNTs 1P[LA]	1.164 ± 0.141	-20.1	30.3 ± 3.6	-27.2	25.7 ± 3.7	6.2	8.2 ± 2.2	-97.0

This plasticising effect can be more clearly observed by examining representative stress-strain curves for the four sets of composites, figure 5.9. The area under the stress-strain curves decreased significantly on addition of MWCNTs alone, but is recovered with increasing P[LA] content in the composites. The critical MWCNT loading at which the effect of P[LA] inclusion can be observed to be between 0.5 and 1 wt%, figure 5.10. The ductility of PP can be seen to be recovered on addition of 1wt% MWCNTs and greater than 4wt% P[LA], figure 5.10 d). It is noteworthy that the change in mechanical properties described originate with CNT and P[LA] addition to PP and not as a consequence of thermal degradation of the components during melt mixing.

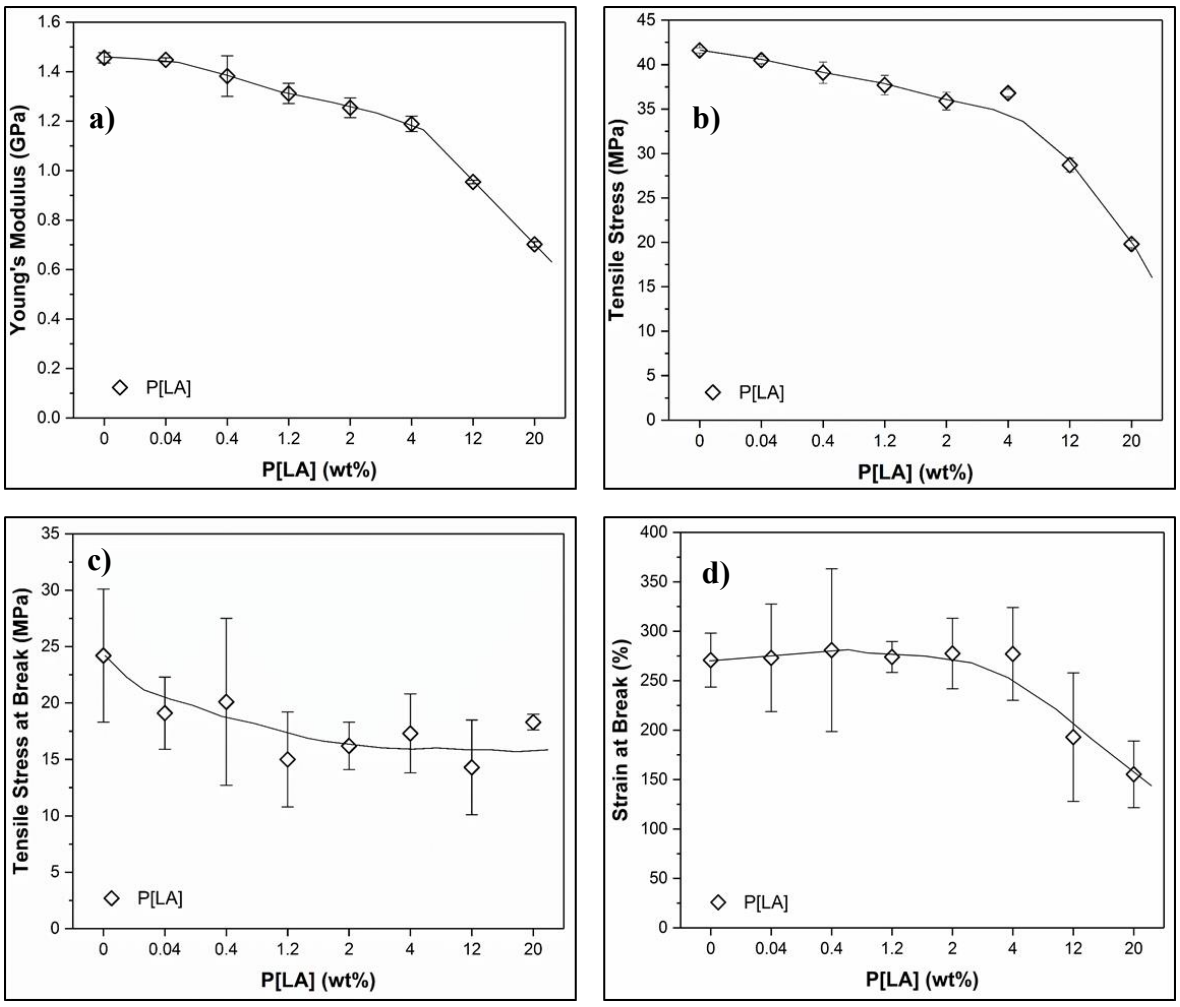

Figure 5.11 Variation in, (a) Young's modulus (E), (b) yield stress (σ_Y), (c) stress at break (σ_B) and (d) elongation at break (ε_B), as a function of P[LA] loading for composites of PP/P[LA].

The previous chapter investigated the thermal stability of P[LA] and its composites with MWCNTs.[24] Our studies confirmed that P[LA] is thermally stable at PP processing temperatures and the addition of P[LA] modified MWCNTs has no effect on the thermal

stability of PP at its typical processing temperature of ~ 165 °C. Interestingly, the thermally stability of PP increased on addition of MWCNTs but the addition of P[LA] modified MWCNTs had no effect.[24] It is likely this behaviour is a consequence of both the known free radical scavenging ability of MWCNTs being altered on P[LA] addition and that P[LA] degrades forming high concentrations of free radicals.

Figure 5.10 and table 5.3 show and list the stress vs strain curves for composites of PP and P[LA] modified MWCNTs with 1:1 ratio of MWCNTs:P[LA]. *E* increases by ~10% for 0.01 wt% P[LA] modified CNT loading. This steadily decreased to ~ -20% for a 5 wt% loading showing small quantities of MWCNTs and P[LA] improve the *E* of the composite compared to using a 1:4 of MWCNTs:P[LA]. The σ_Y increased for loadings below 0.5 wt% compared to unmodified MWCNTs. ε_B decreased upon addition of 1:1 MWCNTs:P[LA] modified MWCNTs, however the decrease was not as dramatic compared to unmodified MWCNTs.

In summary, the use of P[LA] as a compatibiliser results in plasticisation of PP as seen from increases in ε_B ~50% compared to unmodified MWCNTs. The use of P[LA] in a 1:1 ratio of MWCNTs:P[LA] resulted in improved mechanical properties compared to using 1:4 MWCNTs:P[LA] due to the reduced quantity of P[LA] relative to 1:4 MWCNTs:P[LA]. The use of P[LA] modified MWCNTs with a loading of less than 0.5 wt% MWCNTs resulted in increases in *E*, σ_Y and σ_B compared to unmodified MWCNTs. With the exception of σ_B, an increase in *E*, σ_Y and ε_B was not observed compared to neat PP for all samples due to the plasticisation of PP by P[LA]. Only, σ_B increased compared to neat PP upon addition of unmodified MWCNTs, and the incorporation of P[LA] did not affect this.

It is well known in literature that the addition of un-modified MWCNTs can result in some increases in mechanical properties relative to the neat unfilled polymer matrix, for a well dispersed system.[25, 26] Further evidence for the plasticisation of PP by P[LA] was investigated using DMTA which facilitates the measurement of the variation in *E'*, *E''* and tan δ vs temperature. The change in interfacial tension between P[LA] and MWCNTs and the plasticising of PP by P[LA] can also be indirectly proven by studying the changes in the dynamic mechanical thermal (DMTA) properties, in particular the glass transition (T_g), of PP and composites of PP and MWCNTs on addition of P[LA].

Figures 5.12, 5.14, 5.15 and 5.16 show the variation in tan δ, storage modulus (*E'*) and loss modulus (*E''*) as a function of temperature for the various composites with and

without P[LA] addition. From figure 5.12, variations in a) tan δ b) *E'* and c) loss modulus *E''* for unfilled PP and composites of PP and MWCNTs are shown. A modest increase in *E'* was not observed (figure 5.12b) upon addition of unmodified MWCNTs. At low loadings (<0.3 wt%) *E'* remains similar to that of neat PP. An increased MWCNT loading resulted in *E'* remaining relatively unchanged. From SEM and oscillatory rheology measurements, it has been determined that the composites of PP and MWCNTs are well dispersed and interconnected. Addition of P[LA] led to increased dispersion and lower percolation thresholds and therefore, such reinforcement can be readily detected using DMTA through increases in *E'*.

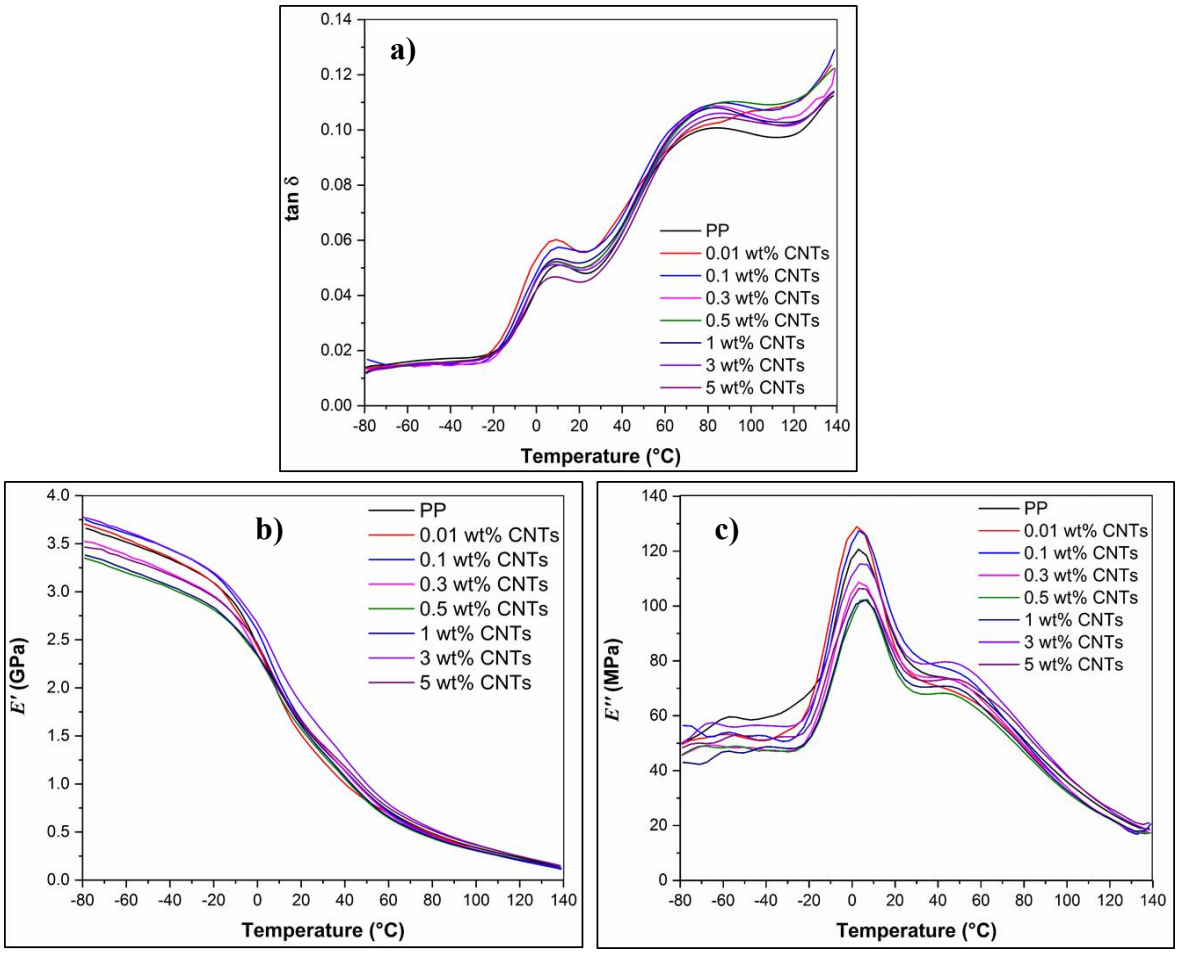

Figure 5.12 Variation in (a) tan δ (b) storage modulus (*E'*) and (c) loss modulus (*E''*) for unfilled PP and composites of PP and MWCNTs.

PP displays three dynamic relaxations.[27] The α-relaxation has been assigned to the lamellar slip and rotation in the crystalline phase. The β-relaxation is due to the dynamic

glass-rubber (T_g) transition of the amorphous phase of PP and the γ-transition is attributed to relaxation of a few chain segments in the amorphous regions of the semi-crystalline polymer.[27] The α-relaxations are clearly observable from DMTA and usually occur at temperatures above 60°C. The β-relaxation (T_g) occurs between -20 – +20 °C for neat PP. The γ-transition is weak and often not observed and is usually observed below -50°C. In theory, addition of MWCNTs are expected to increase the *E'* of the composite due to, the exceptionally high *E* value reported for MWCNTs (~1 TPa idealised), interfacial stress transfer from the nanotubes to the PP and their high aspect ratio creating an interconnected polymer-CNT network. It was expected the MWCNTs would reinforce the PP matrix and enhance stiffness. A lack of increase in *E'* and hence reinforcement, suggests weak interfacial adhesion and stress transfer between the MWCNTs and PP in the composite material.

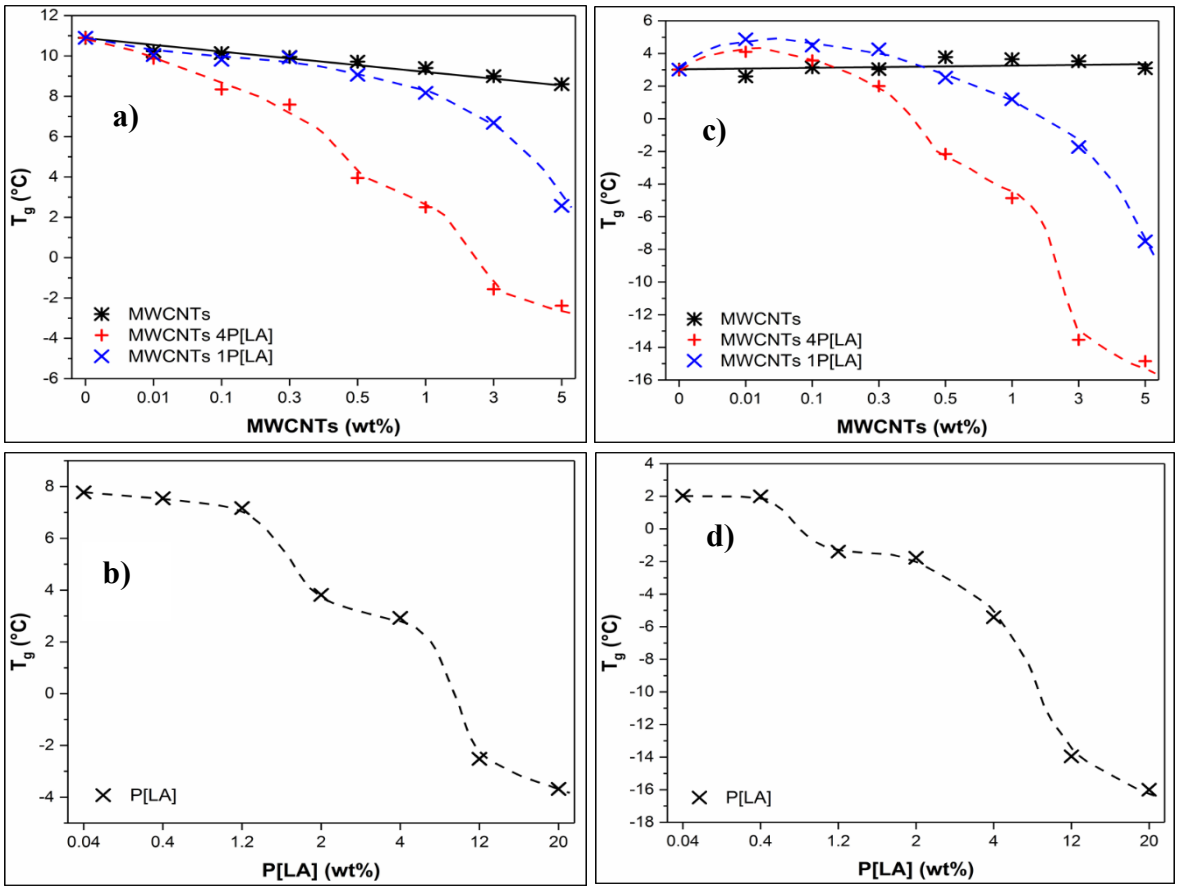

Figure 5.13 Variation in T_g obtained from tan δ maximum a) as function of MWCNT loading for composites of PP and unmodified MWCNTs, PP and 1:4 MWCNT:P[LA] modified MWCNTs and PP and 1:1 MWCNT:P[LA] modified MWCNTs and b) as function of P[LA] loading for composites of PP and P[LA]. Change in T_g obtained from loss modulus (*E''*)

maximum c) as function of MWCNT loading for composites of PP and unmodified MWCNTs, PP and 1:4 MWCNT:P[LA] modified MWCNTs and PP and 1:1 MWCNT:P[LA] modified MWCNTs and d) as function of P[LA] loading for composites of PP and P[LA].

Figure 5.12, 5.13 a) and 5.13 c) show both the *E''* and tan δ peaks (β-relaxation, T_g) to remain largely unaffected upon addition of the unmodified MWCNTs to PP. From figure 5.12 a) a slight decrease in the tan δ maximum upon increasing MWCNT loading, from ~4 °C to ~2 °C up to 5 wt% was observed. The slight decrease in the tan δ (β-peak) temperature maximum indicates a small enhancement in PP chain dynamics. An increase in the local chain mobility as a result of the addition of nanoparticles to polymers has been reported in the literature.[27] It has been proposed that the increase in chain mobility is due to confinement of the polymer between the nanoparticles. The polymer-nanoparticle interactions cause loosened packing behaviour and therefore increased free volume in the composite.[27]

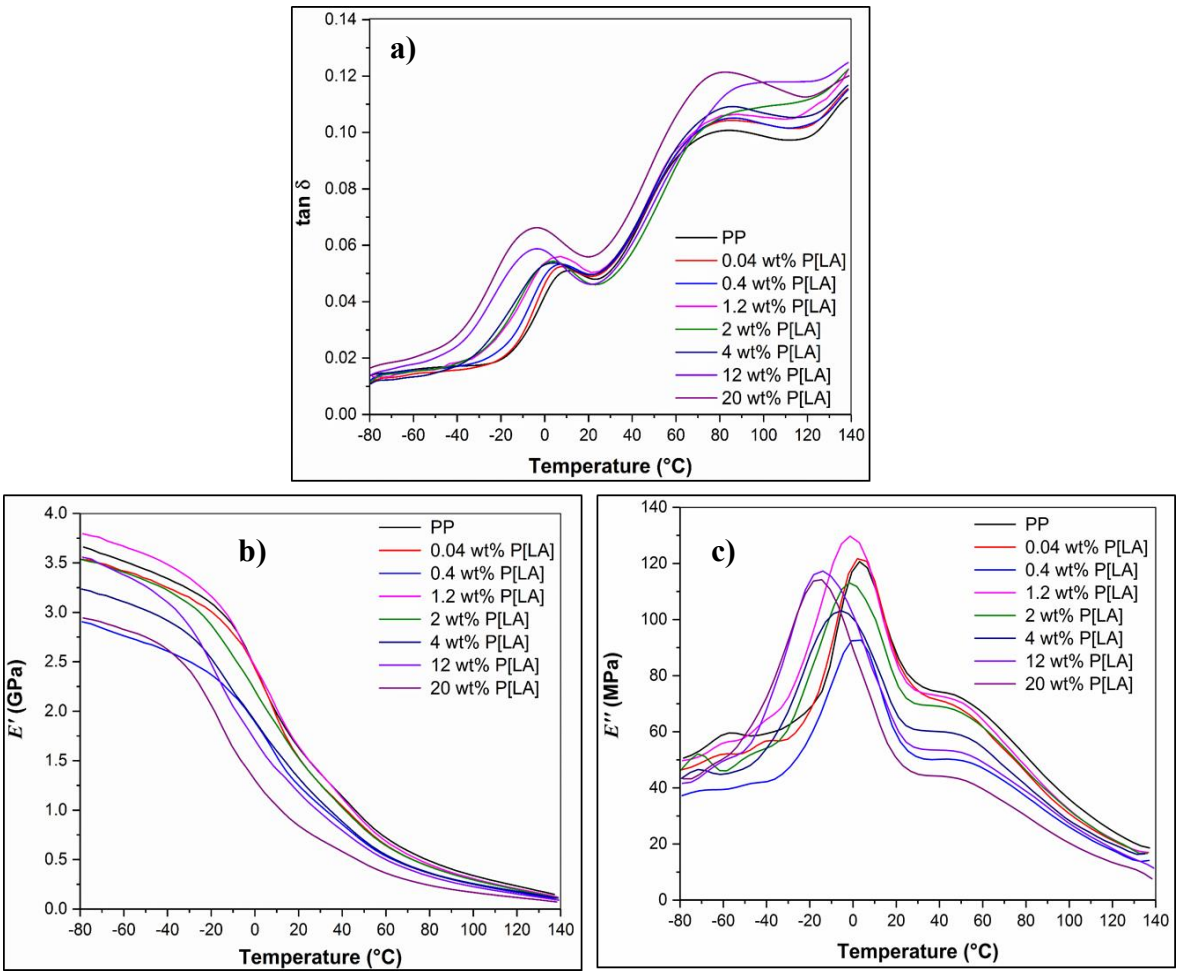

Figure 5.14 Variation in (a) tan δ (b) storage modulus (*E'*) and (c) loss modulus (*E''*) of unfilled PP and composites of PP and P[LA].

The effect of the addition of P[LA] alone on the DMTA of PP is shown in figures 5.14, 5.13 b) and d). Increasing P[LA] content results in significant decrease in T_g, from 8°C to -4°C at 20wt% P[LA] loading when measured using tan δ maximum (figure 5.13 b)) and from 2° to -16°C at 20 wt% P[LA] loading when measured using *E''* maximum (figure 5.13 d)). The T_g (β-peak) shows a significant shift to lower temperatures as a result of the plasticisation effect of P[LA] on the PP matrix. *E'* decreased by ~3.7 GPa for temperatures <40°C after the addition of 20 wt% P[LA] providing further evidence for the plasticisation through reduction in stiffness.

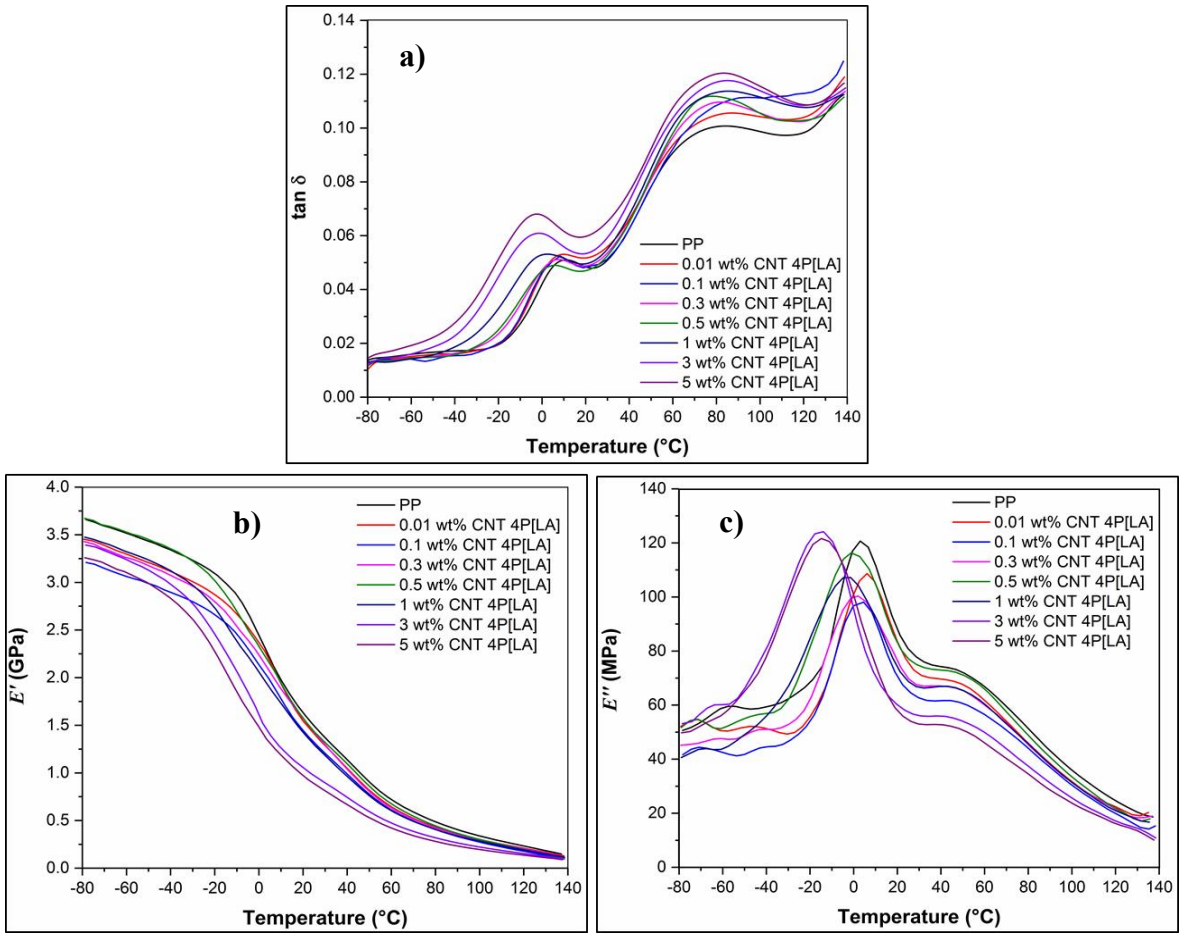

Figure 5.15 Variation in (a) tan δ (b) storage modulus (*E'*) and (c) loss modulus (*E''*) of unfilled PP and P[LA] functionalised MWCNTs with a filler to compatibiliser ratio of 1:4.

From figure 5.15, 5.13 a) and c) the variation in tan δ, *E'* and *E''* vs temperature is shown for composites of PP with 1:4 MWCNT:P[LA] modified MWCNTs. Both the T_g from the tan δ peak (figure 5.13 a)) and *E''* peak (figure 5.13 c)), show a decrease in T_g similar to that of PP when blended with P[LA]. The T_g decreased by ~ 14 °C when determined from

the tan δ peak and by ~ 19 °C when taken from the peak maximum in the *E''* plot. The decrease in T_g and stiffness are a result of increased chain mobility as a result of the plasticisation of P[LA] with PP. Even though the loadings of P[LA] are the same compared to the composite of just PP and P[LA], the decreases in T_g are not to the same extent, but similar. This is due to the CH-π wrapping effect of the surface bound P[LA] on the MWCNTs which reduces the quantity of unbound P[LA] in the matrix and hence, the plasticisation effect. However, this effect is minimal as the T_g decreases to just above that of measured in the composite of PP and P[LA]. At low loadings, <0.3 wt%, there is an increase in T_g when measured by *E''* peak. The 0.1 wt% MWCNT 4P[LA] loading resulted in an increase in T_g by ~1 °C suggesting the P[LA] functionalised MWCNTs increased PP reinforcement because, the increase in T_g was not observed with unmodified MWCNTs at a 0.1 wt% loading.

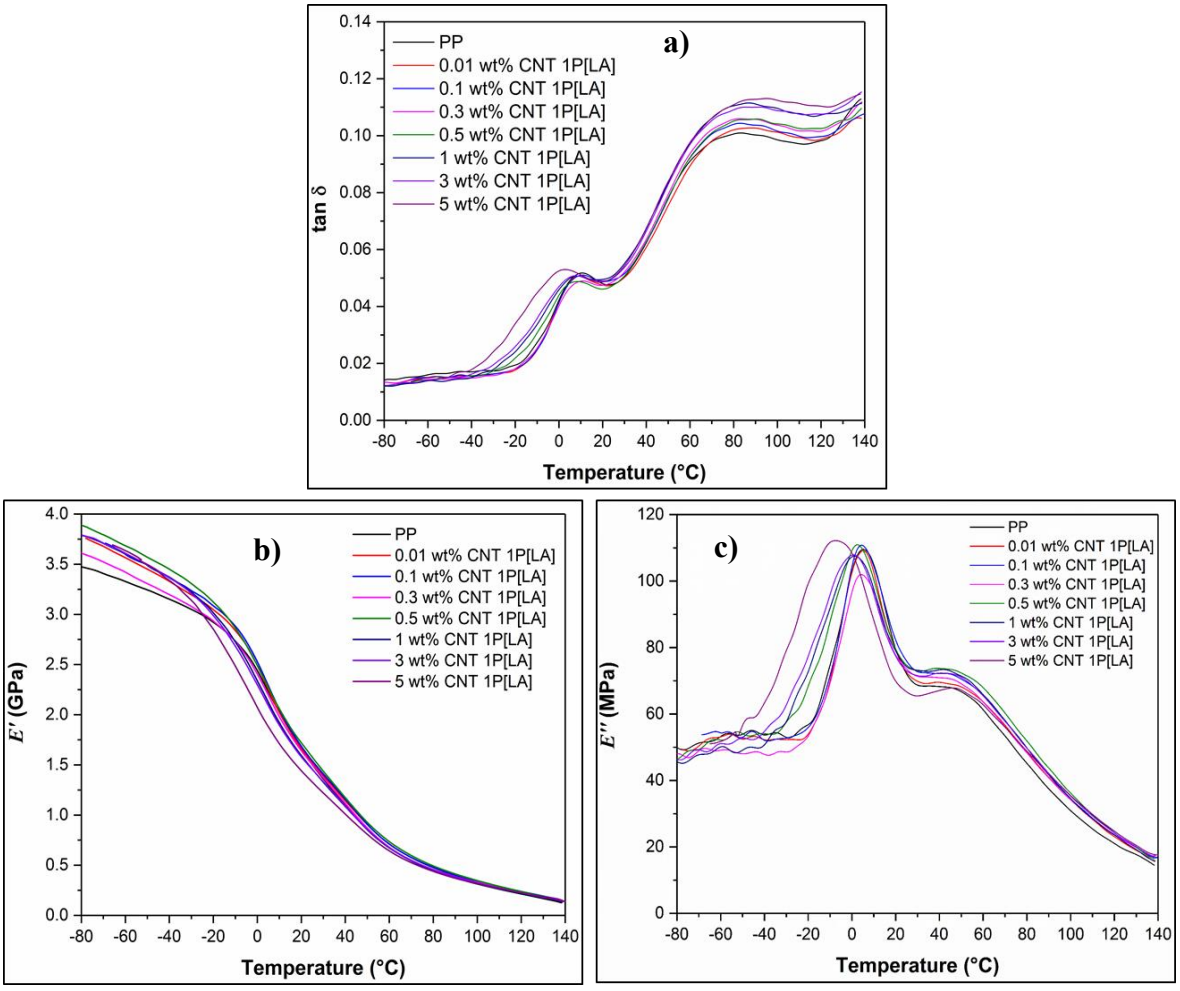

Figure 5.16 Variation in (a) tan δ (b) storage modulus (*E'*) and (c) loss modulus (*E''*) of unfilled PP and P[LA] functionalised MWCNTs with a filler to compatibiliser ratio of 1:1.

Figures 5.13 a) and b) clearly show the critical loading of P[LA] is ~1 wt% for the plasticisation effect to be realised. The results suggest a significant proportion of the P[LA] is not bound/adsorbed onto the MWCNTs and therefore, it is not able to effectively compatibilise the MWCNTs and facilitate reinforcement.

From figures 5.16, 5.13 a) and b) the variation in tan δ, *E'*, *E''* vs temperature for composites of PP with 1:1 MWCNT:P[LA] modified MWCNTs are shown. Utilising a ratio of 1:1 MWCNT to P[LA] resulted in a reduced concentration of P[LA] being added to the composite. The T_g as measured from the maximum in the tan δ peak was consistent with that of the composite with unfilled MWCNTs suggesting the P[LA] content is now not sufficient at facilitating plasticisation of PP to the same extent of that seen for the composites of 1:4 MWCNT:P[LA]. At loadings of 0.5 wt% 1:1 MWCNT:P[LA] and above, the T_g decreased from ~ 10°C to ~ 2 °C when measured from tan δ maximum. The result is consistent with the samples of 1:4 MWCNTs:P[LA] showing that ~ 1 wt% of P[LA] is required to facilitate plasticisation. The T_g taken from the *E''* curve showed an increase in T_g by ~ 2 °C at 0.1 wt% 1:1 MWCNT:P[LA] loading indicating the MWCNTs are reinforcing the composites by increasing stiffness through increase dispersion and network formation. However, at higher loadings, the increased P[LA] content exhibits plasticisation as expected.

From all four sets of data, irrespective of how the T_g is measured, i.e. maxima in tan δ, corresponding decrease in *E'* or peak maxima in *E''*, the incorporation of P[LA] in to these composite materials results in a significant decrease in T_g, see figure 5.13, between 15 °C to 35 °C. The decrease in T_g is first observed when the MWCNT loading is about 0.1 wt% and thus the P[LA] content 0.4wt%. However, for a loading of 5wt% MWCNTs, but critically 20 wt% P[LA], the reduction in T_g of PP is shifted to lower temperatures by as much as 35 °C. This result is most interesting given the technological goal of extending the application of PP hitherto hindered by the relatively poor low temperature (< -20 °C) impact properties of PP.

Further characterisation of the plasticisation effect of P[LA] on PP was determined by way of DSC and WAXD. They provide details of the crystallinity of the PP and importantly, how the addition of P[LA] changes the crystallinity and therefore its plasticisation properties.

The strong nucleating effect of CNTs on polymers cooled from the melt can alter the crystalline content and crystallisation kinetics of semi-crystalline PP. On the assumption that

the majority of MWCNTs are dispersed in the PP amorphous phase, it is important to consider the effect of MWCNT loading on the crystallisation behaviour of PP. It is worth noting recent studies have shown CNTs can reside within the inter-lamella spacing of certain polymers.[28] The crystalline content (X_c) and relevant thermal properties of composites of PP with MWCNT loadings up to 5 wt%, PP with P[LA] modified MWCNTs at ratios of 1:4 and 1:1 MWCNT:P[LA] at loadings up to 5 wt% and PP with P[LA] loadings up to 20 wt%, were determined from a combination of DSC (figure 17) and WAXD (figure 18), the relevant thermal properties are listed in table 5.4.

For composites of PP with MWCNTs (figure 17 a) and b)), an increase in both melt temperature (T_m) of ~ 4 °C and crystallisation temperature (T_c) also of ~ 4 °C was obtained on addition of up to 5 wt% MWCNTs. The increase in T_m and T_c is evidence for the nucleating effect typically exhibited by MWCNTs on semi-crystalline polymers cooling from the melt. This behaviour has previously been reported for PP and other semi-crystalline polymers.[29] For MWCNT loadings less <1 wt%, increases in T_m and T_c were not observed suggesting, nucleation was not significant at these loadings. For loadings >1wt% the nucleating effect becomes more apparent. However, a change in X_c with increasing MWCNT content was not observed from DSC. In fact, X_c remained unchained even after the addition of 5wt% unfunctionalised MWCNTs. At lower loadings, <1 wt%, the crystallinity decreased, ~1%. However, for increased loadings, >1wt% leads to the addition of external nucleating sites, an increase in crystallisation rate and therefore and increase in X_c to neat PP values.

In contrast, a modest decrease in X_c for PP with increasing MWCNT content was obtained from, ~ 37 % to ~ 28 % when measured by WAXD again on addition of 5 wt% MWCNTs. The contrasting values for X_c can be explained by fundamental differences in the two techniques. Full width at half-height values for both the melting ~ 4 °C and cooling ~ 1°C peaks for composites of PP and 5 wt% unfunctionalised MWCNTs showed peak broadening compared to unfilled PP, evidence for heterogeneous nucleation of PP by the MWCNTs. The effect of peak broadening at high MWCNT loadings suggests changes to the spherulite size distribution. The presence of MWCNTs nucleated spherulite growth at higher temperatures resulting in a wider distribution of crystallite sizes and therefore broadening of the melting and cooling peaks.

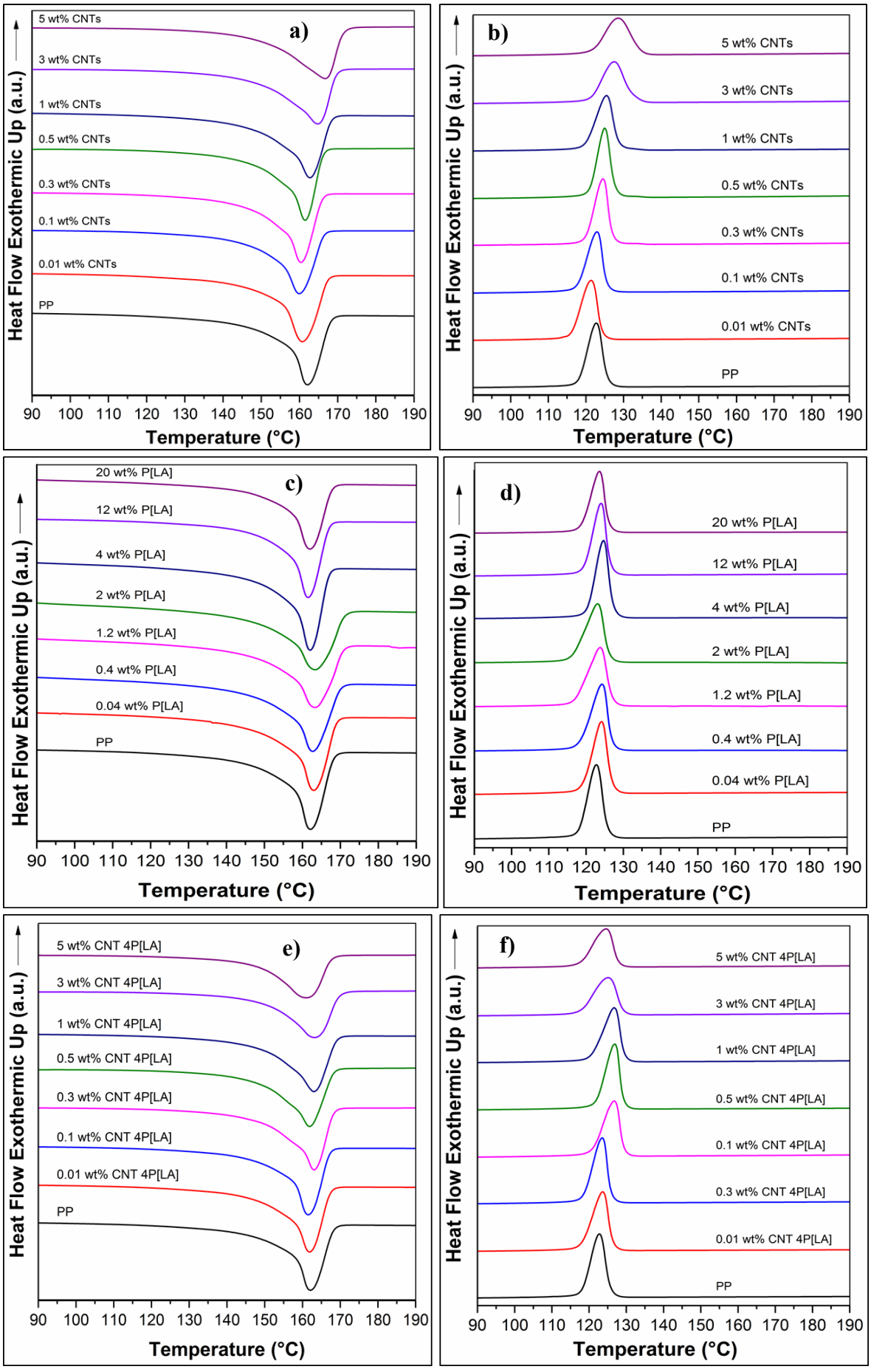
a)
5 wt% CNTs
3 wt% CNTs
1 wt% CNTs
0.5 wt% CNTs
0.3 wt% CNTs
0.1 wt% CNTs
0.01 wt% CNTs
PP
Heat Flow Exothermic Up (a.u.)
90 100 110 120 130 140 150 160 170 180 190
Temperature (°C)
b)
5 wt% CNTs
3 wt% CNTs
1 wt% CNTs
0.5 wt% CNTs
0.3 wt% CNTs
0.1 wt% CNTs
0.01 wt% CNTs
PP
Heat Flow Exothermic Up (a.u.)
90 100 110 120 130 140 150 160 170 180 190
Temperature (°C)
c)
20 wt% P[LA]
12 wt% P[LA]
4 wt% P[LA]
2 wt% P[LA]
1.2 wt% P[LA]
0.4 wt% P[LA]
0.04 wt% P[LA]
PP
Heat Flow Exothermic Up (a.u.)
90 100 110 120 130 140 150 160 170 180 190
Temperature (°C)
d)
20 wt% P[LA]
12 wt% P[LA]
4 wt% P[LA]
2 wt% P[LA]
1.2 wt% P[LA]
0.4 wt% P[LA]
0.04 wt% P[LA]
PP
Heat Flow Exothermic Up (a.u.)
90 100 110 120 130 140 150 160 170 180 190
Temperature (°C)
e)
5 wt% CNT 4P[LA]
3 wt% CNT 4P[LA]
1 wt% CNT 4P[LA]
0.5 wt% CNT 4P[LA]
0.3 wt% CNT 4P[LA]
0.1 wt% CNT 4P[LA]
0.01 wt% CNT 4P[LA]
PP
Heat Flow Exothermic Up (a.u.)
90 100 110 120 130 140 150 160 170 180 190
Temperature (°C)
f)
5 wt% CNT 4P[LA]
3 wt% CNT 4P[LA]
1 wt% CNT 4P[LA]
0.5 wt% CNT 4P[LA]
0.1 wt% CNT 4P[LA]
0.3 wt% CNT 4P[LA]
0.01 wt% CNT 4P[LA]
PP
Heat Flow Exothermic Up (a.u.)
90 100 110 120 130 140 150 160 170 180 190
Temperature (°C)

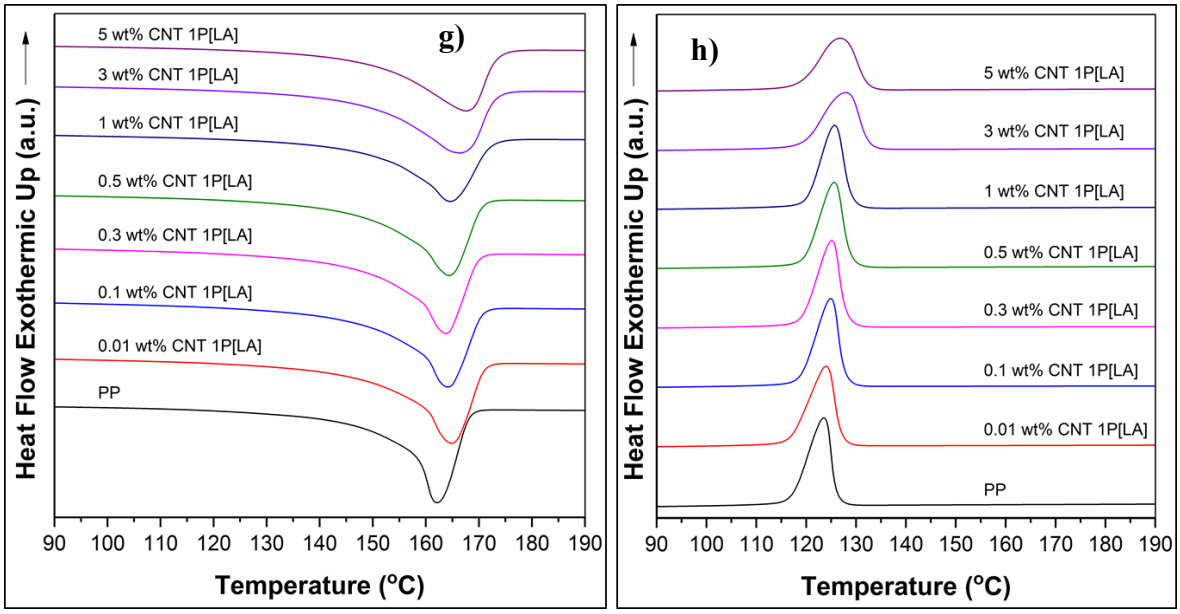

Figure 5.17 DSC a) heating curves and b) cooling curves for unfilled PP and composites of PP and MWCNTs, c) heating curves and b) cooling curves for unfilled PP and composites of PP and P[LA], e) heating curves and f) cooling curves for unfilled PP and composites of PP and P[LA] functionalised MWCNTs (1:4 MWCNTs:P[LA]) and g) heating curves and (h) cooling curves for unfilled PP and composites of PP and P[LA] functionalised MWCNTs (1:1 MWCNTs:P[LA]).

For composites of PP with P[LA] modified MWCNTs (figures 5.17 e) and f)), T_m and T_c of PP remained unchanged at 163 °C and 124 °C respectively, even after the addition of 5 wt% P[LA] modified MWCNTs. The lack of any observable change in T_m and T_c show the P[LA] influences the CNTs ability to nucleate PP. WAXD data (figure 5.18 b)) showed a decrease in X_c with increasing P[LA] modified MWCNT content, from ~ 37 % to ~ 28 %. Presumably, the coating of P[LA] on the CNT surface hinders nucleation and trans-crystallisation of PP. The strong nucleating effect of MWCNTs on polymers cooled after melt mixing has been reported previously and was observed for the un-modified MWCNTs in this study. The non-covalent functionalisation of MWCNTs prior to melt mixing appears to limit the nucleating effect commonly observed. The increase in T_c is directly related to the extent of MWCNT dispersion which promotes nucleation and favours crystal growth. The results suggest the P[LA] is coating and shielding the MWCNTs from the PP matrix and hence reduces nucleation of the MWCNTs.[30]

Table 5.4 Calorimetric data observed from DSC and crystalline content (X_c) determined by DSC and WAXD for PP and composites of PP, P[LA] and MWCNTs.

Sample	T_m [a] (°C)	T_c [b] (°C)	ΔH_m [c] (J/g)	ΔH_c [d] (J/g)	X_c [e] (%)		$FWHH_m$ [f] (°C)	$FWHH_c$ [g] (°C)
					DSC	WAXD		
PP	163	125	-105.5	104.5	51.0	36.6	12.0	5.9
0.01 wt% CNTs	161	122	-104.2	102.0	50.3	36.3	12.7	5.6
0.1 wt% CNTs	160	123	-101.5	98.8	49.0	31.2	12.8	5.2
0.3 wt% CNTs	161	125	-102.5	100.7	49.6	31.7	12.3	4.7
0.5 wt% CNTs	162	125	-103.0	101.6	50.0	32.9	10.7	4.2
1 wt% CNTs	163	125	-103.2	102.5	50.3	33.0	14.6	5.9
3 wt% CNTs	165	127	-101.9	101.1	50.7	31.3	15.3	7.7
5 wt% CNTs	167	129	-100.3	99.1	51.0	28.3	16.1	7.1
0.04 wt% P[LA]	163	124	-103.5	104.0	50.0	38.4	14.2	5.3
0.4 wt% P[LA]	164	124	-100.6	103.1	48.8	37.7	18.0	5.7
1.2 wt% P[LA]	164	124	-98.4	101.8	48.1	37.1	20.0	6.5
2 wt% P[LA]	164	123	-96.6	100.6	47.6	36.7	23.1	6.5
4 wt% P[LA]	163	125	-93.5	98.2	47.0	35.5	12.5	4.5
12 wt% P[LA]	162	124	-85.5	89.8	46.9	32.9	11.7	4.7
20 wt% P[LA]	162	124	-78.5	81.9	47.4	29.0	13.0	4.8
0.01 wt% CNT 4P[LA]	163	124	-105.2	103.3	50.8	37.0	12.7	5.2
0.1 wt% CNT 4P[LA]	162	123	-103.2	101.2	50.1	33.5	11.5	4.8
0.3 wt% CNT 4P[LA]	164	127	-103.3	101.3	50.6	32.2	13.0	5.2
0.5 wt% CNT 4P[LA]	164	127	-103.0	101.4	51.0	32.1	13.8	5.4
1 wt% CNT 4P[LA]	163	126	-101.7	99.9	51.7	28.3	15.2	5.7
3 wt% CNT 4P[LA]	163	125	-91.9	90.7	52.2	29.7	15.2	8.0
5 wt% CNT 4P[LA]	163	124	-82.8	82.9	53.3	28.3	15.8	7.2
0.01 wt% CNT 1P[LA]	165	124	-105.9	104.9	51.2	-	11.3	5.6
0.1 wt% CNT 1P[LA]	164	124	-103.5	102.8	50.0	-	10.3	5.0
0.3 wt% CNT 1P[LA]	163	125	-104.4	103.9	50.6	-	11.0	5.5
0.5 wt% CNT 1P[LA]	164	126	-102.5	102.0	49.7	-	12.0	5.6
1 wt% CNT 1P[LA]	163	125	-97.1	96.7	47.4	-	11.2	5.9
3 wt% CNT 1P[LA]	166	128	-100.1	99.4	49.9	-	14.1	7.5
5 wt% CNT 1P[LA]	167	127	-93.3	92.1	47.4	-	13.7	8.0

[a] T_m = melting temperature.
[b] T_c = crystallisation temperature.
[c] ΔH_m = melting enthalpy.
[d] ΔH_c = crystallisation enthalpy.
[e] X_c = degree of crystallinity computed from equation: $X_c = (\Delta H_m/(1-W_f)\Delta H_{100}) \times 100$ where W_f is the weight fraction of filler and ΔH_{100} is the melting enthalpy of a theoretically 100% crystalline PP (207.1 J/g).
[f] $FWHH_m$ = full width at half height of melting curve.
[g] $FWHH_c$ = full width at half height of cooling curve.

The addition of P[LA] to PP (figures 5.17 c) and d)) had little or no effect on the T_m and T_c of PP. X_c decreased by ~3% for the 20 wt% P[LA] filled PP from DSC and by ~ 9% from WAXD (figure 5.18 b)). Due to the increased loading of P[LA], the reduction in PP accounts for the decreased crystalline content.

From figures 5.17 g) and h) the melting and cooling traces for composites of PP and P[LA] modified MWCNTs with a 1:1 loading of MWCNTs:P[LA] are shown. The reduced quantity of P[LA] re-establishes the nucleating effect for PP with an increase in T_m and T_c of ~2-3 °C. The increase is less than that seen for un-modified MWCNTs but greater than P[LA] modified MWCNTs with a 4:1 loading of MWCNTs:P[LA], as expected. Interestingly, X_c decreased to similar levels as composites of P[LA] modified PP by DSC, even though the corresponding P[LA] loadings for composites of PP and P[LA] at 1:1 MWCNTs:P[LA] are significantly lower.

The normalised diffractograms shown in figure 5.18 show the evolution of a peak at about 18.6° which is associated with the (300) basal plane of the β-polymorph of PP. This peak is absent in the diffractrograms for the composite of PP and unmodified MWCNTs (figure 5.18 a)), confirming the co-crystallisation of PP with P[LA], as expected. Moreover, the intensity of the doublet centred around 25° increased with increasing P[LA] content, particular the peak at lower 2θ which is derived from the (301) basal plane of the β-polymorph of PP.

Figure 5.18 a) shows the WAXD diffractogram for composites of PP and MWCNTs. No significant changes in the PP crystalline structure in the presence of MWCNTs were observed. The reflections unambiguously show that PP remains primarily monoclinic (α-form) with a small presence of hexagonal (β-form). Table 5.4 shows the PP crystallinity decreased significantly however, such results as considered unreliable compared to those obtained from DSC because, DSC only measured the heat flow resulting from the crystalline regions whereas WAXD measures both crystalline and amorphous regions and accurately differentiating between crystalline and amorphous regions in the diffractograms is challenging. The contrasting values obtained for the crystalline content between DSC and WAXS can be explained by the increase in MWCNT loading in the composites. The crystalline content as measured by DSC has been compensated for CNT loading however, the measurements by WAXD have not been compensated for due to overlap of diffraction patterns between PP and MWCNTs. The MWCNTs are contributing to the amorphous halo and therefore, the results show a perceived decrease in total crystalline content. In addition,

it is difficult to accurately and unambiguously determine the cut off between the crystalline peaks and the amorphous halo and therefore, detailed conclusions based on crystallinity data obtained from WAXD will not be made in this thesis.

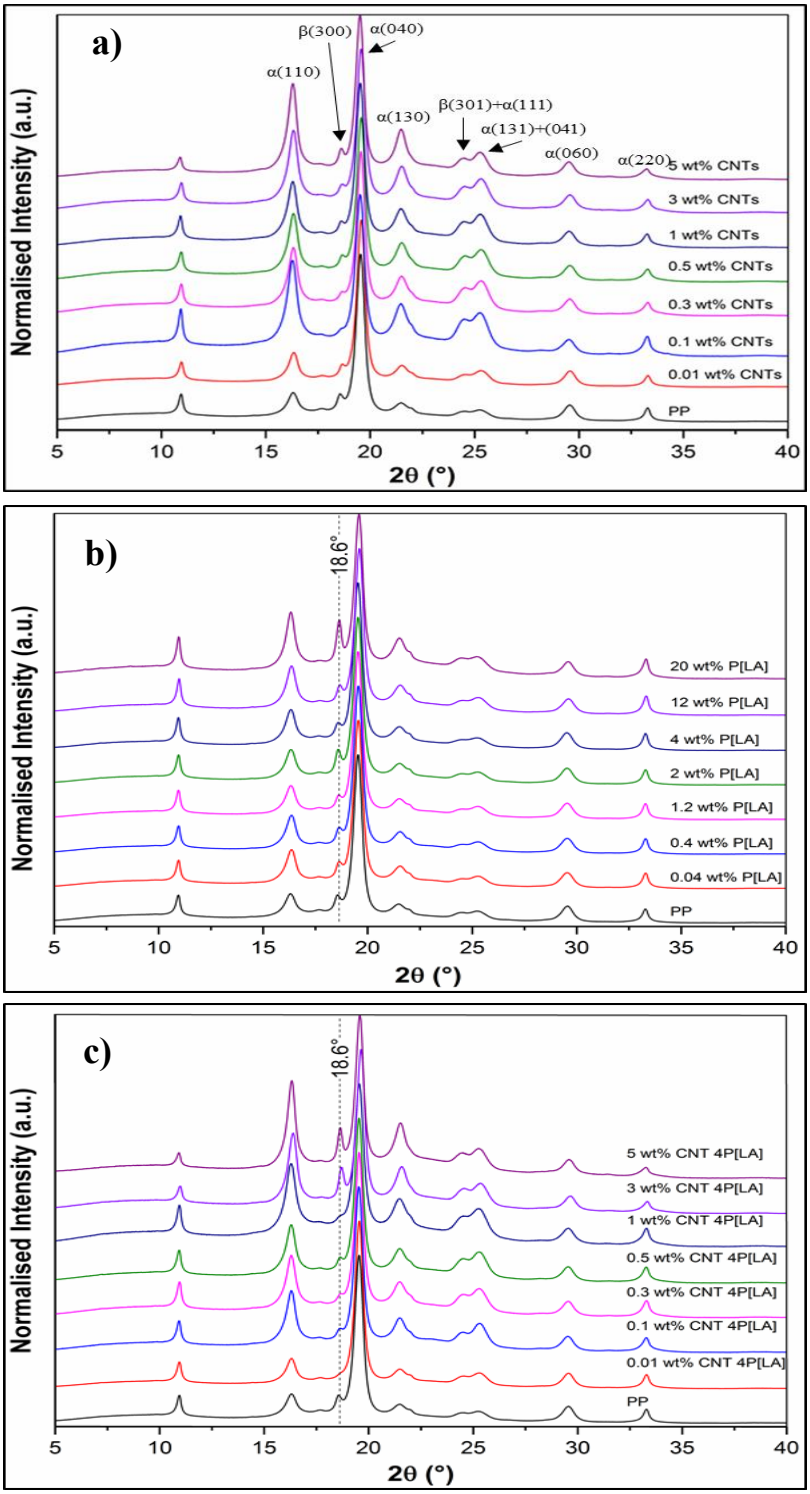

Figure 5.18 WAXD diffractograms for a) unfilled PP and composites of PP and MWCNTs, b) unfilled PP and for blends of P[LA] and PP and c) unfilled PP and for composites of PP and P[LA] modified MWCNTs in a 1:4 MWCNTs:P[LA].

The WAXD for blends of PP and P[LA] are shown in figure 5.18 b). The reflections indicate a predominate retention of monoclinic α polymorph however, an increase in the intensity of a reflection at 2θ = 18.6° corresponding to the hexagonal β(300) morphology suggests the P[LA] is a β nucleating agent at higher P[LA] content. It has been suggested in literature that the β polymorph has excellent thermal and mechanical performance (impact strength and toughness).[31] Additionally, the reflection at 2θ = 21.5° corresponding to the hexagonal β(301) morphology also increased in intensity confirming β nucleation of PP by P[LA]. The determination of β nucleation leads to the determination of shoulder process observed in the melting peaks in the DSC curves (figures 5.29-5.31). These shoulders can be attributed to the melting of the β-crystals in PP.[32]

The WAXD for composites of PP and P[LA] modified MWCNTs with 1:4 MWCNT:P[LA] are shown in figure 5.18 c) and unsurprisingly, the reflections at 2θ = 18.6° and 2θ = 21.5° corresponding to β(300) and β(301) respectively show a substantial increase in intensity. It appears the presence of P[LA] modified MWCNTs leads to an increase in the β-content compared to P[LA]-PP blends providing evidence for the non-covalent wrapping of P[LA] around MWCNTs which leads to increased β nucleation.

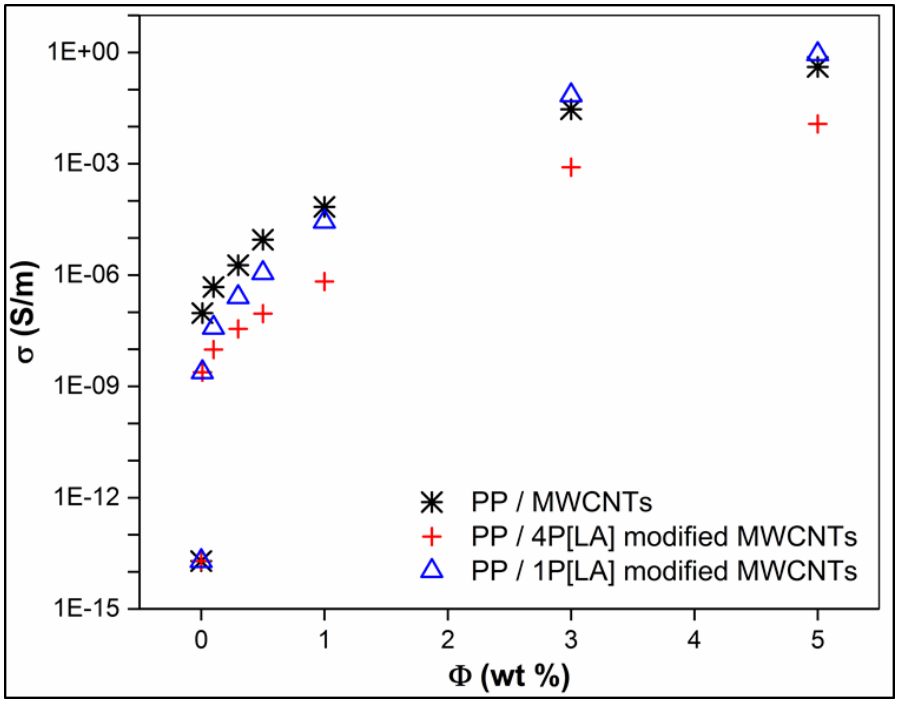

Figure 5.19 DC electrical conductivity (σ) as a function of MWCNT concentration (Φ) at a constant r.t. for unfilled PP, composites of PP and MWCNTs, composites of PP and P[LA] functionalised MWCNTs (1:4 MWCNT/P[LA]) and composites of PP and P[LA] functionalised MWCNTs (1:1 MWCNT/P[LA]).

The incorporation of electrically conducting MWCNTs into a polymer matrix can impart electrical conductivity into the composite and DC electrical conductivity can be used to explore the effective conduction mechanisms. It is well known that the use of MWCNTs as inter-particle charge carrier's trough tunnelling between particle interfaces is the dominant charge carrying mechanism in these types of polymer composites. A highly disperse and percolated network of CNTs will create a highly conductive composite material. If the CNTs are poorly dispersed and a network is not fully formed, there will only be a limited, if any, increase in conductivity as conduction paths are not present and the polymer matrices insulating nature is preserved.[33]

Stauffer and Aharony formulated the relationship between the measured electrical conductivity σ and carbon black concentration Φ which was expressed by the following equation;[33, 34]

$$\sigma \propto (\Phi - \Phi_C)^t, \text{ for } \Phi > \Phi_C \quad (5)$$

where Φ_C is known as the percolation threshold for the filler and t is a 'universal' critical index value predicted by classical theory of lattice percolation.[33, 34] Moreover, in this work, if the P[LA] prevents trans-crystallisation of PP on the surface of the MWCNTs but assisted MWCNT dispersion in the PP matrix via non-covalent interactions, then it is expected the DC conductivity of the composites of PP and P[LA] modified MWCNTs should not be significantly different than that obtained for the composites of PP and unmodified MWCNTs.

Figure 5.35 shows the DC (direct current) electrical conductivity at r.t. as a function of MWCNT weight fraction (Φ). Neat PP shows a very low conductivity of ~1 x 10^{-14} S/m due to the highly insulating nature of PP. An increase in electrical conductivity of composites is generally observed upon formation of a percolated MWCNT structure. A dramatic increase in conductivity was observed upon the addition of just 0.01 wt% MWCNTs to ~5 x 10^{-9} S/m. Further addition of functionalised and un-functionalised MWCNTs caused a small but not dramatic increase in conductivity due to only partial formation of a conductive CNT network. For the addition of 3 wt% MWCNTs, a further dramatic increase in conductivity was observed showing the complete formation of the CNT network at ~1 x10^{-1} S/m. When the CNT loading was increased further to 5 wt%, the improvement in conductivity became less prominent, as additional CNT would not significantly change the conducting network of the composite. The results indicate the possible presence of a double percolation threshold

at 0.01 wt% and 3 wt%. A high conductivity for the un-functionalised MWCNTs (3 – 5 wt%) in PP was observed suggesting good dispersion and good inter-particle charge carrier tunnelling.

For all loadings, the un-functionalised MWCNTs displayed an increased conductivity between 1 and 3 orders of magnitude compared to the 4P[LA] functionalised MWCNT composite. Interestingly, the presence of P[LA] appears to have improved dispersion but, also insulated the MWCNTs from each other and hindered the tunnelling between the MWCNTs. For the 1P[LA] functionalised MWCNT composite, the conductivity is marginally higher than that of un-functionalised MWCNTs for loadings greater than 3 wt%. However, for loadings lower than 3 wt%, the conductivity is lower than that of unfunctionalised MWCNTs but higher than 4P[LA] functionalised MWCNTs.

Interestingly, the DC electrical measurements suggests that any polymer used to non-covalently functionalise MWCNTs to improve dispersion of with a polymer matrix may also need to be electrically conducting in order to prevent the polymer from insulating the CNTs from each other, and thereby increasing tunnelling resistance between the CNTs. The use of P[LA] in a 1:4 ratio of MWCNTs:P[LA] appears to excessively hinder inter-particle tunnelling compared to using a 1:1 ratio which is able to improve dispersion and therefore conductivity, but not insulate the MWCNTs.

5.3 Conclusions

MWCNTs were non-covalently functionalised by surface wrapping of P[LA] synthesised using Cu(0)-mediated LRP and mixed with MWCNTs prior to the manufacture of composites of PP, MWCNTs and P[LA], (1:4 & 1:1 MWCNT:P[LA]). SEM and TEM images showed the MWCNTs were homogenously dispersed within the PP matrix with the addition of P[LA] appearing to improve the extent of MWCNT dispersion and distribution for a ratio of P[LA]:MWCNTs of 4:1. HRTEM also confirmed the P[LA] coats or wraps the MWCNTs. This is likely by a combination of CH-π interactions and physical wrapping of the polymer around the CNTs. Phase separation of P[LA] in composites of PP and P[LA] was not observed by SEM providing further evidence for the good compatibility and co-crystallisation effect between P[LA] and PP. In addition, rheological investigations confirmed the formation of a MWCNT network with a percolation threshold of about 0.5wt% for unmodified MWCNTs. This percolation threshold was reduced to ~0.3 wt% after

the addition of P[LA] modified MWCNTs, again in a 1:4 ratio indicating the P[LA] aided the dispersion of MWCNTs in the PP matrix and in agreement with SEM observations.

The E of PP was unaffected on addition of MWCNTs, but decreased significantly with loadings of P[LA] greater than 2 wt% however, the ε_B increased by over 50% upon addition of P[LA] modified MWCNTs in a ratio of 1:4, evidence that P[LA] has a plasticisation effect on PP. A common observation in the mechanical properties was a significant decrease in ε_B from ~270% for unfilled PP to ~5% after MWCNT addition due to the highly anisotropic behaviour of the MWCNT particles.

T_m and T_c increased by ~ 4 °C for a loading of 5 wt% unmodified MWCNTs, evidence the CNTs can nucleate PP. Upon functionalisation with P[LA], the P[LA] coating hinders MWCNT nucleation and PP crystallinity decreased at higher filler loadings. The addition of P[LA] resulted in a significant decrease in the T_g of PP, to between 15 and 25 °C. This is further evidence that P[LA] effectively reduced the T_g by plasticising PP.

WAXD results indicate the P[LA] is behaving as a α-nucleating agent though the observed increase in intensity of the peak at 2θ = 18.6° corresponding to the hexagonal α(300) for both composites of PP and P[LA] functionalised MWCNTs and composites of PP and P[LA]. However, the β-polymorph is also present in the composites with P[LA] modified MWCNTs which was induced by the inclusion of the P[LA] and not the MWCNTs. Also, there is evidence from the published literature for the β-polymorph being more prominent in low molecular weight (high MFR) PP, as used in this study.

The DC electrical conductivity of PP was increased by about 15 orders of magnitude on addition of 5wt% unmodified MWCNTs. However, the electrical conductivity of the composites of PP and P[LA] modified MWCNTs was only 2 orders of magnitude less than that obtained for composites with as received MWCNTs, across the composition range. The data suggests a double percolation effect for both sets of composites.

In summary, the addition of P[LA] to composites of MWCNTs and PP has shown increases in dispersion and the formation of a highly interconnected network of MWCNTs leading to enhancements in electrical conductivity. In addition, the P[LA] has shown to plasticise the PP through reductions in T_g. Clearly, the most significant changes in properties are observed with loading of P[LA] at a MWCNT:P[LA] ratio of 1:4 and a ratio 1:1 appears to have limited effect on the properties of the composite, except for high MWCNT and therefore P[LA] loadings. It would be interesting to explore the addition of P[LA] to

composites of GNPs and PP. As GNPs are a 2D graphitic nano-filler, they behave differently compared to MWCNTs and the addition of P[LA] could lead to dramatic improvements in mechanical, electrical and thermal properties of composite of PP and GNPs compared to composites of PP and unfunctionalised GNPs.

5.4 References

1. M. Supova, G. S. Martynkova and K. Barabaszova, *Sci. Adv. Mater.*, 2011, **3**, 1-25.
2. A. Chafidz, M. Kaavessina, S. Al-Zahrani and I. Ali, *Polym. Eng. Sci.*, 2014, **54**, 1134-1143.
3. S. Torres-Giner, A. Chiva-Flor and J. L. Feijoo, *Polym. Compos.*, 2016, **37**, 488-496.
4. S. H. Lee, E. Cho, S. H. Jeon and J. R. Youn, *Carbon*, 2007, **45**, 2810-2822.
5. G. Pandey and E. T. Thostenson, *Polym. Rev.*, 2012, **52**, 355-416.
6. M. H. Al-Saleh, *Mater. Des.*, 2015, **85**, 76-81.
7. H. Kim, A. A. Abdala and C. W. Macosko, *Macromolecules*, 2010, **43**, 6515-6530.
8. D. F. Wu, Y. R. Sun, L. Wu and M. Zhang, *J. Appl. Polym. Sci.*, 2008, **108**, 1506-1513.
9. K. Prashantha, J. Soulestin, M. F. Lacrampe, P. Krawczak, G. Dupin and M. Claes, *Compos. Sci. Technol.*, 2009, **69**, 1756-1763.
10. M. El Achaby, F. E. Arrakhiz, S. Vaudreuil, A. E. Qaiss, M. Bousmina and O. Fassi-Fehri, *Polym. Compos.*, 2012, **33**, 733-744.
11. D. Bikiaris, *Materials*, 2010, **3**, 2884-2946.
12. R. T. Zeng, W. Hu, M. Wang, S. D. Zhang and J. B. Zeng, *Polym. Test.*, 2016, **50**, 182-190.
13. N. G. Sahoo, S. Rana, J. W. Cho, L. Li and S. H. Chan, *Prog. Polym. Sci.*, 2010, **35**, 837-867.
14. A. E. Daugaard, K. Jankova and S. Hvilsted, *Polymer*, 2014, **55**, 481-487.
15. T. Fujigaya and N. Nakashima, *Sci. Tech. Adv. Mater.*, 2015, **16**, 1-21.

16. C. McClory, T. McNally, M. Baxendale, P. Pötschke, W. Blau and M. Ruether, *Eur. Polym. J.*, 2010, **46**, 854-868.
17. B. Krause, M. Mende, P. Pötschke and G. Petzold, *Carbon*, 2010, **48**, 2746-2754.
18. B. Mayoral, G. Garrett and T. McNally, *Macromol. Mater. Eng.*, 2014, **299**, 748-756.
19. B. Mayoral, J. Lopes and T. McNally, *Macromol. Mater. Eng.*, 2014, **299**, 609-621.
20. G. Moad, G. Li, R. Pfaendner, A. Postma, E. Rizzardo, S. Thang and H. Wermter, in *Controlled/Living Radical Polymerization*, ed. K. Matyjaszewski, American Chemical Society, 2006, vol. 944, ch. 35, pp. 514-532.
21. T. McNally and P. Pötschke, *Polymer–carbon nanotube composites: preparation, properties and applications*, Woodhead Publishing Ltd, Cambridge, UK, 2011.
22. C. C. Teng, C. C. M. Ma, Y. W. Huang, S. M. Yuen, C. C. Weng, G. H. Chen and S. F. Su, *Compos. Part A*, 2008, **39**, 1869-1875.
23. A. A. Koval'chuk, V. G. Shevchenko, A. N. Shchegolikhin, P. M. Nedorezova, A. N. Klyamkina and A. M. Aladyshev, *Macromolecules*, 2008, **41**, 7536-7542.
24. J. Gupta, D. J. Keddie, C. Y. Wan, D. M. Haddleton and T. McNally, *Polym. Chem.*, 2016, **7**, 3884-3896.
25. M. Micusik, M. Omastova, I. Krupa, J. Prokes, P. Pissis, E. Logakis, C. Pandis, P. Potschke and J. Pionteck, *J. Appl. Polym. Sci.*, 2009, **113**, 2536-2551.
26. J. N. Coleman, U. Khan and Y. K. Gun'ko, *Adv. Mater.*, 2006, **18**, 689-706.
27. R. Kotsilkova, E. Ivanov, E. Krusteva, C. Silvestre, S. Cimmino and D. Duraccio, *J. Appl. Polym. Sci.*, 2010, **115**, 3576-3585.
28. B. Mayoral, P. R. Hornsby, T. McNally, T. L. Schiller, K. Jack and D. J. Martin, *R. Soc. Chem. Adv.*, 2013, **3**, 5162-5183.
29. E. Logakis, E. Pollatos, C. Pandis, V. Peoglos, I. Zuburtikudis, C. G. Delides, A. Vatalis, M. Gjoka, E. Syskakis, K. Viras and P. Pissis, *Compos. Sci. Technol.*, 2010, **70**, 328-335.

30. R. Cardinaud and T. McNally, *Eur. Polym. J.*, 2013, **49**, 1287-1297.
31. F. Luo, K. Wang, N. Y. Ning, C. Z. Geng, H. Deng, F. Chen, Q. Fu, Y. Y. Qian and D. Zheng, *Polym. Adv. Technol.*, 2011, **22**, 2044-2054.
32. B. Zhang, J. B. Chen, X. L. Zhang and C. Y. Shen, *J. Appl. Polym. Sci.*, 2011, **120**, 3255-3264.
33. S. J. Chin, S. Vempati, P. Dawson, M. Knite, A. Linarts, K. Ozols and T. McNally, *Polymer*, 2015, **58**, 209-221.
34. D. Stauffer and A. Aharony, *Introduction to percolation theory*, Taylor & Francis, London, 1994.

Chapter 6 Results and Discussion III

Synthesis and characterisation of composites of PP and PP filled with graphene nano-platelets (GNPs) functionalised by poly(lauryl acrylate) P[LA]

6.1 Introduction

The use of 1D and 2D graphitic fillers for polymers is currently of great interest. The unique mechanical, electrical, optical and thermal properties of various 1D and 2D carbon based materials such as carbon nanotubes (CNTs), diamond, fullerene and graphene have attracted enormous technological interest.[1] In addition to CNTs, graphene is also of a particular interest due to its exceptional thermal, electrical and mechanical properties as well as high surface area and aspect ratio.[1, 2] It is expected the incorporation of GNPs into polymers such as polypropylene (PP) *via* melt blending will lead to functional nanocomposites with enhanced properties, such as improvements in mechanical properties, particularly stiffness, strength and electrical conductivity.[1] The sp^2 hybridized structure of graphene has displayed exceptional levels of stiffness and strength, close to the theoretical limit.[3] In addition, it is possible to influence the crystal nucleation and microstructure of the nanocomposite by the addition of GNPs. However, an examination of the literature reveals simple melt mixing is not sufficient to homogenously disperse these fillers. Interfacial adhesion with the polymer matrix is poor and the orientation of the graphene sheets within the polymer matrix is random and not controlled.[1, 4-12] Interfacial interactions are determinative to the efficiency of reinforcement.[2] Young, Kinloch and co-workers have investigated the fundamental mechanisms of reinforcement of composites of polymers and graphene-based materials. They investigated a variety of factors such as the lateral dimensions of GNPs, the number of layers, surface chemistry and orientation. They concluded such nanomaterials follow the rules of continuum mechanics formulated for macroscopic fibre-reinforced composites with the best properties found for large, well-aligned, few-layer GNPs with good interfacial adhesion.[3] For example, Kinloch *et al*. clearly demonstrated that GNP flakes with large lateral dimensions lead to higher values for Young's modulus compared to smaller flakes within a PP matrix.[13]

In chapters 4 and 5 the incorporation of MWCNTs in to PP to improve the properties of PP and how the use of P[LA] as a compatibiliser can be used to enhance MWCNT

dispersion and interfacial adhesion was described. To further explore the use of P[LA] as a compatibiliser, P[LA] was used to compatibilise composites of GNPs and PP. The present study is concerned with the effect of GNP addition to PP upon PP structure and properties and the effectiveness of P[LA] as a compatibiliser.

PP was chosen as the polymer matrix due to its ease of processing, light-weight, low cost and high recyclability. However, limitations such as high mould shrinkage, low stiffness and poor cold temperature impact toughness reduce its possible applications. GNPs are typically added to PP to improve properties such as electrical, thermal and mechanical (including, tensile, flexural, impact and fracture toughness).[14] The GNPs used in the following work were kindly donated by Thomas Swan & Co (mechanical grade) and were produced based on the high shear exfoliation of graphite flakes. The process is similar to the process published by Coleman *et al*.[15] In addition to producing blends of PP and GNPs, P[LA] was used to further improve the dispersion and interfacial interaction between the PP matrix and the filler as first tested with MWCNTs (Chapter 5). Composites of PP, GNPs, and P[LA] were blended using twin-screw extrusion and injection moulded into disks (rheology and WAXS), tensile bars (static-mechanical) and bars (dynamic-mechanical and electrical). An idealistic representation of P[LA] non-covalently functionalising GNPs is displayed in Figure 6.1 is the initial hypothesis was that the P[LA] will reside on the surface of the graphene and promote exfoliation as well as improve the interfacial adhesion with the PP matrix. The GNPs were premixed with P[LA] by mechanical mixing prior to mixing with powdered PP before being melt compounded using twin-screw extrusion and characterised.

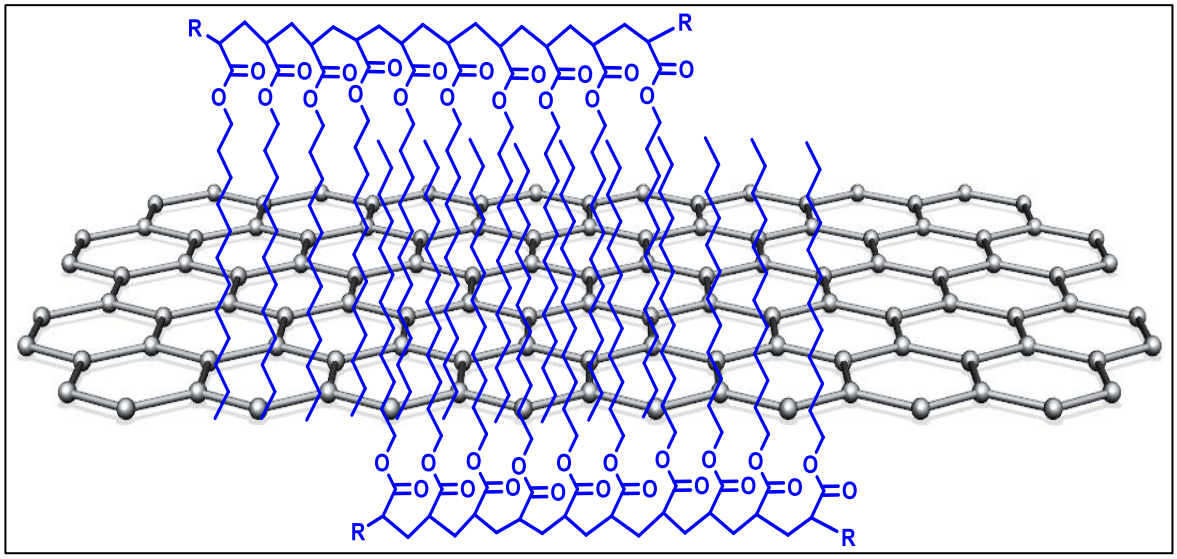

Figure 6.1 Schematic representation of P[LA] interacting with a graphene sheet.

Table 6.1 Composite Formulation.

Composite composition (wt %)	Nomenclature
PP(100)	PP
PP(99.9) / GNPs(0.1)	0.1 wt% GNPs
PP(99.7) / GNPs(0.3)	0.3 wt% GNPs
PP(99.5) / GNPs(0.5)	0.5 wt% GNPs
PP(99.25) / GNPs(0.75)	0.75 wt% GNPs
PP(99) / GNPs(1)	1 wt% GNPs
PP(97) / GNPs(3)	3 wt% GNPs
PP(95) / GNPs(5)	5 wt% GNPs
PP(99.5) / P[LA] 10K(0.4) / GNPs(0.1)	0.1 wt% GNPs P[LA]
PP(98.5) / P[LA] 10K(1.2) / GNPs(0.3)	0.3 wt% GNPs P[LA]
PP(97.5) / P[LA] 10K(2) / GNPs(0.5)	0.5 wt% GNPs P[LA]
PP(96.25) / P[LA] 10K(3) / GNPs(0.75)	0.75 wt% GNPs P[LA]
PP(95) / P[LA] 10K(4) / GNPs(1)	1 wt% GNPs P[LA]
PP(85) / P[LA] 10K(12) / GNPs(3)	3 wt% GNPs P[LA]
PP(75) / P[LA] 10K(20) / GNPs(5)	5 wt% GNPs P[LA]

In the first instance, blends of GNPs and PP were prepared, i.e. without P[LA]. Subsequently, the GNPs were mixed with P[LA] in a 1:4 ratio GNPs:P[LA] in an attempt to understand the effect of P[LA] compatibilising PP and GNPs. Table 6.1 lists the compositions of PP, GNPs and P[LA] used to produce the composites. For clarity, the composite labelled 5 wt% GNPs P[LA] contains 5 wt% GNP loading and 20 wt% P[LA] loading.

6.2 Characterisation of GNPs

Typically, graphene is synthesised by oxidative exfoliation of graphite to produce graphene oxide (GO). The GO is subsequently reduced to produce few-layer graphene however, such forms of graphene are typically littered with defects. An alternative approach, sonication, provides mechanical energy to exfoliate the graphite in stabilizing solvents. However, the scalability of sonication as an energy source is limited for commercial use.[15] The manufacturers of this particular graphene employ the use of high-shear mixing coupled with stabilising liquids without the need for prior treatment with solvent for intercalation to weaken the inter-layer binding strength. The synthesis process involves using high shear

mixer with a closely spaced (~100 μm) rotor/stator combination.[15] The manufactures claim the GNPs are substantially undamaged and non-oxidised by the high-shear exfoliation approach. There are low non-carbon contaminates such as oxygen and transition metals.

6.2.1 Electron microscopy of GNPs

Figure 6.2a-b displays the SEM micrographs of un-functionalised GNPs at various magnifications. Figure 6.2a confirms the presence of multi-layer flakes and appear to be generally homogenous in size distribution. Figure 6.2b displays the flakes have a large number of layers (>10) which confirms the graphene falls into the graphene nanoplatelet (GNP) range rather that the few-layer graphene which is usually reserved for electronic applications. The GNP flake diameters appear to be in the order of 10 μm. Figure 6.2c-f displays HRTEM at various magnifications of the GNP used. The TEM images present the GNPs vary in size and distribution. The Elicarb® are quoted to have lateral sizes of <5 μm. The sheet edges appear to be highly varied with some GNPs displaying smooth and rounded edges (figure 6.2c) and other samples displaying a highly crumpled and folded structure (figure 6.2e). The folding graphene sheets into ‘scrolls’ is a common observation and is as a result of their requirement to minimise internal energy. The individual graphene layers edge-on can be seen in figure 6.2f.

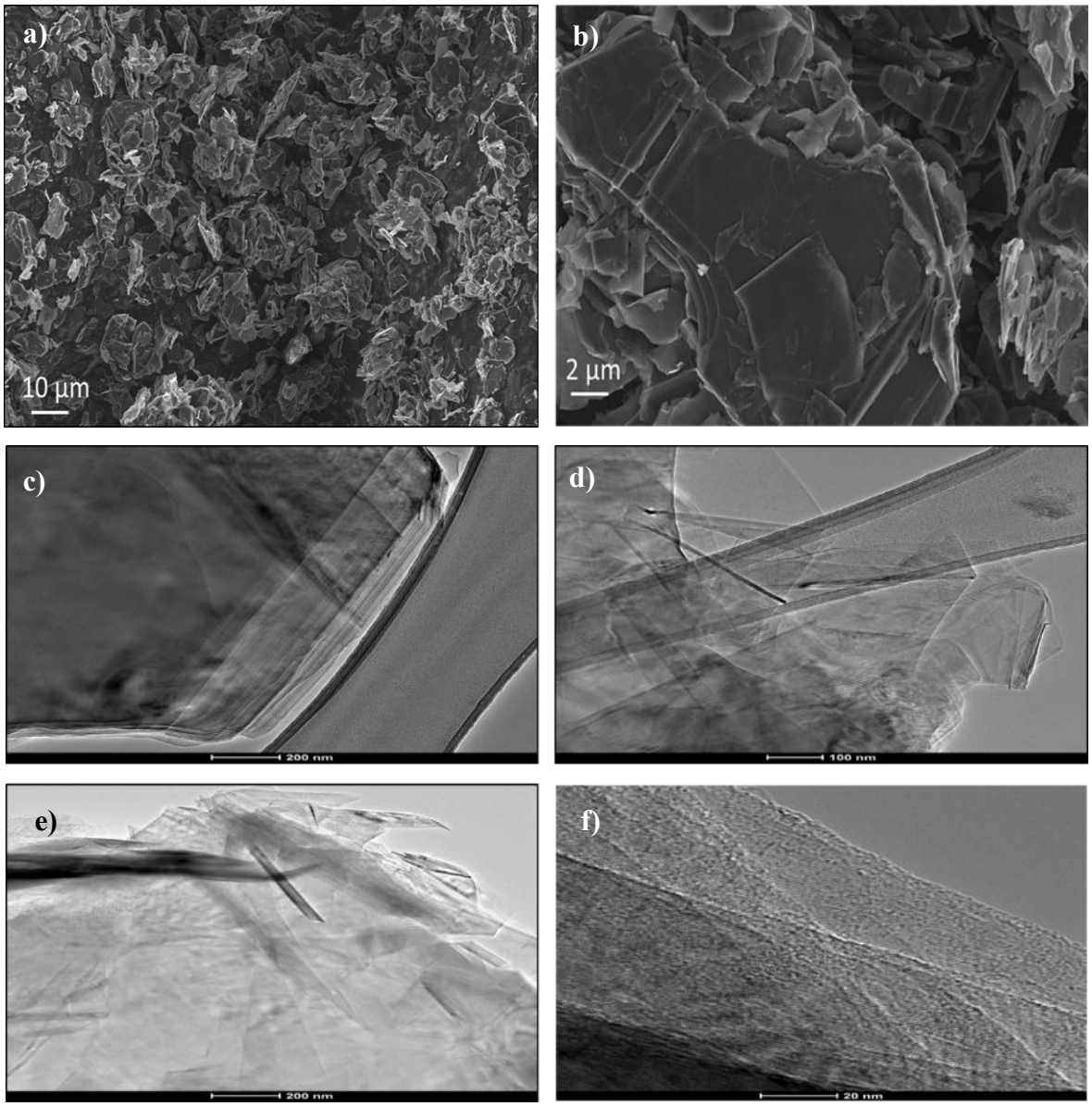

Figure 6.2 SEM micrographs of GNPs at a) x 2k, and b) x 10k magnification. HRTEM images of un-functionalised GNPs at c) x 28.5k, d) x 46k, e) x 28.5k, and f) x 310k magnification.

6.2.2 Raman spectroscopy of GNPs

Figure 6.3 displays the Raman spectra for un-functionalised GNPs. As discussed in chapter 2, I_D/I_G ratio can provide an indication of the quality of the GNPs. The D-band (1349.2 cm^{-1}) is a measure of the disorder or defects present in the graphene and the G-band (1581.0 cm^{-1}) is vibrational in-plane stretching of the C-C bonds. I_D/I_G = 0.12 which demonstrates the GNPs are of high quality due to the low quantity of defects. It is expected

for defects to be present which are mostly as a result of incomplete 'dangling' bonding on the sheet edges. The *G'* band (2718.8 cm-1) is consistent with that of multi-layer graphene.[3]

The *G*-band is associated with the doubly degenerate (iTO and LO) phonon mode with an E_{2g} symmetry. The band is a normal first order scattering process where as the *D*-band and the *G'* bands are second order processes. The *D*-band is as a result of two scattering processes consisting of one elastic scattering event caused by defects in the graphitic crystal and one inelastic event caused by absorbing or emitting a phonon. In the case of the *G'* band, it is also a result of two scattering events which are both inelastic involving two phonons.[16] The line shape of the *G'* band can be used to understand the multi-layer structure of graphene(s). The presence of a shoulder to the left the *G'*-band indicated the GNPs are of a multi-layer structure (>3 layers) which is consistent with the electron microscopy images, see figure 6.1.

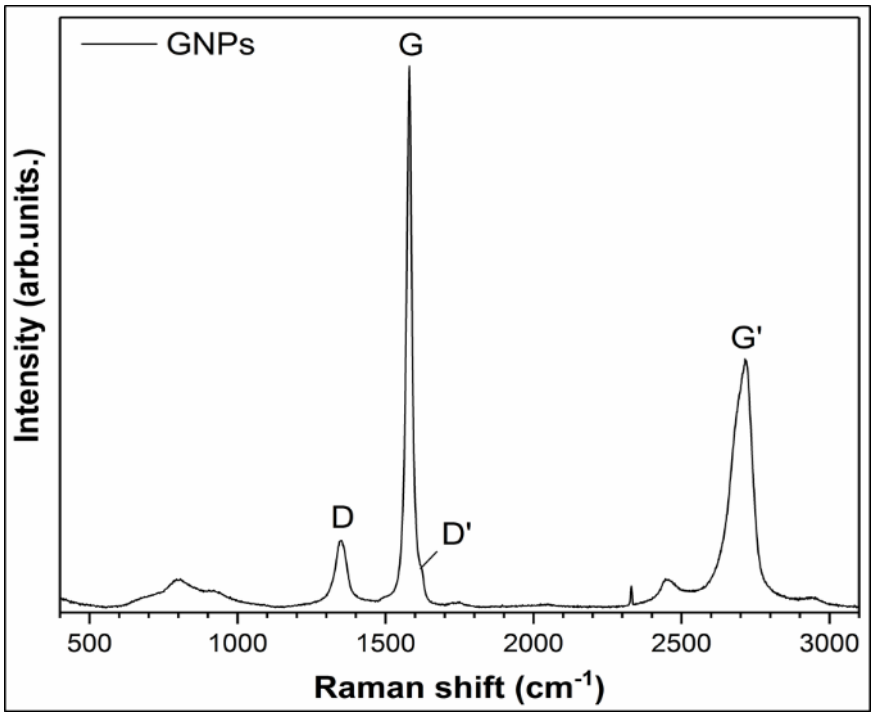

Figure 6.3 Raman spectra for the GNPs used in this study.

6.2.3 X-ray photoelectron spectroscopy of GNPs

From the XPS spectra for un-functionalised GNPs, the survey scan (figure 6.4a) distinctly displays the presence of two main elements, carbon (C) and oxygen (O) along with trace amounts of sodium (Na). The Na is present with an atomic % (at%) of <1 % which displays, we assume, that most but not all of the surfactant used during the high shear exfoliation synthesis procedure was removed.[15] In addition, the survey scan displays the presence of 9 at% O and 90 at% C. The presence of significant quantities of O is consistent with observations obtained from Raman spectroscopy. The Raman confirmed the presence of 12% defects where the XPS indicates the presence of 10% oxygen defects. It can be concluded the defects present are in the form of oxygen based functional groups such as, alcohols and carboxylic acids. It is expected for the concentration of oxygen defects to be concentrated on the sheet edges. The deconvolution of the C1s peak (figure 6.4b) once again confirmed the presence of oxygen based functional groups. Interestingly, the peak shape of the sp^2 C=C and the lack of a sp^3 C-C peak confirms 90% of the carbon atoms are in fact sp^2 hybridized and the sheets are graphene. This particular result is important because, if there was a high concentration of sp^3 hybridized defects in the graphene sheets, then the material would be ineffective at being thermally and electrically conductive and the mechanical properties lower than expected. Most of the defects on the sheets edges are in the form of hydroxyl groups and carboxylic acids as displayed in figure 6.4c. The result confirms the high shear exfoliation synthesis process results in mild oxidation due to the lack of higher order oxidation groups such as ketones and esters.

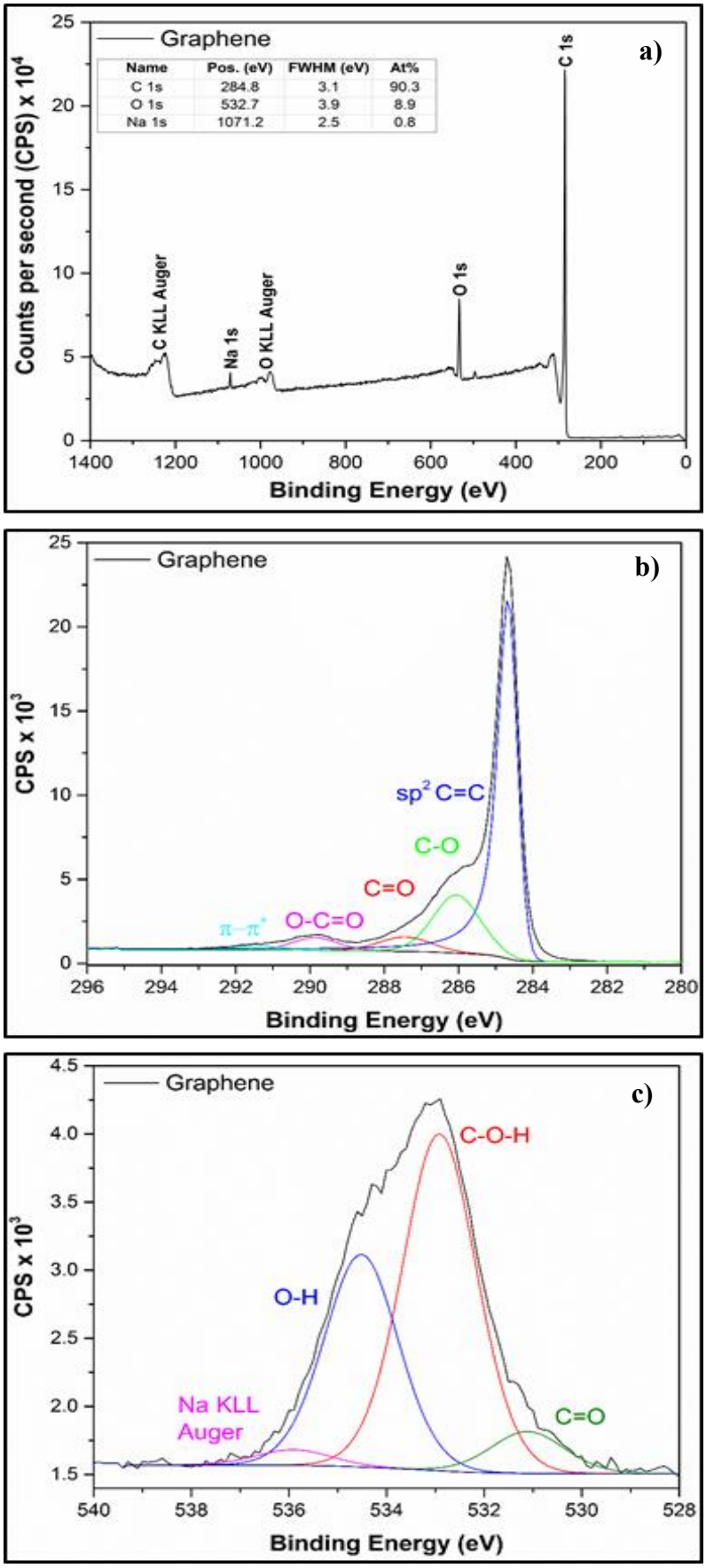

Figure 6.4 XPS spectra of GNPs, a) survey scan, b) Carbon 1s and c) Oxygen 1s.

6.3 Characterisation of composites of PP, GNPs and poly(lauryl acrylate) P[LA]

SEM was used to examine the microstructure of the composites. Figure 6.5a and b display the presence of the GNPs in the PP matrix after cryo-fracturing the samples. The cryo-fractured surface is typical of that of a polymer which is ductile at room temperature determined by the smooth surfaces and randomly orientated ridges, peaks and troughs. For the composites of PP with 1 wt% GNP, the GNP edges can be seen protruding from the fractured surface. The white arrows display the positions of some of the GNPs sheet edges protruding from the fractured surface. The GNPs appear to be randomly distributed with no apparent preferred orientation and appear to be poorly dispersed due to the low quantities of GNPs observed. The GNP lateral dimensions do not appear to be affected by the high shear mixing process. Similar results for poor dispersion were obtained by Kalaitzidou *et al*.[7] when they dispersed exfoliated GNPs within PP *via* melt blending.

Figure 6.5e-h displays the cryo-fractured surfaces of P[LA]-functionalised GNPs dispersed in the PP matrix. Figure 6.5e and f present low magnification images where large quantities of GNP flakes can be seen at the cryo-fractured surface which is in contrast with the un-functionalised GNP composites which display lower quantities of GNPs on the fracture surface. Furthermore, the higher magnification images, figures 6.7c and d depict the PP surface to be rougher compared to the un-functionalised GNP composites suggesting the presence of GNPs. A possible reasoning behind the increased dispersion of the composites of PP and P[LA] functionalised GNPs compared to PP and un-functionalised GNPs is that the P[LA] adsorbs onto the surface of the GNPs during the pre-mixing phase. The pre-mixing causes the GNPs to disperse and the combined compatibilisation and mixing in the extruder is effective at separating GNP agglomerates.

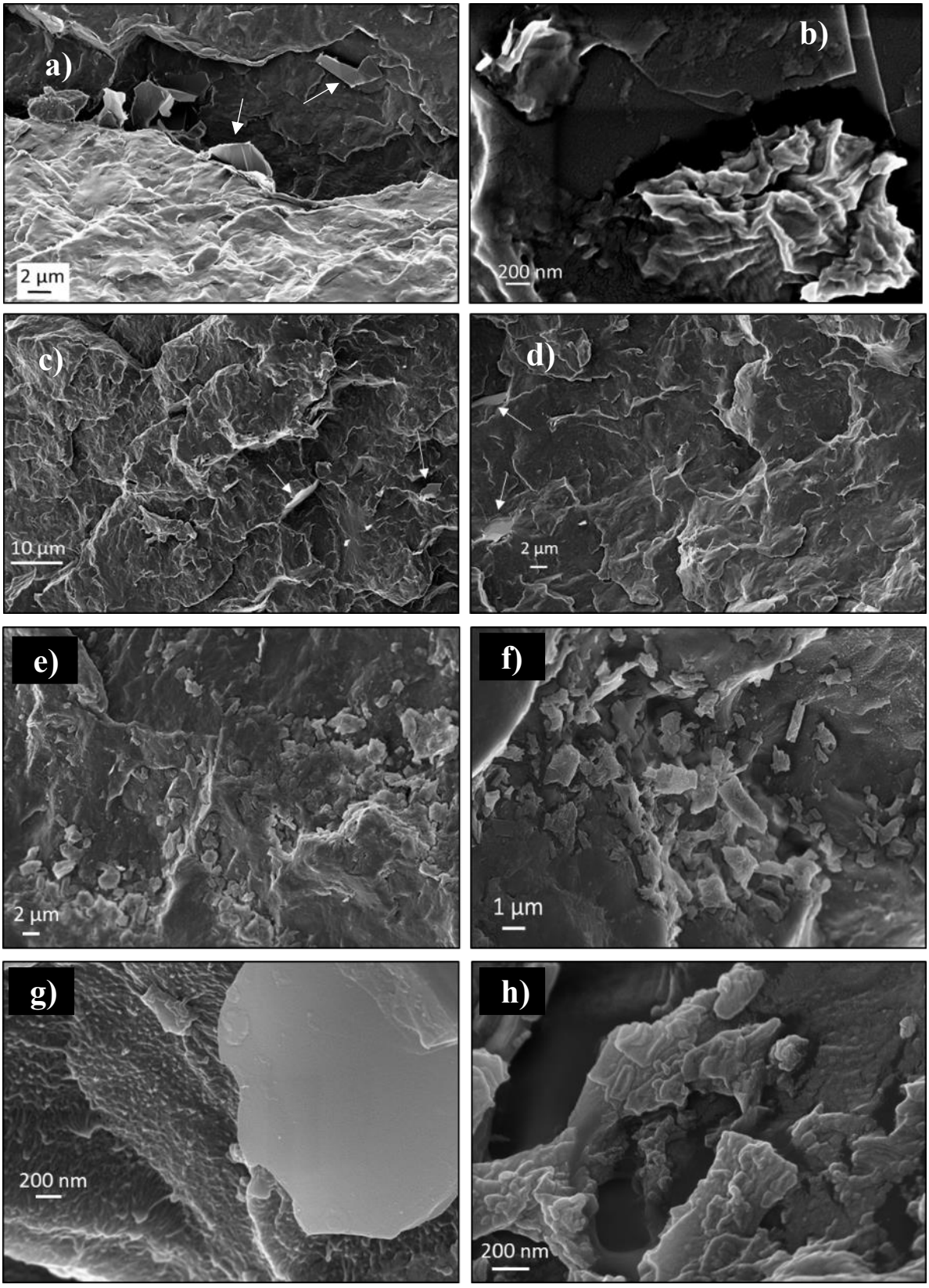

Figure 6.5 SEM micrographs of composites of, PP and GNPs (1 wt% GNPs) at a) x 8k, b) x 80k, c) x 3k and d) x 5k magnification and composites of PP and P[LA] functionalised GNPs (1 wt% GNPs P[LA]) at e) x 5k, f) x 15k, g) x 80k and h) x 120k magnification.

Figure 6.6a and b present the stress vs strain curves for composites of PP and GNPs (figure 6.6a) and for composites of PP and 4P[LA] functionalised 1GNPs (figure 6.6b) for different levels of GNP loading. For the composites of PP and 4P[LA] functionalised GNPs, the ratio of P[LA] to GNP was fixed at 4:1, P[LA]:GNPs with the wt% loading referring to the GNP loading and not the combined P[LA] functionalised GNP loading. For example, the sample 5 wt% GNPs P[LA] contains 5 wt% GNPs and 20 wt% P[LA] as listed in table 6.1. The stress vs strain curves were used to determine the Young's modulus (*E*) (initial gradient of elastic region – strain range of 0.05% and 0.25% – figure 6.7a), the tensile strength (σ) (maximum stress before plastic deformation – figure 6.7b), the strain at yield point (ε_y) (the strain at maximum stress before plastic deformation – figure 6.7c) and the strain at break (ε_B) (figure 6.7d). The values for these parameters are tabulated in table 6.2 and graphically represented in figure 6.7a-d.

E remained unchanged with increasing loading of un-functionalised GNPs. There is a small increase in stiffness of the composite from 3.0 GPa to 3.3 GPa for a 5 wt% loading of un-functionalised GNPs. The result suggests these loadings are too small to achieve a significant increase in stiffness as percolation is not achieved for loadings below 5 wt%. The possible reasons for poor mechanical performance are poor dispersion, weak interfacial adhesion with the PP matrix and poor-quality GNPs, i.e. GNPs with low aspect ratio, high number of layers and a high defect density. Work by Ahmad *et al*. presented the characterisation of composites of PP and GNPs. They used GNPs supplied by XG sciences and processed them with a similar grade of PP using similar processing methods used in this study (twin screw extrusion).[3] They achieved an increase in *E* from 1.3 GPa to over 2.0 GPa suggesting the GNP type is the cause for the lack of increase in *E* rather than poor dispersion.[3]

σ decreased from 41.6 MPa for neat PP to ~ 35 MPa upon addition of un-functionalised GNPs. The decrease in σ appears to be independent of GNP loading suggesting the GNPs are disrupting the crystal morphology of the PP. A combination of DSC and XRD was used to study the changes in crystal morphology. The decrease in σ upon addition of un-functionalised GNPs is due to the poor adhesion between the GNPs and PP. The result is in agreement with that reported by Ahmad *et al*.[3]

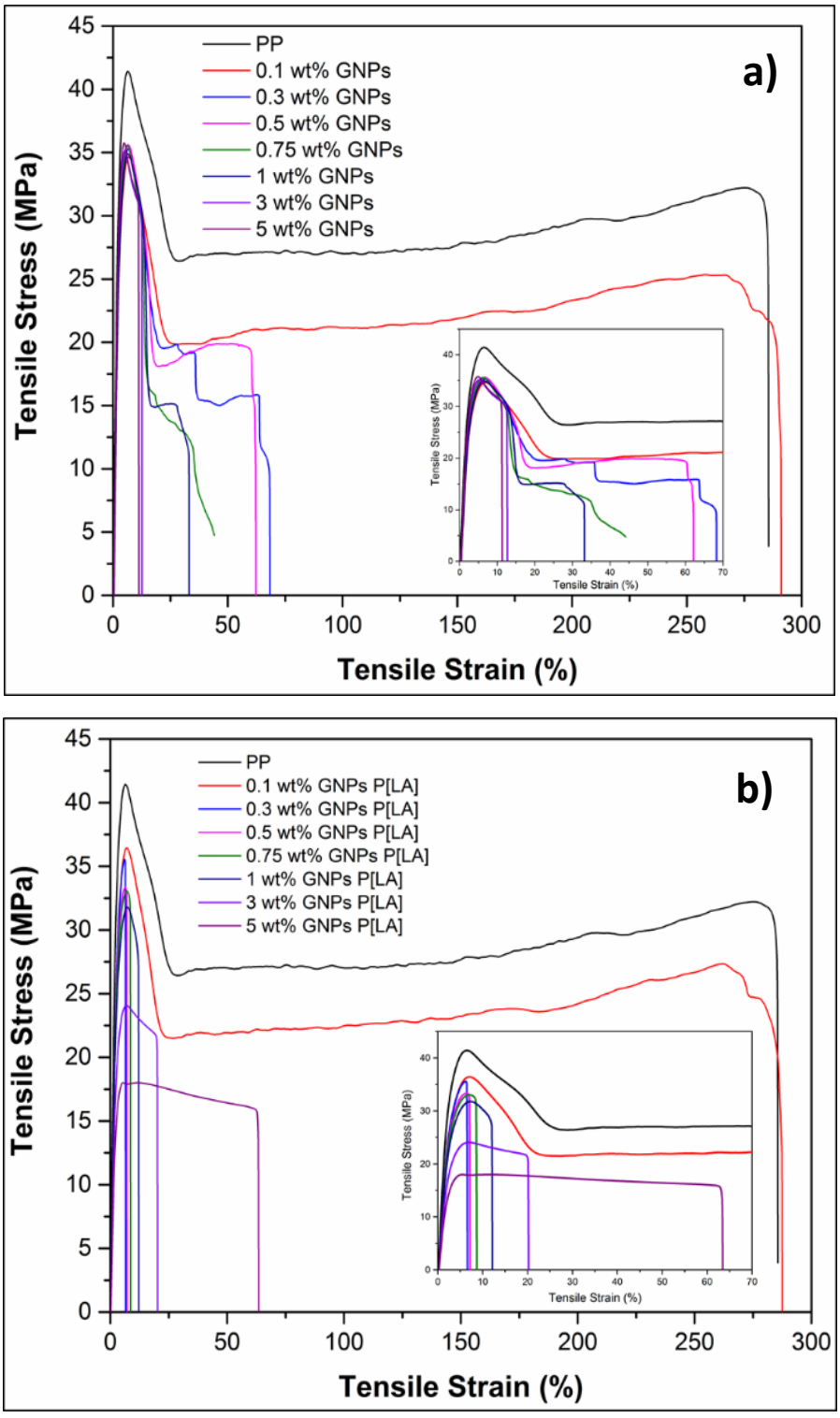

Figure 6.6 Stress vs strain curves for unfilled PP and composites of a) PP and GNPs and b) PP and P[LA] functionalised GNPs.

Table 6.2 Change in mechanical properties for PP and composites of PP, GNPs and P[LA].

Sample (wt%)	Young's modulus (GPa)	↑ GPa (%)	Tensile Strength (MPa)	↑ MPa (%)	Yield Strain (%)	↑ MPa (%)	Strain at break (%)	↑ % (%)
PP	3.0 ± 0.2		41.6 ± 0.3		7.7 ± 1.2		285 ± 40	
0.1 wt% GNPs	2.9 ± 0.2	-3.3	35.1 ± 1.2	-15.6	8.0 ± 1.0	3.8	330 ± 38	15
0.3 wt% GNPs	3.0 ± 0.3	0.0	35.3 ± 0.7	-15.1	8.4 ± 0.8	9.1	34 ± 23	-88
0.5 wt% GNPs	2.8 ± 0.2	-6.6	35.5 ± 0.4	-14.7	8.5 ± 0.2	10.4	77 ± 23	-73
0.75 wt% GNPs	3.0 ± 0.4	0.0	34.1 ± 2.0	-18.0	7.2 ± 1.6	-6.5	23 ± 11	-92
1 wt% GNPs	3.0 ± 0.2	0.0	34.7 ± 0.7	-16.6	7.7 ± 0.6	0.0	14 ± 11	-95
3 wt% GNPs	2.8 ± 0.4	-6.6	31.8 ± 4.1	-23.6	5.6 ± 2.3	-27	10 ± 2.4	-97
5 wt% GNPs	3.3 ± 0.3	10	34.8 ± 0.7	-16.3	5.9 ± 0.5	-23	10 ± 1.0	-97
0.1 wt% GNPs P[LA]	2.5 ± 0.2	-17	35.9 ± 0.7	-13.7	9.0 ± 0.6	17	297 ± 62	4
0.3 wt% GNPs P[LA]	2.6 ± 0.3	-13	30.7 ± 7.7	-26.2	5.0 ± 2.9	-35	5.0 ± 2.5	-98
0.5 wt% GNPs P[LA]	2.5 ± 0.2	-17	28.0 ± 6.3	-32.7	7.4 ± 1.9	-3.9	5.7 ± 4.9	-98.0
0.75 wt% GNPs P[LA]	2.5 ± 0.3	-17	29.0 ± 5.0	-30.3	7.6 ± 2.1	-1.3	7.9 ± 2.5	-97.2
1 wt% GNPs P[LA]	2.5 ± 0.1	-17	30.9 ± 1.3	-25.7	8.4 ± 1.0	9.1	37 ± 25	-87.0
3 wt% GNPs P[LA]	2.0 ± 0.1	-33	24.4 ± 0.8	-41.3	7.5 ± 0.8	-2.6	11 ± 5.4	-96.1
5 wt% GNPs P[LA]	1.7 ± 0.1	-43	18.3 ± 0.7	-56.0	12.2 ± 8.1	58	55 ± 28	-80.1

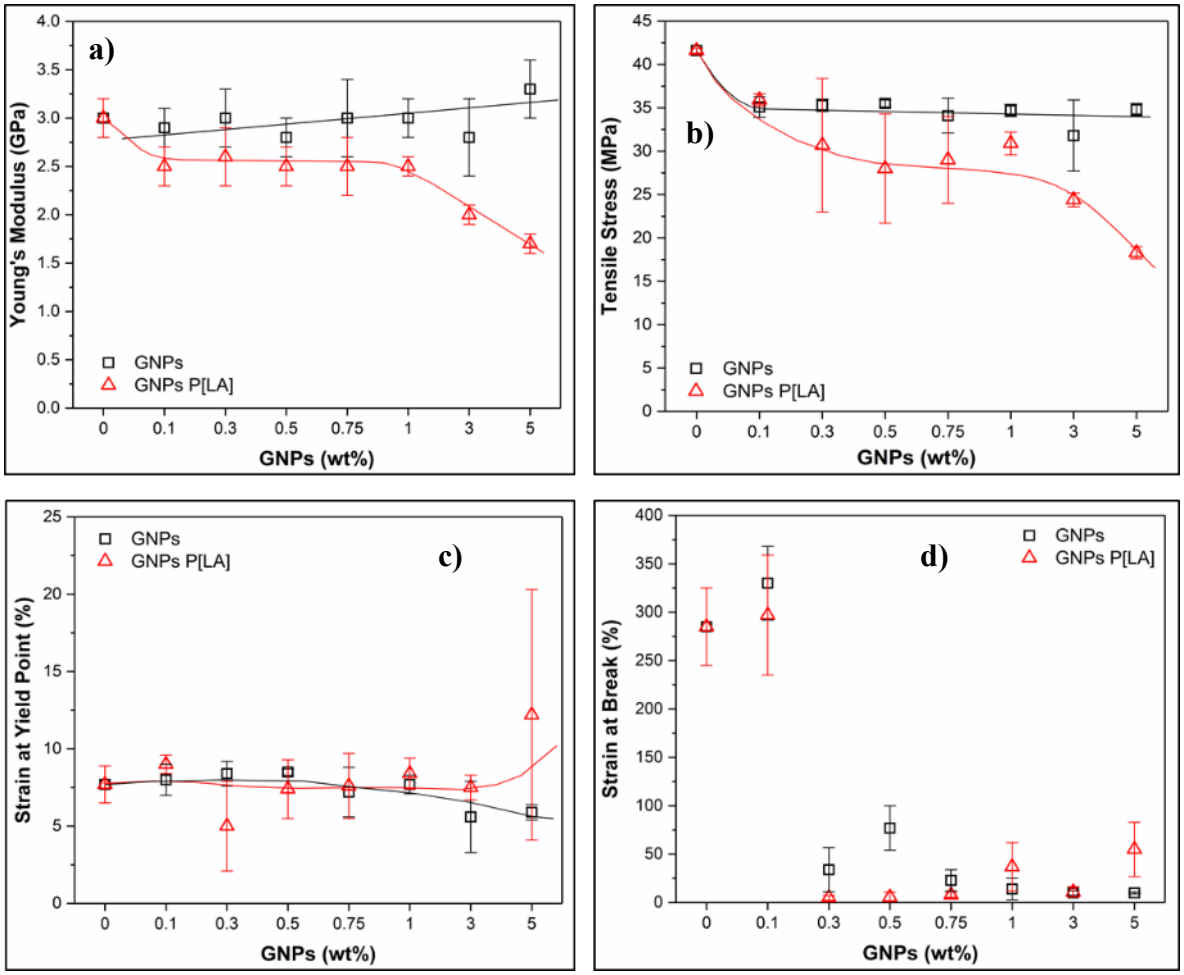

Figure 6.7 Variation in a) Young's modulus (*E*), b) tensile stress (σ), c) strain at yield point (ε_y) and d) tensile strain at break (ε_B), as a function of GNP loading for composites of PP filled with GNPs and PP filled with P[LA] functionalised GNPs.

ε_y was relatively unchanged following the addition of un-functionalised GNPs. GNP loadings >1 wt% depict a relatively small decrease in ε_y (~2%) compared to neat PP and resulted in embrittlement of the composite material. Sharp reductions of ε_B confirms the embrittlement effect with a significant decrease in strain from more than 250% to less than 10% for the highest loadings of GNPs. Defects in the form of GNPs melt blended within the PP matrix alter the arrangements of the PP chains leading to embrittlement of the composite. The crystalline lamella are prevented from sliding past each other due to the presence of the GNPs in the amorphous phase resulting in rapid fracture of the PP crystallites. The result is in agreement with that reported by Ahmad *et al.*[3] The loading of GNPs into the PP matrix results in the formation of a discontinuous network. Physical crosslinking between the GNPs and the polymer chains restrict the movement of the polymer chains during uniaxial

deformation which is expected to improve stiffness (σ) if the physical crosslinking is strong enough and the network is continuous.[14] However, the partial network formation of GNPs restricts polymer chain movement and accounts for the reduction in ε_B.

Work by El Achaby *et al*. produced composites of graphene nanosheets (GNs) with PP. The GNs were produced by chemical reduction of graphene oxide using hydrazine. These workers reported an increase in *E* and σ of 100% and 81%, respectively. The improvements were attributed to the large aspect ratio of the GNs used and the strong interfacial interactions between the GNs and PP.[1] Park *et al*. achieved improvements in flexural modulus, flexural strength and impact strength of 38%, 4% and 34% respectively by covalently functionalising the surface of the GNPs with dodecyl chains to improve interfacial adhesion with the polymer matrix.[17] It is clear, improvements in mechanical properties can only be achieved through functionalisation, therefore it was proposed that P[LA] would functionalise the surface of the GNPs (as displayed in figure 6.1), improve interfacial adhesion and obtain improvements in mechanical properties as described in literature.

The mechanical properties of composites of PP and P[LA] functionalised GNPs were determined. *E* decreased relative to neat PP and composites of PP and un-functionalised GNPs. *E* decreased by ~20% for loadings up to 1 wt% GNPs P[LA] with a further decrease for higher loadings. In addition, σ decreased with increasing GNP P[LA] loadings similar behaviour to the plasticisation effect observed with MWCNTs (Chapter 5). ε_y remained relatively unaffected up to 1 wt% GNP P[LA] loading. Higher loadings resulted in increases in ε_y. A similar effect was observed for ε_B confirming the P[LA] is increasing extensibility at high loadings of P[LA] compared to un-functionalised GNPs but, have very little, if any, effect on the GNPs.

The simple physical melt blending of PP and P[LA] modified GNPs presented reduced mechanical properties compare to composites of neat PP and un-functionalised GNPs. As detailed by Park *et al*. the lack of covalent bonding between the functionalising molecule, in this case, P[LA] results in free P[LA] molecules in the composite which act as plasticisers and impurities.[17] Addition of P[LA] therefore degrades the mechanical properties of PP due to the interaction between the GNPs and P[LA] being too weak.

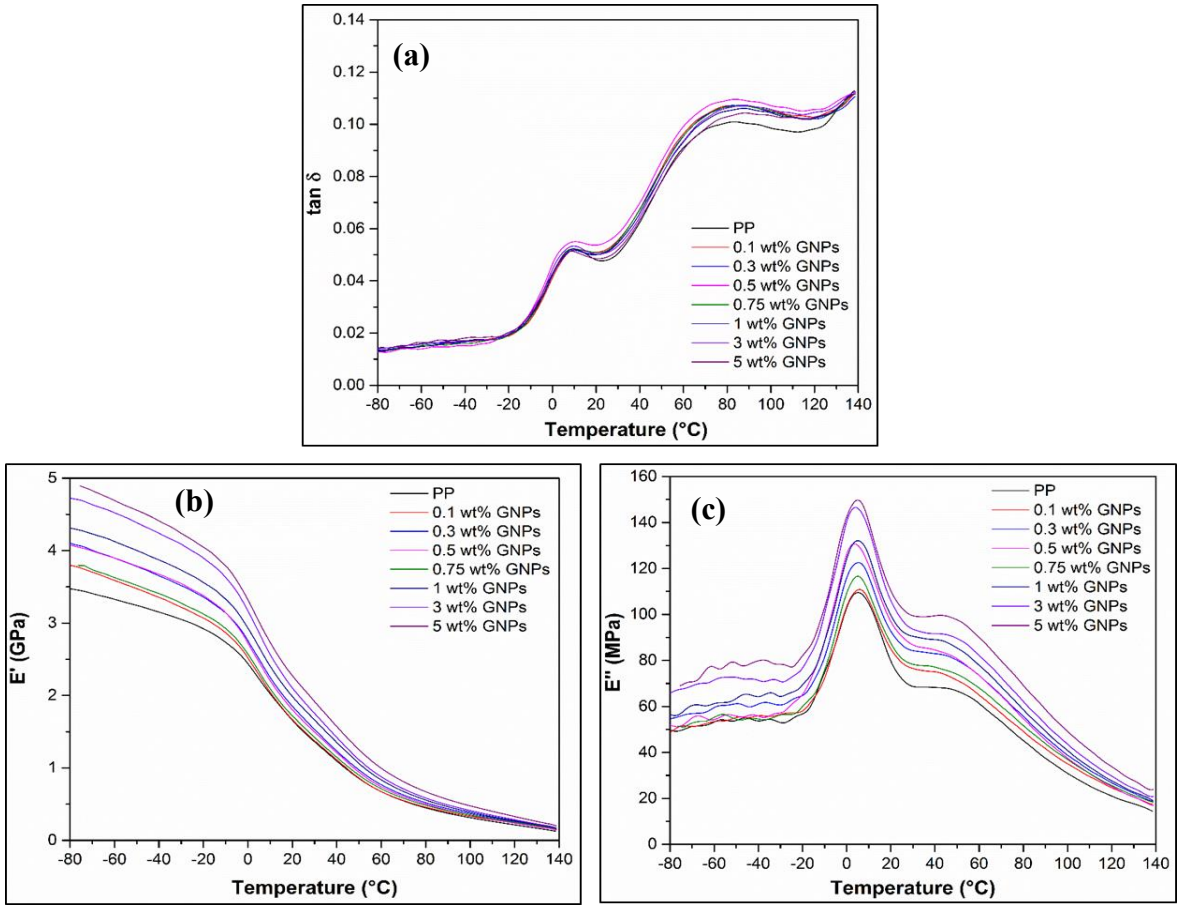

Figure 6.8 DMTA traces for unfilled PP and composites of PP and GNPs, a) tanδ b) storage modulus (E') and c) loss modulus (E'') as a function of temperature.

DMTA was used to characterise the viscoelastic properties of the nanocomposites. The storage modulus (E') is the elastic component of the modulus where the loss modulus (E''), displays the frictional losses incurred (energy dissipated) due to motion of polymer chains.[4] The dynamic mechanical properties for composites of PP and GNPs, (figure 6.8a) displays the tanδ as a function of temperature to be relatively unchanged and unaffected by the addition of GNPs. It was found the values of E' (figure 6.8b) increased with increased GNP loadings for temperatures below the T_g of PP (~ 0-10 °C). Compared to neat PP (3.5 GPa), E' increased to 5 GPa for a 5wt% GNP loading at -80 °C. For temperatures above the T_g, E' remained relatively unaffected compared to temperatures below the T_g but, with a small noticeable increase in E' with increasing GNP loadings. Increasing the loadings of GNPs results in an E' increase of ~1.6 GPa from 1.4 GPa for neat PP to 2.0 GPa for a 5wt% loading at 30 °C (~r.t.). The increase in E' is expected as the GNPs reinforce the PP and increase stiffness. It is expected the GNPs would mostly reside in the amorphous phase of

the semi-crystalline PP. In addition, figure 6.8c displayed no change in the position of the *E″* peak however, *E″* increased with increasing GNP loading across all temperatures confirming the viscous component of the material is becoming stiffer. In fact, the (*E″*) peak maximum increases from ~110 MPa for neat PP to ~150 MPa for a 5 wt% loading of un-functionalised GNPs. The result once again confirms the GNPs are reinforcing the PP.

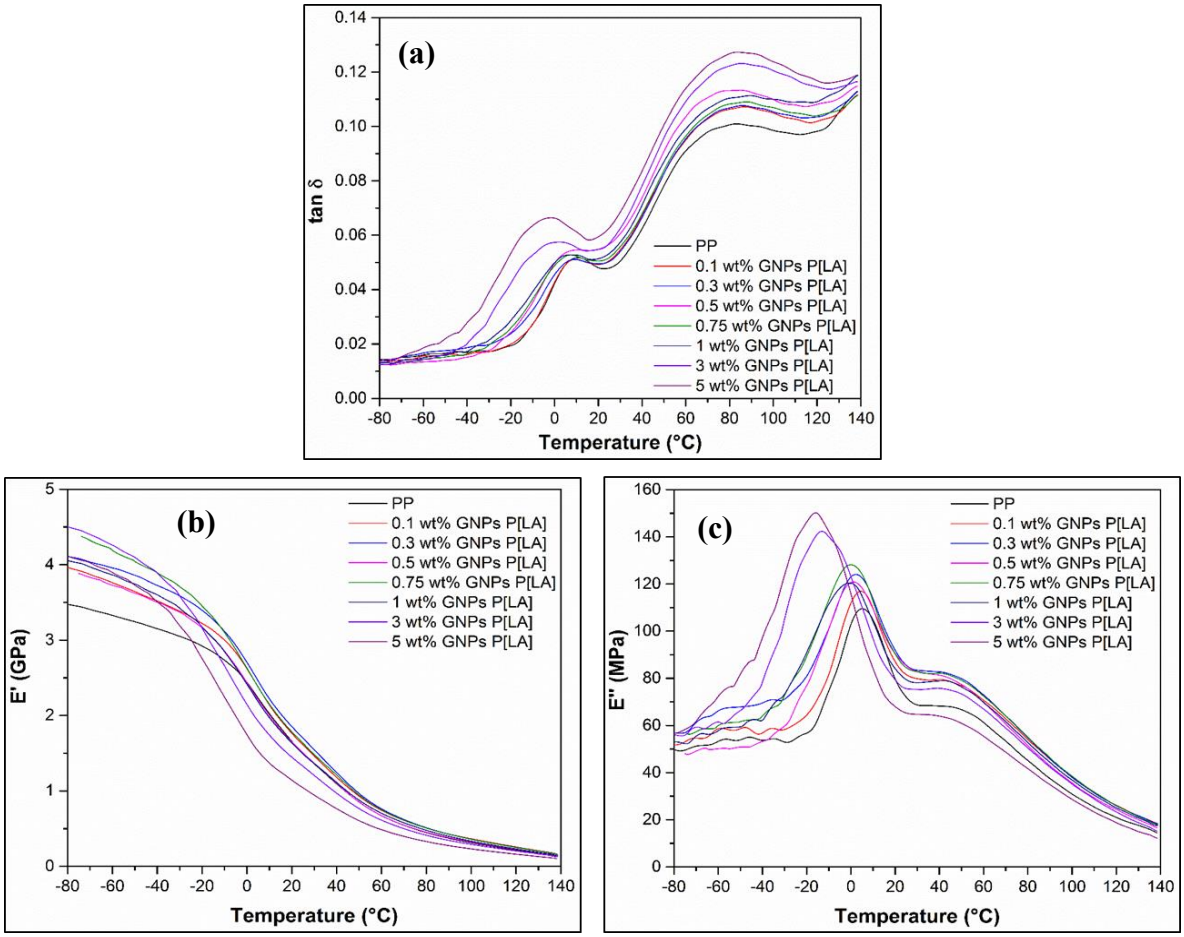

Figure 6.9 DMTA traces for unfilled PP and composites of PP and P[LA] functionalised GNPs, a) tanδ b) storage modulus (*E′*) and c) loss modulus (*E″*) as a function of temperature.

The dynamic mechanical properties of composites of PP and P[LA]-functionalised GNPs, (figure 6.9a) displays an increase in tanδ and a shift to lower temperatures caused by the plasticisation of PP by P[LA] and reinforcement by the GNPs. *E′* increased compared to neat PP but, not to the same extent as seen with the inclusion of un-modified GNPs. *E′* for the composite with 5 wt% GNPs:P[LA] increased to 4 GPa from 3.5 GPa for neat PP at -80 °C. In fact, 3 wt% GNPs P[LA] is as high as 4.5 GPa which suggests possibly some

variability in the mixing across all loadings. For temperatures above the T_g, E' showed the increase in stiffness was negated by the simultaneous shift to lower temperatures by ~20 °C. A key observation from both the E' and E'' traces for composites of PP and P[LA] functionalised GNPs is the simultaneous increase in stiffness and a shift in T_g to lower temperatures. For example, the E'' maxima displayed an increase in stiffness from 110 MPa at 5 °C for neat PP to a maxima of 150 MPa at -15 °C for 5 wt% GNPs P[LA] composite.

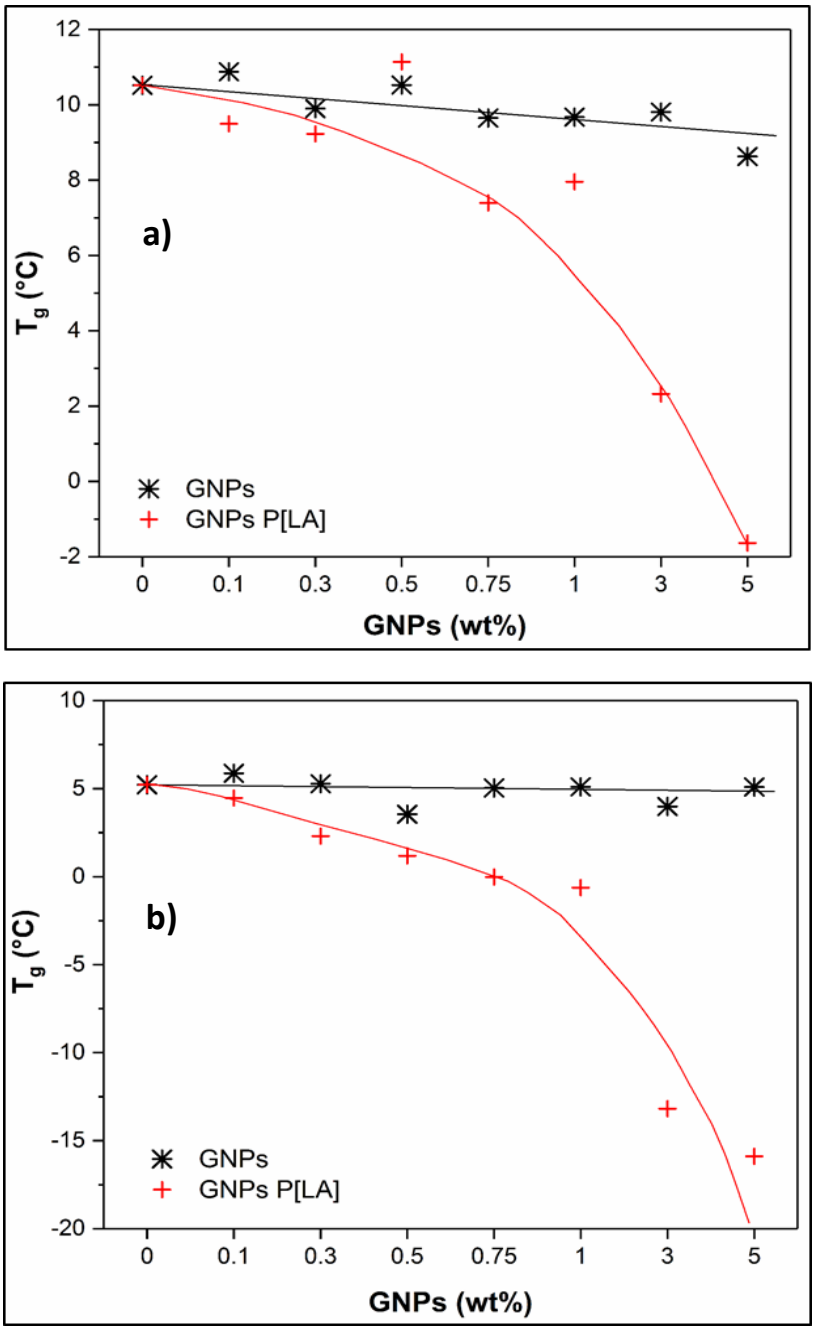

Figure 6.10 Change in T_g obtained from a) tanδ maxima and b) loss modulus (E'') maxima, for composites of PP/GNPs and PP/P[LA] modified GNPs.

Figure 6.10 displays the change in T_g measured from the tanδ maximum (figure 6.10a) and E'' maximum (figure 6.10b) for each composite. It is evident from both figures that the T_g taken from the tanδ or E'' maxima, that the addition of un-functionalised GNPs had very little if any, effect on the T_g. In stark contrast, the addition P[LA] to functionalise the GNPs significantly reduced the T_g of the composites. The T_g decreased by ~ 12 °C (figure 6.10a) for the composite with 5 wt% GNPs P[LA] and by ~ 20 °C from figure 6.10b. This is further evidence the P[LA] is plasticising the PP and reducing the stiffness of the PP the higher the loading of P[LA], i.e. > 1wt% GNPs P[LA]. The GNPs however, are still able to increase the stiffness compared to neat PP for composites <1wt% GNPs P[LA]. Figure 6.9c displays E'' increased with a simultaneous decrease in T_g. This particular result is of great interest because the combination of using GNPs and P[LA] to allow mechanical stiffness to be maintained yet the material has a lower T_g has many applications, where PP is used in car bumpers, which need to be functional at sub-zero temperatures. It would interesting explore the effect of keeping the P[LA] concentration fixed and varying the GNP loading to obtain a greater understanding of the system, see recommendations for future work (Chapter 9).

Neat and filled PP with various GNPs loadings were submitted to small amplitude oscillatory shear flow at 180 °C. Frequency sweeps in the range of 0.01-1000 rad/s were conducted and the dynamic shear storage modulus G', loss modulus G'', dynamic complex viscosity $|\eta^*|$ and the $\tan\delta^{-1}$ are reported for composites of PP and GNPs (figure 6.11a-d) and composites of PP and P[LA] functionalised GNPs (figure 6.12a-d).

PP displays the classic polymer melt behaviour with G' decreasing with decreasing frequency as well as a terminal zone in the low frequency range.[1] Interestingly, the addition of un-functionalised GNPs resulted in a parallel decrease in G' by approximately a single order of magnitude compared to neat PP. It was expected, as seen in recent reports in the literature that the addition of GNPs would result in an increase in G' resulting in the appearance of the 'pseudo-solid' plateau effect in the low frequency region.[4, 12] The appearance of such an effect would distinguish the percolation threshold for the composite. Even with the highest GNP loading (5wt%), there was no significant observable change in melt behaviour. The results display, the loadings do not lead to the formation of interconnected GNP networks. This is mostly likely due the relatively low aspect ratio of the GNPs used and therefore, a much higher concentration would be required to achieve a solid-like viscoelastic response. In addition, GNPs are 2D materials and therefore, it is easy for

the PP chains to slide between the GNP stacks relatively unperturbed compared to a CNT (1D) system, as discussed in chapter 5.

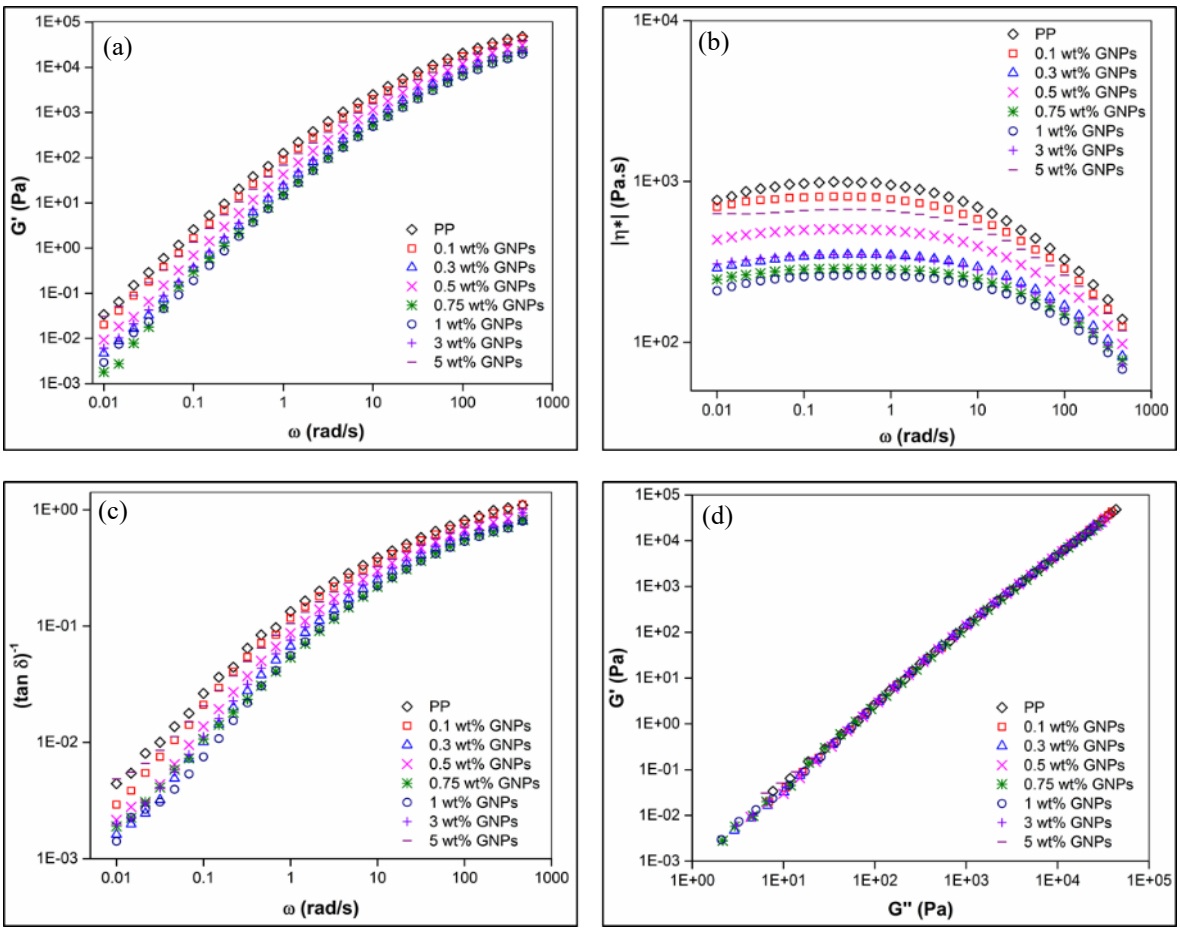

Figure 6.11 Variation in: (a) storage modulus (G'), (b) complex viscosity |η*| and (c) reciprocal of loss tangent ($(\tan \delta)^{-1}$) as a function of angular frequency (ω) for unfilled PP and composites of PP and GNPs and (d) Cole-Cole plot (G' verses G'').

As seen with figure 6.11, figure 6.12 displays similar behaviour where the addition of P[LA] had no effect on the rheological flow behaviour of the composite. It had been thought that the P[LA] would non-covalently adsorb on the surface of the GNPs and improve interfacial adhesion with the PP matrix. However, the data in figure 6.12 indicate the P[LA] has not improved GNP dispersion and there is limited interfacial adhesion between PP and GNP due to the absence of a 'solid-like' response (increase in G' compared to G'') in the rheology data. However, it could be that the GNP aspect ratio (~500) is too low to achieve percolation at these loadings, even for a well dispersed system and therefore, it cannot be

definitively concluded that the P[LA] is not improving dispersion and interfacial adhesion with the PP matrix.

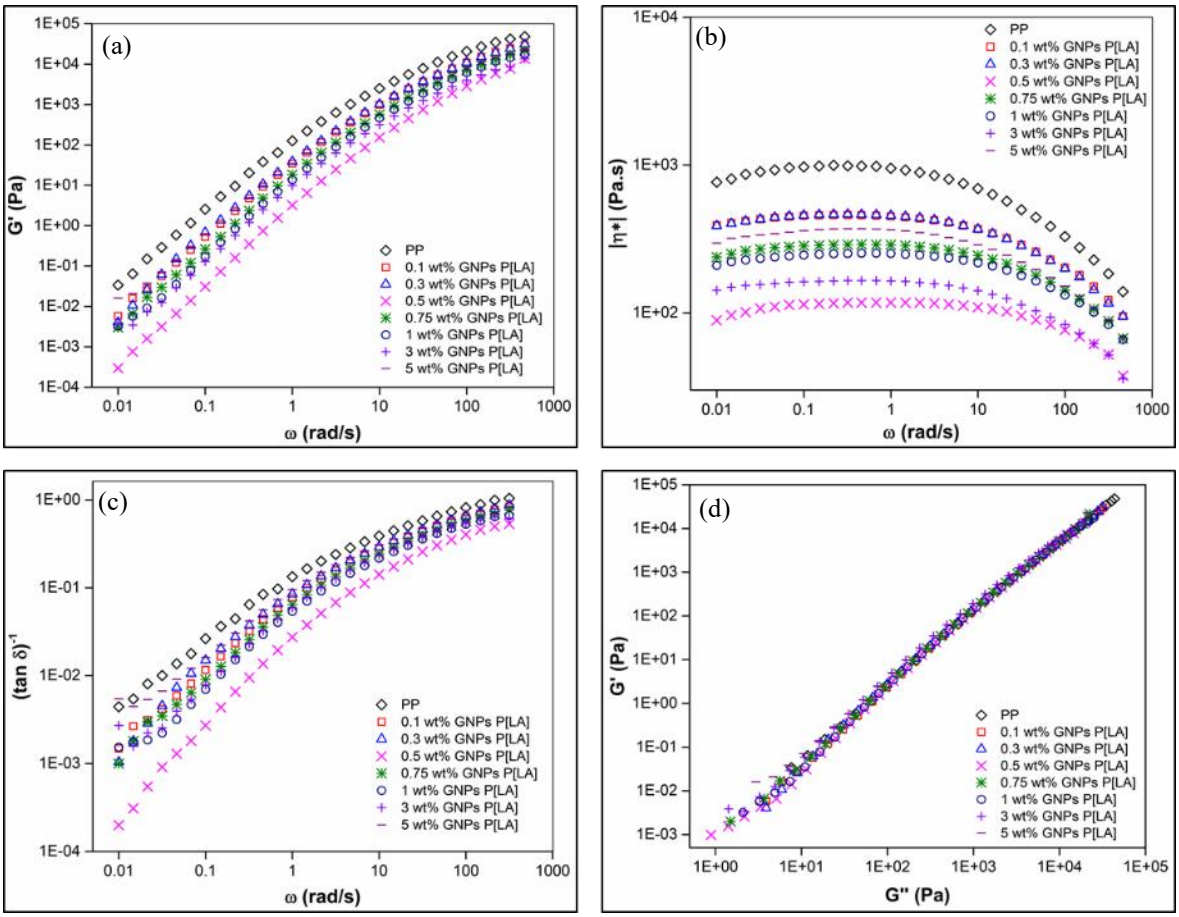

Figure 6.12 Variation in: (a) storage modulus (G'), (b) complex viscosity |η*| and (c) reciprocal of loss tangent ($(\tan \delta)^{-1}$) as a function of angular frequency (ω) for unfilled PP and composites of PP and P[LA] functionalised GNPs and (d) Cole-Cole plot (G' verses G'').

Figure 6.13 displays the respective heating and cooling traces for composites of PP with GNPs and PP with P[LA] functionalised GNPs, from DSC measurements. The values obtained for the melting temperature (T_m), crystallisation temperature (T_c), enthalpy of melting (ΔH_m) and cooling (ΔH_c), degree of crystallinity (X_c) and full width at half maximum (FWHH) for the respective melting and cooling peaks are detailed in table 6.3.

For the neat PP, T_m was observed at 163 °C and it shifted to higher temperatures by ~2 °C upon addition of GNPs (figure 6.13a). Interestingly, the shift is independent of GNP

loading which is contrary to recent results published in literature[3], but it may also reflect the inherent instrument error associated with DSC.

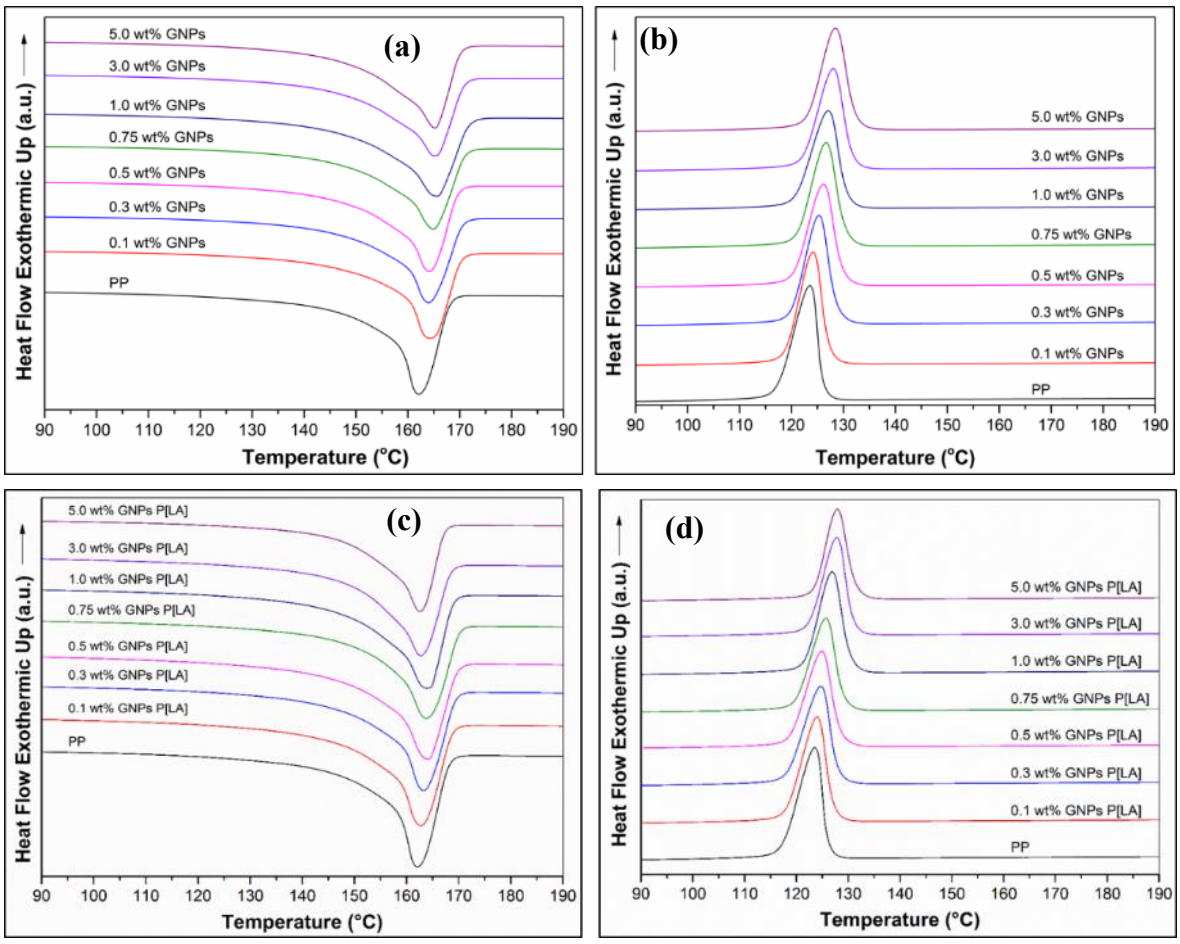

Figure 6.13 DSC (a) heating curves and (b) cooling curves for, unfilled PP and composites of PP and GNPs. DSC (c) heating curves and (d) cooling curves for, unfilled PP and composites of PP and P[LA] functionalised GNPs.

In addition, for neat PP, the T_c was observed to occur at 125 °C and shifted to higher temperatures, as the GNP content was increased for composites of PP and un-functionalised GNPs (figure 6.13b). For the highest GNP loading (5 wt%), T_c increased by ~ 4 °C. The increase in crystallisation temperature demonstrates that the GNPs promote crystallisation of the PP by serving as nucleating agents.[3] The nucleating behaviour of GNPs in thermoplastics such as PP and HDPE has been reported several times in literature.[3]

Table 6.3 Calorimetric data observed from DSC and crystalline content (X_c) determined from DSC for PP and composites of PP and GNPs.

Sample (wt%)	T_m [a] (°C)	T_c [b] (°C)	ΔH_m [c] (J/g)	ΔH_c [d] (J/g)	X_c [e] (%) DSC	$FWHH_m$ [f] (°C)	$FWHH_c$ [g] (°C)
PP	163	125	-105.5	104.5	51.0	12.0	5.9
0.1 wt% GNPs	165	124	-103.7	102.4	50.1	9.9	5.6
0.3 wt% GNPs	164	124	-103.1	101.2	50.0	10.0	5.5
0.5 wt% GNPs	165	125	-101.1	99.8	49.1	10.2	5.7
0.75 wt% GNPs	165	126	-104.8	103.1	51.0	11.3	5.7
1 wt% GNPs	165	127	-104.6	102.7	51.0	11.6	5.7
3 wt% GNPs	164	127	-100.8	98.7	50.2	11.8	5.6
5 wt% GNPs	165	129	-101.8	99.6	51.8	11.7	5.9
0.1 wt% GNPs P[LA]	164	124	-105.1	101.9	50.8	9.6	5.2
0.3 wt% GNPs P[LA]	164	125	-104.1	101.0	50.4	10.2	5.0
0.5 wt% GNPs P[LA]	162	125	-101.8	98.8	49.4	9.2	5.0
0.75 wt% GNPs P[LA]	163	125	-99.2	96.0	48.2	10.6	5.6
1 wt% GNPs P[LA]	164	127	-98.2	94.9	47.9	10.2	5.2
3 wt% GNPs P[LA]	163	128	-93.2	90.6	46.4	10.1	5.1
5 wt% GNPs P[LA]	163	128	-84.9	82.1	43.2	9.2	4.8

[a] T_m = melting temperature.
[b] T_c = crystallisation temperature.
[c] ΔH_m = melting enthalpy.
[d] ΔH_c = crystallisation enthalpy.
[e] X_c = degree of crystallinity computed from equation: $X_c = (\Delta H_m/(1-W_f)\Delta H_{100}) \times 100$ where W_f is the weight fraction of filler + P[LA] and ΔH_{100} is the melting enthalpy of a theoretically 100% crystalline PP (207.1 J/g).
[f] $FWHH_m$ = full width at half height of melting curve.
[g] $FWHH_c$ = full width at half height of cooling curve.

As PP is a semi-crystalline polymer, the melting and cooling peaks in the DSC traces correspond to the thermal transitions of the crystalline lamella only. Therefore, it is possible to determine the degree of crystallinity by integrating the area of the melting peak (ΔH_m) and comparing that to the enthalpy of melting of a theoretically 100% crystalline PP (207.1 J/g). The results in table 6.3 indicate the degree of crystallinity (X_c) is not significantly altered compared to the neat PP (51%) after the addition of GNPs. In addition, the peak width at half height (given by FWHH) are not significantly altered. It can therefore be concluded that even if the GNPs have demonstrated to heterogeneously nucleate the crystallisation of PP at the GNP interfaces, the crystallite size and distribution are not significantly affected by the GNPs.[2]

Similar results were observed for the composites of PP and P[LA] functionalised GNPs. T_m (figure 6.13c) was not significantly affected but T_c (figure 6.13d) increased by ~ 4 °C as result of the nucleating effect of the GNPs. It has been reported that GNPs accelerate polymer crystallisation at the interface when there are strong interactions between the GNPs and the polymer matrix.[2] As the increase in T_c is similar to that obtained for un-functionalised GNPs, this suggests the P[LA] has nether hindered nor promoted the interactions between the GNPs and the PP. It is important to control the microstructures and morphologies at the interface in terms of polymer chain orientation and crystal polymorph. Ordered interfacial microstructures (e.g. trans-crystals) significantly improve interfacial adhesion and load transfer.[2] The PP crystallites are expected to grow perpendicular to the axis of the graphene sheet (trans-crystals) and a soft-epitaxial model has been proposed. Interestingly, it is the trans-crystalline layer which promoted changes in polymorph as it is known that GNPs can promote the formation of β crystallites.[2] The melting curves for both sets of composites display the presence of a shoulder (left of the melting peak maximum) which increased with increasing GNP loading. The shoulder has been identified to be the formation of β crystallites.[2]

However, the ΔH_m and X_c significantly decreased upon addition of P[LA] functionalised GNPs suggesting the P[LA] is disrupting PP crystallisation. The X_c decreased by ~8% for the 5 wt% GNP P[LA] loading suggesting the P[LA] is not completely, only partially co-crystallising with PP.

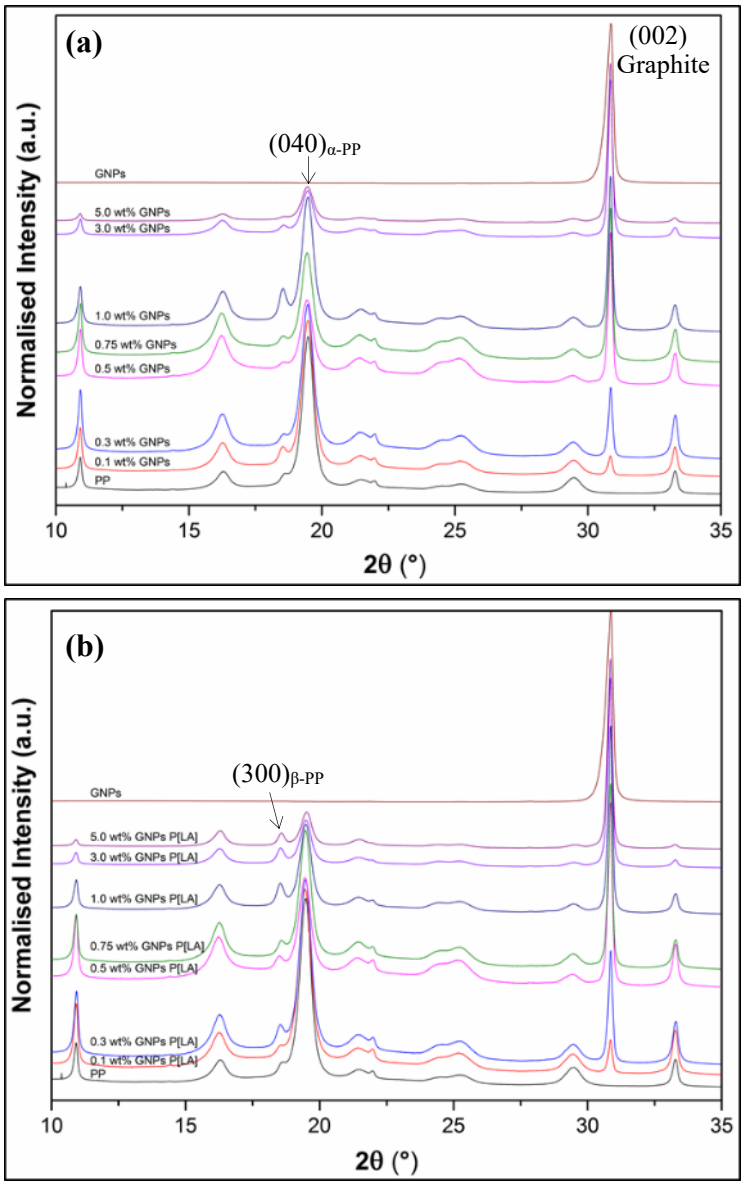

Figure 6.14 WAXD diffractograms for unfilled PP and for composites of a) PP and GNPs and b) PP and P[LA] functionalised GNPs.

Wide angle X-ray diffraction (WAXD) for neat PP and various loadings of un-functionalised GNPs and P[LA] functionalised GNPs are displayed in figure 6.14. The X-ray diffraction patterns can be correlated to a *d*-spacing using Bragg's law ($n\lambda=2d\sin\theta$) where *n* is an integer determined by the given order and λ is the X-ray wavelength.[18] The diffraction patterns are characteristic of αPP (see figure 5.32 for assignment of reflections) with the exception of the peak at $2\theta \approx 30.9°$ corresponding the (002) plane of graphite and a *d* spacing of 0.336 nm. The reflection corresponding to the (002) plane of graphite increases in

intensity relative to the PP reflections due to the increased loadings of GNPs in the composite as expected. The presence of the (002) peak confirms that the GNPs retain their layered and crystalline structure in the nanocomposite, with limited intercalation or exfoliation during the melt mixing process.[3] Furthermore, GNPs have been known to nucleate the β-crystal polymorph of PP and the presence of the (300) β-PP shoulder on the low angle side of the (040) α-PP peak can be observed for both un-functionalised GNP and P[LA]-functionalised GNP samples.[3] The presence of β-form trans-crystals is interesting as they are known to be unstable under normal processing conditions. Moreover, the β-form trans-crystals have excellent impact strength and toughness properties.[2] The concentration of β-form trans-crystals appears to be higher in P[LA]-functionalised GNPs suggesting the P[LA] is aiding the β-nucleation effect. The results agree with the DSC traces through the presence of a shoulder (left of the melting peak maximum) which becomes more prominent with increasing GNP and P[LA] loadings and was attributed to the formation of β-form trans-crystals.

Attempts to determine the degree of crystallinity of the PP from the WAXS diffractograms were attempted however, the presence of the (002) graphitic peak made it challenging to separate the crystalline peaks of the PP with the amorphous halo with suitable accuracy to draw reliable conclusions.

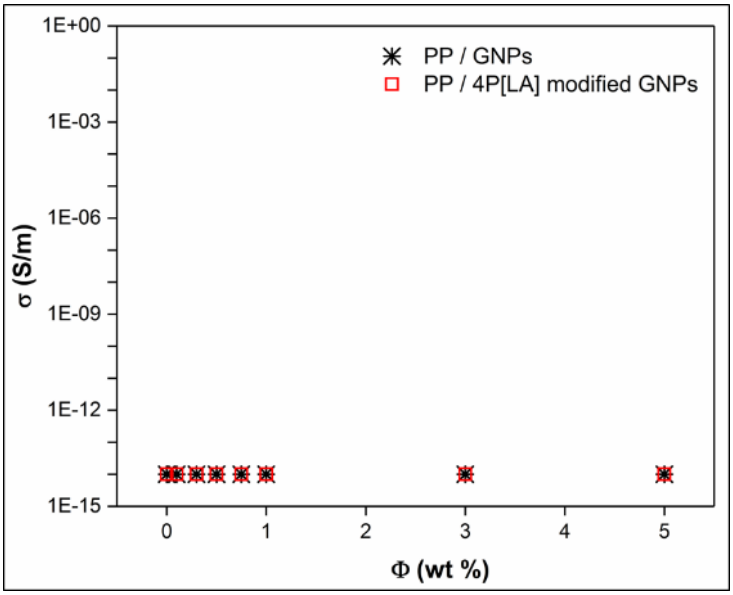

Figure 6.15 DC electrical conductivity (σ) verses GNP concentration (Φ) at a constant r.t (298K).

Figure 6.15 displays the DC electrical conductivity of composites of PP loaded with GNPs and PP and P[LA] functionalised GNPs. The samples were measured by cutting the injection moulded bars into lengths of 1 cm and coating the ends with silver conducting paint to measure the volume resistivity of the sample and minimise the contact resistance. The resistance of the samples was measured as listed in section 3.3.14. Unfortunately, the maximum resistance measured by the instrument is 1TΩ and as all of the samples exhibited a resistance greater than this value (measured as being 'out of limit'), it was assumed all of the samples were not conducting. It is known the conductivity of PP is in the region of $1x10^{-14}$ S m^{-1}, i.e. it is an insulator. This result is not particularly surprising given electrical conduction is only possible upon the formation of an interconnected nanofiller network that forms conduction pathways. This would require all of the GNP sheets to become into to contact with nearby GNP sheets to enable the electrons to 'tunnel' from one side of the sample to the other. It is expected that percolation is harder to obtain when using a 2D material compared to a 1D material such as CNTs. The tubular nature of CNTs and their strong tendency to aggregate during synthesis results in the formation of agglomerates of CNTs. The agglomerates tangle with one another like spaghetti and even with high shear, their low entropy of mixing prevents effective dispersion of the agglomerates. However, percolation requires an inter-connected network to be present and as the CNTs are already interconnected, dispersion of the agglomerates is only required to achieve percolation with the agglomerates largely unaffected by the high shear melt blending. In the case of GNPs, the stacked sheets do not constitute a 3D interconnected network due to their 2D structure. Even though CNTs are classed as 1D, their multi-tubular complex produces a 3D structure which entraps the PP polymer chains. The critical difference between achieving percolation between CNTs and GNPs is that the CNT agglomerates are not required to be interconnected because the CNTs are interconnected within agglomerates and this is enough to restrict the flow of the PP polymer chains during rheological shear whereas GNPs require interconnection between individual sheet stacks to achieve percolation because, their 2D structure on its own is not sufficient to restrict the flow of polymer chains above and below their respective stacks.

To establish whether the GNPs themselves were electrically conducting, the GNPs were pressed into a circular die using 10 tonnes of force. The resulting disk was placed between electrodes and the electrical conductivity was measured to be in the region of 10 Sm^{-1} confirming the GNPs alone are indeed conducting. However, factors such as

processing, loading, GNP aspect ratio and dispersion in the melt state prevent the formation of a network structure.

6.4 Conclusions

In conclusion, the effect of using poly(lauryl acrylate) P[LA] as a compatibiliser for the non-covalent functionalisation of GNPs to improve dispersion and interfacial adhesion with PP with the aim of improving the thermal, electrical and mechanical properties of PP was investigated. Composites of PP with un-functionalised GNPs and P[LA] functionalised GNPs were prepared using twin-screw melt compounding and injection moulding with various loadings of GNPs ranging from 0.1 wt% to 5 wt% and a P[LA] to GNP ratio of 4:1.

Initially, the GNPs were characterised using SEM, TEM, XPS, and Raman. The SEM of un-functionalised GNPs displayed the diameter of the GNP flakes were in the order of 10 μm and in the form of multi-layer flakes. HRTEM imaging confirmed the flakes are multi-layered with the number of layers estimated to be in the region of ≈ 10-20. The GNP structure is varied with some displaying a smooth and rounded surface whereas others are highly crumpled and rounded structures. XPS displayed the presence of residual surfactant used during the processing and 9 at% oxygen. The oxygen groups are predicted to be mainly on the sheets edges with the XPS data supporting the functional groups are mainly in the form of hydroxyl and carboxylic acid groups. The presence of oxygen based functional groups was confirmed from Raman spectroscopy which presented the GNPs to have an I_D/I_G ratio = 0.12.

SEM micrographs of the composites displayed the un-functionalised GNPs were poorly dispersed compared to the P[LA]-functionalised GNPs, due to the greater quantity of GNPs observed at or near the fractured surface of the P[LA]-functionalised GNPs composites. This could be that the P[LA] was adsorbed onto the surfaces of the GNPs during the pre-mixing phase facilitating dispersion. Rheological studies presented no evidence for a percolation threshold and no observation of an apparent ‘pseudo-solid’ network formation as determined from the absence of any change in the dynamic storage modulus (G') with increasing GNP loadings. The results are due to the 2D nature of GNPs which allow the PP polymer chains to move unrestructured during rheological shear compared to CNTs. Therefore, the lack of a rheological percolation threshold does not necessarily constitute poor dispersion of the GNPs but merely illustrates a lack of an interconnected network of GNPs,

possibly due to insufficient loadings of GNPs. The DC electrical conductivity measurements at all loadings confirmed the GNPs did not form an interconnected network, in agreement with the results of oscillatory rheology measurements.

The mechanical properties of the composites of PP and GNPs revealed no significant change in E, σ and ε_y with increasing GNP loadings. The ε_B decreased by over 250% with loadings greater than 0.3 wt% due to embrittlement. The addition of P[LA] functionalised GNPs resulted in a decrease in E and σ, ~ -43 % and ~ -56% respectively for 5 wt% GNP P[LA] loadings. However, there were increases in ε_y and ε_B, ~ 5% and ~ 50% respectively for 5 wt% GNP P[LA] loadings compared to un-functionalised GNPs. The addition of P[LA] plasticises the PP matrix reducing stiffness and strength while increasing extensibility. The DMTA measurements for the composites of PP and un-functionalised GNPs presented an increase in stiffness observed on the E' vs temperature for temperatures below the T_g with no change in the position of the T_g. For temperatures above the T_g, the reinforcement effect of the GNPs was less prominent. The observation can be attributed to the effect that below the T_g, the polymer chains are unable to move freely and can more easily transmit the mechanical energy to the GNPs whereas for temperatures above the T_g, the PP polymer chains are more mobile and therefore dissipate the energy through frictional losses. For composites of PP and P[LA] functionalised GNPs, the T_g decreased with increasing loadings of P[LA]-functionalised GNPs, by as much as ~20 °C for 5 wt% GNPs P[LA] confirming that P[LA] is plasticising the PP and significantly effecting the mechanical properties. In addition, both E' and E'' traces demonstrated simultaneous increases in stiffness and reduction in T_g resulting the in the improvement of the low temperature impact properties of PP.

DSC measurements confirmed the nucleating effect commonly observed with the addition of graphitic nanomaterials to polymers with T_c increasing by ~4 °C for both un-functionalised and P[LA] functionalised GNPs. The overall crystallinity content of PP remained unchanged when un-functionalised GNPs were added however, the addition of P[LA] functionalised GNPs led to a significant decrease in crystallinity of ~ 7%. WAXD results presented the formation of the β-PP morphology upon addition of the un-functionalised GNPs. The extent of the β-PP morphology appeared to increase with addition of P[LA] functionalised GNPs suggesting for the GNPs and the P[LA] are independently β nucleating agents and therefore affecting the crystallinity of PP, as observed also in the DSC traces.

Clearly, P[LA] has its limitations when non-covalently adsorbing onto the surface of graphitic fillers via CH-π wrapping. Even though measurements have portrayed P[LA] to improve dispersion, its plasticisation effect at high loadings is suppressing any improvements in mechanical properties. Moreover, the strength of the interaction between the P[LA] and the 2D filler is too weak for effective interfacial stress-transfer.

Therefore, poly(acrylate)s with aromatic pendent side-groups which can π-π stack with both MWCNTs or GNPs will be now be explored as means of increasing the dispersion and interfacial adhesion of the fillers with PP.

6.5 References

1. M. El Achaby, F. E. Arrakhiz, S. Vaudreuil, A. E. Qaiss, M. Bousmina and O. Fassi-Fehri, *Polym. Compos.*, 2012, **33**, 733-744.
2. J. P. Abdou, K. J. Reynolds, M. R. Pfau, J. van Staden, G. A. Braggin, N. Tajaddod, M. Minus, V. Reguero, J. J. Vilatela and S. J. Zhang, *Polymer*, 2016, **91**, 136-145.
3. S. R. Ahmad, C. Z. Xue and R. J. Young, *Mater. Sci. Eng., B*, 2017, **216**, 2-9.
4. A. P. Bafana, X. R. Yan, X. Wei, M. Patel, Z. H. Guo, S. Y. Wei and E. K. Wujcik, *Compos. Part B*, 2017, **109**, 101-107.
5. K. Kalaitzidou, H. Fukushima and L. T. Drzal, *Compos. Part A*, 2007, **38**, 1675-1682.
6. K. Kalaitzidou, H. Fukushima and L. T. Drzal, *Compos. Sci. Technol.*, 2007, **67**, 2045-2051.
7. K. Kalaitzidou, H. Fukushima, P. Askeland and L. T. Drzal, *J. Mater. Sci.*, 2008, **43**, 2895-2907.
8. M. Y. Song, S. Y. Cho, N. R. Kim, S. H. Jung, J. K. Lee, Y. S. Yun and H. J. Jin, *Carbon*, 2016, **108**, 274-282.
9. M. Wegrzyn, B. Galindo, A. Benedito and E. Gimenez, *J. Appl. Polym. Sci.*, 2015, **132**, 1-8.
10. J. J. Zhang, S. H. He, P. R. Lv and Y. Q. Chen, *J. Appl. Polym. Sci.*, 2017, **134**, 1-9.
11. S. M. Zhao, F. H. Chen, Y. J. Huang, J. Y. Dong and C. C. Han, *Polymer*, 2014, **55**, 4125-4135.
12. J. Zhong, A. I. Isayev and X. P. Zhang, *Eur. Polym. J.*, 2016, **80**, 16-39.

13. C. Valles, A. M. Abdelkader, R. J. Young and I. A. Kinloch, *Faraday Discuss.*, 2014, **173**, 379-390.
14. J. Z. Liang, Q. Du, G. C. P. Tsui and C. Y. Tang, *Compos. Part B*, 2016, **95**, 166-171.
15. K. R. Paton, E. Varrla, C. Backes, R. J. Smith, U. Khan, A. O'Neill, C. Boland, M. Lotya, O. M. Istrate, P. King, T. Higgins, S. Barwich, P. May, P. Puczkarski, I. Ahmed, M. Moebius, H. Pettersson, E. Long, J. Coelho, S. E. O'Brien, E. K. McGuire, B. M. Sanchez, G. S. Duesberg, N. McEvoy, T. J. Pennycook, C. Downing, A. Crossley, V. Nicolosi and J. N. Coleman, *Nat. Mater.*, 2014, **13**, 624-630.
16. L. M. Malard, M. A. Pimenta, G. Dresselhaus and M. S. Dresselhaus, *Phys. Rep.*, 2009, **473**, 51-87.
17. S. M. Park and D. S. Kim, *Compos. Interfaces*, 2017, **24**, 335-345.
18. J. E. An, G. W. Jeon and Y. G. Jeong, *Fibre. Polym.*, 2012, **13**, 507-514.

Chapter 7 Results and Discussion IV

Synthesis and characterisation of homopolymers and co-polymers of poly(lauryl acrylate) P[LA] and 2-phenyl ethyl acrylate P[2PEA] and their composites with multi-walled carbon nanotubes (MWCNTs) and graphene nano-platelets (GNPs)

7.1 Introduction

The following chapter will describe the use of multifunctional copolymers as non-covalent compatibilisers for composites of MWCNTs and GNPs with PP. The hypothesis is that copolymer chemistry can improve dispersion and interfacial adhesion of MWCNTs and GNPs with the PP matrix and, perhaps provide a mechanism for efficient load transfer between components. The use of copolymers with controlled architectures and inherent properties can be used to provide specific functionality.

To further improve the weak interfacial load transfer from the polymer matrix to the filler, bi-functional poly(acrylate) co-polymers were synthesised. The use of poly(lauryl acrylate) P[LA] has previously been investigated and revealed to adsorb on to the surface of MWCNTs via a CH-π mechanism. However, CH-π type bonding is weak compared to the cumulative effect of the Van der Waals interactions between neighbouring MWCNTs in MWCNT agglomerates and the π-π stacking between GNP sheets.

It is proposed that aromatic based poly(acrylates) efficiently adsorb and/or wrap on to the surface of MWCNTs and GNPs. 2-phenylethyl acrylate (2PEA) has had significant use in the contact lens industry for its refractive index properties. To date, polymers prepared from such a monomer has not been used as a dispersing additive for 1D and 2D carbon nanomaterials. Typically, polymers and monomers similar to styrene have been investigated with MWCNTs and GNPs.

Since the structure of the MWCNTs and GNPs are mostly aromatic, the optimal strategy for non-covalent adsorption of the dispersing polymer would be via a π-π aromatic stacking type mechanism between the dispersing polymer and the surface of the filler. It is proposed that the use of an aromatic type polymer would interact with the graphitic filler and hence contribute to the disentanglement/exfoliation of the filler and, in combination the lauryl acrylate component is capable of co-crystallising with PP.

Block co-polymer (P[LA-*block*-2PEA]) and statistical co-polymer (P[LA-*stat*-2PEA]) were selected. P[LA] was selected based upon its good compatibility with PP and because its hydrophobic chains are able to co-crystallise with PP as presented in chapters 4 through 6. 2PEA was selected as it is an aromatic acrylate. An acrylate was selected because it was presented in chapter 4 to be thermally stable at the temperatures used for extrusion of PP. 2PEA is a readily available aromatic acrylate with the benefit of having a molecular spacer between the acrylate group and the phenyl group which allows greater flexibility of the aromatic group, due to reduced steric hindrance with a rigid structure such as styrene for example. The greater flexibility of the phenyl group is thought will improve its binding properties with the filler.

In addition to the co-polymers of P[LA] and P[2PEA], the homo-polymers of P[LA] and P[2PEA] were also prepared as controls also having varying molecular weights ranging from 5,000 g mol^{-1} to 20,000 g mol^{-1}.

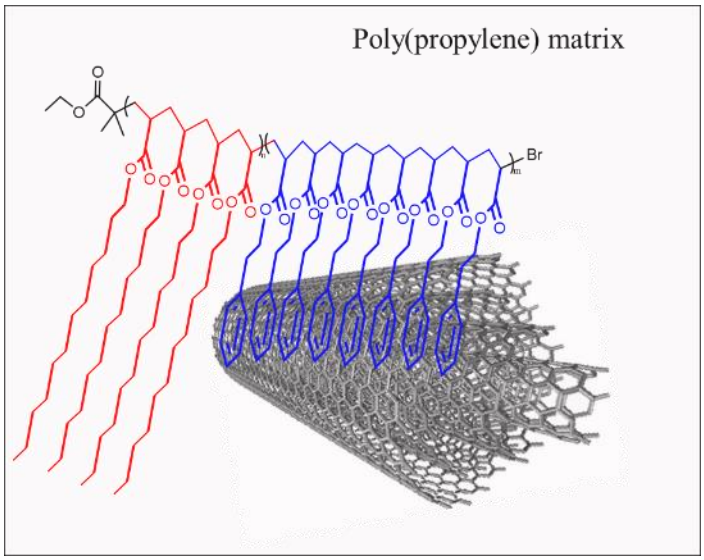

Figure 7.1 Schematic displaying the block copolymer (P[LA-*block*-2PEA]) interacting with MWCNTs within a poly(propylene matrix).

An idealised schematic representation of a block-copolymer comprising of P[LA] and P[2PEA] blocks and possible interaction with a graphene sheet is displayed in figure 7.1. A similar idealised schematic representation (figure 7.2) is presented for the case of GNPs.

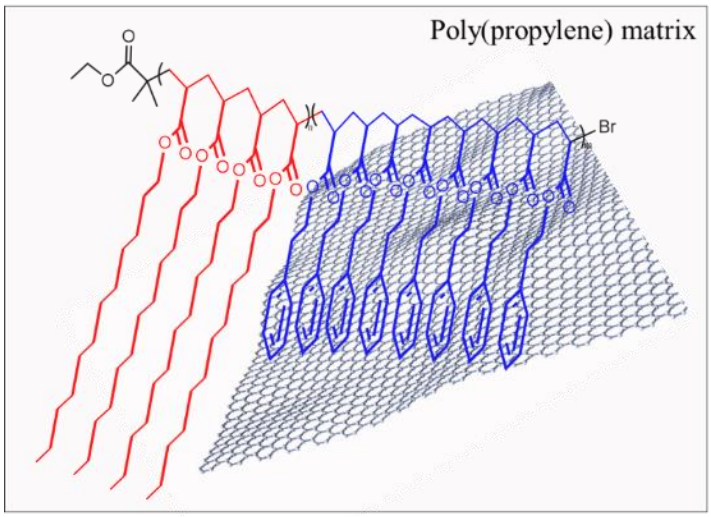

Figure 7.2 Schematic displaying the block copolymer interacting with GNPs within a poly(propylene) matrix.

7.2 Synthesis of homopolymers and co-polymers of P[LA] and P[2PEA]

Homo-polymers and co-polymers of LA and 2PEA were polymerised using Cu(0)-mediated LRP using the methods discussed in chapter 4. The polymerisations were conducted in IPA solvent and performed using the adapted procedure by Anastasaki *et al.*[1] The experimental procedure for the synthesis is detailed in chapter 3.

7.2.1 Synthesis of homopolymers of P[LA]

Initially, P[LA] was synthesised (scheme 7.1) and was characterised using ^{1}H NMR and GPC (table 7.1). The polymerisation of LA was repeated so as to compare its properties with the homo-polymerisations of 2PEA ensuring, that both homo-polymerisations of LA and 2PEA were performed in an attempt to achieve identical targeted molar masses. The synthetic strategy for the polymerisation of LA (scheme 7.1) is presented and table 7.1 lists the targeted degrees of polymerisation (DP_n = 21, 42, 84, $M_{n,th}$ = 5,000-20,000 g mol^{-1}). The ^{1}H NMR (figure 7.3) and GPC (figure 7.4) confirm the polymerisation of LA was successful. The minimal presence of vinylic peaks in the range of 5.5-6.5 ppm demonstrates a high conversion from monomer to polymer. In addition, the sequential increase in molar mass calculated from the GPC confirms the polymerisations proceeded as expected.

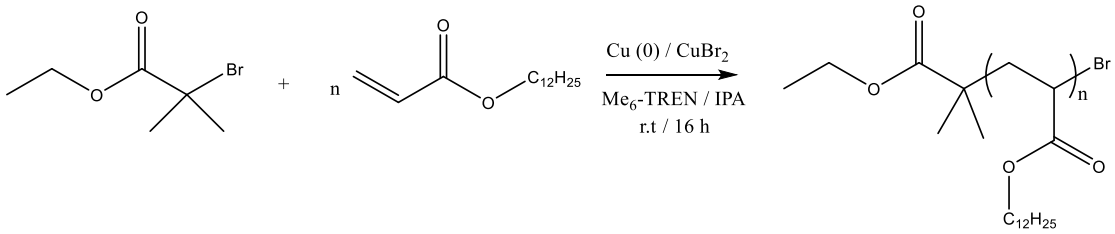

Scheme 7.1 Synthetic strategy for homo-polymerisation of LA *via* Cu(0)-mediated living radical polymerisation.

Table 7.1 Theoretical and experimental data for the preparation of homo-polymers of P[LA] *via* Cu(0)-mediated LRP process and the associated number average molar masses.

Nomenclature	[LA]/[I]	Conv.[a] [%]	$M_{n,\,th}$ [g mol^{-1}]	$M_{n,\,GPC}$ [b] [g mol^{-1}]	$Đ^b$
P[LA] 5K	21	85	5 000	6 800	1.10
P[LA] 10K	42	99	10 000	13 300	1.15
P[LA] 20K	84	97	20 000	21 300	1.19

[a] ^{1}H NMR. [b]$CHCl_3$ SEC analysis *via* RI detection using linear PMMA standards.

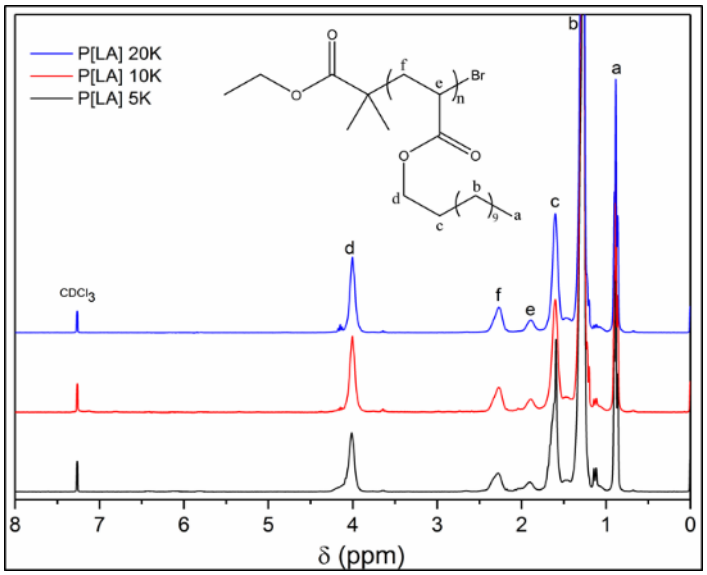

Figure 7.3 ^{1}H NMR spectra of P[LA] of various molecular weights recorded in $CDCl_3$ synthesised *via* Cu(0)-mediated polymerisation.

From table 7.1 and figure 7.4, it can be deduced that there is a linear increase in molar mass with increasing monomer concentration, ($M_{n,exp}$ = 6 800, 13 300, 21 300 g mol^{-1}). ^{1}H

NMR of P[LA] (figure 7.3) revealed the polymerisations proceeded with excellent conversion (~98%) and high levels of purity after purification. As presented in chapter 4, lower molar mass polymers are not as efficient at proceeding to high levels of conversion. The dispersity achieved was $Đ \sim 1.15$ with low molar mass tailing observed for two higher molar mass polymers of P[LA].

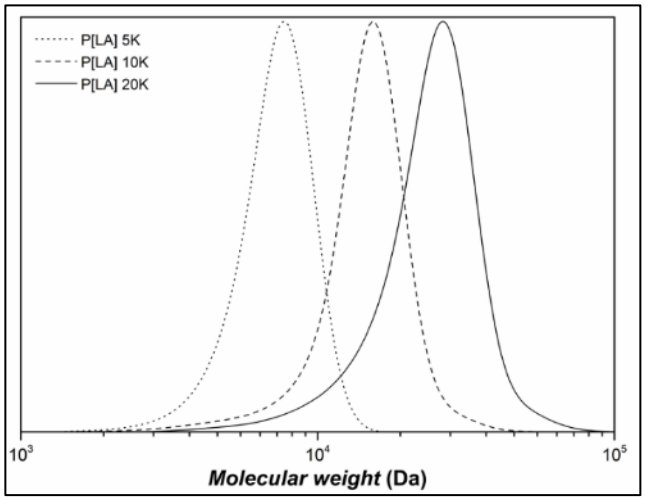

Figure 7.4 SEC traces of P[LA] of various molecular weights synthesised *via* Cu(0)-mediated polymerisation.

7.2.2 Synthesis of homopolymers of P[2PEA]

2-phenyl ethyl acrylate (2PEA) was polymerised using similar conditions to that of P[LA] (IPA, identical ratios of Cu and Me_6TREN). The synthetic strategy used to polymerise 2PEA (scheme 7.2) demonstrates the Cu(0)-mediated LRP polymerisation is versatile and effective at polymerising a wide range of acrylates. It is important to determine if 2PEA can be polymerised by Cu(0)-mediated LRP with the same control of molar mass and dispersity as that of LA. The copolymers can only be synthesised if the monomers can copolymerise under the same polymerisation conditions.

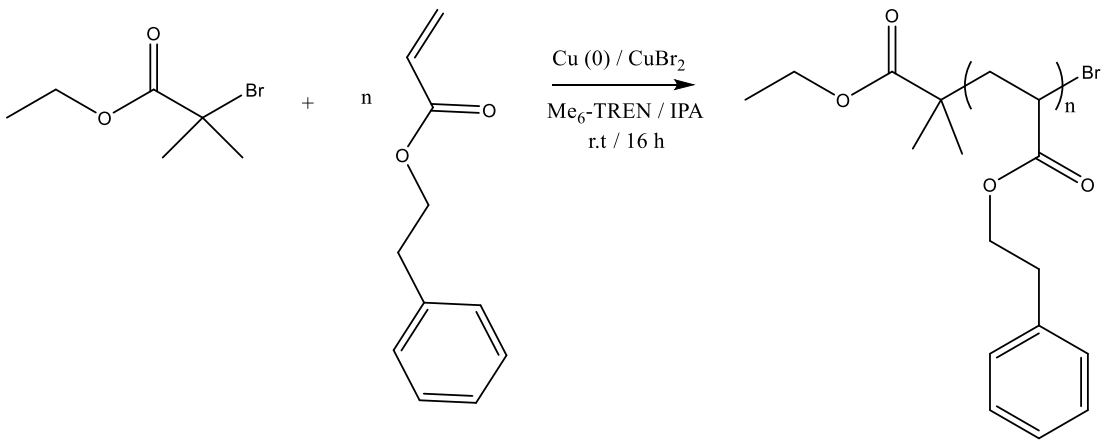

Scheme 7.2 Synthetic strategy for homo-polymerisation of 2PEA *via* Cu(0)-mediated LRP.

Table 7.2 Theoretical and experimental data for the preparation of homo-polymers of P[2PEA] *via* Cu(0)-mediated LRP process and the associated number average molar masses.

Nomenclature	[LA]/[I]	Conv.[a] [%]	$M_{n,\,th}$ [g mol^{-1}]	$M_{n,\,GPC}$ [b] [g mol^{-1}]	$Đ^b$
P[2PEA] 5K	28	96	5 000	6 300	1.22
P[2PEA] 10K	57	99	10 000	10 000	1.18
P[2PEA] 20K	114	95	20 000	23 400	1.18

[a] ^{1}H NMR. [b]$CHCl_3$ SEC analysis *via* RI detection using linear PMMA standards.

The data for homo-polymerisation of 2PEA *via* Cu(0)-mediated LRP is tabulated (table 7.2) and lists the targeted degrees of polymerisation (DP_n = 28, 57, 114, $M_{n,th}$ = 5 000-20 000 g mol^{-1}). The targeted molecular weights are the same as that for P[LA] in order to be consistent when investigating the differences between the two polymers when blended with MWCNTs and GNPs. The ^{1}H NMR of P[2PEA] revealed the polymerisation proceeded with high conversion (~97%) and the copolymers obtained had high purity (after purification) due to the minimal presence of vinylic peaks in the range of 5.5-6.5 ppm. The ^{1}H NMR of 2PEA monomer is displayed in appendix 7. Conversion appears to be independent of molecular weight. Table 7.2 and figure 7.6 confirm the linear increase in molar masses with increasing monomer concentration. The obtained molecular weights ($M_{n,exp}$ = 6 300, 10 000, 23 400) are in good agreement with the theoretical molar masses and low dispersities were obtained ($Đ$ ~ 1.2; Table 7.2) displaying a narrow distribution of molar masses. The results confirm 2PEA can be polymerised using Cu(0)-mediated LRP.

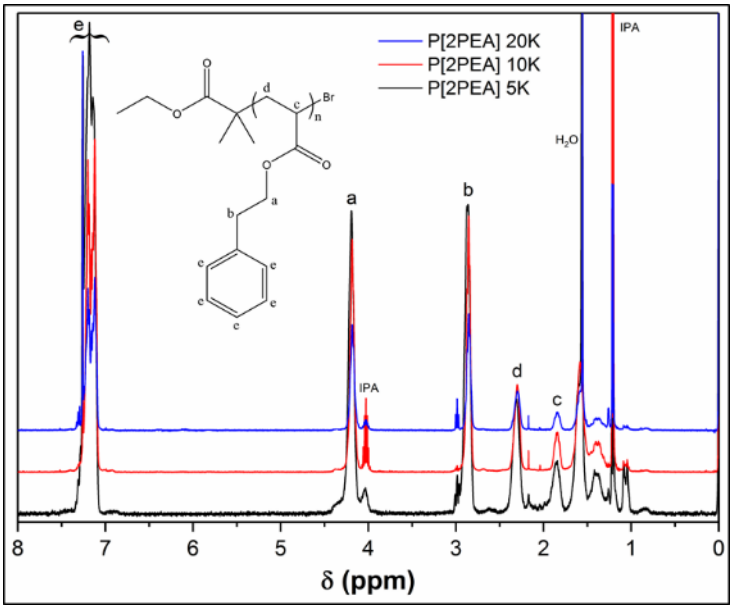

Figure 7.5 ^{1}H NMR spectra of P[2PEA] of various molecular weights recorded in $CDCl_3$ synthesised *via* Cu(0)-mediated polymerisation.

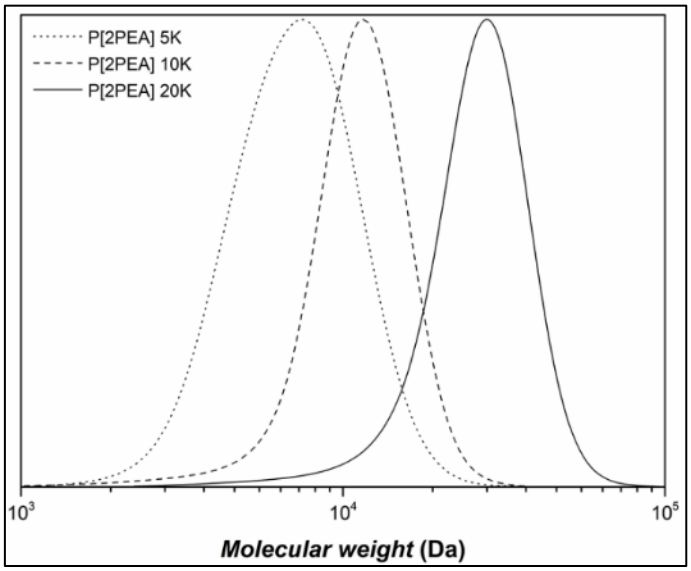

Figure 7.6 SEC traces of P[2PEA] of various molecular weights synthesised *via* Cu(0)-mediated polymerisation.

7.2.3 Synthesis of co-polymers of P[LA] and P[2PEA]

Copolymers of LA and 2PEA were prepared using Cu(0)-mediated LRP and with similar polymerisation procedures to that for the homopolymers of P[LA] and P[2PEA]. The architectures of the copolymers are depicted pictorially in scheme 7.3 for a block and statistical copolymers. The block copolymer involves firstly homo-polymerising LA and

subsequently chain extending with 2PEA and is denoted P[LA-*block*-2PEA]. The statistical copolymer involves polymerising both LA and 2PEA simultaneously at the start of the polymerisation to produce a random copolymer and is denoted P[LA-*stat*-2PEA]. The reactivity ratios are predicted to be similar between LA and 2PEA and therefore, it can be expected that the polymerisation will lead to a random statistical copolymer. Reactivity ratios are a measure of the probability a monomer will homo-propagate (polymerise with itself) or cross-propagate (polymerise with the co-monomer).

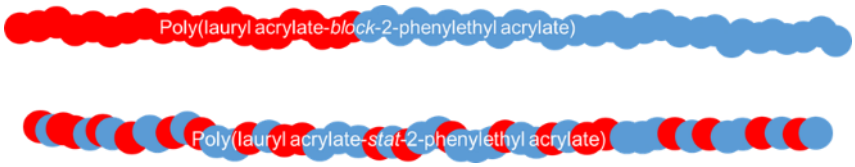

Scheme 7.3 Ball and stick schematics for the copolymer architectures of LA and 2PEA *via* Cu(0)-mediated LRP.

Scheme 7.4 exhibits schematically the polymerisation strategy used for the copolymers and table 7.3 lists the targeted degree of polymerisation for each monomer in the copolymer (DP_n = 42 (LA), 57 (2PEA), $M_{n,th}$ = 20 000 g mol^{-1}). The statistical and block copolymers were polymerised to identical targeted molecular weights, $M_{n,th}$ = 20 000 g mol^{-1}. For subsequent discussion, the P[LA-*block*-2PEA] nomenclature will be abbreviated to *block* 20K and the P[LA-*stat*-2PEA] abbreviated to *stat* 20K. As well as characterising both the *block* 20K and *stat* 20K, the initial homo-polymerisation of LA before chain extension with 2PEA was also characterised (P[LA] *block* 10K).

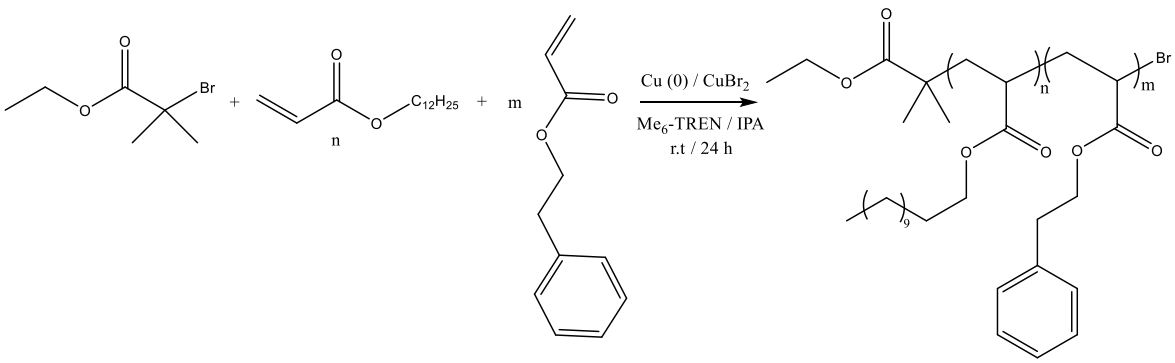

Scheme 7.4 Synthetic strategy for co-polymerisation of LA and 2PEA *via* Cu(0)-mediated LRP.

The ^{1}H NMR for the copolymers (figure 7.7) indicated the copolymers proceeded to high conversion (~99 %) and were obtained in high purity after purification. The minimal presence of vinylic peaks in the range of 5.5-6.5 ppm confirms the high conversion from monomer to polymer. Peaks **a** and **h** (figure 7.7) confirm conversion of LA and 2PEA due to the broadening of the peaks. In addition, integration of peaks **a** and **h** in the copolymers was used to determine the monomer composition in the copolymer. As listed in table 7.3, the DP_n of 2PEA in the copolymers (~56) is relatively close to the targeted DP_n of 57 suggesting the polymerisation conditions are well optimised for 2PEA. However, the DP_n of LA in the copolymers (~ 33 for *stat 20K* and ~38 for *block* 20K) are significantly lower than the targeted DP_n of 42 suggesting the polymerisation are not optimised for LA. LA polymerises more efficiently in the *block* 20K compared the *stat* 20K illustrating that LA does not polymerise efficiently in the presence of 2PEA compared to its absence.

The GPC traces (figure 7.8) present the molar masses of the *stat* 20K and the *block* 20K copolymers are similar, $M_{n,exp}$ = 17 900 and 19 000 g mol^{-1} respectively. The *block* 20K displayed broader low molar mass tailing relative to the *stat* 20K. Differences in the GPC trace between the *block* 20K and the *stat* 20K are expected as they would have a significantly different hydrodynamic volumes and radius of gyration in solution compared to each other and therefore, behave differently in the GPC column. This is due to the *block* 20K possibly self-assembling whereas the *stat* 20K is likely to randomly orientate in solution. Additionally, the measured dispersities of $Đ$ = ~ 1.15 for both the *block* 20K and *stat* 20K indicate the polymerisations were well controlled with fast initiations and low termination rates. The traces demonstrate the polymerisations were successful for the purpose of investigating their non-covalent adsorption with 1D and 2D graphitic nanomaterials.

Table 7.3 Theoretical and experimental data for the preparation of co-polymers of LA and 2PEA *via* Cu(0)-mediated LRP process and the associated number average molar masses.

Nomenclature	[LA]/[I]	[2PEA]/[I]	Conv.[a] [%]	$M_{n,th}$ [g mol^{-1}]	$M_{n,GPC}$[b]	$Đ$[b]	Co-polymer composition [DPn] LA	2PEA
stat 20K	42	57	99	20 000	17 900	1.15	33	57
P[LA] *block* 10K	42	-	98	10 000	11 200	1.11	47	-
block 20K	42	57	99	20 000	19 000	1.15	38	56

[a] ^{1}H NMR. [b]$CHCl_3$ SEC analysis *via* RI detection using linear PMMA standards.

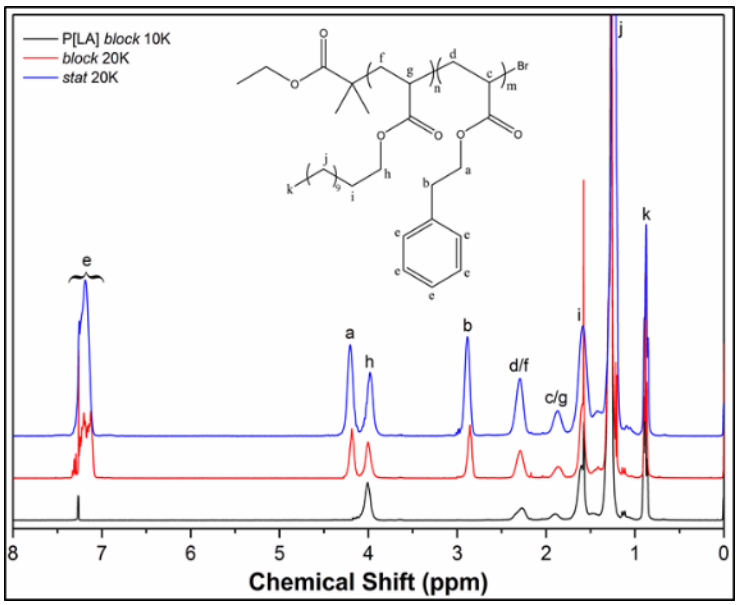

Figure 7.7 ^{1}H NMR spectra of co-polymers of P[LA] and P[2PEA] recorded in $CDCl_3$ synthesised *via* Cu(0)-mediated polymerisation.

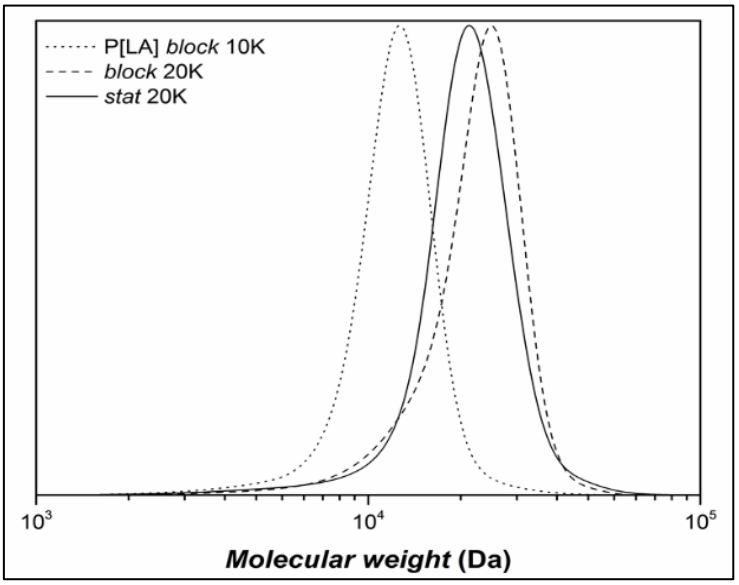

Figure 7.8 SEC traces of co-polymers of P[LA] and P[2PEA] synthesised *via* Cu(0)-mediated polymerisation.

7.3 Homopolymers and copolymers of P[LA] and P[2PEA]

7.3.1 TGA of homopolymers and co-polymers of P[LA] and P[2PEA]

TGA was used to investigate the thermal stability of the homopolymers and copolymers of LA and 2PEA. The onset of thermal degradation for P[LA] 10K and P[LA] 20K (figure 7.9a) was ~ 300-320 °C. P[LA] 5K has a significantly lower onset of degradation at ~120-130 °C which can be attributed to the presence of unreacted monomer and IPA (see Appendix 10a). This is confirmed by the lower conversion (~ 85%) calculated from the ^{1}HMR.

The onset of thermal degradation for P[2PEA] 5, 10, 20K was ~ 300-320 °C. However, all homopolymers of P[2PEA] exhibited a 10 wt% mass loss prior to the main loss observed at ~ 300-320 °C. The 10 wt% mass loss occurred in two 5 wt% mass events with the first having an onset at ~ 90-110 °C and the second at ~ 200-220 °C. Using the TGA and DTA curves from the reagents used during the polymerisation (see Appendix 10 a) and b)) the first mass loss event at ~ 90-110 °C can be attributed to the presence of IPA which was not removed fully during the drying process. The ^{1}H NMR also confirmed the presence of IPA. The second mass loss event at ~ 200-220 °C can be attributed to unreacted 2PEA monomer which was also confirmed by ^{1}H NMR as conversion did not reach 100% for all polymers. Thermal degradation of the main mass loss event achieved 95 wt% mass loss by 440-460 °C. The onset of thermal degradation for P[2PEA] was independent of molar mass.

The onset of thermal degradation remains unchanged for the copolymers at ~ 300-320 °C suggesting the onset of degradation is independent of monomer and architecture and dependent on monomer type only. The *block* 20K had a mass loss event of ~ 10 wt% with an onset of ~ 90-110 °C which can be attributed to IPA. *Stat* 20K and P[LA] 10K exhibited minor losses at ~ 90-110 °C suggesting they contained less IPA solvent (~ 1-2 wt%) compared to the *block* 20K. In conclusion, the TGA measurements of homo- and copolymers of P[LA] and P[2PEA] demonstrated that they are thermally stable up to 300 °C. They are suitable for the purpose of non-covalently compatibilising with 1D and 2D graphitic nanomaterials when added to PP *via* extrusion.

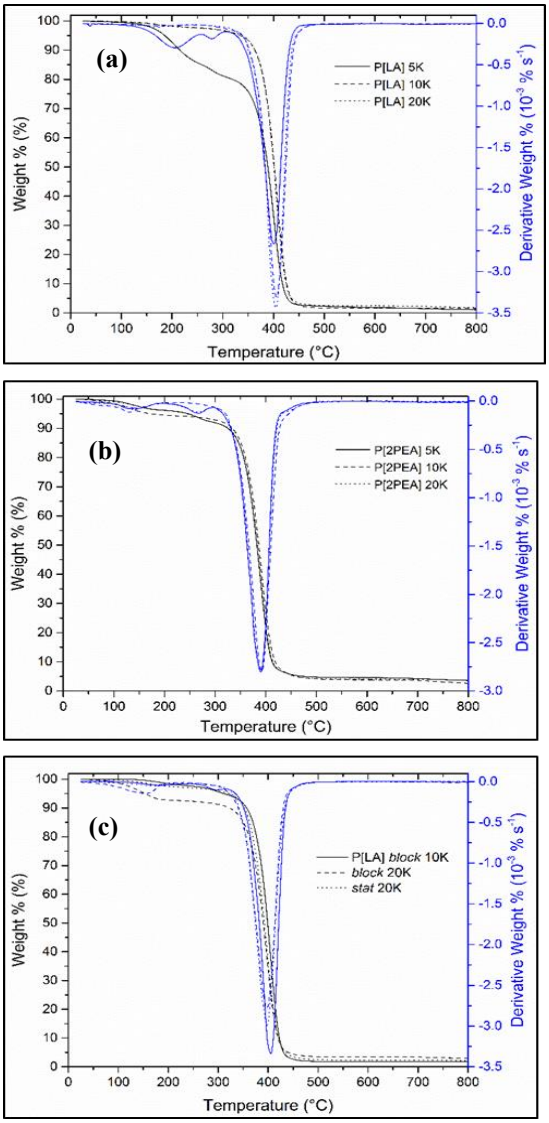

Figure 7.9 TGA and DTA curves of (a) homopolymers of P[LA], (b) homopolymers of P[2PEA] and (c) copolymers of P[LA] and P[2PEA] synthesised *via* Cu(0)-mediated LRP.

7.3.2 DSC of homopolymers and copolymers of P[LA] and P[2PEA]

The homopolymers and copolymers of P[LA] and P[2PEA] were further characterised using DSC to investigate the correlation between composition and thermal properties. The DSC traces of homopolymers of P[LA] (figure 7.10a) exhibit a melting event (T_m ~ 0 °C) and a crystallisation event (T_c ~ -10 °C). The presence of a T_m and T_c illustrates that the long alkyl hydrophobic side chains of the P[LA] are able to pack together in an ordered, possibly lamella type structure.

In contrast, homopolymers of P[2PEA] exhibit a step change in heat flow between -20 °C and 0 °C representing the possible presence of a T_g ~ -10 °C (figure 7.10b). The chemical structure of P[2PEA] is similar to poly(styrene) (PS) with the added difference of the acrylate group and the two carbon units between the acrylate group and the benzene ring. PS is well known to be an amorphous polymer with a T_g ~ 100 °C and therefore, P[2PEA] is expected to be amorphous but with a lower T_g. The lack of rigidity along the polymer backbone of P[2PEA] compared to PS would account for the lower T_g.

The DSC traces of the copolymers (figure 7.10c) clearly represent the differences in polymer architecture between the *block* 20K and the *stat* 20K. The *block* 20K has a T_m ~ 0 °C and T_c ~ -10 °C which is consistent with the P[LA] homo-polymers whereas for the *stat* 20K, these peaks are absent. The peak in the DSC trace for the *block* 20K can be attributed to the sequential ordering of P[LA] units in the polymer backbone and therefore, the alkyl chains can facilitate close packing and subsequently crystallise. In the case of the *stat* 20K, the LA and 2PEA are randomly ordered and close packing between P[LA] chains is not possible. The absence of any peak in the *stat* 20K suggests the monomer is in addition likely to be alternating. This observation is supported from the published literature which details 2PEA prefers to cross-propagate when copolymerised with acrylates.[2, 3] In addition, the copolymer feed of 40:60 of LA:2PEA would also promote cross propagation of LA.

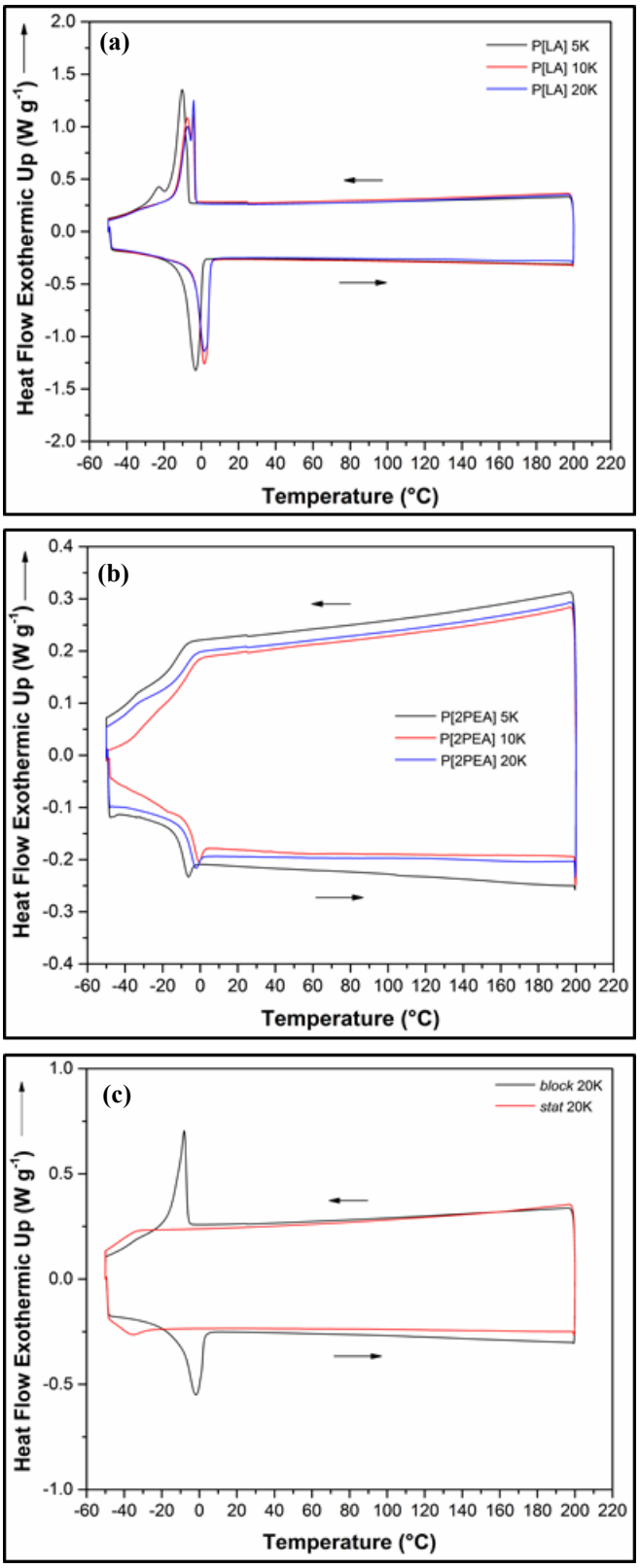

Figure 7.10 DSC traces (first cooling and second heating cycle) of (a) homopolymers of P[LA], (b) homopolymers of P[2PEA] and (c) copolymers of P[LA] and P[2PEA] synthesised *via* Cu(0)-mediated LRP.

7.3.3 Oscillatory rheology of homopolymers and copolymers of P[LA] and P[2PEA]

Oscillatory rheology was used to investigate the viscoelastic properties of the poly(acrylate)s and the extent of nanofiller dispersion in the PP matrix and, *de facto* the effectiveness of these polymers as compatibilisers for GNP and PP. Understanding the viscosity of the polymers (i.e. the internal resistance to flow and deformation) is crucial when designing polymers which can compatibilise 1D and 2D graphitic fillers with polymers. For example, the PP will have a specific melt viscosity while in the extruder, but this can be altered on addition of any nanofiller. To enable the poly(acrylate) to effectively disperse the GNPs within the PP matrix, the viscosity of the poly(acrylate) must be such that the extruder is able to efficiently mix the two components.

An oscillatory shear force is applied to measure the storage modulus (G') (figure 7.11a) i.e. the elastic component (energy stored) by the polymer and the loss modulus (G'') (figure 7.11b) i.e. the viscous component (energy lost) by the polymer as a result of an applied deformation. G' as a function of shear rate (figure 7.11a) decreased with decreasing shear rate because, the G' of the poly(acrylates) is shear rate dependent. At high shear rates, the bulk properties are probed as all polymer chains are subjected to shear stress. Due to the non-Newtonian behaviour of the poly(acrylate), the bulk material is being broken down which has a high combined resistance to flow making it behave solid like however, at low shear rates, only the microstructure is sheared which has a low resistance to flow making it behave fluid like. G' does not deviate with increasing molar mass for both P[LA] and P[2PEA] homopolymers. The bulk properties of the *stat* 20K are almost identical to P[LA]. G' for the P[2PEA] homopolymers is 3 orders of magnitude higher (at 1 rad/s) compared to P[LA] suggesting that the π-π stacking between the P[2PEA] chains is over 1000 times stronger (increased resistance to flow) than the alkyl side chain packing interactions in P[LA]. Interestingly, G' for the *block* 20K is a further order of magnitude higher compared to the P[2PEA] suggesting the *block* 20K is able to self-assemble, the resultant material has an increased elastic response. G'' for the P[LA] 5K is lower than P[LA] 10K, 20K suggesting the polymer chains are too short to pack effectively. The increased complex viscosity $|\eta^*|$ (measured as a function of shear rate) of P[2PEA], by some 3 orders of magnitude than that determined for P[LA], confirms the π-π interactions between P[2PEA] chains are stronger than the side-chain packing interactions between P[LA] chains. The *block* 20K has viscosity similar to the homo polymers of P[2PEA] and the *stat* 20K is intermediate of the P[2PEA] and the P[LA], as might be expected.

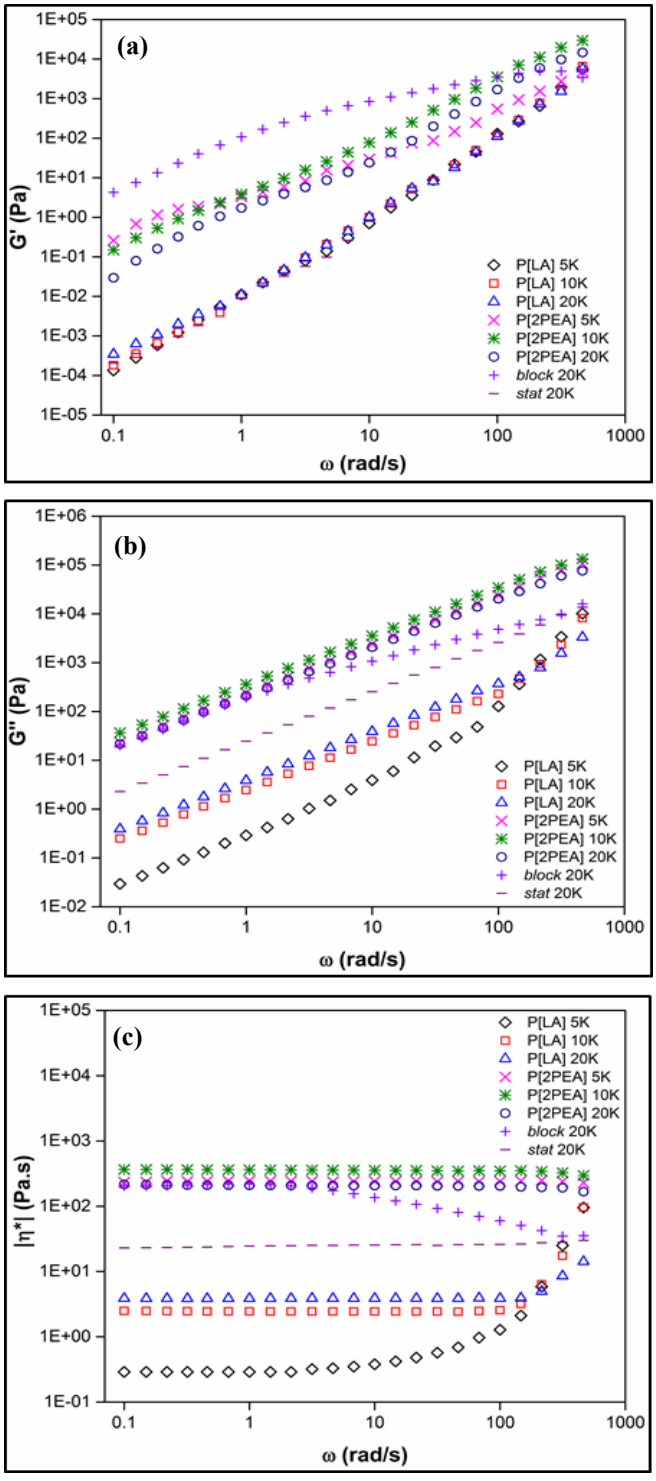

Figure 7.11 Variation in: (a) storage modulus (G'), (b) loss modulus (G'') and (c) complex viscosity ($|\eta^*|$) as a function of angular frequency (ω) for homopolymers and copolymers of P[LA] and P[2PEA] at r.t.

7.4 Composites of MWCNTs and GNPs with homopolymers and copolymers of P[LA] and P[2PEA]

Composites of MWCNTs and GNPs with homo and copolymers of LA and 2PEA were produced, see table 7.4 for the composite formulations prepared. The composites were characterised to investigate the non-covalent adsorption of the poly(acrylate)s onto the surface of both graphitic nanomaterials. The composites were prepared using the procedure detailed in section 3.2.5. and, with a 4:1 ratio of poly(acrylate):nanofiller and therefore all blends contain 5 wt% additives, i.e. compatibiliser plus nanofiller.

Table 7.4 Descriptions of loadings of poly(acrylate)s and filler in the composites.

Composite composition (wt %)	Nomenclature
MWCNTs	MWCNTs
P[2PEA] 5K(4)/MWCNTs(1)	P[2PEA] 5K MWCNTs
P[2PEA] 10K(4)/MWCNTs(1)	P[2PEA] 10K MWCNTs
P[2PEA] 20K(4)/MWCNTs(1)	P[2PEA] 20K MWCNTs
block 20K(4)/MWCNTs(1)	*block* 20K MWCNTs
stat 20K(4)/MWCNTs(1)	*stat* 20K MWCNTs
GNPs	GNPs
P[LA] 5K(4)/GNPs(1)	P[LA] 5K GNPs
P[LA] 10K(4)/GNPs(1)	P[LA] 10K GNPs
P[LA] 20K(4)/GNPs(1)	P[LA] 20K GNPs
P[2PEA] 5K(4)/GNPs(1)	P[2PEA] 5K GNPs
P[2PEA] 10K(4)/GNPs(1)	P[2PEA] 10K GNPs
P[2PEA] 20K(4)/GNPs(1)	P[2PEA] 20K GNPs
block 20K(4)/GNPs(1)	*block* 20K GNPs
stat 20K(4)/GNPs(1)	*stat* 20K GNPs

7.4.1 Composites of MWCNTs with homopolymers and copolymers of P[LA] and P[2PEA]

The SEM micrographs of MWCNTs blended with the different poly(acrylate)s are displayed in (figure 7.12). For the composite of P[2PEA]10K and MWCNTs, the MWCNTs

appear well dispersed within the P[2PEA] matrix (figure 7.12a and b) and randomly orientated with what seems to be an even covering of P[2PEA]. The well dispersed MWCNTs confirms the P[2PEA] is favourably interacting with the surface of the MWCNTs, via a π-π interactions. In the case of the composite of *stat*20K and MWCNTs (figure 7.12c and d), the MWCNTs are not as well dispersed compared to that observed for the P[2PEA]10K MWCNT composite because, the micrographs suggest the MWCNTs are not uniformly coated with polymer. The bulk of the MWCNTs are embedded within the *stat*20K polymer however, there are MWCNTs on the surface which appear to be uncoated with polymer. The observation is expected as the random copolymer backbone of LA and 2PEA will reduce the effectiveness of 2PEA to adsorb onto the surface of MWCNTs compared to the P[2PEA] homopolymer. For the composite of *block*20K and MWCNTs (figure 7.12e and f), there is a clear difference between the two components of the block copolymer. It is assumed the MWCNTs prefer to reside in the P[2PEA] phase rather than the P[LA] phase. The dark smooth areas are deduced to be the P[LA] phase as there is very limited presence of MWCNTs. Whereas in the case of the of the P[2PEA] phase, the MWCNTs are clearly embedded. This observation confirms π-π stacking is occurring between the P[2PEA] and the MWCNTs and any CH-π interactions between the P[LA] and the MWCNTs are considerably weaker. *This observation is in agreement with the hypothesis that it is possible to use a block copolymer to compatibilise MWCNTs with PP as the PP is expected to readily disperse and co-crystallise in the P[LA] phase and the block copolymer will bridge the incompatibility between the PP and the MWCNTs.*

Further investigations were performed using HRTEM to aid the understanding of the interactions between the block copolymers and MWCNTs (figure 7.13). Composites of MWCNTs and both *stat* 20K and *block* 20K were examined. The composite *stat*20K and MWCNTs (figure 7.13a and b) present minimal, if any coating of copolymer on the surface of the MWCNTs. The walls of the MWCNTs (~ 5 nm) appear uniform throughout the sample. However, in the case of the composite of *block* 20K and MWCNTs (figure 7.13c and d) evidence for the block copolymer coating the surface of the MWCNTs is very clear and unequivocal. The lower magnification image (figure 7.13c), the core and walls of the MWCNTs can be observed and the grey shell surrounding the MWCNTs is attributed to the block copolymer. The stark difference between the statistical copolymer and the block copolymer can only be assigned to the sequential repeating pattern of the 2PEA monomer units in block copolymer and their combined π-π stacking leading to the adsorption on the

surface of the MWCNTs. Interestingly, the block copolymer has a high affinity for the MWCNTs but not with itself. For example, the MWCNTs are all coated but the gaps between the MWCNTs are free of polymer suggesting that it is the interaction between the block copolymer and the MWCNTs causing the effect and not a simple case of the MWCNTs embedded within a polymer matrix. Further investigations were carried out to investigate the observation between the block copolymer and the MWCNTs.

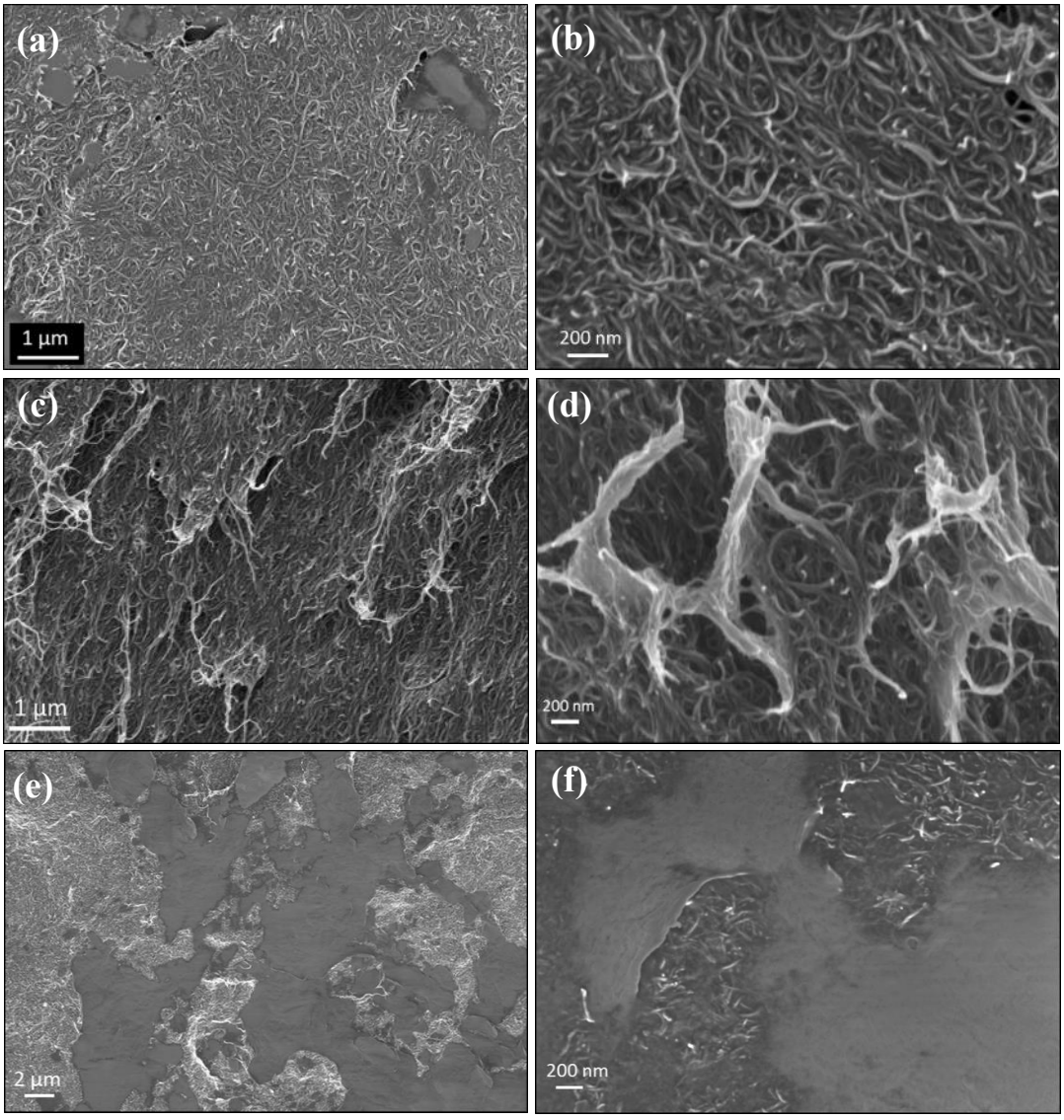

Figure 7.12 SEM micrographs of composites of P[2PEA]10K and MWCNTs at a) x35k and b) x115k; of *stat*20K and MWCNTs at c) x35k and d) x80k and, of *block*20K and MWCNTs at e) x8k and f) x75k magnification.

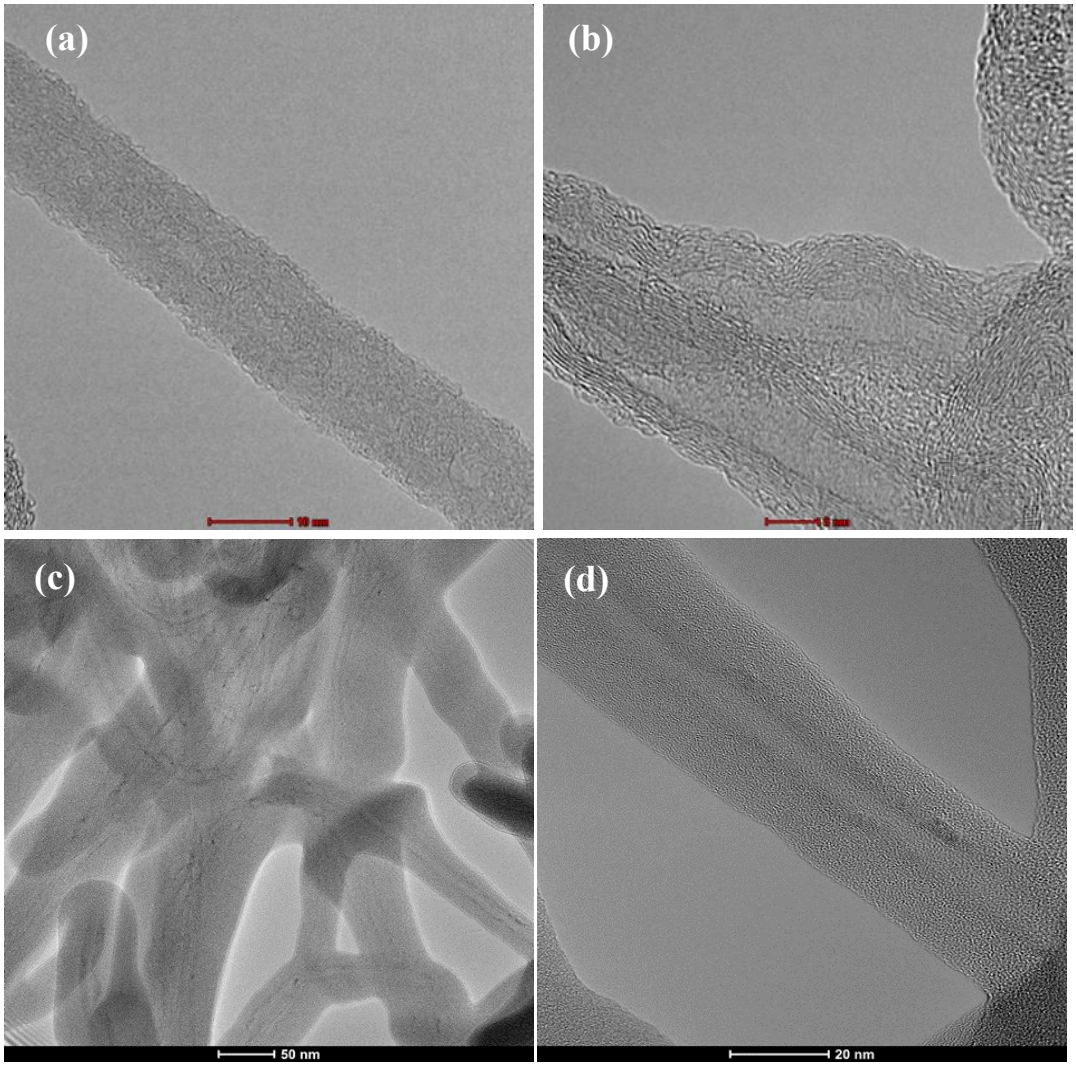

Figure 7.13 TEM images of composites *stat*20K and MWCNTs at a) x630k and b) x820k; and of *block*20K and MWCNTs at c) x94k and d) x390k magnification.

The process of producing the composite of the *block*20K and MWCNTs (*block* 20K MWCNTs) is detailed in figure 7.14. The polymer architecture of using a block copolymer is important in obtaining this coating. The combined π-π stacking of ~57 2PEA units adjacent to each other produces a highly aromatic chain that adsorbs onto the surface of the MWCNTs using the same intermolecular interactions responsible for the aggregation of MWCNTs. The use of ultrasonication and mechanical stirring assists in the breaking up of MWCNT agglomerates of the MWCNTs and block copolymer are subsequently able to self-assemble onto the surface of the MWCNTs leading to an almost perfect uniform coating around the surface of the MWCNTs (~ 10 nm). The coating length can possibly be controlled by altering the lengths of the block-copolymer.

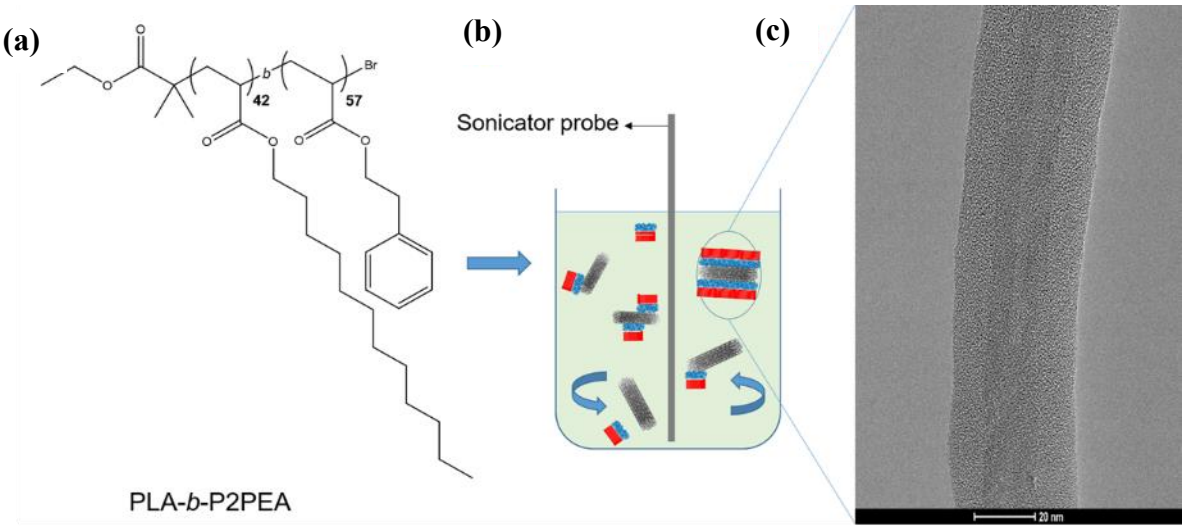

Figure 7.14 a) Structure of di-block copolymer P[LA-*block*-2PEA] ($M_{n,GPC}$ = 19,000 Da, DPn = 1.15) (b) Ultrasonication and mechanical stirring of P[LA-*block*-2PEA] with MWCNTs in $CHCl_3$ (c) HRTEM image depicting evidence for non-covalent functionalization.

The HRTEM and scanning TEM (STEM) images below (figure 7.15) present a uniform ~15 nm coating of the block copolymer on a MWCNT. In addition, HRTEM images suggest that the graphitic structure is preserved along the entire length of the MWCNTs.

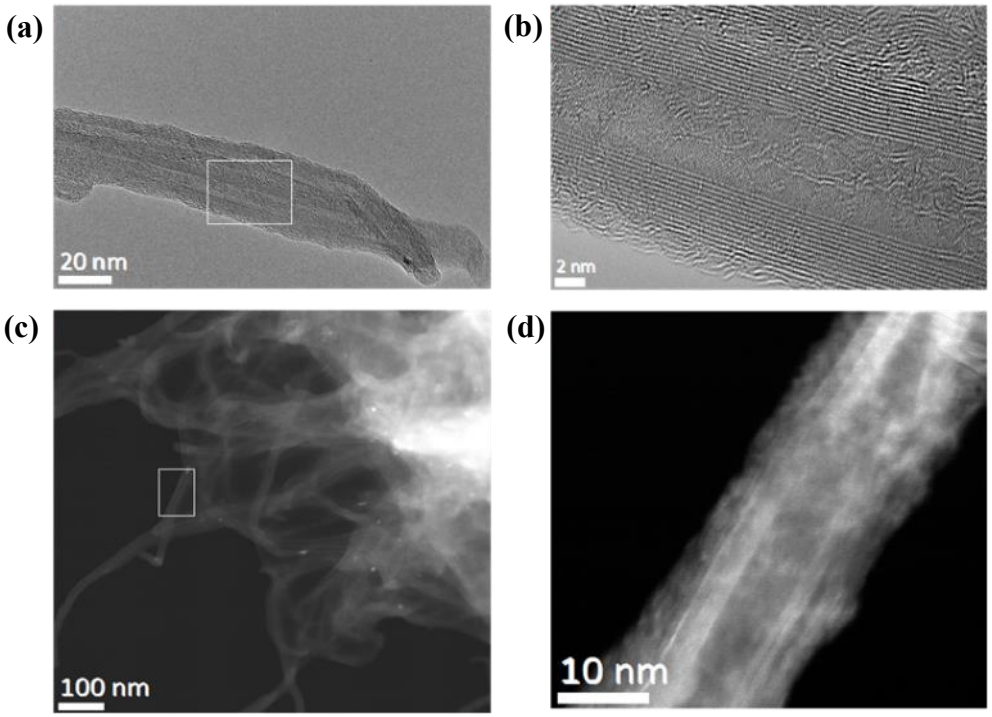

Figure 7.15 a) TEM image of the *block*20K coating a MWCNT and b) a HRTEM image of boxed region in (a); (c) Low magnification dark-field STEM image of *block* 20K MWCNT and (d) HR STEM image of boxed region in (c).

Further work was carried out to determine the bonding state between the block copolymer and the MWCNTs by comparing the electron energy loss near-edge fine structure (ELNES) of the carbon K-edge, which presents the transition from the 1s electronic core state to the unoccupied states above the Fermi level. As reported previously in the literature[4], Figure 7.16a exhibits the shape of the edge for graphite corresponding to a material with 100% (sp^2) bonding. It is composed of two major peaks at 285 eV and 292 eV, which are related to the transition from the 1s to the unoccupied π* states and the transition from the 1s to the unoccupied σ* states, respectively. Figure 7.16b displays only one major σ* peak at around 292 eV, presenting the 100% sp^3 bonding of diamond. By comparing the ELNES spectra at the interphase between the block copolymer and the walls of the MWCNTs, the type of interaction (σ or π) can be determined to establish whether the interaction is indeed π-π stacking.

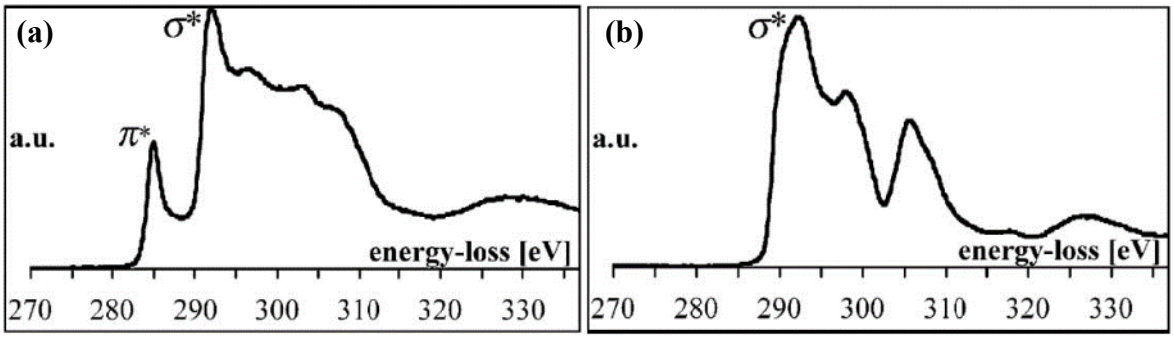

Figure 7.16 Carbon K-edge spectra of a) graphite presenting two peaks of the (sp^2 + $2p_z$) bonding and b) diamond presenting only one major peak of the sp^3 bonding.[4]

Using the STEM imaging mode, a MWCNT coated with block copolymer was imaged (figure 7.17a). EELS was performed on the sample to obtain a spectral image (green box) whereby the electrons passing through the region of interest were analysed to measure their energy loss relative to their initial energy before interacting with the sample. The data analysis was used to produce individual fitting maps, see figure 7.17c and d. In addition, point analysis was performed (blue and red boxed region in figure 7.17a). Figure 7.17b displays EEL spectra obtained from the interface (red) and the centre (blue) of the MWCNT. Both spectra contain the two peaks at 285 eV and 292 eV respectively, suggesting different type of strong interactions. For example, the interactions at the interface are most likely via π-π stacking due to the increased intensity of the π* peak at 285 eV. The spectra suggests the interface contains a greater concentration of sp^2 bonding compared to the centre of the

MWCNT which contains less sp^2 character. The greater sp^2 character at the interphase can be attributed to the presence of aromatic groups on the surface of the MWCNTs confirming the π-π stacking between the P[2PEA] in the block copolymer and the MWCNTs.

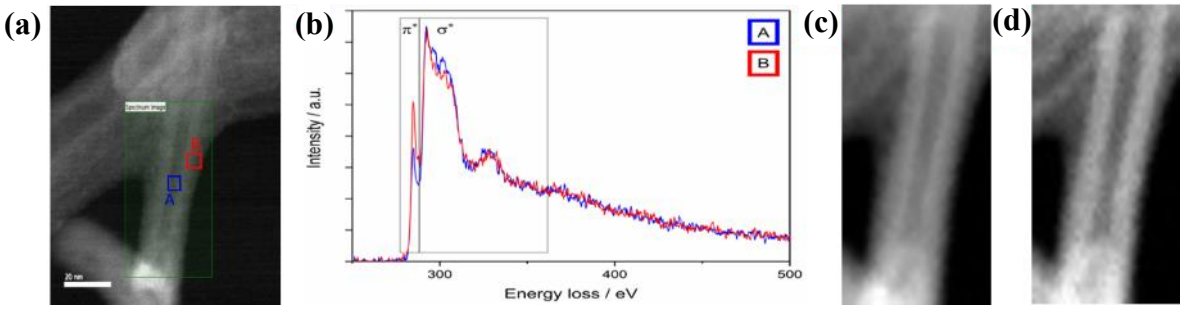

Figure 7.17 EELS analysis. a) High magnification STEM image clearly displaying ~15nm coating of the block copolymer on a MWCNT. b) Carbon K-edge EELS spectra (high-loss) from the green boxed region in (a) from regions A and B, where the peaks at 285 and 292 eV correspond to electron transitions from the 1s level to π* and σ* states, respectively. c) and d) the individual maps of the fitting components from peaks A and B in (a).

DMA and rheology (figure 7.18) was used to further investigate the composite of the *block* 20K (PLA-*b*-P2PEA) and MWCNTs to further aid the understanding of the interactions between the block-copolymer and MWCNTs. The presence of a strong π-π interaction between *block* 20K and the MWCNTs was predicted to promote microstructural reinforcement of the block copolymer. DMA and rheological measurements provided evidence for changes in the viscoelastic properties of the composite relative to the unfilled polymer supporting the observations suggesting the block copolymer absorbs onto the surface of MWCNTs via π-π bonding. The DMA was performed in compression mode by placing the sample between two compression plates. The tan δ (ratio of loss modulus to storage modulus) (figure 7.18a) is a measure of the energy dissipation of the material. At temperatures below -30 °C, the material has a very low tan δ suggesting the material is not losing energy under compression. This is due to the P[LA] block crystallising (determined from DSC – figure 7.10c) and hence the block copolymer is solid. Upon melting of the P[LA] block at ~ -20 °C, the tan δ increases significantly from ~ 0 to ~ 2.2 for the neat block copolymer suggesting the block copolymer is becoming fluidic (more viscous than elastic). However, for the composite, the MWCNTs keep the tan δ below 0.5 revealing the *E'* (storage

modulus) remains greater than the *E″* (loss modulus). The significant difference in tan δ confirms the MWCNTs are interacting with the MWCNTs and are able to form a network. *E′* remains greater for the composite compared to the neat block copolymer after melting of the P[LA] block (> 20 °C) by ~ 50 MPa confirming the reinforcement effect.

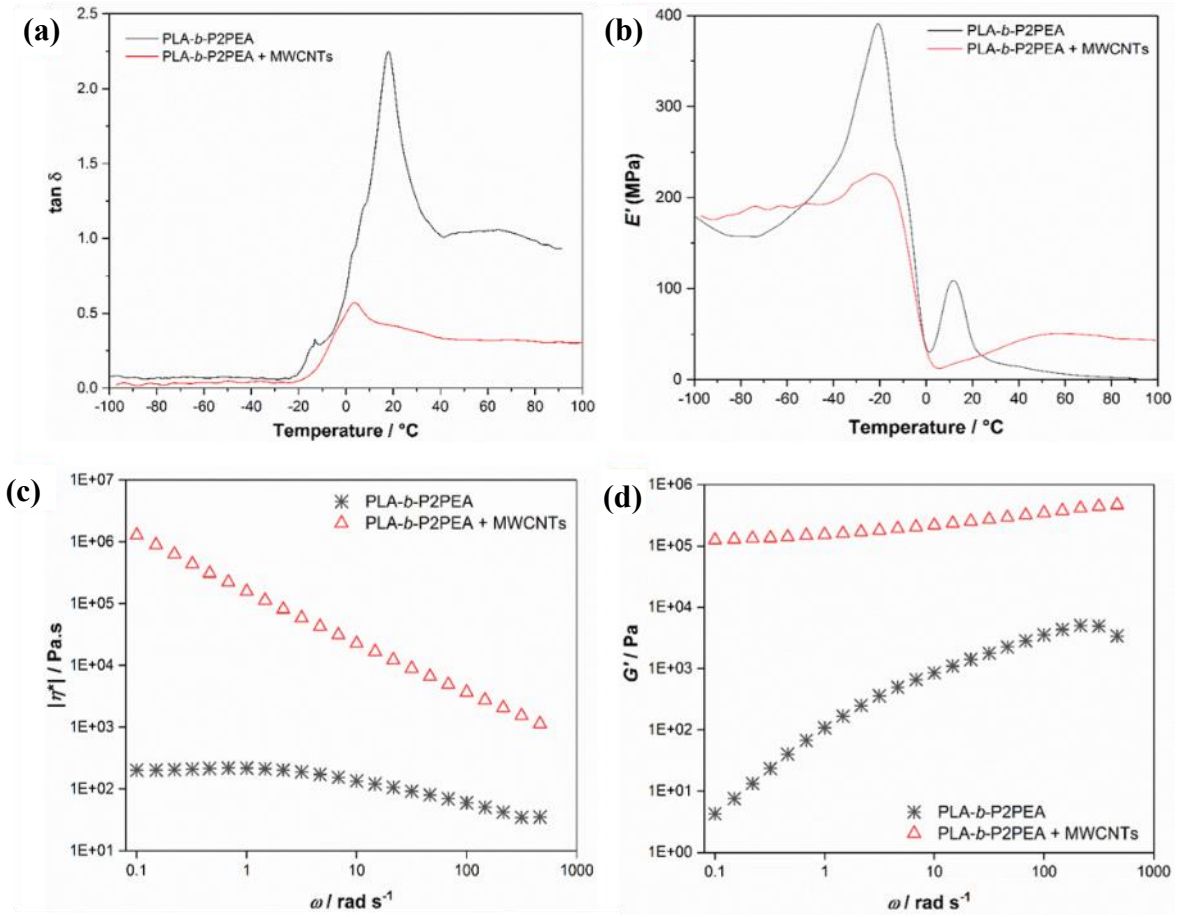

Figure 7.18 DMA and rheological analysis. Variation of a) tan δ and b) storage modulus (*E′*), verses temperature for PLA-b-P2PEA (*block* 20K) and its composite with MWCNTs. Variation (at RT) of (c) storage modulus (*G′*) and (d) complex viscosity (|*η**|), as a function of angular frequency (*ω*) for PLA-*b*-P2PEA and its composite with MWCNTs.

Oscillatory shear rheology was performed on the unfilled block copolymer and the composite (figure 7.18) to further understand the reinforcement effect observed from the DMA measurements. The complex viscosity (|*η**|) (figure 7.18c) and storage modulus (G′)-figure 7.18d) of the composite increased by over 3 orders of magnitude (at 1Hz). The attractive forces between the MWCNTs and the block copolymer are strong with the 'pseudo solid' behaviour displayed by the composite and plateauing of *G′* indicating network formation and strong elastic character which is required for mechanical reinforcement.

Small- and wide-angle X-ray scattering data was used to elucidate the structure and compatibility of the MWCNTs with the copolymer. SAXS provides information on the self-assembly and long-range ordering in the copolymer and on the copolymer/MWCNT composite, whilst WAXS provides information on the crystal lattice structure. Figure 7.19, exhibits the SAXS/WAXS patterns of the pure copolymer, MWCNTs and corresponding composite, including the molecular packing detail which is obtained from this data. In figure 7.19a, the WAXS patterns of the MWCNTs and block copolymer materials are presented.

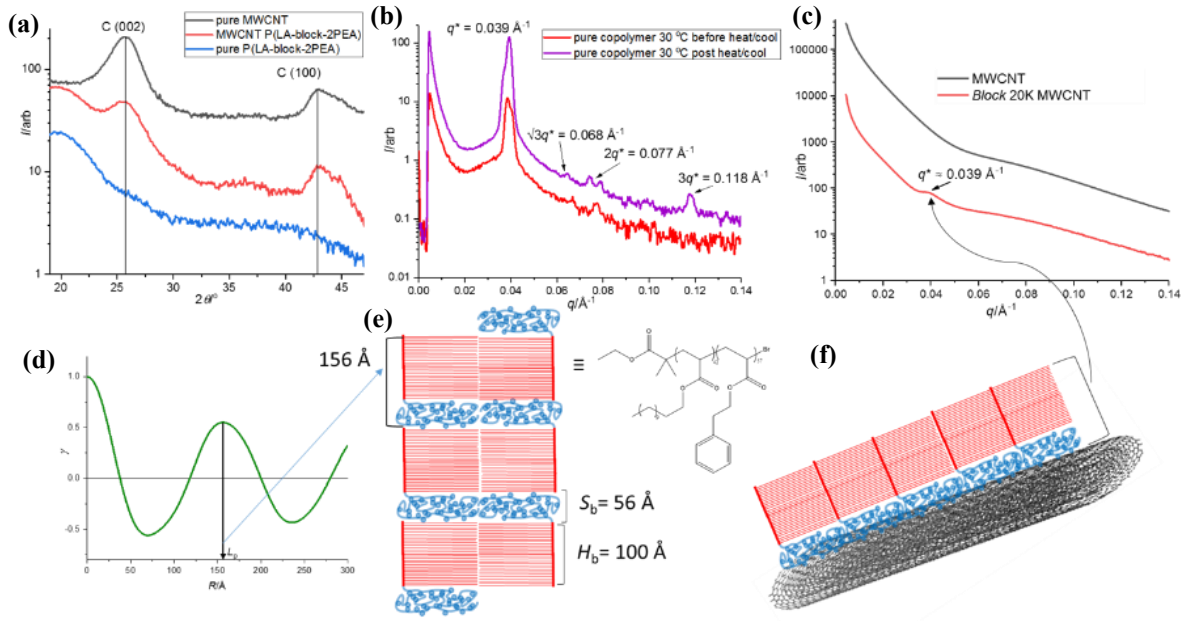

Figure 7.19 Small and wide-angle X- ray scattering data (SAXS/WAXS) of pure copolymer (*block* 20K), MWCNTs and corresponding blend, with molecular packing detail. (a): WAXS patterns of pure MWCNT and MWCNT blend displaying prominent (002) and (100) graphite peaks but, absent in the pure block copolymer pattern. (b): SAXS patterns of pure block copolymer at 30 °C (pre and post-heating to 100 °C), indicating regular lamellar structure. (c): SAXS patterns of pure MWCNT and MWCNT block copolymer blend, where q* at 0.039 Å is still observed in the copolymer blend. (d): Computed correlation function of pure block copolymer SAXS profile displaying long period (Lp) as ~ 156 Å. (e): Lamellar structure of block copolymer with length-scales extracted from the correlation function; Lp = 156 Å, hard block (Hb) is the P[LA] block being ~ 100 Å and soft block (Sb) being P[PEA] block being ~ 56 Å. (f): Schematic of block copolymer on surface of a MWCNT with indication of length-scale in SAXS.

All SAXS and WAXS data were normalized for sample thickness, transmission and background scattering. X-ray data reduction and analysis was performed using the Xeuss 2.0

instrument data processing and analysis software. Both 2D SAXS/WAXS data were reduced to 1D scattering profiles of intensity (I) versus scattering vector (q) for SAXS and 2θ for WAXS (where $q = (4\pi/\lambda) \sin(\theta)$, 2θ is the scattering angle and λ is the X-ray wavelength), by sector averaging around the beam stop by a fixed angle and radius, q. The SAXS data peak positions (D_{max}), were determined by the relationship $D_{max} = 2\pi/q$.

Correlation functions[5] $\gamma(R)$, were performed on the 1D SAXS scattering profiles.[6] The correlation function is given by the expression:

$$\gamma(R) = \frac{1}{Q_s}\int_0^\infty I(q)q^2 \cos(qR)\mathrm{d}q \tag{6}$$

where, $I(q)$ is the scattering intensity and Q_s, is the invariant profile from the SAXS scattering profile between the experimental limits of q_1 (the first real data point) and q_2 (the region where $I(q)$ is constant):

$$Q_s(t) = \int_0^\infty q^2 I(q)\mathrm{d}q \approx \int_{q_1}^{q_2} q^2 I(q)\mathrm{d}q \tag{7}$$

The SAXS data was extrapolated ($q \rightarrow \infty$) using a Porod[7] tail fit and a linear back extrapolation ($q \rightarrow 0$) was applied. Various parameters were extracted from the correlation function such as, the long period, Lp which is the average dimension of the block copolymer lamellar repeat unit which comprises of the 'hard block' (H_b) and 'soft block' (S_b) regions.

With regards to the pure MWCNTs, two prominent peaks are seen relating to the (002) and (100) graphite structure. The (002) at $2\theta = 25.5^o$ indicates and interlayer spacing (sp^2-carbon layers), in the MWCNTs of 3.46 Å, which is seen to be broader than that of graphite (being 3.35 Å), due to the layering in the MWCNTs.[8, 9] The (002) and (100) peaks are also evident in the composite of the block copolymer MWCNTs. However, the block copolymer itself has no obvious crystalline unit cell structure from WAXS as only very broad peaks are seen. Figure 7.19b, presents 1D SAXS patterns of the pure block copolymer at 30 ºC before and after heating to 100 ºC. Various peaks can be observed, the strong first order peak $q^* = 0.039$ Å^{-1}. The heat/cool cycle refines the peaks which are seen in the ratio of 1:2:3, which strongly supports a classical self-assembled lamellar morphology[10-12] with sharp interfaces. A small peak is seen at $\sqrt{3}q^*$ which indicates a mixture of a hexagonal morphology, however it is evident that in this particular di-block copolymer the chains are arranged predominantly in a periodically ordered lamellar structure.

Figure 7.19c, exhibits 1D SAXS scattering patterns of the pure MWCNTs and the composite of MWCNTs and the block copolymer, obtained at 30 ºC. The pure MWCNT SAXS pattern displays a very broad peak in the region of 0.06-0.09 $Å^{-1}$, relating to the average MWCNT shell thickness of ~80 Å[13, 14] (Confirmed for TEM imaging, see figure 7.14). The MWCNT broad peak can still be observed in the SAXS pattern of the MWCNT block copolymer blend, as well as the first order copolymer peak at ~ 0.039 $Å^{-1}$. However, the peak at 0.039 $Å^{-1}$ is broadened and no evidence of the 2nd and 3rd order peaks for the block copolymer are seen, so on addition of the MWCNTs to the block copolymer the sharp interface of the lamellar packing is disrupted. The lamellar repeat distance in the pure copolymer distance was determined by correlation function analysis on the 1D SAXS pattern (in b) and is displayed in figure 7.19d. Figure 7.19e, relates the parameters obtained from the correlation function with the lamellar structure of the block copolymer. Here, the long period (L_p) represents the lamellar repeat distance where the red 'hard block' (H_b) relates to the lauryl acrylate monomer units and the blue 'soft block' (S_b) is the phenyl ethyl acrylate monomer units. Finally, figure 7.19f, presents a schematic packing representation of the copolymer around the MWCNT surface, where the phenyl ethyl acrylate monomer units form non-covalent π-π interactions on the MWCNT surface, whilst the lauryl acrylate monomer units still assemble with a lamellar packing morphology.

Further characterisation of composites of MWCNTs and poly(acrylate)s was performed using TGA (figure 7.20). The neat MWCNTs exhibited an onset of thermal degradation at ~ 700-710 °C as result of the degradation of amorphous carbon and residual catalysts. The quantity of amorphous carbon and residual catalysts was calculated to be ~ 5 wt%. The onset of degradation of the composites of MWCNTs and poly(acrylate)s was typically 300 -320 °C except for the composite of P[2PEA]5K and MWCNTs which had an onset of degradation of 250-260 °C which can be attributed to the presence of unreacted 2PEA monomer, confirmed by TGA of the monomer (Appendix 10), figure 7.5 and table 7.2. The onset of degradation is unchanged to that of neat P[2PEA] (figure 7.9b) suggesting the MWCNTs have not had an effect on the onset of degradation for the composites. The DSC traces of the composites of MWCNTs with poly(acrylate)s (figure 7.21) are unchanged by the addition of MWCNTs compared to the neat composites (figure 7.10). Even though P[2PEA] non-covalently adsorbs onto the MWCNTs, the thermal properties are not affected such as increase in onset of thermal degradation or change in DSC traces.

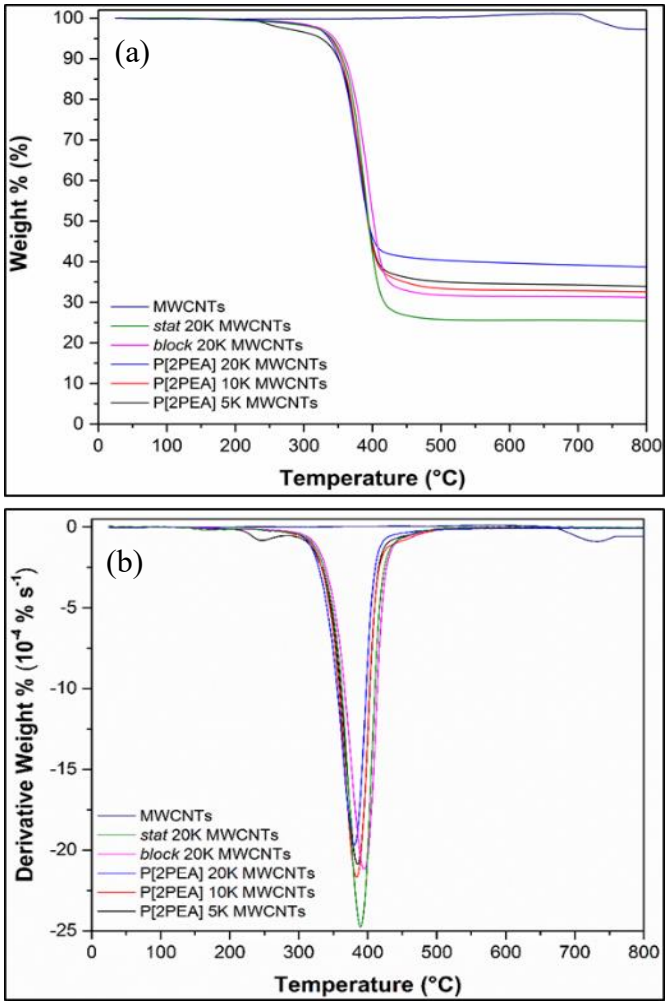

Figure 7.20 a) TGA and b) DTA curves of composites of MWCNTs with homopolymers and copolymers of P[LA] and P[2PEA].

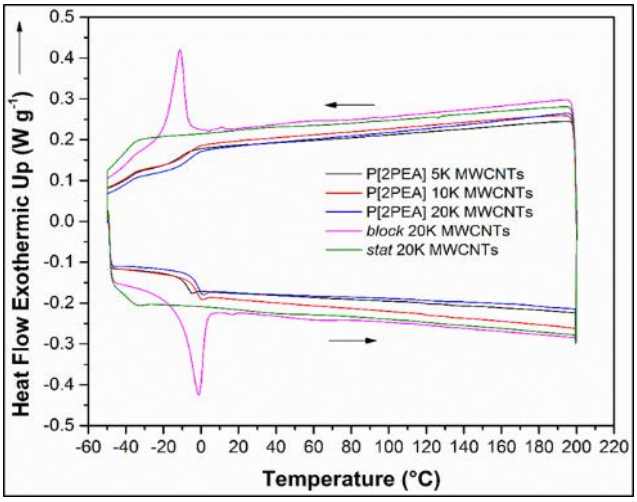

Figure 7.21 DSC traces of composites of MWCNTs with homopolymers and copolymers of P[LA] and P[2PEA].

The extent of intermolecular interaction between the poly(acrylate)s and the MWCNTs was further studied using Raman spectroscopy (figure 7.22). Shifts in the

frequency of the bands can provide a measure for the effect of compressive or tensile forces imposed by the poly(acrylate)s (table 7.5) on the walls of the MWCNTs.[15] A significant upshift in frequency was observed for all three bands major bands associated with graphitic structures. The *D*-band upshifted by ~7.7 cm^{-1} for the P[2PEA] homo-polymer. The block copolymer MWCNT composite had a lower shift of ~ 4.4 cm^{-1} whereas the statistical copolymer composite had an upshift of the *D*-band of ~6 cm^{-1}. In the case of the *G*-band, the P[2PEA] homo-polymer composites demonstrated the greatest and significant upshift of ~14 cm^{-1}. The composites having block or statistical copolymer MWCNT had an upshift of ~10.7 and ~12.4 cm^{-1}, respectively. It is clear the greatest upshift as result of the π-π stacking was obtained for the composite of the P[2PEA] homo-polymer and MWCNTs. The P[2PEA] component is applying a cohesive energy to the MWCNT sidewalls resulting in a compressive force acting on the MWCNT C-C bonds. The composites of block copolymer and statistical copolymer with MWCNTs are not as efficient at applying cohesive stress due to the presence of P[LA] which does not interact with the MWCNTs as strongly as the P[2PEA] homopolymer.

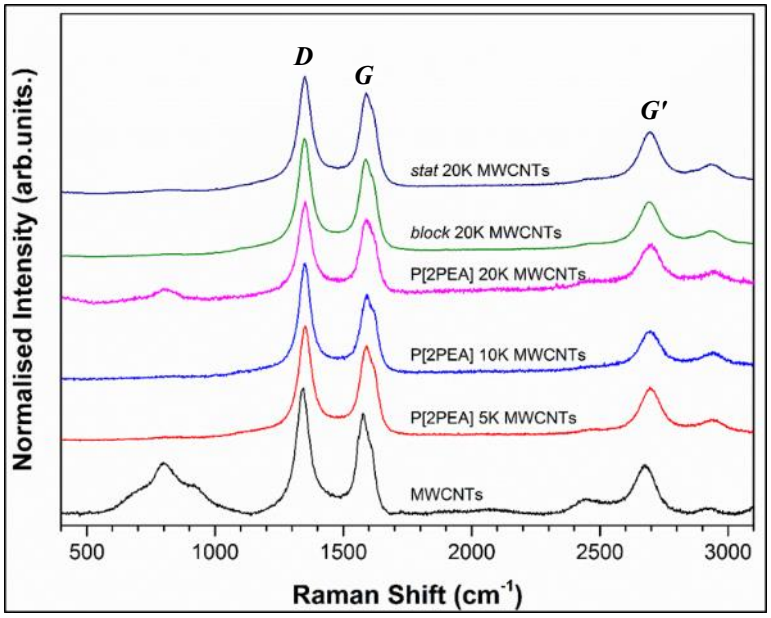

Figure 7.22 Raman spectra of MWCNTs alone and composites of MWCNTs with homopolymers and copolymers of P[LA] and P[2PEA].

Furthermore, the intensity ratios between the *D*-band and *G*-band can be used establish changes in the chemical structure of the MWCNTs (table 7.6). The *D*-band located between 1250 cm^{-1} and 1450 cm^{-1} and is present due to the defects which distort the quasi-infinite crystalline lattice symmetry and therefore gives a direct indication of the level of disorder of the MWCNTs.[16] Changes in intensities between the *D*-band, *G*-band and *G′*-band are inconclusive to either support or deny the presence of π-π interactions between the poly(acrylates) and the surface of the MWCNTs.

Table 7.5 Raman bands for neat MWCNTs and composites of MWCNTs with homopolymers and copolymers of P[LA] and P[2PEA].

Sample	*D* band peak (cm^{-1})	*D* band FWHH (cm^{-1})	*G* band peak (cm^{-1})	*G* band FWHH (cm^{-1})	*G′* band peak (cm^{-1})	*G′* band FWHH (cm^{-1})
MWCNTs	1344.2	63	1577.8	68	2674.2	101
P[2PEA] 5K MWCNTs	1351.9	63	1591.8	76	2694.6	100
P[2PEA] 10K MWCNTs	1351.9	57	1591.8	73	2697.4	99
P[2PEA] 20K MWCNTs	1351.9	58	1591.8	74	2698.8	114
block 20K MWCNTs	1348.6	62	1588.5	76	2691.8	107
stat 20K MWCNTs	1350.2	63	1590.2	74	2696.0	109

Table 7.6 Raman properties of MWCNTs and composites of MWCNTs with homopolymers and copolymers of P[LA] and P[2PEA].

Sample	I_D / I_G	I_D / $I_{G'}$	$I_{G'}$ / I_G	*G* minus *D* (cm^{-1})	*G′* minus *D* (cm^{-1})	*G′* minus *G* (cm^{-1})
MWCNTs	1.26	2.71	0.464	232.0	1332.8	1100.8
P[2PEA] 5K MWCNTs	1.23	2.28	0.538	239.9	1342.7	1102.8
P[2PEA] 10K MWCNTs	1.39	2.64	0.527	241.5	1345.8	1104.2
P[2PEA] 20K MWCNTs	1.25	1.91	0.656	239.9	1345.5	1105.6
block 20K MWCNTs	1.23	2.32	0.529	238.3	1343.0	1104.7
stat 20K MWCNTs	1.24	2.02	0.584	239.9	1347.2	1107.3

7.4.2 Composites of GNPs with homopolymers and copolymers of P[LA] and P[2PEA]

The morphology of composites of GNPs and the poly(acrylate)s were examined using SEM, figure 7.23. SEM micrographs of composites of P[LA]10K and GNPs (figure 7.23a and b) demonstrate the GNPs are dispersed within the P[LA] matrix (GNPs indicated by white arrows). The GNPs appear well dispersed and are embedded within the P[LA] polymer matrix. The observation suggests the GNPs have a high affinity for the P[LA]. For composites of P[2PEA]10K and GNPs, the GNPs are scattered within and on the surface of the P[2PEA] (figure 7.23c and d). The SEM micrographs depict the GNPs are well dispersed within the P[2PEA] matrix across the two length scales suggesting the GNPs have a high affinity for the P[2PEA] also. The composite of *stat*20K and GNPs (figure 7.23e and f) is similar to that of the composite of the P[2PEA] where the GNPs are present on the fractured surface of the polymer and embedded within the polymer as observed with the composite of P[LA] and GNPs. Furthermore, the SEM micrographs for the composite of *block* 20K GNPs (figure 7.23g and h) also demonstrate the GNPs are well dispersed with the block copolymer matrix. The polymer surface is highly wrinkled which is due to the reinforcement effect of the GNPs which lead to an increase in viscosity of the bulk polymer matrix.

TEM micrographs of composites of GNPs with poly(acrylate) (figure 7.24) are presented. Due to the limited phase contrast between the GNPs and the poly(acrylate), it was challenging the distinguish between the GNPs and the poly(acrylate)s. The TEM process involves imaging electrons in transmission through the GNPs and because both the GNPs and poly(acrylate)s are carbon based, the limited elemental contrast makes quantifying the functionalisation challenging. However, the images clearly display the multi-layer structure of the GNPs and the boundary edges of the multi-layer sheets are marked with white lines. Changes in grey-scale contrast can be used to distinguish between each of the individual layers of the GNPs for example, on the GNP edge, the sheets with fewer number of layers appear brighter because, there are less layers to restrict the transmission of electrons that are used to generate the image. The darker areas present a greater number of layers which absorb and scatter a greater proportion of electrons producing a darker image.

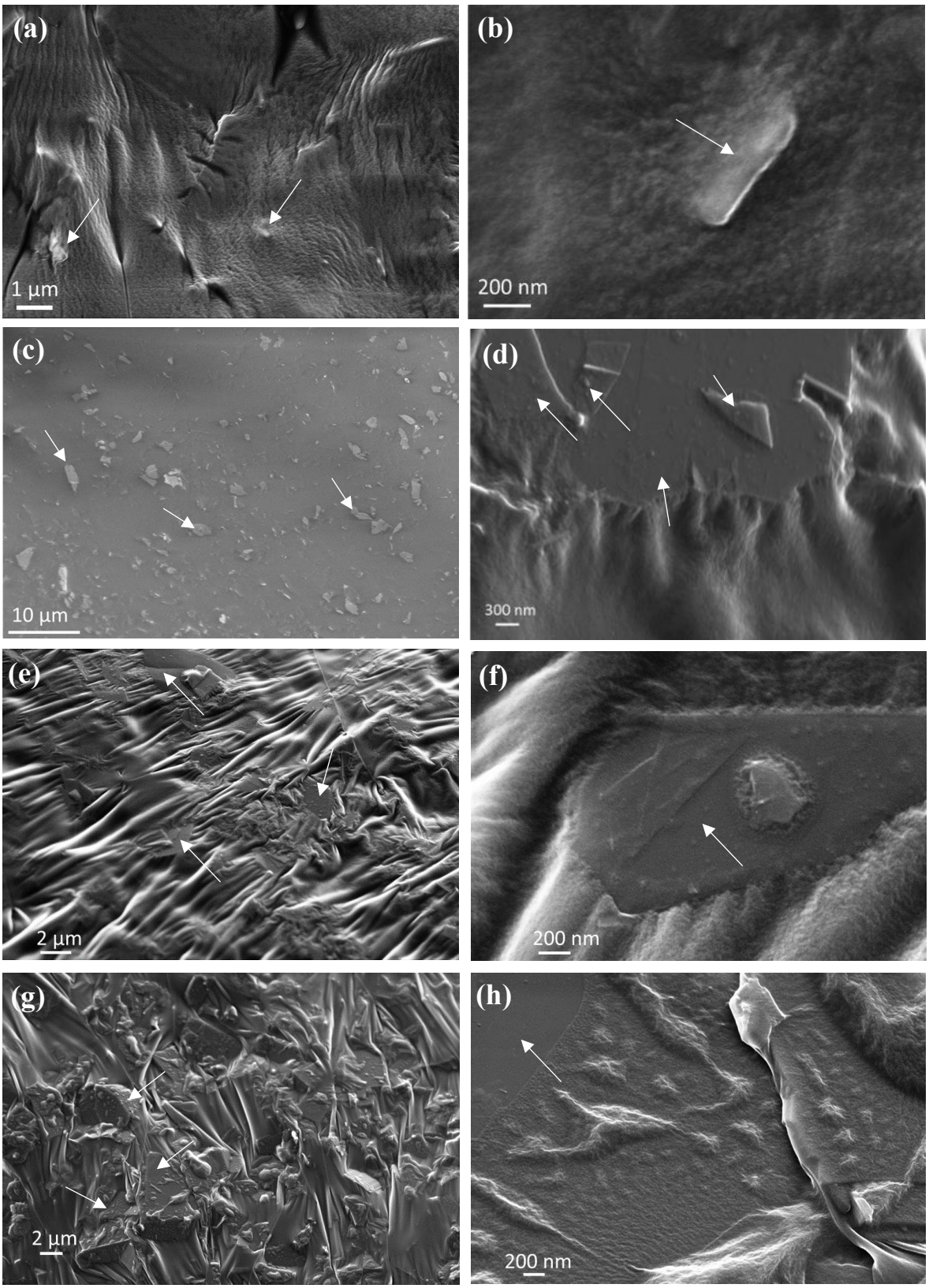

Figure 7.23 SEM micrographs of composites of GNPs and poly(acrylate). P[LA] 10K GNPs a) x25k and b) x150k; P[2PEA] 20K GNPs c) x5k and d) x50k; *stat* 20K e) x10k and f) x100k; *block* 20K g) x7k and x70k magnification.

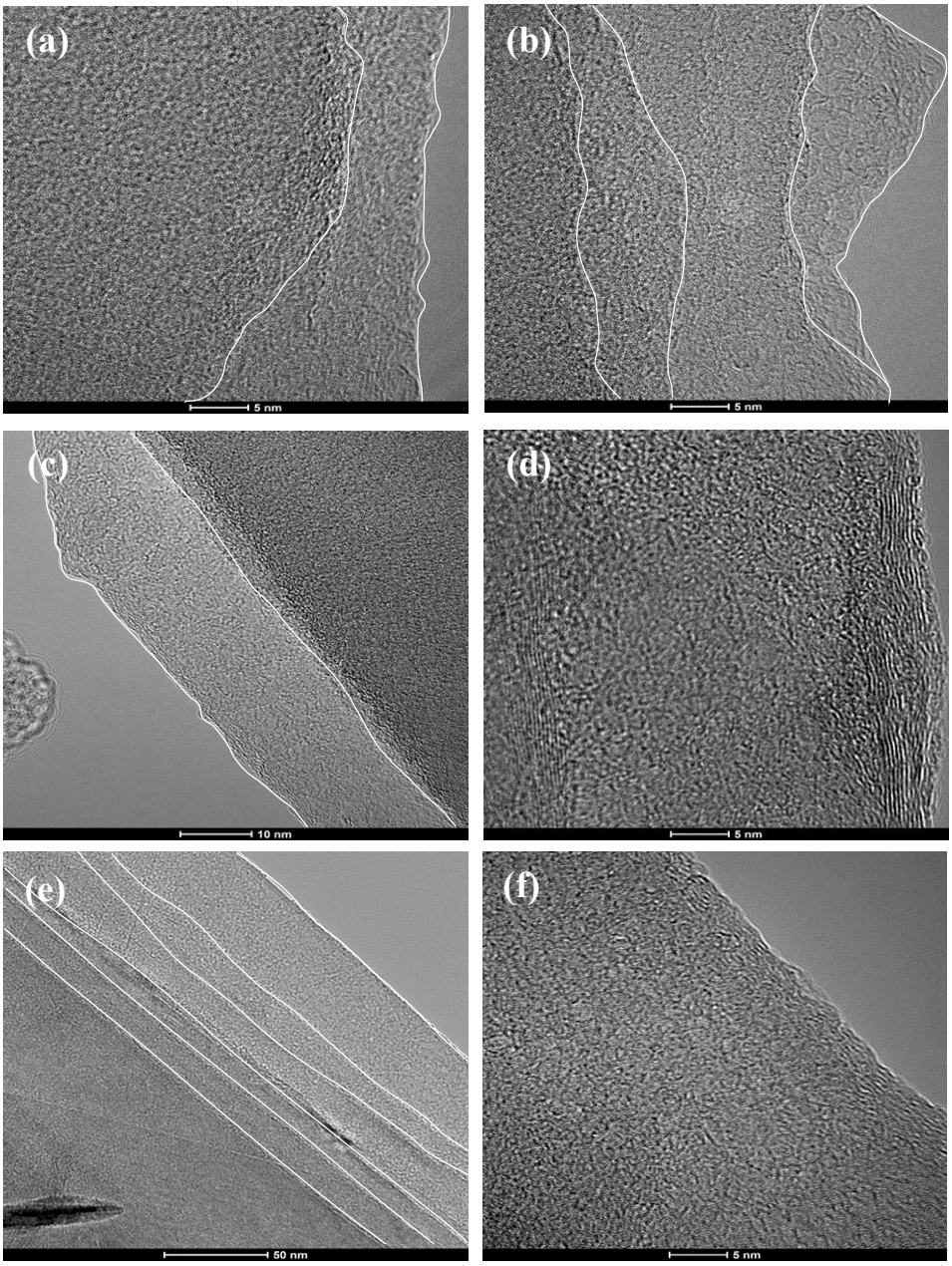

Figure 7.24 TEM images of unfunctionalised GNPs a) x1,050k and b) x1,050k. Composites of GNPs and poly(acrylate). *Stat* 20K GNPs c) x650k and d) x1,050k. *Block* 20K GNPs e) x190k and f) x1,050k magnification.

The thermal degradation properties of un-functionalised GNPs and its composites with the poly(acrylate)s (figure 7.25) exhibits the onset of degradation (~300-320 °C) is similar for all except the composites of P[LA]5K and GNPs and P[2PEA]5K and GNPs. The neat GNPs exhibit minimal if any mass loss over the measured temperature range. The onset of degradation is consistent with unfilled poly(acrylate)s suggesting the addition of GNPs does not influence the thermal degradation properties of these poly(acrylate)s. The lower onset of degradation for the P[LA]5K/ GNP composite (~100-110 °C) is due to its lower

molecular weight and presence of un-polymerised monomer (see Appendix 10). The slightly lower onset of degradation for the composite of P[2PEA]5K and GNPs (~270-280 °C) is also due to presence of un-polymerised monomer and low molecular weight oligomers (Appendix 10).

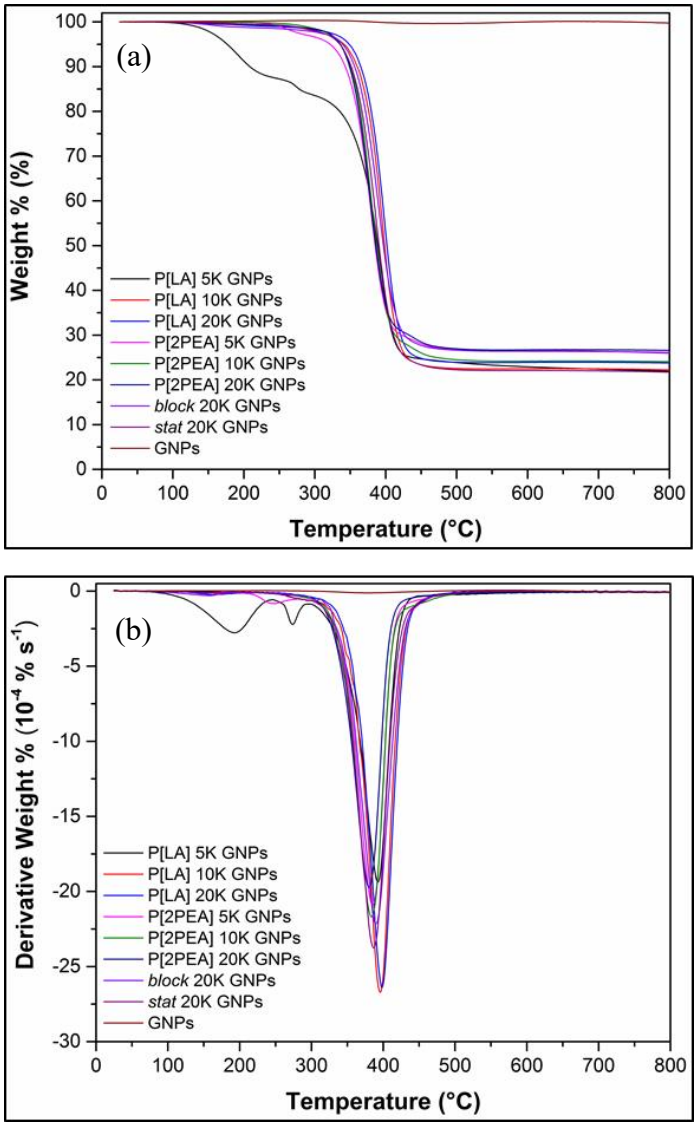

Figure 7.25 (a) TGA and (b) DTA curves of composites of GNPs with homopolymers and copolymers of P[LA] and P[2PEA].

The DSC traces for the composites of GNPs and the poly(acrylate)s (figure 7.26) are not dissimilar to the DSC traces for the unfilled poly(acrylate)s (figure 7.10). The homo-polymers of P[LA] retain their T_m and T_c at ~ 0 and -10 °C respectively upon addition of GNPs. The homo-polymers of P[2PEA] also retain their T_g between -5 and -10 °C. The

thermal properties of both copolymers are also unchanged suggesting the GNPs are not affecting the thermal properties of these poly(acrylate)s.

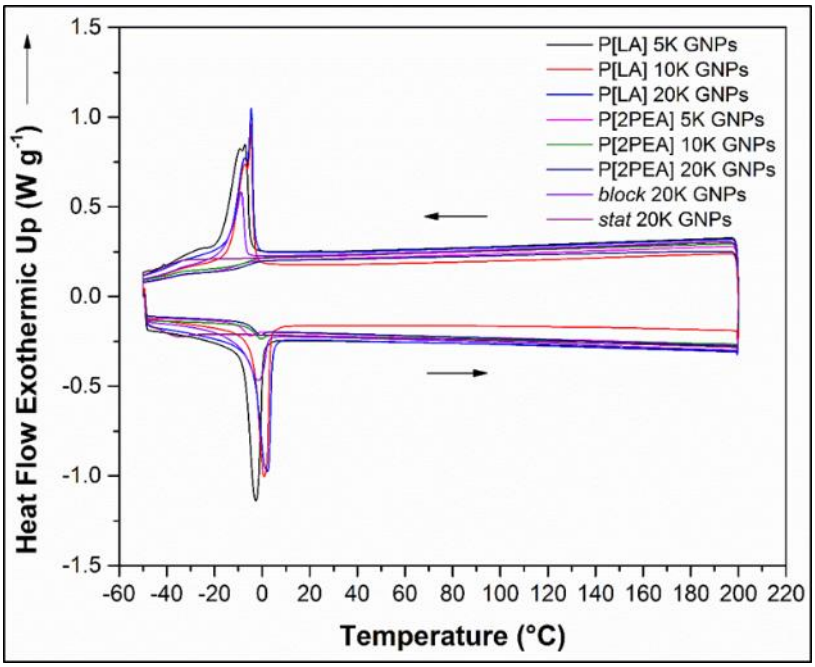

Figure 7.26 DSC traces of composites of GNPs with homopolymers and copolymers of P[LA] and P[2PEA].

Raman analysis (figure 7.27) revealed limited if any shifting (table 7.7) in the *D* and *G* band for all the poly(acrylate)s which may be attributed to the planer structure of the GNPs.[17] The poly(acrylate)s are unable to apply a compressive stress to the surface of the GNPs which is detectable by Raman spectroscopy, in contrast to that observed with MWCNTs. However changes to the I_D/I_G particularly for the P[2PEA]5K/ GNPs composite demonstrate the P[2PEA] does π-π stack with the surface of the GNPs. The I_D/I_G decreased from 0.12 to 0.02. A possible reason for the reduction in *D*-band could be that the P[2PEA] 5K is able to efficiently coat the GNPs and particularly the sheets edges due to its shorter chain length. The presence of P[2PEA] 5K adsorbed on the surface of the GNPs renders the *D*-band signal undetectable. However, this hypothesis is unproven and requires further investigation.

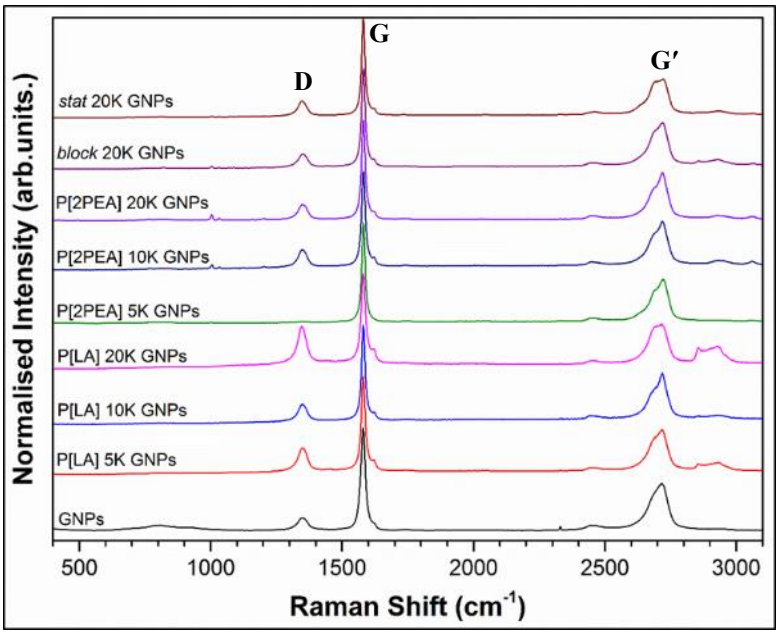

Figure 7.27 Raman spectra for neat GNPs and composites of GNPs with homopolymers and copolymers of P[LA] and P[2PEA].

Table 7.7 Raman peaks for GNPs and composites of GNPs with homopolymers and copolymers of P[LA] and P[2PEA].

Sample	D band peak (cm^{-1})	D band FWHH (cm^{-1})	G band peak (cm^{-1})	G band FWHH (cm^{-1})	G′ band peak (cm^{-1})	G′ band FWHH (cm^{-1})
GNPs	1349.2	45	1581.0	21	2718.8	78
P[LA] 5K GNPs	1350.2	40	1580.4	18	2718.3	74
P[LA] 10K GNPs	1350.2	37	1580.4	18	2718.3	68
P[LA] 20K GNPs	1346.9	38	1580.4	21	2716.9	82
P[2PEA] 5K GNPs	1351.9	17	1582.1	16	2721.1	75
P[2PEA] 10K GNPs	1346.9	40	1582.1	18	2718.3	74
P[2PEA] 20K GNPs	1351.9	42	1580.4	18	2718.3	70
block 20K GNPs	1351.9	40	1582.1	18	2719.7	78
stat 20K GNPs	1348.6	38	1580.4	15	2723.8	82

Table 7.8 Raman of GNPs and composites of GNPs with homopolymers and copolymers of P[LA] and P[2PEA].

Sample	I_D / I_G	I_D / $I_{G'}$	$I_{G'}$ / I_G	G minus D (cm^{-1})	G′ minus D (cm^{-1})	G′ minus G (cm^{-1})
GNPs	0.120	0.262	0.457	231.9	1369.6	1137.8
P[LA] 5K GNPs	0.242	0.553	0.438	230.2	1368.1	1137.8
P[LA] 10K GNPs	0.166	0.335	0.495	230.2	1368.1	1137.8
P[LA] 20K GNPs	0.416	0.961	0.433	233.5	1370.0	1136.5
P[2PEA] 5K GNPs	0.002	0.004	0.429	230.2	1369.2	1139.0
P[2PEA] 10K GNPs	0.174	0.368	0.473	235.2	1371.4	1136.2
P[2PEA] 20K GNPs	0.150	0.317	0.472	228.5	1366.4	1137.8
block 20K GNPs	0.129	0.286	0.449	230.2	1367.8	1137.6
stat 20K GNPs	0.143	0.388	0.369	231.9	1375.3	1143.4

The rheological behaviour of the composite of GNPs with the block copolymer (figure 7.28) similar to that obtained for the composites of the same block copolymer with MWCNTs in that the composite material responded more like a ‘pseudo-solid’. Similarly, the viscosity and storage modulus increased by ~ 3 orders of magnitude (at 1 rad/s) indicating the strong reinforcement by the GNPs. Network formation was established for a 20 wt% GNP loading determined by the plateau effect in *G′* at low frequencies.

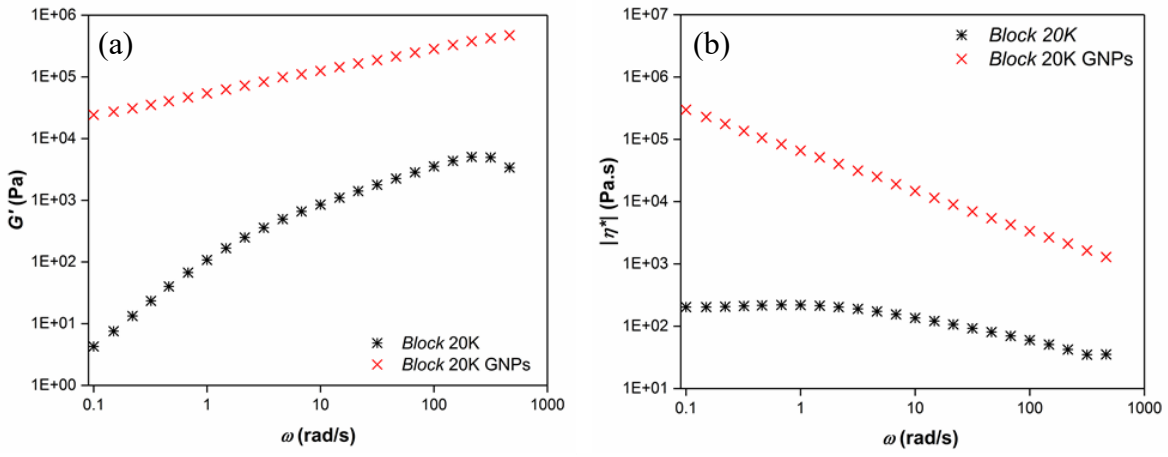

Figure 7.28 Variation (at RT) of (a) storage modulus (*G′*) and (b) complex viscosity (|*η**|), as a function of angular frequency (*ω*) for a composite of *block* 20K and GNPs.

7.5 Conclusions

Bi-functional copolymers comprising of P[LA] and P[2PEA] were synthesised using Cu(0)-mediated LRP and their potential for non-covalently functionalising MWCNTs and GNPs for the purpose of compatibilisation with PP investigated. As well as homo polymers of P[LA] and P[2PEA], copolymers consisting of a block copolymer and statistical random copolymer were characterised and their composites with MWCNTs and GNPs were studied to determine the extent to which they functionalise both fillers. The hypothesis was for them to adsorb onto the surface of the 1D and 2D graphitic fillers though a combination of π-π stacking between the aromatic side chains, in the case of P[2PEA] and CH-π wrapping in the case of P[LA]. In addition, the role of polymer architecture, such as statistical or block copolymer was explored to determine the optimal adoption and compatibilisation mechanism.

Poly(acrylate)s were effectively synthesised using the Cu(0)-mediated LRP process with the polymers achieving high conversion (>97%) and in good agreement with theoretical M_n. The dispersities were generally below $Đ \sim 1.2$ revealing the poly(acrylate)s had narrow distributions. Low molecular weight poly(acrylate)s, P[LA]5K and P[2PEA] 5K were not well controlled with lower than expected (<97%) conversion and broad distributions. Low molecular weight control in LRP polymerisations has often been challenging due to the high initiator concentrations and lack of monomer, leading to a greater rate of terminating side reactions compared to polymers with higher DP_n.

Thermal degradation studies using TGA showed the poly(acrylate)s consistently degraded with an onset temperature of ~300-320 °C resolving the fact that the thermal degradation is independent of side chain, filler or molecular weight but governed by the poly(acrylate) backbone. These poly(acrylate)s are sufficiently stable for melt extrusion with PP. Minor thermal degradation (of up to 10 wt%) at temperatures below ~300-320 °C occurred in some samples, particularly the low molecular weight samples due to the presence of unreacted monomer, oligomers and solvent. Further characterisation with DSC established the homopolymers of P[LA] exhibit a $T_m \sim 0$ °C and $T_c \sim -10$ °C due to crystallisation of the alkyl chains in a predicted lamella morphology. However, in the case of homopolymers of P[2PEA] a presumed $T_g \sim -10$ °C was observed. In addition, DSC confirmed the block copolymer exhibited a crystallisation event similar to the homo-polymer P[LA] but in the case of the statistical copolymer, no thermal transitions were observed.

Oscillatory shear measurements of the poly(acrylate)s determined the shear modulus and viscosity of the homopolymers of P[2PEA] were 3 orders of magnitude higher compared to homopolymers of P[LA] demonstrating the attractive π-π interactions in the aromatic polymer are stronger than the alkyl hydrophobic interactions in P[LA]. Incidentally, the block copolymer behaves similar to the P[2PEA] homopolymer whereas the statistical copolymer behaves closer to the P[LA] homopolymer in terms of inherent viscosity.

Composites of the copolymers with MWCNTs and GNPs were prepared by solution mixing with the aid of ultrasonication so as to study the interfacial interactions in more detail. SEM micrographs revealed the MWCNTs preference for P[2PEA] compared to P[LA]. The block copolymer demonstrates immiscibility between the two blocks and MWCNT migration to the predicted P[2PEA] phase. HRTEM images clearly demonstrate a uniform coating (~10 nm) of block copolymer on the surface of the MWCNTs with a proposed mechanism of the P[2PEA] block π-π stacking on the walls of the MWCNTs. EELS was used to establish that the surface of the MWCNTs have a greater concentration of sp^2 hybridized bonding compared to their centre due to the presence of aromatic groups from the block copolymer. DMA and oscillatory rheology provided (indirectly) further evidence for such strong π-π interactions between the block copolymer and the MWCNTs by establishing an increase in stiffness (storage modulus) of the composite compared to the neat polymer. Further confirmation of π-π stacking from Raman spectroscopy was observed for composites of homo and copolymers of P[2PEA] determined by the upshifting in *D* and *G* bands as a result of the compressive stress applied by the polymers on the filler surface.

Consequently (Chapter 8), the bi-functional compatibilisers were investigated by producing composites of MWCNT or GNP functionalised poly(acrylate) and PP. The hypothesis is to improve the mechanical and electrical properties of the PP matrix concomitantly by efficiently dispersing the MWCNTs or GNPs and improving interfacial adhesion with the PP.

7.6 References

1. A. Anastasaki, C. Waldron, V. Nikolaou, P. Wilson, R. McHale, T. Smith and D. M. Haddleton, *Polym. Chem.*, 2013, **4**, 4113-4119.
2. U. Senthilkumar, K. Ganesan and B. S. R. Reddy, *J. Polym. Res.*, 2003, **10**, 21-29.
3. H. Lee, G. Tae and Y. H. Kim, *Macromol. Res.*, 2008, **16**, 614-619.

4. A. L. Hamon, J. Verbeeck, D. Schryvers, J. Benedikt and R. Van der Sanden, *J. Mater. Chem.*, 2004, **14**, 2030-2035.
5. G. R. Strobl and M. Schneider, *J. Polym. Sci. Part B: Polym. Phys.*, 1980, **18**, 1343-1359.
6. P. G. Grady, Simple SAXS and WAXS Software written in Excel, http://coecs.ou.edu/Brian.P.Grady/saxssoftware.html#Allprograms, (accessed 14/08/17).
7. G. Porod, *Colloid. Polym. Sci.*, 1951, **124**, 83-114.
8. O. Zhou, R. M. Fleming, D. W. Murphy, C. H. Chen, R. C. Haddon, A. P. Ramirez and S. H. Glarum, *Science*, 1994, **263**, 1744-1747.
9. H. B. Zhang, G. D. Lin, Z. H. Zhou, X. Dong and T. Chen, *Carbon*, 2002, **40**, 2429-2436.
10. F. S. Bates and G. H. Fredrickson, *Annu. Rev. Phys. Chem.*, 1990, **41**, 525-557.
11. I. W. Hamley and V. Castelletto, *Prog. Polym. Sci.*, 2004, **29**, 909-948.
12. A. J. Meuler, M. A. Hillmyer and F. S. Bates, *Macromolecules*, 2009, **42**, 7221-7250.
13. B. N. Wang, R. D. Bennett, E. Verploegen, A. J. Hart and R. E. Cohen, *J. Phys. Chem. C*, 2007, **111**, 5859-5865.
14. T. Inada, H. Masunaga, S. Kawasaki, M. Yamada, K. Kobori and K. Sakurai, *Chem. Lett.*, 2005, **34**, 524-525.
15. M. S. Dresselhaus, G. Dresselhaus, R. Saito and A. Jorio, *Phys. Rep.*, 2005, **409**, 47-99.
16. D. Linton, P. Driva, B. Sumpter, I. Ivanov, D. Geohegan, C. Feigerle and M. D. Dadmun, *Soft Matter*, 2010, **6**, 2801-2814.
17. S. R. Ahmad, C. Z. Xue and R. J. Young, *Mater. Sci. Eng., B*, 2017, **216**, 2-9.

Chapter 8 Results and Discussion V

Characterisation of composites of PP filled with multi-walled carbon nanotubes (MWCNTs) and graphene nano-platelets (GNPs) compatibilised with homo-polymers and co-polymers of poly(lauryl acrylate) P[LA] and 2-phenyl ethyl acrylate P[2PEA]

8.1 Introduction

The following work describes the effectiveness of poly(acrylate) homo-polymers and co-polymers as compatibilisers for MWCNTs and GNPs with PP. To accurately explore the effect of the poly(acrylate)s on composite properties, the filler concentration (MWCNT or GNP wt%) was fixed at 1 wt%. The rationale for this is to firstly evaluate the effect of the poly(acrylate) before evaluating the effect of changing the filler concentration which has been independently studied in earlier chapters. In addition, it has been reported that the percolation threshold of MWCNT and GNP filled composites is usually less than 1 wt%[1] for a well dispersed system and therefore, any changes in percolation threshold observed will be due to the compatibilisation of the fillers by the poly(acrylate)s. Theoretically, all composites should be above percolation.[2]

The composites were produced with a filler:poly(acrylate) ratio of 1:4. Such a ratio was chosen due to the high aspect ratio of the fillers, which gives them an exceptionally large surface area.[3, 4] To achieve the maximum possible improvement in composite properties, the filler requires maximum surface coverage with poly(acrylate) and therefore, the 1:4 ratio of filler:poly(acrylate) was chosen to ensure sufficient poly(acrylate) covers and compatibilises the filler surface but, ensures excessive quantities are not used which can influence the bulk properties of the PP and dampen the effects of interest from the filler. Earlier results (chapter 5) indicated improvements in dispersion were observed when the filler:P[LA] was 1:4 compared to 1:1. For example, the composites of MWCNTs and P[LA] (1:1) were less well dispersed and subsequently, the properties (mechanical and electrical) of the PP matrix diminished. The composite formulations studied are listed in table 8.1.

To accurately evaluate the effect of the combination of filler and poly(acrylate) on the PP matrix, reference samples were prepared, including PP and MWCNTs, PP and GNPs, and PP and poly(acrylates). The reference samples contain identical loadings for either the fillers or the poly(acrylate) compared to the composites containing all three components, see

table 8.1. For the reference samples containing the homo-polymer poly(acrylate)s and PP, a single median molecular weight of 10,000 g mol^{-1} for the poly(acrylate) was selected.

Table 8.1 Loadings of PP, filler and poly(acrylate) in the composites studied.

Composite composition (wt %)	**Nomenclature**
PP(100)	PP
PP(99)/MWCNTs(1)	PP MWCNTs
PP(95)/P[LA] 5K(4)/MWCNTs(1)	P[LA] 5K MWCNTs
PP(95)/P[LA] 10K(4)/MWCNTs(1)	P[LA] 10K MWCNTs
PP(95)/P[LA] 20K(4)/MWCNTs(1)	P[LA] 20K MWCNTs
PP(95)/P[2PEA] 5K(4)/MWCNTs(1)	P[2PEA] 5K MWCNTs
PP(95)/P[2PEA] 10K(4)/MWCNTs(1)	P[2PEA] 10K MWCNTs
PP(95)/P[2PEA] 20K(4)/MWCNTs(1)	P[2PEA] 20K MWCNTs
PP(95)/*block* 20K(4)/MWCNTs(1)	*block* 20K MWCNTs
PP(95)/*stat* 20K(4)/MWCNTs(1)	*stat* 20K MWCNTs
PP(99)/GNPs(1)	PP GNPs
PP(95)/P[LA] 5K(4)/GNPs(1)	P[LA] 5K GNPs
PP(95)/P[LA] 10K(4)/GNPs(1)	P[LA] 10K GNPs
PP(95)/P[LA] 20K(4)/GNPs(1)	P[LA] 20K GNPs
PP(95)/P[2PEA] 5K(4)/GNPs(1)	P[2PEA] 5K GNPs
PP(95)/P[2PEA] 10K(4)/GNPs(1)	P[2PEA] 10K GNPs
PP(95)/P[2PEA] 20K(4)/GNPs(1)	P[2PEA] 20K GNPs
PP(95)/*block* 20K(4)/GNPs(1)	*block* 20K GNPs
PP(95)/*stat* 20K(4)/GNPs(1)	*stat* 20K GNPs
PP(96)/P[LA] 10K(4)	PP P[LA] 10K
PP(96)/P[2PEA] 10K(4)	PP P[2PEA] 10K
PP(96)/*block* 20K (4)	PP *block* 20K
PP(96)/*stat* 20K (4)	PP *stat* 20K

The composites included homo-polymers of P[LA] and P[2PEA]. Molecular weights of 5,000, 10,000 and 20,000 $gmol^{-1}$ (denoted as 5K, 10K and 20K respectively) were used

to understand if differences in molecular weight of the compatibilising poly(acrylate) influenced the properties of the composite. The *block* and *statistical* (*stat*) co-polymers were synthesised with a molecular weight of 20,000 $gmol^{-1}$, to ensure there is sufficient quantity of each monomer (LA and 2PEA) in the co-polymer to interact with the filler component of the composite.

The purpose of the following series of composites is to investigate how the monomer type (alkane or aromatic), effects the interaction between the filler and poly(acrylate) and which type of monomer and architecture provides significant improvement in properties of the composites, i.e. mechanical and rheological. The hypothesis is to focus on the use of a *block* co-polymer which is designed to compatibilise the filler (MWCNTs or GNPs) with PP (scheme 8.1). The first monomer (aromatic based) in the copolymer is expected to non-covalently physisorb onto the surface of the filler by a means of strong intermolecular interactions such as, π-π stacking[5] or CH-π.[6] The co-monomer (aliphatic based) will co-crystallise with PP and therefore, the interfacial adhesion between the filler and the polymer matrix is enhanced,[7, 8] as displayed schematically in scheme 8.1.

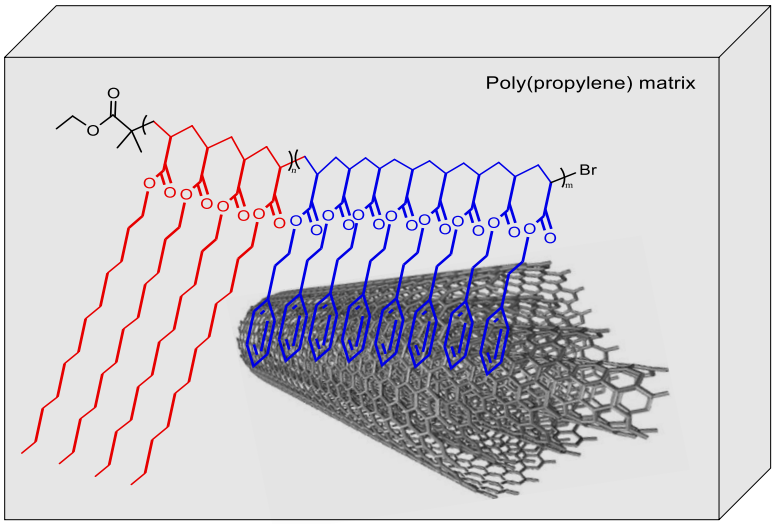

Scheme 8.1 Schematic representation for the non-covalent compatibilisation of P[LA-*block*-2PEA] with MWCNTs within a PP matrix.

To the best of my knowledge, little scientific exploration into the physical chemistry of blends of PP and low molecular weight poly(acrylate)s has been conducted. Such blends are often referred to as 'polymer alloys' and are composed of miscible and immiscible polymer blend systems which can lead to multiple phase separation within the bulk matrix.[9] Hosoda

et al. investigated the role of a poly(propylene-*block*-methyl methacrylate) block copolymer as a compatibiliser for the immiscible blend of PP and poly methyl methacrylate (PMMA).[9] PMMA can be considered similar (but not the same) as the poly(acrylate)s investigated herein and therefore, their findings can be used to support the observations made within this chapter. SEM micrographs of blends of PP-PMMA (70:30) conducted by Hosoda *et al* clearly demonstrated micro-phase separation of the PMMA within the PP matrix in the form of droplets caused by a lack of interfacial adhesion between the two polymer systems. Upon addition of their block copolymer, the PMMA particle size significantly reduced and the block copolymer was assumed to be thermodynamically driven to the PP/PMMA interface.[9] In addition, Seemork *et al*. also found PMMA to form droplets within a PP matrix.[10]

8.2 Characterisation of composites of PP, MWCNTs or GNPs with poly(acrylate)s

SEM provides a visual microscale representation of the location, dispersion and distribution of the filler within the PP matrix. The impact of the poly(acrylate)s on the dispersion of the fillers in composites with PP was determined by imaging the cryo-fractured surfaces of composite samples. However, it is worth noting such images may not necessarily be representative and any conclusive arguments should not be made based on electron microscopy images alone. Nevertheless, it provides a vital contribution to the overall understanding of the effect of the poly(acrylate)s on composite structure. SEM micrographs of neat PP (fig. 8.1a-b) depict a smooth surface even after cryo-fracture. Figure 8.1c-f) displays the SEM micrographs of PP blended with homo and copolymers of P[LA] and P[2PEA]. When comparing the SEM micrograph of PP blended with 4 wt% P[LA] 10K (fig. 8.1c) with neat PP, no significant difference was observed. A smooth surface with the absence of micro-phase separation indicates the P[LA] is miscible with the PP matrix. If P[LA] was immiscible with PP, P[LA] droplets would be observed. The result demonstrates the P[LA] can co-crystallise with PP or at least reside in the amorphous phase of PP. In contrast, SEM micrographs of composites of PP with 4 wt% P[2PEA] 10K (fig. 8.1d) reveal the presence of P[2PEA] 10K droplets (labelled with white arrows). The droplets, containing P[2PEA], clearly demonstrate that P[2PEA] micro-phase separates when dispersed with PP and is immiscible with PP. The morphology is as expected because, P[2PEA] is an aromatic poly(acrylate) and not expected to be miscible with PP.

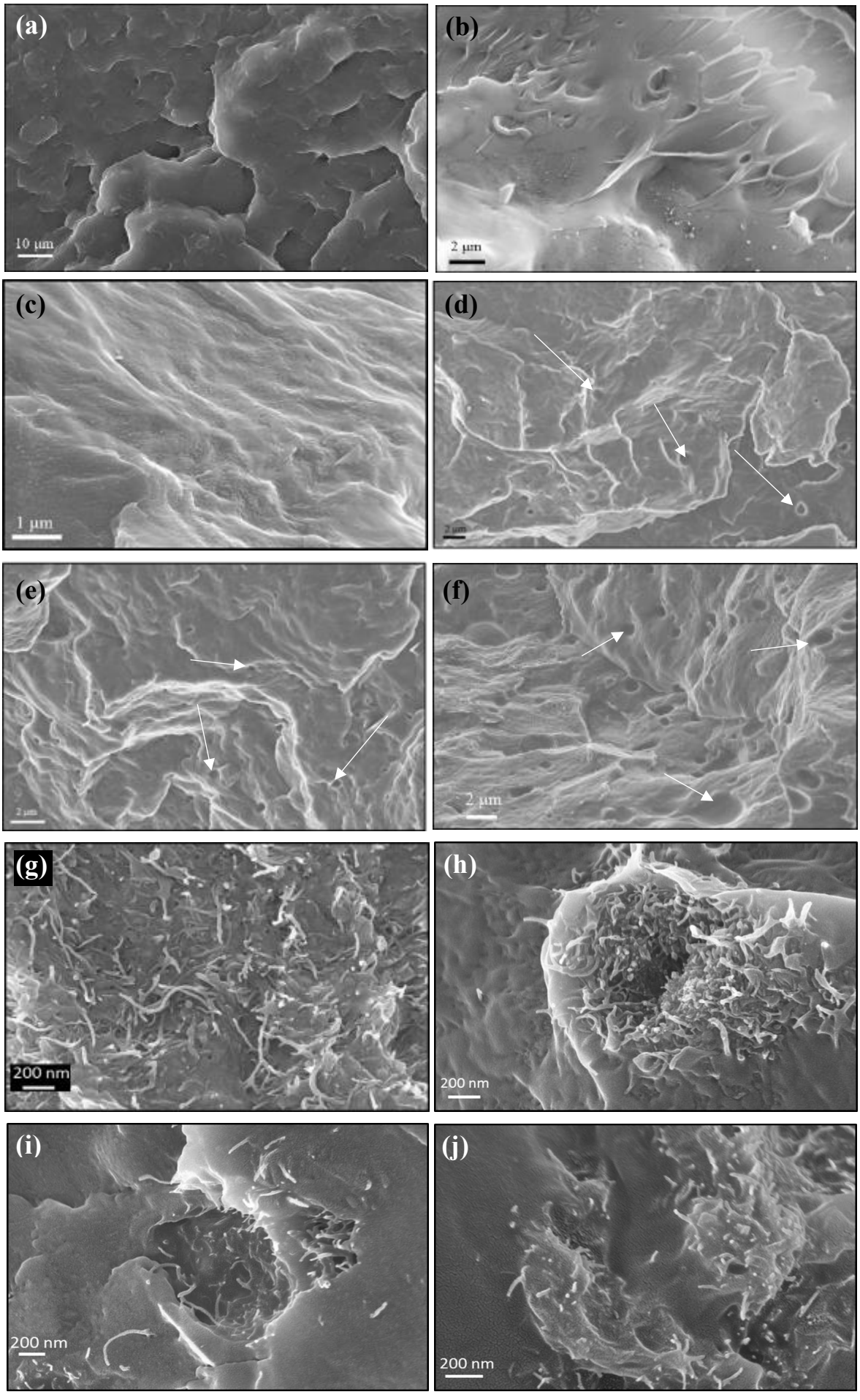
(a)
10 µm
(b)
2 µm
(c)
1 µm
(d)
(e)
(f)
2 µm
(g)
200 nm
(h)
200 nm
(i)
200 nm
(j)
200 nm

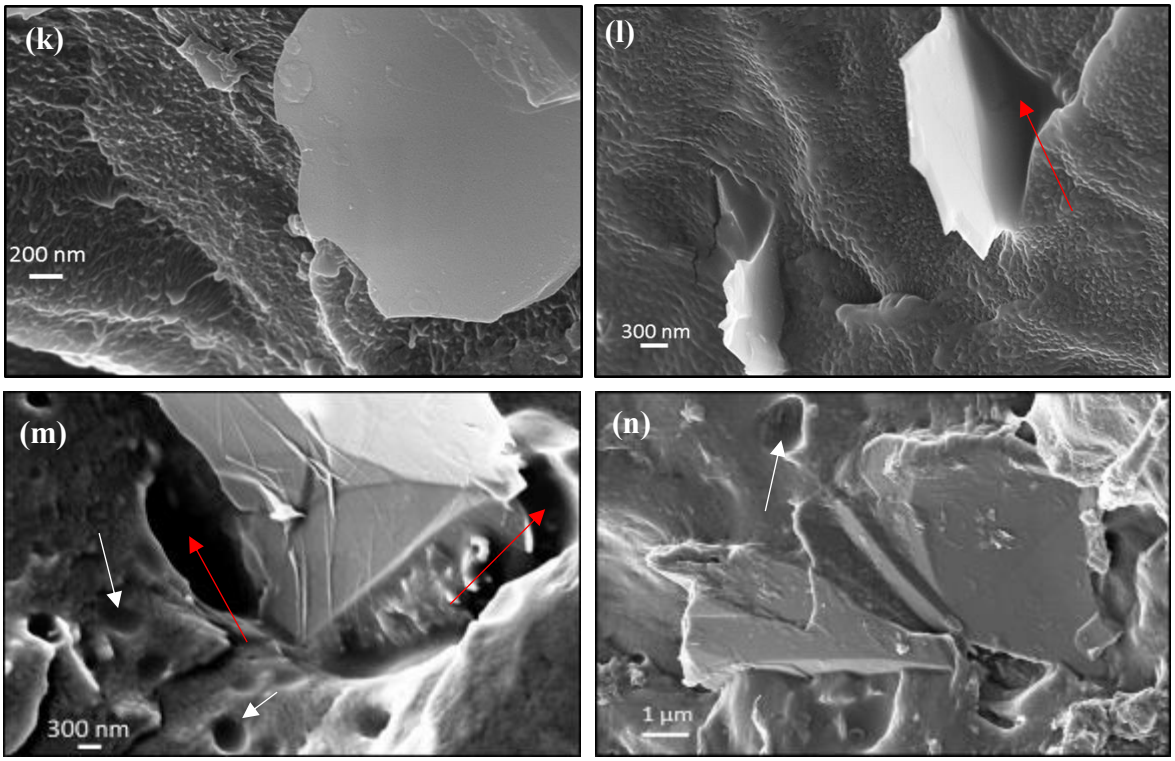

Figure 8.1 SEM micrographs of unfilled PP at **a**) x2.5k, **b**) x3k, **c**) PP/P[LA]10K at x35k, **d**) PP/P[2PEA]10K at x28k, **e**) PP/*block*20K at x23k, **f**) PP/*stat* 20K at x11k, **g**) P[LA]10K/MWCNTs at x110k, **h**) P[2PEA]10K/MWCNTs at x110k, **i**) *block* 20K/MWCNTs at x95k, **j**) *stat* 20K/MWCNTs at x130k, **k**) P[LA]10K/GNPs at x80k, **l**) P[2PEA]10K/GNPs at x50k, **m**) *block* 20K/GNPs at x40k and **n**) *stat* 20KGNPs at x25k magnification.

An aromatic polymer would not be expected to co-crystallise with PP due to the differences in chemical structure between the two components. The P[2PEA] droplets appear to be well dispersed within the PP matrix with the P[2PEA] droplets in the order of ~1 µm in diameter. Composites of PP and *block* 20K (fig. 8.1e) contain droplets similar to those observed with composites of PP P[2PEA]10K however, the droplets appear smaller, < 1 µm in diameter, compared to PP P[2PEA] 10K. The droplets containing the *block* 20K are well distributed throughout the PP matrix. The smaller droplets can be attributed to the P[LA] block miscibility with PP which contributes to effectively dispersing the *block* 20K. The presence of droplets is the result of the P[2PEA] blocks' immiscibility with PP leading to micro-phase separation. As the chain length of the P[2PEA] block is the same as the homopolymer of P[2PEA]10K, it is interesting to observe the smaller droplet size for the composites of PP *block* 20K compared to the composites of PP and P[2PEA]10K. A possible

explanation for the smaller droplet size is the P[LA] block is dispersing the P[2PEA] block within the PP leading to small droplets of P[2PEA] whereas in the case of PP P[2PEA]10K, the P[2PEA] is completely immiscible with PP leading to larger droplet sizes.

For composites of PP and *stat*20K (fig. 8.1f) the droplets containing the *stat*20K polymer are significantly larger (> 2 μm) compared to the composites of PP and P[2PEA]10K (fig. 8.1d) and PP and *block* 20K (fig. 8.1e). The larger droplets are due to the reduced miscibility and associated with the chemical structure of the *stat* 20K. It is assumed the *stat* 20K consists of a chain of random 2PEA and LA monomer units. The random monomer sequence prevents the LA from dispersing and crystallising with PP and hence results in the overall poly(acrylate) being immiscible with PP compared to just a block of the poly(acrylate). The SEM micrographs of poly(acrylate)s blended with 1 wt% MWCNTs and PP are presented in figure 8.1g-j). For the blend of PP and MWCNTs with P[LA]10K (fig. 8.1g), the MWCNTs are well dispersed but, the presence of agglomerates cannot be excluded when one considers an SEM image a 2D representation of a 3D material. For the blend of PP and MWCNTs with P[2PEA]10K (fig. 8.1h), the MWCNTs are poorly dispersed and present in large agglomerates, >1μm. The micrograph reveals large areas which are empty of MWCNTs indicating the P[2PEA] is hindering dispersion of the MWCNTs. The observation is not unexpected as the P[2PEA] is expected to strongly physisorb onto the surface of the MWCNTs and the micrograph in fig. 8.1d clearly exhibits the P[2PEA] is not miscible with the PP. The introduction of P[2PEA] results in a biphasic system where the MWCNTs are preferentially located in the P[2PEA] phase. The blend of PP and MWCNTs with *block* 20K (fig. 8.1i) also reveals the presence of MWCNT agglomerates in the composite. A similar observation was observed for the composite of PP and MWCNTs with *stat*20K (fig. 8.1j). The addition of P[2PEA] reduces the extent of MWCNT dispersion in the PP matrix due to its immiscibility with PP. Composites of PP and MWCNTs with P[LA]10K display the greatest level of MWCNT dispersion of all the composites.

Herein lies the challenge when designing a polymer compatibiliser specifically for non-covalently assisted dispersion of MWCNTs in PP. A polymer (P[2PEA]) which strongly adsorbs onto the surface of the MWCNTs will inherently be incompatible with the PP matrix and the addition of a compatible polymer (P[LA]), whether through a block or statistical architecture does not appear to resolve the incompatibility. The predicted chemical interaction between the copolymer and the MWCNTs (scheme 8.1) assumes the P[2PEA] block does not come into contact with the PP but, in reality this is not the case. The optimal

dispersion and distribution of the MWCNTs within the PP matrix can only be achieved if the P[2PEA] block does not interact with the PP and remains completely bound to the MWCNT surface with the P[LA] block bridging the PP/P[2PEA] interface. However, such a phenomenon is almost impossible to achieve without controlling the microstructure of the block copolymer on the MWCNT surface through self-assembly.

Further investigations were performed with GNPs to understand the chemical interactions between the poly(acrylate)s and GNPs (1 wt%) at the interface with PP (fig. 8.1k-n). For the blend of PP and GNPs with P[LA]10K (fig. 8.1k), droplets within the PP matrix are not observed which is consistent with the corresponding MWCNT composite. The GNPs are of various size and can be easily identified but the presence of P[LA] is difficult to distinguish. The observation once again confirms the miscibility of P[LA] with the PP matrix. For the blend of PP and GNPs with P[2PEA]10K (fig. 8.1l), the presence of P[2PEA] droplets throughout the PP matrix are not observed. The lack of droplets contrasts with the composites of PP and P[2PEA]10K (fig. 8.1d). A possible explanation for the lack of droplets is the P[2PEA]10K is migrating to the interface between the GNP sheets and the PP matrix (red arrows). The droplet between the GNP sheet and the PP matrix (fig. 8.1l) is likely to contain P[2PEA]. The P[2PEA] can migrate through the PP matrix and adsorb into the surface of the GNPs during melt-compounding in the extruder. On the other hand, SEM micrographs are not representative as they are 2D representations of a 3D material and therefore, the P[2PEA]10K could be poorly dispersed and not visible on the micrographs. The surrounding void around the GNPs (red arrows) could indicate poor wetting between the PP matrix and the GNP. To further investigate the morphology of the composites, an SEM micrograph of the blend of PP and GNPs with *block*20K (fig. 8.1m) is displayed. The GNPs appear encapsulated by the block copolymer within the PP matrix (red arrows). Additional droplets are present (white arrows) within the PP matrix revealing the block copolymer is unable to completely migrate to the surface of the GNPs. However, the droplet surrounding the GNP is considerably larger (~ 5 μm) compared to the droplet in the PP matrix (~ 300 nm) revealing most of the block copolymer does migrate to the GNP surface. The SEM micrograph (fig. 8.1m) depicts two competing effects. The poly(acrylate) blocks of the block copolymer (containing both a P[LA] block and P[2PEA] block) are competing with each other in that the P[LA] block prefers to be dispersed in the PP matrix (resulting in small droplets in the PP matrix from the covalently attached P[2PEA] block – white arrows) while, the P[2PEA] block prefers to adsorb onto the surface of the GNPs *via* π-π stacking –

red arrows). The larger droplet surrounding the GNP sheet compared to the droplets in the PP suggest the π-π interaction between the P[2PEA] block and the GNP is stronger than the hydrophobic interactions between the P[LA] block and PP. The observation poses an interesting paradox where the block copolymer is required to migrate and self-assemble on the surface of a 1D or 2D graphitic nano-filler. The migration process of the block copolymer in the PP matrix during extrusion requires the adsorbing block (P[2PEA]) to strongly bind to the graphitic nano-filler which by definition will phase separate and be immiscible with PP. Additionally, the dispersing block (P[LA]) must not strongly disperse with the PP because, this will counteract the migration of the polymer compatibiliser to the surface of the graphitic nano-filler. However, once the block copolymer has self-assembled on the surface of the graphitic nano-filler, the dispersing block must strongly disperse and co-crystallise with the PP matrix to facilitate effective stress transfer from the polymer matrix to the graphitic nano-filler. This observation details how important it is to accurately design and control the properties of the block polymer, for not only the interface between the graphitic nano-filler but also during its migration to the interface during the melt-mixing process in the extruder. For the blend of PP and GNPs with *stat*20K (fig. 8.1n), droplets within the PP matrix are visible however, the size of the droplets surrounding the GNPs are not as large as that seen for the composite of PP with GNPs and *block*20K (fig. 8.1m). This observation demonstrates the poly(acrylate) is not able to effectively migrate to the surface of the GNPs due to a disruption of the aromatic monomer sequence. Further characterisation using oscillatory rheology was used to study the extent of nanofiller dispersion and understand in more detail the observations made from SEM imaging.

Oscillatory rheology was used to probe the microstructure of the polymer matrix and determine rheological percolation. At high frequencies (>10 rad/s), the bulk properties dominate the viscos-elastic response whereas at low frequencies, the nano-filler microstructure and its presence on polymer chain dynamics readily detected. The filled PP will form a percolated network which is manifest by 'pseudo-solid' behaviour which in turn is detected by increases in storage modulus (G') and complex viscosity ($|\eta^*|$) as a function of frequency. $tan\ \delta^{-1}$ (G'/G'') is used to compare the rate of change of G' relative to G'' and G' vs G'' (Cole-Cole plot) is also used to detect changes in G' relative to G''. When investigating the addition of poly(acrylate)s to PP (fig. 8.2), it is evident the poly(acrylate)s do not significantly alter the bulk rheology properties of the PP. The rheological data can be correlated back to the DMTA as such, in that the P[LA] reduced $|\eta^*|$ and G' of PP by

plasticisation. It was evident (Chapter 5 - DMTA), the P[LA] is disrupting the packing of the PP polymer chains using its bulk pendent side chains to increase chain mobility and free volume. The disruption leads to reduced resistance to flow and hence reduced melt viscosity. Interestingly, the block copolymer does not plasticise the PP which hints the block copolymer may not be efficiently dispersed within the PP matrix.

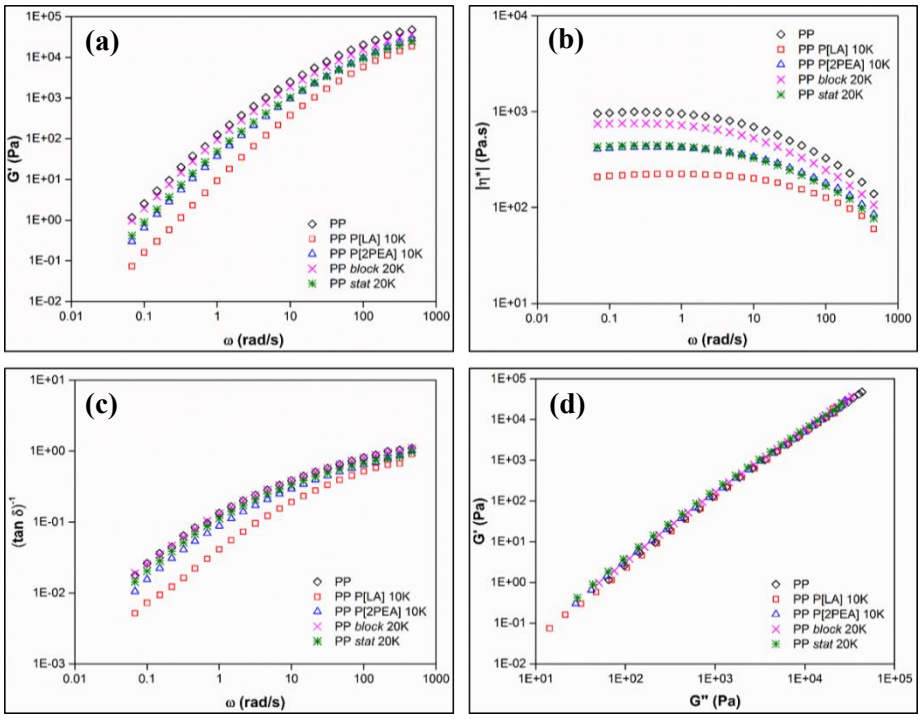

Figure 8.2 Variation in (a) storage modulus (G'), (b) complex viscosity ($|\eta^*|$) and (c) reciprocal of loss tangent ($(\tan \delta)^{-1}$) as a function of angular frequency (ω) for unfilled PP and composites of PP blended with homo and co-polymers of P[LA] and P[2PEA]; and (d) Cole-Cole plot (G' versus G'').

Composites of PP, MWCNTs and poly(acrylate)s were characterised using oscillatory rheology (fig. 8.3) and used to investigate differences in percolation behaviour with varying poly(acrylate)s as well as their effect on MWCNT dispersion. In order to focus the study on the combined MWCNT and poly(acrylate) effect rather than the MWCNTs alone, the MWCNT concentration was fixed to 1 wt% for all composites. On first examination, it is evident the composites of PP, MWCNTs and poly(acrylate)s produce a wide range of responses, ranging from (G' ~6 x 10^2 Pa to ~5 x 10^{-1} Pa (at 0.1 rad/s), indicating the poly(acrylate)s are indeed non-covalently interacting with the MWCNTs. However, some poly(acrylates) promoted dispersion of the MWCNTs more than others. The

MWCNTs functionalised with homo-polymers of P[LA], resulted in the most highly dispersed systems with G' increasing by over 2 orders of magnitude compared to neat PP (at 0.1 rad/s) and by as much as 1 order of magnitude compared to the composite of PP and un-functionalised MWCNTs. Increases in G' represent 'pseudo-solid' behaviour and formation of a percolated network demonstrating in an increased state of dispersion relative to neat PP and composites of PP and MWCNTs. Composites of PP, MWCNTs and homopolymers of P[2PEA] revealed no such increases in G' (at 0.1 rad/s) compared with composites PP, MWCNTs and homopolymers of P[LA]. The observation demonstrates a less well dispersed system due to a lack of microstructure network formation and is in agreement with SEM morphological examinations. The observation is not unexpected as there is microscopic evidence that there is poor compatibility between the P[2PEA] and PP, notwithstanding the differences in morphology and chemical structure between P[2PEA] and P[LA]. In addition, the P[2PEA] is expected to strongly physisorb onto the surface of the MWCNTs and promote agglomeration by adhering to the MWCNTs, hence lack of increase in G' and $|\eta^*|$ in comparison to homopolymers of P[LA]. Disappointingly, the addition of the block copolymer does not improve MWCNT dispersion over and above that observed for the homopolymer P[LA]. This is due to the competing effect (see SEM micrographs) where the P[LA] block prefers to disperse and the P[2PEA] prefers to adhere to the MWCNTs. However, it not always possible for both to occur simultaneously and therefore, the desired improvement in dispersion and reduction in percolation threshold was not observed. This result demonstrates, that the concept is worthy of investigation however, the pre-mixing of the block copolymer and MWCNTs prior to extrusion with PP is critical to achieving the desired composite properties. Complete adsorption of the P[2PEA] on the MWCNTs is required to prevent agglomeration of MWCNTs within PP as observed with the SEM micrographs. On closer inspection, fig 8.3d (Cole-Cole plot) reveals all composites deviate towards G' with exception of neat PP revealing all composites are displaying varying levels of percolation behaviour. Comparisons between the composites can be easily deduced for example, the *block*20K MWCNTs composite reveals the MWCNTs are better dispersed compared with the MWCNTs in the *stat*20K MWCNTs composite. The composites containing the homopolymers of P[2PEA] demonstrate the MWCNTs are the least well dispersed of all the composites with the composites containing the homopolymers of P[LA] exhibited the greatest levels of dispersion.

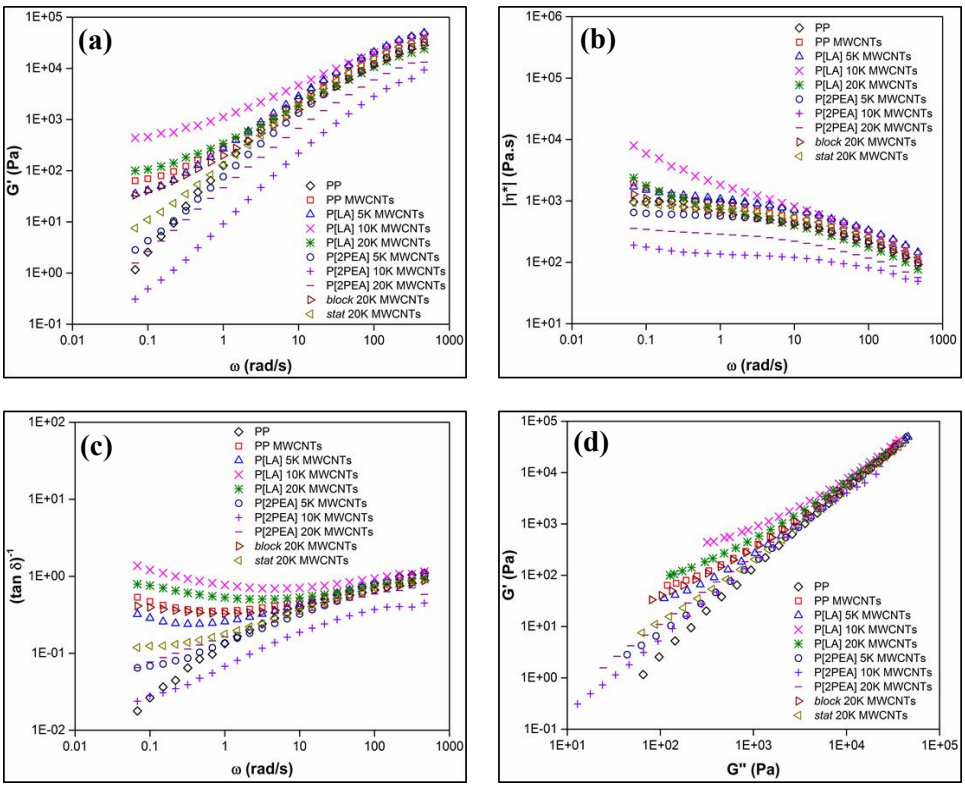

Figure 8.3 Variation in (a) storage modulus (G'), (b) complex viscosity ($|\eta^*|$) and (c) reciprocal of loss tangent ($(\tan \delta)^{-1}$) as a function of angular frequency (ω) for unfilled PP and composites of PP blended with MWCNTs functionalised with homo and co-polymers of P[LA] and P[2PEA]; and (d) Cole-Cole plot (G' versus G'').

Further rheological investigations were performed with composites of PP, GNPs and poly(acrylate)s. As discussed in chapter 6, percolation and filler network formation even at loadings up to 5 wt% was limited for composites filled with GNPs. The nanocomposite microstructure can be examined by investigating the low frequency moduli which provides information on the platelet dispersion. The presence of a low frequency storage modulus (G') plateau is indicative to rheological percolation and 'pseudo-solid' network formation. In literature, G' has been found to increase across all frequencies with the dispersion of rigid nanoplatelets and percolations to be less than 2 vol%.[11] In addition, the orientation of the GNP platelets has been stated to affect the onset of percolation with randomly orientated platelets exhibiting lower percolation thresholds compared to aligned platelets.[11] The oscillatory rheology studies of composites of PP, GNPs (1 wt%) and poly(acrylate)s (fig. 8.3) present limited if any deviation from standard thermoplastic behaviour. Small relative decreases in $|\eta^*|$ and G' were observed following the addition of poly(acrylates) and it

reveals the general plasticisation of PP, with P[LA] most effective and P[2PEA] least effective at plasticisation. It is proposed that the poly(acrylate)s would improve GNP dispersion and induce percolation. The lack of evidence for 'pseudo-solid' network formation, even at 5wt% loadings suggests the GNPs are not rigid platelets and therefore, are unable to induce percolation as these loadings compared to other forms of GNPs.[11] Further characterisation by way of static mechanical and dynamic mechanical analysis can provide further insight into the observations made from SEM imaging.

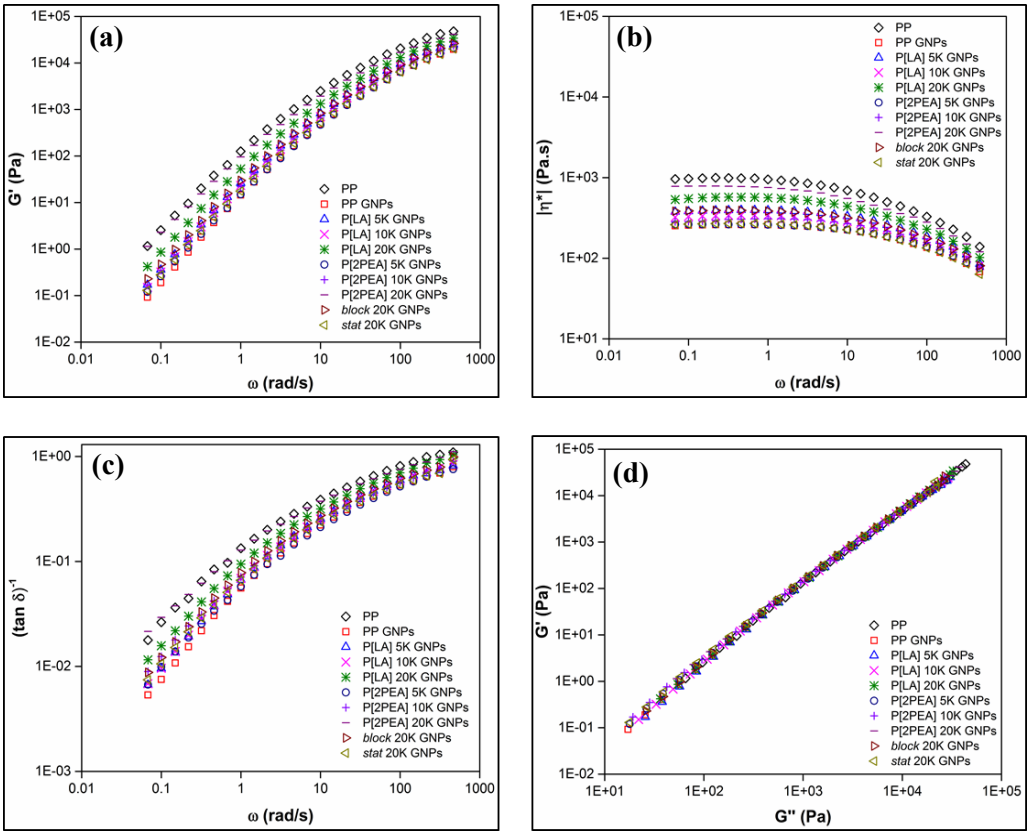

Figure 8.4 Variation in (a) storage modulus (G'), (b) complex viscosity ($|\eta^*|$) and (c) reciprocal of loss tangent ($(tan\ \delta)^{-1}$) as a function of angular frequency (ω) for unfilled PP and composites of PP blended with GNPs functionalised with homo and co-polymers of P[LA] and P[2PEA]; and (d) Cole-Cole plot (G' versus G'').

The r.t. static mechanical properties were investigated to understand the correlation between the poly(acrylate) architecture and its effect on the reinforcement of the filler in the PP composite. The stress vs strain curves for composites of PP and poly(acrylate)s (fig 8.5a) revealed the additions of poly(acrylate)s leads to a significant decrease in elongation at break (ductility) (ε_B) from ~285 % to ~10% of PP in the composites.

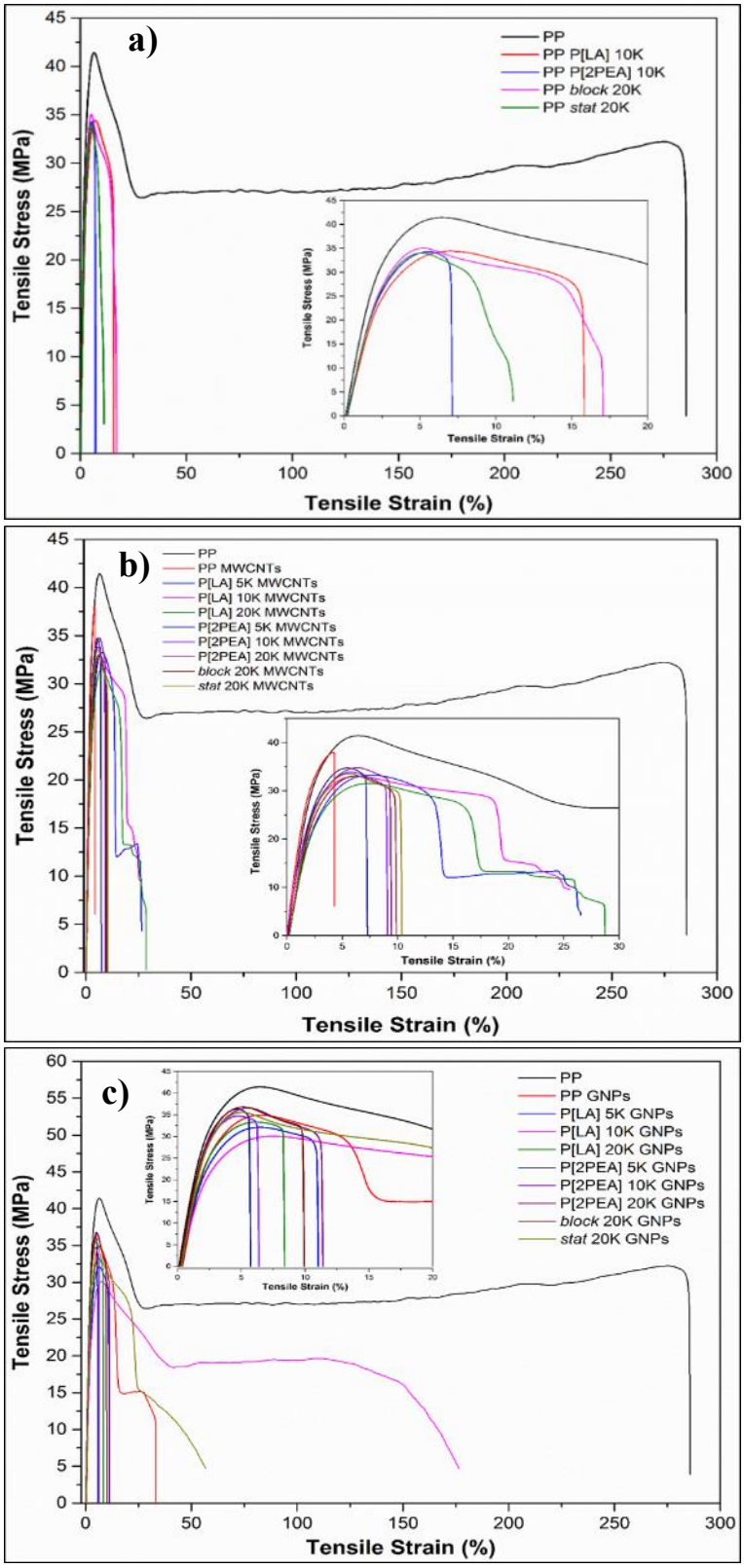

Figure 8.5 Stress vs strain curves for unfilled PP and composites of **a**) PP blended with homo and co-polymers of P[LA] and P[2PEA], **b**) PP blended with MWCNTs functionalised with homo and co-polymers of P[LA] and P[2PEA] and **c**) PP blended with GNPs functionalised with homo and co-polymers of P[LA] and P[2PEA].

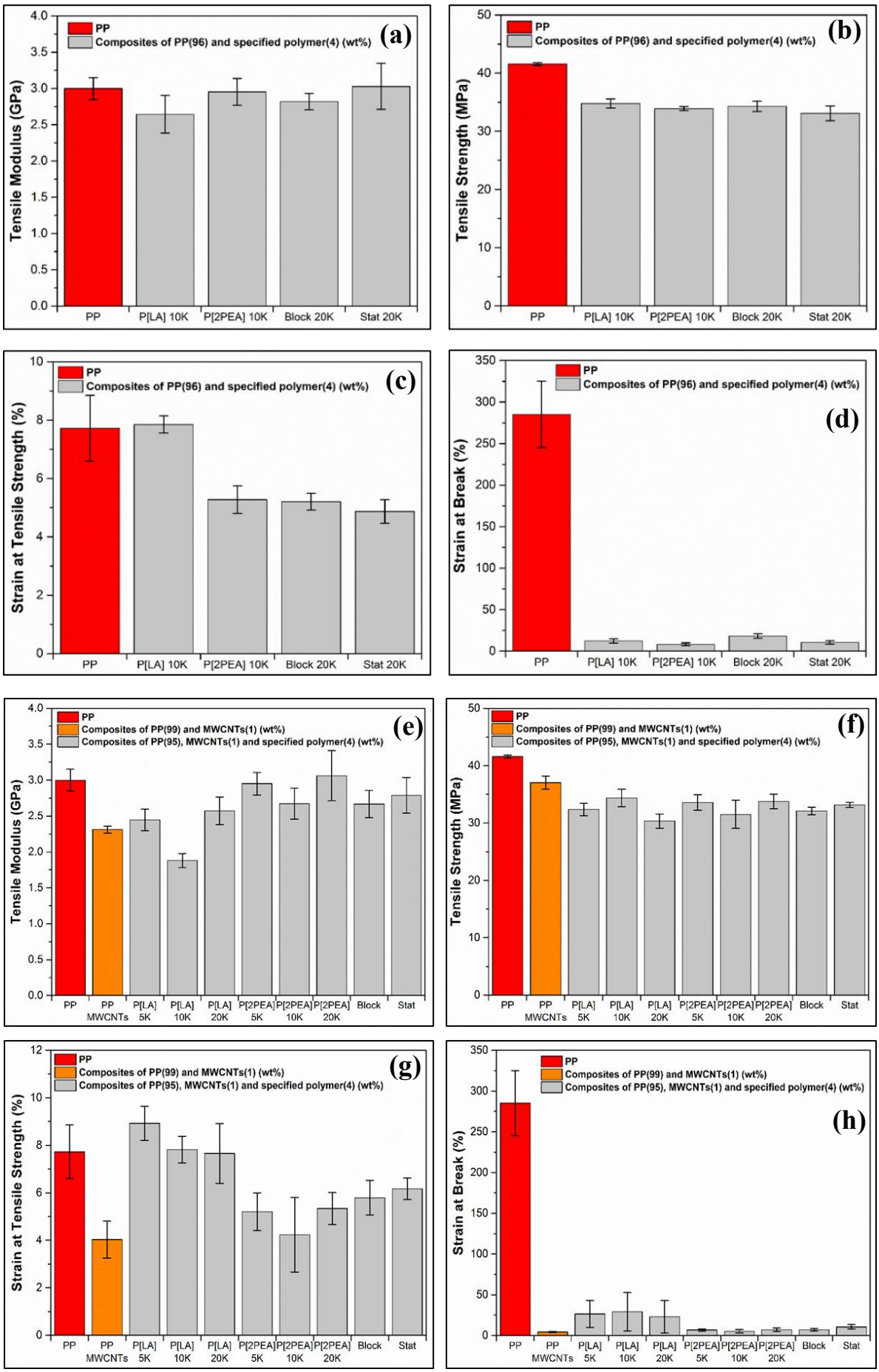
(a)
PP
Composites of PP(96) and specified polymer(4) (wt%)
Tensile Modulus (GPa)
PP
P[LA] 10K
P[2PEA] 10K
Block 20K
Stat 20K
(b)
Tensile Strength (MPa)
(c)
Strain at Tensile Strength (%)
(d)
Strain at Break (%)
(e)
Composites of PP(99) and MWCNTs(1) (wt%)
Composites of PP(95), MWCNTs(1) and specified polymer(4) (wt%)
PP MWCNTs
P[LA] 5K
P[LA] 20K
P[2PEA] 5K
P[2PEA] 10K
P[2PEA] 20K
Block
Stat
(f)
(g)
(h)

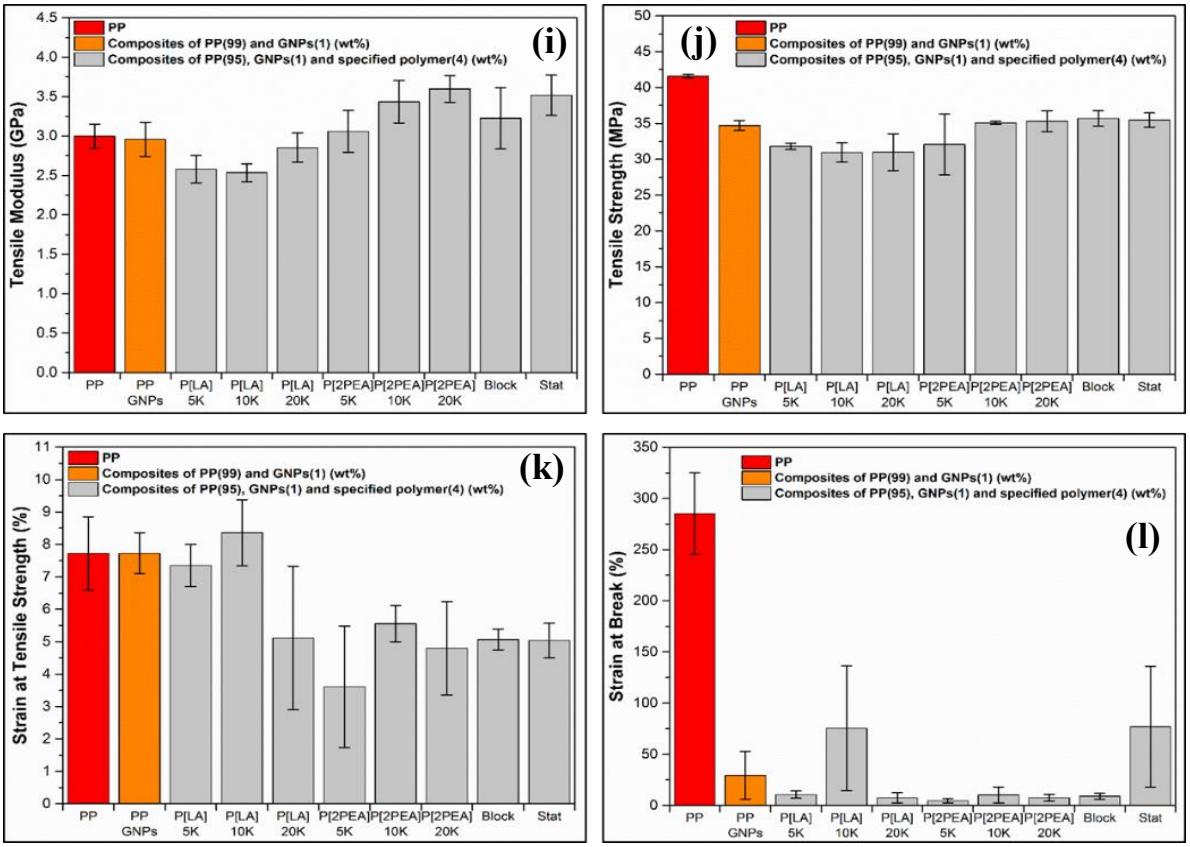

Figure 8.6 Mechanical properties for unfilled PP and composites of PP blended with homo and co-polymers of P[LA] and P[2PEA], **a**) Young's Modulus (E), **b**) tensile strength (σ), **c**) yield strain (ε_Y) and **d**) elongation at break (ε_B). Mechanical properties for unfilled PP and composites of PP blended with MWCNTs functionalised with homo and co-polymers of P[LA] and P[2PEA], **e**) Young's Modulus (E), **f**) tensile strength (σ), **g**) yield strain (ε_Y) and **h**) elongation at break (ε_B). Mechanical properties for unfilled PP and composites of PP blended with GNPs functionalised with homo and co-polymers of P[LA] and P[2PEA], **i**) Young's Modulus (E), **j**) tensile strength (σ), **k**) yield strain (ε_Y) and **l**) elongation at break (ε_B).

The stress-strain curves are displayed in fig. 8.6a-d and the relevant mechanical properties listed in Appendix 12. The Young's modulus (E) is relatively unchanged compared to neat PP after the addition of poly(acrylate)s. The droplets formed (SEM) by the presence of P[2PEA] have not led to a significant change in the E however, the use of poly(acrylate)s has led to a notable and consistent decrease in tensile strength (σ) from ~42 MPa to ~34 MPa compared to neat PP.

The poly(acrylate)s disrupt the morphology of the PP matrix (SEM) and the decrease in σ is independent of poly(acrylate) architecture. Further characterisation into how the poly(acrylate) addition changes PP crystalline behaviour and crystal morphology was investigated using DSC and WAXD and will be discussed below. The yield strain (ε_Y) revealed a notable decrease from ~8% to ~5% for the composites containing the P[2PEA] component. The composite of PP and P[LA]10K revealed no change in ε_Y compared to neat PP suggesting the P[LA]10K compatibilises with the PP matrix where the poly(acrylate)s containing the P[2PEA] polymer component are not compatibilising with the PP, in agreement with observations made from the SEM micrographs. In conclusion, the mechanical properties of the composites of PP and poly(acrylate)s exhibited reduced mechanical performance relative to neat PP. The significant reduction in ε_B suggests the loading of 4 wt% poly(acrylate) is excessive as it leads to significant reduction in mechanical performance compared to neat PP.

The mechanical properties of composites of MWCNTs, poly(acrylate) and PP are displayed in figure 8.5b, 8.6e-h and Appendix 12. The addition of poly(acrylate) functionalised MWCNTs results in the reduction of ε_B from ~285% to ~25% for composites of PP and P[LA] functionalised MWCNTs and to ~6% for composites of PP and P[2PEA] functionalised MWCNTs. The copolymer composites display a minimal increase in ε_B (~10%) compared to the P[2PEA] composites. The composite of MWCNTs and PP possessed the lowest ε_B ~4% with all poly(acrylate) composites displaying a greater ε_B. Evidence for the plasticising effect from the P[LA] is clearly visible on the stress vs strain curve (fig.8.5b) identified by the high extensibility post yield compared to the composites containing homo and copolymers of P[2PEA].[8] Minimal if any correlation between molecular weight and extensibility was observed for the poly(acrylate) composites however, there is some evidence for an underlying trend for higher extensibility positively correlated with increased molecular weight. However, a greater molecular weight range is required to fully examine this hypothesis.

Fundamentally, the addition of nano-scale fillers, such as MWCNTs, leads to the embrittlement of PP, resulting in significantly reduced ε_B values compared to neat PP.[12] In the case of neat PP, the inter-spherulitic boundaries are larger compared to filled composites.[13] Under mechanical stress, a fracture will originate from a highly stress-localized region.[12] The movement of the fracture via smooth progression of the large crystal

planes in the spherulites allows extensive ductile yielding.[12, 14] The addition of nano-scale fillers leads to predominantly α-nucleation as the fillers promote surface crystal nucleation. The significant increase in nucleation centres leads to the formation of considerably smaller spherulites compared to larger domains in neat PP. The narrowing of the inter-spherulitic boundaries from excessive nucleation, suspends extensive ductile yielding and therefore, results in lower ε_B values and embrittlement.[12, 15-17] High loadings of nano-scaled fillers leads to percolation and stress localization around the dense filler network leading to matrix cracking due to a modulus mismatch.[12, 14] However, for the composites of PP, MWCNTs and P[LA] homo-polymers, P[LA] coating surrounding the MWCNT surfaces facilitates a bridging effect between the MWCNTs and PP, allowing a reduction in modulus mismatch and enabling ductile yielding behaviour to re-emerge.[12] Addition of P[LA] homopolymer to composites of PP and MWCNTs resulted in plasticisation and a reduction in E by up to 30%, whereas for addition of P[2PEA] no change in E was observed. Use of either the *block*20K or the *stat*20K copolymers results in a decrease in E (~10%) relative to neat PP. Regarding σ, a consistent decrease (~20%) for all poly(acrylate) composites was observed indicating the poly(acrylate)s are not facilitating effective stress transfer between the MWCNTs and PP matrix as predicted. In fact, σ of the composite of PP and un-functionalised MWCNTs only decreased by ~10% suggesting the poly(acrylate)s are further reducing the mechanical performance compared to neat PP. The results are similar to the composites of PP and poly(acrylate)s demonstrating the poly(acrylate)s are primarily dispersed within the PP matrix rather than at the interface between the MWCNTs and the PP. ε_Y increased by ~100%, compared to the composite with un-functionalised MWCNTs, for the P[LA] homo-polymer filled composites due to plasticisation. In conclusion, the use of homo and copolymers of P[LA] and P[2PEA] has not led to significant improvements in mechanical properties of composites of PP and MWCNTs. This is primarily due to the poly(acrylate)s remaining in the PP matrix rather than locating at the interface between the MWCNTs and the PP matrix and therefore, not facilitating effective stress transfer between components.

The mechanical properties for the composites of PP, GNPs and poly(acrylate)s are displayed in figure 8.5c, 8.6i-l and Appendix 12. For composites of PP and GNPs containing homo-polymers of P[LA] a reduction in E (~10%) was obtained which is consistent with that recorded for the corresponding MWCNT composites. However, E increased by as much as ~20% for the composite of PP, GNPs and P[2PEA]20K relative to neat PP and the composite of PP and unfunctionalised GNPs. Moreover, a clear trend between the increase

in *E* and P[2PEA] molecular weight was observed demonstrating that higher molecular weight P[2PEA] provided enhanced compatibilisation between the GNPs and the PP matrix. In addition, the composite containing the *stat*20K displayed the greatest increase in *E* (~15%) compared to the *block*20K (~5%) which is contradictory to the hypothesis that the block copolymer should lead to the greatest improvement in mechanical properties. An increase in *E* compared to neat PP confirms the SEM observations which suggested the P[2PEA] migrates to the GNP surface facilitating compatibilisation, and promoting interfacial stress transfer. The values for the σ decreased by (~10-20%) compared to neat PP which is consistent with the composites of PP/MWCNTs/poly(acrylate)s and PP/poly(acrylate)s. In the case of ε_Y, the composites of P[LA] homo-polymers maintained ε_Y compared to neat PP whereas, the composites containing P[2PEA] have a reduced ε_Y (~5%) compared to neat PP (~8%). The addition of GNPs to PP resulted in a significant reduction of ε_B from ~ 285% to ~10%. Interestingly, the composite containing the statistical copolymer demonstrated plasticisation behaviour similar to the composite of PP, GNPs and P[LA] homopolymers. This result demonstrates that the statistical copolymer behaves similar to the P[LA] whereas, the block copolymer behaves similar to the P[2PEA].

DMTA was extensively employed to characterise the changes in the glass transition temperature (T_g) of PP and composites of PP and poly(acrylate)s. The three relaxations noted for PP are evident from the tan δ curve (fig. 8.7a).[12, 18] The α-relaxation has been attributed to the lamellar slip and rotation in the crystalline phase. The β-relaxation is due to dynamic glass-rubber transition (T_g) of the amorphous phase of PP and the γ-transition is attributed to relaxation of a few chain segments in the amorphous regions of the semi-crystalline polymer.[18] The α-relaxations are clearly observable in DMTA traces and usually occur at temperatures above 60 °C. The β-relaxation (T_g) occurs between -20 °C to 20 °C for neat PP. The γ-transition is weak and often not observed and usually occurs below -50 °C.[18] The relaxation of interest is the β-relaxation and the T_g is often measured by measuring the peak maximum of the β-relaxation (in tan δ) (Fig. 8.7a) or the loss modulus (E'') maximum (Fig. 8.8b). Comparisons between the T_g values for composites of PP and poly(acrylates) are displayed in fig 8.7b. The addition of P[LA] resulted in a decrease in T_g of ~ 8 °C whereas the composite with P[2PEA] resulted in a decrease of ~ 5 °C. Interestingly, the composite with the *block*20K added had a decrease of ~ 1 °C and the composite with the *stat*20K decreased by ~ 2 °C.

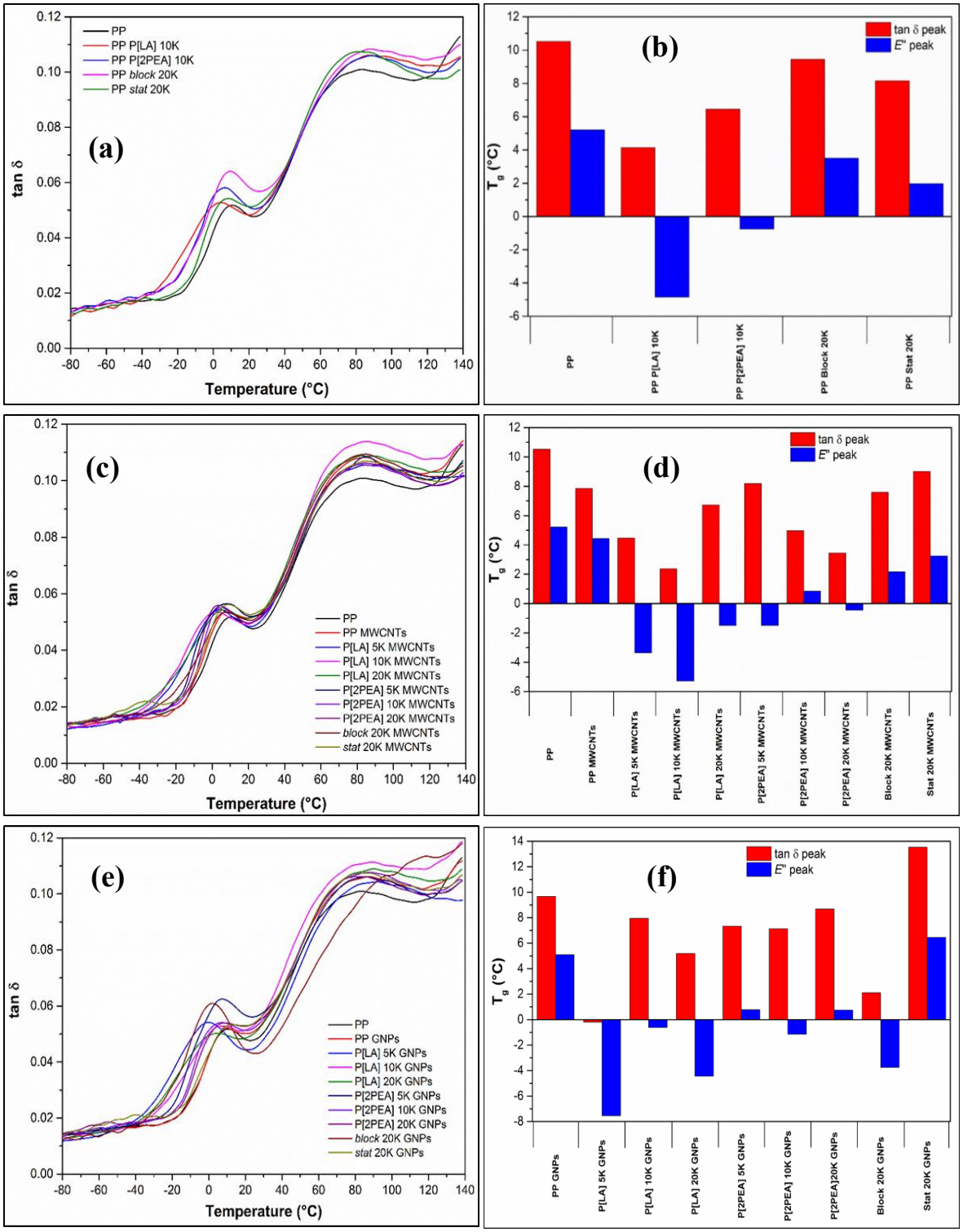

Figure 8.7 a) DMTA tan δ traces as a function of temperature and **b**) comparisons for change in T_g by tan δ peak and E'' peak, for unfilled PP and composites of PP blended with homo and co-polymers of P[LA] and P[2PEA]. **c**) DMTA tan δ traces as a function of temperature and **d**) comparisons for change in T_g by tan δ peak and E'' peak, for unfilled PP and composites of PP blended with MWCNTs functionalised with homo and co-polymers of

P[LA] and P[2PEA]. **e**) DMTA tan δ traces as a function of temperature and **f**) comparisons for change in T_g by tan δ peak and E'' peak, for unfilled PP and composites of PP blended with GNPs functionalised with homo and co-polymers of P[LA] and P[2PEA].

The reduction in T_g resulted from the addition of poly(acrylate)s is expected due to their plasticizing properties when dispersed in PP.[8] The bulky pendent side chains in P[LA] increase the chain mobility of the PP chains by spacing them out and preventing them from getting close together.[19] The increased free volume of the amorphous phase accounts for the reduced T_g.[20, 21] In addition, the lack of methyl group on the backbone of the poly(acrylate)s also contributes to chain mobility comparable to a methacrylate for example.[19] However, significant reductions in T_g require effective dispersion of the poly(acrylate)s throughout the amorphous phase. Addition of P[LA] exhibited the greatest reduction in the T_g of PP due to its bulky pendent side groups and good compatibility with the amorphous PP phase, facilitating effective dispersion. The T_g for the composites containing P[2PEA] revealed limited decrease in T_g as the side chains are not as bulky and their aromatic character prevents good compatibility with the amorphous phase of PP.

Further investigations into the changes in T_g for composites of PP, MWCNTs and poly(acrylate)s were performed to evaluate the effect of the addition of poly(acylate) functionalised MWCNTs to PP, on the thermomechanical properties of PP. Temperature sweeps at a fixed frequency (1 Hz) were performed and tan δ, E' and E'' vs temperature recorded and are displayed in figure 8.7c, figure 8.8c and d, respectively. On first inspection, significant shifts in T_g were not observed. Furthermore, the addition of MWCNTs resulted in an increase in E' for the composite of PP, MWCNTs and P[2PEA]20K, E' by ~ 1 GPa at -80 °C (below T_g). All composites, except for those containing homopolymers of P[LA] exhibited increases in E' relative to neat PP at temperatures below the T_g of PP, T_g ~0-20 °C. The improvement in E' ranged from ~ 7% for composites of PP and unfunctionalised MWCNTs to ~30% for composites of PP and P[2PEA]20K MWCNTs compared to neat PP within the glassy region. The result demonstrates the nanotubes are contributing to the overall modulus of the composite due to their exceptionally high Young's moduli.[18] Interestingly, composites containing poly(acrylate)s; P[2PEA]5K, P[2PEA]10K, P[2PEA]20K, *block*20K and *stat*20K all demonstrated increased values of E' within the glassy region compared with the composite of PP and unfunctionalised MWCNTs. The

results suggest the P[2PEA] component is enhancing the dispersion and interfacial adhesion between the MWCNTs and the PP matrix which leads to increased reinforcement and enhanced stiffness.[18] At temperatures above the T_g, the global relaxation of the bulk matrix caused by the absorption of energy by the polymeric chains leads to the convergence of E' for all the composites to the values of neat PP.[18] Shifts in T_g are displayed in fig. 8.7d for composites of PP, MWCNTs and poly(acrylate)s. On first inspection, the composites containing homopolymers of P[LA] revealed reductions in T_g (of 5-8 °C) due to plasticisation of PP by P[LA] which is as a result of the bulk pendent side chains increasing the free volume of the amorphous phase.[8] For the composites containing the homopolymers of P[2PEA], the reductions in T_g (of 2-5 °C) are not as significant due to the less bulky P[2PEA] and its poor compatibility with the PP amorphous phase, as observed via SEM. Both copolymers revealed reductions in T_g similar to the homopolymers of P[2PEA] exhibiting the incompatibility between the aromatic groups in 2PEA and PP prevents an increase in free volume to the same extent as homopolymers of P[LA]. The hypothesis was to non-covalently functionalise MWCNTs using a poly(acrylate) which can shield the MWCNTs and enable them to reinforce the PP amorphous phase where yielding increased stiffness and T_g of the composite. However, such observations were not observed with all samples revealing reductions in T_g due to plasticisation effects. Furthermore, with the exception of composites of PP/P[LA]5K/MWCNTs and PP/P[PLA]10K/MWCNTs, all other composites exhibited a strong increase in E'' relative to composites of PP and unfunctionalised MWCNTs. This suggests the other poly(acrylate)s are enhancing dispersion of the MWCNTs and interfacial adhesion with the PP matrix through the suppression of the overall chain dynamics of PP.[18]

Investigations into the changes in T_g for composites of PP, GNPs, and poly(acrylate)s were performed (fig. 8.7e and fig. 8.8e-f) to evaluate the effect of the addition of poly(acylate) functionalised GNPs to PP, on the thermomechanical properties of PP. Changes in T_g are detailed in figure 8.7f. The addition of P[LA] 5K to a composite of PP and GNPs resulted in a decrease in T_g of ~ 10 °C. The decrease in T_g from ~ 10 °C to 0 °C is significantly greater than the decrease obtained by both P[LA] homopolymers of molecular weights 10K and 20K (of ~ 5 °C), suggesting the lower molecular weight P[LA] is more efficient at plasticising PP, increasing free volume by promoting chain mobility.[8, 18] The composites containing homopolymers of P[2PEA] reveal a minimal decrease in T_g (~ 1 °C) explained by their poor compatibility with the amorphous phase of PP.

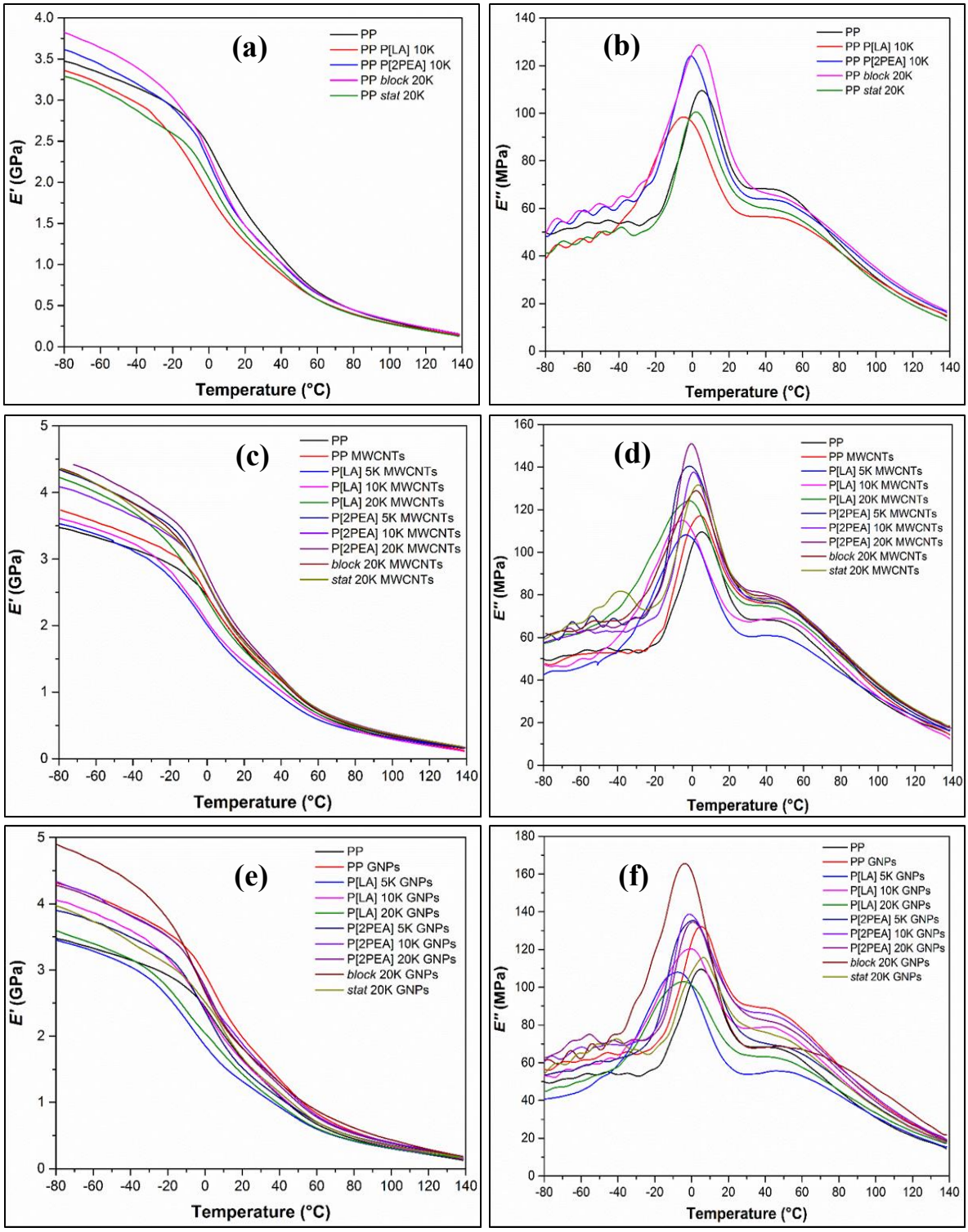

Figure 8.8 DMTA traces for unfilled PP and composites of PP blended with homo and co-polymers of P[LA] and P[2PEA], **a**) storage modulus (*E′*) and **b**) loss modulus (*E″*) as a function of temperature. DMTA traces for unfilled PP and composites of PP blended with MWCNTs functionalised with homo and co-polymers of P[LA] and P[2PEA], **c**) storage modulus (*E′*) and **d**) loss modulus (*E″*) as a function of temperature. DMTA traces for unfilled PP and composites of PP blended with GNPs functionalised with homo and co-

polymers of P[LA] and P[2PEA], **e**) storage modulus (*E′*) and **f**) loss modulus (*E″*) as a function of temperature.

Interestingly, stark differences in T_g were measured for the composites containing the *block*20K and *stat*20K. The composite with the block copolymer had a decrease in T_g from 10 °C to 2 °C whereas the statistical copolymer revealed an increase in T_g from 10 °C to 13 °C when examining the tan δ maximum compared to neat PP. In addition, the DMTA traces displayed the composite with the block copolymer functionalised GNPs is able to simultaneously increase the moduli (through increases in *E′* and *E″*) as well as decrease the T_g. *Such an observation is of great interest as it reveals the addition of block copolymer functionalised GNPs allows PP to be used at lower temperatures without comprising its mechanical performance which is a key requirement for its expanded use in non-structural components.* The increase in T_g of the composite containing PP, GNPs and *stat*20K demonstrated improved GNP dispersion within the PP amorphous phase as well as improved interfacial compatibility compared with the composite containing the *block*20K.

DSC was used to correlate the poly(acrylate) functionalisation with the microstructure of the composite by comparing relevant thermal properties such as, crystallinity and melting behaviour.[22] The DSC traces of composites of PP and poly(acrylate)s are displayed in figure 8.9a and b. On first observation, the melting trace for the composite of PP and P[LA]10K exhibits a shoulder process indicating the presence of multiple crystal structures and polymorphs.[23] The identity of the PP crystal structures can be identified in more detail using wide angle X-ray diffraction (WAXD) and is discussed below.[24] The relevant thermal properties are listed in table 8.2. T_m and T_c are relatively unchanged at ~162 °C and ~124 °C respectively for all poly(acrylate) composites. The crystallinity decreased significantly upon addition of poly(acrylate)s indicating that they are hindering spherulite growth by acting as defects and therefore, increasing amorphous content.[25] The composite containing the P[LA]10K revealed the lowest decrease in crystallinity, from ~50% to ~46% whereas the P[2PEA] composite demonstrated the greatest decrease in crystallinity, from ~50% to ~42%. The differences in crystallinity can be correlated to differences in compatibility between the poly(acrylate)s and the PP matrix, for example, P[LA] has long hydrophobic chains which are able to reside within the inter-lamella spacing, whereas the P[2PEA] contains bulky, π-π stacking aromatic segments,

which are incompatible with the crystalline phase due to its contrasting chemistry. However, optimal composite properties, (mechanical) require greater compatibility, such that the crystallinity of PP is unaffected. Unfortunately, such compatibility may only be achievable using a poly(olefin) apolar based compatibiliser. In the case of the *block*20K composite with PP, the crystallinity was 45.4%, higher than the 43.6% for the *stat*20K composite. The *block*20K facilities partial co-crystallisation with PP as the P[LA] block can partially reside in the inter-lamella spacing whereas, the *stat*20K polymer is unable to achieve this and hence the lower crystallinity results. Evidence for peak broadening (FWHH) confirms the nucleation of multiple polymorphs.

Composites of PP, MWCNTs and poly(acrylate)s were studied using DSC (figure 8.9c and d) to understand the independent and combined effects of MWCNT and poly(acrylate)s addition to PP on the thermal properties of the composite. As the MWCNT loading was fixed at 1 wt%, a consistent shift in T_c from ~125 °C to ~127 °C was observed due to the nucleating of PP by MWCNTs cooled from the melt.[26] The MWCNTs nucleated PP crystallisation during cooling which results in a substantial increase in spherulite concentration.[27] In addition, the T_m also shifted by ~2 ºC to higher temperatures however, the shift is not consistent for all samples. The T_m for samples containing P[LA] shifted to higher temperatures whereas the composites with homopolymers of P[2PEA] were unchanged. This is due to the P[LA] promoting MWCNT dispersion and promoting nucleation but, the P[2PEA] promotes agglomeration and hinders nucleation. PP crystallinity was reduced by poly(acrylate) addition due to the preference of the poly(acrylate)s to disrupt the amorphous phase. The composite of MWCNTs and poly(acrylate) did not significantly change PP crystallinity and any changes appear to be dominated by the poly(acrylate) on its own. This result suggests the majority of the poly(acrylate)s are dispersed within the PP matrix rather than bound to the surface of the MWCNTs.

The calorimetric pattern for behaviour for composites of PP, GNPs and poly(acrylate)s (figure 8.9e and f) is similar to that of obtained for the MWCNT based composites. The GNPs nucleate PP from the melt as observed by the consistent shift in T_c to higher temperatures (again from 125 °C to 127 °C). The GNPs promote crystallisation at higher temperatures by providing more surface area for PP crystallisation.[28]

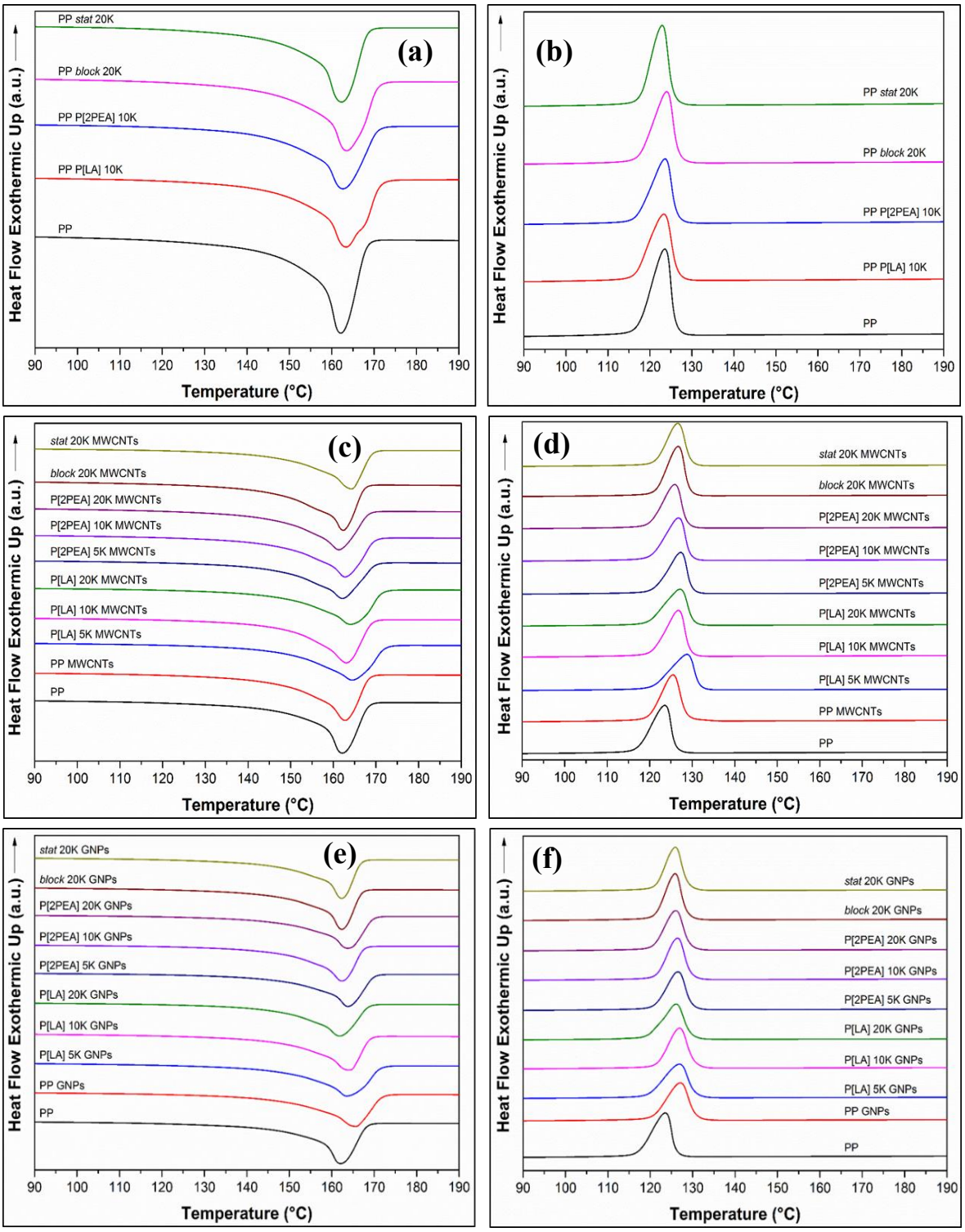

Figure 8.9 DSC **a**) heating curves and **b**) cooling curves for unfilled PP and composites of PP blended with homo and co-polymers of P[LA] and P[2PEA]. DSC **c**) heating curves and **d**) cooling curves for unfilled PP and composites of PP blended with MWCNTs functionalised homo and co-polymers of P[LA] and P[2PEA]. DSC **e**) heating curves and **f**) cooling curves for unfilled PP and composites of PP blended with GNPs functionalised with homo and co-polymers of P[LA] and P[2PEA].

Table 8.2 Calorimetric data observed from DSC and crystalline content (X_c) determined from DSC for PP and composites of; PP blended with homo and co-polymers of P[LA] and P[2PEA], PP blended with MWCNTs functionalised homo and co-polymers of P[LA] and P[2PEA] and PP blended with GNPs functionalised homo and co-polymers of P[LA] and P[2PEA].

Sample	T_m [a] (°C)	T_c [b] (°C)	ΔH_m [c] (J/g)	ΔH_c [d] (J/g)	X_c [e] (%) DSC	$FWHH_m$ [f] (°C)	$FWHH_c$ [g] (°C)
PP	162	125	-104.2	104.9	50.3	10.5	4.5
PP P[LA] 10K	163	123	-91.6	88.9	46.1	15.7	6.7
PP P[2PEA] 10K	163	124	-83.8	82.0	42.1	15.2	6.3
PP *block* 20K	163	124	-90.2	88.1	45.4	15.5	6.3
PP *stat* 20K	162	123	-86.7	86.7	43.6	11.8	5.2
PP MWCNTs	163	125	-103.2	102.5	50.3	14.6	5.9
P[LA] 5K MWCNTs	164	129	-91.9	92.3	46.7	18.8	7.2
P[LA] 10K MWCNTs	163	127	-98.9	99.1	50.3	15.2	5.7
P[LA] 20K MWCNTs	164	127	-93.0	91.6	47.3	18.3	7.0
P[2PEA] 5K MWCNTs	162	127	-88.2	89.1	44.8	17.1	5.5
P[2PEA] 10K MWCNTs	163	127	-97.1	95.0	49.3	17.3	6.7
P[2PEA] 20K MWCNTs	161	126	-92.9	93.3	47.2	17.8	6.0
block 20K MWCNTs	162	126	-95.5	94.4	48.5	14.6	5.3
stat 20K MWCNTs	164	127	-87.9	86.7	44.7	13.8	5.3
PP GNPs	165	127	-100.2	100.0	48.9	11.6	5.7
P[LA] 5K GNPs	163	127	-98.0	97.5	49.8	18.6	7.3
P[LA] 10K GNPs	164	127	-96.9	95.6	49.2	15.7	5.7
P[LA] 20K GNPs	162	126	-94.9	91.5	48.2	15.2	6.5
P[2PEA] 5K GNPs	164	126	-91.8	89.0	46.7	14.0	5.7
P[2PEA] 10K GNPs	162	126	-92.8	91.7	47.2	13.0	5.4
P[2PEA] 20K GNPs	164	126	-93.2	91.6	47.4	14.5	5.5
block 20K GNPs	162	126	-97.3	94.7	49.5	11.5	4.8
stat 20K GNPs	162	126	-94.6	91.1	48.1	11.5	5.0

[a] T_m = melting temperature.
[b] T_c = crystallisation temperature.
[c] ΔH_m = melting enthalpy.
[d] ΔH_c = crystallisation enthalpy.
[e] X_c = degree of crystallinity computed from equation: $X_c = (\Delta H_m/(1-W_f)\Delta H_{100}) \times 100$ where W_f is the weight fraction of filler and ΔH_{100} is the melting enthalpy of a theoretically 100% crystalline PP (207.1 J/g), [Filler W_f refers to filler + poly(acrylate)].
[f] $FWHH_m$ = full width at half height of melting curve.
[g] $FWHH_c$ = full width at half height of cooling curve.

It was possible to determine the degree of crystallinity for the PP nanocomposites by integrating the DSC melting curves (taking into account GNP/poly(acrylate) loading), see table 8.2. Once again, the addition of poly(acrylate)s resulted in the reduction of PP crystallinity by forming defects and hindering large spherulite growth.[27] Peak broadening, especially for the sample containing the composite of GNP and P[LA]5K suggests the poly(acrylate)s are inducing multiple polymorphs of PP, most likely the β-phase, which is known to be brittle has a negative effect on the mechanical properties of the composite.[29]

The WAXD diffractograms for composites of PP and poly(acrylate)s (figure 8.10a) presents significant nucleation of the β (hexagonal) polymorph, especially for the composites containing the P[2PEA] poly(acrylate). The β-phase is evident from the increase in intensity of the reflections at 2θ = 19.0° (300) and 24.8° (301).[23] Typically, the quantity of α-phase and β-phase can be calculated by integrating the relevant peaks and crystallinity data can be obtained by comparing those values to the amorphous halo however, this method is inaccurate and only an estimation.[24] A more practical approach to determining the relative quantity of α and β phases is to compare the intensities of the α(040) and β(300) reflections (I_β/I_α) (see table 8.3).[23] As detailed in chapter 5, an increase in intensity of the β-phase by the addition of P[LA] was determined however, β nucleation was limited and relatively insignificant. The strong incompatibility between the aromatic groups of P[2PEA] and PP induces substantial β-nucleation such that the PP could be considered to be as much as 20% β-phase for the composites of PP and poly(acrylate) copolymers. The evidence for the strong incompatibility between PP and P[2PEA] from WAXD is in agreement with the droplets observed in the SEM images and the shoulder observed in the DSC melting traces. The formation of the β-phase is not desired and can lead to reduced mechanical properties in terms of stiffness and strength however, there have been reports to suggest that the β-phase improves toughness, drawability, and impact properties.[23]

The WAXD diffractograms for the composites of PP, MWCNTs and poly(acrylate)s (figure 8.10b) reveal a wide variability in terms of the quantity of β-phase (2θ = 19.0°) induced during PP crystallisation. This variability can be attributed to the addition of the MWCNTs. From figure 8.10a, it was established that the presence of P[2PEA] in the polymer matrix strongly nucleates the β-phase however, some composites, such as, that with P[2PEA]20K and MWCNTs reveal little β-nucleation compared to other composites, such as the copolymer composites with MWCNTs and PP. The variability in β-phase nucleation can be attributed possible to inconsistent mixing in the extruder. In addition, the samples exhibiting a low quantity of β-phase are those having well dispersed MWCNTs as the poly(acrylate) is predominantly bound to MWCNTs rather than unbound in the PP matrix. The composites containing the poly(acrylate) copolymers display the highest quantities of β-phase.

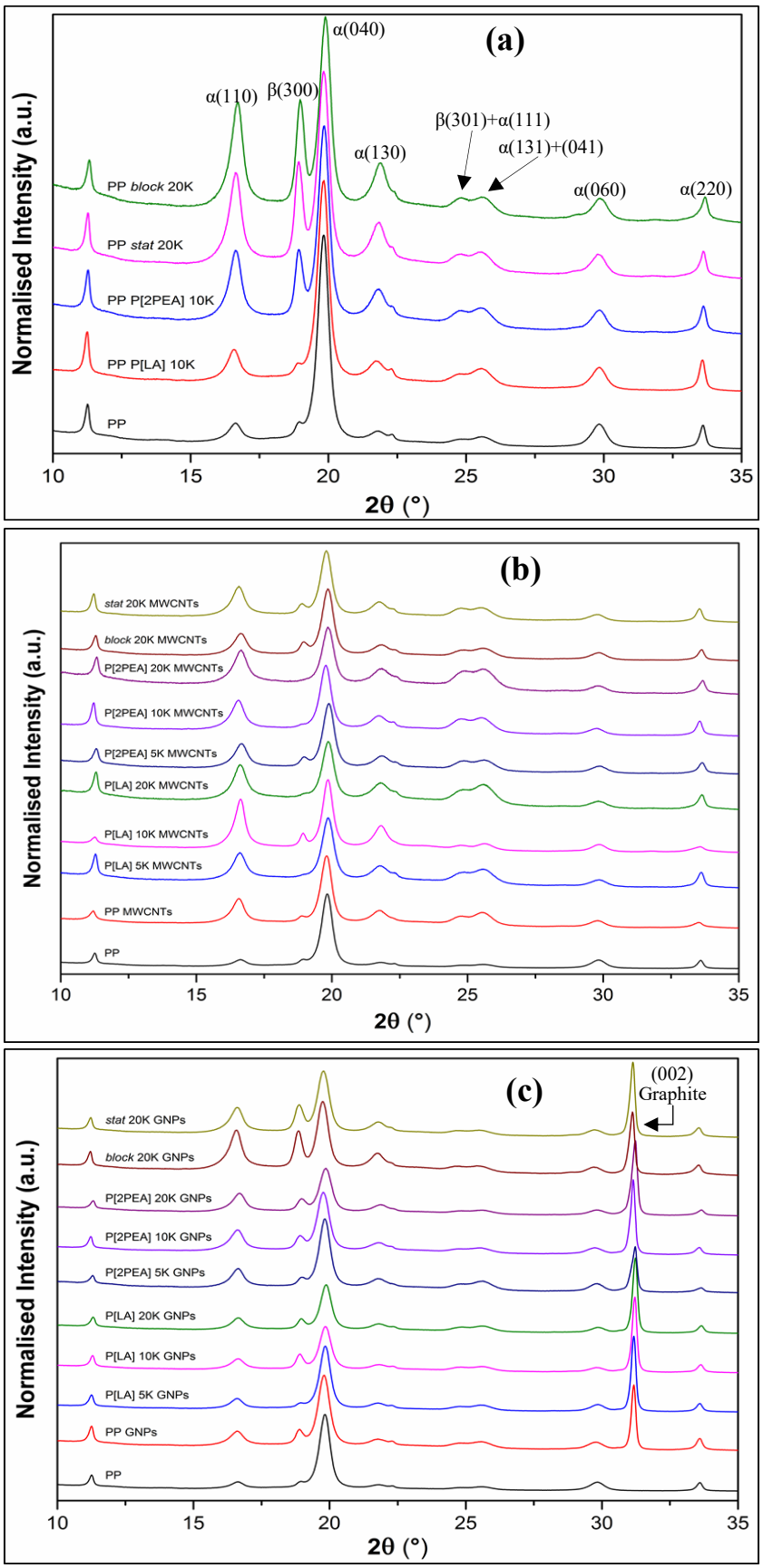

Figure 8.10 WAXD diffractograms of PP and **a**) composites of PP and poly(acrylates), **b**) composites of PP blended with MWCNTs functionalised with homo and co-polymers of

P[LA] and P[2PEA] and **c**) composites of PP blended with GNPs functionalised with homo and co-polymers of P[LA] and P[2PEA].

Table 8.3 Crystallographic properties of composites of PP, GNPs/MWCNTs and poly(acrylate)s listing the relative intensity ratios between the β(300) and α(040) reflections.

Sample	$I_{\beta(300)} / I_{\alpha(040)}$
PP	0.13
PP P[LA] 10K	0.13
PP P[2PEA] 10K	0.41
PP *stat* 20K	0.56
PP *block* 20K	0.60
PP MWCNTs	0.17
P[LA] 5K MWCNTs	0.19
P[LA] 10K MWCNTs	0.26
P[LA] 20K MWCNTs	0.23
P[2PEA] 5K MWCNTs	0.24
P[2PEA] 10K MWCNTs	0.17
P[2PEA] 20K MWCNTs	0.21
block 20K MWCNTs	0.26
stat 20K MWCNTs	0.26
PP GNPs	0.28
P[LA] 5K GNPs	0.14
P[LA] 10K GNPs	0.41
P[LA] 20K GNPs	0.30
P[2PEA] 5K GNPs	0.21
P[2PEA] 10K GNPs	0.31
P[2PEA] 20K GNPs	0.37
block 20K GNPs	0.60
stat 20K GNPs	0.49

The WAXD diffractograms of composites of PP, GNPs and poly(acrylate)s (figure 8.10c) also contain variable quantities of β-phase (2θ = 19.0°) with composites of PP, GNPs and *block*20K containing the highest relative quantity of β-phase. Figure 8.10c suggests that the composites of GNPs and homopolymers of P[2PEA] have lower intensity β peaks relative to the copolymer GNP composites, providing evidence for the migration of P[2PEA] onto the surface of GNPs, again in agreement with SEM observations. Therefore, the concept of using copolymers to improve the compatibility and interfacial adhesion between

MWCNTs or GNPs with PP requires further modification due to the lack of filler surface migration from the PP matrix compared to homopolymers in the case of P[2PEA].

8.3 Conclusions

The initial hypothesis was to use poly(acrylate)s which can non-covalently physisorb onto the surface of 1D and 2D graphitic fillers, such as MWCNTs and GNPs, to improve compatibility between these fillers and the PP matrix. It was anticipated that the effect of improving compatibility would translate to improved filler dispersion and interfacial adhesion leading to improved mechanical and thermomechanical properties of the composite. Poly(acrylate)s were chosen for their suitable thermal stability for processing with PP as well as the ability to be synthesised by Cu(0)-mediated LRP techniques giving rise to various architectures. Copolymers were synthesised in the form of block and statistical copolymers which contain P[LA] or P[2PEA] where the P[LA] is known to co-crystallise with the PP matrix and P[2PEA] can physisorb onto the surface of MWCNTs or GNPs via interactions such as π-π stacking. Composites were prepared containing, PP, MWCNTs/GNPs and poly(acrylate)s and were evaluated to determine which poly(acrylate) architecture exhibits the best performance in terms of improving filler dispersion and interfacial adhesion with PP. To accurately explore the effect of the poly(acrylate)s on composite properties, the filler concentration (MWCNT or GNP wt%) was fixed at 1 wt%. Using extrusion to produce the composites resulted in the inevitable blend of PP and poly(acrylate) and blends of multi-component polymers are often referred to as ‘polymer alloys’. SEM micrographs revealed for composites of PP and poly(acrylate)s that P[2PEA] formed droplets within the PP matrix due to the incompatibility and immiscibility between the hydrophobic PP chains and the pendant aromatic structure of P[2PEA], caused by the differing chemistries between the two polymer systems. However, the composite with P[LA] demonstrated good compatibility with the PP matrix determined by the lack of droplets within the composite and absence of micro-phase separation. The result demonstrated that P[LA] can co-crystallise with PP or at least reside in the amorphous phase of PP. Both composites of PP and copolymers revealed micro-phase separation in the form of droplets caused by the presence of P[2PEA]. The composites containing homo-polymers of P[LA] displayed the highest degree of filler dispersion whereas, the composites containing the homopolymers of P[2PEA] displayed reduced filler dispersion. SEM micrographs of

composites of PP, MWCNTs and P[LA]10K exhibited the MWCNTs were well dispersed but the presence of agglomerates remained. When examining composites of PP, MWCNTs and P[2PEA]10K, the MWCNTs were poorly dispersed indicating the P[2PEA] is hindering dispersion. The composites of PP, MWCNTs and copolymers also revealed poor dispersion of the MWCNTs due the P[2PEA] components' immiscibility with PP. Evidence for the copolymers forming a coating or surrounding the fillers (especially for the GNPs) was observed, suggesting the P[2PEA] can physisorb onto the surface of the fillers via π-π stacking. The SEM micrographs reveal two competing effects. The P[LA] components of the *block*20K prefers to be dispersed within the PP matrix and the P[2PEA] prefers to π-π stack with the surface of the filler. Oscillatory rheology analysis revealed the composites containing homopolymers of P[LA] and the block copolymer promoted dispersion of the MWCNTs, displayed by the increase in 'pseudo solid' like behaviour however, the composites containing homopolymers of P[2PEA] and statistical copolymer promoted dispersion to a lesser extent observed by reduced increases in G' at low frequencies. The rationale for this behaviour is the P[2PEA] is causing the MWCNTs to π-π stack with each other thereby hindering dispersion during the extrusion process in agreement with the SEM observations. Unfortunately, the block copolymer did improve the dispersion of the MWCNTs over and above that of the homo-polymers of P[LA]. Composites with GNPs did not demonstrate a 'pseudo solid' like behaviour due to the low rigidity of the GNPs which was also observed in chapter 6. The results highlight the importance of efficient pre-mixing of the fillers with the poly(acrylate)s prior to extrusion. Static mechanical properties revealed composites of PP/filler and poly(acrylate)s, especially P[LA], plasticized the PP through increased ductility post yield compared to without the addition of the poly(acrylate)s. However, the introduction of nano-fillers resulted in heterogeneous nucleation of PP, resulting in reduced ductility of PP, compared to neat PP. Significant decreases in ε_B from ~285% for neat PP to <50% for filled composites was observed. Composites containing homopolymers of P[LA] enabled increases ε_B due to the increased chain mobility relative to filled, functionalised composites. E, σ and ε_Y values were either reduced or unchanged, revealing the functionalisation process has not improved the mechanical properties as hypothesised. Only composites of PP, GNPs and homo-polymers of P[2PEA] displayed an increase E (20%) relative to neat PP demonstrating it is possible to improve the mechanical properties if the local microstructure surrounding the fillers can be controlled with the P[2PEA] migrating to the surface of the GNPs as observed in SEM observations. DMTA

analysis revealed reductions in T_g to lower temperatures due to the plasticisation of the amorphous phase which was primarily attributed to the increased chain mobility caused by the bulky pendant lauryl groups in P[LA]. The less bulky P[2PEA] did not plasticize the PP to the same extent as P[LA]. For composites of PP, MWCNTs and poly(acrylate)s, all composites, except for those containing homopolymers of P[LA] exhibited increases in E' relative to neat PP at temperatures below the T_g of PP, T_g ~0-20 °C. The improvement in E' ranged from ~ 7% for composites of PP and unfunctionalised MWCNTs to ~30% for composites of PP and P[2PEA]20K MWCNTs compared to neat PP within the glassy region. The result demonstrates the nanotubes are contributing to the overall modulus of the composite due to their exceptionally high Young's moduli. In addition, the DMTA traces displayed the composite with the block copolymer functionalised GNPs is able to simultaneously increase the moduli (through increases in E' and E'') as well as decrease the T_g. Such an observation is of great interest as it reveals the addition of block copolymer functionalised GNPs allows PP to be used at lower temperatures without comprising its mechanical performance which is a key requirement for its expanded use in non-structural components. DSC analysis of the composites revealed the MWCNTs and GNPs promoted heterogenous nucleation observed by shifts in T_m and T_c to higher values. In addition, the crystallinity values decreased significantly for all composites containing the P[2PEA]. The rationale being the P[2PEA] is incompatible with the crystalline phase causing defects and reducing crystalline content, whereas the P[LA] is more compatible and the crystalline content was relatively unaffected. The results agreed with SEM and rheological observations. Optimal composite properties (mechanical), require greater compatibility, such that the crystallinity of PP is unaffected. Unfortunately, such compatibility may only be achievable using a poly(olefin) apolar based compatibiliser. Melting traces for all composites containing poly(acrylate)s exhibited varying forms of peak broadening and the emergence of a peak shoulder indicating the presence of multiple crystal structures and polymorphs. WAXD revealed the composites containing, homopolymers of P[2PEA], *block*20K and *stat*20K induced β-crystallinity significantly which contributed to the reduced mechanical properties observed. The result reinforces the observation that P[2PEA] is incompatible with the PP matrix compared to P[LA]. In conclusion, the characterisation of the composites exposed the lack of compatibility between P[2PEA] and PP which resulted in reduced mechanical properties and decreased dispersion. Further improvement requires the poly(acrylate) to be redesigned in way that prevents the P[2PEA] from dispersing within

the PP matrix through more efficient surface functionalisation. A possible solution is to increase the length of the P[LA] block. However, the optimal solution hypothesised is to synthesise a block copolymer of a PP olefin and P[2PEA] which can provide better compatibility with the PP matrix. In addition, further investigations into optimising the pre-functionalisation of the fillers with poly(acrylate) prior to extrusion is required to ensure the P[2PEA] is not disperse within the PP matrix.

8.4 References

1. D. Das and B. K. Satapathy, *Mater. Chem. Phys.*, 2014, **147**, 127-140.
2. S. H. Lee, E. Cho, S. H. Jeon and J. R. Youn, *Carbon*, 2007, **45**, 2810-2822.
3. N. G. Sahoo, S. Rana, J. W. Cho, L. Li and S. H. Chan, *Prog. Polym. Sci.*, 2010, **35**, 837-867.
4. K. Kalaitzidou, H. Fukushima and L. T. Drzal, *Compos. Part A*, 2007, **38**, 1675-1682.
5. C. A. Hunter and J. K. M. Sanders, *J. Am. Chem. Soc.*, 1990, **112**, 5525-5534.
6. D. Baskaran, J. W. Mays and M. S. Bratcher, *Chem. Mater.*, 2005, **17**, 3389-3397.
7. J. Gupta, D. J. Keddie, C. Y. Wan, D. M. Haddleton and T. McNally, *Polym. Chem.*, 2016, **7**, 3884-3896.
8. J. Gupta, C. Wan, D. M. Haddleton and T. McNally, *Polymer*, 2017, **133**, 89-101.
9. S. Hosoda, H. Kihara, K. Kojima, Y. Satoh and Y. Doi, *Polym. J.*, 1991, **23**, 277-284.
10. J. Seemork, T. Sako, M. A. B. Ali and M. Yamaguchi, *J. Rheol.*, 2017, **61**, 1-11.
11. J. R. Potts, D. R. Dreyer, C. W. Bielawski and R. S. Ruoff, *Polymer*, 2011, **52**, 5-25.
12. D. Bikiaris, *Materials*, 2010, **3**, 2884-2946.
13. M. Aboulfaraj, B. Ulrich, A. Dahoun and C. Gsell, *Polymer*, 1993, **34**, 4817-4825.
14. K. Prashantha, J. Soulestin, M. F. Lacrampe, P. Krawczak, G. Dupin and M. Claes, *Compos. Sci. Technol.*, 2009, **69**, 1756-1763.
15. S. R. Ahmad, C. Z. Xue and R. J. Young, *Mater. Sci. Eng., B*, 2017, **216**, 2-9.
16. C. Valles, A. M. Abdelkader, R. J. Young and I. A. Kinloch, *Faraday Discuss.*, 2014, **173**, 379-390.
17. Z. Zhou, S. F. Wang, Y. Zhang and Y. X. Zhang, *J. Appl. Polym. Sci.*, 2006, **102**, 4823-4830.

18. R. Kotsilkova, E. Ivanov, E. Krusteva, C. Silvestre, S. Cimmino and D. Duraccio, *J. Appl. Polym. Sci.*, 2010, **115**, 3576-3585.
19. C. E. Corcione and M. Frigione, *Materials*, 2012, **5**, 2960-2980.
20. S. Y. Choi, H. Rodriguez, H. Q. N. Gunaratne, A. V. Puga, D. Gilpin, S. McGrath, J. S. Vyle, M. M. Tunney, R. D. Rogers and T. McNally, *R. Soc. Chem. Adv.*, 2014, **4**, 8567-8581.
21. S. Y. Choi, H. Rodriguez, A. Mirjafari, D. F. Gilpin, S. McGrath, K. R. Malcolm, M. M. Tunney, R. D. Rogers and T. McNally, *Green Chem.*, 2011, **13**, 1527-1535.
22. S. Boncel, J. Gorka, M. S. P. Shaffer and K. K. K. Koziol, *Mater. Lett.*, 2014, **116**, 53-56.
23. B. Zhang, J. B. Chen, X. L. Zhang and C. Y. Shen, *J. Appl. Polym. Sci.*, 2011, **120**, 3255-3264.
24. K. Nakamura, S. Shimizu, S. Umemoto, A. Thierry, B. Lotz and N. Okui, *Polym. J.*, 2008, **40**, 915-922.
25. R. T. Zeng, W. Hu, M. Wang, S. D. Zhang and J. B. Zeng, *Polym. Test.*, 2016, **50**, 182-190.
26. D. F. Wu, Y. R. Sun, L. Wu and M. Zhang, *J. Appl. Polym. Sci.*, 2008, **108**, 1506-1513.
27. J. Zhong, A. I. Isayev and X. P. Zhang, *Eur. Polym. J.*, 2016, **80**, 16-39.
28. K. Kalaitzidou, H. Fukushima, P. Askeland and L. T. Drzal, *J. Mater. Sci.*, 2008, **43**, 2895-2907.
29. F. Luo, K. Wang, N. Y. Ning, C. Z. Geng, H. Deng, F. Chen, Q. Fu, Y. Y. Qian and D. Zheng, *Polym. Adv. Technol.*, 2011, **22**, 2044-2054.

Chapter 9 Conclusions and Recommendations for Future Work

9.1 Conclusions

Initially, the suitability for polymers synthesised using reversible deactivation radical polymerisation techniques (RAFT and Cu(0)-mediated LRP)) for melt mixing using extrusion was explored. The thermal and thermo-mechanical behaviour of such polymers, by way of example, poly(acrylates) was investigated. In the first instance, poly(lauryl acrylate) P[LA] was selected based upon its known compatibility with PP through the work conducted by ICT ltd. The synthesis of P[LA] was conducted using RAFT and Cu(0)-mediated LRP. Polymerisation of lauryl acrylate (LA) via RAFT involved firstly preparing a chain transfer agent (CTA), cyanomethyl dodecyltrithiocarbonate. The correct choice of CTA is imperative to producing a polymer with well controlled molecular weight and narrow dispersity. Successful synthesis of the CTA agent was determined by ^{1}H NMR and this subsequently led to the successful polymerisation of LA of three different targeted molecular weights, (DP_n = 25, 50 and 100, $M_{n,th}$ = 6,000 – 24,000 g mol^{-1}). By way of example, three different molecular weights of P[LA] were selected to investigate how differing molecular weights influence the thermal stability of P[LA] and the study was then extended to investigate non-covalent interactions with MWCNTs. Characterisation of these polymers via ^{1}H NMR and GPC revealed molecular weights of $M_{n,GPC}$ = 5,300, 13,800, 21,500 g mol^{-1} demonstrating the polymerisations were in good agreement with theoretical M_n. Low molar mass tailing was observed for high molar mass polymers suggesting further optimisation is required to achieve narrower dispersities however, for the purposes of this project, further optimisations were not necessary.

Further characterisation via DSC was used to investigate the thermal properties of P[LA] to further understand its behaviour with PP during extrusion. The traces revealed a single-phase transition corresponding to a T_m at ~2 °C and a T_c at ~ -10 °C. Such transitions revealed that P[LA] is a viscous fluid at r.t and therefore, will be a low viscous liquid during extrusion with PP (~ 165 °C). In comparison to RAFT, P[LA] was also synthesised via Cu(0)-mediated LRP to investigate how changes in polymerisation method effected both the thermal stability of P[LA] and its potential to non-covalently coat the surface of MWCNTs via CH-π wrapping. P[LA] was polymerised with similar targeted degrees of polymerisation (DP = 25, 50, 100, $M_{n,th}$ = 6 000-24 000 g mol^{-1}) to RAFT to effectively compare the two methods. ^{1}H NMR and GPC of P[LA] polymerised using Cu(0)-mediated LRP revealed

polymerisations achieved excellent conversion (~98%) and good agreement with theoretical M_n and low dispersity ($Đ \approx 1.2$) with the molecular weights of $M_{n,GPC}$ = 5,500, 11,900, 17,500 g mol^{-1} obtained. Low molar mass tailing can also be observed causing broadening of dispersities for the two higher molar mass polymers. Comparatively, both methods successfully polymerised LA however, polymerisation via Cu(0)-mediated was markedly simpler as there is no requirement for a CTA. Even though Cu(0)-mediated LRP required the use of a ligand (Me_6TREN), the polymerisation experimental set-up did not require increased temperatures and such stringent deoxygenation measures compared to RAFT. As a consequence, further polymerisations throughout the project were performed using Cu(0)-mediated LRP.

In addition to investigating the thermal stability of P[LA] for its suitability for extrusion and its potential for non-covalently CH-π wrapping MWCNTs, the use of aromatic end-functionalised P[LA] polymers was also explored. It was proposed that π-π stacking would provide a more efficient pathway to non-covalent functionalisation as it is known that π-π stacking forms stronger intermolecular interactions compared to CH-π. Based on this rationale, aromatic initiators in the form of Hostasol-ATRP and pyrene-ATRP were used to synthesise P[LA]. Hostasol was selected for its use as a fluorescent pigment with excellent heat resistant properties. Hostasol-P[LA] was successfully polymerised via Cu(0)-mediated LRP, ($M_{n,\,GPC}$ = 10,000, $Đ$ = 1.5). Even though conversion was limited to 85% and dispersity was broad, its thermal stability and potential for non-covalently functionalising MWCNTs was still investigated. The onset for the degradation of the Hostasol-ATRP initiator was relatively close to the processing temperature of PP (~170-210 °C) suggesting it would not be suitable for functionalisation of P[LA]. The Hostasol-P[LA] had an onset degradation temperature of ~140-150 °C suggesting the Hostasol is not as thermally stable when attached to P[LA] compared to Hostasol-ATRP. In addition, DSC traces of Hostasol-P[LA] revealed a significant melting or sublimation process at ~165 °C for the Hostasol-ATRP initiator suggesting the Hostasol is thermally altered after this temperature. Further investigations into the thermal stability of Hostasol were performed using variable temperature FTIR. The FTIR spectra showed the Hostasol-ATRP changes molecular structure when heated from r.t. to even 200 °C and therefore, it was not possible to use Hostasol end-functionalised P[LA] for the purpose of non-covalently functionalising MWCNTs when melt blended with PP. In addition to Hostasol, pyrene end-functionalised P[LA] was also investigated. LA was successfully polymerised *via* Cu(0)-mediated LRP with a pyrene-ATRP initiator with a

conversion of ~95%, broad dispersity ($Đ \approx 1.52$) and poor agreement with theoretical M_n = 14,100 g mol^{-1}. This outcome was attributed to the lack of solubility of pyrene in the IPA solvent used for the polymerisation. TGA revealed that pyrene-ATRP had an onset of thermal degradation at ~150-160 °C and therefore, it was not possible to use pyrene end-functionalised P[LA] to non-covalently functionalise MWCNTs. It appeared the ester bond linking the aromatic moiety to the polymer backbone may not be thermally stable to >300 °C and therefore, alternative methods of incorporating aromatic functionalities into poly(acrylates) were required, for example, the use of block copolymers containing pendent aromatic side-chain groups which was then adopted.

After establishing that Hostasol and pyrene end-functionalised P[LA] were not sufficiently thermal stable for extrusion with PP, a detailed analysis of the thermal stability of P[LA] itself was conducted. TGA of P[LA] synthesised *via* RAFT showed onset of degradation occurred at ~340-350 °C however, this decreased to ~250-260 °C for lower molar mass polymers. TGA of the RAFT agent revealed an onset of degradation of ~200-250 °C. Free radicals generated from the thermal degradation of end groups did not influence the thermal stability of the P[LA] backbone and 'unzipping' commonly seen with methacrylates was not observed with respect to the processing of PP using extrusion at temperatures of 170 °C. TGA of P[LA] using Cu(0)-mediated LRP revealed similar degradation to that of P[LA] using RAFT. Therefore, the thermal stability of P[LA] is sufficient for melt processing with PP. P[LA] prepared *via* RAFT was solution mixed with MWCNTs and ~10-25 wt% P[LA] adsorbed onto the surface of the MWCNTs by means of TGA. The onset of thermal degradation of the P[LA] remained unchanged after the adsorption on to the surface of the MWCNTs. P[LA] *via* the Cu(0)-mediated method adsorbed up to 85 wt% P[LA] and an increase in thermal stability of ~50 °C of the P[LA] was recorded. Increasing P[LA] and MWCNT concentration independently also resulted in an increase in the quantity of polymer adsorped, possibly due to increased CH-π interactions, however sufficient evidence to confirm this observation was not obtained. The increased thermal stability of the P[LA] after adsorbing onto the surface of MWCNTs could possibly be due to heat transfer from the P[LA] to the MWCNTs, resulting in delayed pyrolysis of P[LA], however sufficient evidence to confirm this observation was not obtained. Evidence from transmission electron micrographs (TEM) showed the P[LA] adsorbing onto the MWCNT surface. Size exclusion chromatography (SEC) and matrix-assisted laser desorption/ionization time of flight mass spectrometry (MALDI-TOF) of P[LA] after

heating to 200 °C for 30 mins in an air atmosphere showed loss of end groups but, the P[LA] backbone remained preserved for both polymer types. TEM images showed the P[LA] adsorbing onto the MWCNT surface. Melt processing of composites of P[LA] prepared *via* Cu(0)-mediated LRP with MWCNTs and PP was possible as the P[LA] was thermally stable during both extrusion and during TGA when studied post melt mixing. MWCNTs were characterised using electron microscopy, Raman spectroscopy and XPS. Characterisation revealed the tubes have diameters ranging from 5-20 nm and the number of walls in the region of 10-20. XPS revealed the presence of 2 at% oxygen and Raman spectra confirmed a high intensity D band, possible due to presence of oxidised amorphous carbon. The interactions between P[LA] and MWCNTs were characterised using SEM, TEM, DSC, and Raman spectroscopy and all supported interactions between both components.

Further investigations on the effect of functionalisation of P[LA] on the surface of MWCNTs were carried out by producing composites of PP, MWCNTs and P[LA] with various MWCNT concentrations and MWCNT to P[LA] ratios. The hypothesis was to investigate the wrapping of P[LA] on MWCNTs post extrusion and study if the wrapping of P[LA] led to an improvement in mechanical, electrical and rheological properties of the composites compared to the composites without the addition of P[LA]. Subsequently, the use of various graphitic fillers (e.g. GNPs) or poly(acrylate) architectures (e.g. block copolymers) and monomers were investigated. Initially, P[LA] was synthesised in bulk via Cu(0)-mediated LRP due to the prior assumption of CH-π adsorption, determined by the ~50 °C increase in degradation temperature of P[LA] when adsorbed onto the surface of MWCNTs (from TGA). The P[LA] was subsequently melt blended with MWCNTs and PP to produce four sets of composites; PP and MWCNTs, PP and P[LA], PP and P[LA] functionalised MWCNTs with a MWCNT:P[LA] ratio of both 1:4 and 1:1. The composites were later characterised to understand the role of P[LA] in improving the dispersion and interfacial adhesion between the MWCNTs and P[LA]. A poorly dispersed and entangled network of MWCNTs within the PP matrix was determined by SEM imaging post melt mixing. As well as the composites of MWCNTs and PP being poorly dispersed, they were not homogenously distributed throughout the PP matrix and MWCNT pull-out was observed demonstrating weak interfacial compatibility. Upon addition of P[LA] functionalised MWCNTs in a MWCNT:P[LA] ratio of 1:4, the agglomerate size was reduced and MWCNT dispersion enhanced further from an poorly dispersed system. Changing the loading ratio

between MWCNT:P[LA] to 1:1 led to increased agglomerate size and reduced dispersion, from SEM imaging.

Further evidence for the formation of percolated MWCNT networks was obtained using oscillatory rheology. For composites of PP and MWCNTs, a well-defined rheological percolation threshold at ~0.5 wt% was established and upon P[LA] functionalisation, (MWCNT:P[LA] at 1:4) this was reduced to 0.3 wt% which provided further evidence, along with SEM, that P[LA] not only altered PP chain dynamics and but also the interfacial interactions between the MWCNT filler and PP resulting in enhanced but still poor MWCNT dispersion. Further indirect evidence for these changes in composite morphology was gained from static mechanical and dynamic mechanical analysis of these composite systems. A common observation in the mechanical properties was a significant decrease in elongation at break (ε_B) from ~270% for unfilled PP to ~5% after MWCNT addition due to the highly anisotropic behaviour of the MWCNT particles. The Young's modulus (E) of PP was unaffected on addition of MWCNTs, but decreased significantly with loadings of P[LA] greater than 2 wt% however, the elongation at break increased by over 50% upon addition of P[LA] modified MWCNTs in a ratio of 1:4 ratio, evidence that P[LA] has a plasticisation effect on PP. T_m and T_c increased by ~ 4 °C for a loading of 5 wt% unmodified MWCNTs, evidence the CNTs can nucleate PP. Upon functionalisation with P[LA], the P[LA] coating hinders MWCNT nucleation and PP crystallinity decreased at higher filler loadings. The addition of P[LA] resulted in a significant decrease in the T_g of PP, to between 15 and 25 ºC. This is further evidence that P[LA] effectively reduced the T_g by plasticising PP. WAXD results indicated the P[LA] was behaving as a α-nucleating agent though the observed increase in intensity of the peak at $2\theta = 18.6°$ corresponding to the hexagonal α(300) for both composites of PP and P[LA] functionalised MWCNTs and composites of PP and P[LA]. However, the β-polymorph is also present in the composites with P[LA] modified MWCNTs which was induced by the inclusion of the P[LA] and not the MWCNTs. Also, there is evidence from the published literature for the β-polymorph being more prominent in low molecular weight (high MFR) PP, as used in this study.

The DC electrical conductivity of PP was increased by about 15 orders of magnitude on addition of 5wt% unmodified MWCNTs. However, the electrical conductivity of the composites of PP and P[LA] modified MWCNTs was only 2 orders of magnitude less than that obtained for composites with the as received MWCNTs, across the composition range. The data suggests a double percolation effect for both sets of composites.

To further explore the use of P[LA] as a compatibiliser, P[LA] was used to compatibilise GNPs and PP. The present study is concerned with the effect of the addition of GNPs to PP upon the structure and properties of the material and the influence of P[LA] as a compatibiliser. The investigation involved firstly blending various loadings of GNPs with PP and understanding the effect of unfunctionalised GNPs on PP properties. Subsequently, the GNPs were functionalised with P[LA] in a 1:4 ratio GNPs:P[LA] to understand the effect of P[LA] at compatibilising GNPs. In the first instance, the GNPs were characterised using SEM and HRTEM. The GNPs were in the form of multi-layer flakes with >10 layers. The sheet edges were highly smooth and rounded along with many platelets folding into scrolls. Raman spectroscopy was used to calculate a I_D/I_G = 0.12 which demonstrates the GNPs are of high quality due to the low quantity of defects. Further characterisation of the chemical structure of the GNPs was determined by XPS which confirmed <1 at% sodium and ~9 at% oxygen. Both XPS and Raman detected similar quantities of oxygen confirming the high quality of the GNPs used in this study. Subsequently, composites of PP, GNPs and P[LA] were prepared with a GNP:P[LA] ratio of 1:4 to compare the differences between the use of MWCNTs and GNPs. For composites of PP and GNPs, cryo-fractured SEM micrographs show the presence of GNPs protruding from the surface of the PP. They appear randomly distributed with no preferred orientation and but poorly dispersed. However, the addition of P[LA] lead to an increased quantity of GNPs observed on the fractured surface suggesting the P[LA] is assisting dispersion of the GNPs, as predicted. For the composite of PP and GNPs, E of PP remained unchanged with increasing GNP loading. Moreover, the σ decreased and the ε_y remained unchanged. The lack of an increase in static mechanical properties was in agreement with SEM observations in that the GNPs were poorly dispersed and did not form a well-connected network structure due to poor interfacial compatibility. As expected, the GNPs embrittled the PP with ε_B decreasing from 250% for unfilled PP to 10% for a 5 wt% GNP loading. Composites of PP, GNPs and P[LA] showed a ~20% decrease in E and σ with ε_y remaining unchanged for loadings up to 1 wt% P[LA] functionalised GNPs. Further increased GNP loadings resulted in increases in ε_y and ε_B relative to un-functionalised GNPs confirming a similar plasticisation effect to that observed for P[LA] functionalised MWCNTs. DMTA was used to further quantify the extent of plasticisation observed from the mechanical properties and the reductions in T_g of ~12 °C when determined from the tanδ maximum and ~ 20 °C when taken from the maximum in loss modulus, E'' upon addition of 5 wt% P[LA] functionalised

GNPs compared to unfunctionalised GNPs. This behaviour is consistant with the observations made for composites of P[LA] functionalised MWCNTs. No observable changes in *G'*, *G''* and |η*| as function of frequency for both un-functionalised and P[LA] functionalised GNPs were detected when characterised using oscillatory rheology. The expected appearance of the 'pseudo-solid' plateau effect in the low frequency region was not observed suggesting percolation was not achieved, even at 5 wt% loadings. Most critically, this result clearly demonstrates the effect of nanofiller geometry when quantifying an interconnected filler structure in 3D. The more flexible nature of CNTs facilitated network formation at lower loadings compared to the more rigid and small GNPs. When the composites were examined by DSC, both the T_m and T_c shifted to higher temperatures due to the GNPs promoting the nucleation of PP crystallites. This observation was also observed with MWCNTs. X_c was relatively unchanged after the addition of un-functionalised GNPs however, this decreased significantly upon addition of P[LA] functionalised GNPs. As observed with P[LA] functionalised MWCNTs, the P[LA] disrupted the crystallisation of PP. WAXD was used to further quantify the change in crystallinity however, accurately determining the X_c through this method was challenging. However, the diffractograms did appear to show the P[LA] nucleating the β-crystal polymorph of PP which would account for the changes in crystallinity observed in the DSC traces. Furthermore, DC electrical conductivity measurements supported the rheological observations in that the poorly interconnected GNP system was electrically conducting and well below percolation due to no observable increase in conductivity with GNP loading even up to 5 wt% GNPs.

A further approach to improve the dispersion and interfacial compatibility of MWCNTs and GNPs with PP, was developed using copolymers of LA and 2PEA, synthesised again using Cu(0)-mediated LRP. P[2PEA] was chosen for it π-π stacking potential with graphitic fillers. After successful synthesis of P[LA-*block*-2PEA] and P[LA-*stat*-2PEA] characterised by ^{1}H NMR, GPC and DSC, the thermal stability of such polymers was investigated and confirmed up to 300 °C. Oscillatory rheology measurements on the copolymers clearly demonstrated the P[2PEA] to have higher viscosity than P[LA] due to the π-π stacking between neighbouring polymer chains. Composites of these copolymers with MWCNTs and GNPs were prepared by solution mixing with the aid of ultrasonication. Examination of these composites by EM showed the MWCNTs preference for P[2PEA] compared to the P[LA]. The block copolymer demonstrated immiscibility between the two blocks but MWCNT migration to the predicted P[2PEA] phase. HRTEM images clearly

demonstrated a uniform coating (~10 nm) of block copolymer on the surface of the MWCNTs. The P[2PEA] block was π-π stacked on the outer walls of the MWCNTs. EELS experiments were used to establish that the surface of the MWCNTs have a greater concentration of sp^2 hybridized bonding compared to the MWCNT centre due to the presence of aromatic groups of the block copolymer. DMA and oscillatory rheology provided further evidence for the strong π-π interactions between the block copolymer and the MWCNTs by establishing an increase in stiffness (storage modulus) of the composite compared to the neat polymer. Further confirmation of π-π stacking from Raman spectroscopy was observed for composites of the homo- and copolymers of P[2PEA] determined by the shifts in the *D* and *G* bands as a result of the compressive stress applied by the polymers on the MWCNTs. Consequently, the efficiency of the bi-functional compatibilisers was investigated by producing composites of MWCNT or GNP functionalised with a poly(acrylate) based copolymer and PP. The hypothesis is to simultaneously improve the mechanical and electrical properties of the PP matrix by efficiently dispersing the MWCNTs or GNPs and improving interfacial adhesion with the PP.

Composites of PP, MWCNTs or GNPs and poly(acrylate)s were characterised using a range of techniques to investigate the effect of the homo and copolymers of P[LA] and P[2PEA] on the dispersion and interfacial adhesion of MWCNTs or GNPs with PP. EM was used to interpret the effect of adding poly(acrylate)s into composites of PP and MWCNTs/GNPs. EM provided inconclusive evidence for the dispersion of the fillers and the interfacial interaction between the fillers and the poly(acrylate)s and therefore, observations were purely speculative due to the fact that alternative means of assessing dispersion and interfacial interactions were not available. EM studies revealed the samples containing P[2PEA] formed droplets within the PP matrix due to the incompatibility between the hydrophobic PP chains and the pendant aromatic structure of P[2PEA]. However, the composite with P[LA] added demonstrated good compatibility with the PP matrix, no droplets were observed. The composites containing homo-polymers of P[LA] displayed the highest degree of nanofiller dispersion whereas, the composites containing the homopolymers of P[2PEA] displayed reduced dispersion. Evidence for the copolymers forming a shell of poly(acrylate) surrounding the fillers (especially for the GNPs) was observed, proving the P[2PEA] can physisorb onto the surface of the fillers via π-π stacking. Static mechanical testing revealed further evidence for the plasticisation of PP by P[LA].

The addition of poly(acrylate)s to PP did not show significantly improved mechanical properties compared to neat PP irrespective if the filler was MWCNTs or GNPs. Dynamic mechanical analysis provided further evidence for the plasticisation of PP due to reductions in T_g for composites containing P[LA]. Thermal properties characterised by DSC confirmed the nucleation of PP on addition of MWCNTs and GNPs.

9.2 Recommendations for Future Work

The use of poly(acrylate)s as compatibilisers to assist the dispersion of 1D and 2D graphitic nanofillers in a PP has proven to be a concept with limited potential to alter the mechanical, electrical and thermal properties of polymers. The excellent thermal stability demonstrated by poly(acrylate)s for the purpose of melt blending with PP provides scope for further work through alternative functionalisation strategies e.g. covalent functionalisation. Throughout the project, the discussion has centred around the use of P[LA] and P[2PEA] due their potential to adsorb onto surface of 1D and 2D graphitic fillers and promote their dispersion in a PP matrix however, further work should investigate a range of poly(acrylate)s with various structures, chemistries, molecular weights and dispersities. For example, the use poly(acrylate)s with longer side chains such as poly(octadecyl acrylate) or poly(acrylate)s containing aromatic side chains with a greater number of benzene rings such as pyrene, for example pyrene acrylate. Further expansion could include the use of coupling the aromatic poly(acrylate)s with poly(propylene) oligomers to further improve compatibility. It is evident that the viscosity of the compatibilising polymer influences the extent of dispersion of the compatibiliser in the PP and matrix and therefore, it would be interesting to investigate if there is a correlation between the viscosity of the polymer compatibiliser and the extent of its dispersion in the PP matrix. Another further topic, would be to use a PP having a lower MFI with a higher melt viscosity compared to the PP used in this project. Lower MFI PP would have a greater melt viscosity and therefore impart greater shear forces on the mixture during the extrusion process.

While this study was focused on compatibiliser chemistries systematic studies with regard the processing conditions used, including screw profiles, on filler dispersion should also be completed. An example of this would be scale up the process and use larger diameter screws with deeper screw edges and counter-rotating screws to increase the shear force during mixing and assist further the polymer compatibiliser and the dispersion process.

Further work is also required to investigate the effect of increasing the aspect ratio of GNPs on percolation for these composite systems. GNPs with a greater aspect ratio are predicted to achieve percolation at lower loadings, increase electrical and thermal conductivity as well as improve the mechanical properties. Additionally, it would be interesting to explore what GNP quantity is required to achieve electrical and rheological percolation with the same type of GNPs and correlate those findings with graphenes with different aspect ratios to understand the role of flake dimensions. It is clear, P[LA] is not particularly successful in compatibilising the GNPs used in this study. In addition, it would useful to conduct dynamic cross-polarized optical microscopy and WAXS/SAXS scattering experiments during heating and cooling to investigate trans-crystallinity phenomena at the interface between GNPs and the PP matrix.

Journal Papers and Conference Presentations

Journal papers published and submitted

1. J. Gupta, D. J. Keddie, C. Y. Wan, D. M. Haddleton, T. McNally, **Functionalisation of MWCNTs with poly(lauryl acrylate) polymerised by Cu(0)-mediated and raft methods.** *Polym. Chem.* 2016, **7**, 3884-3896. (11 citations)
2. J. Gupta, C. Y. Wan, D. M. Haddleton and T. McNally, **Plasticisation and compatibilisation of poly(propylene) with poly(lauryl acrylate) surface modified MWCNTs.** *Polymer*, 2017, **133**, 89-101. (0 citations)
3. J. Gupta, E. Heeley, H. Amari, C. Y. Wan, D. M. Haddleton and T. McNally, **Non-covalent interfacial interactions between MWCNTs and block copolymers having pendent aromatic groups.** *Nat. Nanotechnol.,* 2017, submitted.
4. J. Gupta, E. Heeley, H. Amari, C. Y. Wan, D. M. Haddleton and T. McNally, **Non-covalent functionalisation of MWCNTs and GNPs using copolymers of lauryl acrylate and 2-phenyl ethyl acrylate.** Submission to *Macromolecules,* 2017.
5. J. Gupta, E. Heeley, C. Y. Wan, D. M. Haddleton and T. McNally, **Compatibilisation of poly(propylene) with MWCNTs and GNPs using acrylate copolymers.** Submission to *E. Polym. J.,* 2017.

Conference presentations

6. J. A. Gupta, C. Wan, D. M. Haddleton, Tony McNally, **Non-covalent functionalisation of carbon nanotubes for compatibilisation and melt mixing with polymers.** Nanomaterials and composites: Preparation, characterization, processing, modelling, application (NANO) poster session. Poster Ref: **NANO-P-174**. Poster presented at the *European Polymer Federation, European Polymer Congress,* 21-26 June **2015**, Dresden, Germany.
7. J. A. Gupta, C. Y. Wan, D. M. Haddleton, Tony McNally, **Non-covalent functionalisation of carbon nanotubes for compatibilisation and melt-mixing with polymers.** Poster presented at the *WMG Doctoral Research and Innovation Conference*, 30 June to 1 July **2015**, University of Warwick, Coventry, UK. (Awarded second prize for poster presentation).

8. J. A. Gupta, D. J. Keddie, C. Y. Wan, D. M. Haddleton, Tony McNally, **Functionalisation of MWCNTs with poly(lauryl acrylate) polymerised by Cu(0)-mediated and RAFT methods.** Poster presented at the *Macro Group UK Polymer Physics Group – Young Researchers Meeting*, 5-6 April **2016**, University of Liverpool, UK.
9. J. A. Gupta, D. J. Keddie, C. Y. Wan, D. M. Haddleton, Tony McNally, **Thermal stability of poly(lauryl acrylate) polymerised by Cu(0)-mediated and RAFT methods: For functionalisation of multi-walled carbon nanotubes.** Poster presented at the *WMG Doctoral Research and Innovation Conference*, 28 June **2016**, University of Warwick, Coventry, UK.
10. J. A. Gupta, D. J. Keddie, C. Y. Wan, D. M. Haddleton, Tony McNally, **Thermal stability of poly(lauryl acrylate) polymerised by Cu(0)-mediated and RAFT methods: For functionalisation of multi-walled carbon nanotubes.** Poster Presentation. Poster Ref: **P67**. Poster presented at the *Warwick Polymer Conference*, 11-14 July **2016**, University of Warwick, Coventry, UK.
11. J. A. Gupta, D. J. Keddie, C. Y. Wan, D. M. Haddleton, Tony McNally, **Functionalisation of MWCNTs with poly(lauryl acrylate) for compatibilisation with poly(propylene).** Oral presentation. Presented at the *IXth ECNP International Conference on Nanostructured Polymers and Nanocomposites*, 19-21 September **2016**, Rome, Italy.
12. J. A. Gupta, C. Y. Wan, D. M. Haddleton, Tony McNally, **Design of Multi-functional Poly(acrylates) and their role in non-covalent compatibilisation of composites of MWCNTs and graphene with PP.** Oral presentation. Presentation ref: **Stream 2, Block 2**, Composites and Nanocomposites session, talk 3. Presented at the *WMG Doctoral Research and Innovation Conference*, 28 June **2017**, University of Warwick, Coventry, UK.
13. J. A. Gupta, C. Wan, D. M. Haddleton and Tony McNally, **A unique approach to non-covalent functionalization of MWCNTs and graphene for compatibilisation with PP.** Oral presentation. Presentation ref: **IT-1**. Presented at *the 8th Asia-Europe Symposium on Processing and Properties of Reinforced Polymers* and *3rd China-UK Bilateral Symposium on Polymer Nanocomposites Special Session*, 29 June to 2 July, **2017**, Chengdu, China.

14. J. A. Gupta, C. Wan, D. M. Haddleton and Tony McNally, **Design of multi-functional poly(acrylates) and their role in non-covalent compatibilisation of composites of MWCNTs and graphene with PP.** Oral presentation. Presentation ref: **PROC-K08 McNally**. Presented at the *European Polymer Federation, European Polymer Congress,* 2-7 July **2017**, Lyon, France.
15. J. A. Gupta, C. Wan, D. M. Haddleton and Tony McNally, **Non-covalent interfacial interactions between MWCNTs and block copolymers having pendent aromatic groups.** Oral presentation submitted to the *World Polymer Congress*, 1-5 July, **2018**, Cairns, Queensland, Australia.